Studies on the horizontal and vertical distribution of clouds and their impact on energetics of the Atmosphere over the Indian Region

Thesis Submitted to

Cochin University of Science and Technology

In Partial Fulfillment of the Requirements

for the Award of

Doctor of Philosophy

in

Atmospheric Science

under the Faculty of Marine Sciences

by

Anish Kumar M. Nair

Space Physics Laboratory

Vikram Sarabhai Space Centre

Indian Space Research Organisation

Thiruvananthapuram - 695022

India

June 2013

Declaration

This is to declare that the work presented in this thesis was carried out at the Space Physics Laboratory (SPL), Vikram Sarabhai Space Centre (VSSC), Thiruvananthapuram for the award of the degree of Doctor of Philosophy in Atmospheric Science from the Cochin University of Science and Technology, Cochin, Kerala State, India. This Thesis is the outcome of the original work done by me and the work did not form part of any dissertation submitted for the award of any degree, diploma, associateship or any other title or recognition from any University/Institution.

26 June, 2013
Thiruvananthapuram

Anish Kumar M. Nair
(Author)

भारत सरकार
अंतरिक्ष विभाग
विक्रम साराभाई अंतरिक्ष केन्द्र
तिरुवनन्तपुरम-695 022
केरल, भारत
फोन : (0471) 2563886
फैक्स : (0471) 2706535
तार/Gram: SPACE

सत्यमेव जयते

Government of India
Department of Space
Vikram Sarabhai Space Centre
Thiruvananthapuram-695 022
Kerala, INDIA
Telephone : (0471) 2563886
Fax : (0471) 2706535
e-mail: k_rajeev@vssc.gov.in

SPACE PHYSICS LABORATORY

Dr. K. Rajeev
Scientist-SG & Head, BLPAM

CERTIFICATE

Certified that the thesis entitled **"Studies on the horizontal and vertical distribution of clouds and their impact on energetics of the Atmosphere over the Indian Region"** submitted by **Mr.Anish Kumar M. Nair** (Ph.D. Reg.No.3643) to Cochin University of Science and Technology, Cochin, embodies the original results of the investigations carried out at the Space Physics Laboratory, Vikram Sarabhai Space Centre, Thiruvananthapuram, under my supervision. The work presented in this thesis has not been submitted for the award of any other degree, diploma or associateship to any other University or Institution.

26 June 2013

Dr. K. Rajeev
(Thesis Supervisor)

Countersigned

Dr. K. Krishnamoorthy
Director

भारत सरकार
अंतरिक्ष विभाग
विक्रम साराभाई अंतरिक्ष केन्द्र
तिरुवनन्तपुरम-695 022
केरल, भारत
फोन : (0471) 2563886
फैक्स : (0471) 2706535
तार/Gram: SPACE

सत्यमेव जयते

Government of India
Department of Space
Vikram Sarabhai Space Centre
Thiruvananthapuram-695 022
Kerala, INDIA
Telephone : (0471) 2563886
Fax : (0471) 2706535
e-mail: k_rajeev@vssc.gov.in

SPACE PHYSICS LABORATORY

Dr. K. Rajeev
Scientist-SG & Head, BLPAM

CERTIFICATE

This is to certify that all the relevant corrections and modifications suggested by the audience during the Pre-synopsis Seminar and recommended by the Doctoral Committee of **Mr.Anish Kumar M.Nair** (Ph.D. Reg.No.3643) have been incorporated in the thesis.

Dr. K. Rajeev
(Thesis Supervisor)

26 June 2013

Dedicated to My
Parents & ***Sister***

Acknowledgements

'Research is a way of life dedicated to discovery'

In the last few years of humble beginning of my Research life, the role played by several people and institutions needs to be gratefully acknowledged. It was through guiding, sharing the knowledge and intellect, supporting, encouraging, energising, examining, providing the necessary facilities, working in a team, sharing the data, providing feedback and giving suggestions for improvement that the work progressed. The research problem has been a challenge to me. I have wholeheartedly enjoyed the different phases of the research.

First and foremost, gratitude and thanks to my friend, philosopher and Guide Dr.K.Rajeev. I am highly indebted to him for leading me the way, empowering me with knowledge, training me with a vision, and encouraging me minute by minute. It has been an honour and a privilege working with him.

I would like to acknowledge ISRO for the Research Fellowship for 5 years and Vikram Sarabhai Space Centre (VSSC) for all facilities and amenities including the excellent research ambience at Space Physics Laboratory (SPL). Sincere thanks to Dr.K.Krishnamoorthy Director, SPL for his guidance, support as well as encouragement throughout the course of this research work. I am grateful to former director of SPL, Dr.R.Sridharan for his encouragement, advice and support.

The role played by the Academic, Research, Doctoral and Centre level monitoring committees in streamlining the progress of my research needs special mention. The reviews and seminars have always been helpful for developing confidence, improving presentation skill and refining the research work. I thank Dr.Anil Bhardwaj, Chairman of Academic Committee, SPL for his highly critical reviews and suggestions. Thanks are due to Dr.M.Mohan, Dr.Prabha R.Nair, Dr.Geetha Ramkumar, Dr.C.Suresh Raju, Dr.Tarun Kumar Pant, Dr.K.Kishore Kumar, Dr.Rajkumar Choudhary, Dr.S.Suresh Babu and Dr.D.Bala Subrahmanyam for constant encouragement, suggestions and advices.

The feedbacks, advice and encouragements from the Research Committe members – Prof.H.S.Ram Mohan, Prof.K.Mohankumar, Prof.C.A.Babu, Dr.K.R.Santosh and Prof.K.Sajan during different stages of my research is also gratefully acknowledged. Encouragement from other faculty and staff of the Dept. of Atmospheric Sciences, Cochin University of Science and Technology (CUSAT) as well as from the administrative staff of CUSAT is also thankfully acknowledged.

I would like to thank the anonymous referees whose comments and suggestions had definitely aided to increase the the quality of science in our journal publications.

Sincere thanks are due to Dr.K.Parameswaran for taking me into new realm of scientific analyis and for the insightful discussions. I would like to thank my senior, Dr.S.Meenu for the discussions and help provided for the analysis of AVHRR data. I would like to express my gratitude for the support extended by Mr.Manoj Kumar Mishra for conducting the micropulse lidar (MPL) observations, as well as the extensive scientific discussions. The overnight Lidar observations and experimental campaigns have provided me opportunities to have hands on experience to probe the atmosphere for aerosols and clouds using MPL and profile meteorological parameters using radiosonde. It was indeed a pleasure having worked with a strong team which also inclues Dr.S.V.Sunil Kumar, Dr.S.Sijikumar and Dr.Bijoy V.Thampi. I wish to record my thanks to Mr.S.V.Mohan Kumar, Dr.N.V.P.Kiran Kumar, and Dr.Sandhya K.Nair for their encouragement.

Thanks are also due to Library, Administrative and other support staff of VSSC. I express my sincere gratitude for the support from SPL office. Support from Smt.P.R.Suseela, Smt.Geetha.C, Ms.Salini M.S., Ms.Sisira R., Ms.Shiji D. and Mr.M.Jihas are thankfully acknowledged. Five years in VSSC have credited me with many friends and well wishers from different age groups. I thank them for their friendship, encouragement and memorable moments.

Motivation was the key driving force to enter the challenging field of research. I sincerely thank Dr.P.V.Manoranjan Rao, Late.Dr.Sudha Raveendran, Dr.B.N.Suresh, Dr.C.K.Rajan, Dr.V.Adimurthy and Prof.S.N.Sukumaran Nair for their encouragements.

Thanks and appreciation to all research fellows and associates including seniors & juniors. Last few years have provided a handful of memorable events with their company. Special mention to my batchmates Ms.Sherine, Mr.Prijith, Mr.Raghuram & Mr.Sumod. I acknowlede the support extended by all scientists, engineers, technical, office and support staff of SPL.

Thanks are also extended to my classmates specially Mr.Jayakrishnan and Mr.Sivaprasad for the memorable events at Cochin. Thanks to a handful of friends, seniors and juniors at CUSAT. I recall the friendship and encouragement from Nithin, Anila, Resmi, Krishnamohan, Dileep, Reynold, Shinto, Lijeesh, Eldhose, Albin and Midhun.

Modern day research demands use of multiple soft-tools. I would like to thank Linux users group, Ubuntu, Mendeley, GrADS-, GIMP-, LaTeX user groups. Thanks are due to Mr.Raghuram, Mr.Sonal and Dr.Sijikumar for their help and support in the learning process which was fun.

Special thanks to CloudSat, CALIPSO, TRMM and Megha Tropiques projects data processing centres. CloudSat 2BGEOPROF and 2BGEOPROF-LIDAR data were obtained from http://cloudsat.cira.colostate.edu. *AVHRR data were obtained from* http://www.class.noaa.gov. *The ERS-1/2 and QuikSCAT scatterometer data were obtained from CERSAT, at IFREMER, Plouzane (France). The GPCP combined precipitation data were developed and computed by the NASA/Goddard Space Flight Centers Laboratory for Atmospheres as a contribution to the GEWEX Global Precipitation Climatology Project. TRMM-Convective and stratiform heating data were obtained from NASA-GES DISC through* http://disc.sci.gsfc.nasa.gov/precipitation/documentation/TRMM_README. *TMI data are produced by Remote Sensing Systems and sponsored by the NASA Earth Science MEaSUREs DISCOVER Project and are available at* www.remss.com. *MERRA data used in this study/project have been provided by the Global Modeling and Assimilation Office (GMAO) at NASA Goddard Space Flight Center through the NASA GES DISC online archive. NCEP Reanalysis Derived data was provided by the NOAA/OAR/ESRL PSD, Boulder, Colorado, USA, through their Web site at* http://www.esrl.noaa.gov/psd.

Last but not the least, acknowledging the true whole hearted support, encouragement, patience and prayers from my beloved father Shri.N.Muralidharan Nair, mother Smt.Sreekumari M.Nair, loving sister Ms.Asha Sree and brother-in-law Mr.Manoj A.S are beyond words to express. Besides, the blessings of almighty have given inner strength to take up the assignment and move forward. Thank God!.

Anish Kumar M.Nair

Contents

Publications in Journals

1. **Nair,A.K.M.**, and K.Rajeev, Multi-year CloudSat and CALIPSO Observations of the Dependence of Cloud Vertical Distribution on Sea Surface Temperature and Tropospheric Dynamics, *Journal of Climate (Revised, 2013)*.

2. **Nair,A.K.M.**, K.Rajeev, M.K.Mishra, B.V.Thampi, and K.Parameswaran (2012), Multi-year Lidar observations of the descending nature of tropical cirrus clouds, *J. Geophys. Res.*, 117, D18201, doi:10.1029/2011JD017406.

3. Mishra,M.K., K.Rajeev, **A.K.M.Nair**, K.Krishna Moorthy and K. Parameswaran (2012), Impact of a noon-time annular solar eclipse on the mixing layer height and vertical distribution of aerosols in the atmospheric boundary layer, *J. Atmos. Sol. Terr. Phys.*, 74, 232-237, doi:10.1016/j.jastp.2011.10.012.

4. **Nair,A.K.M**, K. Rajeev, S. Sijikumar, and S. Meenu (2011), Characteristics of a persistent 'pool of inhibited cloudiness' and its genesis over the Bay of Bengal associated with the Asian summer monsoon, *Ann. Geophys.*, 29, 12471252, doi:10.5194/angeo-29-1247-2011.

5. Mishra,M.K., K. Rajeev, B.V.Thampi, K.Parameswaran, and **A.K.M.Nair** (2010), Micropulse Lidar observations of the dust layer in the lower troposphere over the southwest coast of Peninsular India during the Asian Summer Monsoon, *J. Atmos. Sol. Terr. Phys.*, 72, 12511259, doi:10.1016/j.jastp.2010.08.012.

6. K. Rajeev, K. Parameswaran, B.V. Thampi, M.K. Mishra, **A.K.M.Nair** and S. Meenu (2010), Altitude distribution of aerosols over Southeast Arabian Sea coast during pre-monsoon season: Elevated layers, long-range transport and atmospheric radiative heating, *Atmos. Environ.*, 44, 2122, 2597-2604, doi:10.1016/j.atmosenv.2010.04.014.

7. Meenu, S., K. Rajeev, K. Parameswaran, and **A.K.M.Nair** (2010), Regional distribution of deep clouds and cloud top altitudes over the Indian subcontinent and the surrounding oceans, *J.Geophys.Res.*, 115, D05205, doi:10.1029/2009JD011802.

Publications in Proceedings

1. **Nair A.K.M.** and K.Rajeev, Dependence of the Cloud Vertical Distribution on Sea Surface Temperature and Tropospheric Dynamics–New Insights, International Tropical Meteorology Symposium (INTROMET), S.R.M. University, Chennai, India, 27–30 August 2013. *(accepted),*

2. **Nair A.K.M.** and K.Rajeev, Three-dimensional distribution of clouds and its association with tropical circulation, Proceedings of the XXV Kerala Science Congress, Thiruvananthapuram, India, 29 January–01 February 2013.

3. **Nair A.K.M.**, K.Rajeev, S.Sijikumar and Meenu S, On the genesis of a 'Pool of inhibited cloudiness' over the Bay of Bengal during the Asian summer monsoon, Proceedings of the International Conference on Opportunities and Challenges in Monsoon Prediction in a Changing Climate (OCHAMP), Indian Institute of Tropical Meteorology, Pune, India, 21–25 February 2012.

4. Mishra, M. K., K. Rajeev, **A. K. M Nair**, B. V. Thampi, K. Krishnamoorthy and K. Parameswaran, Impact of noon-time annular Solar Eclipse on the vertical distribution of aerosols and mixing height over Thumba, Proceedings of the National Workshop: Results on Solar Eclipse, Vikram Sarabhai Space Centre, Thiruvananthapuram, 27–28 January 2011.

5. Mishra, M. K., B.V.Thampi, **A.K.M.Nair**, K. Rajeev and K.Parameswaran, Lidar Observations of contrasting Aerosol layers over Trivandrum (8.5°N,77°E) during pre-monsoon and summer monsoon seasons, Proceedings of the Indian Aerosol Science and Technology Association Conference, Bose Institute, Darjeeling, 24–26 March 2010.

6. **Nair A.K.M.**, B.V. Thampi, Mishra, M. K., S. Meenu, K. Rajeev and K. Parameswaran, Lidar observations of the descending nature of tropical cirrus clouds, Proceedings of the Indian Aerosol Science and Technology Association Conference, Bose Institute, Darjeeling, 24–26 March 2010.

7. Meenu, S., K. Rajeev, K. Parameswaran, **A.K.M. Nair**, C.Suresh Raju, Regional mean vertical distribution of deep clouds over the Indian Subcontinent and surrounding oceans estimated from AVHRR and CALIPSO observations, Proceedings of the International Conference on Megha-Tropiques, Bangalore, India, 2009.

8. Rajeev, K., S.Meenu, K.Parameswaran, **A.K.M. Nair**, C.Suresh Raju, S.V. Sunilkumar, KALPANA-1-VHRR and CALIPSO observations of semi-transparent cirrus clouds over the Indian subcontinent and surrounding oceans, Proceedings of the International Conference on Megha-Tropiques, Bangalore, India, 2009.

Conference presentations

International

1. K. Rajeev, **Nair,A.K.M.** and K.Krishna Moorthy, Direct observations of Cloud Radiative Forcing over Tropics using Megha-Tropiques ScaRaB data, Indo-French Megha Tropiques Workshop, ISRO HQ, Banglore, India, 17–19 December 2012.

2. **Nair,A.K.M.**, K. Rajeev, Multi-year analysis of the three-dimensional distribution of clouds using CloudSat data and inferences on atmospheric circulation features over the Indian region, Committee on Space Research (COSPAR) 39^{th} Scientific Assembly, Mysore, India, 14–22 July 2012.

3. K. Rajeev, **A.K.M.Nair**, Mishra M.K., B.V.Thampi, K.Parameswaran, Characteristics of the descending nature of tropical cirrus clouds derived from long-term Lidar observations and their potential impact, Committee on Space Research (COSPAR) 39^{th} Scientific Assembly, Mysore, India, 14–22 July 2012.

4. Mishra M.K., B.V.Thampi, **A.K.M.Nair**, K. Rajeev, K.Parameswaran, K. Krishnamoorthy, Micropulse lidar observations of the annual cycle of altitude profiles of aerosols and delineation of the effect of long-range transport over a tropical coastal Indian station, Committee on Space Research (COSPAR) 39^{th} Scientific Assembly, Mysore, India, 14–22 July 2012.

5. **Nair, A.K.M.**, K. Rajeev, S.Sijikumar and Meenu S, On the genesis of a 'Pool of inhibited cloudiness' over the Bay of Bengal during the Asian summer monsoon, International Conference on Opportunities and Challenges in Monsoon Prediction in a Changing Climate (OCHAMP), Indian Institute of Tropical Meteorology, Pune, India, 21–25 February 2012.

6. K. Rajeev and **A.K.M.Nair**, Dependence of the Vertical Distribution of Clouds on Sea Surface Temperature: Results from CloudSat & CALIPSO Combined Analysis, International Conference on Opportunities and Challenges in Monsoon Prediction in a Changing Climate (OCHAMP), Indian Institute of Tropical Meteorology, Pune, India, 21–25 February 2012.

7. **Nair,A.K.M.**, S. Sijikumar, Meenu, S., K. Rajeev, K. Parameswaran, A Pool of Reduced Cloudiness over the South Bay of Bengal during the Asian Summer Monsoon Season: Characteristics and Genesis, Asia Oceania Geosciences Society (AOGS) 7^{th} annual general meeting, Hyderabad, India, 5–9 July 2010.

8. Mishra,M.K., B.V.Thampi, **A.K.M.Nair**, K. Rajeev, K. Parameswaran, Seasonal Variations in the Altitude Distribution of Aerosols and Characteristics of the Elevated Layers over Trivandrum (8.5°N, 77°E), Asia Oceania Geosciences Society (AOGS) 7^{th} annual general meeting, Hyderabad, India, 5–9 July 2010.

9. Meenu, S., K.Rajeev, K.Parameswaran, **A.K.M.Nair**, C.Suresh Raju, Regional mean vertical distribution of deep clouds over the Indian Subcontinent and surrounding oceans estimated from AVHRR and CALIPSO observations, International Conference on Megha-Tropiques, ISRO-HQ, Bangalore, India, 2009.

10. Rajeev,K., S.Meenu, K.Parameswaran, **A.K.M.Nair**, C. Suresh Raju, S. V. Sunilkumar, KALPANA-1-VHRR and CALIPSO observations of semi-transparent cirrus clouds over the Indian subcontinent and surrounding oceans, International Conference on Megha-Tropiques, ISRO-HQ, Bangalore, India, 2009.

National

1. **Nair A.K.M.** and K.Rajeev, Three-dimensional distribution of clouds and its association with tropical circulation, XXV Kerala Science Congress, Thiruvananthapuram, India, 29 January–01 February 2013.

2. Rajeev, K and **A.K.M.Nair**, Cloud distribution over the Indian Region and Surrounding Ocean, Variability of monsoons in Kerala, Indian Meteorological Society Seminar, Thiruvananthapuram, 21 August 2012.

3. **Nair A.K.M.**, K. Rajeev, S.Sijikumar and Meenu S, On the genesis of a 'Pool of inhibited cloudiness' over the Bay of Bengal during the Asian summer monsoon, National Seminar on Climate change and variability, Cochin University of Science and Technology, Cochin, 26–27 March 2012.

4. **Nair A.K.M.** and K. Rajeev, Vertical distribution of clouds and associated latent heating over the Indian region, National Space Science Symposium, Sri Venkateswara University, Tirupati, 14–17 February 2012.

5. Rajeev K., **A.K.M.Nair**, Mishra, M. K., B.V.Thampi, and K.Parameswaran, Multi-year lidar observations of descending tropical cirrus clouds and their potential impact, National Space Science Symposium, Sri Venkateswara University, Tirupati, 14–17 February 2012.

6. Mishra, M. K., B.V.Thampi, **A.K.M.Nair**, K. Rajeev, K.Parameswaran and K.Krishnamoorthy, Multi-year Micropulse Lidar observations of the vertical distribution and non-sphericity of aerosols over Trivandrum, National Space Science Symposium, Sri Venkateswara University, Tirupati, 14–17 February 2012.

7. **Nair A.K.M.**, K. Rajeev, Mishra, M. K., B.V.Thampi, and K.Parameswaran, Potential Dehydration of TTL by Descending Cirrus, Tropical Tropopause Dynamics Workshop, Vikram Sarabhai Space Centre, Thiruvananthapuram, 23–24 January 2012.

8. Mishra, M. K., K. Rajeev, **A. K. M Nair**, B. V. Thampi, K. Krishnamoorthy and K. Parameswaran, Impact of noon-time annular Solar Eclipse on the vertical distribution of aerosols and mixing height over Thumba, National Workshop: Results on Solar Eclipse, Vikram Sarabhai Space Centre, Thiruvananthapuram, 27–28 January 2011.

9. Mishra, M. K., B.V.Thampi, **A.K.M.Nair**, K. Rajeev and K.Parameswaran, Lidar Observations of contrasting Aerosol layers over Trivandrum (8.5°N,77°E) during pre-monsoon and summer monsoon seasons, Indian Aerosol Science and Technology Association Conference, Bose Institute, Darjeeling, 24–26 March 2010.

10. **Nair A.K.M.**, B.V. Thampi, Mishra, M. K., S. Meenu, K. Rajeev and K. Parameswaran, Lidar observations of the descending nature of tropical cirrus clouds, Indian Aerosol Science and Technology Association Conference, Bose Institute, Darjeeling, 24–26 March 2010.

11. Meenu S.,K.Rajeev, **A.K.M.Nair** and K.Parameswaran, On the regional distribution and characteristics of semi-transparent cirrus clouds over the Indian region derived from CALIPSO observations, National Space Science Symposium, Rajkot, 2010.

12. Meenu S.,K.Rajeev, **A.K.M.Nair** and K.Parameswaran, Direct observations of the modulation of the Tropical Tropopause Layer by deep convective clouds over the Indian Subcontinent, National Space Science Symposium, Saurashtra University, Rajkot, 24–27 February 2010.

13. **Nair A.K.M.**, Meenu S., S.Sijikumar, K.Rajeev and K.Parameswaran, Characteristics of the pool of reduced cloudiness over the southwest Bay of Bengal during the Asian summer monsoon season, National Space Science Symposium, Rajkot, 2010.

14. **Nair A.K.M.**, K. Rajeev, Mishra, M. K., B.V. Thampi, S. Meenu and K. Parameswaran, Micropulse Lidar observations of the descending nature of tropical cirrus clouds, National Space Science Symposium, Saurashtra University, Rajkot, 24–27 February 2010.

15. Mishra, M. K., B.V.Thampi, **A.K.M.Nair**, K. Rajeev and K.Parameswaran, Observations of Arabian dust over the southwest coast of Peninsular India during the Asian summer monsoon season, National Space Science Symposium, Saurashtra University, Rajkot, 24–27 February 2010.

16. K. Rajeev, K.Parameswaran, B.V.Thampi, Mishra, M. K., **A.K.M.Nair** and Meenu.S, Vertical distribution of aerosols associated with the Southeast Arabian Sea plume during pre-monsoon season: Elevated layers and atmospheric heating, National Space Science Symposium, Saurashtra University, Rajkot, 24–27 February 2010.

Frequently Used Acronyms

ADM	Angular Distribution Models
ASM	Asian Summer Monsoon
AVHRR	Advanced Very High Resolution Radiometer
BoB	Bay of Bengal
CALIPSO	Cloud-Aerosol Lidar and Infrared Pathfinder Satellite Observation
CAPE	Convective Available Potential Energy
CCN	Cloud Condensation Nuclei
CERES	Cloud and the Earth's Radiant Energy System
COD	Cloud Optical Depth
CPR	Cloud Profiling Radar
CRF	Cloud Radiative Forcing
DJF	December, January, February
DPC	Data Processing Centre
ERBE	Earth Radiation Budget Experiment
FOC	Frequency of Occurrence of Clouds
GCM	Global Circulation Models
GPCP	Global Precipitation Climatology Project
IN	Ice Nuclei
IPCC	Intergovermental Panel on Climate Change
ISCCP	International Satellite Cloud Climatology Project
ISRO	Indian Space Research Organisation
ITCZ	Inter Tropical Convergence Zone
JJAS	June, July, August, September
LDR	Linear Depolarization Ratio
LHR	Latent Heating Rate
LIDAR	LIght Detection And Ranging
LTS	Lower Tropospheric Stability
LWC	Liquid Water Content
LWCRF	Longwave Cloud Radiative Forcing
LWF	Longwave Flux
MADRAS	Microwave Analysis and Detection of Rain and Atmospheric Systems
MAM	March, April, May
MERRA	Modern-Era Retrospective Analysis for Research and Applications
MODIS	Moderate Resolution Imaging Spectroradiometer
MPL	Micro Pulse Lidar
MT	Megha Tropiques

NASA	National Aeronautics and Space Administration
NCEP	National Centre for Environment Prediction
NCRF	Net Cloud Radiative Forcing
NIR	Near Infrared
NOAA	National Oceanographic and Atmospheric Administration
OLR	Outgoing Longwave Radiation
ON	October, November
SAGE	Stratospheric Aerosol and Gas Experiments
SAPHIR	Sondeur Atmosphérique du Profil d'Humidité Intertropicale par Radiométrie
ScaRaB	Scanner for Radiation Budget
SNR	Signal to Noise Ratio
SST	Sea Surface Temperature
STC	Semi Transparent Cirrus
SVC	Sub-Visual Cirrus
SWCRF	Shortwave Cloud Radiative Forcing
SWD	Surface Wind Divergence
SWF	Shortwave Flux
TIR	Thermal Infrared
TMI	TRMM Microwave Imager
TOA	Top of the Atmosphere
TRMM	Tropical Rainfall Measuring Mission
TTL	Tropical Tropopause Layer
UTLS	Upper Troposphere Lower Stratosphere
VHRR	Very High Resolution Radiometer
VIS	Visible Band

List of Frequently used Symbols

δ_L	Linear Depolarization Ratio
δ_{MPL}	Depolarization ratio
λ	Wavelength
μ	micro- ($\times\ 10^{-6}$)
ν	Number of ions resulting from the dissolution of one solute molecule
π	pi $= 4 \times \tan^{-1}(1)$
ρ	Density of air
ρ_w	Density of water
σ_w	Surface Tension of water
τ	Cloud Optical Depth
BT	Brightness Temperature
D_p	Diameter of the droplet
D_{pc}	Critical droplet diameter
e_s	equilibrium saturation vapour pressure
e'_s	equilibrium saturation vapour pressure for a droplet
F_{ALT}	Frequency of occurrence of clouds at each altitude
F_C	Frequency of occurrence of clouds (total)
FOC	Frequency of occurrence of Cirrus clouds
L_{LW}	Longwave radiance
LWF_{clear}	Longwave flux during clear sky condition
M_s	Molecular weight of the solute
m_s	mass of the solute
M_w	Molecular weight of water
P	Pressure
P_0	Lidar backscattered signal received (cross polarized channel)
$P_{\pi/2}$	Lidar backscattered signal received (co-polarized channel)
R	Gas Constant
S	Supersaturation
SWF_{clear}	Shortwave flux during clear sky condition
T	Temperature

Preface

Clouds play a paramount role in the weather and climate of the earth-atmosphere system through a host of direct and feedback processes, which results in the vertical and horizontal transport of energy and moisture as well as the modulation of radiation balance, large-scale dynamics and thermal structure of the atmosphere and hydrological cycle. Impact of clouds on the radiation budget and latent heating of the atmosphere depends on the cloud properties, the most prominent among them being their frequency of occurrence, spatial distribution and water content. An excess surface radiative heating produces instability in the atmosphere, resulting in convection and transfer of energy from the surface and its subsequent cooling. This, in turn, affects the large-scale atmospheric circulation, triggering a chain of non-linear processes and affects the meteorology of the regions that are even well separated from the initial source of instability. Cloud feedback processes are highly non-linear and complex and are among the largest sources of uncertainties in the modelling and prediction of weather and climate. As a result, the response of clouds to climate change differs widely among general circulation models (GCMs). Detailed knowledge of the spatial and vertical distribution of clouds, their properties and temporal evolution are of fundamental importance for understanding the genesis and impact of clouds and their feedback on the above processes and their subsequent accurate parametrization in weather and climate models. This is also important for investigating the aerosol-cloud interaction, radiative impact of aerosols under cloudy conditions and heterogeneous chemistry in the atmosphere.

Horizontal distribution of clouds and their temporal evolution had been extensively investigated in the past using about three decades of systematic observations employing passive remote sensing imagers onboard various satellites and had immensely contributed to the understanding of cloud processes and their impact as well as to the assessment of GCMs and climate change. Such extensive studies have also been carried out over the Indian region and the surrounding oceans. However, investigations on the vertical distribution of clouds, especially the optically thicker clouds, have been sparse, though these are crucial and offer the best avenue for improving the understanding and modelling of most of the processes listed above. Major gaps in the accurate knowledge of the three-dimensional distribution of clouds, their properties and temporal variations as well as the atmospheric processes involving clouds exist at present. Further, the observed 3-dimensional distribution of clouds can act as a proxy for some of the atmospheric dynamical processes which are not explored hitherto.

Spatial distribution of clouds, their temporal evolution and impact on the energetics of the earth-atmosphere system over the Indian subcontinent and the surrounding oceans have several unique features, which mainly include: (i) substantial, but sys-

tematic, annual variation in the distribution and properties of clouds associated with the massive monsoon circulation caused by the largest annual migration of ITCZ over the entire globe, (ii) occurrence of the deepest convection and highest cloud tops over the entire globe over the north and east Bay of Bengal during the June to August period, (iii) the strongest ascending limb of the Walker circulation located in the east equatorial Indian Ocean and the western Pacific and its descending limb at the west equatorial Indian Ocean/east Africa, (iv) large spatial variations in SST from <23°C to >30°C over the Indian Ocean region and the associated changes in cloud development, and (v) significantly large negative net cloud radiative forcing (NCRF) over the Indian region (<-30 Wm^{-2}) during the Asian summer monsoon season, which is distinctly different from the near-zero NCRF over the tropics.

Motivation for the present study is to improve the scientific understanding on the prominent gap areas in the average three-dimensional distribution of clouds and their impact on the energetics of the earth-atmosphere system. This study is focused on the Indian subcontinent and the surrounding oceans bound within the latitude-longitude bands of 30°S to 30°N and 30°E to 110°E. Main objectives of this study are to : (i) estimate the monthly and seasonal mean vertical distributions of clouds and their spatial variations (which provide the monthly and seasonal mean 3-dimensional distributions of clouds) using multi-year satellite data and investigate their association with the general circulation of the atmosphere, (ii) investigate the characteristics of the 'pool of inhibited cloudiness' that appear over the southwest Bay of Bengal during the Asian summer monsoon season (revealed by the 3-dimensional distribution of clouds) and identify the potential mechanisms for its genesis, (iii) investigate the role of SST and atmospheric thermo-dynamical parameters in regulating the vertical development and distribution of clouds, (iv) investigate the vertical distribution of tropical cirrus clouds and their descending nature using lidar observations at Thiruvananthapuram (8.5°N, 77°E), a tropical coastal station at the southwest Peninsular India, and (v) assessment of the impact of clouds on the energetics of the earth-atmosphere system, by estimating the regional seasonal mean cloud radiative forcing at top-of-the-atmosphere (TOA) and latent heating of the atmosphere by precipitating clouds using satellite data.

General introduction to clouds and the background for this study are provided in **Chapter 1**. **Chapter 2** provides the details of the satellite data, experimental details of the Micropulse lidar system, methods used for the analyses, and advantages, limitations and uncertainties of the derived parameters. **Chapter 3** describes the monthly and seasonal mean vertical distributions of clouds, their spatial variations, and association with atmospheric circulation. Detailed characteristics and potential generation mechanisms of the 'pool of inhibited cloudiness' over the southwest Bay of Bengal during the Asian summer monsoon season are presented in **Chapter 4**. The role of SST

and its spatial gradient, and atmospheric thermo-dynamical parameters on the vertical distribution and development of clouds are investigated in **Chapter 5**. **Chapter 6** presents the characteristics of cirrus clouds and their prominent descending nature over a tropical coastal station Thiruvananthapuram, based on multi-year dual polarization lidar observations. **Chapter 7** presents the impact of clouds on the energetics of the earth-atmosphere system, investigated using the satellite-based estimations of clouds radiative forcing at TOA and latent heating of the atmosphere by precipitating clouds. **Chapter 8** provides the summary of the results obtained from the present study and scope for future research.

List of Figures

List of Tables

Chapter 1

Introduction to Clouds: Characteristics and Measurement Techniques

I bring fresh showers for the thirsting flowers,
From the seas and the streams;
I bear light shade for the leaves when laid
In their noon-day dreams.
'The Cloud' (P.B.Shelley)

1.1 Introduction

Clouds are among the most vital elements of the earth-atmosphere system, which play a pivotal role in regulating the weather and climate by modifying the radiation balance, vertical and horizontal transfer of energy, thermo-dynamical structure and hydrological cycle [e.g., *Rogers and Yau*, 1979; *Pruppacher and Klett*, 1980; *Ramanathan et al.*, 1989; *Kiehl and Trenberth*, 1997; *Seinfeld and Pandis*, 1997; *Trenberth et al.*, 2009]. Feedback processes that further modify the impact of clouds are highly non-linear and complex [*Stephens*, 1988; *Rossow*, 1989]. Accurate parameterization of the cloud processes are challenging and major sources of uncertainties in climate and weather prediction [e.g., *Pruppacher and Klett*, 1980; *Schiffer and Rossow*, 1983; *Cess et al.*, 1990]. Clouds also play a vital role in aerosol scavenging and hence atmospheric residence time of aerosols – as well as aqueous phase chemical reactions leading to the production of secondary species [*Seinfeld and Pandis*, 1997]. The occurrence of clouds in the upper troposphere and lower stratosphere (UTLS) modifies the chemistry, moisture content and thermal structure of this region [*Sherwood and Dessler*, 2001].

Aerosols can act as cloud condensation nuclei, thereby modifying the microphysical properties, residence time and precipitation efficiency of clouds. This, known as the indirect effect of aerosols, is one of the highly uncertain and least understood problems in climate modelling and is a major hindrance in the assessment of aerosol impact on climate [*Twomey*, 1977; *Koren*, 2004; *Metz et al.*, 2007]. Clouds are also major components in the exchange of electric charges between the atmosphere and earth's surface and hence are important in the global electric circuit [*Siingh et al.*, 2007]. Release of latent heat associated with deep convective clouds significantly warms the tropospheric column, while clouds in the convective cores as well as the large anvils emanating from them influence the synoptic and mesoscale radiation balance [*Ramanathan et al.*, 1989; *Grossman and Garcia*, 1990]. Formation of deep convective clouds is the most effective mechanism for the transport of heat and moisture from the earth's surface and atmospheric boundary layer to the upper troposphere. Despite their enormous importance, clouds still remain one of the least understood components of the earth-atmosphere system and are major stumbling blocks in the prediction of weather and climate.

Understanding of the physical, microphysical, optical and radiative properties of clouds as well as the three-dimensional distribution of clouds and their temporal evolution are essential for estimating their impact on the energetics of the earth-atmosphere system. This information is also required for parameterization of cloud properties for incorporating in the weather and climate models and understanding their role in climate and the associated feedback mechanisms. Though the horizontal distribution of clouds has been extensively studied using satellite observations [*Fu et al.*, 1990; *Mapes and Houze*, 1993; *Zhang*, 1993; *Hall and Vonder Haar*, 1999; *Gettelman et al.*, 2002; *Hong et al.*, 2007; *Rossow and Pearl*, 2007; *Meenu et al.*, 2007, 2010, 2011, 2012; *Meenu*, 2010; *Sunilkumar et al.*, 2010], the vertical distribution of clouds is less explored [*Nair et al.*, 2011; *Rajeevan et al.*, 2012]. The impact of clouds on the energetics of the earth-atmosphere system (both radiative and latent heating) over the Indian region are also less explored [e.g., *Rajeevan and Srinivasan*, 2000; *Sathiyamoorthy et al.*, 2004; *Patil and Yadav*, 2005; *Roca et al.*, 2005].

Main purpose of the present study is to improve the understanding on the vertical and horizontal distributions of clouds and their impact on the energetics of the earth-atmosphere system over Indian subcontinent and the surrounding oceanic regions based on the analysis of multi-year satellite data. As the monthly and seasonal mean horizontal distributions of total cloudiness over this region were investigated in detail in the earlier studies [e.g., *Meenu et al.*, 2007, 2010, 2011, 2012; *Meenu*, 2010], this thesis focuses on the monthly and seasonal mean vertical distribution of clouds, its spatial variations, the role of sea surface temperature (SST) and atmospheric dynamics in regulating the vertical development of clouds and the impact of clouds on the energetics of

the earth-atmosphere system (in terms of cloud radiative forcing and latent heating). The three-dimensional distribution of clouds reveals certain atmospheric dynamical features which are not explored hitherto and are investigated in detail. Background information on the generation of clouds and their classification, in situ and remote sensing methods for investigating the cloud properties, global and regional distribution of clouds and their association with atmospheric general circulation, effect of clouds on the radiation budget and atmospheric energetics, importance of the cloud studies over the Indian subcontinent and the surrounding oceans and scope of the present study are presented in this chapter.

1.2 Physics of cloud formation

Clouds are formed by the condensation of water vapour. They can be produced by the updraft of warm moist air - driven by processes such as convection, frontal movements, or forced ascent due to flow over orography - which lead to adiabatic cooling of the air parcel and condensation of water vapour above the altitude at which supersaturation is attained [*Rogers and Yau*, 1979; *Pruppacher and Klett*, 1980; *Seinfeld and Pandis*, 1997]. Clouds can also be formed by radiative cooling (e.g., fog formation) at a given location or advection of warm humid air over to a cold surface. In principle, radiative cooling can also result in the in situ production of cirrus clouds. Cooler air has a lower saturation vapour pressure so that the air-mass with a given water vapour content becomes saturated upon sufficient cooling. The specific cloud morphologies are mainly determined by atmospheric water vapour content and thermo-dynamical processes that govern the cloud formation. For example, localized vertical motions caused by hydrostatic instability produce cumuliform clouds while much larger scale wave motions from a variety of sources produce stratiform clouds. Thus, the vertical structure of clouds is diagnostic of the atmospheric motions that produce the clouds [*Rossow and Schiffer*, 1991, 1999].

1.2.1 Condensation and growth of cloud droplets

Cloud droplets are formed by the condensation of water vapor through heterogeneous or homogeneous nucleation, under appropriate conditions of supersaturation. The condensation process is governed by the supersaturation (S), which is defined as the relative humidity (RH) exceeding 100%; S=0 for RH=100%; S<0 for unsaturation and S>0 for supersaturation. The unsaturated airmass can become saturated or supersaturated by undergoing various thermodynamic processes such as adiabatic expansion (e.g., updraft of air parcel), isobaric cooling (e.g., radiative cooling in a stable atmosphere) or incursion of moisture through mixing or advective processes. Produc-

tion of cloud droplets occurs through homogeneous nucleation when the water vapour condenses on embryos comprised of water molecules only. On the other hand, cloud droplets are formed through heterogeneous nucleation when the condensation of water vapor occurs over a foreign particle called cloud condensation nuclei (CCN). Initial size of a droplet formed through homogeneous nucleation is very small (typically the size of an aggregate comprising of a few tens or hundreds of water vapour molecules). Due to the energy associated with the surface tension of a droplet it is energetically unfavourable for a small droplet to grow. In contrast, the initial size of a droplet formed through condensation over a CCN will have relatively larger size. As the equilibrium saturation vapor pressure required for the maintenance of a droplet is quite large for small droplets (Kelvin effect), very tiny droplets get vaporized immediately after formation unless the airmass is highly supersaturated. Hence, the homogeneous nucleation takes place only at very high supersaturation.

In practice, clouds in the atmosphere are formed as a result of heterogeneous nucleation. Sufficiently large-sized aerosols can act as CCN. Regions having larger concentration of CCN would produce larger number of smaller cloud droplets compared to those having clean air which would produce fewer but larger droplets for the same total water content (indirect effect of aerosols). Nucleation efficiency of CCN depends on its physical size and water affinity, which considerably limits the percentage of aerosols that can act as CCN. For a given size of CCN, a water soluble particulate can act as better CCN compared to a non-soluble particulate. A non-soluble CCN can provide only the core area for the condensation to take place. In contrast, in addition to providing the surface area required for condensation, some of the dissolved foreign molecules in the water soluble CCN also appear at the surface of the droplet and reduce the equilibrium supersaturation required for the maintenance of the droplet (solute effect).

1.2.2 Köhler equation

Growth of a cloud droplet with supersaturation in the atmosphere can be estimated by considering the Kelvin and solute effects and is given by the Köhler equation [*Seinfeld and Pandis*, 1997]:

$$ln\left(\frac{(e_s^{'}(D_p)}{e_{s(\infty)}}\right) = \frac{A}{D_p} - \frac{B}{D_p^3} \tag{1.1}$$

where $e_s^{'}(D_p)$ is the equilibrium saturation vapor pressure for a droplet having diameter D_p, and $e_{s(\infty)}$ is the equilibrium saturation vapour pressure over a flat surface of water. The first term on the right-hand-side of Equation 1.1 represents the Kelvin effect and the second term represents the solute effect. The coefficients A and B are given by:

$$A = \left(\frac{4M_w\sigma_w}{RT\rho_w}\right) \cong \frac{0.66}{T} \tag{1.2}$$

$$B = \frac{6M_w n_s}{\pi \rho_w} \cong \frac{3.44 \times 10^{13} \nu m_s}{M_s} \tag{1.3}$$

where A has the unit of μm while B is in μm^3. In the above equations, M_w is the molecular weight of water, σ_w is the surface tension, R is the gas constant, T is the temperature (in K), ρ_w is the density of water, M_s is the molecular weight of the solute (in g/mole), m_s is the mass of solute (in g), n_s is the number of moles of solute and ν is the number of ions resulting from the dissolution of one solute molecule.

As seen in Equation 1.1, for CCNs that are insoluble in water, the equilibrium saturation vapour pressure decreases with increase in droplet size. Note that the sign of the solute effect in Equation 1.1 is negative. Hence, the Kelvin effect tends to increase the equilibrium saturation vapor pressure, while the solute effect tends to decrease it. However, magnitudes of both these effects decrease with increase in droplet size. As the solute effect decreases much faster (as cube of D_p), the Kelvin effect dominates in large droplets. Figure 1.1 shows the Kohler curves representing the variations of equilibrium supersaturation as a function of cloud droplet diameter for droplets formed from NaCl particulates acting as CCN. The curves correspond to different dry diameters of NaCl.

The value of S rapidly increases with droplet diameter and attain a maximum at the critical droplet diameter $D_{pc}=(3B/A)^{1/2}$. The corresponding value of $S(D_{pc})$ is the critical equilibrium saturation ratio. Figure 1.1 shows that, for a droplet with $D_p < D_{pc}$, any increase in the droplet size will require larger equilibrium vapor pressure than the prevailing value of atmospheric saturation vapor pressure e_s and hence is not favourable for growth. On the other hand, the value of S decreases with further increase in droplet diameter above the critical radius. Hence, for droplets with $D_p > D_{pc}$, any increase in the size of the droplet will decrease the equilibrium vapor pressure to less than e_s and the drop can grow further. Thus, for a droplet to grow in a cloud, the size of the droplet has to be larger than D_{pc}. If the saturation ratio of the atmosphere exceeds that for D_{pc}, the particulates having size larger than D_{pc} start growing through condensation and are said to be activated. Hence, only those particulates which are having size above the critical size D_{pc} can act as CCN.

The percentage of aerosols which can act as CCN varies considerably with the physical and chemical properties of aerosols. Though a generalization is rather complicated due to the spatial and temporal variations of aerosols, one of the most commonly used relationships between CCN and supersaturation S (in %) is given by [*Seinfeld and Pandis*, 1997]:

$$CCN(S) = CS^K \tag{1.4}$$

where C corresponds to the CCN at 1% supersaturation. The values of C and K show large temporal and spatial variations; typical the values of C and K are in the range of 100 to 2000 cm^{-2} and 0.3 to 1.3 respectively [*Hegg and Hobbs*, 1992; *Seinfeld and*

Pandis, 1997]. The cloud droplet concentration is largest (200 to 1000 cm^{-3}) over continents and least (10 to 200 cm^{-3}) over pristine oceans [e.g., *Seinfeld and Pandis*, 1997].

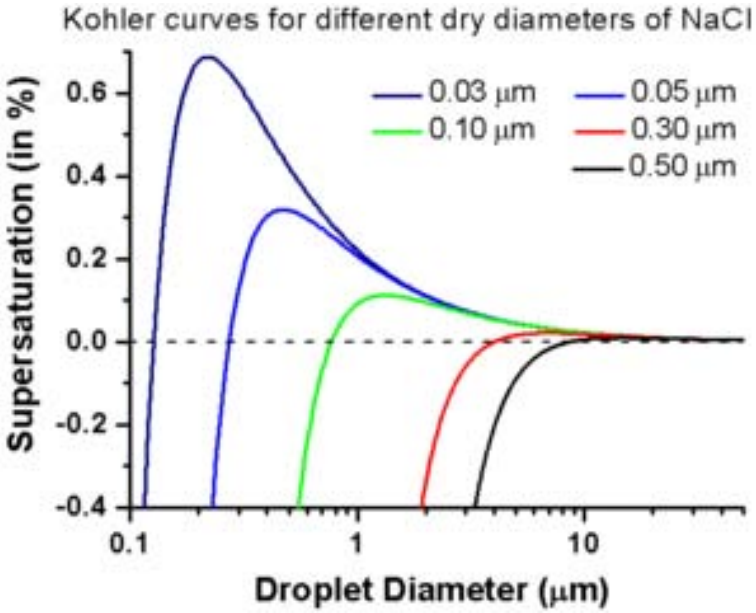

Figure 1.1: Köhler curves for NaCl particles as solute with dry diameters of 0.03, 0.05, 0.10, 0.30 and 0.50 μm at temperature of 293 K. Supersaturation is expressed in percentage (for RH=100.6%, supersaturation = 0.6%).

1.2.3 Lifting condensation level

The critical supersaturation required for the growth of a cloud droplet can be achieved in the atmosphere through several processes such as adiabatic cooling of a rising moist air parcel in an unstable atmosphere (convective processes), isobaric radiative cooling of an air parcel and the entrainment of warm moist air in a cold airmass. Processes such as heating of the surface layer and evolution of convective boundary layer during the day, low-level wind convergence and atmospheric instability can lead to convection. As a moist air parcel ascends, the temperature of the rising air parcel initially decreases at the dry adiabatic lapse rate (-9.76 K/km) up to the altitude where the parcel becomes supersaturated. Condensation can occur at this altitude - referred as the lifting condensation level (LCL) - and is usually very close to the cloud base. In practice, the rising air will mix with the surrounding air which leads to the formation of cloud base above the LCL. Because of the heating of air parcel due to latent heat released during the condensation of water vapor, further rising of the moist air parcel above the cloud base will result in a temperature decrease at the moist adiabatic lapse rate up to the cloud top. Magnitude of the moist adiabatic lapse rate depends on the amount of moisture condensed and is less than the dry adiabatic lapse rate. Ascending

of the airmass can continue so long as the air parcel is warmer than the environment and instability prevails. This is the main mechanism responsible for the formation of convective clouds.

1.2.4 Ice nuclei and cloud ice crystals

Cloud droplets can exist in liquid form even below 0°C (i.e., even above ∼5 km altitude in the atmosphere). Such supercooled water droplets are very common in clouds warmer than -10°C. Formation of pure ice particles through homogeneous nucleation occurs only at very low temperatures, typically below -40°C [*Hobbs*, 1993]. However, the presence of an ice nucleus (IN) allows ice formation at temperatures well above -40°C. Insoluble aerosols having chemical bonding and crystalline structure similar to that of ice can act as efficient IN. Likelihood of ice crystal occurrence increases with decrease in temperature. At -20°C, only ∼10% of the clouds consist entirely of supercooled water droplets [*Seinfeld and Pandis*, 1997]. Ice crystals and water droplets can co-exist in the same cloud, which is typically the case with the tropical clouds occurring around 6 to 8 km altitude. Interestingly, for clouds comprising of ice crystals alone, the number of ice crystals in clouds are generally larger than the IN concentration [*Rangno and Hobbs*, 1991]. Potential reasons for this conspicuous feature include breaking of primary ice particles, ice splitter productions during droplet freezing and unusually high supersaturation.

The IN concentrations in the atmosphere varies with space and time. Similar to CCN, the potential of particulates to act as IN depends on their microphysical properties as well as the water vapour pressure and temperature of the atmosphere. Nucleating efficiency of IN increases with their size. Freezing temperature decreases with decrease in the size of ice particles and is more pronounced for crystal diameter smaller than 0.02 μm. Thus, the ice nucleating 'active' fraction of an aerosol population increases with decrease in temperature [*Pruppacher and Klett*, 1980; *Seinfeld and Pandis*, 1997]. Ice crystals in clouds have a variety of shapes such as plates, poly-crystalline bullet rosettes, single bullets, and banded columns [*Pruppacher and Klett*, 1980].

1.2.5 Growth of droplets through collision and coalescence processes

Increase in the size of a water droplet by condensation of water vapor slows down as the droplet size increases. Growth of a droplet through condensation process alone takes considerable time before they attain sizes large enough to fall as precipitation. In the atmosphere, once the droplet has attained significant size through condensation, their further growth take place rapidly through the collision-coalescence process in

which the relatively small droplets are collided with bigger drops and coalesce to form large rain drops. Convection and turbulence significantly aid the collision-coalescence process. In the absence of significant convection and turbulence, the size of the cloud droplet produced is typically a few micrometers. Clouds produced thus (e.g., scattered fair-weather cumulus, stratocumulus) do not produce precipitation and dissipate unless supported by upward motions since such small droplets fall very slowly and evaporate within a few minutes after they leave the cloud environment. Typical lifetime of a cumulus is 10 to 20 minutes. Stronger vertical motions of moist-laden air tend to produce larger droplets, typically having radius of ∼15 to 30 μm which fall more rapidly and collide with each other to grow further.

Probability for collision is low for small droplets and the collision efficiency increases with the size of the droplets. However, for much larger drops, the efficiency decreases because droplets tend to follow the streamlines around the drop. Further, two colliding droplets need not always coalesce permanently but can coalesce temporarily before breaking into a number of small drops. They are quantified through a factor called coalescence efficiency, which is the ratio of number of coalescence to the total number of collisions. Thus the droplet growth through collision-coalescence depends on collection efficiency which is the product of collision and coalescence efficiencies. In effect, the collision and coalescence processes cause much rapid increase in droplet sizes compared to the growth by condensation of water vapour. Those clouds containing only a very few droplets having size larger than ∼18 μm will be relatively stable with respect to growth by collision and coalescence while clouds with significant number of larger drops may develop precipitation [*Rogers and Yau*, 1979]. Very strong vertical motions result in the generation of deep convective clouds such as the cumulonimbus clouds in which the growth (as well as breaking) of the cloud droplets (water or ice droplet) is very rapid and causes intense rainfall with large droplet sizes.

1.2.6 Growth of ice crystals

In mixed clouds (having both ice crystals and liquid droplets) which occur at sub-freezing temperature, the saturation vapor pressure over water surface is greater than that over ice. This causes vapor molecules to diffuse from water droplet towards ice. This process by which an ice crystal grows at the expense of the surrounding super-cooled water droplets is known as Wegener-Bergeron-Findeisen process (usually referred as Bergeron process). The consequence is that the ice crystals grow much more quickly to larger sizes in the range from 20 to 100 μm and keep growing below the cloud, reaching sizes of a few hundred micrometers, because the relative humidity is still >100% with respect to ice below the initial cloud base. As the ice crystals fall, they may collide with each other and stick together (aggregation) or collide and stick with other

supercooled water droplets (accretion/rimming), which support the growth of ice crystals. In practice, violent collisions take place in a vertically developing cloud with large updraft velocity (typically 5 to 15 ms^{-1}) and turbulence, which considerably amplifies the growth and break up of ice crystals through collision and coalescence. For example, in the violent vertical motions of strong thunderstorms, the particles can fall and rise many times, producing large hail stones that have been known to reach sizes >10 cm.

1.2.7 Effect of aerosols on clouds

Any increase in the concentration of aerosols (especially the coarse particles) will increase the concentration of CCN. For a given amount of water vapor available in the atmosphere, the effective size of the droplets will decrease with increase in CCN. Smaller size of cloud droplets causes an increase in cloud albedo, increase in cloud lifetime and decrease in the precipitation efficiency of the cloud. This will increase the solar radiation scattered back to space while decreasing the insolation at earth's surface. This effect of aerosols on clouds, termed as the indirect effect of aerosols [*Twomey*, 1977; *Albrecht*, 1989; *Charlson et al.*, 1992; *Ramanathan et al.*, 2001; *Koren*, 2004] and is demonstrated using observations of cloud albedo and size of cloud droplets above ship stacks as well as over major pollution sources [e.g., *Charlson et al.*, 1992; *Andreae and Rosenfeld*, 2008; *Pandithurai et al.*, 2012]. Recent studies also point to their impact on the large-scale weather systems [*Rosenfeld et al.*, 2008; *Zhang et al.*, 2009; *Krall and Cottom*, 2012; *Rosenfeld et al.*, 2012]. Notwithstanding these studies, the indirect effect of aerosols is among the most uncertain factors while modelling the aerosol-cloud interaction and predicting climate change [e.g., *IPCC*, 2007]. In addition, the absorption of radiation by aerosols (especially those having small values of single scattering albedo, such as soot) can cause heating of the atmosphere and increase the atmospheric temperature, eventually causing the 'burning of clouds'. This effect is termed as semi-direct effect of aerosols [*Ackerman*, 2000]. Both these effects have considerably large spatial and seasonal variations as the atmospheric residence time of tropospheric aerosols are rather short (typically 3 to 10 days) and their properties and concentrations undergo substantial regional variations [e.g., *Prospero et al.*, 1983; *Moorthy et al.*, 1997; *Parameswaran et al.*, 1997; *Satheesh et al.*, 1998; *Ramanathan et al.*, 2001; *Rajeev and Ramanathan*, 2001; *Tahnk and Coakley*, 2002; *Babu*, 2004; *Nair et al.*, 2005; *Jayaraman et al.*, 2006; *Niranjan et al.*, 2007; *Nair et al.*, 2008; *Satheesh and Krishna Moorthy*, 2005; *Lawrence and Lelieveld*, 2010; *Menon et al.*, 2011; *Moorthy et al.*, 2013].

Cirrus clouds are also influenced by the ice-forming properties of the aerosol precursors [*Kärcher and Solomon*, 1999]. Modification of cloud microphysical properties by aerosols depends on the altitude structure of their size distribution and chemical

composition. On the contrary, cloud processing of aerosols can significantly modify the properties of aerosols [*Seinfeld and Pandis*, 1997]. Further, the washout, rainout and scavenging of aerosols by clouds and precipitation are the main processes that control the aerosol residence time and their abundance in the atmosphere [*Prospero et al.*, 1983; *Seinfeld and Pandis*, 1997].

1.3 Cloud types and classification

Differences in the cloud dynamics under different meteorological conditions produce different cloud types. Depending on their texture, physical properties, and rain bearing nature, clouds are generally classified into four basic types [*Battan*, 2003]. Their names and meaning are (i) Cirrus (curl of hair) (ii) Stratus (layer), (iii) Cumulus (heap), and (iv) Nimbus (rain). In addition, alto-clouds refer to the middle level clouds. Other cloud types are a combination of the above basic types (e.g., stratocumulus, nimbostratus, altostratus, altocumulus, cirro-startus, cirro-cumulus, cumulonimbus). Combinations that include nimbus are the most common precipitating clouds (e.g., Nimbostratus, Cumulonimbus). Different cloud types often co-exist over a given location. Generation mechanisms for different cloud types are different. For example, cumulonimbus clouds occur during intense convection of highly humid air from the lower-troposphere into the upper troposphere in a highly unstable atmosphere. The updraft velocity of airmass in such clouds from typically ranges from 1 to 20 m s^{-1} [*Pruppacher and Klett*, 1980]. For stratiform clouds, the updraft velocity and supersaturation are very small (0 to 1 m s^{-1} and about 0.05% respectively). Fog (which is classified as the stratus cloud reaching the ground) is formed under stable conditions and the maximum supersaturation is ∼0.1% [*Seinfeld and Pandis*, 1997]. Based on the altitude of cloud base above the surface, clouds are classified into 4 major groups: low-level clouds (0 to ∼2 km), middle-level clouds (∼2 to ∼8 km in the tropics, ∼2 to ∼7 km in the mid-latitudes and ∼2 to ∼4 km in the high latitudes), high-level clouds (∼8 to ∼18 km in tropics, ∼7 to ∼13 km in mid-latitudes and ∼4 to 8 km in high latitudes) and vertically developing clouds (∼500 m to the upper troposphere).

1.3.1 Low-level clouds

They include the status, cumulus, and stratocumulus. Cumulus is fair weather cloud while stratus can be rain-bearing. They are warm clouds composing of water droplets. Base altitudes of these clouds are usually at the lifting condensation level or just above. Majority of the vertically developing clouds originate as low level clouds. Under favourable conditions, they can develop vertically to cumulus congestus. Cumulus with small vertical development is called Cumulus humulis (fair weather cumulus).

Ragged edge cumulus which are often smaller than cumulus humulis and scattered across the sky are called cumulus fractus. Such cumiliform clouds often cap the atmospheric boundary layer. In general, the individual low-level clouds have relatively short residence time and small horizontal extent which is comparable to their vertical extent. This leads to large spatio-temporal variations in their occurrence over a given location. Very often they appear as a cluster of individual clouds and have significant diurnal variation in the frequency of occurrence. Over the continents, their frequency of occurrence usually increases during the development of daytime convective boundary layer, with peak occurrence around the afternoon.

1.3.2 Middle-level clouds

They mainly include altocumulus and altostratus clouds. Though the Nimbostratus have cloud base occurring in the lower troposphere, their top altitude often extend above ∼4 km and hence are classified as middle level clouds. Altocumulus is optically thinner than altostratus, with typical physical thickness of <1 km. Optical depth of these clouds is generally larger than that for the high-altitude cirrus clouds. Nimbostratus are rain-bearing clouds and have considerably large optical depth (COD>23). In most of the middle level clouds, water exists in liquid phase (either warm or supercooled). However, those clouds occurring at altitudes above 5 to 6 km may contain a mixture of supercooled water droplets and ice crystals. The altocumulus and altostratus clouds may spread out to several kilometres horizontally.

1.3.3 High-level clouds

The most common high-level clouds are cirrus clouds, which are either formed in situ or through the outflow of deep convective clouds (anvils of cumulonimbus or remnants of deep convective precipitating clouds). A large fraction of these clouds are optically and physically thin and are referred to as semitransparent cirrus clouds [e.g., *Wang et al.*, 1996; *Dessler and Yang*, 2003; *Meenu et al.*, 2011]. The visible band COD may vary from <0.01 (ultra-thin cirrus) to >10 (thick cirrus). In most of the cases, the horizontal dimension of cirrus clouds far exceeds their thickness and can be considered as a nearly homogeneous sheet of cloud. These cold clouds are mostly composed of ice crystals, though those having relatively low cloud base (e.g., at 8 km) may contain supercooled water droplets as well [*Stith et al.*, 2002]. Cirrus clouds can have considerably long lifetime (few hours to 2 days) compared to other clouds and hence can spread to large distances. Advection of cirrus clouds originating from deep convective outflows are very frequent and often dominate the total cloud occurrence [*Sathiyamoorthy et al.*, 2004; *Meenu et al.*, 2010, 2011]. Most of them are physically thin (<1 km) and the frequency of occurrence of cirrus clouds decrease with increase

in physical thickness [*SunilKumar et al.*, 2003; *Meenu et al.*, 2011].

1.3.4 Clouds with large vertical development

Under favourable conditions (moisture availability, lower-level convergence, upper-level divergence, atmospheric instability, and high value of convective available potential energy), clouds originating in the lower troposphere can develop vertically and extend upto near-tropopause. The Cumulonimbus (Cb) clouds are examples of this cloud type. If a cumulus congestus continues to grow vertically, it develops into a giant cumulonimbus cloud. Mesoscale convective systems (MCS) mainly comprise of these clouds [*Houze*, 2004]. Strong winds at the high altitudes can reshape the cloud top by flattening it into thin anvils, which is one of the major sources of cirrus generation. The deep convective clouds are generally mixed phase clouds with lower part (below 5 km in tropics) in liquid phase, middle part composed of a mixture of supercooled water droplets and ice crystals and the upper part (>8 km) almost completely in ice phase. These clouds play a crucial role in the upward transport of energy and moisture from the surface to the upper troposphere and latent heating of the atmosphere. They result in the lifting of convective tropopause and significantly modulate the characteristics of the tropical tropopause layer (TTL). They are also important in the global electrical circuit [*Siingh et al.*, 2007].

1.3.5 Other cloud types

In addition to the above there are a large number of cloud types which are subgroups or variants of the above cloud types. Examples of this include (i) 'Fractus clouds' which are ragged stratiform or cumuliform clouds that are normally unattached to large thunderstorms, (ii) Mammatus, which droop underside of a cumulonimbus cloud in its latter stage of development. (iii) Shelf Cloud which are low-level wedge-shaped clouds associated with the leading edge of a thunderstorm outflow or gust front, (iv) Hole-Punch Clouds which are usually formed when the cloud temperature is below freezing but the water has not frozen. They occur when part of the water starts to freeze and begin to descend, leaving a rounded hole in the cloud. Another important cloud type is the anthropogenically produced contrails, which are the narrow, elongated clouds formed as jet aircraft exhaust condenses in cold air at high altitudes.

1.3.6 Cloud classification using satellite observations

Mesoscale and synoptic features of clouds are well discernible in passive satellite remote sensing. However, the passive observations in the visible and IR spectral bands are biased towards the cloud top altitude as these satellites detect only the radiation

emitted or reflected from the cloud top. In such observations, clouds are conventionally classified into low, middle- or high-level clouds by applying threshold criteria on the cloud top brightness temperature (CTBT) as summarized elsewhere [*Nakazawa*, 1988; *Fu et al.*, 1990; *Lau et al.*, 1991; *Mapes and Houze*, 1993; *Machado et al.*, 1998; *Roca et al.*, 2002; *Zuidema*, 2003; *Meenu et al.*, 2007, 2010]. Though different authors follow different criteria and threshold, overall they are somewhat consistent [*Meenu et al.*, 2010]. For example, *Roca et al.* [2002] identified the cloudy pixels with CTBT>275 K as low level clouds, 245⩽CTBT<275 K as middle-level clouds and CTBT<245K as high-level clouds. *Mapes and Houze* [1993] classified the clouds as very cold and moderately cold if their CTBT are less than the threshold values of 208 K and 235 K respectively.

The International Satellite Cloud Climatology Project (ISCCP) has evolved a similar scheme for the classification of clouds into different altitude groups and types based on the cloud top pressure and cloud optical depth [*Rossow and Schiffer*, 1999], as shown in Figure 1.2. In this scheme, the low, middle and high-level clouds have cloud top in the pressure band of 1000 to 680 hPa, 680 to 440 hPa and 440 to 50 hPa respectively. The cloud types are identified on the basis of COD (derived from cloud reflectance in the visible band). Relatively thin clouds with COD<3.6 are classified as cumulus, altocumulus or cirrus clouds. Those with COD in the range of 3.6 to 23 are classified as stratocumulus, altostratus or cirrostratus, while the optically dense clouds (COD>23) are classified as stratus, nimbostratus, or deep convective clouds.

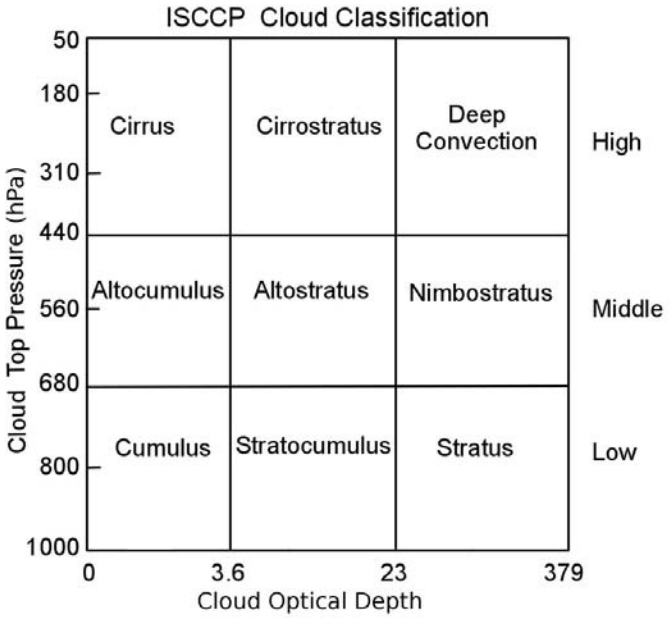

Figure 1.2: ISCCP classification of clouds using cloud top pressure and cloud optical depth.

1.4 Microphysical and optical properties of clouds

The physical (e.g., amount, altitude of occurrence, thickness), microphysical (e.g., droplet size distribution, phase, cloud water content) and radiative (e.g., reflectance, emissivity, optical depth) properties of clouds regulate their impact on the energy budget and hydrological cycle as well as the cloud feedback processes. Some of the above parameters are inter-related. For the warm (water) clouds, the cloud droplet size distribution can be assumed to follow a Gamma distribution given by *Deirmendjian* [1969]

$$n(r) = Nar^{\gamma}exp(-Gr^{\gamma}) \tag{1.5}$$

where,

$$G = \frac{\alpha}{\gamma.r_{mod}^{\gamma}} \tag{1.6}$$

N is the total droplet number density in cm^{-3}, 'r' is the droplet radius, and r_{mod} is the mode radius of the droplets expressed in micrometers. The constants α and γ describe the slope of the size distribution, and 'a' is a normalization constant for ensuring that the integral of the size distribution over all radii yields N. In general, the size distribution of stratus cloud droplets is broader than that of cumulus, but they contain fewer droplets per volume than cumulus clouds. Clouds over the oceans tend to have broader distributions than clouds over the continents, and polluted clouds contain more but smaller droplets than clean ones. The model values of the parameters defining the Gamma distribution for cumulus and stratus clouds over continent and maritime under clean and polluted conditions are given in *Hess et al.* [1998]. Typical values of r_{mod} are ~10.4 μm for marine cumulus, 3.5 to 4.8 μm for continental cumulus, ~4.7 μm for continental stratus and ~6.7 μm for marine stratus [*Hess et al.*, 1998]. Typical mode radius of fog is ~8 μm. The difference between the mode radii of cloud droplets over ocean and continental regions are mainly caused by the relatively larger number of CCN concentration over continents (indirect effect of aerosols).

In general, the size of warm cloud droplets vary from a few micrometers to 100 μm, with typical average droplet diameter in the range of 10-20 μm. In general, the frequency distribution of stratus clouds peaks in the size range of 10 to 14 μm. In general, droplet spectra are wider for orographic clouds, less wide for stratus and rather narrow for cumulus clouds [*Seinfeld and Pandis*, 1997; *Hess et al.*, 1998]. The altostratus and altocumulus clouds have relatively larger droplet sizes compared to stratus and cumulus clouds. Using airborne sampling of tropical convective clouds, *Stith et al.* [2002] showed that the strength of convection is a major factor in determining the microphysical characteristics of droplets. Stronger updrafts (>5 ms^{-1}) contained smaller droplets or ice particles at the cloud mid-level than in the regions with weaker updrafts.

The liquid water content of clouds (LWC) varies from almost zero during the cloud formation to reach a maximum during the mature stage of the cloud and decreases to zero during cloud evaporation. In general, the LWC increases with altitude up to the upper half of the cloud and decreases towards the cloud top [*Pruppacher and Klett*, 1980]. Typical values of LWC in clouds vary in the range of approximately 0.05 to 3 gm^{-3}, with most of the values occurring in the region of 0.1 to 0.3 g m^{-3} [*Seinfeld and Pandis*, 1997]. The cloud water volume mixing ratio (defined as the volume of water/volume of air in the cloud) typically ranges from 5×10^{-8} to 3×10^{-6} (in m^3/ m^3). The cloud optical depth is larger for clouds having large LWC and varies over a very wide range from <0.1 (e.g., thin cirrus clouds) to >50 (e.g., nimbostratus, cumulonimbus). The typical range of COD for different cloud types are given in Figure 1.2. Liquid water path (LWP) in a cloud is the integral of LWC over the vertical column from the base to top of the cloud. Assuming a constant vertical distribution of LWC within a cloud, the relationship between the LWP and COD can be approximated as:

$$COD = \frac{3}{2}\frac{LWP}{\rho_{LW} R_{eff}} \tag{1.7}$$

where ρ_{LW} is the density of liquid water and R_{eff} is the effective radius of the cloud droplets in a cloud. Typical value of LWP is ~100 $gm.m^{-2}$ for COD=10 and R_{eff}=14 μm. Obviously, cumulonimbus clouds have the largest values of LWP. As the transmittance of clouds increases exponentially with COD, the longwave and shortwave radiative fluxes are very sensitive to small perturbations of LWP when the LWP is small (typically <100 $gm.m^{-2}$) [*Turner et al.*, 2007].

Cloud albedo depends on the droplet size distribution, COD, cloud phase and solar zenith angle and varies over a very wide range from <5% (for thin semitransparent cirrus clouds) to >60% for the thick high-altitude cirrus clouds. In general, cloud albedo is larger for high solar zenith angle compared to the zenith. This is especially the case with cirrus clouds having planar crystals whose principal axis is aligned horizontally. On average, the single scattering albedo (the ratio of scattering coefficient to extinction coefficient) of all cloud types are close to unity in the visible and near-IR wavelengths below 1.3 μm and decreases with further increase in wavelength. The value of single scattering albedo is quite low (<0.6 for water clouds and <0.8 for cirrus) at the wavelength bands centered around 3 μm and 6 μm where the absorption of radiation by water is strong. The lowest values of single scattering albedo (generally <0.4 for both water clouds and cirrus) are observed in the thermal IR bands, especially between 11 μm and 40 μm. The asymmetry factor varies spectrally and the spectral variation depends on the droplet size. It is generally in the range of 0.8 to 0.95 below the wavelength of ~10 μm and decreases with further increase in wavelength.

1.4.1 Properties of Cirrus clouds

Cirrus clouds constitute the largest fraction of tropical clouds [*Wang et al.*, 1996; *Meenu et al.*, 2011]. They are distinctly different from the other clouds in terms of the horizontal extent, cloud phase, and impact on the energetics and hydrological cycle. They are non-precipitating and are made predominantly or wholly of ice crystals. A series of in situ measurements of the microphysical properties of cirrus clouds [e.g., *Heymsfield and Knollenberg*, 1972; *Turner and Radke*, 1973; *Heymsfield*, 1975] showed that the predominant ice crystal types are poly crystalline bullet rosettes, single bullets, banded columns and plates. The particle size, shape and concentration vary with temperature. The number size distribution of ice crystals is found to maximize in the lower size range (of <50 μm) followed by an exponential decrease with increase in size. However, these crystals can have sizes up to ~1000 μm in one dimension. The size distribution of ice crystals in cirrus clouds is different from that for the water droplets in warm clouds. The analytical function defining the ice crystal size distribution is given by [*Heymsfield and Platt*, 1984; *Hess et al.*, 1998]:

$$\frac{dN}{dx} = N f a_1 x^{b_1} I \tag{1.8}$$

where 'x' is the maximum dimension (e.g., length in columnar crystals), dN is the number density of ice crystals within the size interval of 'dx' the maximum dimension of the ice crystals, 'I' the ice water content, 'f' is a normalization factor (Strauss et al. 1997) and a_1 and b_1 are temperature dependent constants. The ice water content is typically less than 0.02 g/m^3. In general, the effective size of ice crystals is considerably larger than that of the water droplets. The effective crystal size is typically ~91 μm at -25°C and ~57 μm at -50°C [*Hess et al.*, 1998].

It is hypothesized that the cylinder shaped ice crystals fall with their long axes horizontal [*Liou*, 1986] which has important implications on the reflectance of the clouds. Investigations using polarization lidar signals showed that the ice crystals at -15°C are predominantly plates oriented horizontally [*Platt*, 1978]. These ice crystals generally have a basic hexagonal structure. *Jensen et al.* [2009] showed that the concentrations of tiny ice crystals in tropical anvil cirrus are considerably smaller than those inferred from earlier measurements. Ice crystal concentrations in fresh anvil cirrus may often exceed 1 cm^{-3} and are observed to exceed 10 cm^{-3} in turrets. In aged anvils, it is typically 0.1 cm^{-3} and rarely exceeds 1 cm^{-3}. Ice crystal size distribution of sub-visible cirrus in the tropical upper troposphere exhibits a pronounced peak at ~10 μm with ice crystal number concentrations ranging between 0.04 and 0.87 cm^{-3} [*Thomas*, 2002]. Observations of sub-visible cirrus layers over the tropical central Pacific showed a typical ice water content between 10^{-6} and 10^{-4} g m^{-3} and maximum ice crystal sizes of 30 to 140 μm [*McFarquhar et al.*, 2000]. Aircraft observations in the upper

tropospheric cirrus showed the prominence of ice crystals (plates and columns) with sizes up to 50 μm at temperatures of -83°C [*Heymsfield*, 1986]. In situ measurements of ice crystal size distribution in the tropical troposphere and lower stratosphere (on-board the high-altitude research aircraft M55 'Geophysica') over Darwin, Australia showed the presence of large ice crystals, with a maximum size up to 400 μm, in the lower stratosphere up to 1.4 km above the local tropopause [*de Reus et al.*, 2009]. The effective size of the ice particles decreased from ∼100 μm at about 10 km, to ∼3 μm at the tropopause, while the ice water content decreased from 0.04 to 10^{-5} gm^{-3}.

In general, COD of cirrus clouds range from <0.01 (ultra-thin cirrus) to >3. Among all cirrus types, the anvil clouds produced by deep convective outflows generally have the largest COD, while those produced in situ have the least COD. A substantial fraction of these clouds are semitransparent (COD<1) to the shortwave and longwave radiations. Ultra-thin cirrus clouds characterized by very low optical depth (typically <0.01) and low ice crystal number concentration (0.05 cm^{-3}) are observed just below the tropical tropopause. These ultra-thin tropical tropospheric clouds may exist for many hours as a cloud layer of 200 to 300 m thick covering thousands of square kilometres area [*Peter et al.*, 2003; *Sunilkumar et al.*, 2010; *Meenu et al.*, 2011]. In situ and remote sensing measurements are also used to parameterize the radiative and optical properties of cirrus clouds as a function of temperature [e.g., *SunilKumar et al.*, 2003]. CALIPSO and in situ observations show the occurrence of thin cirrus clouds even above the cold point tropopause. Using CALIPSO data, *Meenu et al.* [2011] showed that the occurrence of semitransparent cirrus within 1 km below the cold point tropopause is >30% while that above the cold point tropopause is ∼3 to 6% over the north Bay of Bengal during the Asian summer monsoon season; most of these clouds were sub-visible type with COD <0.03. Based on the spatial variations of cirrus properties, *Meenu et al.* [2011] proposed that the presence of high-altitude clouds below the cirrus clouds reduces their dissipation rate resulting in their longer lifetime (∼1 to 2 days).

1.5 Measurement techniques for deriving cloud properties

Both in situ and remote sensing techniques are used for measuring or estimating the cloud properties. Laboratory studies on cloud microphysics and aerosol-cloud interaction are being extensively carried out using Cloud chamber [*Pradeep Kumar et al.*, 2003; *Jish Prakash and Pradeep Kumar*, 2010]. Though the remote sensing techniques are used more extensively and provide the cloud properties on a regional and global scale, highly accurate measurements of the microphysical properties of clouds require in situ techniques, especially using aircrafts and balloons. Accurate measurements of

some of the cloud properties such as shape and aspect ratio of ice crystals as well as the number densities of aerosols, CCNs, and droplets within a cloud can be obtained only through in situ measurements [e.g., *Pandithurai et al.*, 2012]. In situ observations are also essential for validating the cloud microphysical properties estimated using remote sensing data. Major limitations of the in situ measurements of clouds are: (i) they are highly limited in space and time and hence cannot provide the regional or global characteristics, (ii) have only limited access to deep convective clouds, and (iii) they are cost intensive. In contrast, the satellites can provide very frequent observations of cloud properties (though not all the properties) regionally and globally. Further, the satellite data can be used for investigating the cloud properties during a past unplanned event. However, apriori knowledge of some of the cloud parameters is essential for inversion of the satellite remote sensing data for retrieving cloud properties. Both in situ observations and satellite measurements have their inherent errors, limitations and advantages and an optimal usage of these multi-platform observations are essential for the accurate estimation of the cloud parameters. Some of the in situ and remote sensing techniques used for measuring the cloud properties are summarized below.

1.5.1 Visual observations

The oldest and longest records of clouds are available through visual observations at several geographical locations. The cloud cover (usually as multiples of 1/8) and cloud type (based on their appearance) are regularly recorded as part with the visual meteorological observations at fixed time intervals of the day at the meteorological observatories worldwide. Over the oceanic regions, ship-based visual observations provide vital information on cloud cover and cloud type [*Hahn et al.*, 1996; *Pincus et al.*, 1999], though they are highly limited in space and time [e.g., *Grossman and Garcia*, 1990]. Surface-based visual observations have the advantage of obtaining reliable information on the cloud types and sometimes, the multilayer of clouds present. Usually, the surface observations are biased towards the lower level clouds, since the upper level cloud information cannot be obtained when overcast low altitude clouds are present. Though the accuracy of these observations is not very high, they provide vital information required for the validation of the satellite derived cloud amount [e.g., *Rossow and Schiffer*, 1999].

1.5.2 In situ measurements

The microphysical properties of clouds and droplet size distribution can be reliably measured in situ using instruments mounted on aircrafts and balloons. Experimental campaigns using airborne sensors for the measurement of cloud microphysical properties and thermodynamic environment are carried out in several parts of the world

[e.g., *Pandithurai et al.*, 2012], which are generally focused on measurement of CCN and aerosol concentrations, cloud droplet size distribution, liquid/ice water content and droplet/ice crystal images. The CCN Counter samples aerosols from outside the aircraft to measure their potential to act as CCN. In this system, the air sample is introduced in the CCN chamber at the top of a vertical cylindrical column and is surrounded by an aerosol-free humidified uniform supersaturation flow environment. As the air sample flows through the chamber, the CCN gets activated in response to the exposed supersaturation and grow to droplets. An optical particle counter at the base or outlet of the chamber detects all the droplets with diameters larger than ∼0.5 μm, providing the number concentration of CCN. The number of cloud droplets at different size ranges, typically between 2 to 50 μm, can be measured using Cloud Droplet Probe (CDP), in which the air collected through the inlet is passed through a laser beam; the cloud droplets that hit the beam scatters light and are detected and counted. The Forward Scattering Spectrometer Probes (FSSP), which measures the light scattered from droplets and retrieve their sizes using Mie scattering theory, are used to determine the size distribution of particulates with sizes ranging from ∼2 to ∼47 μm. The Cloud Imaging Probe (CIP) is used to image the cloud particle over a large size range of ∼10 μm to >1500 μm and consists of a linear array of laser beams focused on a sampling area where the shadows of the particles are recorded through imagers. Cloud liquid water content (LWC) can be determined using King Hot Wire Probe [*Gerber et al.*, 1994; *Lin et al.*, 2001]. However, the sensitivity of these probes decreases for large cloud droplets, typically above the size of ∼45 μm [*Lin et al.*, 2001]. The liquid water path (LWP) is derived by integrating the measured LWC. Overall uncertainties of the above measurements is <30% for thin clouds and <10% for thicker clouds [*Lin et al.*, 2001].

Aircraft-based instruments have also been used to measure the properties and concentrations of ice crystals in cirrus clouds in the UTLS region [e.g., *Knollenberg et al.*, 1993; *Heymsfield and McFarquhar*, 1996; *McFarquhar and Heymsfield*, 1996; *Baum et al.*, 2005; *Heymsfield*, 2007]. The high-altitude research aircraft M55 'Geophysica' have been used to probe even above the cold point tropopause [e.g., *de Reus et al.*, 2009]. In the lower end of the cirrus ice size spectrum (<50 μm diameter), the ice crystal size distributions are made using Forward-Scattering Spectrometer Probes. Counter-flow Virtual Impactors (CVIs) are used to infer ice crystal concentrations [*Ström et al.*, 1997]. These in situ measurements have been used to characterize the microphysical and radiative properties of tropical cirrus clouds [e.g., *Platt et al.*, 1989; *Knollenberg et al.*, 1993; *Garrett et al.*, 2005] as well as mid-latitude cirrus [e.g., *Ivanova et al.*, 2001; *Lawson et al.*, 2006]. However, in almost all the above measurements, speed of the aircraft produces artifacts due to shattering of large crystals [*Baum et al.*, 2005; *Jensen et al.*, 2009].

1.5.3 Ground based Lidar and Radar remote sensing of clouds

Detailed measurements of the structure and properties of clouds and their time evolution at a given location are best achieved using active remote sensing techniques employing lidar and radar. In the former, the range-resolved backscattered signal from a transmitted laser pulse (or laser beam, in the case of continuous wave lidar) is used to probe the cloud and aerosol properties. In most of the cases, the laser wavelength used in lidars for probing clouds and aerosols is in the visible or near-IR band (e.g., 532 nm and 1064 nm) and the backscattered lidar signal are primarily contributed by air molecules (Rayleigh scattering), aerosols and clouds (Mie scattering). Radar technique for probing clouds is the same as that for lidar, except that the wavelength used is quite larger (typically several millimeters or a few centimeters) so that the scattered signals are primarily contributed by cloud droplets through Rayleigh scattering and the contribution of aerosols and molecules are negligible. Hence, the lidar technique is ideal for probing optically thinner clouds (e.g., semitransparent cirrus, boundary layer clouds), while the radar techniques are best suited for probing optically thick and precipitating clouds. Both lidar and radar can be used in scanning mode (both elevation and azimuth) so that the spatial structure of clouds can also be derived from these measurements. Notwithstanding this, a majority of lidar systems are used only in the vertical probing mode.

1.5.3.1 Lidar remote sensing of clouds

Lidar systems used for cloud studies include: (i) single or multiwavelength backscatter lidars which determine cloud boundaries, cloud extinction coefficient profiles, and internal cloud structures; (ii) backscatter lidar with dual polarization capability which clearly discriminate ice clouds from water droplets; (iii) Raman or High Spectral Resolution Lidar, which provides intrinsically calibrated optical attenuation coefficient and optical depth data; and (iv) Differential Absorption Lidar, which characterizes particle backscattering and the water vapor density of the cirrus cloud environment. The backscattered lidar signals from clouds provide highly accurate estimates of the physical properties of relatively thin clouds and reasonably accurate estimates of their optical properties [*Sassen et al.*, 1989; *Dowling and Radke*, 1990; *Spinhirne and Hart*, 1990; *Sassen and Chow*, 1992; *Sassen and Campbell*, 2001; *SunilKumar et al.*, 2003; *Sunilkumar and Parameswaran*, 2005; *Seifert et al.*, 2007; *Nair et al.*, 2012]. Even the sub-visual clouds with optical depths <0.01 can be detected by the a sensitive lidar system. However, depending on the overall system sensitivity, the backscattered lidar signals from altitudes above the cloud base of optically dense clouds (especially with COD>1) can be attenuated considerably and may not be detected by the lidar. Lidars can also characterize the structural inhomogeneities present in cirrus [*Quante and*

Starr, 2002].

Measurement of the depolarized backscattered lidar signal provides a simple and reliable means for unambiguously discriminating between water and ice clouds through its ability to sense particle shape [*Sassen*, 2000]. The linear depolarization ratio observed using the dual polarization lidar is a function of non-sphericity of the scatterers [e.g., *Takano and Liou*, 1995; *Sassen*, 2000; *Mishra et al.*, 2010; *Rajeev et al.*, 2010]. The spherical droplets yield very small depolarization of the incident radiation while the large non-sphericity associated with ice crystals gives rise to significant depolarization. Thus, the linear depolarization ratio estimated from the co- and cross-polarized lidar returns can be used to identify the cloud phase. While the identification of the crystal structure would be difficult from the depolarization measurements, magnitude of the depolarization provide information on the relative sphericity of the particulates. Water vapor amount surrounding the cirrus can be determined using Raman lidar techniques and can reveal basic information on ice crystal nucleation processes in cirrus clouds [*Comstock*, 2004].

Ceilometer is a rugged but relatively less-sensitive lidar system, which is used to measure the profiles of multi-layer clouds (when the clouds are optically thin) and cloud base (for optically dense clouds) [*Varikoden et al.*, 2009]. They are increasingly being used at meteorological observatories and airports. Unlike the high-sensitive lidars, ceilometers are more rugged and used under all-weather conditions. However, the ceilometers (as well as other lidars) will not be able to provide the cloud information during precipitation as the transmitted laser beam and the backscattered signal get strongly attenuated by the rain drops.

Lidar observations of cirrus clouds have been carried out over many parts of the world, including the Indian region [*Sassen and Campbell*, 2001; *SunilKumar et al.*, 2003; *Parameswaran et al.*, 2003; *Sivakumar et al.*, 2003; *Sunilkumar and Parameswaran*, 2005; *Immler et al.*, 2007; *Nair et al.*, 2012]. Such studies are also important for validating and improving the satellite cloud algorithms and weather/climate model predictions. Extensive and long-term measurements of cirrus clouds were carried out at the Indian tropical station, Gadanki (13.5°N, 79.2°E) using a dual polarization lidar [*Bhavani Kumar et al.*, 2001; *Sivakumar et al.*, 2003; *Sunilkumar and Parameswaran*, 2005; *Thampi et al.*, 2012], which showed that cirrus clouds are generally observed in the altitude region of 10 to 18 km, with mid-cloud temperature in the range -85°C to -40°C and a mean cloud thickness in the range 0.7 to 1.7 km [e.g., *Sunilkumar and Parameswaran*, 2005]. The cloud thickness showed a tendency to decrease at lower temperatures while the cloud extinction and optical depth increased with increase in temperature.

1.5.3.2 Radar remote sensing of clouds

Optically thick clouds as well as the precipitating clouds are best studied using cloud radars. In general, the millimeter-wave cloud radars [*Moran et al.*, 1998] operates mostly in the vertical mode and at high frequency (typically at ∼35 or ∼94 GHz) and are capable of detecting tiny water droplets and ice crystals [*Hogan and Illingworth*, 2000]. Radars with still lower frequencies (e.g., ∼13 GHz) are used to probe precipitation. Although most meteorological radars lack the sensitivity to detect small cloud droplets (as they are operated at longer wavelengths), millimeter-wavelength cloud radars (MWCR) provide opportunities for remotely monitoring the properties of non-precipitating clouds. It measures the range-resolved radar reflectivity (typically over a dynamic range of approximately -50 to +20 dBZ) of the atmosphere, which is used to identify the structure of the clouds and estimate the cloud microphysical properties such as such as droplet size (effective radius) and water content. Most of them are also equipped with Doppler measurement capability and can be used to determine the velocities of the cloud particles [e.g., *Clothiaux et al.*, 1999]. Conversion of the radar reflectivity into cloud and precipitation properties requires the development of relationships connecting the measured parameters with the desired quantities. This is done through theoretical analysis, modeling, or empirical relationships. The cloud reflectivity observed by MMCR is a function of cloud liquid water content (LWC) and effective radius of the droplet. Empirical relationships connecting these parameters are derived based on aircraft measurements [*Fox and Illingworth*, 1997]. The effective droplet diameter can be estimated from radar reflectivity by assuming the number concentration of the cloud droplets.

Coincident 35- and 94- GHz radars can be used to measure ice crystals of larger sizes (typically >100 μm) in cirrus clouds [*Hogan and Illingworth*, 2000]. In the presence of larger crystals, the 94-GHz radar scatters sufficiently beyond the Rayleigh regime, so that the difference in reflectivity factor measured by the two can be directly related to size. This enables more accurate estimation of ice water content than that would have been possible using single radar [*Hogan and Illingworth*, 2000]. Combined airborne and ground-based 94 GHz radar measurements could be used to estimate the extinction and rain rate in precipitation [*Li et al.*, 1999].

Hybrid techniques that combine lidar with millimeter-wave radar or radiometer measurements are also being used to derive the visible and infrared optical depths, the most popular among them being the combined lidar and mid-IR radiometer (LIRAD) [*Platt*, 1973; *Platt et al.*, 1987; *Comstock and Sassen*, 2001] and combined lidar-radar-radiometer methods, which can characterize the basic cloud type also [*Wang and Sassen*, 2001]. The LIRAD method uses the downwelling radiation in the atmospheric window (after corrections for propagation losses and gaseous emissions), lidar-measured

cloud heights and integrated backscatter for deriving the infrared emittance and improved estimates of visible cloud optical depth. The LIRAD method also allows the estimation of path-integrated infrared emittance.

1.6 Satellite remote sensing techniques of clouds

Spatial coverage of the above techniques employing in situ measurements or ground-based remote sensing techniques is rather limited. In contrast, satellite measurements of the radiation reflected or emitted from the earth-atmosphere system provides a highly potential tool for determining cloud properties on a regional or global scale. The satellite remote sensing techniques can be broadly divided into two groups: (i) passive and (ii) active. Passive remote sensing makes use of sensors that measure the scattered, reflected or emitted electro-magnetic radiation from natural sources. Detection of solar radiation reflected from the earth-atmosphere system or the IR radiation emitted by the earth's surface, atmospheric constituents or clouds are examples of this technique. The radiance observed by a passive radiometer will be the total radiance from a column atmosphere and the surface (with varying contribution from the earth's surface and/or atmospheric levels). In contrast, the active satellite remote sensing employs a radiation source onboard the satellite as the transmitter (instead of the natural source such as the Sun) and detects the backscattered or reflected radiation from this source by the earth-atmosphere system. Spaceborne radars and lidars are examples of this category. Main advantage of the active remote sensing technique is that the range-resolved backscattered signal detected can provide the altitude profiles of clouds (or other factors such as aerosols) with very high vertical resolution spanning typically from a few tens to a few hundred meters. In general, the hardware realization of the active remote sensing satellites is more complex compared to the passive technique.

The spatial resolutions, area of coverage, and repetivity of both active and passive satellite observations depend on the satellite platform and payload characteristics. A radiometric imager onboard a geostationary satellite can provide the regional observations over a wide region around the sub-satellite point (typically over a latitude-longitude region of $\pm 45^{\circ}$ around the sub-satellite point) with a repetivity of $\sim$30 minutes, while a payload with wide swath onboard a polar orbiting Sun-synchronous satellite can provide global observations of clouds twice in a day (separated by 12 hours) at the same local time. At high latitudes, the frequency of observation by the polar orbiting satellite can be larger due to the overlapping swath of adjacent orbits. A low inclination satellite can provide more frequent observations of the tropics, but cannot observe the high-latitudes. Because of the relatively lower altitude of the polar orbiting satellites (typically 850 km) compared to that of the geostationary satellites ($\sim$36000 km), the spatial resolution (in the visible and IR bands) of the former are

relatively better (typically 250 m to 1 km) than the latter (typically 2 to 8 km). Swath, number of pixels in a scan line and spatial resolution are also limited by the earth's curvature (leading to poorer spatial resolution away from the sub-satellite point), onboard data storage capacity and the down-linking communication speed between the satellite and the ground station (for data reception of the satellite). The active sensors also can be of scanning type (e.g., Scatterometer onboard QuikScat) or non-scanning type (e.g., Cloud Profiling Radar onboard CloudSat). The horizontal coverage and repetivity of observations over a given location in the latter case are highly limited.

1.6.1 Passive remote sensing of clouds

Operational passive satellite remote sensing technique for cloud studies has a history of more than three decades and is one of the most effective methods used for the systematic long-term observations of regional and global distribution of clouds with high spatial resolution. Several satellite payloads have been flown with detector systems for measuring the radiance in the spectral bands in Visible (VIS), near-IR (NIR), Mid-IR, thermal IR (TIR) and Microwave part of the of the electromagnetic spectrum. While the observations in the visible and near-IR spectral bands provide information on cloud albedo (which can also be inverted to cloud optical depth and effective droplet size), the brightness temperatures derived from the thermal IR observations provide information on the cloud top altitude (this can also be used to estimate the outgoing longwave radiation). Clouds are clearly identifiable from these data as their reflectance in the visible band is generally larger than that of the Earth's surface (particularly outside the sun-glint regions and ice-covered surfaces) and does not show significant spectral dependence in the visible and near-IR bands. More importantly, clouds are colder than the earth's surface and the cloud top temperature decreases with altitude of their occurrence. These characteristics are used in the passive remote sensing to detect clouds and measure their properties. Passive microwave radiometers provide a suitable platform for determining cloud liquid water content, but generally with a coarser spatial resolution than that could be detected by the visible and IR radiometers [e.g., *Puranik and Karekar*, 2006]. Satellite observed microwave radiance combined with visible and IR radiances are used to retrieve precipitation information over many parts of the world, particularly over the oceans [e.g., *Kummerow*, 1998; *Lin et al.*, 1998; *Masunaga*, 2002].

1.6.1.1 Radiometric imagers onboard polar orbiting Sun-synchronous satellites

The National Oceanic and Atmospheric Administration Polar Orbiting Environmental Satellites Series (NOAA-POES) provides the longest set of global observations

of clouds, spanning for more than three decades. The Advanced Very High resolution Radiometer (AVHRR) onboard the NOAA-POES observe the earth-atmosphere system in the visible, near-IR and thermal IR bands. The NOAA-AVHRR has a pixel resolution of 1.1 km at nadir and a swath of approximately 2900 km. The earlier version of AVHRR had 4 spectral channels (VIS, near-IR, Mid-IR and TIR), while an additional channel was added in the TIR band in the later versions (AVHRR/2 and AVHRR/3). In AVHRR/3, a new channel is added in the shortwave IR at the wavelength of ∼1.6 μm. The spectral bands of NOAA-AVHRR are suitable for studying clouds. The most important advantage of NOAA-AVHRR is the continuity of the spectral channels for the series of satellites and the highly systematic updating of the post-launch calibration coefficients, which make the AVHRR data suitable for the climate change research and long-term analysis of clouds. The NOAA-POES usually will have a minimum of 2 satellites in orbit; one having an equatorial crossing time around 1:30 AM/PM and the other around 7:30 AM/PM. These two satellites provide at least 4 observations everyday over any location in the world. More details of the NOAA-AVHRR is given in Chapter 2.

The Moderate Resolution Imaging Spactroradiometer (MODIS) flown onboard the polar Sun-synchronous satellites, Terra (equatorial crossing time ∼10:30 AM/PM) and Aqua (equatorial crossing time ∼01:30PM/AM) is another example of a resourceful payload that provide well-calibrated multi-spectral observations of clouds. It has 36 spectral channels (in the spectral band of 0.405 to 14.385 μm). The horizontal resolution at nadir is 0.250 to 1 km (varies with spectral channels) and swath width is 2330 km. Repeativity of the observations in every 1 to 2 days. In addition to the conventional analysis of clouds, MODIS has the potential to identify the overlapping water clouds [*Chang and Li*, 2005] by combining the data from MODIS CO_2-slicing channels and the visible (0.65 μm) and IR (11 μm) channels. Further, MODIS has a channel at 1.375 μm, which is specifically designed to detect thin cirrus clouds with COD as low as 0.02 [*Dessler and Yang*, 2003]. The spectral radiance data from MODIS data can also be used to derive cloud parameters (cloud top temperature, albedo, effective droplet size, COD).

Multispecrtral data obtained from Atmospheric Infrared Sounder (AIRS) are also being used extensively for deriving the cloud physical and microphysical properties [e.g., *Bréon and Doutriaux-Boucher*, 2005; *Li et al.*, 2005; *Yue and Liou*, 2009]. The AIRS is a cross-track scanning instrument with a swath of ∼1600 km. It mainly consists of an IR spectrometer operating in the wavelength range of 3.7 to 15.4 μm with a total number of 2378 spectral channels. The spatial resolution in this spectral band is 13.5 km at nadir. AIRS also makes observations in 4 spectral bands in the visible and near-IR band, which has a spatial resolution of 2.3 km at nadir. The VIS and

NIR channels provide a diagnostic imaging capability for observing low-level clouds. The term 'sounder' in the instrument's name refers to the fact that temperature and water vapor can be derived as functions of altitude. Thick clouds block the infrared radiation from the sub-cloud layers and surface. However, by combining with the microwave instruments onboard other satellites (e.g., Aqua), the AIRS provide highly accurate measurements in most of the cloud conditions. The AIRS retrieval consists of cloud and surface properties, and altitude profiles of retrieved temperature, water vapor, ozone, carbon monoxide and methane. The AIRS data has the potential to detect even very thin cirrus clouds. The retrieved temperature profile consists of the temperature at 24 vertical levels between 1000 hPa and 1 hPa, while the moisture profile consists of 14 atmospheric layers between 1000 hPa and 50 hPa. The horizontal resolution of the retrieval is 50 km.

1.6.1.2 Radiometric imagers onboard geostationary satellites

In contrast to the temporally limited observations of clouds using the polar orbiting satellites, the geostationary satellites can observe a wide region almost continuously with high repetition rate of <30 minutes. Such near-continuous observations are essential for investigating the life cycle of mesoscale convective systems and cyclones, and diurnal evolution of clouds. However, because of the large distance from the earth, the spatial resolution of geostationary observations is rather poor compared to the polar orbiting satellites, especially in the thermal IR bands. For example, the spatial resolution of Kalpana-1-VHRR data is 2 km in visible and 8 km in the thermal IR at nadir. (The visible and near-IR band data observed using the CCD camera onboard INSAT has a resolution of ∼1 km at nadir. However, thermal IR band measurements are not carried out using these CCDs). Similarly, the pixel resolution of METEOSAT data is 5 km at nadir. Because of this, small sub-pixel level clouds having scale sizes considerably smaller than the pixel size may not be detected.

The Very High Resolution Radiometer (VHRR) onboard the Indian geostationary satellites in the INSAT series (including INSAT-1A, -1B, -1C, -1D, INSAT-2A, -2B , -2E , Kalpana-1, INSAT-3A) observe the earth-atmosphere system in the visible and IR bands, providing long-term data since the end of 1983. In addition to the visible (0.55 to 0.75 μm) and thermal IR bands (at 10.5 to 12.5 μm), the VHRR onboard Kalpana-1, INSAT-2E and INSAT-3A also has a channel in the water vapor absorption band of 5.7 to 7.1 μm, which has the potential to identify upper tropospheric humidity and optically thin cirrus clouds [e.g., *Rajeev et al.*, 2008; *Sunilkumar et al.*, 2010]. Among this, the INSAT-1B data has been extensively used by the world scientific community for cloud studies during January 1988 to March 1989 [e.g., *Bony et al.*, 2000; *Rajeevan and Srinivasan*, 2000; *Roca and Ramanathan*, 2000; *Gambheer and Bhat*, 2000, 2001]

and was also used in ISCCP (April 1988 to March 1989).

The INSAT-3D consists an imager and a sounder and is scheduled for launch during the second half of 2013. The INSAT-3D-Imager makes observations in the visible, near-IR and thermal IR at six spectral bands (Ch1: 0.55–0.75 μm; Ch2: 1.55–1.70 μm; Ch3: 3.7–3.95 μm; Ch4: 6.50–7.10 μm; Ch5: 10.2–11.3 μm; Ch6: 11.5–12.5 μm). Spatial resolution of Ch1 and 2 is 1 km, Ch3, 5, 6 is 4 km, and Ch4 is 8 km. Radiometric resolution of these channels is 10 bits. The sounder consists of 19 spectral bands (18 in the mid- to thermal IR spectral band of 3.74 to 14.71 μm and one in the visible band at 0.69 μm). Spatial resolution is 10 km at nadir and the radiometric resolution is 14 bits for all the sounder channels. While the imager provide information on clouds and surface properties (similar to that from Kalpana-1-VHRR and INSAT-VHRR), the INSAT-3D Sounder data can be inverted to derive the altitude profiles of temperature (typically at 40 levels in the altitude band of 1000 to 0.1 hPa) and humidity at 12 levels in the troposphere between 1000 and 100 hPa.

Geostationary satellites developed by the European Space Agency (ESA), METEOSAT, provide data over the African and European longitudes as well as over the Indian Ocean [METEOSAT-5, -6, -7]. In these satellites, the Earth is viewed in the visible, water vapor absorption band and thermal IR bands. The METEOSAT-5 satellite, moved to the Indian Ocean in 1998, provides observations over the Indian region since then [e.g., *Sèze and Pawlowska*, 2001]. The spectral bands of observations in METEOSAT are also similar to that of Kalpana-1-VHRR. Currently, the METEOSAT second generation (MSG) series is in operation, the first in the series being METEOSAT-8 launched in 2004. In addition to the main optical payload Spinning Enhanced Visible and Infrared Images (SEVIRI), METEOSAT-8 also carries a secondary payload, Geostationary Earth Radiation Budget (GERB) instrument. The Japanese Multifunctional Transport Satellites (MTSAT) provide coverage for the hemisphere centered on 140°E. They replace the Geostationary Meteorological Satellites (GMS) and provide imagery in five wavelength bands: one in visible and four in the infrared, including the water vapor channel. The visible band has a spatial resolution of 1 km while the IR channels have a resolution of 4 km at nadir. The Chinese FY-2 and FY-4 series are geostationary weather satellites which carry a 3-channel Visible and Infrared Spin Scan Radiometer (VISSR) observing the Earth in the visible/near-IR (0.55–1.05 μm), Thermal IR (10.5–12.5 μm) and WV (6.2–7.6 μm) channels with a nadir pixel resolution of 1.25 km in visible and 5 km in IR and WV channels. The subsatellite point of FY-2 is at 105°E over the equator. The Russian Geostationary Operational Meteorological Satellite (GOMS)/Elektro series placed over the Indian Ocean (∼76°E) has 3 spectral bands of observations: visible (0.46–0.7 μm), thermal IR (10.5–12.5 μm) and the WV band (6.0–7.0 μm). It has a nadir pixel resolution of 1.25 km in visible and 6.25 km in

IR.

The NOAA normally operates two meteorological satellites in geostationary orbit over the equator. Each satellite views almost one-third of the Earth's surface: one monitors North and South America and most of the Atlantic Ocean and the other monitors North America and the Pacific Ocean basin. The GOES-12 (or GOES-East) is positioned at 75°W longitude over the equator, while GOES-11 (or GOES-West) is positioned at 135°W longitude over the equator. Together, they cover the geographical region from ∼20°W longitude to ∼165°E longitude. The five channel GOES imager (0.55–0.75, 3.80–4.00, 6.50–7.00, 10.20–11.20, 11.50–12.50 μm) has a spatial resolution of 1 km in visible, 4 km in IR and 8 km in the water vapor absorption band (WV) of 6.50–7.00 μm.

1.6.1.3 Detection of clouds using passive radiometric imagers

Retrieval of cloud properties from satellite observations involve methods based on the relationships derived from radiative transfer theory [*Rossow et al.*, 1985]. First step in the analysis of satellite data for clouds is the identification of a pixel as clear, partially cloudy or fully cloudy. Cloud detection schemes differ primarily by whether they make use of radiance variation in wavelength, space or time [*Coakley and Bretherton*, 1982; *Rossow et al.*, 1985; *Rossow*, 1989; *Wielicki and Parker*, 1992; *Nair et al.*, 2005]. The common cloud detection methods include: (i) Radiance or Brightness temperature thresholds, (ii) Space contrast test applied to individual IR images, (iii) Time contrast test applied to consecutive IR images at constant time and (iv) Spatial coherence test. Details of the above tests are provided in *Rossow and Garder* [1993] and *Coakley and Bretherton* [1982].

The most widely used cloud detection technique employs radiance threshold [*Rossow*, 1989]. In this method, all pixels colder than a threshold value of brightness temperature are considered as cloudy. The threshold brightness temperature is determined based on a statistical analysis of the IR image data and can be fixed or varied in space and time. In the space contrast test, all pixels which are much colder than the warmest pixel in a small spatial domain are treated as cloudy. However, the warmest pixel remains unclassified. In the time contrast test, all pixels which have considerably lower brightness temperature compared to a day before or a day after (in the same diurnal phase) are classified as cloudy. In the spatial coherence test, the standard deviation of the brightness temperature of a 3×3 array of pixels is estimated and if this standard deviation is above a threshold value, the central pixel is classified as cloudy. This procedure is repeated for other pixels by shifting the array by one pixel. Cloud albedo has little spectral variation in the visible and near-IR band. This property also can be used to detect clouds since the spectral dependence of clear-sky pixels over ocean

and land is quite large. However, this method might fail over ice sheets and sunglint regions.

Detection of tiny and broken clouds which occupy only a small fraction of the pixel as well as the ultrathin cirrus clouds is a major challenge. Spatial coherence technique has the potential to detect the partially cloudy pixels, particularly over the oceans where the surface reflectance is fairly uniform [*Coakley and Bretherton*, 1982]. This principle is mainly based on the fact that the partially cloud-filled pixels will have larger pixel-to-pixel variability compared to overcast pixels. The brightness temperature observed in the water vapour band (∼6.3 μm) together with that in the thermal IR band has the potential to detect thin cirrus clouds [*Roca et al.*, 2002; *Rajeev et al.*, 2008; *Meenu et al.*, 2010; *Sunilkumar et al.*, 2010]. A comparison between the visible and near-IR reflectances observed at multiple wavelengths also can be used to identify thin cirrus clouds, since the absorption coefficients for ice and water are similar in the VIS band (0.7 μm) whereas it is different in certain wavelength bands in the near-IR spectral region [*Dessler and Yang*, 2003]. For example, at 1.68 μm or 1.37 μm, ice has large absorption compared to water. In practice, a combination of different cloud detection methods (employing all the simultaneous measurements from a given satellite) is essential for reliably detecting clouds. In general, the cloud detection over ocean is relatively more accurate compared to land due to the less spatial and temporal variabilities of the background surface features (temperature, emissivity and reflectance).

1.6.2 Solar occultation technique for the altitude profiling of cirrus clouds

A satellite orbiting around the Earth encounters a sunrise and a sunset in each orbit. It encounters a sunset when the spacecraft moves from the sunlit hemisphere to the dark side of the Earth. Solar occultation technique is a passive remote sensing technique in which the radiometer points towards the Sun and measures its intensity at different wavelength bands in the visible and near-IR during the solar occultation (sunrise and sunset time) [*Kent et al.*, 1995; *Wang et al.*, 1996]. The advantage of this technique is its capability to provide the altitude profiles of thin cirrus clouds in the upper troposphere and lower stratosphere. As the satellite descends or ascends during the occultation, the solar radiation reaching the radiometer pass through different atmospheric layers and get attenuated. Magnitude of this attenuation depends on the extinction coefficient of the atmosphere (contributed by aerosols, molecules and clouds). Thus, the altitude profiles of extinction coefficient can be derived from these observations using 'onion peeling method', assuming a horizontal stratification within the ray path.

As the path length that is traversed by the solar radiation through the atmosphere during the occultation is very large, even ultra-thin clouds can be detected using this method. The clouds and aerosols are discriminated using observations made at multiple spectral bands in the visible and near-IR, as the clouds do not show strong spectral dependence of extinction coefficient. The observations are also taken before (after) the actual solar occultation during the sunset (sunrise) which provide the calibration information for the detectors as the solar radiation does not enter the atmospheric medium during this period. The major disadvantages of this method are: (i) the path length is quite large that only average profiles over large spatial extent (typically 150 km) can be derived, (ii) the profiles are valid only when the horizontal variations of clouds and aerosols are negligible, (iii) it cannot be used for profiling the middle and lower troposphere as the spatial inhomogeniety and opacity are very large, and (iv) the profiles are not continuous in space and time and occurs at different geographical regions and local time (only about 28 to 32 profiles per day can be obtained by a polar orbiting satellite at different parts of the globe).

The solar occultation data from the Stratospheric Aerosol and Gas Experiments (SAGE-I, SAGE-II and SAGE-III) have provided the first observations of the altitude profiles of cirrus clouds on a global scale; as of now this data spans for about three decades [*Wang et al.*, 1996; *Kent et al.*, 1995]. The SAGE spacecraft orbits the Earth (in polar orbit) approximately once every 90 minutes (16 times/day), depending on orbital parameters. Each orbit provides two occultations: one for each sunset and one for each sunrise. The SAGE-II provides altitude profiles of extinction due to aerosols and thin clouds at wavelengths of 0.525 and 1.02 μm, above $\sim$8 km with an altitude resolution of 1 km. The SAGE-III, an improved version of SAGE-II, can provide the above observations at the wavelengths of 0.525, 1.020 and 1.55 μm, with an altitude resolution of 0.5 km. The lower altitude is practically limited by the presence of opaque clouds. Over the tropics, the lower altitude limit is mostly above 8 km because of the presence of thick clouds during most of the time. Wavelength dependence of the extinction due to aerosols differs from that of clouds and this feature is used as the basis for separating these two components [*Kent et al.*, 1995]. The SAGE observations have produced climatology of thin cirrus clouds over the globe [*Wang et al.*, 1996], which showed the predominance of cirrus clouds over the tropics, particularly around the deep convective areas.

1.6.3 Active remote sensing of clouds using satellites

Active remote sinsing techniques employing spaceborne lidars and radars can provide the altitude profiles of clouds and their spatial variations. Such observations using polar sun-synchronous satellites CloudSat and CALIPSO (Cloud-Aerosol Lidar and In-

frared Pathfinder Satellite Observation) have provided multi-year observations on the global 3-dimensional distribution of clouds with unprecedented vertical resolution [e.g., *Ellis et al.*, 2009; *Haladay and Stephens*, 2009; *Cetrone and Houze*, 2009; *Nair et al.*, 2011; *Rajeevan et al.*, 2012]. They are part of the 'A-Train' formation of Earth Observing satellites, which is a constellation of six satellites. All satellites in the 'A-Train' have the same orbital tracks with a 16-day repeating cycle, but the equatorial crossing time of the individual satellites differ by less than few minutes. This formation flying enables these satellites (having different payloads) to near-simultaneously observe different features of clouds and other geophysical parameters of the earth-atmosphere system at any location along the orbital track. Combined analysis of all these observations substantially enhances the potential of the observations from the individual satellites [*Mace et al.*, 2009].

CloudSat is a spaceborne radar, mainly indented to provide the altitude profiles of clouds at very high vertical and horizontal resolutions along the satellite track. It carries onboard the Cloud Profiling Radar (CPR) operating at 94-GHz in the nadir-looking mode [*Stephens et al.*, 2008]. The CPR detects the backscattered signal from the atmosphere (mainly clouds) as a function of distance from the radar and provides the altitude profile of clouds along the sub-satellite track with a vertical resolution of 480 m and horizontal resolution of 1.4 km in the cross-track direction and 1.7 km along the track. As the operating wavelength is 94 GHz, it mainly detects the Rayleigh scattered radiation from optically thick clouds and may not detect the weak signals from optically thin clouds (typically having COD$<$1). Observations on the vertical profiling of optically thick clouds are done for the first time. Main limitation of this system is that it provides data only along the sub-satellite track and hence the coverage across the orbital track is highly limited. Details of the CloudSat and potential of this data are presented in Chapter 2.

The CALIPSO is a spaceborne Lidar, which carries onboard the Cloud Aerosol Lidar with Orthogonal Polarization (CALIOP) and is primarily indented to provide the vertical profiles of aerosols and clouds. It inherits its scientific heritage and design from the Lidar In-space Technology Experiment [LITE, *Winker et al.*, 1996]. (LITE was flown on the Space Shuttle Discovery as part of the STS-64 mission between September 9 and September 20, 1994). The CALIOP is a dual wavelength (532 nm and 1064 nm) lidar with orthogonal polarization capability at 532 nm [*Winker et al.*, 2007], operated in a near-nadir viewing geometry. It has an Nd:YAG laser as transmitter that emits laser pulses at a PRF of 20 Hz at 532 nm and 1064 nm. The receiver comprises of a telescope having 1 m diameter and the range resolved orthogonal polarization components of the backscattered signal at 532 nm total backscattered intensity at 1064 nm are measured [*Winker et al.*, 2007]. The vertical resolution of the profile is $\leqslant$60 m below

the altitude of ∼20 km. Dual polarization observations provide the altitude profiles of depolarization ratio, which is a measure of the shape of the scatterer [*Rajeev et al.*, 2010; *Mishra et al.*, 2010]. The total backscattered intensity at 532 nm and 1064 nm are inverted to obtain the altitude profiles aerosol backscatter coefficient, cloud optical depth and colour ratio. CALIPSO can detect very thin clouds (mainly semitransparent cirrus, even with COD<0.01) and multiple cloud layers. Their detection capability is better during the night due to absence of background noise from solar radiation. However, as the backscattered lidar signal from the optically thick clouds cannot penetrate the cloud depth to reach the satellite, this instrument cannot provide complete information of such clouds. Main limitations of CALIPSO are: (i) the observations are limited to the sub-satellite track, (ii) cannot profile optically thick clouds due to the poor transmittance of such clouds. Details of CALIPSO are described in Chapter 2.

While CALIPSO mainly observes optically thin clouds, the CloudSat is more sensitive to optically thick clouds and may underestimate the optically thin clouds. Thus, the CALIPSO and CloudSat observations are complementary and can be used together to provide vertical cross section of all types of clouds [*Haladay and Stephens*, 2009]. However, the combined analysis of these two satellites is not straightforward due to the following reasons: (i) the foot-print size of CALIPSO at the Earth's surface is ∼70 m, which is significantly smaller than that for CloudSat (∼1.4 km), (ii) the scattering mechanisms and the cloud droplet size ranges that generate the backscattered signals in these two instruments are completely different and hence the cloud boundaries identified by them also can be different. (iii) any small changes in the sensor attitudes will lead to different areas of scanning (note that the foot print size of CALIPSO is only ∼70 m). Algorithm for the combined analysis of these two data sets, accounting for the above factors are developed at NASA and the CALIPSO data are used for identifying cloud features as part of the CloudSat analysis.

Data from the Geoscience Laser Altimeter System (GLAS) onboard the ICESat (Ice, Cloud and land Elevation Satellite), which was primarily indented to be used as an altimeter for geomorphological studies, can also determine the altitude profiles of aerosols and clouds on a global scale along the sub-satellite track. Similar to CALIPSO, it measures the backscattered lidar signal at 532 and 1064 nm, which are inverted to derive the aerosol and cloud characteristics [*Yang et al.*, 2008]. It does not have the dual polarization capability. GLAS operates at a PRF of 40 Hz. The ground track is ∼70 m 'spots' separated along-track by ∼170 m. The repeat cycle is 183 days, which is considerably larger than that of CALIPSO (16 days). However, the spacing between two adjacent tracks is only 15 km at equator, which is better than that for CALIPSO (∼160 km at the equator).

1.7 Satellite observations on radiation budget of the earth-atmosphere system

Observations on the spatio-temporal variations of the shortwave radiation reflected and the longwave radiation emitted from the earth-atmosphere system are essential for estimating the radiative impact of clouds on the earth-atmosphere system and the associated feedback processes. These measurements are best accomplished using well-calibrated broadband sensors onboard satellites. First of such measurements were carried out using the Earth Radiation Budget Experiment (ERBE) aboard the NOAA satellites [*Ramanathan et al.*, 1989; *Harrison et al.*, 1990] and was followed by several missions such as Earth Radiation Budget (ERB), CERES, ScaRaB, the latest in the category being the Megha-Tropiques-ScaRaB.

Ideally, a satellite dedicated for the measurement of earth radiation budget should make observations in the shortwave (0.2 to 4 μm) and longwave (4 to 100 μm) bands at high spatial resolution at different times of the day and for different Sun-earth-satellite geometry. Such satellites should also be equipped with sensors for observing the radiance at narrow spectral bands in the visible and thermal IR for the accurate detection of clouds, aerosols and surface features. Observations at different time of the day are required for estimating the diurnal variation of radiative fluxes at the TOA (note that the incoming solar radiation systematically changes during the day while the corresponding variations in cloud occurrence as well as the bi-directional cloud reflectance are not highly systematic). Observations at different viewing geometry are required for the development of angular distribution models (ADMs) for converting the observed shortwave radiances to shortwave fluxes at TOA. All the above satellites satisfy the essential requirement on the spectral bands of observations. However, majority of the above missions were flown onboard the Polar orbiting sun-synchronous satellites with observations limited to fixed time of the day/night. However, the CERES satellite onboard the Tropical Rainfall Measuring Mission (TRMM) and the ScaRaB onboard the Megha-Tropiques satellite have low orbital inclinations and make observations as a function of time. However, due to the low inclination of the above satellites, these observations are limited to the tropics. Further, these observations are not uniformly separated in local time over a given region, and hence data for a longer period is required for determining the 'equivalent' diurnal variation of radiative fluxes. On the contrary, the observations onboard the polar orbiting satellites are very regular, but at fixed time of the day.

The radiances at the TOA observed by the satellites should be converted to broadband fluxes. For shortwave flux, this is achieved by using the angular distribution models developed for different solar and satellite angles for different surface types and

cloud conditions [*Smith et al.*, 1986; *Suttles et al.*, 1988, 1989; *Wielicki et al.*, 1996]. Estimation of the longwave flux from the observed radiance is straightforward as it does not depend on the Sun-pixel geometry. The cloud radiative forcing is estimated by differencing the observed fluxes under all-sky conditions from that for the cloud-free condition at the same geographical location and local time (assuming all other atmospheric parameters are invariant). The estimates are done separately for the shortwave CRF (SWCRF) and longwave CRF (LWCRF). Sum of the SWCRF and LWCRF is the net CRF (NCRF). Details of the sensors, method of analysis and estimation of CRF are provided in Chapter 2.

1.8 Limitations of the satellite observations of clouds and radiation

Complexities involved in the satellite remote sensing of clouds and retrieval of the cloud parameters include: (i) Bias in time: Observations using polar orbiting sun-synchronous satellites take place at fixed local time of the day and hence represent the same diurnal phase. The diurnal variation of clouds cannot be studied using such observations. (ii) Under cloudy conditions, the radiation detected by a passive radiometric imager mostly originates from the cloud top. Hence these observations are biased towards the high-altitude clouds and the lower layer clouds would be underestimated. This problem can be solved using the active radiometric observations. (iii) When the cloud is optically thin, the radiation reaching the sensor (in the thermal IR, visible or near-IR) will have contribution from any cloud present below this cloud as well as from the earth's surface. Cloud properties estimated from such measurements will be erroneous as the individual contributions from these sources are unknown. However, these measurements in combination with passive radiometric observations made in the water vapour band ($\sim$6.3 μm) can detect even optically thin clouds. In general, the spaceborne lidars also do not suffer from this problem. (iv) Sub-pixel scale clouds may not be detected by the satellite sensor (when they are detected, their amount is overestimated as the clouds might not have filled the full pixel). This uncertainty increases with pixel size. (v) Periodically updated absolute post-launch calibration of the satellite sensor over long period of observations is essential for eliminating the biases in the retrieved cloud properties as well as radiation budget. (vi) Frequency of observation by the nadir-looking spaceborne lidar and radar observations (e.g., CALIPSO, CloudSat, ICESat) are rather poor in the cross-track direction. This is a major limitation compared to the passive radiometric images. (viii) Accuracy of most of the cloud properties and radiative forcing derived from satellite remote sensing data depend on the reliability of the parameters assumed in the inversion.

1.9 Atmospheric circulation and spatial distribution of clouds

1.9.1 Circulation features and clouds

Formation and distribution of clouds are primarily controlled by the atmospheric dynamics and moisture availability. A host of atmospheric and surface meteorological parameters affect cloud formation. On a mesoscale scale, this includes the surface temperature, availability and incursion of moisture, low-level vorticity and convergence of airmass, atmospheric instability, convective available potential energy, vertical wind shear and upper-level divergence. The mesoscale convection can also be modulated by the large-scale scale atmospheric circulation. In contrast, the synoptic scale cloud distributions are controlled by large-scale circulations and moisture transport rather than the local effects. Atmospheric waves (e.g., Rossby waves, easterly waves), large-scale oscillations (e.g., Madden-Julian Oscillation) as well as the development of the low-level vorticity to lows, depressions and cyclones by positive feedback processes under favourable conditions are among the dominant factors that regulate the synoptic-scale cloud distributions.

On a seasonal mean basis, the latitude variation of cloud distribution is closely linked with the general circulation of the atmosphere in the meridional direction, which is constituted by the Hadley, Ferrell and Polar circulation cells [*Wallace and Hobbs*, 1977]. The large-scale ascending of airmass at the Inter Tropical Convergence Zone (ITCZ; the ascending limb of Hadley circulation cell) gives rise to large amount of deep convective clouds in the tropics, while the cloudiness is the least at the mid-latitudes where large scale downdraft of airmass occurs at the descending limb of the Hadley cell. The sub-polar regions where the ascending branch of the Polar cell is located also has large cloud amount, though their cloud tops are considerably lower than that of the tropical deep convective clouds.

Associated with the annual variation of the latitude zone of maximum solar heating, the ITCZ undergoes systematic annual migration [e.g., *Ramage*, 1971; *Srinivasan and Smith*, 1996]. However, the spatial extent of this migration varies substantially with longitude, primarily as a result of the variations in the land-ocean distribution around the globe. The annual migration of ITCZ is largest over the Indian region where the northern hemisphere is mostly occupied by the continents and the southern hemisphere is covered mostly by the Indian Ocean, resulting in large differential heating of the land and the sea. During the northern hemispheric summer, the ITCZ over the Indian region can be located as north as 30°N while during the winter, it will reach as south as ∼20°S (southwest Indian Ocean); the ITCZ locations, however, has large

longitudinal variations during any season [*Das*, 1968; *Ramage*, 1971]. This systematic annual migration is the primary cause of the summer and winter monsoons over the Indian region. In contrast, the annual migration of ITCZ is considerably small over the open oceanic regions in the Pacific and the Atlantic.

The monsoon area, as defined by *Ramage* [1971], should satisfy the following criteria: (i) the prevailing wind direction should shift by at least 120° between January and July, (ii) average frequency of prevailing wind directions in January and July should exceed 40%, (iii) the mean resultant winds in at least one of the months should exceed 3 ms^{-1}, and (iv) fewer than one cyclone – anticyclone alternation only should occur every two years in either month (January, July) in a 5° latitude – longitude grid. These conditions are stipulated to emphasize the highly systematic seasonal nature of change in circulation. Broadly, the area between 35°N and 25°S and 30°W and 170°E satisfies this definition and India and the surrounding oceans are covered within this area [*Ramage*, 1971; *Rao*, 1976]. The cloud distribution undergoes large and systematic annual variations over the monsoon region, with minimum cloudiness during winter and maximum during summer.

The non-uniform land-sea distribution, surface properties, SST and its spatial gradient, and moisture availability causes significant zonal variations in the general circulation in the meridional plane. These variations cause zonal circulations such as the Walker circulation in the equatorial region and produce convection and downdraft at specific regions around the globe [*Wallace and Hobbs*, 1977]. They regulate the zonal variations in the monthly and seasonal mean cloud distributions on a regional and global scale. For example, the strongest ascending limb of the Walker cell is located over the east equatorial Indian Ocean and the Western Pacific, which surround the Indonesian region. On average, this region has the largest annual mean frequency of occurrence of clouds [e.g., *Rossow and Schiffer*, 1999; *Meenu et al.*, 2007, 2010]. However, the location of the ascending and descending limbs of these circulations undergo considerable variations during the El Niño period and during the positive phase of the Indian Ocean Dipole [*Saji et al.*, 1999].

1.9.2 Global distribution of clouds

The International Satellite Cloud Climatology Project (ISCCP) provides the most comprehensive and long-term (July 1983 to December 2009) analysis of the satellite data on a global scale, which has immensely contributed to the present understanding of the global distribution and properties of clouds and their spatio-temporal variations [*Rossow and Schiffer*, 1991, 1999; *Rossow and Garder*, 1993; *Schiffer and Rossow*, 1983]. The ISCCP incorporates data from various sources, including five geostationary meteorological satellites (GOES-E, GOES-W, GMS, INSAT and METEOSAT) and at

least one polar orbiting NOAA satellite. Data from the polar orbiting satellites are essential to cover the Polar Regions. The ISCCP provides the 30 km mapped pixel-level cloud parameters derived from individual satellites and global cloud data products (280 km equal area grid). The data from INSAT satellite is used only for the period of April 1988 to March 1989. However, since 1998, geostationary satellite data from METEOSAT-5 (moved to 63°E over the Indian Ocean) is incorporated in the ISCCP analysis.

Analysis of the ISCCP data [http://isccp.giss.noaa.gov] shows a long-term global mean total cloud coverage of 66.32±1.48%. The corresponding mean values of cloud top pressure is 573 hPa, cloud top temperature is 261.6 K and COD is 3.9. The monthly mean properties and occurrence of clouds undergo systematic, but significant, spatial and month-to-month variations [*Rossow and Schiffer*, 1999], which are well correlated with the general circulation of the atmosphere. The ISCCP data shows that, associated with the zonal mean descending limb of the Hadley cell, the cloud occurrence is the least at mid-latitude regions centered at ∼30° latitude on both hemispheres where the long-term zonal mean cloud occurrence is in the range of 50 to 55%. The corresponding values are relatively larger at the tropics (55 to 70%), which is the mean region of the ITCZ. This is also the region of the highest cloud top altitude. However, the largest cloud occurrence is observed at the sub-polar regions, especially at the southern hemisphere where the long-term cloud occurrence is ∼90% at ∼55°S, which is associated with the ascending limb of the polar cell.

Cirrus clouds constitute the largest fraction of clouds occurring globally. Though their physical and optical thicknesses are smaller than the vertically developing clouds, they play an important role in regulating the radiation budget, thermal structure and moisture content of the upper troposphere and lower stratosphere [e.g., *McFarquhar et al.*, 2000; *Hartmann et al.*, 2001; *Holton and Gettelman*, 2001; *Jensen et al.*, 2001; *Dessler and Yang*, 2003; *Sunilkumar et al.*, 2010; *Meenu et al.*, 2011]. Considerable amount of thin tropical cirrus clouds occur in the altitude region of 9 to 18 km with the maximum occurrence around 13 to 15 km altitude [*Wang and Sassen*, 2001; *Sunilkumar and Parameswaran*, 2005; *Liu et al.*, 2007; *Sassen et al.*, 2009; *Haladay and Stephens*, 2009; *Meenu et al.*, 2011].

Horizontal scale sizes of clouds vary over a wide range from several hundred kilometres (e.g., wide-spread cirrus clouds) down to <100 m (e.g., highly localized cumulus). Thickness of clouds also vary over a wide range from <100 m (e.g., cumulus and thin cirrus) to as large as ∼16 km (deep convective tropical cumulonimbus clouds). The tropical clouds are significantly different from their counterparts in the higher latitudes, mainly due to their largest possible vertical development, large cloud water content and the quantum of heat and moisture transported from the surface to higher altitudes. At

the Inter-tropical convergence zone (ITCZ) and other tropical deep convective regions, the vertical extent of clouds can reach up to the tropical tropopause [e.g., *Newell and Gould-Stewart*, 1981; *Meenu et al.*, 2010]. Occasionally, deep convective clouds can penetrate into the upper troposphere and lower stratosphere (UTLS), transporting humid surface air parcels rapidly upward. Only <10% of the total clouds produce precipitation [*Seinfeld and Pandis*, 1997]. The mesoscale convective systems (MCSs) that have horizontal scales typically >100 km account for a considerable fraction of tropical precipitation and produce much of the latent and radiative heating in the tropics [*Cetrone and Houze*, 2009].

1.9.3 Cloud distribution over the Indian region

Observations using satellite data have significantly contributed to the understanding on the regional distribution of cloudiness over the Indian region [e.g., *Saha*, 1971, 1972; *Grossman and Garcia*, 1990; *Bony et al.*, 2000; *Gambheer and Bhat*, 2000, 2001; *Roca and Ramanathan*, 2000; *Roca et al.*, 2002; *Zuidema*, 2003; *Sathiyamoorthy et al.*, 2004; *Puranik and Karekar*, 2006; *Meenu et al.*, 2007, 2010, 2012; *Haynes and Stephens*, 2007; *Srinivasan and Joshi*, 2007; *Devasthale and Grassl*, 2009; *Wonsick et al.*, 2009; *Sunilkumar et al.*, 2010; *Nair et al.*, 2011; *RameshKumar et al.*, 2012; *Sabin et al.*, 2012; *Rajeevan et al.*, 2012], their radiative impact [*Pai and Rajeevan*, 1998; *Rajeevan and Srinivasan*, 2000; *Patil and Yadav*, 2005; *Roca et al.*, 2005; *Samala and Krishnan*, 2008] and atmospheric latent heating [e.g., *Magagi and Barros*, 2004]. Based on NOAA-AVHRR data, *Meenu et al.* [2010] have derived the long-term (1996 to 2008) monthly and seasonal mean cloud distributions over the Indian subcontinent and the surrounding oceanic regions. The above studies revealed several interesting features of the cloud distribution over the Indian region, including the occurrence of the deepest convective clouds in the entire globe over the north Bay of Bengal during the Asian summer monsoon season, occurrence of double ITCZ over the Indian Ocean during November-December and April months, large spreading of cirrus clouds originating from the deep convective outflows in the Bay of Bengal over to the Indian region and the Arabian Sea during the summer monsoon season, large occurrence of thin cirrus clouds in the upper troposphere around the cold point tropopause, the role of deep convection on the structure of tropical tropopause layer and the considerable negative cloud radiative forcing over the Indian region during the Asian summer monsoon season. Monthly variations in the spatial distribution of total and high-altitude clouds were found to be in tandem with corresponding variations of the Hadley and Walker cells. The ITCZ is manifested by cloud occurrence of >70% and its annual migration is well discernible from the monthly mean frequency of occurrence of clouds. The minimum cloudiness (<15%) over the Indian region occurs during winter, when the de-

scending limb of Hadley cell is located over the north-central Arabian Sea and Central Indian region. The double ITCZ over the Indian Ocean is manifested as two bands of large cloud occurrence on either side of the equator which are clearly separated by a dip in the cloud occurrence at the equator; their occurrence is most prominent over the west equatorial Indian Ocean during the November, December and April months, when the bands appear centered at ∼60° latitude on either side of the equator. The occurrence of clouds undergoes diurnal variations, phase of which varies with season [*Wonsick et al.*, 2009]. The dominance of deep convective clouds with brightness temperature <233 K during the active monsoon period and suppression of convective activity over the Arabian Sea and the west coast of India during break monsoon periods are clearly discernible in the satellite-derived spatial distribution of deep convective clouds [*Devasthale and Grassl*, 2009].

During the summer monsoon period, the convective areas over the tropical Indian Ocean stand out for the presence of deep precipitating clouds with cloud top height >11 km [*Haynes and Stephens*, 2007; *Rajeevan et al.*, 2012]. Under this intense deep convection, the convective tropopause over the north Bay of Bengal gets lifted upwards to 13 to 15 km altitude while the thickness of tropical tropopause layer (TTL) shrinks to <3 km during June to August period [*Meenu et al.*, 2010]. In contrast, the TTL thickness is larger (∼4 to 5 km) over the regions away from deep convection. *Rajeevan et al.* [2012] investigated the mean spatial and vertical distribution of clouds over the Indian monsoon region during the active and break spells of the Asian summer monsoon season using CloudSat data (2007 to 2010), which showed that the active spells are characterized by negative anomalies of cloud water content extending up to 16 km over the equatorial Indian Ocean and positive anomalies over the Bay of Bengal, along the west coast of India and northeast Arabian sea. In contrast, the break spells are characterized by negative anomalies of cloud water content along the west coast of India and the Bay of Bengal and enhancement of deep convection over the equatorial Indian Ocean.

Analysis of the Kalpana-1 VHRR and CALIPSO data [*Rajeev et al.*, 2008; *Sunilkumar et al.*, 2010; *Meenu et al.*, 2011] clearly showed that the semitransparent cirrus (STC) occurrence is largest (70 to 100%) over the Bay of Bengal and the Indian region during the Asian summer monsoon season, when the whole region north of ∼15°S latitude is characterized by widespread cirrus occurrence. Most of these cirrus clouds originate from the deep convective zones over the north Bay of Bengal and spread westwards by the tropical easterly jet [*Sathiyamoorthy et al.*, 2004; *Sunilkumar et al.*, 2010; *Meenu et al.*, 2011]. The large occurrence of STCs during the other seasons is mostly confined to the vicinity of the ITCZ and their occurrence is rather sparse (<10%) over the descending limbs of Hadley circulation cell during all seasons. Most of the STCs

are of sub-visual type and contribute as large as 80% to the total STC occurrence over the regions of largest occurrence.

1.10 Impact of clouds on the energy budget of the earth-atmosphere system

Clouds have a pivotal role in the radiation and energy budget of the earth-atmosphere system as well as on the vertical and horizontal transport of energy through transfer of latent heat. They reflect part of the incoming solar radiation and significantly absorb the thermal IR radiation emitted from the surface and sub-cloud regions of the atmosphere. The absorbed energy is re-emitted, depending on the cloud temperature. Reflection of the incoming shortwave radiation back to space reduces the shortwave flux at the earth's surface, causing a cooling at the surface. This is referred as the shortwave cloud radiative forcing (SWCRF) at surface. In contrast, the cloud absorption of IR radiation emitted from the surface and its re-emission partly back to the earth's surface (referred as the greenhouse effect of clouds) increases the longwave radiative flux at the earth's surface, causing a heating of the surface. This is called the longwave cloud radiative forcing (LWCRF) at surface. The net effect of clouds depends on the sum of SWCRF and LWCRF. The SWCRF depends primarily on the cloud amount and cloud optical depth while the LWCRF depends on the amount, temperature, emissivity and optical depth of clouds. Though the magnitude of LWCRF increases with COD, the rate of increase of LWCRF decreases with increase in COD an becomes almost insignificant at high CODs, typically when COD>10. This is primarily because of the decrease in transmittance of clouds with increase in COD, the rate of increase of which is more significant at lower values of COD. Thus, for an optically thick cloud, the LWCRF mainly depends on the cloud temperature. Higher the cloud altitude (i.e., smaller the cloud temperature), larger will be the LWCRF. For optically thick low-altitude clouds, the cooling caused by the SWCRF can exceed the warming by LWCRF and hence the net effect of such clouds will be cooling. On the contrary, the warming caused by the LWCRF can be larger than the cooling by the SWCRF, especially for optically thin clouds. This is the case with cirrus clouds, which generally have a warming effect on the earth's surface. The cloud radiative forcing discussed above also alters the radiative forcing due to other greenhouse gases such as water vapour and CO_2 by providing a shielding effect [*Kiehl and Trenberth*, 1997]. On average, the global mean LWCRF is about 30 Wm^{-2}, while the corresponding longwave radiative forcing by all the greenhouse gases is 125 Wm^{-2}.

Advancements in satellite remote sensing during the past three decades have substantially improved the understanding on the radiative impact of clouds, the first among

them being the ERBE data during 1985 to 1989 [*Ramanathan et al.*, 1989; *Harrison et al.*, 1990]. These observations showed that, on average, clouds cool the Earth-atmosphere system [*Ramanathan et al.*, 1989], magnitude of which were found to vary in the range of 14 to 21 W m^{-2} between April 1985 and January 1986 [*Harrison et al.*, 1990]. The global mean longwave and shortwave cloud forcings were found to nearly cancel each other in the winter hemisphere, while the magnitude of the SWCRF significantly exceed that of the LWCRF during summer, producing a strong cooling [*Harrison et al.*, 1990]. The ERBE data also showed that clouds modify the spatial gradient of atmospheric and surface radiative heating, effectively reducing the equator-to-pole radiative heating gradient of the planet [*Harrison et al.*, 1990]. Clouds also reduce the seasonal changes in the net radiative heating of the earth-atmosphere system.

In the tropics, the LWCRF and SWCRF attain their peak values over the regions of strong convection; on average, they tend to nearly cancel each other [*Kiehl*, 1994]. Large magnitudes and near-cancellation of the shortwave and longwave CRF in the tropical convective regions imply that clouds have a considerable influence on the vertical distribution of radiative heating between the atmosphere and the surface. However, the NCRF at the TOA is negative over the Indian region during the Asian summer monsoon season, magnitude of which exceeds 30 W/m^2 over a quarter of the Asian summer monsoon region [*Rajeevan and Srinivasan*, 2000]. This large negative value of the regional mean NCRF might have been caused by the presence of large amount of high-altitude optically thick clouds present over the summer monsoon region, especially at the north Bay of Bengal and the monsoon trough zone in the Indian region [*Rajeevan and Srinivasan*, 2000]. Cloud radiative forcing in the Asian summer monsoon season is also affected by the large spreading of cirrus clouds from the deep convective areas of the Bay of Bengal into the Indian landmass and the Arabian Sea [*Sathiyamoorthy et al.*, 2004].

Many well-calibrated spaceborne radiometers followed the ERBE, especially the CERES on several satellite platforms [*Wielicki et al.*, 1996, 2006]. An excellent consolidation on the energy flow on the earth-atmosphere-space system and the radiation balance based on satellite observations and reanalysis is given by *Trenberth et al.* [2009], which clearly shows the dominance of clouds in the radiation budget and redistribution of energy from the surface to the atmosphere through latent heat. On average, the net radiation balance at the Earth's surface (balance between the incoming solar radiation absorbed at the Earth's surface and the terrestrial radiation emitted from the Earth's surface) is positive at the tropics. Exchange of this 'excess energy' to the atmosphere takes place through the sensible and latent heat fluxes [e.g., *Trenberth et al.*, 2009]. Latent heating of the tropical atmosphere is estimated to account for about 75% of the total atmospheric heating [e.g., *Riehl and Simpson*, 1979; *Zuluaga et al.*, 2010]. The

cloud feedback processes are essentially regulated through the latent heating as well as the radiative forcing.

1.11 Importance of the cloud studies over the Indian region

Earlier observations clearly showed that the deep convective regions over the tropics are characterized by the occurrence of clouds extending up to ∼16 km [e.g., *Liou*, 1986; *Rossow and Schiffer*, 1999; *Wylie et al.*, 1994; *Liu et al.*, 1995; *Wang et al.*, 1996; *Wang and Rossow*, 1998; *Wylie and Menzel*, 1999; *Dessler and Yang*, 2003; *Luo and Rossow*, 2004; *Wylie et al.*, 2005; *Stubenrauch and Schumann*, 2005; *Meenu et al.*, 2010, 2011; *Rajeevan et al.*, 2012]. These regions are also characterized by the widespread occurrence of thick and thin cirrus clouds, which can be transported to large distance from their source regions [*Nazaryan et al.*, 2008; *Rajeev et al.*, 2008; *Haladay and Stephens*, 2009; *Sunilkumar et al.*, 2010; *Meenu et al.*, 2011].

Spatial distribution of clouds and their temporal evolution over the Indian subcontinent and the surrounding oceans have several unique features [*Saha*, 1971, 1972; *Sikka and Gadgil*, 1980; *Rajeevan and Srinivasan*, 2000; *Roca et al.*, 2002, 2005; *Sathiyamoorthy et al.*, 2004; *Simon et al.*, 2006; *Meenu et al.*, 2007, 2010; *Meenu*, 2010; *Meenu et al.*, 2011, 2012; *Samala and Krishnan*, 2008; *Ramesh Kumar et al.*, 2009; *Rajeevan et al.*, 2012; *Sabin et al.*, 2012]. The foremost among them is that the largest annual migration of ITCZ over the entire globe occurs over the Indian region, which drives the monsoons. The spatial distribution and properties of clouds as well as their temporal evolutions associated with the monsoons have several interesting features. For example, the highest clouds over the entire globe occur over the north and east Bay of Bengal during the June to August period [*Newell and Gould-Stewart*, 1981; *Meenu et al.*, 2010]. Large amount of semitransparent cirrus clouds occur near the cold point tropopause over this region, a small part of which (∼5%) even penetrate into the lower stratosphere [*Meenu et al.*, 2011], which will have significant impact on the moisture budget and heterogeneous chemistry of the UTLS region. The strongest ascending limb of Walker circulation is located in the east equatorial Indian Ocean and the western Pacific surrounding the Indonesian landmass. The SST undergoes considerable spatial variations from <24°C to >30°C over this region, which makes it an ideal natural laboratory for testing the hypothesis on the role of SST and atmospheric thermodynamics on the vertical development of clouds. Unlike the near-cancellation of the shortwave and longwave cloud radiative forcing at TOA over the tropics, the occurrence of optically thick high-altitude clouds leads to significantly large negative net cloud radiative forcing over the Indian region (<-30 Wm^{-2}) [*Rajeevan and Srinivasan*, 2000]. Large westward

transport of cirrus clouds generated at the deep convective regions over the Bay of Bengal during the summer monsoon season [*Sathiyamoorthy et al.*, 2004; *Sunilkumar et al.*, 2010; *Meenu et al.*, 2010] suggests that the cirrus lifetime over these regions could be ∼1 to 2 days. The Indian Ocean Dipole [*Saji et al.*, 1999] and El Niño/La Niña conditions significantly influence the meteorology and cloud distribution over the Indian region [e.g., *Gadgil et al.*, 1984; *Behera et al.*, 1999; *Ashok et al.*, 2001, 2004; *Meenu et al.*, 2010].

1.12 Scope and objectives of the present study

Horizontal distribution of clouds over the Indian region and the surrounding oceans is reasonably well explored using satellite data [*Saha*, 1971, 1972; *Sikka and Gadgil*, 1980; *Grossman and Garcia*, 1990; *Laing and Fritsch*, 1993; *Pai and Rajeevan*, 1998; *Gambheer and Bhat*, 2000, 2001; *Rajeevan and Srinivasan*, 2000; *Roca and Ramanathan*, 2000; *Wilcox and Ramanathan*, 2001; *Roca et al.*, 2002, 2005; *Sathiyamoorthy et al.*, 2004; *Patil and Yadav*, 2005; *Devasthale and Grassl*, 2009; *Wonsick et al.*, 2009; *Meenu et al.*, 2007, 2010, 2011; *Meenu*, 2010; *Rajeevan et al.*, 2012]. However, vertical distribution of clouds and its spatial variations [*Nair et al.*, 2011; *Rajeevan et al.*, 2012] and the impact of clouds on the energetics of the earth-atmosphere system [*Rajeevan and Srinivasan*, 2000] are less explored. Direct observations on the dependence of the vertical development of clouds on SST and other atmospheric thermo-dynamic variables are least (if not never) explored. Improvements in these aspects are essential to quantify the effect of clouds and their feedback mechanisms and their parameterizations in the weather and climate models. Though the regional distribution of cirrus clouds were investigated in the past [e.g., *Bhavani Kumar et al.*, 2001; *SunilKumar et al.*, 2003; *Sunilkumar and Parameswaran*, 2005; *Sunilkumar et al.*, 2010; *Meenu et al.*, 2011], the time evolution of their vertical structure has not been investigated in detail. Detailed investigations on the monthly and seasonal mean vertical distribution of clouds and their spatial variations, the role of SST and atmospheric thermodynamic parameters on the vertical development of clouds, the vertical structure of cirrus clouds and their time evolution, and the impact of clouds on the radiation budget and atmospheric latent heating are investigated in this thesis.

The study focuses over the Indian region and the surrounding oceans in the geographical region bounded between 30°S to 30°N latitude and 30°E to 110°E longitude (Figure 1.3). This study extensively utilizes multi-year and multi-satellite observations; the CloudSat data during 2006 to 2011 forms its backbone. Impact of clouds on the radiation budget of the earth-atmosphere system is investigated using the data from ScaRaB flown onboard the Megha-Tropiques satellite, while the latent heating of the atmosphere by precipitating clouds are estimated using TRMM-Precipitation

radar data. Cirrus cloud characteristics and its time evolution are investigated using the Micropulse lidar (MPL) observations carried out Thiruvananthapuram (8.5°N, 77°E) during 2008 to 2011. The location is marked with a red * in the Figure 1.3. Three-dimensional distribution of clouds can act as a tracer for some of the atmospheric dynamical features which are not understood hitherto. One such aspect is the occurrence of a large pool of inhibited cloudiness over the Bay of Bengal during the Asian summer monsoon season. This aspect is also investigated in detail.

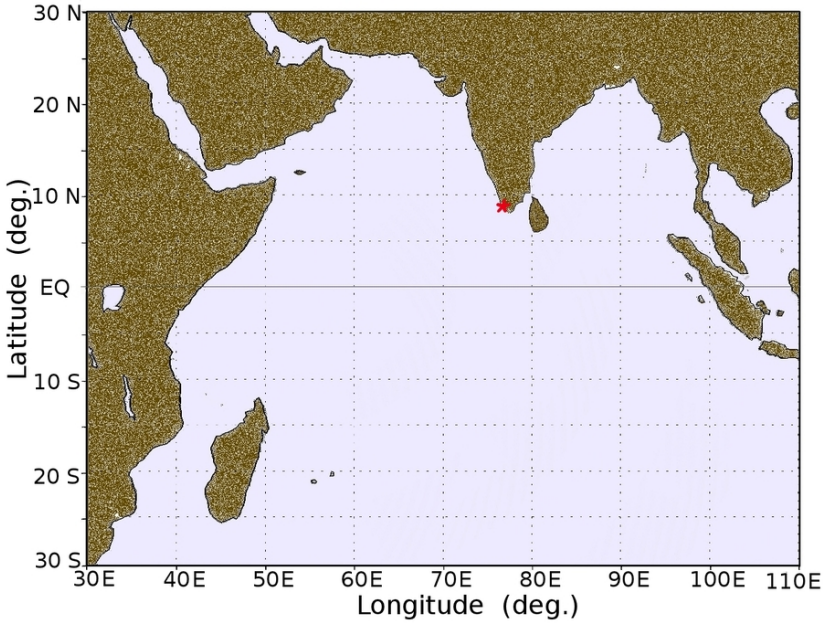

Figure 1.3: Region of study (30°S to 30°N, 30°E to 110°E). The location of tropical coastal station –Thiruvananthapuram (8.5°N, 77°E) is marked by '*'.

The main objectives of this study are:

1. To estimate the monthly and seasonal mean vertical distribution of clouds and their spatial variations (which provide a monthly and seasonal mean 3-dimensional distribution of clouds) and investigate their association with the atmospheric circulation over the Indian subcontinent and the surrounding oceans.

2. Investigate the characteristics and genesis of the 'pool of inhibited cloudiness' that appear over the southwest Bay of Bengal during the Asian summer monsoon season.

3. Exploration of the role of SST and atmospheric thermo-dynamical parameters in regulating the vertical development of clouds.

4. To investigate the vertical distribution of tropical cirrus clouds and time evolution of their vertical structure using lidar observations at Thiruvananthapuram, a tropical coastal station at the southwest Peninsular India.

5. Assessment of the impact of clouds on the energetics of the earth-atmosphere system, by estimating the regional seasonal mean cloud radiative forcing at top-of-the-atmosphere and latent heating of the atmosphere by precipitating clouds.

Chapter 2 provides the details of the satellite data, experimental details of the micropulse lidar system, methods used for the data analyses, advantages and disadvantages of each data set, and potential sources errors and uncertainty limits. Chapter 3 describes the monthly and seasonal mean vertical distribution of clouds, their spatial variations, and association with atmospheric circulation. Results presented in Chapter 3 reveals the presence of a large 'pool of inhibited cloudiness' over the southwest Bay of Bengal during the Asian summer monsoon season. Detailed characteristics and potential generation mechanisms of this 'pool' are presented in Chapter 4. The role of SST and its spatial gradient, and atmospheric thermo-dynamic parameters such as the lower tropospheric stability, convective available potential energy, and wind convergence on the vertical distribution and development of clouds are investigated in Chapter 5. Chapter 6 presents the characteristics of cirrus clouds over a tropical coastal station, Thiruvananthapuram, based on multi-year dual polarization lidar observations. The time evolution of the structure of cirrus clouds generally shows a prominent descending nature. Detailed characteristics of the descending nature of cirrus clouds are also presented here. Impact of clouds on the energetics of the earth-atmosphere system is investigated using the satellite-based estimations of cloud radiative forcing at TOA and latent heating of the atmosphere by precipitating clouds. These results are presented in Chapter 7. Chapter 8 provides the summary of the results obtained from the present study and scope for future research.

Chapter 2

Experimental Techniques, Data and Method of Analysis

2.1 Introduction

The present study is mainly based on multi-year observations of the spatial and vertical distributions of clouds derived from different satellite observations and the temporal variation of cirrus clouds observed using Micropulse Lidar (MPL) at Thiruvananthapuram (8.5°N, 77°E). Impact of clouds on the energetics of the earth-atmosphere system is also investigated using satellite data. Meteorological processes and physical mechanisms responsible for the observed features of the cloud distribution are investigated using the satellite-derived Sea Surface Temperature (SST) and surface wind divergence and the atmospheric circulation obtained from Reanalysis data (MERRA). Summary of these data used in the present study are given in Tables 2.1 and 2.2.

Vertical distribution of clouds and their spatial variations are derived using the data obtained from the spaceborne Cloud Profiling Radar (CPR) flown on board the polar orbiting Sun-synchronous satellite, CloudSat during June 2006 to February 2011, which form the backbone for the present study. This data is unique as it provides, for the first time, the altitude profiles of all types of clouds (except semitransparent clouds) globally from a spaceborne platform. However, its spatial coverage and repetivity are limited as the profiling is carried out only along the sub-satellite track. On the other hand, the across-track scanning NOAA-AVHRR provides long-term high resolution spatial distribution of clouds with high repetivity (twice daily), but are limited to the horizontal distribution of total cloudiness which are biased to the high-altitude clouds. The AVHRR data have been extensively used for studying the spatial distribution of clouds over the study region in the past [e.g., *Meenu et al.*, 2007, 2010, 2012; *Meenu*, 2010]. In the present study, the long-term (1996 to 2010) monthly mean horizontal cloud dis-

tributions derived from AVHRR data are used to further improve the insight into the 3-dimensional distribution of clouds obtained from the relatively less frequent observations using CloudSat. The spaceborne Lidar onboard CALIPSO provides observations on the semitransparent cirrus clouds, which are underestimated by CloudSat. As the CloudSat and CALIPSO are part of the same 'A-train' constellation of satellites (having the same orbital track, with their equatorial crossing separated by a few minutes) their combined analysis provides information on all cloud types. This data are used to study the role of SST and atmospheric thermo-dynamic parameters on the vertical distribution of clouds. None of the above satellite data can provide temporal evolution of the structure of clouds over any given region at short time intervals. In the present study, continuous time evolution of the vertical structure of cirrus clouds over several hours are investigated using the ground-based Micropulse Lidar observations carried out at Thiruvananthapuram during March 2008 to May 2011. Latent heating of the atmosphere by clouds (precipitating clouds) are investigated using the data obtained from Precipitation Radar onboard the TRMM satellite during 2006 to 2011. Cloud radiative forcing at the Top-of-atmosphere (TOA) are estimated using the broad band shortwave and longwave fluxes observed using ScaRaB onboard the Megha-Tropiques (MT) satellite. The MT was launched on 12 October 2011 and MT-ScaRaB data since July 2012 have been released for scientific studies. The MT-ScaRaB data during July to November 2012, which typically represents the Asian summer monsoon and post-monsoon seasons, are used to estimate the cloud radiative forcing (CRF) in the present study.

Main objective of this chapter is to provide details of different data sets used in this thesis, experimental setup (MPL), method of analysis, accuracies and potential sources of uncertainties in these data.

2.2 CloudSat data and its processing

The orbital characteristics of CloudSat and specifications of the Cloud Profiling Radar (CPR) onboard are given in Tables 2.3 and 2.4 respectively [*Durden and Boain*, 2004]. The CloudSat and CALIPSO were launched together by NASA on 28 April 2006. They fly in orbital formation as part of the 'A-Train' constellation of earth observing satellites. All satellites in the A-Train formation have the same orbital tracks with a 16-day repeating cycle, but the equatorial crossing time of the individual satellites differ by less than a few minutes. This enables these satellites (having different payloads) to observe different features of clouds and other geophysical parameters near simultaneously at the same location. Combining the observations of CloudSat with those from CALIPSO and Aqua-MODIS is the observing philosophy of the CloudSat mission to extract maximum scientific information from these observations [*Mace et al.*,

Table 2.1: Summary of the satellite data used in the present study

Sl.No.	Satellite-Payload	Data Duration	Data Type & Resolution
1	CloudSat-CPR	Jun.2006-Feb.2011	Level-2: 2B-GEOPROF Vertical resolution: 240 m Horizontal resolution (along track): 1.7 km Data along sub-satellite track at 1.30 PM/AM (Local Time)
2	CALIPSO-CALIOP (Combined analysis of CloudSat and CALIPSO)	Jun.2006-Dec.2011	Level 2: 2B-GEOPROF-LIDAR Horizontal resolution: 40 km Vertical resolution: 60 m (0-8 km) 180 m (>8 km) Data along sub-satellite track at 1.30 PM/AM (Local Time)
3	NOAA-AVHRR NOAA-14-AVHRR NOAA-16-AVHRR NOAA-18-AVHRR	Dec.1995-Dec.2010 Dec.1995-Dec.2000 Mar.2001-Dec.2003 Jun.2005-Dec.2010	Leve-1B Global Area Coverage (GAC) Binary data (10 bits) Spatial resolution: 4.4 km (nadir) Daily afternoon passes (01:40 or 02:00 PM Local Time)
4	Megha-Tropiques: ScaRaB	Jul.2012-Nov.2012	Level-2: Instantaneous fluxes at TOA Spatial Resolution: 40 km at Nadir Temporal coverage: up to 6 observations/day (low-inclination orbit) at different local times
5	TRMM-PR	Jun.2006-Feb.2011	Level-3: Monthly mean convective and stratiform latent heating (CSH) Spatial resolution: 0.5° Vertical resolution: 1 km
6	TRMM-TMI	Jun.2006-Feb.2011	Level-3: SST Spatial resolution: 0.25° Temporal: Daily mean
7	Scatterometer data ERS-1 and -2 QuikSCAT	1991-2009	Monthly Mean Surface Wind Divergence over Ocean Spatial Resolution: 1.0° (ERS1 & 2) 0.5° (QuikSCAT)

Table 2.2: Summary of the ground based data used in the present study

Sl.No.	Instrument	Data Duration	Data Type & Resolution
1	Ground-based Micropulse Lidar (MPL) at Thiruvananthapuram (8.5°N, 77°E)	Mar.2008-May2011	Raw data: Backscattered Dual Polarization Lidar signal. Vertical resolution ∼30 m. Time resolution : 1 minute

Table 2.3: Orbital characteristics of CloudSat

Orbital elements	Values
Orbit	Polar Sun synchronous
Semi-Major Axis	7083.44 km
Eccentricity	0.0012
Altitude	705 km (Approx.)
Inclination	98.2°
Equatorial crossing	01:31/13:31 Local Time
Orbital period	98.88 min
No. of Orbits per day	14.563
Repetitivity	16 days (every 233 orbits)

Table 2.4: Specifications of CloudSat-Cloud Profiling Radar

Parameter	Value
Frequency	94.05 GHz
Wavelength	3.19 mm
Pulse Width	3.3 μs
Pulse Repletion Frequency	4340 Hz
Transmitted Peak Power	~1.7 kW
Average Transmitted Power	~24.3 W
Antenna Size	1.85 m (Parabolic reflector type)
Beam width	0.108° (both azimuth and elevation)
Foot print size	1.4 km (approx.) at Earth's surface
Nadir Angle	0.16° (15 Aug. 2006 onwards; 1.7° and 0° earlier)
Dynamic Range	70 dB
Minimum Detectable Signal	<-29 dBZ
Vertical resolution	240 m (By over-sampling of the returned signal)
Data window	0 to 25 km altitude
Data Integration Time	0.16 s
Cross-track Resolution	1.4 km
Along-Track Resolution	1.7 km

2009].

The CPR onboard CloudSat observes the altitude profiles of cloud reflectivity along the sub-satellite track [*Haynes and Stephens*, 2007; *Marchand et al.*, 2008, 2009]. The CPR transmits microwave pulses at the frequency of 94 GHz (wavelength = 3.19 mm) having pulse width of 3.3 μs and peak energy of ~5.6 mJ at a pulse repletion rate (PRF) of 4340 Hz. The receiver detects the range-resolved radar signals backscattered from hydrometeors with a vertical resolution of 240 m along the sub-satellite track. Though the pulse width is 3.3 μs, the range resolution of 240 m is achieved by over-sampling the returned signal. The radar beam width generated by the parabolic reflector type antenna is 0.108° along the azimuth and elevation, which produces an instantaneous foot-print size of ~1.4 km at the surface. This is the across-track resolution of the

radar footprint. The radar backscattered signals are integrated in time for 0.16 s (688 pulses). After accounting for the satellite movement within this time (∼7 km/s.), the convolution calculations show that the along-track resolution of CPR is 1.7 km (based on pure geometrical consideration, this will be ∼2 km). In order to minimize the surface reflectance effects and specular reflection, the CPR is set to point at 0.16° from the nadir from orbit number 1595 (In the initial period, the CPR was kept at 1.7° and 0° from the nadir). The dynamic range of the system is 70 dB, while the minimum detectable signal is <-29 dBZ (which is the equivalent radar reflectivity that gives a mean power equal to the standard deviation after integration and noise subtraction).

Figure 2.1 shows all the orbital tracks of CloudSat (both ascending and descending) during the 16-day orbital cycle. Each ascending tracks are separated longitudinally by ∼1.6° at the equator. As stated earlier, the CloudSat-CPR does not scan across the orbital track, but only observes the altitude profiles of radar backscattered signal along the sub-satellite track. No observations are made between the tracks. Hence each satellite orbit produces only a curtain (2-dimensional cross section along the vertical and orbital track) of the cloud distribution along the sub-satellite track. A given track is repeated only once is 16 days (after every 233 orbits). This limits the frequency of observations of CloudSat compared to that of an imager (e.g., NOAA-AVHRR) and is one of the main limitations of CloudSat. The implication of this is that the CloudSat data for a longer period is to be averaged to produce any meaningful representation of the cloud distribution over a region. Hence, this thesis mainly focuses on the monthly and seasonal mean cloud distributions derived from multi-year observations rather than their variations over short time scales (such as intra-seasonal variations).

2.2.1 Cloud detection by CPR-CloudSat

This study utilizes the cloud geometrical profile product, 2B-GEOPROF (Version-4) provided by NASA, which gives the cloud mask containing the information on cloud layers and their top and base altitudes for the individual profiles along the satellite orbit [*Mace et al.*, 2007]. The occurrence of clouds is identified from the backscattered CPR signals based on threshold criteria for the detected signal after noise subtraction. As the typical size range of cloud droplets (8 to 100 μm) is substantially smaller than the CPR wavelength (3.19 mm), the backscattered signal from clouds arises mainly from Rayleigh scattering. As the backscattering coefficient depends on the number density of droplets and their individual backscattering scattering cross sections, the CPR mainly detects optically thick clouds, which produce sufficiently strong Rayleigh lidar signals above the detectability limit of -29 dBz. The signal from semitransparent cirrus clouds will be considerably weak and are mostly undetectable using CloudSat. Though the lower boundary of the cloud optical depth (COD) for CloudSat detection is not well-

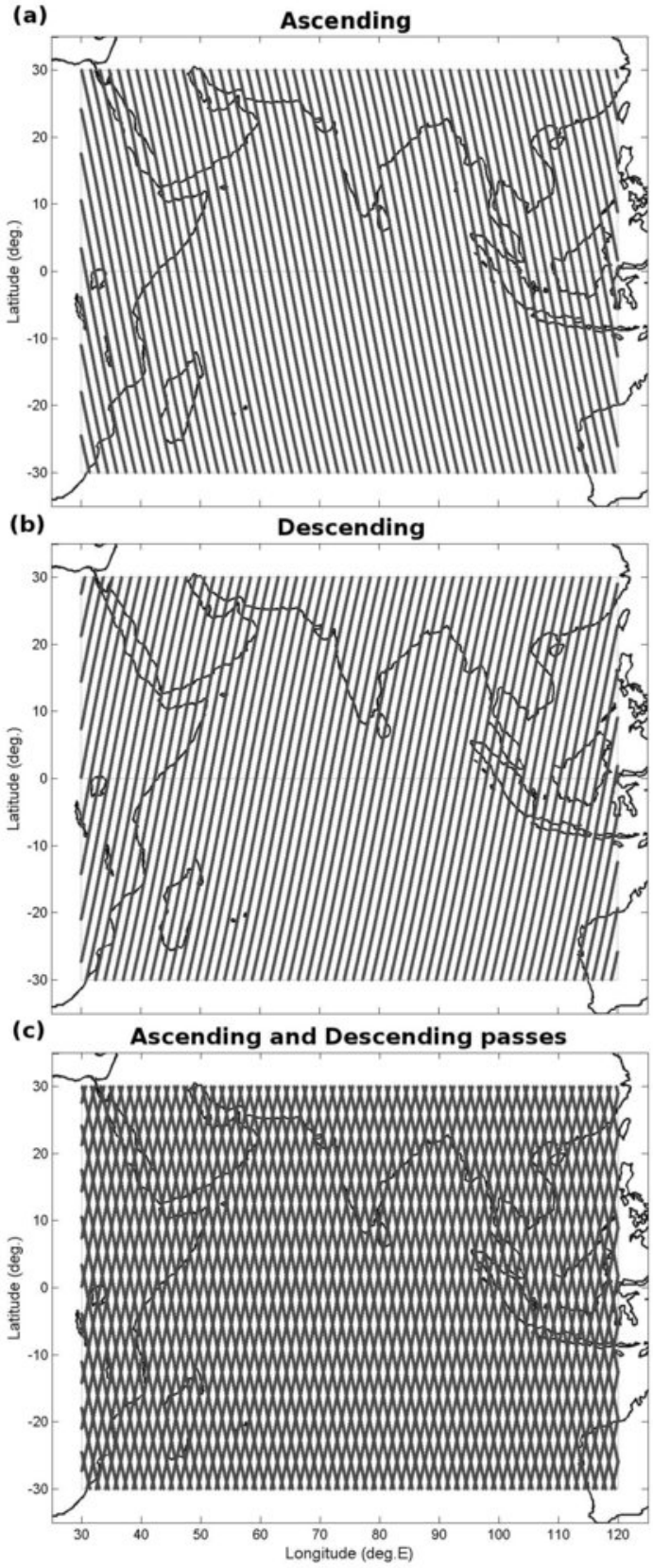

Figure 2.1: All orbital tracks of CloudSat for (a) the ascending mode, (b) the descending mode, and (c) combined ascending and descending modes over the study region during the 16-day orbital cycle. These tracks are also valid for CALIPSO and other satellites in the A-Train constellation and get repeated after 233 orbits (once in 16 days).

defined, an intercomparison between CloudSat and CALIPSO (which can detect thin clouds, but cannot penetrate thick clouds) observations clearly indicate that the clouds having optical depth less than 1.0 are mostly undetectable by CloudSat. The signal strength and reliability of cloud detection by CloudSat increases with COD. For clouds with COD>1.0, the accuracy of cloud detection using CloudSat is more than ∼90%. In addition to COD, the uncertainty in cloud detection is also caused by physically thin clouds having thickness <240 m [*Mace et al.*, 2009]. Thus, the altitude profiles of clouds obtained from CloudSat data mainly represents the optically thick clouds and not the semitransparent clouds. However, the results presented in Chapter 3 clearly show that the CloudSat can detect thick cirrus clouds which originate from deep convective anvils

Each profile of CPR has 125 vertical bins - each bin having a thickness 240 m – covering a total vertical window of 30 km. One 'granule' of CloudSat data is defined as one orbit and starts at the first profile that falls on or past the equator on the descending node. Each granule contains ∼37088 profiles. On average, ∼112 granules (ascending and descending) of data will be available over the present study region during the 16-day cycle. The CloudSat CPR data is analyzed together with the Aqua-MODIS and CALIPSO data to extract maximum information from these data sets. All these satellites are part of the A-Train, and hence observe the same location within a few seconds to a few minutes. Details on the analysis of CloudSat-CPR data are provided in *Mace et al.* [2007, 2009] and *Marchand et al.* [2008].

The raw, Level 0 data from CPR transmitted to the ground station are converted to calibrated Level 1B data using the pre-launch and in-flight calibration measurements. The Geometrical Profile algorithm (Level-2) takes the Level-1B granule and the corresponding auxiliary data from MODIS (for presence of clouds along the sub satellite track) and ECMWF (for atmospheric thermo-dynamic parameters) to produce the radar reflectivity profile and identify the bins containing clouds following threshold criteria and comparing with the cloud information derived from MODIS [*Stephens et al.*, 2001]. The Aqua-MODIS provides information on the horizontal distribution of clouds within the CloudSat footprint and is used to evaluate the characteristics of the CPR hydrometeor returns. Essentially, the CloudSat data processing algorithm does the following: (i) examines the characteristics of each range resolution volume to determine if the CPR reflectivity data for that volume is significantly above the radar noise and, thus, deemed to contain hydrometeors, (ii) quantify the likelihood that a given range resolution volume with characteristics different from noise actually contains hydrometeors, and (iii) compare the radar significant echo profile with the information from the MODIS cloud mask. An exhaustive description of the Algorithm Theoretical Basis (ATB) is given in *Mace et al.* [2007]. This section provides a summary of the steps involved for processing the CloudSat-CPR data to identify cloud layers as given

in the 2B-GEOPROF data.

The Significant Echo Mask (SEM) Algorithm identify the altitude bins in which the radar reflectivity is significantly above the noise and establish the likelihood that such bins contain hydrometeors. It maximizes the identification of hydrometeor echo while minimizing the occurrence of false alarms. Since the CPR minimum detectable signal is -29 dBZ, some hydrometeor layers will have a backscatter cross section per unit volume that generates signal near or below the detection threshold of the CPR. As in any threshold method, there is some amount of arbitrariness associated with the selection of threshold. The threshold was developed based on the data from the combined analysis of CloudSat, MODIS and CALIPSO data as well as the past microwave radar data from ground stations. In order to identify the relatively weak but significant radar returns, a statistical approach is followed that effectively increases the separation between signal and noise by assuming some degree of spatial and vertical continuity of the hydrometeor field on the scales of the CloudSat observations. MODIS cloud-mask data available at 1 km (day and night) and 250 m (daytime only) horizontal resolutions are used for further verifying the CloudSat-CPR cloud-mask generated by the GEOPROF algorithm by assuming that the backscatter cross section per unit volume is due to a reasonably uniform distribution of hydrometeors within that volume.

2.2.2 CloudSat 2B-GEOPROF

The CPR Level 2 GEOPROF data provide information on cloud mask for each profile. The cloud mask (CM) contains a value between 0 and 40 for each range bin with values greater than 5 indicating the location of likely hydrometeors [*Mace et al.*, 2007]. Higher values of the Cloud Mask variable indicate a reduced probability of a false detection. An intercomparison with CALIPSO shows that the CloudSat false detection is 44% for CM=6 to 10, 5% for CM=20, 4.3% for CM=30 and 0.6 for CM=40. The lower values of CM mainly arise from the weak radar echoes, which are rather noisy. However, the total number of bins having CM$<$20 are substantially smaller than those with CM$\geqslant$20 (this is also evident in Figure 2.2 and is explained later). In order to avoid the spurious detections, those cloud-masks having values greater than or equal to 20 only are considered as cloudy in the present analysis. In order to further reduce the uncertainties, it is also ensured that the radar reflectivity is >-28 dBZ for CM=20.

Figure 2.2 shows an example of the altitude variation of Radar Reflectivity factor (in dBZ) along a CloudSat track on 2 June 2007 over the Arabian Sea region, and the corresponding cross-section of the cloud mask obtained from the GEOPROF algorithm. The spatial distribution of clouds derived from AVHRR data (description given in Section 2.3) around the CloudSat path is also shown for comparison. The AVHRR-derived spatial distribution of cloudiness is in agreement with that obtained from CloudSat.

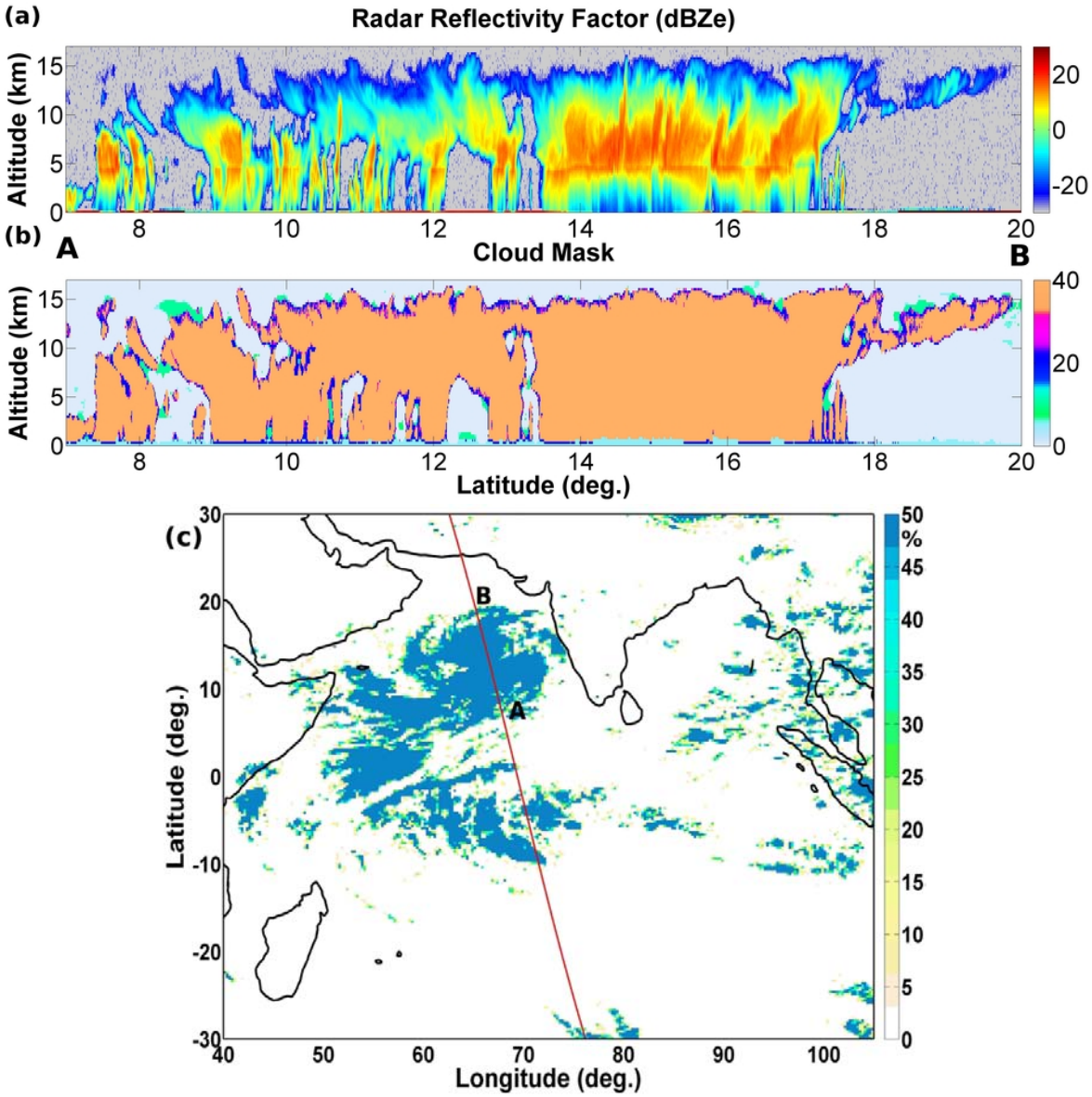

Figure 2.2: (a) Altitude variation of Radar reflectivity factor (dBZ) along a CloudSat track on 2 June 2007 over the Arabian Sea, and (b) the corresponding cross-section of the cloud mask obtained from the GEOPROF algorithm. (c) Spatial distribution of clouds derived from AVHRR over the region within 1 hour from the CloudSat path. The straight line indicates the CloudSat track. The CloudSat Radar reflectivity and cloud mask shown in (a,b) are between the points A and B marked in (c).

In general, the cloud radar reflectivity is larger in the middle portion of the clouds and the least at their top. This is essentially because of the large liquid or ice water content in the middle portion of the vertically developing clouds (as seen in Chapter 7, in general, the cloud latent heating is also larger between ∼5-10 km altitude); at still higher altitudes, the availability of moisture for condensation decreases and clouds become thinner. It is likely that the clouds might be extending still farther above the region seen in Figure 2.2, but the backscatter coefficient might be too small to be detected

by CloudSat – such thin semitransparent clouds can be detected by CALIPSO. Note that most of the Cloud Mask values are >30 and the contribution from those having values <20 are negligible. Even the cirrus cloud outflows (observed at 18 to 20°N) have radar reflectivity of >-25 dB and are well detectable in the GEOPROF algorithm. This shows that, neglecting the values having CM<20 does not significantly underestimate the vertical distribution of optically thick clouds.

2.2.3 Cloud geometrical profile from combined CloudSat and CALIPSO analysis

2.2.3.1 Characteristics of CALIOP-CALIPSO

As stated earlier, the CALIOP onboard CALIPSO can detect the semitransparent cirrus clouds that might be below the detectable limit of CloudSat. The orbital characteristics of CALIPSO and the observation geometry - providing the altitude profiles of backscatter coefficient along the sub-satellite track - are the same as that for CloudSat. The specifications of CALIOP are summarized in Table 2.5. The lidar is operated in a near-nadir viewing geometry. It has an Nd:YAG laser as transmitter that emits laser pulses at a PRF of 20 Hz (pulse energy =110 mJ) at 532 nm and 1064 nm and detects the backscattered lidar signals at these two wavelengths. The foot-print of the laser beam at the Earth's surface is ∼70 m, which is significantly smaller than that for CloudSat (∼1.4 km). The backscattered lidar signal is collected by a telescope having 1 m diameter. The range resolved orthogonal polarization components (co- and cross-polarization components) at 532 nm are measured using a PMT while the range-resolved total backscattered intensity at 1064 nm is measured using Avalanche Photodiode [*Winker et al.*, 2007]. The dual polarization observations provide the altitude profiles of depolarization ratio, which is a measure of the shape of the scatterer: larger the depolarization ratio, larger is the non-sphericity [*Rajeev et al.*, 2010; *Mishra et al.*, 2010]. The total backscattered intensity (sum of the co- and cross-polarized components) at 532 nm and 1064 nm are inverted to obtain the altitude profiles aerosol backscatter coefficient, cloud optical depth (for semi-transparent clouds) and colour ratio. The vertical resolution of the profile is ⩽60 m below the altitude of ∼20 km.

2.2.3.2 The CALIOP Level 2 algorithm

The CALIPSO data are analyzed by the Data Processing Centre at NASA to derive the altitude profiles of backscatter coefficient (532 and 1064 nm) and depolarization ratio (532 nm) due to aerosols and clouds using CALIOP Level-2 algorithm. The aerosol and cloud layers are detected by the Selective Iterated BoundarY Locator (SIBYL) algorithm, the layer type is identified using the Scene Classification Algorithm (SCA)

Table 2.5: Specifications of CALIPSO-CALIOP. (The orbital characteristics are same as that for CloudSat given in Table 2.3).

Parameter	Value
Laser Transmitter	Nd:YAG (Solid State Diode Pumped)
Transmitted Wavelengths	532 nm, 1064 nm
Pulse Energy (each wavelength)	∼110 mJ
Pulse Repetition Frequency	20.2 Hz
Foot print size at Earth's surface	∼70 m
Telescope Diameter	100 cm
Detectors	523 nm: PMT 1064 nm: APD
Detection of backscatter signal	a) Parallel and perpendicular polarized components of backscattered radiation at 532 nm b) Total backscattered radiation at 1064 nm.
Vertical resolution	60 m (at 532 nm, vertical resolution is 30 m below 8.2 km altitude)

and the backscatter and extinction coefficient profiles are determined using the Hybrid Extinction Retrieval Algorithm (HERA). Details of these algorithms are provided in "CALIOP Algorithm Theoretical Basis Document, Part 1: CALIOP Instrument, and Algorithms Overview and Part 2: Feature Detection and Layer Properties Algorithms".

The range-corrected Lidar signal ($z^2P(z)$ (where z is the distance from the satellite up to the altitude 'h' and P(z) is the corresponding backscattered signal) is used for the layer identification after normalizing to the system efficiency. Search for the aerosol and cloud 'features' begins at the top of the normalized range-corrected lidar profile. A 'feature' is identified at that altitude region where the profile data exceed their corresponding range-dependent threshold values. The aerosols and clouds are differentiated using the Cloud Aerosol Discrimination (CAD) algorithm [*Winker et al.*, 1996; *McGill et al.*, 2002], which essentially utilizes the spatial variability and optical properties of the particulates. The SCA discriminates cloud from an aerosol layer, primarily using the layer mean value of the attenuated backscatter coefficient at 532 nm and the ratio of the mean attenuated backscatter coefficients at 1064 nm and 532 nm (the attenuated colour ratio). Since the cloud droplet sizes are significantly larger than the laser wavelength, the backscatter coefficient does not show significant spectral variation for clouds. Hence the colour ratio will be close to unity for clouds. On the contrary, the aerosol sizes are generally comparable to or smaller than the laser wavelength and hence the aerosol backscatter coefficients show spectral dependence: in general, the aerosol backscatter coefficients will be smaller at 1064 nm than that at 532 nm, thereby giving a backscatter colour ratio <1. However, dust particles may have colour ratio close to unity and large values for depolarization ratio. They are

distinguishable from cloud droplets occurring below ∼7 km as the latter are in liquid phase (in the tropics) and have very small values of depolarization ratio, though the colour ratio would be close to unity. Ice droplets with large values of depolarization ratio appear only above ∼7 km. The aerosol-cloud discrimination also employs the vertical and horizontal variations of the 'features': clouds show more rapid variations compared to aerosols, especially across the cloud boundaries. If a layer is classified as cloud, the SCA will then determine whether it is an ice cloud or water cloud using the depolarization ratio along with the ancillary information such as layer height: ice clouds have distinctly large depolarization ratio and occur in the upper troposphere.

One of the major limitations of CALIOP is its inability to profile the optically thick clouds. This is because of the large attenuation suffered by the laser beam as it passes through optically thick clouds. The CALIOP can provide observations on optically thin semitransparent cirrus clouds, especially for visible band COD<1.0. As the COD increases, the CALIOP observations increasingly get biased towards top of the uppermost cloud layer.

2.2.3.3 Combined analysis of CALIPSO and CloudSat: 2B-GEOPROF-Lidar

The synergy of the combined observational capability of CloudSat-CPR and CALIPSO-CALIOP is significant. With the ability of the CPR to probe optically thick cloud layers and that of CALIOP to detect semitransparent clouds, the two instruments have the potential of providing as complete a picture of the occurrence of clouds as has been compiled to date. However, the scattering processes as well as the targets of these two instruments are different. The macroscopic characteristics of observations such as vertical resolution, spatial resolution, and spatial coverage are also different from one another. The pointing accuracy of the two payloads adds further complexity while combining the two data streams. The CloudSat DPC optimally merges these two data streams in order to produce the most accurate quantitative description of the location of hydrometeor layers in the atmosphere that is possible.

In the present study, the CloudSat-CALIPSO combined data set (2B-GEOPROF-Lidar) is used to investigate the role of SST and atmospheric thermo-dynamics on cloudiness (including cirrus). For the vertical distribution of clouds (presented in Chapter 3), the present study uses only the 2B-GEOPROF, which is derived from CloudSat data alone. This is mainly because the 2B-GEOPROF-Lidar will be limited to the profiles having overlap; this will limit its availability to the period during which both these sensors are operational and have exact overlap. With the already limited frequency of observation as described earlier, this additional requirement will further reduce the combined observation points to produce a meaningful 3-dimensional distri-

bution of clouds on a monthly and seasonal basis. On the contrary, the combined data (2B-GEOPROF-Lidar) provides sufficient number of observations for a wide range of SSTs (23 to 31°C) to explore the relationship between cloudiness and SST (presented in Chapter 5).

2.3 Horizontal distribution of clouds using NOAA-AVHRR

Though the present study is mainly based on the horizontal and vertical distribution of clouds observed using CloudSat data, the data from the polar orbiting sun-synchronous satellites NOAA-AVHRR are used here to derive the long-term (December 1995 to December 2010) monthly mean horizontal distributions of clouds at high horizontal resolution, which provide better insight and confidence on the features observed using CloudSat whose spatial resolution (along a latitude circle) and frequency of observation are rather limited. Data from the NOAA-14, -16, and -18 satellites are used in this study. They belong to the NOAA Polar orbiting Operational Environmental Satellites (NOAA-POES), which is the longest series of polar orbiting satellites providing meteorological imageries in the visible (VIS), near-IR (NIR), mid-IR (MIR) and thermal IR (TIR) bands. This study utilizes the level-1B Global Area Coverage (GAC) binary data for the day-time pass (equatorial crossing time of ∼01:40 PM local time) containing the pixel-level digital counts corresponding to the visible, near-IR and thermal IR radiances and appended calibration information and geo-location points. The cloud detection and analysis procedure used here are the same as that reported by [*Meenu et al.*, 2007, 2010, 2012; *Meenu*, 2010].

2.3.1 Characteristics of NOAA-AVHRR

The AVHRR is an across-track scanning passive radiometer for detecting the radiance reflected and/or emitted by the earth-atmosphere system in the visible, near-IR, mid-IR and thermal IR wavelength bands. Specifications of the AVHRRs flown onboard NOAA-14, -16 and -18 are given in Table 2.6. The AVHRR sensor onboard the NOAA-14 satellite was AVHRR/2 which made observations at five spectral bands: (i) 0.58–0.68 μm (Ch-1), (ii) 0.725–1.1 μm (Ch-2), (iii) 3.55–3.93 μm (Ch-3), (iv) 10.3–11.3 μm (Ch-4) and (v) 11.5–12.5 μm (Ch-5). The AVHRR/3 onboard the NOAA-16 and NOAA-18 have 6 channels of observation. Spectral characteristics of AVHRR/2 and AVHRR/3 are similar, except for the addition of a new channel in AVHRR/3 in the spectral band of 1.58 to 1.64 μm. This channel is identified as channel 3A (Ch-3A) while the Ch-3 of AVHRR/2 (3.55 to 3.93 μm) is named as channel 3B (Ch-3B) in AVHRR/3. In AVHRR/3, the data from either Ch-3A (daytime) or Ch-3B (night

Table 2.6: General characteristics of NOAA-AVHRR.

Parameter	Ch-1	Ch-2	Ch-3A	Ch-3B	Ch-4	Ch-5
Spectral Range (μm)	0.58-0.68	0.725-1.0	1.58-1.64	3.55-3.93	10.3-11.3	11.5-12.5
Original Pixel Resolution (km)	1.1	1.1	1.1	1.1	1.1	1.1
SNR at 0.5% albedo	$\geqslant$9:1	$\geqslant$9:1	$\geqslant$20:1	-	-	-
NEdT at 300 K	-	-	-	$\leqslant$0.12 K	$\leqslant$0.12 K	$\leqslant$0.12 K
Temperature Range (K)	-	-	-	180 - 335	180 - 335	180 - 335

time) only are transmitted to ground at any given time, so that the number of channels of data transmitted at any time is five, which is same as that for AVHRR/2. These observations provide the radiance and albedo in Channels-1, 2, and 3A and brightness temperature (BT) in Channels 3B, 4 and 5. The present study primarily employs the brightness temperature derived from the thermal IR channels (Channels-4 and 5) for the detection of cloudy pixels. At high brightness temperatures (BT>280 K), the cloud detection is also confirmed using the high and comparable albedo values observed in visible and near-IR (Channels-1 and 2). The data from Channels 3A and 3B are not used here.

The swath of AVHRR is ∼2900 km and every point on the earth is observed once during the day and night (more than one observation occurs at high latitudes). The instantaneous field of view of the detectors (for all channels) is 1.4 μrad, yielding a pixel horizontal resolution of ∼1.1 km at nadir at the earth's surface. However, in global area coverage (GAC) data, the radiances observed by 4 sequential pixels in a scan line are averaged before transmitting to the ground (This is done for reducing the data volume, while storing the global data for each pass onboard the satellite). Hence, the spatial resolution of the GAC data is 4.4 km at nadir. The dynamic range of albedo measured in Channels 1 and 2 is 0-100%, with a signal to noise ratio (SNR) of $\geqslant$9 when the albedo is 0.5%. The smallest change in temperature that the sensor will be able to detect (given by the Noise Equivalent Temperature Difference, NEdT) is $\leqslant$0.12 K at BT=300 K. This signal is digitized using a 10 bit analog-to-digital converter and recorded as digital counts (DC), which is an integer ranging from 0 to 1023. The DC values can be converted to albedo (in Ch-1, 2, 3A) or BT (in Ch-3B, 4, 5) using the appropriate calibration coefficients for each channel appended with the satellite data and the conversion relationships provided in the NOAA-AVHRR users handbook [*Kidwell*, 1998].

The AVHRR channels are well characterized and calibrated before launch. Sys-

tematic and periodic post launch calibrations of the visible and near-IR channels are carried out using long-term satellite observations of reflectance at radiometrically stable regions [e.g., *Rao and Chen*, 1995, 1999] as well as vicarious calibrations by intercomparing with other satellite sensors (e.g., MODIS). The post-launch calibration of the TIR channels is achieved by recording the data obtained when AVHRR views the space (due to rotation of the telescope) and an internal blackbody, which give two extreme points on the calibration curve for every scan line.

2.3.2 Detection of clouds using AVHRR data and uncertainties

The cloud detection method used in this study is the same as that reported by *Meenu et al.* [2007, 2010] and *Meenu* [2010]. It utilizes a combination of several well-established techniques for this purpose reported in the literature [*Saunders and Kriebel*, 1988; *Durkee et al.*, 1991; *Derrien et al.*, 1993; *Franya and Cracknell*, 1995]. The main criterion for the selection of these methods is that they are applicable over the entire region and the artefacts in the spatial distribution of clouds contributed by the methodology when applied to different regions should be minimal. Due to the significant variability of albedo and temperature in the land, the threshold method having region-specific thresholds applied to the VIS or NIR albedo and spatial coherence method [*Coakley and Bretherton*, 1982] are not uniformly applicable over the whole study region.

The present study mainly employs threshold method applied to the BTs observed in Ch-4 and Ch-5 (BT4 and BT5 respectively). Here, a pixel is considered as cloudy if BT4 and BT5 are less than 280 K. The threshold of 280 K is arrived at after extensive analysis of the minimum possible BT value at the whole region under clear-sky condition during any season and ensure that all pixels having BT<280 K are indeed cloudy. The threshold BT of 280 K is well in agreement with that used in the literature, including that over the Indian subcontinent and the surround oceans [*Roca and Ramanathan*, 2000; *Roca et al.*, 2002]. Cloudy pixels with 280K<BT<288K are identified using the normalized difference vegetation index

$$NDVI = \frac{(Ch2 - Ch1)}{(Ch2 + Ch1)} \tag{2.1}$$

Detailed analysis of the NDVI shows that a pixel having NDVI>0.2 is vegetated and cloud-free while the one with NDVI<-0.2 is clear-sky ocean surface [*Meenu*, 2010]. Based on this, those pixels with BT4 or BT5<288 K and -0.2<NDVI<0.2 are also marked as cloudy.

However, some pixels having BT>288 K also may have low-level clouds or semi-

transparent clouds. The present analysis might underestimate the occurrence of low-altitude clouds over cold ocean and semitransparent cirrus which have BT>288 K. It may be noted that the SST over the study region is mostly >295 K. On average, the cloud top brightness temperature of 288 K would be sufficient to detect the clouds which are >1.5 km above these cold oceans. Further reducing the threshold might increase spurious detection of clouds over the cold oceans. As shown in Chapter 3, significant fraction of the low-altitude clouds over the southern hemispheric Indian Ocean (which are detected using CloudSat) are not detected by the AVHRR. This is the major limitation of the present method. In summary, the spatial distribution of clouds derived here from AVHRR data are mainly corresponding to optically thick clouds with top altitude >1.5 km. The low-level and semitransparent clouds might be underestimated.

2.4 Megha-Tropiques – ScaRaB: shortwave and longwave fluxes at TOA

In the present study, the cloud radiative forcing is estimated using the upwelling shortwave and longwave radiative fluxes at TOA observed using ScaRaB flown onboard the low-inclination Megha-Tropiques (MT) satellite, which is an Indo-French mission launched on October 2011. The uniqueness of the Megha-Tropiques mission is the high repetivity of observations over the tropics (due to the low orbital inclination) and the suitable selection of payloads for simultaneously measuring three interrelated components of the energy and hydrological cycle of the earth-atmosphere system. The Megha-Triopiques carries onboard three Indo-French payloads, viz. SAPHIR (Sondeur Atmosphrique du Profil d'Humidité Intertropicale par Radiométrie), MADRAS (Microwave Analysis and Detection of Rain and Atmospheric Systems), ScaRaB (SCAnner for RAdiation Budget). A fourth payload (ROSA- Radio Occultation Sounder for Atmosphere) is also flown onboard the MT to derive altitude profiles of temperature and humidity using radio occultation technique. The ScaRaB measures the radiative fluxes in the short and longwave domains, while the spatial and altitude variations of water vapour at different layers in the atmosphere are measured by the microwave sounder SAPHIR and the column integrated water vapour and ice/water content are measured by the microwave radiometer MADRAS.

2.4.1 MT Orbital characteristics

Orbital characteristics of the Megha-Tropiques are given in Table 2.7. Key factor of the MT mission is the high repetitivity of measurements in the tropics. Though the inclination of MT is only 19.98°, the regions up to ±30° latitude can be observed

Table 2.7: Orbital characteristics of the Megha-Tropiques satellite.

Parameter	Value
Orbit type	Low inclination, near-circular
Inclination	19.98°
Semi-major axis	7243.679 km
Eccentricity	0.001294
Mean altitude	859.9 km
Period	101.93 minutes
Recurrent cycle	6.87 days (97 revolutions in the cycle)
Precession cycle of the orbit	51 days

because of the wide swath of the science payloads carried onboard the satellite. The orbital characteristics of MT enables to obtain a repetivity of more than 3 visibilities at different local time per day of each point of the region situated between 22°S and 22°N. The repetivity is ∼5 per day around 13°N and 13°S. Figure 2.3(a) shows all the 14 orbital tracks of the Megha-Tropiques on 08 November 2012. The thick line in Figure 2.3(a) shows a single orbit and its continuation into the subsequent orbit, which is shifted westward due to the rotation of earth. The extent of this westward shift is determined by the rotation speed of earth in its axis and the orbital period of the satellite. For the Megha-Tropiques, the westward longitudinal shift of adjacent orbits at the equator is 25°. Figure 2.3(b) shows the orbits subtended by the Megha-Tropiques during the 7-day recurrent cycle. Though the orbit is repeated after the recurrent cycle, the local time of the overhead passes will be different. The precessing cycle of the orbit is 51 days, which is the time interval needed for the hour angle of ascending node to vary by 24 h. Hence the similar orbital paths and time of pass are repeated once in 51 days.

2.4.2 Characteristics of ScaRaB and measurement of TOA radiances

Specifications of MT-ScaRaB are summarized in Table 2.8. Details of the ScaRaB instrument are described elsewhere [*Monge et al.*, 1991; *Kandel et al.*, 1998; *Viollier and Raberanto*, 2010]. Two flight models of ScaRaB had flown earlier onboard the Russian satellites, METEOR and RESURS which were launched in 1994 and 1997 respectively. The ScaRaB/3 flown onboard the Megha-Tropiques satellite is similar to the earlier versions [*Viollier and Raberanto*, 2010]. The ScaRaB is an optical radiometer comprising of 4 independent telescopes focusing the reflected solar and emitted thermal IR radiation from the earth-atmosphere system on four detection channels, viz. visible (Channel-1: 0.55–0.65 μm), shortwave (Channel-2: 0.2–4.0 μm), total spectral band (Channel-3: 0.2–100 μm), and IR atmospheric window (Channel-4: 10.5–12.5 μm).

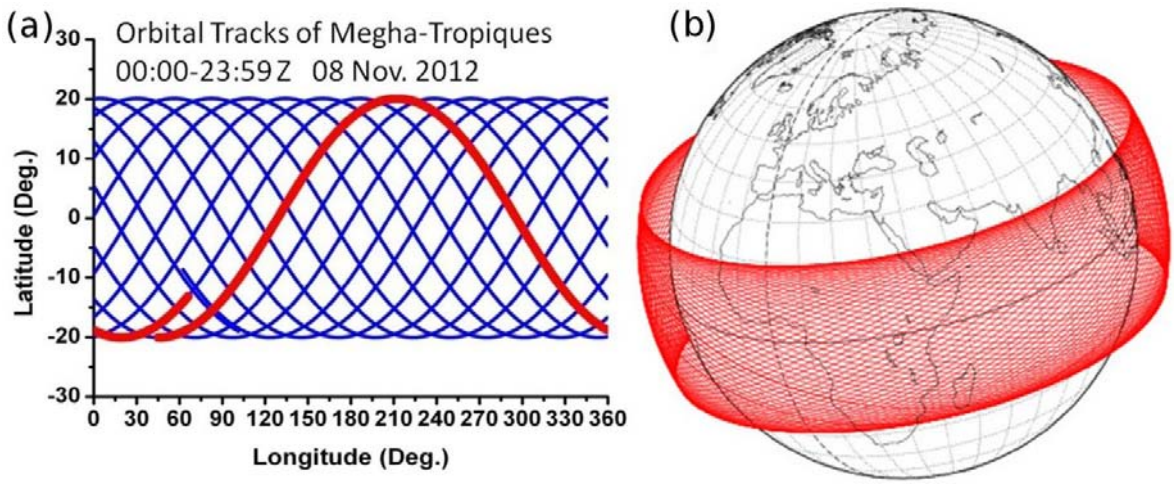

Figure 2.3: All the 14 orbital tracks of the Megha-Tropiques on 08 November 2012 (00:00 to 23:59Z). The thick red line indicates a single orbit and its continuation into the subsequent orbit. (b) Orbital tracks of the Megha-Tropiques during the 7-day recurrent cycle. As the inclination is 19.98°, the sub-satellite tracks are always limited to 19.98°S and 19.98°N (Courtesy for Figure 2.3(b): LMD, France)

The absolute accuracy of the radiances measured in these channels is better than 2% [*Viollier and Raberanto*, 2010].

The broadband Channels 2 and 3 are the main channels used for radiative flux estimates: Channel 2 provides the solar shortwave radiance (L_{SW}) reflected by the earth-atmosphere, while Channel 3 measures the total radiance (L_{Total}) in the solar shortwave and the terrestrial longwave bands. The observed radiances (filtered by the spectral characteristics of the respective ScaRaB channels) are normalized with the filter response functions for each channel to obtain the unfiltered radiances, which are subsequently used to derive the TOA fluxes. During the nighttime, the longwave radiance (L_{LW}) is directly given by the Channel 3. The ScaRaB Channels 2 and 3 have very similar spectral response in the shortwave spectral domain, and hence the longwave radiance during the daytime is calculated as:

$$L_{LW(daytime)} = L_{Total} - A' \times L_{SW} \tag{2.2}$$

where A' depends on the spectral responses of the Channels 2 and 3. For the ScaRaB onboard the Megha-Tropiques, the value of A' is 0.910 [*Viollier and Raberanto*, 2010]. The radiances observed in Channels 1 and 4 (Visible and thermal IR window channels) are used to identify clouds. The detector systems are calibrated using onboard sources and have an absolute radiance accuracy of 1 to 2%.

As seen in Figure 2.3(a,b), the sub-satellite tracks of Megha-Tropiques are limited to ±19.98° latitude. However, as the swath of ScaRaB is about 2200 km, these observations cover the tropical regions between 30°N to 30°S. This is indicated in Figure 2.4,

Table 2.8: Characteristics of ScaRaB

Parameter	Value	
Type of scanning	Across track	
Number of pixels/scan line	51	
Instantaneous field of view	48 milliradians	
Spatial resolution	40 km at nadir	
Swath	2200 km	
Number of spectral bands	4	
Channels & Spectral bands	Channel	Wavelength band
	Visible	0.55 to 0.65 μm
	Solar	0.2 to 4.0 μm
	Total	0.2 to 100 μm
	IR Window	10.5 to 12.5 μm
Radiance accuracy	Better than 2%	

which depicts a zoomed version of Figure 2.3(a) in the longitude band of 75 to 135°E. The shaded area indicates the ScaRaB swath for one orbital track. On average, a given location in the tropics will be covered up to a maximum of 6 times in a day, each observation corresponding to different local time. Variation in the number of observations of a geographical location on a given day is also evident in Figure 2.4. Superposition of the swaths for all orbits in Figure 2.4 shows that the location 'A' will be observed less frequently compared to the location 'B': while the former will be 'seen' in 4 orbits on this day, the latter will be 'seen' in 5 orbits. However, it is important to note that the frequency of observation of a location at a given local time interval varies considerably during the precessing MT orbital cycle of 51 days. This is one limitation of the MT to study the diurnal variation of radiative fluxes, as a given region will not be observed during a given local time continuously for several days: for the latitudes between 10° and 25° (North and South latitudes), the temporal sampling is represented by a pack of overpasses followed by a lack (without overpass). This requires that, for studying the diurnal evolution of radiative fluxes at a give region, the analysis needs to be carried out on an 'equivalent day' basis by combining the data during the same local time (for each pixel) over a period of at least 51 days (or typically a season).

2.4.3 Conversion of TOA radiance to TOA fluxes

Similar to the ERBE, CERES and other scanning radiometers flown earlier for Earth radiation budget studies, the ScaRaB measures radiances at different solar zenith, satellite zenith and relative azimuth angles. The angular distribution models (ADMs), which account for the anisotropy of the radiation field, are then applied to the unfiltered SW and LW radiances to obtain the SW and LW fluxes at TOA [*Suttles et al.*, 1988, 1989]. The conversion of radiance to fluxes using ADMs is the largest

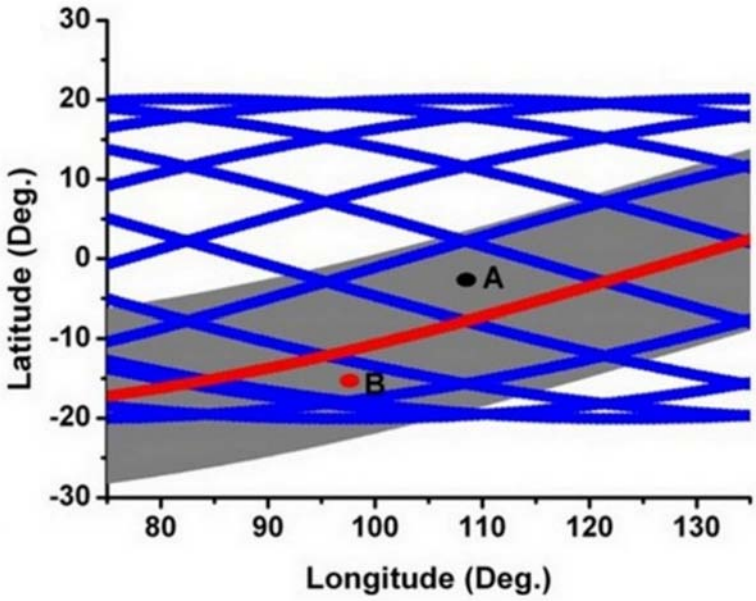

Figure 2.4: Same as Figure 2.3(a), but zoomed in the longitude band of 75 to 135°E. The shaded area indicates the swath for one orbital track indicated by the red line. The points 'A' and 'B' denotes two different geographical locations: Considering the swath of 2200 km, 'A' will be observed in 4 orbits while 'B' will be 'seen' in 5 orbits.

source of uncertainty in any ERB measurement. In ScaRaB, the unfiltered radiances in the shortwave and longwave bands are converted to shortwave and longwave fluxes at the TOA using the ERBE-like inversion [e.g., *Smith et al.*, 1986], employing the ERBE–Angular Distribution Models for different surface types and cloud conditions [*Smith et al.*, 1986; *Suttles et al.*, 1988, 1989; *Wielicki et al.*, 1996]. The algorithm for scene identification is the maximum likelihood estimation (MLE) [*Wielicki and Green*, 1989], which compares the unfiltered LW and SW radiances to apriori statistics developed. The ERBE-ADM corresponds to 12 scene classifications based on a combination of five geo-types (ocean, land, snow, desert, coast) and four cloud categories: clear (0 to 5% cloud cover), partly cloudy (5 to 50% cloud cover), mostly cloudy (50 to 95% cloud cover), overcast (95 to 100% cloud cover).

2.4.3.1 Uncertainties of ScaRaB-derived SW and LW fluxes

Potential sources of uncertainty in the radiative fluxes derived from the ScaRaB data are:

1. Measurement errors of instantaneous filtered radiances. Studies made by the instrument team shows that this error is less than 2% [*Viollier and Raberanto*, 2010].

2. Conversion of filtered radiances to unfiltered radiances. The well-characterized

ScaRaB filter response curves minimize this uncertainty. This error is scene-dependent and is less than ±1% [*Chomette et al.*, 2012; *Sathiyamoorthy et al.*, 2013]

3. Conversion of instantaneous shortwave radiance to shortwave fluxes using Angular Distribution Models. This is the largest contributor to the error budget of SW flux (SWF) at TOA. Uncertainty in the instantaneous shortwave fluxes derived from radiance is about 12% [*Wielicki et al.*, 1998]. Uncertainties arising from this can be reduced by averaging the fluxes or the estimated SWCRF over a month or season: the uncertainty of the monthly mean fluxes is typically a few percent [*Wielicki et al.*, 1998]. Utilization of the ERBE-ADMs ensures that the continuity is maintained with respect to the long-record of ERBE observations.

4. Errors associated with scene inhomogeneity arising from large pixel size. This error is scene-dependent and is insignificant for absolutely cloud-free and overcast cloudy pixels with homogeneous cloud coverage. Partially cloudy pixels contribute to increase in errors as the exact fractional cloud coverage of a given pixel can have larger uncertainty. This error is included in the error estimate stated above due to ADMs.

Comparisons of the ScaRaB-derived instantaneous fluxes with those from CERES for the same sun-pixel-satellite geometry were carried out by the instrument/project team [*Chomette et al.*, 2012; *Sathiyamoorthy et al.*, 2013]. These studies showed a constant bias error of ∼19 Wm^{-2} in the ScaRaB-derived shortwave fluxes. After correcting for this bias error, the instantaneous SW fluxes were found to follow a 1:1 relationship with the CERES data, with an RMS error of <26 Wm^{-2}. The longwave fluxes (LWF) do not show any significant bias errors: the intercomparison showed an RMS error of <8 Wm^{-2}.

The ScaRaB Level-2 data (Version: MT1SCAS-1.02) contains the instantaneous TOA fluxes in the shortwave and longwave spectral bands for the observed foot-print. This data during July to November 2012 are used in the present study. The data prior to this is yet to be released. Hence, estimates of the cloud radiative forcing in this study are limited to July to November 2012. Though this period is rather limited, it almost covers the summer monsoon and post-monsoon seasons and has produced a few very important features on cloud radiative forcing, as described in Chapter 7.

2.5 Latent Heating Rates (LHR) from TRMM Precipitation Radar data

The Topical Rainfall Measuring Mission (TRMM), a joint program between NASA and the National Space Development Agency of Japan (NASDA), launched in November 1997 in a low inclination orbit is designed to monitor the tropical and subtropical precipitation and energy. The TRMM orbit is near circular with an inclination of 35° to the equator. The low satellite orbital inclination enable it to observe the tropical region more frequently compared to the polar orbiting satellites. The satellite altitude was 350 km till 06 August 2001 and was raised to 403 km afterwards. The TRMM has five instruments onboard: Precipitation Radar (PR), TRMM Microwave Imager (TMI), Visible Infrared Scanner (VIRS), Clouds & Earths Radiant Energy System (CERES) and Lightning Imaging Sensor (LSI). The Precipitation Radar is an active microwave radar while all other payloads are passive instruments operating in the visible, near-IR, thermal IR and microwave bands.

The Precipitation Radar onboard TRMM provided the first-ever estimate of the vertical profile of latent heat that is released by precipitating clouds. The Precipitation Radar (PR) is a scanning radar operating at 13.8 GHz and employs an active phased array. It detects the altitude-resolved radar signal scattered/reflected from precipitating clouds, which in turn is used to derive the radar reflectivity of these clouds. Unlike the CloudSat, the backscattering or reflection detected by PR occurs mainly from precipitation. The contribution of non-precipitating clouds on the TRMM-PR signal is negligible. This is because of the substantially longer wavelength of TRMM-PR (λ ~2.17 cm) compared to the droplet size of non-precipitating clouds (typically 8-100 μm). The TRMM-PR has a horizontal resolution of 4.3 km at nadir, range resolution of 250 m and scanning swath width of 220 km. The radar reflectivity observed by TRMM-PR can define the layer depth of the precipitation in the atmosphere and provide information about the rainfall reaching the surface, which are essential to determining the latent heat input to the atmosphere.

Estimates of the rainfall (R) are carried out using the altitude profiles of radar reflectivity (Z) observed by the PR radar, employing the Z-R relationship [*Tao et al.*, 2006]. The data processing procedures were developed based on the application of rain gauge and disdrometer observations of rain rate and droplet size distribution in conjunction with the radar measurements to provide the necessary calibration of the radar rain estimates [*Tao et al.*, 2006]. The technique was thoroughly tested and evaluated by the TRMM validation team during the pre-mission phase as well as using ground validations [*Tao et al.*, 2006]. The estimated rain rates are used to derive the altitude profiles of latent heating of the atmosphere by the convective and stratiform

precipitating clouds.

Methodologies for estimating latent heating based on precipitation rate profile retrievals from TRMM-PR measurements are described in *Tao et al.* [2006]. The present study uses the TRMM-PR-Level-3 product on the monthly mean convective and stratiform latent heating (CSH-LH) to investigate the altitude variations of latent heating by precipitating clouds and its spatial variations. This data set is provided with a spatial resolution of $0.5^\circ \times 0.5^\circ$ at 19 vertical levels from the surface to a height of 18 km. The CSH-LH data during 2006 to 2011, which also covers the duration of CloudSat observations, are used in this thesis. The CSH algorithm also uses surface precipitation rates, percentage of its stratiform and convective components, and location of the observed cloud system for deriving the latent heat profile. The inversion to derive latent heating rate (LHR) is based on a look-up table of LHR profiles derived from simulations using the Goddard Cumulus Ensemble model and diagnostic heating budgets [*Tao et al.*, 2001]. The main drawback of this data set is that the CSH algorithm does not estimate the LHR in the absence of surface rainfall. However, the net LHR in the absence of surface precipitation is generally very small [*Zuluaga et al.*, 2010].

Direct observations of LHR in the atmosphere do not exist for validation of the LHR estimated from the PR data. *Tao et al.* [2001] have evaluated the LHR derived from TRMM-PR using those estimated from ground-based rainfall measurements and were found to be in agreement for different regions of the tropics. Spatial structure of the rainfall distribution and its temporal evolution on monthly and seasonal scales derived from TRMM-PR are found to be in agreement with that derived from in situ observations [*Mitra et al.*, 2009]. Overall, the uncertainty in the instantaneous values of LHR estimated from TRMM-PR is expected to be quite large. However, the spatial and temporal averaging will reduce the overall uncertainty of the seasonal mean LHR to less than 30%.

Despite the relatively large uncertainty of the LHR, this data have been extensively used to investigate the role of tropical clouds in the latent heating and thermodynamics of the atmosphere [e.g., *Tao et al.*, 2006, 2010; *Xie et al.*, 2009; *Lau and Wu*, 2010; *Zhang et al.*, 2010; *Zuluaga et al.*, 2010; *Guimond et al.*, 2011; *Jiang et al.*, 2011; *Ling and Zhang*, 2011; *Park and Elsberry*, 2013]. This is primarily because of the absence of better datasets that can provide the regional or global distribution of the atmospheric latent heating, understanding of which is crucial for assessing the impact of clouds on the energetics of the earth-atmosphere system.

2.6 Micro Pulse Lidar (MPL) system

Though the spaceborne observations can provide the vertical and horizontal distribution of clouds over a given region, they cannot provide the continuous evolution of the vertical structure of clouds. Though high-resolution geostationary satellite data can provide observations on the spatio-temporal evolution of clouds, these observations are limited to the top layer cloud and at time intervals of ∼20 to 30 minutes. On the other hand, ground-based radar and lidar observations can provide information on the time evolution of clouds, but limited to a given geographical location. A Dual Polarization Micro Pulse Lidar system (Model: MPL-4B-POL of Sigma Space Corporation, USA) has been operational at Thumba, Thiruvananthapuram [8.5°N, 77°E] since March 2008. This station is located at the southwest coast of Peninsular India adjoining the southeast Arabian Sea and the lidar site is located at ∼500 m inland from the Arabian Sea coast.

2.6.1 MPL Configuration

The MPL is a compact system which is capable of continuous observations during both day and night time. A photograph of the MPL system and its schematic diagram are shown in Figure 2.5. Major features of the MPL system are given in Table 2.9. The lidar system consists of a diode-pumped solid state Nd:YAG laser transmitter emitting laser pulses at the wavelength of 532 nm at a PRF of 2500 Hz. The pulse width is ∼7 ns and maximum pulse energy is 8 μJ. The laser pulse energy is controlled by a laser controller. A Maksutov-Cassegrain type telescope having a primary mirror diameter of 179 mm is used in 'transceiver' mode which serves as transmitter for the outgoing laser pulses and receiver for collecting the backscattered lidar signal. The telescope also acts as beam expander for the transmitted laser beam. The linearly polarized laser pulses from the laser source are directed to a negative lens followed by a polarizing beam splitter which reflects the laser pulses towards the secondary and primary mirrors of the telescope, through which the laser beam is transmitted. The transmitted laser radiation has a diameter of 179 mm at the exit of the telescope and is collimated with an effective divergence of ∼14 μrad. A liquid crystal retarder (LCR) placed between the polarizing beam splitter and the secondary mirror of the telescope modulates the polarization of the transmitted and received radiation, which enables the dual polarization lidar observations. The Maksutov-Cassegrain type telescope collects the backscattered radiation, which is passed through the liquid crystal retarder (LCR), polarization beam splitter and a field limiting iris. Light passing through the iris is collimated and passed through two identical narrow-band interference filters (central wavelength = 532 nm; Full-width at Half Maximum = 0.14 nm, Out-of-band rejection

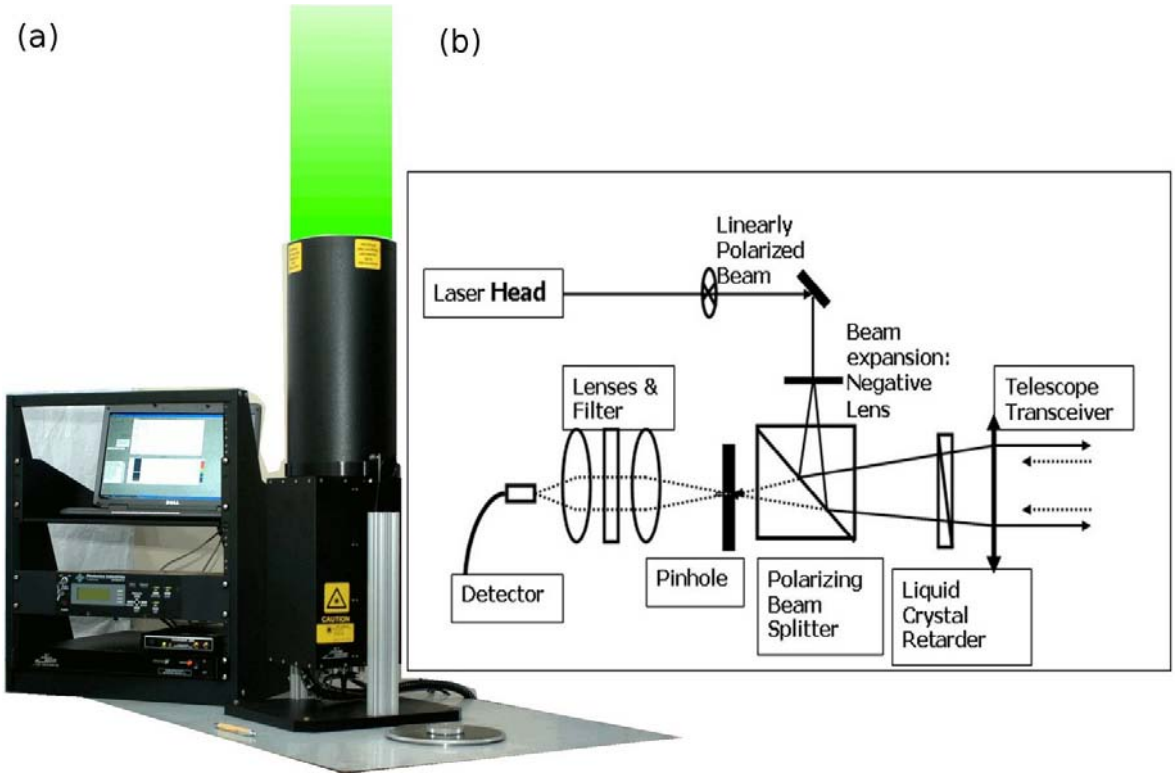

Figure 2.5: (a) Photograph of the Micropulse Lidar (MPL) system at Thumba and (b) schematic diagram of the MPL.

$= 10^5$) in order to reduce the background light, and is focused onto a photon counting Avalanche Photodiode (APD) detector.

A programmable multi-channel scalar (MCS) is used for range-resolved photon counting (which is synchronized with a trigger pulse from the laser transmitter). The photon counts are made with a range resolution of 30 m. The MCS also does the time integration at preset intervals, which is generally set as 60 s. The range-resolved photon count data, integrated for 60 s, are recorded in the computer along with the auxiliary information such as the average pulse energy, range resolution, duration of time-integration and temperatures of the detector and laser source.

2.6.2 Detection of Co- and Cross-polarized lidar signal

Conventionally, the co- and cross polarized backscattered signals are measured by transmitting one type of polarization and detecting the co- and cross polarization using two independent detector channels. This requires that the two detector channels are calibrated and the calibration constants are stable. In MPL, detection of the co- and cross-polarized lidar signals is realized using a different approach by altering the polarization state of the transmitted pulse and received signal using an actively controlled liquid crystal retarder (LCR) and employing a single detector. The advantage this

Table 2.9: Features of the MPL system at Thumba.

Transmitter	
Laser	Diode pumped Nd-YAG
Wavelength	532 nm
Maximum energy per pulse	8 μJ
Pulse width	7 ns
Pulse repetition rate	2500 Hz
Transceiver	
Telescope type	Maksutov-Cassegrain
Diameter	179 mm
Fild of view	96 μrad
Interference filter band width	0.14 nm (FWHM, 2 filters)
Polarization	Liquid Crystal Retarder (LCR)
Detector & Data Acquisition System	
Detector	APD in photon counting mode
Range resolution	30 m
Detector Dead Time (@ <1MHz)	47.6 ns
Detection	Co- and Cross-Polarization Channels
Synchronization and Data acquisition	Multi-channel scalar
Computer interface	USB

method is that the detector efficiency and range-dependent corrections are the same for both the polarizations and cancel out while estimating the depolarization ratio. The detected signals at the two polarizations are converted to the linear depolarization ratio following the method of *Flynn et al.* [2007]. This method of the co-polarization and depolarization measurements is explained below.

Detection of co-polarized signal: When the LCR is operated with quarter-wave retardation, the polarization state of the linearly polarized laser pulses (which is the polarization state at the output of the laser source) will be changed to circular polarization before transmitting to the atmosphere. When circularly polarized light undergoes non-depolarizing scattering in the atmosphere, the backscattered light is circularly polarized but with reversed rotational sense. For example, if the outgoing laser beam has right-hand circular polarization, the backscattered non-depolarized light will have left-hand circular polarization. After passing through the LCR, this will again become linearly polarized but with orientation orthogonal to the original laser polarization. The polarization beam splitter will pass this radiation towards the detector. In contrast, the depolarized backscattered signal will have right-hand circular polarization, which will be changed by the LCR to linear polarization having same orientation as the original laser polarization. This will be reflected by the polarization beam splitter, and will not reach the detector. Quarter-wave retardation of the LCR is achieved by

applying electric pulses with amplitude of 2.9 volts to the LCR.

Detection of depolarized lidar signal: When the LCR is operated with zero retardation, polarization state of the radiation passing through it will not be altered. In this condition, the transmitted laser beam will be linearly polarized. Backscattered lidar signal with identical polarization will be reflected by the polarizing beam splitter and will not pass through it towards the detector. In contrast, the depolarized lidar signal will have a polarization orthogonal to the transmitted laser beam, which will pass through the polarizing beam splitter towards the detector, and will be detected by the system. Zero retardation of the LCR is achieved by applying electric pulses with amplitude of 5.0 volts to the LCR.

2.6.2.1 Estimation of the Linear Depolarization Ratio (LDR)

In the present configuration, the lidar system alternates between the two states of polarization at an interval of 60 s and the range-resolved co-polarized and depolarized lidar signals are integrated for 60 s and recorded. Note that the above technique does not exactly represent the conventional depolarization measurements, since the observations are carried out at two different polarization states: one with linear and the other with circular polarization. The co-polarized and cross-polarized lidar signals measured using the above techniques are used to estimate the conventional linear depolarization ratio (LDR) using the following equations [*Flynn et al.*, 2007]:

$$LDR(z) = \frac{\delta_{MPL}(z)}{\delta_{MPL}(z) + 1} \tag{2.3}$$

$$\delta_{MPL}(z) = \frac{|P_{(0,z)}|}{|P_{(\pi/2,z)}|} \tag{2.4}$$

where Z represents the altitude, and $P_{(0,z)}$ and $P_{(\pi/2,z)}$ are the received power when the LCR is operated with zero and quarter wave retardation respectively. The total lidar backscattered signal power is estimated as [*Flynn et al.*, 2007]:

$$P_{(z)} = 2P_{(0,z)} + P_{(\pi/2,z)} \tag{2.5}$$

2.6.2.2 Correction of the lidar signal

Backscattered signals detected by the MPL are affected by the errors caused by detector dead-time, after-pulse effects, and the range-dependent lidar geometrical correction factor. All the above corrections are incorporated in the off-line processing of the MPL data [*Rajeev et al.*, 2010; *Mishra et al.*, 2010, 2012]. The geometrical correction factor for the MPL is determined experimentally following the method described

by *Welton* [2002] and *Mishra et al.* [2012]. For the present MPL system, the geometrical correction factor is unity (no correction required) beyond a range of 1080 m. The 'dead-time' correction for the APD detector is carried out using the calibration curve provided by the manufacturer. In order to minimize the effect of detector dead-time and multiple photon counts (as the count rate is directly proportional to the laser pulse energy), the MPL system is usually operated at low energy of ~2.5 μJ/pulse, which can provide good signal strength up to about 20 km during night in the absence of opaque clouds.

After emission from the laser source and before transmission into the atmosphere, the laser pulse interacts with various reflective surfaces inside the telescope which cause multiple reflections of the outgoing pulse from these surfaces. This causes large amount of reflected photons to reach the detector even before the laser pulse enters the atmosphere [*Campbell et al.*, 2002]. The 'after-pulse' effect is minimized by blanking the detector for the first 200 ns after the transmission of a laser pulse. Even after this duration, the energy at the detector surface is sufficiently large to momentarily saturate the APD detector. A run-on signal is created by this event, which decays gradually with time through the length of the sampling period. These transient photon counts due to initial saturation of the APD from the outgoing laser pulse are known as 'after pulse counts' and are quite large at short ranges (typically <120 m). The 'after pulse counts' are measured by operating the lidar after covering the transceiver output by a black cloth (rough and thick), which prevents the transmission of most of the pulse energy to the atmosphere as well as any photons scattered from the atmosphere before reaching the telescope. The 'after pulse counts' are subtracted from the measured photon counts to get the actual lidar backscattered signal.

2.6.2.3 MPL data

In summary, the MPL provide altitude profiles of backscattered lidar signal with a vertical resolution of 30 m and time integration of 60 s. The polarization state of the lidar is altered at every 60 s so that the co- and depolarized lidar signals are acquired alternately. The system is operated only during non-rainy periods. In general, the MPL is operated almost continuously for about 60 h per week (except for short breaks). The data recorded during March 2008 to May 2011 are used in this study for investigating the cirrus cloud properties and the time evolution of cirrus structures over Thiruvananthapuram. Methodology used for the identification of cirrus clouds and temporal evolution of their structure from the MPL data, determination of their optical and physical properties and the sources of uncertainties are explained in Chapter 6.

2.7 Auxiliary data

2.7.1 Sea Surface Temperature (SST) from TRMM-Microwave Imager

The Microwave Imager on-board TRMM (TRMM Microwave Imager–TMI) has the heritage of SSM/I and is a multi-channel passive microwave radiometer operating at five frequencies: 10.65, 19.35, 37.0, and 85.5 GHz at dual polarization and 22.235 GHz at single polarization. These observations can provide information on the integrated column precipitation content, cloud liquid water, cloud ice, rain intensity and SST. The TMI makes a conical scanning at 53° and has a swath of 878 km. The field of view and hence horizontal resolution of the data varies with spectral band.

Estimation of SST from microwave observations is advantageous over the infrared radiometer measurements as the latter requires a cloud-free field of view [*Reynolds et al.*, 2010]. In contrast, the microwave retrievals of SST using observations made at 10.7 GHz can be carried out under cloudy conditions also (except rain), as clouds are nearly transparent to this radiation. However, the microwave retrievals are sensitive to sea-surface roughness, while the infrared retrievals are not. A primary function of the TRMM SST retrieval algorithm is the removal of surface roughness effects. The microwave and infrared SST retrievals are complementary and can be combined to obtain a reliable global data set. Algorithm for the retreival of SST from TMI is similar to that followed for AMSR and is described in *Wentz and Meissner* [2000] and Meissner [2000].

The TMI-SST data are available from December 1997 to the present as daily maps (separated into ascending and descending orbit segments), 3-day mean maps, weekly mean maps and monthly mean maps, covering all longitudes in the latitude band of 38°S to 38°N with a pixel resolution of 0.25°. Comparison of the TMI-SST with in situ observations using buoys shows that, on average, the former is accurate to better than 0.5°C.

2.7.2 Surface Wind Divergence from scatterometer

Surface winds over ocean can be derived from space borne scatterometers under all weather conditions. The scatterometer is essentially a microwave radar which transmits the microwave pulses (e.g., at the frequency of 5.3 GHz in ERS-1/2) and detects the signal that is backscattered by surface roughness (ripples) over ocean. The magnitude of the backscattered power increases with increase in surface roughness. The wind speed is a measure of the strength of the backscattered signal and the wind direc-

tion is estimated from the angle that is most likely to be consistent with the observed backscattered power from different angles. The surface wind characteristics are determined using an empirical model which relates the wind speed and direction to the sea surface radar reflectivity.

The present study utilizes the monthly mean data of the surface wind divergence (SWD) derived from the surface wind observations carried out using the space borne scatterometers onboard the Earth Remote Sensing satellites (ERS-1 and ERS-2) and QuikSCAT obtained from Centre ERS d'Archivage et de Traitment (CERSAT), France. The ERS-1 data during August 1991-May 1996, ERS-2 data during June 1996 to December 2000 and QuikSCAT data during January 2001 to October 2009, covering a period of ∼18 years are used. These are Sun-synchronous polar orbiting satellites and hence make observations at the same local time of the day. The scatterometer onboard ERS-1/ERS-2 operates at 5.3 GHz while the QuikSCAT operate at 13.4 GHz. The ERS-scatterometer has a swath of ∼500 km while that of QuikSCAT is 1800 km. The spatial resolution of surface wind obtained from ERS-1/ERS-2 is 1°× 1°, while that of the QuikSCAT data is 0.5°×0.5°. The overall accuracy of the surface wind derived from the scatterometer data is ∼3 ms^{-1}. Details of the scatterometer observations, the method of deriving surface wind, and validation of the wind data are widely discussed in literature [e.g., *Quilfen*, 1993; *Bentamy et al.*, 1996; *Liu*, 2002]. In the present study, the main purpose of using SWD data is to understand the association of surface wind divergence with certain features associated with the frequency of occurrence of clouds which are explained in Chapter 4.

2.7.3 Reanalyses data on atmospheric dynamics

Reanalyses (Retrospective-analyses) integrate the data from a variety of observing systems with numerical models to produce a temporally and spatially consistent synthesis of observations and analyses of variables that cannot be easily observed (e.g., global 3-dimensional wind and their time evolution). The reanalysis products are extensively used in climate studies as well as for generating the maps of meteorological variables. In the present study, reanalysis data is used to present the atmospheric dynamics for better understanding of the observed variations in cloud distribution. Several reanalysis products were used during the course of this study, including the NCEP (National Centre for Environmental Prediction) reanalysis, MERRA (Modern-Era Retrospective analysis for Research and Applications) and ECMWF Reanalysis (ERA), all of which generally yield consistent results. However, most of the reanalysis outputs presented in this thesis is based on MERRA as it has better spatial resolution (horizontal and vertical resolutions) and frequency at which the output are available. MERRA is a NASA reanalysis using the Goddard Earth Observing System Atmospheric Data Assimilation

System - version 5 (GEOS-5) and incorporates a large number of insitu observations and satellite data to maximize their impact in the analysis and prediction of climate and weather through integrated Earth system modelling and data assimilation [*Rienecker et al.*, 2011]. It covers the time period from 1979 (starting of the regular and systematic satellite observations of meteorological parameters) through the present. MERRA provides the 6-hourly three-dimensional atmospheric analyses at a spatial resolution of 0.5° latitude × 0.66° longitude at 72 vertical levels. It also provides 3 hourly data at 1° spatial resolution at 42 pressure levels extending from 1000 hPa to 0.1 hPa level, which is used in the present study. It has 17 levels from 1000 to 500 hPa, 8 levels from 450 to 100 hPa and 17 levels above.

Comparison of the MERRA output with other reanalyses shows that there is little difference in the new reanalyses in most of the aspects of atmospheric dynamics and climate variability, though significant differences remain in poorly constrained quantities such as precipitation and surface fluxes. Comparisons with in situ observations show that the MERRA is one of the best reanalyses products available at present with minimum biases, though deficiencies still exist [e.g., *Decker et al.*, 2012; *Roberts et al.*, 2012].

2.7.4 Other gridded climate data products

The other gridded climate data products used here include the monthly mean Outgoing Longwave Radiation (OLR) during 1974 to 2011, which were obtained from the National Center for Atmospheric Research (NCAR) archives of NOAA. The Monthly mean of OLR is created from the daily OLR files obtained from NOAA twice-daily OLR values [*Liebmann and Smith*, 1996] having a 2.5° grid resolution. This data has a gap during March to December period of 1978 because of the satellite failure. The monthly mean precipitation data obtained from the Global Precipitation Climatology Project (GPCP V2) [*Huffman et al.*, 1997; *Gruber et al.*, 2000] during the period of 1996 to 2008 are also used in the present study. This data is a combination of the rain-gauge observations, satellite measurement of precipitation and the numerical model output and have a spatial resolution of 2.5°× 2.5°.

2.8 Summary

Details of the experimental techniques, satellite data and methods of analyses employed in the present study are presented in this chapter. The characteristics, advantages, limitations and potential uncertainty limits of the data are discussed. This thesis mainly utilizes multi-year satellite observations to study the spatial and vertical distribution of clouds and their impact on the energetics of the earth-atmosphere

system. The temporal variation of cirrus structures are investigated using Micropulse Lidar observations carried out at Thiruvananthapuram (8.5°N, 77°E).

Characteristics of the vertical distribution of clouds and their spatial variations are derived from CloudSat-CPR data during June 1996 to February 2011. These observations provide vertical profiles of optically thick clouds (generally for COD>1) along the sub-satellite track with a spatial resolution of 1.4 km × 1.7 km and vertical resolution of 240 m. CloudSat is part of NASA's A-Train constellation and has a 16-day repeating orbit cycle; the ascending tracks are separated longitudinally by ∼1.6° at the equator. The main limitations of CloudSat-CPR are: (i) its limited frequency of observation of a given location due to non-scanning, which limits the observations to produce only a curtain (2-dimensional cross section along the vertical and orbital track) of the cloud distribution along the sub-satellite track, and (ii) thin semitransparent clouds will be undetected. Due to the limitation in the frequency of observation, CloudSat data should be averaged for longer period to produce the mean spatial and vertical distributions. Hence, this thesis primarily focuses on the multi-year monthly and seasonal mean cloud distributions rather than their variations over short time scales (such as intra-seasonal variations).

In contrast to CloudSat, the spaceborne Lidar, CALIOP onboard CALIPSO (which is also part of the A-Train constellation) observations can detect thin semitransparent clouds, but cannot penetrate optically thick clouds. The orbital characteristics of CALIPSO and observation geometry along-track observations providing the altitude profiles of backscatter coefficient along the sub-satellite track are the same as that for CloudSat. With the ability of the CPR to probe optically thick cloud layers and that of CALIOP to detect semitransparent clouds, the two instruments have the potential of providing as complete a picture of the occurrence of clouds as has been compiled to date. In the present study, the CloudSat-CALIPSO combined data (2B-GEOPROF-Lidar) during June 2006 to December 2010 are used to investigate the role of SST and atmospheric thermo-dynamics on cloudiness. However, as the 2B-GEOPROF-Lidar will be limited to the profiles having overlap of CPR and CALIOP, the vertical distribution of clouds are derived only from the 2B-GEOPROF data, which is based on CloudSat data alone.

The across-track scanning NOAA-AVHRR provides long-term high resolution (spatial resolution of 4.4 km at nadir for GAC data) spatial distribution of clouds with high repetivity (twice daily), but are limited to the horizontal distribution of total cloudiness which are biased to the high-altitude clouds. Data from the polar orbiting sun-synchronous satellites NOAA 14/16/18-AVHRR are used here to derive the long-term (December 1995 to December 2010) monthly mean horizontal distributions of clouds at high horizontal resolution, which further improve the insight and confidence

on the features observed using CloudSat whose spatial resolution (along longitude) and frequency of observation are rather limited. The cloud detection is carried out using threshold method and the spectral dependence of albedo in the visible and near-IR bands. While this analysis can detect all optically thick high altitude clouds, it underestimates the optically thin semitransparent cirrus and the low altitude clouds over cold ocean.

The shortwave, longwave and net cloud radiative forcing at the TOA during the summer monsoon and post-monsoon seasons of 2012 are estimated using the data from ScaRaB onboard the recently launched low-inclination Megha-Tropiques satellite. This data has a spatial resolution of 40 km at nadir and a swath of 2200 km. High repetivity of these observations over the tropics (due to the low orbital inclination of MT) at different local times enables the estimation of cloud radiative forcing (CRF) as a function of local time (for each pixel) and hence produce the true diurnal variation of the shortwave and longwave cloud radiative forcing. The Megha-Tropiques has a 7-day recurrent cycle, but with different local time of the overhead passes. As the precession cycle of the orbit is 51 days, similar orbital paths and time of pass are repeated once is 51 days. Due to this limitation, the data needs to be averaged over a season by combining the data for different local times during the period to produce an 'equivalent day' analysis and elucidate the diurnal variation of CRF. After correcting for the bias error, the instantaneous SW fluxes were found to follow a 1:1 relationship with the CERES data, with an RMS error of $<$26 Wm^{-2}. Bias error of the longwave flux is negligible and the RMS error is $<$8 Wm^{-2}.

Altitude profiles of the latent heating of the atmosphere by precipitating clouds are obtained using the data from the Precipitation Radar onboard TRMM during June 2006 to February 2011 (same period as CloudSat data used here). Horizontal resolution of the TRMM-PR is 4.3 km at nadir, the range resolution is 250 m and the scanning swath width is 220 km. The present study uses the TRMM-PR-Level-3 product on the monthly mean convective and stratiform latent heating (CSH) to investigate the altitude variations of latent heating by precipitating clouds and its spatial variations. This data set has a spatial resolution of $0.5^\circ \times 0.5^\circ$ and has 19 vertical levels from the surface to a height of 18 km. Uncertainty in the instantaneous values of LHR estimated from TRMM-PR is expected to be quite large. However, the spatial and temporal averaging will reduce the overall uncertainty of the seasonal mean LHR to less than 30%. Despite the relatively large uncertainty of the LHR, the CSH data has been extensively used to investigate the role of tropical clouds in the latent heating and thermodynamics of the atmosphere. This is mainly because of the absence of better datasets which can provide the regional or global distribution of the atmospheric latent heating.

The ground-based Dual polarization Micropulse Lidar has been used to observe the structure of cirrus clouds and their time evolution over Thiruvananthapuram. The MPL data are recorded continuously for about 60 hours (with short breaks) with a time resolution of 1 minute and vertical resolution of 30 m. The MPL data recorded during March 2008 to May 2011 are used to estimate the altitude profiles of clouds and time evolution of their structure. Linear depolarization ratio estimated from the dual prolaizartion observations provides information on the non-sphericity of the cloud droplets/ice particles.

The daily SST data are obtained from the TRMM Microwave Imager (TMI) during 2006 to 2011. The TMI-SST has a spatial resolution of 0.25°, but are limited to the latitude band of 38°S to 38°N. Comparison of the TMI-SST with in situ observations using buoys shows that, on average, the former is accurate to better than 0.5°C. Observations of the surface wind under all weather conditions are obtained from space borne scatterometers QuikSCAT and ERS-1/2. The spatial resolution of surface wind obtained from ERS-1/ERS-2 is 1°× 1°, while that of the QuikSCAT data is 0.5°× 0.5°. The overall accuracy of the surface wind derived from the scatterometer data is ∼3 ms^{-1}. Information on the 3-dimensional winds and atmospheric general circulation are obtained from the Modern-Era Retrospective analysis for Research and Applications (MERRA).

Chapter 3

General Characteristics of the Spatial and Vertical Distribution of Clouds, their Seasonal Variations and Association with General Circulation of the Atmosphere

3.1 Introduction

Clouds and their genesis play a key role in the redistribution of energy and water vapour in the earth-atmosphere system [*Kiehl and Trenberth*, 1997; *Ringer and Shine*, 1997; *Moore et al.*, 2001; *Trenberth et al.*, 2009]. Temperature of the Earth's surface and the thermal structure of the atmosphere are considerably modulated by clouds through interaction with radiation and latent heat released [*Ramanathan et al.*, 1989; *Harrison et al.*, 1990; *Rossow and Lacis*, 1990; *Gupta et al.*, 1993; *McFarlane and Grabowski*, 2007]. Magnitude of these effects depends on several factors, such as the horizontal and altitude distributions, geometrical thickness, optical depth, liquid/ice water content, droplet size distribution and emissivity of clouds: the first and foremost among them being the spatial and vertical distribution of clouds. Horizontal and vertical distributions of clouds as well as the cloud properties are strongly coupled to general circulation of the atmosphere, moisture convergence, and efficiency of air-surface (land/sea) interactions. Conversely, clouds play a dominant role in modulating the energy and moisture budget of the earth-atmosphere system, meteorological parameters and atmospheric general circulation through feedback processes. Genesis of clouds and the cloud feedback take place through a sequence of complex and highly

non-linear processes [e.g., *Hartmann and Short*, 1980; *Liebmann and Hartmann*, 1982; *Gadgil et al.*, 1984; *Graham and Barnett*, 1987; *Slingo and Slingo*, 1988; *Hartmann et al.*, 1992; *Pai and Rajeevan*, 1998; *Wang and Rossow*, 1998]. One key difficulty in modeling the radiative and climate effects of clouds is in the treatment of the complex space-time variabilities in cloudiness [*Stephens*, 1988; *Rossow*, 1989]. Further, an adequate understanding of the air-sea interaction processes requires a detailed analysis of the cloud distribution under different conditions of Sea Surface Temperature (SST) and atmospheric thermo-dynamics. Knowledge of the cloud distribution is also essential for the estimation of the actual impact of aerosols on climate.

Parameterization of the cloud generation and feedback processes are major challenges in numerical models for weather prediction and climate simulation [e.g., *Bony et al.*, 2000]. Improvement in understanding the cloud processes essentially requires detailed studies on the spatial and vertical distribution of clouds, their properties, and variations under variety of meteorological conditions. The spatio-temporal variations in cloud distribution can also act as tracers of some of the important aspects of atmospheric dynamics and air-sea interaction [*Meenu et al.*, 2007] that are not understood hitherto. Studies focusing on the spatial distribution of clouds, their temporal variations and impact on the atmospheric energetics over the Indian subcontinent and the surrounding oceanic areas are rather limited [e.g., *Saha*, 1971; *Grossman and Garcia*, 1990; *Gambheer and Bhat*, 2000; *Rajeevan and Srinivasan*, 2000; *Roca and Ramanathan*, 2000; *Roca et al.*, 2002; *Zuidema*, 2003; *Sathiyamoorthy et al.*, 2004; *Meenu et al.*, 2007, 2010, 2011; *Nair et al.*, 2011, 2012; *Rajeevan et al.*, 2012] compared to those over the other regions [e.g., *Hanson et al.*, 1991; *Fu et al.*, 1990; *Klein and Hartmann*, 1993; *Zhang*, 1993; *Mapes and Houze*, 1993; *Norris*, 1998a, b; *Hall and Vonder Haar*, 1999; *Gettelman and Forster*, 2002; *Rossow and Pearl*, 2007; *Hong et al.*, 2008]. Long-term regional distribution of clouds over the Indian region has been carried out using the spaceborne imager data [*Meenu et al.*, 2007, 2010, 2011]. Vertical distribution of the upper tropospheric semitransparent cirrus clouds and their spatial variations were also investigated earlier based on ground-based and spaceborne lidars [*Sunilkumar and Parameswaran*, 2005; *Sunilkumar et al.*, 2010; *Meenu et al.*, 2011].

While the passive radiometer imager data can provide information on the horizontal distribution of clouds and cloud top temperature (and hence an idea about the cloud top altitude), they cannot 'see' the clouds that are present underneath the top layer and hence cannot provide the vertical distribution of clouds. The spaceborne Lidar onboard CALIPSO can provide the vertical distribution of clouds (mainly optically thin semitransparent cirrus clouds), but cannot penetrate through thick clouds, including thick cirrus. The CloudSat can provide the vertical distribution of all optically thick clouds (except the semitransparent ones), and is the first and only such satellite to

monitor the altitude profiles of clouds around the globe as of now. Barring a few [*Nair et al.*, 2011; *Rajeevan et al.*, 2012], studies on the vertical distribution of clouds occurring over the entire troposphere and their spatial variations over the Indian region and the surrounding oceans are extremely sparse. Main driving force for the present study is to fill this gap. This is essential for improving the understanding on clouds, their genesis and potential impact on the atmospheric thermo-dynamics over the Indian region and the surrounding oceans which have several unique dynamical features.

Importance of the tropical clouds and their distribution over the Indian region, in particular, are discussed in Chapter 1. Main aspects of this uniqueness are:

1. The deepest convection over the entire globe occurs over the north Bay of Bengal during the Asian summer monsoon season.

2. Associated with the largest annual migration of the Inter Tropical Convergence Zone (ITCZ) and the resulting monsoons, cloudiness over the Indian region undergoes large variations in space and time.

3. Considerable spatio-temporal variations of SST and atmospheric dynamics over this region make it a natural laboratory to test some of the important hypotheses on air-sea interactions such as the SST-convection-cloudiness relationship [e.g., *Gadgil et al.*, 1984; *Graham and Barnett*, 1987; *Meenu et al.*, 2012].

General characteristics of the altitude distribution of distribution of clouds and its spatial variations over the Indian subcontinent and the surrounding oceanic regions over the geographical region from 30°S to 30°N and 30°E to 110°E derived from CloudSat data during July 2006 to February 2011 are presented in this chapter. A picture on the long-term monthly mean regional distribution of total cloudiness (all cloud types) derived using the daily data of NOAA-AVHRR during 1996 to 2010 is also presented for comparison. Association between the horizontal and vertical distribution of clouds and atmospheric general circulation is investigated using the circulation data obtained from MERRA.

The main objectives of this chapter are:

1. To provide a quantitative estimate of multi-year monthly and seasonal mean vertical distribution of clouds and its spatial variations over the Indian subcontinent and the surrounding oceans.

2. To understand the influence of atmospheric general circulation - especially the ITCZ, Hadley and Walker circulation cells - on the vertical distribution of clouds and its spatial variations.

This chapter also provides the background information on the horizontal-vertical distributions of clouds and the prevailing atmospheric circulation, which are essential for the topics investigated in the subsequent chapters.

3.2 Data and method of analysis

3.2.1 Altitude variations of the frequency of occurrence of clouds using CloudSat data

Vertical distribution of clouds and its spatial variations are obtained from the polar orbiting sun-synchronous satellite, CloudSat, having a Cloud Profiling Radar (CPR) operating at 94 GHz, which provides the altitude profiles of backscattered radar signal from hydrometeors with a vertical resolution of 240 m along the sub-satellite track [*Haynes and Stephens*, 2007]. Details of the CloudSat data are provided in Chapter 2. This study utilizes the cloud geometrical profile product, 2B-GEOPROF (Version-4) provided by NASA, which gives the cloud mask containing the information on cloud layers and their top and base altitudes for the individual profiles along the satellite orbit [*Mace et al.*, 2007]. The vertical resolution of the cloud mask is 240 m and the horizontal resolution (along track) is 1.7 km. This provides the vertical distribution of clouds only along the sub-satellite track. Note that the repetivity of CloudSat orbits is 16 days and the individual orbits are separated longitudinally by $\sim$1.6° at the equator (Chapter 2). This is one of the major limitations of CloudSat compared to the conventional imager data (e.g., NOAA-AVHRR) wherein the across-the-track scan with a large swath ($\sim$2600 km) ensures that each geographical location is observed everyday. In the case of CloudSat, the same region (located along the well-defined orbital tracks) will be observed twice during the 16-day period: one during daytime and the other during night. Due to this limitation in the frequency of observation, the data are analyzed here to study the latitude and longitude variations of the vertical distribution of clouds at different longitude and latitude bands of sufficiently large width (typically 10°).

Operating wavelength of the Cloud Profiling Radar (CPR) onboard the CloudSat is 3.19 mm. As the typical size range of cloud droplets (8 to 100 μm) is substantially smaller than the CPR wavelength, the signal detected by CPR from clouds arises mainly from Rayleigh scattering. It is found that the CPR mainly detects optically thick clouds, which produce sufficiently strong Rayleigh lidar signals. The signal from optically thin clouds (mainly the semitransparent cirrus clouds) will be considerably weak and are not detectable using CloudSat. Though the lower boundary (in terms of cloud optical depth) of CloudSat detection is not well-defined, an inter-comparison

between CloudSat and CALIPSO observations indicate that the clouds having optical depth less than 1.0 are mostly not detected by CloudSat. The reliability of cloud detection by CloudSat increases with cloud optical depth (COD). For optically thick clouds (COD>1.0), the accuracy of cloud detection using CloudSat is more than 90% (in addition to the COD, physically thin clouds especially those with thickness <240 m also contributes to the uncertainty of ∼10%) [*Mace*, 2007]. Hence, the present study using CloudSat data mainly shows the vertical distribution of optically thick clouds and not the semitransparent cirrus clouds. However, as demonstrated by the results presented in the following sections, the CloudSat can detect thick cirrus clouds, most of which originate from deep convective anvils.

The CloudSat data are used to estimate the monthly and seasonal mean altitude profiles of the frequency of occurrence of clouds and their zonal and meridional distributions during the June to September period of 2006 to 2010. For each individual satellite track, the 2B-GEOPROF data provide the base and top altitudes of the cloud layer for up to 5 cloud layers as a function of profile number. This data also provides the latitude and longitude of the footprint corresponding to each profile. The individual profiles are separated by 1.7 km. The monthly mean latitude-altitude cross section of the frequency of occurrence of clouds for a given longitude band (of 10° width) is determined as described below:

1. For each individual profile, all the altitude bins (of 240 m vertical resolution) that occur between the base and top of the cloud layer (as given by 2B-GEOPROF data) are filled with a value of 1 to identify the presence of cloud; all other altitude bins are filled with zeros. This provides a two-dimensional matrix (as a function of profile number and altitude) of cloud occurrence for the given track.

2. The above matrix of cloud occurrence for all satellite orbits, that occur within this given longitude band of 10° width (say, between 60 to 70°E) during a month (say, January 2007), are averaged and gridded into a uniform latitude-altitude matrix having cell sizes of 0.1° (latitude) and 240 m (altitude). This is obtained by summing all the observations occurring within each latitude grid (of 0.1° size) and altitude bin (240 m size) and dividing by the total number of observations within each latitude grid (the number of observations at all altitude bins within a latitude grid is the same). This provides the monthly mean latitude-altitude cross section of the frequency of clouds within the given longitude band. As the polar orbiting CloudSat provides data at very fine spatial intervals long its track (somewhat aligned along the longitude circle), the latitude grid size of 0.1° is used in this study. However, it is important to note that, though the estimates are carried out at fine latitude grid size of 0.1°, this analysis can provide only the longitudinally averaged gross features of cloud distribution during each month.

Very small scale features (spanning for, say, less than few degrees) cannot be discerned using this analysis. However, reducing the longitudinal band width is also not advisable as the number of satellite orbits for small longitude bands are highly limited.

3. The multi-year (2006 to 2011) monthly and seasonal mean latitude-altitude cross sections of the frequency of occurrence of clouds are determined by averaging the corresponding frequency of occurrence of clouds observed during individual years.

The longitude-altitude cross sections of the frequency of occurrence of clouds within a given latitude band of 10° width (say, between 10° to 20°N) are estimated following the same method as explained above, but for a longitude grid size of 2°. The coarser longitude grid size of 2° is used here as the individual tracks of the Polar orbiting CloudSat satellite within the 16-day orbit cycle are distinctly separated in longitude.

3.2.2 Spatial distribution of the frequency of occurrence of total cloudiness using NOAA-AVHRR data

As explained earlier, the frequency of observation of a given location using CloudSat are limited. Observations using NOAA-AVHRR can provide the information on cloud occurrence at high spatial resolution (4 km at nadir) on a daily basis and has been extensively used to study the regional distribution of clouds over the Indian region [*Meenu et al.*, 2007, 2010, 2012; *Meenu*, 2010]. The main advantage of this data is its high spatial resolution and availability over a long duration. However, it cannot provide the vertical distribution of clouds as the IR and visible radiation detected by the passive sensors onboard AVHRR mainly originate from top of the cloud or surface layer. Further, the cloud discrimination using NOAA-AVHRR data on brightness temperature might underestimate the low-altitude clouds (especially when the cloud top temperature is comparable to the surface temperature). In the present study, the features observed using multi-year observations of the vertical and spatial distribution of clouds derived from CloudSat data are compared with those observed using the long-term (1996 to 2010) monthly and seasonal mean frequency of occurrence of total clouds derived using NOAA-14/16/18-AVHRR. While the former provides the vertical distribution clouds and their zonal and meridional variations, the latter provides the spatial distribution of total cloudiness with high spatial resolution which is not vertically resolved.

Daily data obtained from the polar orbiting NOAA-14/16/18-AVHRR (equatorial crossing time: approx. 01:30 PM/AM) during the period of 1996 to 2009 over the Indian region and surrounding oceans (30°S to 30°N and 40°E to 105°E) are used in

this analysis. The Global Area Coverage (GAC) data used here has a pixel resolution of 4 km at nadir. The occurrence of clouds in a pixel is identified using the methods explained in Chapter 2 and is same as that followed in *Meenu et al.* [2010, 2012] and *Meenu* [2010]. The pixel-wise cloud amount derived from each satellite pass is composited for each day and transformed into a uniform geographical grid of size 0.2°× 0.2° to derive the frequency of occurrence of clouds. The monthly mean frequency of occurrence of clouds in each grid is obtained by averaging the observed daily mean fractional cloud amount in that grid in the respective month.

Role of atmospheric circulation on the vertical and horizontal distribution of clouds is investigated using the atmospheric circulation data obtained from MERRA. This is one among the most extensively used datasets for understanding the atmospheric circulation features. The MERRA data provides the atmospheric wind and temperature with a horizontal resolution of 1° at 42 vertical levels. Monthly mean spatial distributions of SST are examined using the TRMM Microwave Imager (TMI). The TMI-SST is based on observations of TMI at 10.7 GHz which are nearly transparent to clouds. This data is advantageous over the infrared SST observations that require a cloud-free field of view. The TMI-SST provides daily observations covering the global region extending from 40°S to 40°N at a pixel resolution of 0.25°. Comparison of the TMI-SST with insitu observations using buoys shows that, on average, the former is accurate to better than 0.5°C [*Reynolds et al.*, 2010].

3.3 Monthly mean features of atmospheric circulation and SST

Gross features of the monthly mean atmospheric circulation and SST, which are closely linked to the cloud distribution, are briefly presented in this section.

3.3.1 Atmospheric circulation

Figure 3.1 shows the monthly mean horizontal winds at the isobaric level of 950 hPa prevailing over the study region (2006 to 2011). During January, the Hadley circulation is manifested by the convergence of lower-tropospheric airmass from the northern hemisphere and southern hemisphere at the south of the equator: typically between 10°S to 5°S over the west and central equatorial region and near the equator over the equatorial Indian Ocean. This is the Inter-Tropical Convergence Zone (ITCZ: the rising limb of Hadley cell), which has a small north-south tilt over the Indian Ocean region during this month. The high-pressure area, manifested by the anticyclonic circulation centered on the central Indian region and Arabia represents the descending limb of Hadley cell in the northern hemisphere. The lower tropospheric winds during

this month are predominantly northerly (northeasterly/northwesterly) from the continental regions into the Arabian Sea, the Bay of Bengal and the tropical Indian Ocean. A similar anticyclonic system prevails around 30°S in the southern hemispheric Indian Ocean, which represents the descending limb of Hadley cell in the southern hemisphere during January. Largest wind speeds are observed at the south Indian Ocean (between 15°S to 25°S) and western parts of the equatorial Indian Ocean and the Arabian Sea. Convergence of air is largest over the east equatorial Indian Ocean and least over the west. This east-west asymmetry is due to the Walker circulation cell. The general circulation features during the other months of winter (December to February) are more or less similar.

General circulation of the atmosphere during the pre-monsoon season (March to May) is characterized by the transition from the winter pattern to the summer monsoon pattern. Overall characteristics of the Hadley and Walker cells, including the locations of their ascending (ITCZ) and descending limbs during March are more or less similar to that during February. In April, the ITCZ over the west and central Indian Ocean migrates towards the north and the region of lower tropospheric convergence over the equatorial Indian Ocean is rather broad. The descending limb of Hadley cell in the northern hemisphere during April is located over the north Arabian Sea and central India. The lower tropospheric winds are strongly diverging near the western equatorial Indian Ocean (indicating strengthening of the descending limb of the Walker cell over this region), while the convergence associated with the Walker circulation prevails over the east equatorial Indian Ocean. By May, the anticyclonic vortex over the Indian subcontinent is replaced by a low pressure area, resulting in the trough regions observed in the central and north-western parts of the Indian subcontinent. The prevailing lower tropospheric winds in the northern hemisphere change from northerlies to southerlies/westerlies/southwesterlies over the Arabian Sea, the equatorial Indian Ocean, and the Bay of Bengal. Though the high-pressure area over the southern hemispheric Indian Ocean prevails during March to May, its location is slightly shifted towards the north during May.

Most important features of the atmospheric circulation during the Asian summer monsoon season (June to September) are the occurrence of a persistent low-pressure system (Heat Low; mean sea level pressure <999 hPa) over the north-western parts of the Indian subcontinent, the monsoon trough generally extending from the Heat Low to the north Bay of Bengal, the high-pressure zone over the Tibetan plateau (Tibetan High, at ∼600 hPa level), the low-level jet (LLJ) extending from the west Arabian Sea to the Peninsular India, the equatorial trough over the equatorial Indian Ocean, the subtropical high-pressure area over the southern hemispheric Indian Ocean (Mascarenes High: mean sea level pressure >1023 hPa), and the tropical easterly jet stream (TEJ)

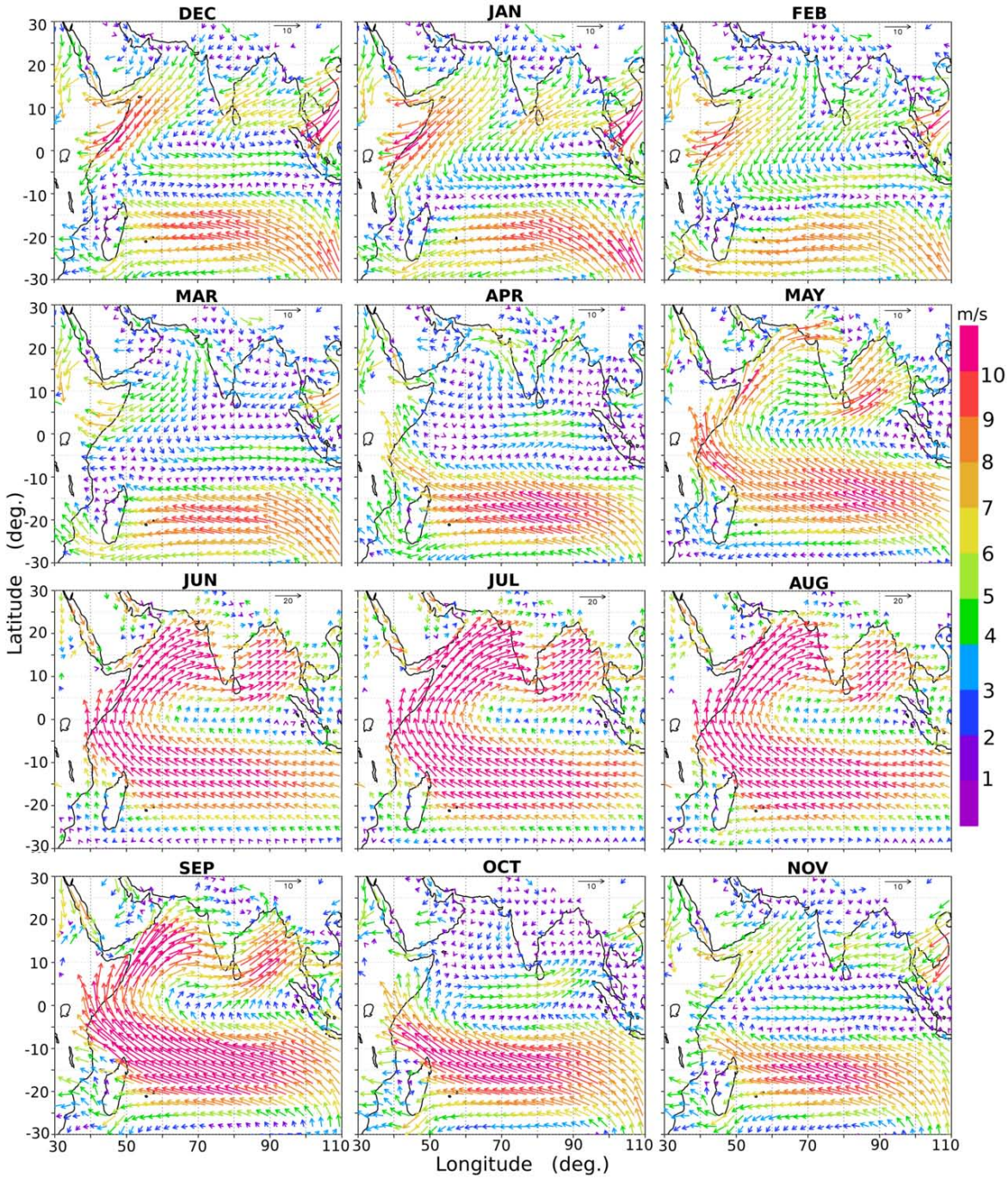

Figure 3.1: Monthly mean horizontal winds at 950 hPa level obtained from MERRA data during 2006 to 2011.

in the upper troposphere [e.g., *Das*, 1968; *Rao*, 1976]. On average, latitude gradient of the mean sea level pressure is >4.8 hPa/10° between the Mascarenes High and Heat Low, which is the primary driving force for the massive monsoon circulation from the southern hemispheric Indian Ocean to the Indian subcontinent. The convergence zones at the monsoon trough and the equatorial trough regions and the anticyclonic circulation at the Mascarenes High are well discernible in Figure 3.1. The anticyclonic

circulation over the Mascarenes High is the seat of the strong descending limb of the Hadley cell and closes the circulation loop by the strong ascending of airmass at the Monsoon Trough and the equatorial trough regions and upper tropospheric flow towards the south. The availability of lower tropospheric vorticity available at the north Bay of Bengal (associated with the extension of the Monsoon trough up to this region) is conducive for the generation of monsoon depressions over this area. On average, wind speeds are largest over the western Arabian Sea and the Bay of Bengal. Orographic lifting of this high velocity air current (which appear as bursts, producing breaks and active precipitation over the region) over the western parts of the Indian subcontinent by the Western Ghats and over the northern and eastern boundaries of the Bay of Bengal are evident in Figure 3.1 as a rather abrupt reduction in horizontal wind in the upwind direction. This causes convection over the east Arabian Sea and the north and northeast Bay of Bengal. Horizontal winds over the western Arabian Sea (Figure 3.1) as well as the Arabian region have significant divergence at the lower tropospheric level. In general, the lower-tropospheric circulation is similar during June to September. However, strength of the summer monsoon circulation gets diminished during September, especially in the northern parts of the Indian subcontinent.

By October, anticyclonic circulation prevails over the central and northern parts of the Indian subcontinent and Arabia, which manifests the descending limb of the Hadley cell. Under its influence, the lower-tropospheric circulation over the northern and central parts of the Indian subcontinent and the Arabian Sea turns to northerly. A strong cyclonic vorticity appears at the south peninsular India. The ITCZ, as seen from the extended cyclonic circulation patterns in Figure 3.1, is very broad and straddles on either side of the equator between ∼10°S to ∼15°N. The descending branch of the Hadley cell over the southern hemispheric Indian Ocean is located at south of ∼15°S where the lower tropospheric wind is anticyclonic. Associated with the Walker cell, an anticyclonic circulation (descending limb) appears over western parts of the equatorial Indian Ocean while the eastern equatorial Indian Ocean is manifested by the strong ascending limb with cyclonic vortex. By November, the anticyclonic circulation over the northern hemispheric continents strengthens (including over most parts of the Peninsular India), resulting in the equatorward movement of the ITCZ in the northern hemisphere. The cyclonic circulation at just south of the equator (part of ITCZ) and the location of the descending limb of Hadley cell at the southern hemispheric Indian Ocean observed during October continue to prevail during November as well. Interestingly, the ITCZ during this month has a tendency to appear as two independent bands on either side of the equator, producing a double-ITCZ feature [*Saha*, 1972; *Meenu et al.*, 2007; *RameshKumar et al.*, 2012].

3.3.2 Spatial variations of SST

The spatial distribution of clouds are also strongly influenced by the SST [*Gadgil et al.*, 1984; *Graham and Barnett*, 1987; *Waliser and Graham*, 1993; *Fu et al.*, 1990, 1994; *Joseph and Sabin*, 2008; *Meenu et al.*, 2012]. Further, the absolute magnitude and spatial gradient of SST significantly influence the atmospheric circulation and convection. Figure 3.2 shows the monthly mean spatial distribution of SST over the Arabian Sea, the Bay of Bengal and the tropical Indian Ocean. Throughout the year, the warmest SSTs are observed over the equatorial region. The SST over this region increases from January to April-May. The largest SST (∼30.5°C) over the study region is observed over the central Arabian Sea and the equatorial Indian Ocean (called the 'Warm Pool') around 53 to 70°E and 0 to 10°N during April-May; such warm pockets with SST>30°C are also observed at the south Bay of Bengal and the east equatorial Indian Ocean during these months. A reduction of SST (by ∼1°C) occurs over most regions during the summer monsoon season, especially from July to September; the warmest SSTs (SST>29°C) during this season are observed near the equator. However, most of the areas of the east Arabian Sea, the equatorial Indian Ocean and the Bay of Bengal have SST>28.5°C during this season. The SST further reduces during October to January, when most of the regions have SST<29°C). In general, the SSTs are the least at the south Indian Ocean, especially at south of ∼15°S to 20°S during all seasons. The SSTs are typically <26°C over this region. Low SSTs (SST<27°C) are also observed at the north Arabian Sea during winter and early part of pre-monsoon seasons.

3.4 Spatial distribution of clouds derived from NOAA-AVHRR

Figure 3.3 shows the monthly mean spatial distribution of the frequency of occurrence of clouds (F_C) derived from NOAA-AVHRR data over the study region, averaged during 1996 to 2010. This figure is mainly shown here to discern the gross features of the spatial distribution of clouds over the study region based on long-term data (1996 to 2010). Together with the features of atmospheric circulation described in the earlier section, the cloud distribution presented in Figure 3.3 shows the following major features.

During January to February, the ITCZ is manifested in Figure 3.3 as an east-west oriented band of large cloudiness with F_C >70% at the centre of the band, which decreases to <50% within 10° on either side of the ITCZ. The slight north-south tilt of the ITCZ observed in the atmospheric convergence is clearly manifested in the cloud distribution as well. The total width of this band of large cloudiness is about 20°. The

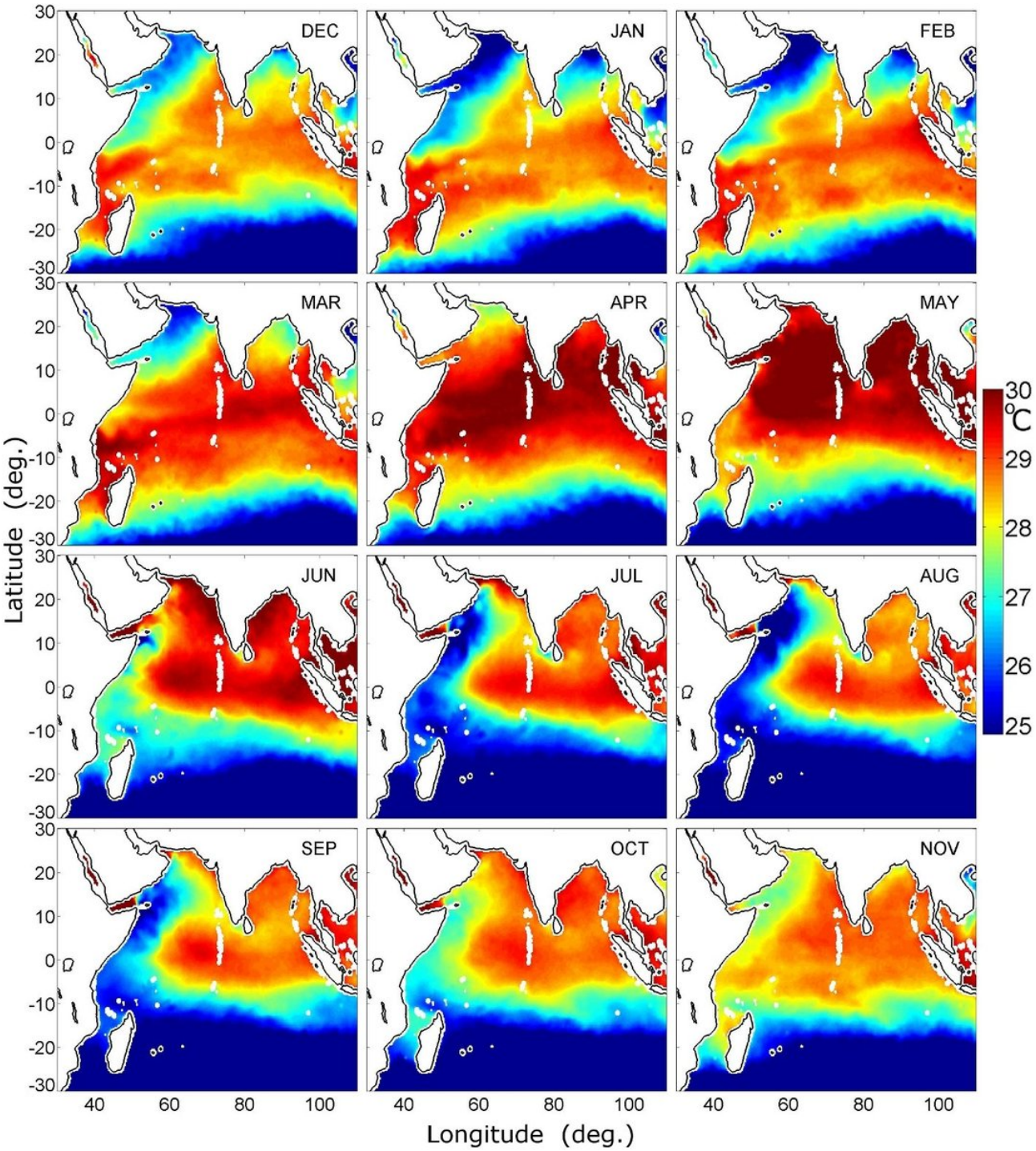

Figure 3.2: Long term(2000 to 2011) monthly mean SST over the Arabian Sea, the Bay of Bengal and the Indian Ocean obtained from TMI-SST.

cloudiness undergoes remarkable latitude variations across the northern and southern boundaries of this cloud band, with substantially less cloud occurrence (<20%) at the regions where the descending limbs of the Hadley cell are located in the northern (centered over Central India and the Arabian Sea) and southern hemispheres (south Indian Ocean at south of 20°S). The ascending branch of the Walker cell at the east

equatorial Indian Ocean is manifested by larger cloudiness (F_C ~80%) while the western equatorial Indian Ocean (descending branch of the Walker Cell) has substantially smaller cloudiness. A zone of large cloudiness (F_C ~80%) is observed at the southwestern Indian Ocean near Madagascar in January and February. This region has warm SST (>29°C) and has a large cyclonic vortex (associated with the ITCZ), leading to convection and large-scale cloudiness.

Overall, the spatial distribution of cloudiness during March is similar to that during January-February, especially with respect to the locations of the enhanced cloudiness associated with the ITCZ and the descending limbs of the Hadley and Walker cells. However, the cloud amount shows an overall reduction in March, especially over the western Indian Ocean. Compared to March, the latitudinal width of the band of enhanced cloudiness associated with the ITCZ broadens further in the central and eastern equatorial Indian Ocean during April. Despite the warm SSTs (SST>30°C) over the western equatorial Indian Ocean, the cloudiness in this region is substantially reduced to <40% in April. This is associated with the strengthening of the descending limb of the Walker cell over this region. The cloudiness over the north-eastern parts of the Indian subcontinent increases from March to April. Cloudiness over the Bay of Bengal as well as the northern parts of the Indian subcontinent increases to 40 to 80% in May, and is associated with the corresponding increase in lower tropospheric convergence (Figure 3.3). Further, the eastern branch of the summer monsoon current (originating from the Australian region) appears in the Bay of Bengal during May [e.g., *Singh and Salvekar*, 2004]. An increase in cloudiness (F_C ~60%) is also observed at the southeast Arabian Sea in May and is caused by an enhancement in the westerly wind from the warm Arabian Sea region. The descending limb of Hadley cell in the southern hemisphere Indian Ocean as well as in the northern parts of the Indian subcontinent and Arabia have cloudiness <20% during all months of the pre-monsoon season.

In general, the horizontal distributions of cloudiness over the study region during June to September are similar, with substantially large cloudiness over the east Arabian Sea, Indian subcontinent, the Bay of Bengal and the equatorial Indian Ocean. Largest cloudiness during this season is observed over the north and east Bay of Bengal (F_C of 80 to 100%), with most intense cloudiness during July to August. This is among the most intense deep convective regions in the world [e.g., *Newell and Gould-Stewart*, 1981; *Meenu et al.*, 2010; *Meenu*, 2010]. The large spatial gradient of F_C across the coastal regions at the north and east Bay of Bengal are particularly notable and are significantly contributed by the orographic lifting, in addition to the favourable conditions prevailing over the Bay of Bengal for convection and moisture convergence during this season. Cloudiness over the east Arabian Sea also enhances (F_C >70%) during the summer monsoon season. The high wind speed associated with the LLJ and the

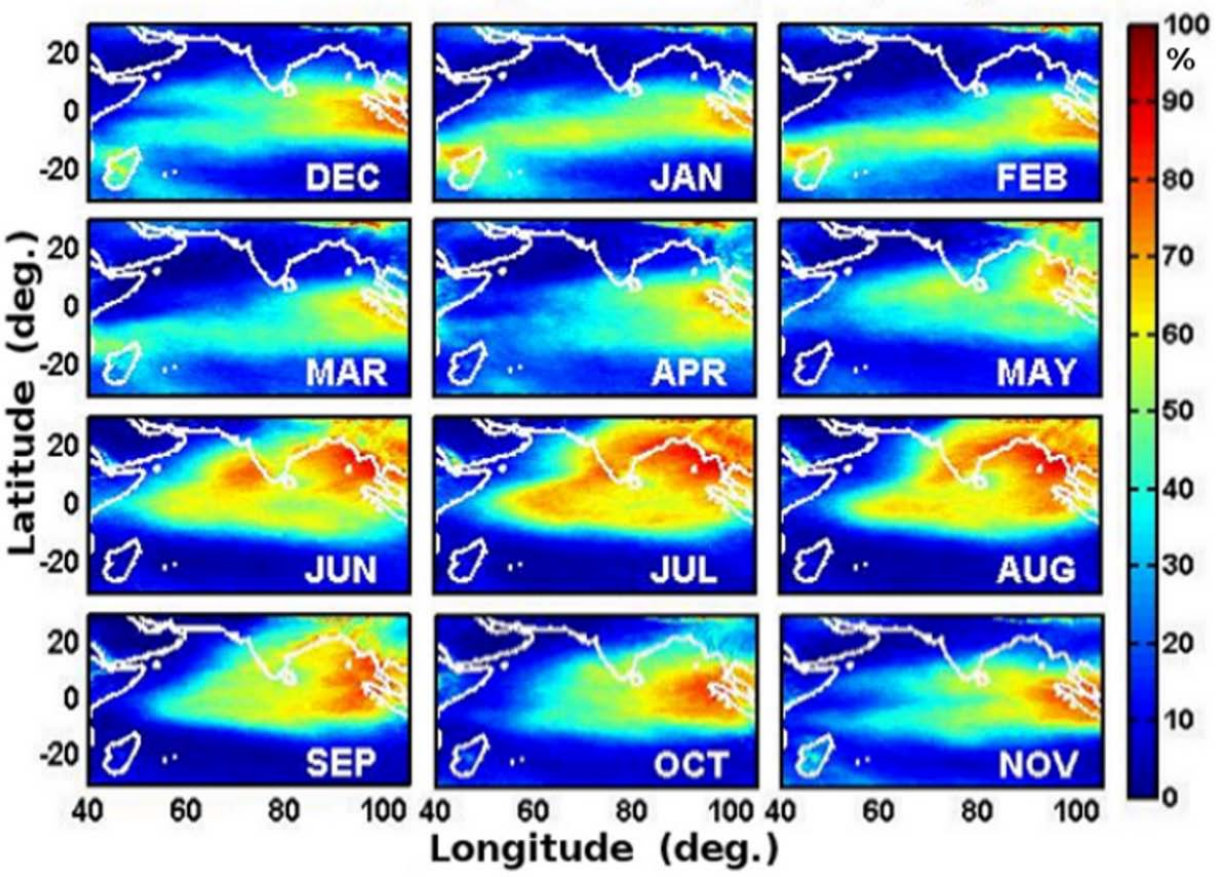

Figure 3.3: Long term (1996-2010) monthly mean spatial variations of the frequency of occurrence of clouds (F_C) observed using NOAA-AVHRR.

orographic lifting of this moist airmass over the Arabian Sea at west of the Western Ghats (Figure 3.1) contribute to this enhanced cloudiness. The large cloudiness along an east-west oriented band between the equator and ∼7°S is caused by the equatorial trough [*Meenu*, 2010; *Meenu et al.*, 2010]. Minimum cloudiness over the entire region occurs at the Mascarenes High over the south Indian Ocean, the west equatorial Indian Ocean, the west Arabian Sea, and Arabia where the values of F_C are usually less than 20%. All these regions are manifested by strong subsidence associated with the prevailing tropical circulation cells. Reduction in cloudiness between the southern boundary of the equatorial trough and the Mascarenes High is remarkably sharp. One important feature of the cloud distribution during the summer monsoon season is the appearance of a region of distinctly small cloudiness over the southwest Bay of Bengal near Sri Lanka, which is surrounded by large scale cloudiness on all sides. The characteristics and genesis of this 'pool of inhibited cloudiness' are presented in detail in Chapter 4.

Associated with placement of the descending limb of Hadley cell over the northern parts of the Indian subcontinent in October, the frequency of occurrence of clouds over this region decreases considerably (F_C <30%). The broad ITCZ and the cyclonic

vortex over the Peninsular India results in considerable cloudiness (F_C >50%) over the south Peninsular India and the central and eastern equatorial Indian Ocean. The most remarkable feature observed in October is the strengthening of the Walker cell, with large cloudiness (∼80%) over the eastern equatorial Indian Ocean and substantially reduced cloudiness (<20%) over the western part. Cloudiness at the southern hemispheric descending limb of Hadley cell is also <20%. Overall, the spatial distribution of cloudiness during October is similar to that in April. One of the most remarkable features observed in November is the double-ITCZ structure around the equator. This feature is more prominent in the 50°E to 85°E longitude region [*Meenu et al.*, 2007]. The northern band is centered at ∼5°N, while the southern band is centered at ∼7°S. The double band structure of the ITCZ during November is clearly discernible in the atmospheric circulation also (Figure 3.1). In December, cloudiness increases considerably over the western part of the south Indian Ocean and Madagascar, due to the influence of the prevailing cyclonic circulation over the west of Madagascar. The double-band structure of ITCZ is discernible during December as well.

3.5 Vertical and horizontal distributions of clouds derived from CloudSat and their association with atmospheric circulation

Altitude distribution of clouds and their spatial variations observed using CloudSat data are presented in this section. Vertical cross sections of the frequency of occurrence of clouds (F_{ALT}) averaged along different longitude and latitude bands are presented to obtain a 3-dimensional distribution of the monthly and seasonal mean cloud distribution. Notwithstanding the uniqueness of the CloudSat data in terms of the high-resolution observations of the vertical distribution of clouds at very small fine spatial scales along the satellite track, these observations are limited to the sub-satellite track for a 16-day orbit cycle, as explained in Section 3.2. Due to this limitation, the latitude-altitude cross sections of F_{ALT} are averaged for different longitude bands of 10° width. Similarly, the longitude-altitude cross sections are presented for latitude bands of 10° width. As seen in Figure 3.3, all major features of cloud distributions have sufficiently large spatial scales to be detected in the present analysis. Structures having very fine spatial scales (of the order of a couple of degrees) may not be detectable in this analysis and are not examined in detail.

3.5.1 Winter season

3.5.1.1 Altitude-latitude cross sections of cloud distribution and atmospheric circulation

The latitude-altitude cross sections of the multi-year (2006 to 2011) seasonal mean F_{ALT} during the winter season (December to February) for different longitude bands (30 to 40°E, 40 to 50°E, ... 100 to 110°E) are depicted in Figure 3.4. The corresponding monthly mean pictures are shown in Figure 3.5. Overall, the features observed in the vertical distribution of F_{ALT} during the individual months are similar to the seasonal mean pattern. The vertical distribution of clouds and its spatial variations are well in agreement with the mean spatial distribution of total cloudiness observed using AVHRR data (Figure 3.3). As seen from the lower tropospheric circulation (Figure 3.1) and AVHRR-observations of cloud occurrence (Figure 3.3), the ITCZ is located around the equator and south of it during this season. CloudSat observations show that the vertical distribution of clouds over the ITCZ is marked by large values of F_{ALT} at all altitudes in the troposphere below ∼14 km. The small northward tilting of the ITCZ from the west Indian Ocean to the east is clearly discernible in the vertical distribution of clouds shown in Figures 3.4 and 3.5. Compared to December, this feature is more prominent during January-February. The amount of cloudiness as well as the strength of the ITCZ (as inferred from the values of F_{ALT} and its vertical distribution) varies considerably at different longitudes. Strength of the ITCZ is largest over the eastern equatorial Indian Ocean (especially at the east of 90°E) and consistently decreases towards the west upto 50 to 60°E. This feature is more prominent during December. The east-west asymmetry in the strength of the ITCZ is caused by the Walker circulation, with the ascending limb over the east equatorial Indian Ocean and the descending limb over the west.

The cloudiness in the middle and upper troposphere in the deep convective regions generally increases with altitude to attain the peak occurrence around 9 to 13 km. This is because of the occurrence of thick cirrus clouds, whose probability of occurrence increases with altitude at least up to 12 km. Most of these clouds might have been formed from the outflow of deep convective clouds as anvils or might be the remnants of deep convective clouds after precipitation. The cirrus clouds are non-precipitating and have large atmospheric residence time (of several hours to 2 days) compared to the low- and middle-level clouds (few minutes to few hours). The enhanced cloudiness observed in the upper troposphere (typically between 9 to 13 km altitude) which spread to either side of the ITCZ is the result of the strong outflow from the deep convective clouds at the ITCZ. Figures 3.4 and 3.5 clearly shows that the meridional winds associated with the Hadley cell carries the outflow to considerably large distances (∼10 to 20° latitude)

from the ITCZ. This aspect is further examined using the meridional cross sections of the Hadley cell inferred using MERRA data.

Figure 3.6 shows the meridional circulation averaged in the longitude bands of 50 to 60°E, 70 to 80°E and 90 to 100°E, indicated by the vector plots of the meridional and vertical winds as a function of altitude and latitude. As the magnitudes of vertical winds are very small compared to the horizontal winds, the former are multiplied by 50 while plotting, for clearly representing the circulation pattern. Figure 3.6 reveals that the ITCZ (marked by horizontal wind convergence and large updraft) is indeed strongest over the east equatorial Indian Ocean where strong convection extends upto ∼150 hPa level (∼14 km) in the latitude band confined between ∼10°S and ∼8°N. In the longitude band of 90 to 100°E, the largest vertical winds are observed between 600 hPa and 250 hPa levels, above which the meridional outflow becomes prominent. Strength of the sinking branch of the Hadley cell as well as the meridional outflow from the ITCZ in the upper troposphere in this longitude sector is more prominent in the northern hemisphere compared to the southern hemisphere. Though the downdraft associated with the Hadley cell is observed at the north and south of the ITCZ, the core of the sinking branches are located at south of 25°S in the southern hemisphere and 20 to 30°N in the northern hemisphere. Meridional cross section of the vertical distribution of clouds is in agreement with this meridional circulation. Largest vertical development of clouds occurs between 10°S and 5°N, where the cloudiness is quite large upto ∼14 km altitude. The upper tropospheric cloudiness associated with the outflow from the ITCZ is larger in the northern hemisphere where the cloudiness associated with the outflow is significant at least up to 8° away from the northern boundary of the convective core. A careful examination of the meridional cross-section of cloudiness suggests that the clouds originating from deep convective outflow from the ITCZ extend upto the core of the descending limb of Hadley cell, though the overall cloudiness is quite small. The cloudiness is considerably weak at the descending branches, with the least values observed in the middle and upper troposphere in the sinking core region indicated by the meridional circulation. It is important to note that the latitudinal width of the ITCZ inferred from the meridional circulation as well as the vertical distribution of clouds (∼15°) are in agreement, while the width of the large-scale cloudiness in the ITCZ region observed using AVHRR data (Figure 3.3) are significantly larger (>20°). This is primarily because of the optically thick cirrus clouds caused by the outflows from the ITCZ which could not be discriminated in the observations using passive radiometer (AVHRR) data.

As seen in Figure 3.6, strength of the Hadley cell (including the convection at the ITCZ and the meridional circulation) weakens towards the west. Except for this, the gross features of the Hadley cell over the central Indian Ocean region (70 to 80°E

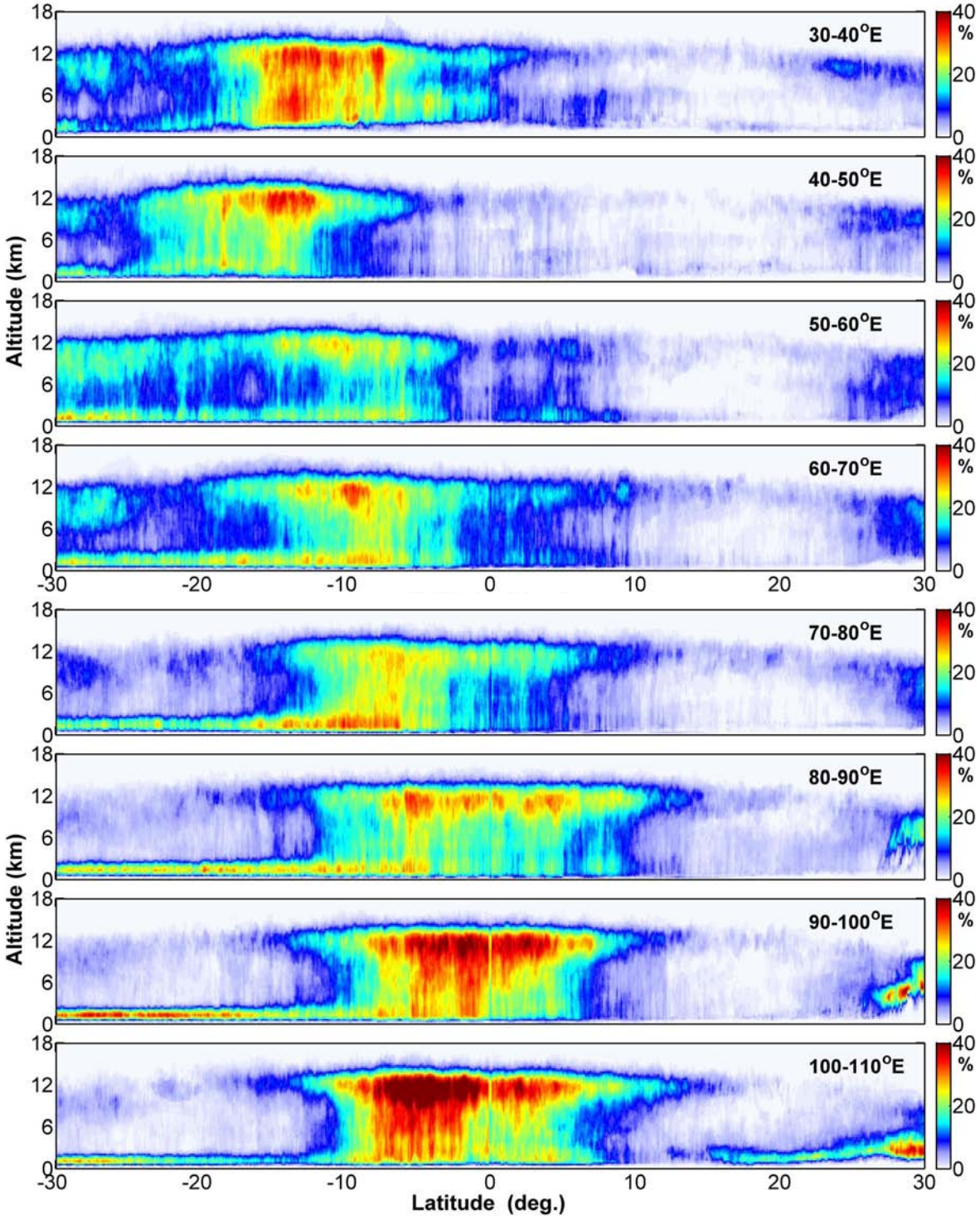

Figure 3.4: Multi-year (2006 to 2011) seasonal mean latitude-altitude cross sections of the frequency of occurrence of clouds averaged for different longitude bands of 10° width (30 to 40°E, 40 to 50°E, ..., 100 to 110°E) over the Indian subcontinent and the surrounding oceanic regions during winter (DJF).

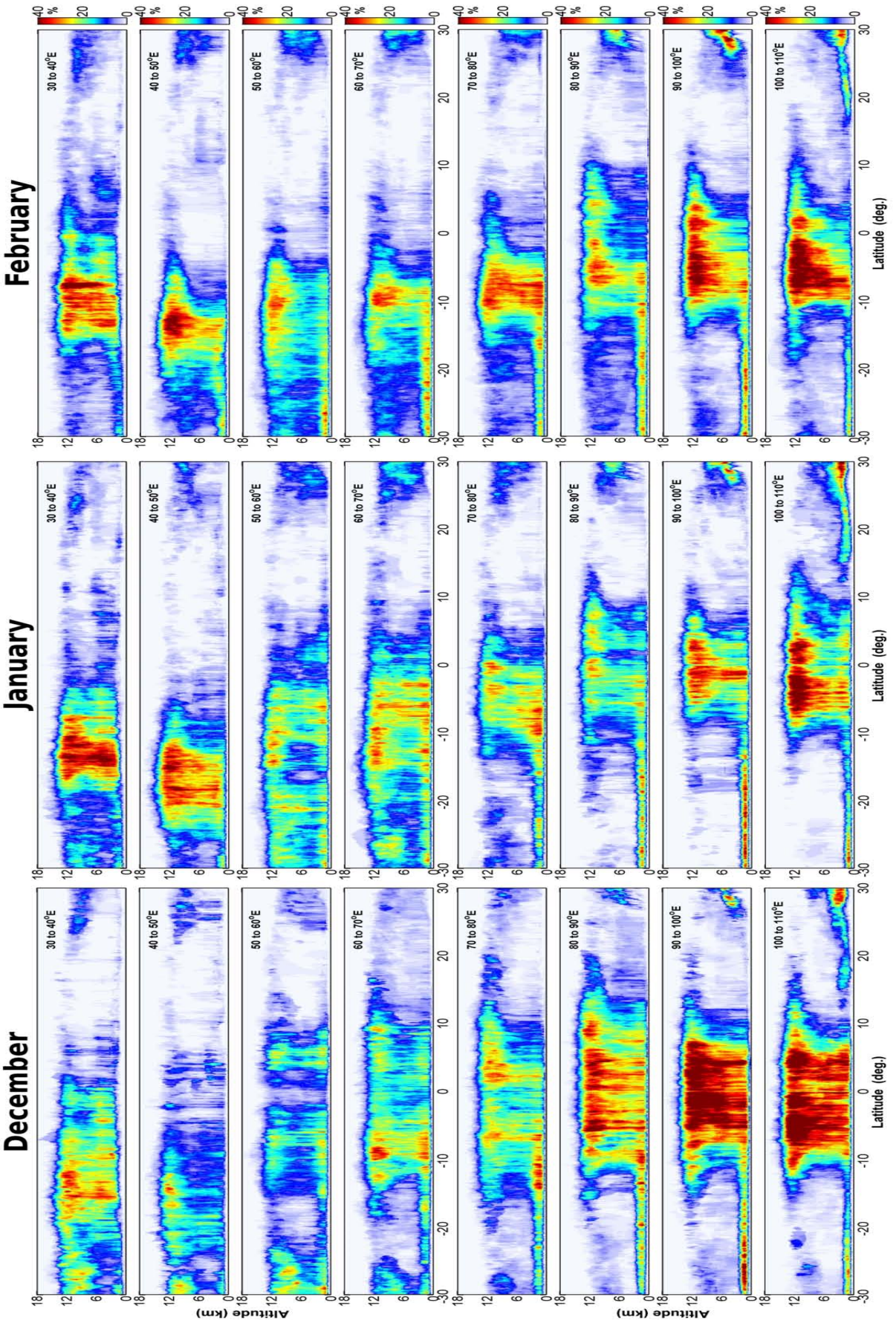

Figure 3.5: Multi-year (2006 to 2011) monthly mean latitude-altitude cross sections of the frequency of occurrence of clouds averaged for different longitude bands of 10° width (30 to 40°E, 50 to 50°E, ..., 100 to 110°E) over the Indian subcontinent and the surrounding oceanic regions during December, January and February.

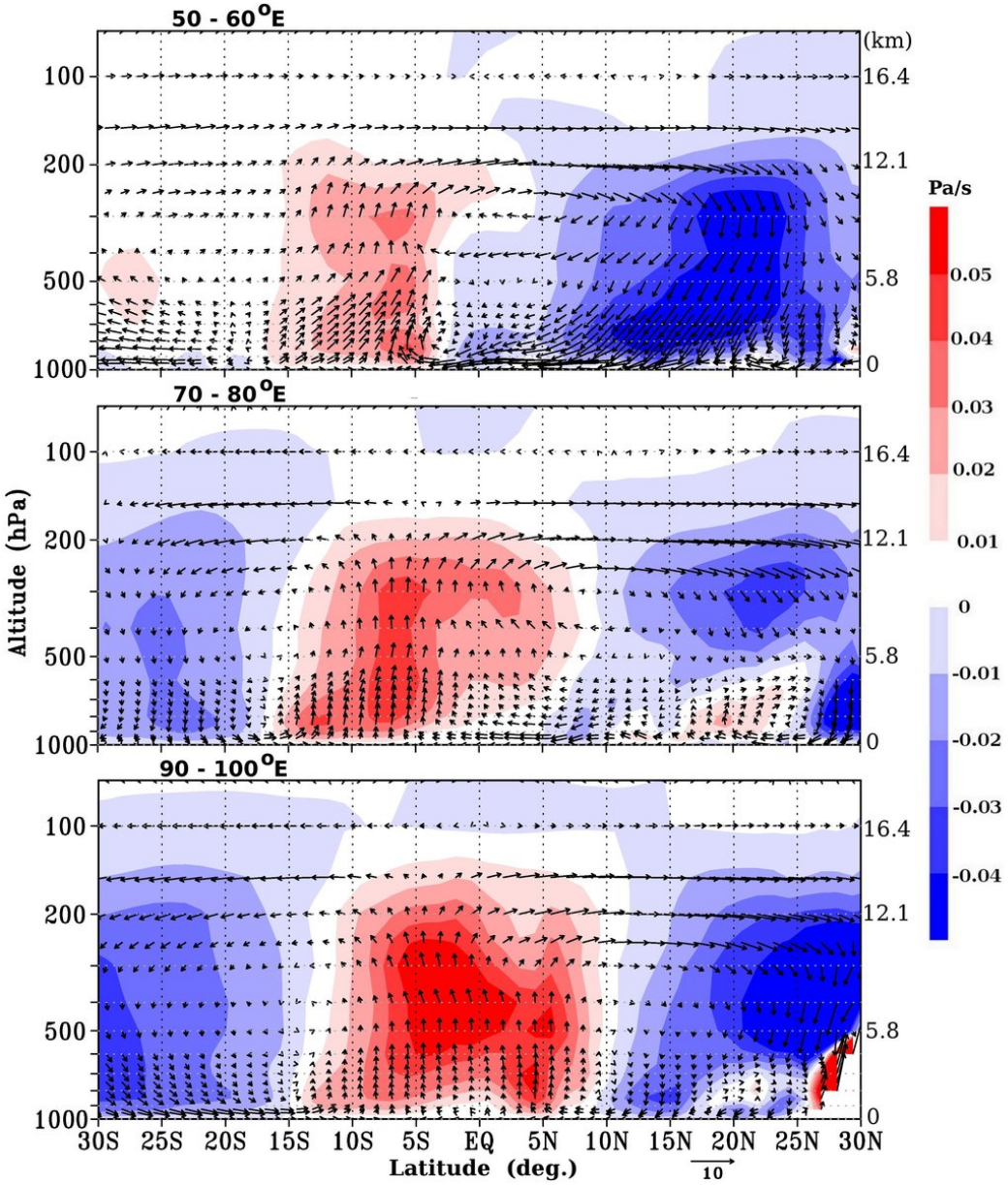

Figure 3.6: Longitudinally averaged seasonal mean meridional circulation during winter, shown by vector plots of the average meridional and vertical winds in the longitude bands of 50 to 60°E, 70 to 80°E and 90 to 100°E as a function of altitude and latitude. The vertical winds are multiplied by 50 for clearly representing the circulation pattern. Blue shade indicates downdraft and red shade indicates updraft.

longitude band) are somewhat similar to those over the east equatorial Indian Ocean (90 to 100°E). The convection associated with the ITCZ in the longitude band of 70 to 80°E mainly occurs in the latitude band of 13°S to 5°N, with the maximum convection centered about 10°S to 5°S (Figure 3.6). This convection is limited to <200 hPa level and the outflow is quite significant above 300 hPa level. Core of the descending branches of the Hadley cell are located at 15 to 25°N in the northern hemisphere and 20 to 25°S in the southern hemisphere, with downdraft occurring at poleward of the northern

and southern boundaries of the ITCZ. Meridional cross section of cloudiness in this longitude band (Figures 3.4 and 3.5) is in agreement with the meridional circulation discussed above. The largest vertical development of clouds occurs between 12°S and 5°S, which extends up to ∼13 km. The overall cloudiness in this region is significantly lesser than that over the east equatorial Indian Ocean. As the separation between the ITCZ and core of the sinking cell is larger in the northern hemisphere compared to the southern hemisphere, the outflow also extends to larger distance (at least 10° from the northern boundary of the ITCZ) in the former region. Though quite small, the cloudiness associated with this outflow extends upto core of the descending limb of the Hadley cell. Cloudiness caused by the outflow from the ITCZ is weaker in the southern hemisphere. Cloudiness at the descending branches of the Hadley cell is considerably smaller, with the least values observed in the middle and upper troposphere in the core region.

Figure 3.6 shows that the Hadley circulation cell is quite weak over the east Arabian Sea. In the longitude band of 50 to 60°E, convection associated with the ITCZ is substantially weak both in terms of spatial extent of the convection and magnitude of the updraft in this region. Updraft is observed between 15°S to 5°S with the largest vertical winds between 7°S to 5°S. The updraft is prominent below ∼250 hPa level and ceases above 200 hPa level. The downdraft associated with descending branch is significant only in the northern hemisphere (with core between 15°N to 25°N) while it is feeble in the southern hemisphere where significant descending is not seen up to 30°S. Vertical distributions of F_{ALT} (Figures 3.4 and 3.5) are in agreement with the above dynamical features. Associated with the descending limb of Walker cell, substantially reduced cloudiness is observed in this longitude band. Relatively larger cloudiness is observed between 15°S to 5°S, which is the mean location of the ITCZ. As the ITCZ is very weak, cloudiness in the mid-troposphere is distinctly small in this region compared to the ITCZ in the central and east equatorial Indian Ocean. Cloudiness is negligible at the descending branch of the Hadley cell in the northern hemisphere. On the contrary, the reduction in cloudiness towards the south of the ITCZ is rather insignificant as the downdraft in the southern hemisphere in this longitude sector is very weak.

3.5.1.2 Persistent occurrence of low altitude clouds over the South Indian Ocean

One of the most remarkable features observed in Figures 3.4 and 3.5 is the persistent occurrence of low altitude clouds below 3 km at the descending limb of the Hadley circulation over the southern hemispheric Indian Ocean. They are present throughout the southern hemisphere Indian Ocean, right up to the ITCZ. In contrast, a similar feature is almost completely absent in the northern hemisphere, except at 100 to 110°E. These

clouds are very shallow and occur mostly in the altitude band of 1 to 3 km, with a peak around 1.5 km. Their frequency of occurrence is about 30 to 40% at the peak altitude of occurrence. However, the frequency of occurrence of these clouds is significantly underestimated in the AVHRR data (Figure 3.3), which is primarily based on the observed brightness temperature. This under estimation arises mainly because of the small difference between the temperatures at the surface and cloud top altitude, which makes the discrimination of these clouds by AVHRR more ambiguous. As explained earlier, the AVHRR observations of clouds using the methodology followed here employing the brightness temperature would underestimate the low-altitude clouds, especially those occurring below ∼1 to 2 km altitude over regions of cold SST.

It may be noted that the cold ocean surface over this region, where the SST is in the range of 25 to 27°C, cannot provide large amount of moisture flux to the atmosphere for generating clouds (This is clearly shown in Chapter 5 which deals with the relationship between cloudiness and SST). It is likely that the lower tropospheric moisture required for the observed cloud development might have been mainly produced by the sea agitation arising from strong surface winds in this region. The moisture thus produced (through evaporation of water droplets from sea spray) gets mixed in the atmospheric boundary layer by the turbulence generated by large wind shears. The moisture is trapped in the lower troposphere by the strong downdraft at the descending branch of the Hadley cell which effectively prevents their upward transport from the lower troposphere. This leads to accumulation of moisture and subsequent development of shallow clouds in this region. In contrast, compared to the southern hemispheric Indian Ocean, the surface wind speeds, sea agitation and wind shears are rather weak in the northern hemisphere. Further, spatial extent of the north Arabian Sea region (where the downdraft occurs during winter) is rather small and the prevailing dry winds from the continents in this region would further decrease the water vapour mixing ratio generated by the evaporation from ocean surface. In contrast, the south Indian Ocean is considerably vast and the influence of dry winds from the continents is negligible over most of the regions. A combination of the above mechanisms might prevent significant development of lower tropospheric clouds over the Arabian Sea region while the south Indian Ocean might have larger moisture accumulation in the lower troposphere and occurrence of low altitude clouds, as seen in the CloudSat observations. However, this needs to be ascertained based on observations of moisture and atmospheric thermodynamics in this region.

3.5.1.3 Altitude-longitude cross sections of cloud distribution and atmospheric circulation

Figure 3.7 shows the multi-year (2006 to 2011) seasonal mean longitude-altitude cross sections of F_{ALT} averaged for different latitude bands of 10° width (30°S to 20°S, 20°S to 10°S, ..., 20 to 30°N) over the Indian subcontinent and the surrounding oceanic regions during winter. As shown earlier, the ITCZ during this season generally persists around the equator and south of it in the equatorial Indian Ocean, with a small shift towards the north at the east equatorial Indian Ocean. The longitude-altitude cross section of cloudiness (Figure 3.7) at 0 to 10°S represents the zonal cross section of the cloud distribution along the ITCZ, which clearly shows the effect of the Walker circulation in the vertical development of clouds. The F_{ALT} is largest over the east equatorial Indian Ocean between 90 to 110°E at all altitudes, while the cloud vertical development is almost fully suppressed between 40 to 55°E. The zonal cross section of cloudiness at 0 to 10°N shows largest deep convective clouds at 100 to 110°E and the near-absence of clouds between 40 to 55°E. This aspect of the Walker circulation is further examined using Figure 3.8, which depicts the seasonal mean zonal circulation during winter averaged in the latitude bands of 0 to 10°S and 0 to 10°N during winter. The updraft is largest at east of 90°E where the convection crosses 150 hPa level (Figure 3.8). It systematically decreases towards the west and turn to downdraft in the longitude between 40 to 55°E. In the 0 to 10°N latitude band, this downdraft exists at eastward of 70°E. Vertical distribution of clouds is in agreement with this circulation.

It may be noted that the increase in the vertical development of clouds seen at west of 40°E is the result of the convergence and convection at the ITCZ region over the south African region, which is more prominently seen in the latitude band of 10 to 20°S. This is seen in Figure 3.7, which shows large updraft extending upto ∼200 hPa level at west of 40°E. Associated with the descending limb of the Hadley cell, cloudiness in the longitude band of 10 to 30°N is <20% at all altitudes at west of 100°E. Similar feature is also observed in the middle and upper troposphere at south of 20°S in the southern hemisphere. The south Indian Ocean is manifested by the large occurrence of lower tropospheric clouds at <3 km altitude in all the longitudes.

3.5.2 Pre-monsoon season

3.5.2.1 Altitude-latitude cross sections of cloud distribution and atmospheric circulation

Figure 3.9 shows the multi-year mean meridional cross sections of F_{ALT} averaged for 10° longitude bands during the pre-monsoon season. Figure 3.10 shows the corre-

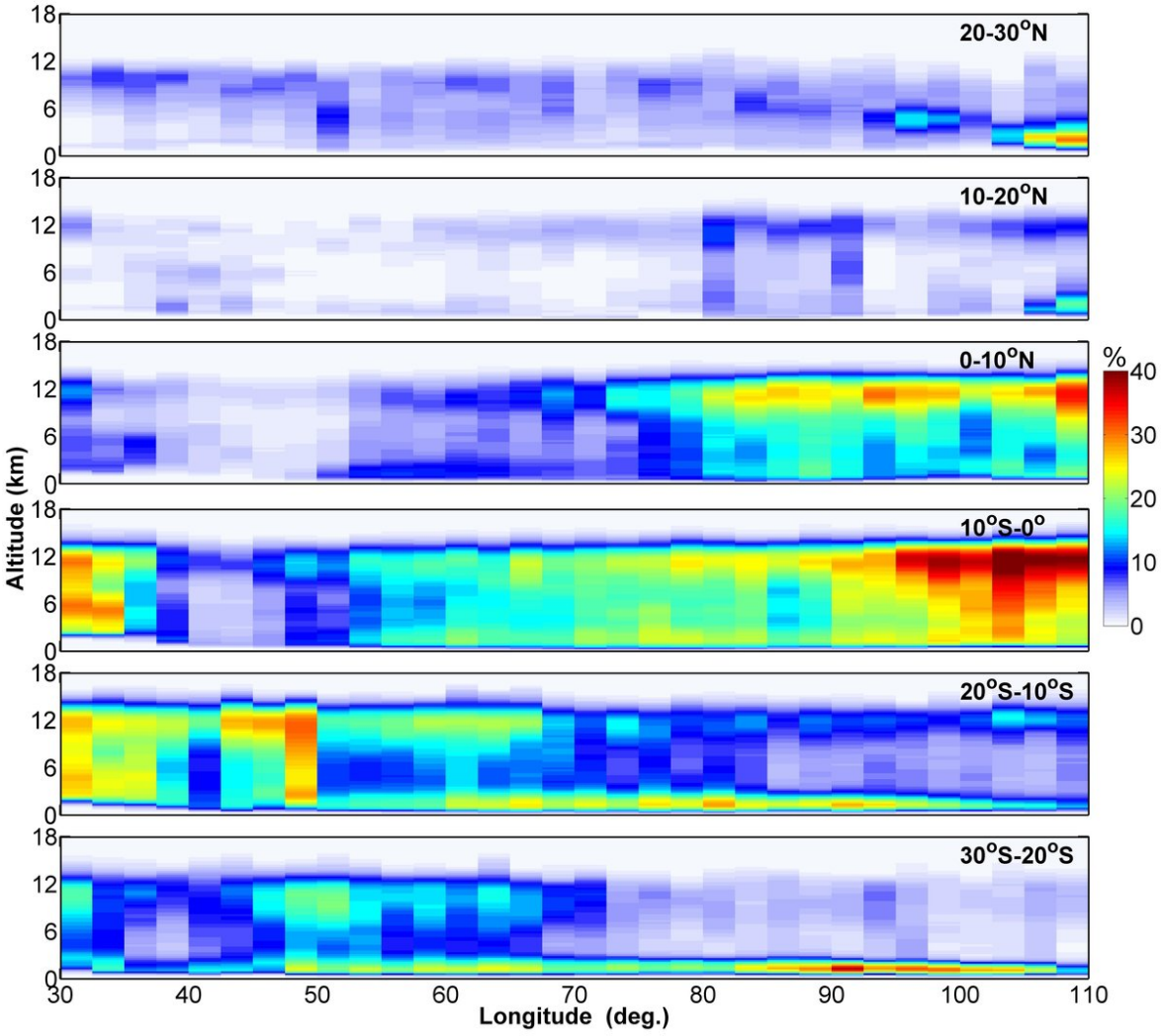

Figure 3.7: Multi-year (2006 to 2011) seasonal mean longitude-altitude cross sections of the frequency of occurrence of clouds averaged for different latitude bands of 10° width (20 to 30°N, 10 to 20°N, ..., 30°S to 20°S) over the Indian subcontinent and the surrounding oceanic regions during winter.

sponding plots for the individual months: March, April and May. Overall, the spatial distribution of clouds observed in Figure 3.9 and 3.10 are similar to that observed using NOAA-AVHRR (Figure 3.3). Similar to winter, spatial variations of the vertical distribution of cloudiness during this season are strongly coupled to the Walker and Hadley cells. This season represents the transition period: the vertical distribution of clouds observed during March has several similarities to those during January-February months. This is especially the case with the location of ITCZ, its north-south tilt and the east-west asymmetry. The ITCZ over the central and west equatorial Indian Ocean moves equatorward during April and May and the north-south tilt of ITCZ almost completely disappears by May. However, the east-west asymmetry in the vertical distribution of clouds (intense deep convection over the east equatorial Indian Ocean and

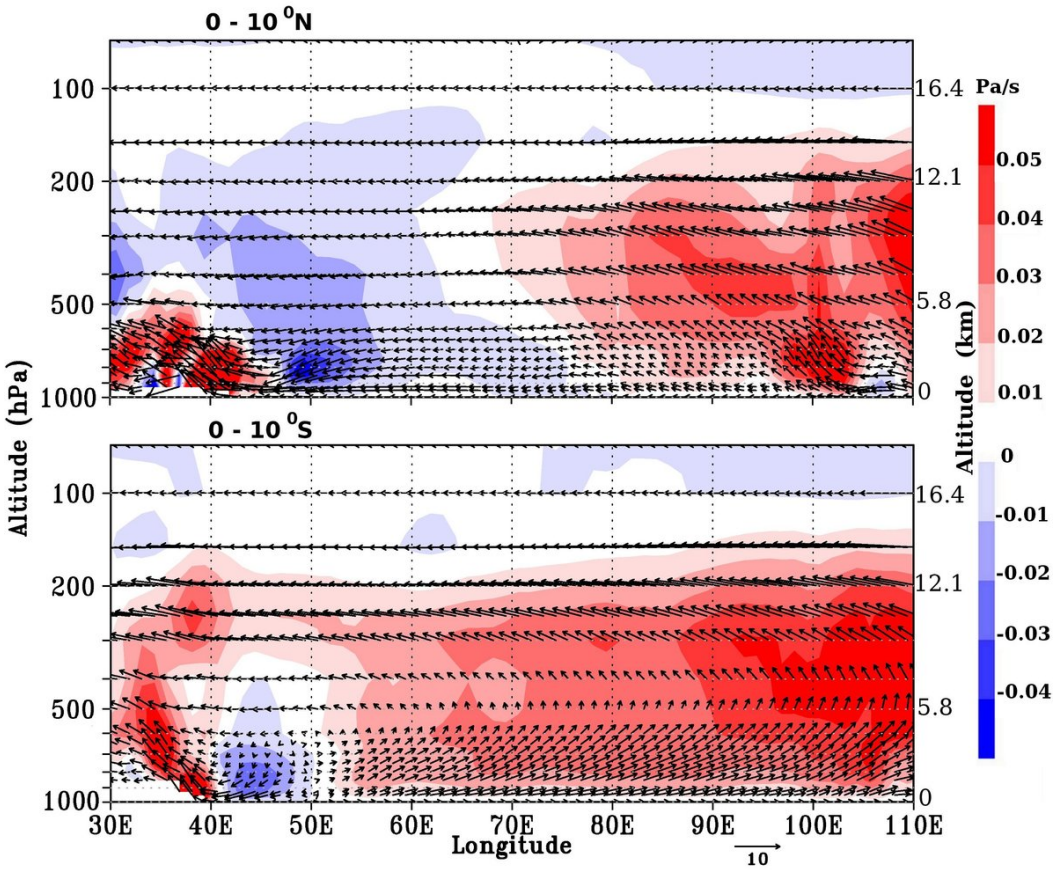

Figure 3.8: Latitudinally averaged seasonal mean zonal circulation during winter, shown by vector plots of the average zonal and vertical winds in the latitude bands of 0 to 10°N and 0 to 10°S as a function of altitude and longitude. The vertical winds are multiplied by 50 for clearly representing the circulation pattern. Blue shade indicates downdraft and red shade indicates updraft.

rather weak convection over the western parts) associated with the Walker circulation prevails during all months of this season.

The vertical development of clouds during this season is largest in the longitude band of 90 to 110°E, with strong outflows to either side of the ITCZ. The vertical cross sections of the meridional circulation during this season, depicted in Figure 3.11 for the longitude bands of 40 to 50°E, 70 to 80°E and 90 to 100°E, show a wide region of large-scale convection over the east equatorial Indian Ocean between ∼12°S and 25°N (larger width of this convective region in Figure 3.11 is partly contributed by the seasonal averaging, as the summer monsoon current advances to the Bay of Bengal sector during the second half of May). Figure 3.11 shows that, in the longitude band of 90 to 100°E, the convection is largest between 8°S and 15°N and extends up to ∼150 hPa level. However, the magnitude of convection reduces substantially above ∼200 hPa level, giving rise to large scale divergence which is manifested in the vertical distribution of clouds as outflow from the ITCZ band. Over this longitude region,

descending limb of the Hadley cell is stronger over the southern hemisphere compared to the north. This results in the substantially reduced amount of cloudiness in the south Indian Ocean with the minimum cloudiness observed around 20°S, which almost coincides with the core of the sinking branch. In contrast, the vertical development of clouds is quite significant at most of the northern latitudes, except around 20°N. The region at north of 20°N witnesses significant cloudiness (F_{ALT} 40%) below ∼6 to 8 km altitude, with rapid reduction in cloudiness above. Though less prominent, a similar feature is observed in the longitude band of 80 to 90°E as well. This feature is also seen in the total cloudiness observed using NOAA-AVHRR (Figure 3.3). Note that this feature appears at the orographically dominated Sub-Himalayan region at the northeastern parts of the Indian subcontinent (the presence of mountains and their average altitude are also seen from the white band appearing at the bottom of Figures 3.9 and 3.10 at north of 26°N in the longitude band of 70 to 90°E). Figure 3.11 shows a region of strong updraft below ∼600 to 500 hPa level, capped by an equally strong downdraft above. However, the vertical distribution of cloudiness shows peak values at ∼6 to 7 km, which is ∼1 to 2 km above the base altitude of the region of strong subsidence. This difference between the regions of maximum cloudiness and downdraft might be because of the uncertainties in the MERRA data arising from the orographic influence.

Meridional circulation shows that, in the Indian longitude band of 70 to 80°E, the descending limbs of the Hadley cell are strong (with comparable strengths) in both the hemispheres. Correspondingly, the cloudiness is quite small at these descending limbs of Hadley cell centered around 20°S and 20°N. In the western longitude band of 40 to 50°E, the ITCZ is very weak as this region is occupied by the descending limb of the Walker cell. Except for a weak convection at 6°S to equator, all latitudes in this region experiences strong subsidence in the middle and upper troposphere. Cloud occurrence is the least in this region and the occurrence of vertically developing clouds is almost negligible. Clouds in the middle and upper troposphere that occur in this longitude band at south of 25°S are primarily the result of convection at the southeast African region/Madagascar observed in March–April period.

As seen in the winter season, cloudiness in the upper troposphere increases with altitude, especially between 8 and 12 km. Most of these clouds are thick cirrus clouds having larger atmospheric residence time compared to the other cloud types, which lead to increase in their frequency of occurrence. As revealed by the meridional cross section of F_{ALT}, clouds in the upper troposphere generated by the outflow from the ITCZ prevail at all longitudes. Maximum cloudiness due to the outflow occurs in the altitude band of 9 to 13 km, with the base of this cloud band increasing (and its thickness reducing) away from the ITCZ. They extend meridionally to as large as 8

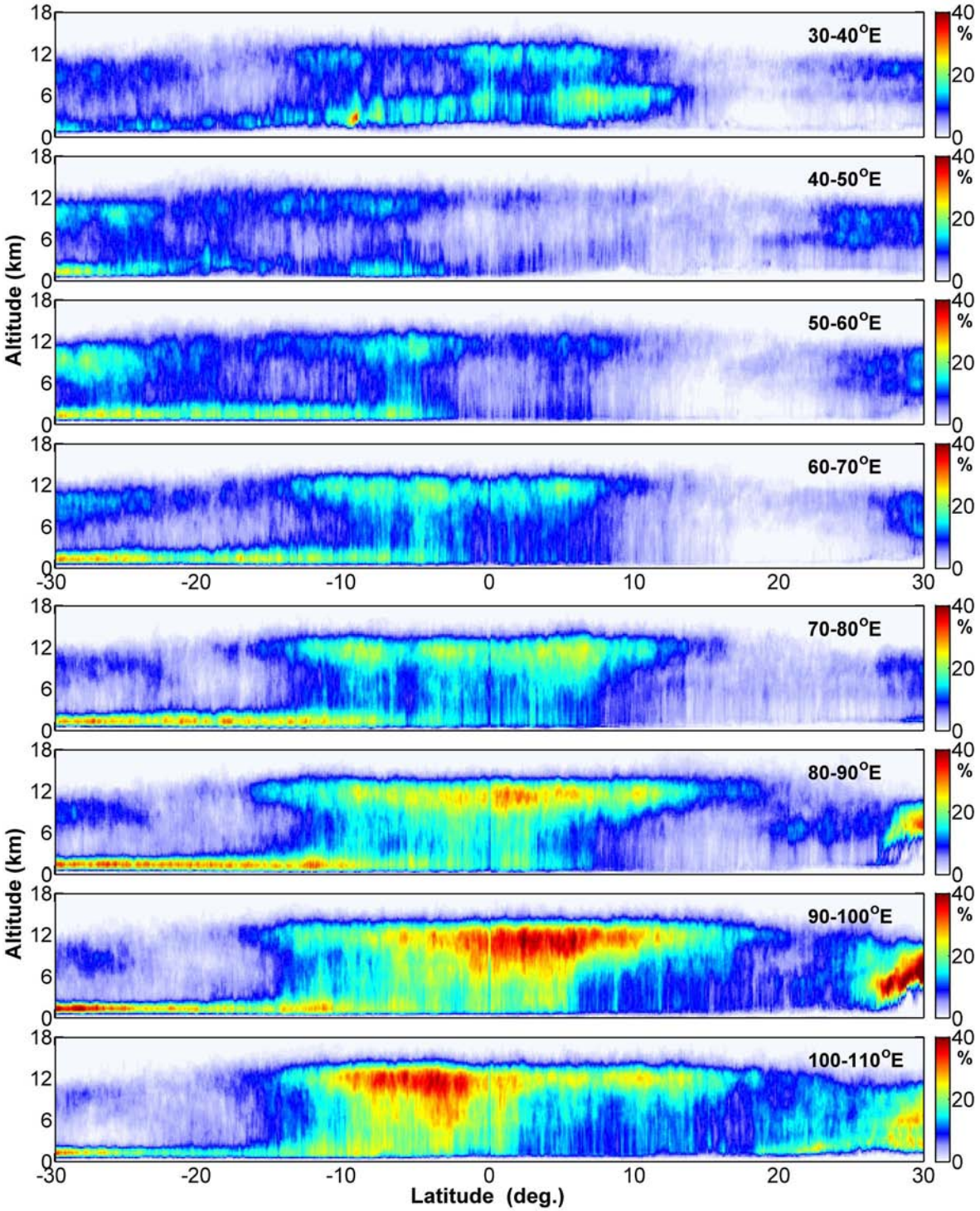

Figure 3.9: Multi-year (2006 to 2011) seasonal mean latitude-altitude cross sections of the frequency of occurrence of clouds averaged for different longitude bands of 10° width (30 to 40°E, 40 to 50°E, ..., 100 to 110°E) over the Indian subcontinent and the surrounding oceanic regions during the pre-monsoon season (MAM).

to 10° from the boundary of the ITCZ. Considering that the typical meridional wind speed at 9 to 13 km altitude is <10 m/s, it takes >24 hours for these clouds to spread meridionally as observed. This provides an indirect evidence for the relatively long residence time of cirrus clouds. Weaker meridional winds in the southern hemisphere results in the smaller distance to which the outflow of cirrus clouds occur at south of the ITCZ.

High frequency of occurrence of lower tropospheric clouds persists over the south Indian Ocean during all months of the pre-monsoon season. These clouds occur in the downdraft zones associated with the Hadley cell, which effectively prevents the penetration of moisture into the middle and upper troposphere. Largest frequency of occurrence of these clouds is observed at ∼1.5 km altitude and they seldom penetrate ∼3 km altitude. Such clouds are almost absent in the descending branch of the Hadley cell in the northern hemisphere. All features of their occurrence as well as their absence in the northern hemisphere are similar to those observed in winter. The generation mechanisms for their occurrence in the southern hemisphere and their absence in the northern hemisphere proposed for the winter Section 3.5.1.2 hold good during the pre-monsoon season as well.

3.5.2.2 Altitude-longitude cross sections of cloud distribution and atmospheric circulation

Figure 3.12 shows the multi-year mean meridional cross sections of F_{ALT} averaged at 10° latitude bands during the pre-monsoon season. The longitudinal variations around the equator represents the zonal cross section of cloudiness within the ITCZ, which clearly reveals the systematic decrease in deep convection from the east equatorial Indian Ocean to the west. The most intense (in terms of cloudiness) and deepest convection occurs in the latitude band of 0 to 10°S over the east equatorial Indian Ocean between 95 to 100°E longitude. The convection and vertical development of clouds are considerably weaker at west of 80°E. It is likely that a significant fraction of the clouds appearing in the upper troposphere at west of 80°E might be the clouds transported westward by the prevailing easterlies in the tropics. The frequency of occurrence of clouds is insignificant between 40 and 55°E in the latitude band of 0 to 10°S. The longitude of least cloudiness is wider (40 to 65°E) in the latitude belt of 0 to 10°N compared to that at 0 to 10°S. These features are in agreement with the altitude-zonal cross section of the zonal winds averaged in the 0 to 10°S latitude band (Figure 3.13) which shows persistent easterlies in the upper troposphere over the equatorial Indian Ocean.

The zonal cross section of the vertical distribution of clouds shows deep convective clouds at 10 to 30°N in the longitudes at east of 90°E (the northeast Bay of Bengal

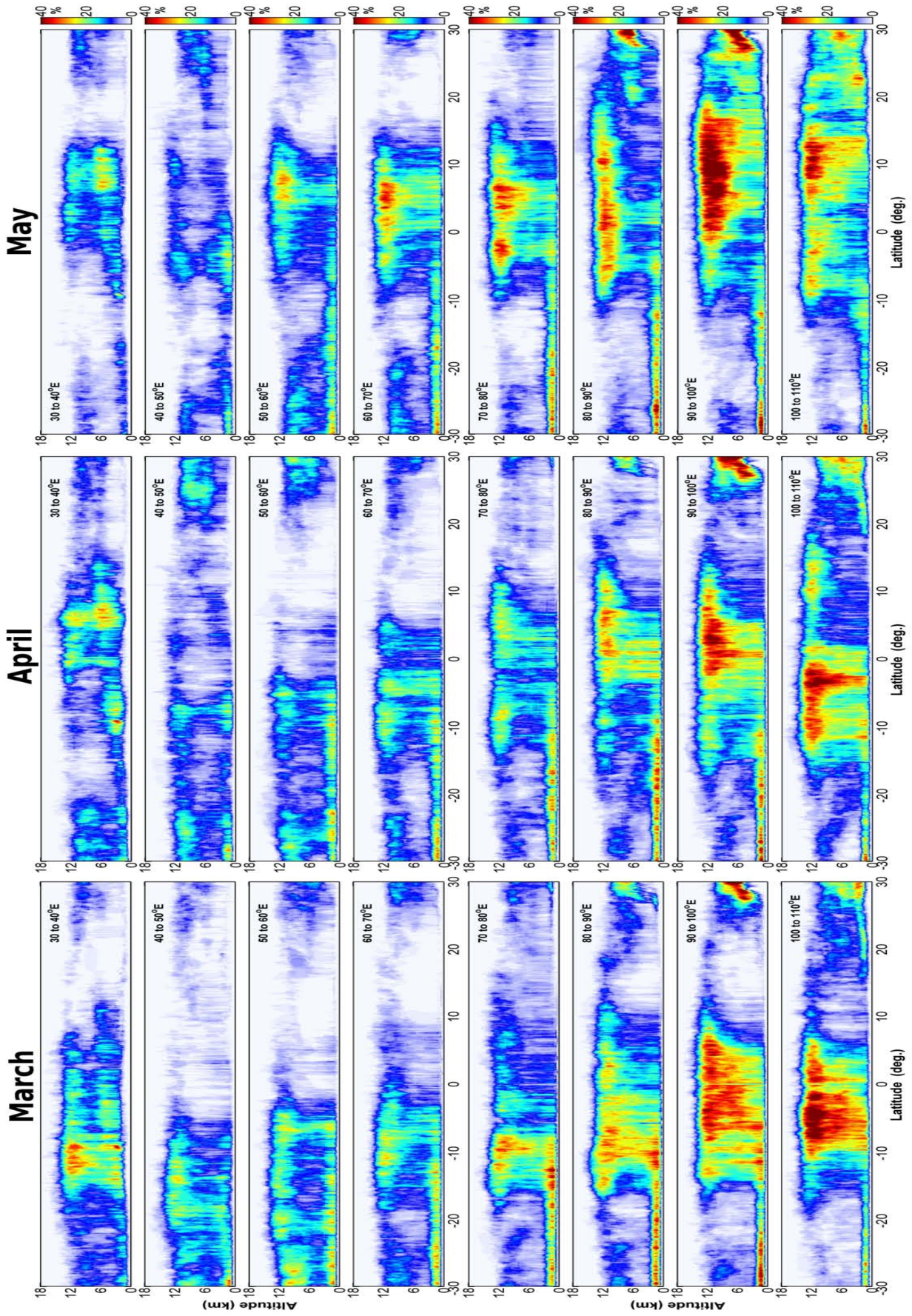

Figure 3.10: Multi-year (2007 to 2010) monthly mean latitude-altitude cross sections of the frequency of occurrence of clouds averaged for different longitude bands of 10° width (30 to 40°E, 40 to 50°E, ..., 100 to 110°E) over the Indian subcontinent and the surrounding oceanic regions during March, April and May.

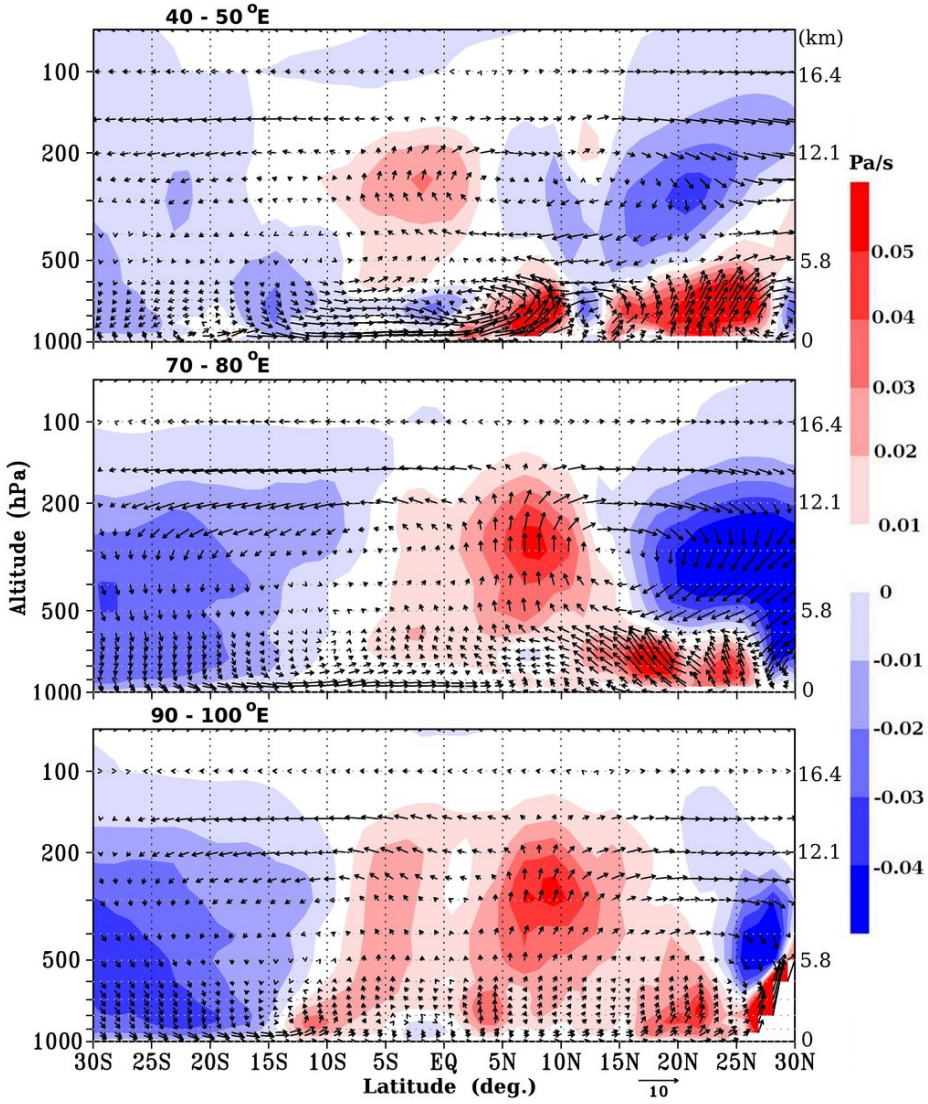

Figure 3.11: Longitudinally averaged seasonal mean meridional circulation during the pre-monsoon season, shown by vector plots of the average meridional and vertical winds in the longitude bands of 40 to 50°E, 70 to 80°E and 90 to 100°E as a function of altitude and latitude. The vertical winds are multiplied by 50 for clearly representing the circulation pattern. Blue shade indicates downdraft and red shade indicates updraft.

and northern parts of the Indian subcontinent). In the latitude belt of 20 to 30°N, this enhancement is mainly caused by the convective clouds in the Sub-Himalayan region. At 10 to 20°N, the deep convection primarily occurs over the warm (SST>29°C) east Bay of Bengal during May, leading to large-scale vertical development of clouds in this region. In contrast, the convection is almost fully suppressed in the latitude band of 10°S to 30°S, where the occurrence of clouds are primarily limited to <3 km altitude (especially at 20 to 30°S).

One of the most interesting features observed in the cloud distribution over the equatorial Indian Ocean is the rather weak convection that prevails over the warm

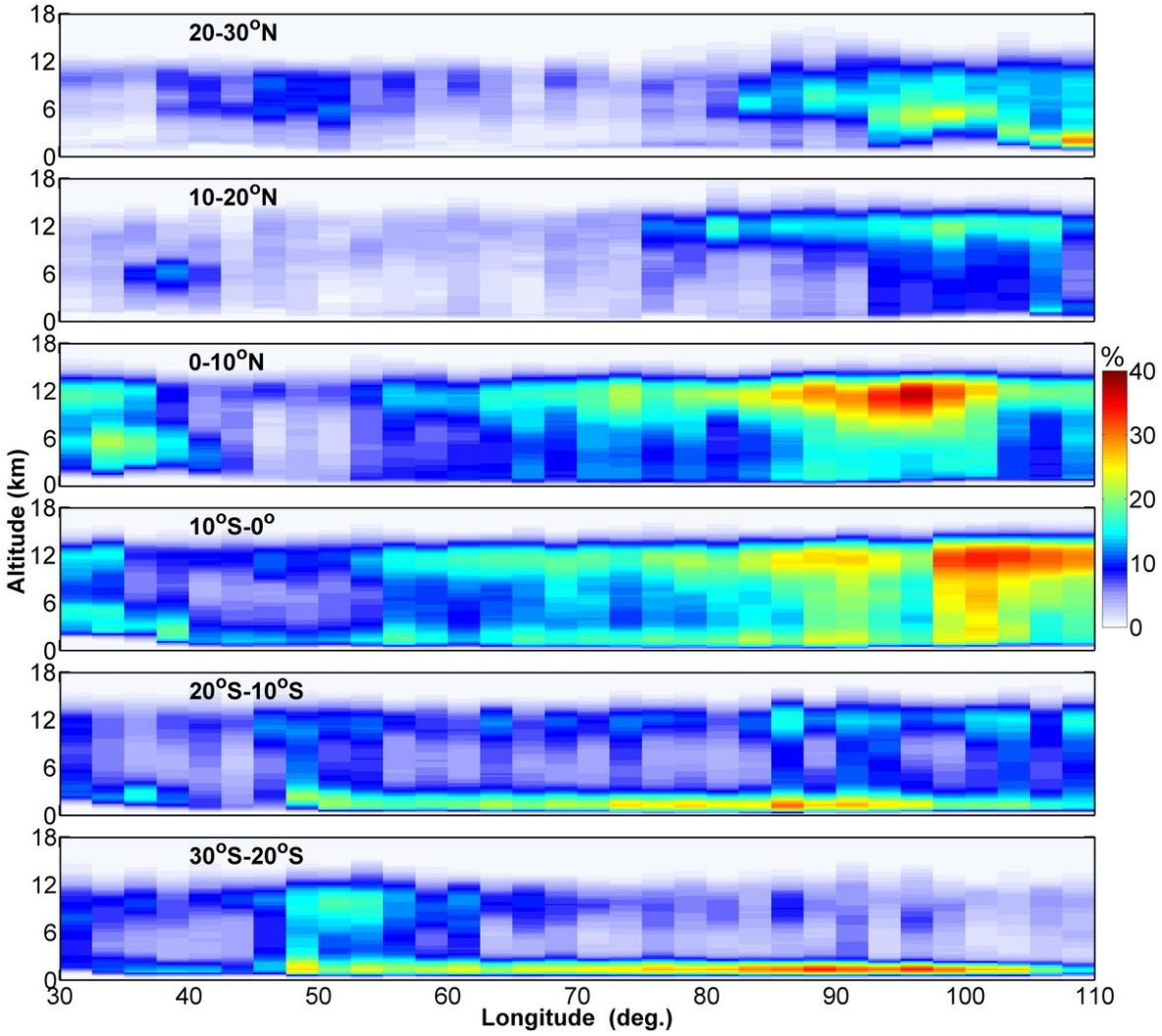

Figure 3.12: Multi-year (2006 to 2011) seasonal mean longitude-altitude cross sections of the frequency of occurrence of clouds averaged for different latitude bands of 10° width (20 to 30°N, 10 to 20°N,..., 30 to 20°S) over the Indian subcontinent and the surrounding oceanic regions during the pre-monsoon season.

pool region in the west equatorial Indian Ocean and southern parts of the Arabian Sea, where the SST exceeds 30°C over a vast region, especially between 60 to 70°E and 0 to 10°N during May (Figure 3.2). This is clearly seen in Figure 3.10, which shows the occurrence of convection over the equatorial Indian Ocean in the longitude band of 60 to 70°E and latitude region of 0 to 10°N during May. (The absence of large-scale cloudiness in this region in Figure 3.12 is because of the averaging of data during March to May; the warm pool does not exist in March). Notwithstanding this, the convection and vertical development of clouds over the Indian Ocean Warm Pool is considerably less than the convection and cloudiness over several other regions which are relatively cooler than the warm pool (e.g., in March, the deep convective clouds over the east equatorial Indian Ocean between 90 to 100°E at 0 to 10°S with SST of

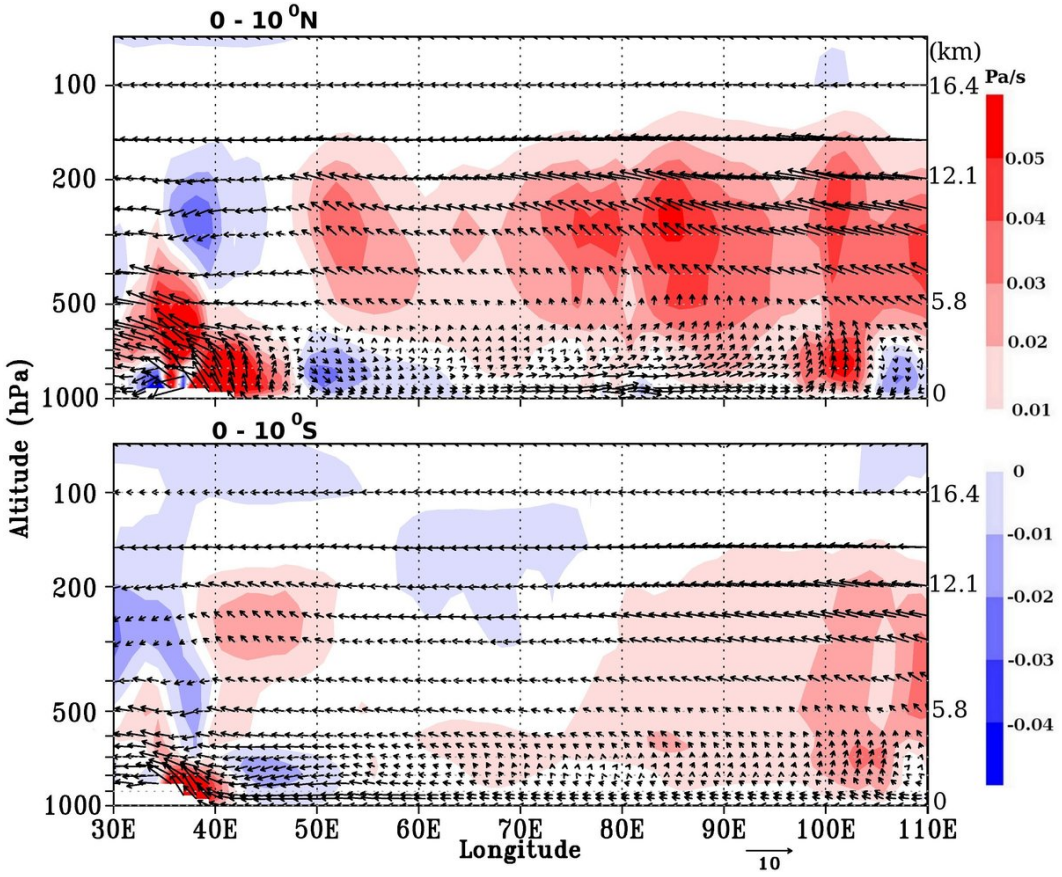

Figure 3.13: Latitudinally averaged seasonal mean zonal circulation during the pre-monsoon season, shown by vector plots of the average zonal and vertical winds in the latitude bands of 0 to 10°N and 0 to 10°S as a function of altitude and longitude. The vertical winds are multiplied by 50 for clearly representing the circulation pattern. Blue shade indicates downdraft and red shade indicates updraft.

∼29°C is substantially larger than that over the warm pool region where the SST is >30°C). This indicates that the cloudiness over a given region is not controlled by the SST alone, but is modified by other thermo-dynamical factors. This aspect on the SST–convection–cloudiness relationship is investigated in detail in Chapter 5.

3.5.3 Asian Summer Monsoon (ASM) Season

3.5.3.1 Altitude-latitude cross sections of cloud distribution and atmospheric circulation

Multi-year (2006 to 2011) seasonal mean latitude-altitude cross sections of the frequency of occurrence of clouds averaged for different longitude bands of 10° width over the Indian subcontinent and the surrounding oceanic regions during the Asian summer monsoon season (JJAS) are shown in Figure 3.14. A better graphical representation of the longitude variations of F_{ALT} depicted in Figure 3.14 is shown in Figure 3.15 ex-

cept for partial masking of the F_{ALT} values in the lower altitudes. The corresponding monthly mean variations of F_{ALT} during the individual months (June, July, August and September) are shown in Figure 3.16. One of the most remarkable features of the cloud distribution during the ASM is the deepest convection over the entire study domain and among the deepest global convective regions [*Newell and Gould-Stewart*, 1981] occurring over the north and northeast Bay of Bengal in the longitude bands of 80 to 90°E and 90 to 100°E. Though these features prevail throughout the season, they are more intense during July to August compared to June and September. The zone of intense convection is centered around 16 to 22°N over the north Bay of Bengal (80 to 90°E, which cover the north Bay of Bengal adjoining the east coast of Peninsular India) and around 12 to 20°N over the northeast Bay of Bengal (90 to 100°E). Figures 3.14 and 3.16 shows that the altitude of largest cloud occurrence over both these deep convective zones tends to shift southward. Frequency of occurrence of clouds over the northeast Bay of Bengal is larger than that over the north Bay of Bengal. These features are in agreement with the total frequency of occurrence of clouds depicted in Figure 3.3, which shows that the total cloudiness exceeds 90% over most of these regions.

Over most parts of the north and northeast Bay of Bengal, F_{ALT} exceeds 40% at all altitudes during July to August. A significant fraction of the deep convective clouds reach up to ∼15 km altitude in this region, above which the values of F_{ALT} rapidly decreases. In contrast, the occurrence of deep convective clouds almost ceases at the altitude of ∼13 to 14 km over all other regions (including the east and central equatorial Indian Ocean, the Arabian Sea sector, and the Indian landmass) during the ASM; similar is the case with the vertical distribution of clouds during the other seasons as well. This clearly shows that the top altitudes of deep convective clouds over the north/northeast Bay of Bengal extends at least 1 to 2 km above that over the other deep convective regions. These results on the largest deep convection over the north Bay of Bengal are in agreement with the inferences made by *Meenu et al.* [2010] based on the brightness temperature data, which showed that the deep convective cloud tops over the north and northeast Bay of Bengal is about 10 to 15 K cooler than that over the other regions. It is also important to note that only optically thick clouds are detected by CloudSat. Based on CALIPSO observations, *Meenu et al.* [2011] showed that the frequency of occurrence of semitransparent cirrus clouds (which are not detectable using CloudSat) extends up to 16.5 km altitude over the north and northeast Bay of Bengal, while the corresponding altitude over the other deep convective regions is 14 to 15 km. A small fraction (<5%) of these semitransparent cirrus clouds were found to cross the cold point tropopause over the north and northeast Bay of Bengal [*Meenu et al.*, 2011].

Throughout the summer monsoon season, the frequency of occurrence of clouds consistently decreases northward and southward of the deep convective regions observed at 80 to 100°E. One of the most remarkable features observed in Figures 3.14 and 3.16 is the persistence of a large region of negligible cloudiness occurring below ∼7 km altitude in the region encompassed between ∼5 to 12°N latitude and 80 to 90°E longitude. This appear like a dome structure with cloudiness <10% at all altitudes below ∼7 km. Though this structure appears throughout the season, it is most prominent during July to August. The cloudiness systematically increases away from this region (in all directions), though the signature of relatively less cloudiness is seen in the longitude bands of 70 to 80°E and 90 to 100°E, especially during July to August. This is one of the least explored aspects of the Asian summer monsoon [*Nair et al.*, 2011] and is investigated in detail in Chapter 4.

Deep convection is also prominent between the latitudes of ∼10 to 22°N in the 70 to 80°E longitude band, which covers most of the India landmass. This deep convection, mainly caused by the monsoon trough, is most prominent towards the northern latitudes, and extends up to ∼14 km altitude. However, the overall cloudiness in this convective region is lesser (typically, F_{ALT} <35%) than that over the north and north-east Bay of Bengal. Cloudiness in this region is most prominent during June-July and starts weakening from August onwards. Intensity of this convection reduces substantially towards the west, and is rather feeble in the longitude band of 60 to 70°E. On average, cloudiness over the northern hemisphere is the least in the longitude band of 40 to 60°E.

In addition to the above regions in the northern hemisphere, a zone of large-scale convection is observed around the equator and south of it, which is associated with the equatorial trough. This region of enhanced cloudiness is also observed in total cloudiness shown in Figure 3.3. This feature is prominent at the central and east equatorial Indian Ocean at east of ∼60°E. Deep convection associated with the equatorial trough extends between the equator and ∼5°S latitude. The upper altitude of limit of this deep convection is ∼13 km, above which the cloudiness rapidly decreases; this upper altitude limit of deep convection is at least 2 km below that over the north and north-east Bay of Bengal. Thick cirrus outflows in the upper troposphere from the equatorial trough extends up to 5° southward of the southern boundary of the trough region.

South of the equatorial trough is marked by the persistent occurrence of low altitude clouds in the south Indian Ocean. These clouds have maximum occurrence at ∼1.5 km and are confined to less than 3 km altitude. These features are similar to that observed during the other seasons as well and are associated with the descending limb of the Hadley cell. However, the frequency of occurrence of these clouds is largest (>50% at the peak altitude of occurrence) during the summer monsoon season.

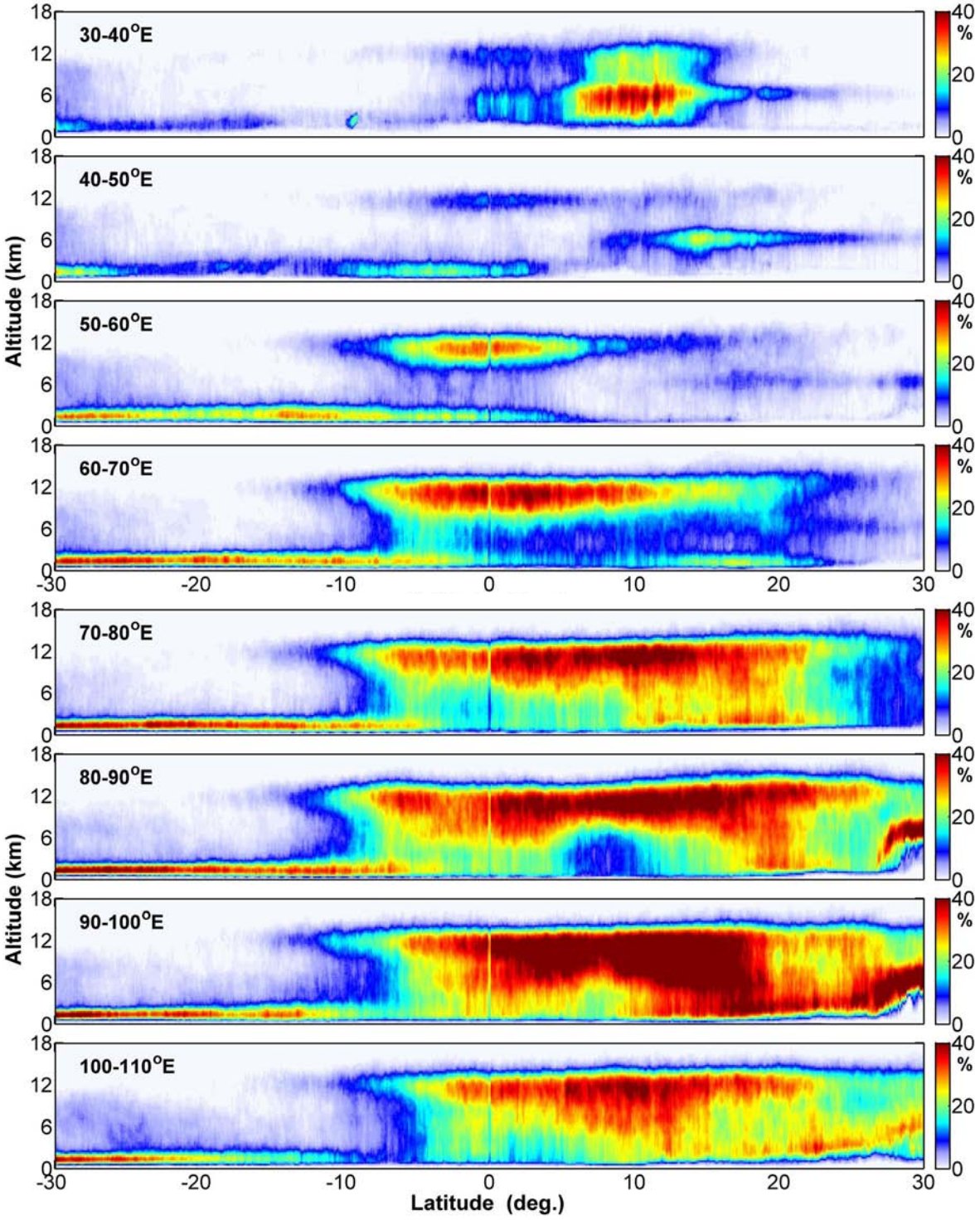

Figure 3.14: Multi-year (2006 to 2011) seasonal mean latitude-altitude cross sections of the frequency of occurrence of clouds averaged for different longitude bands of 10° width (30 to 40°E, 40 to 50°E, ..., 100 to 110°E) over the Indian subcontinent and the surrounding oceanic regions during the Asian summer monsoon season (JJAS).

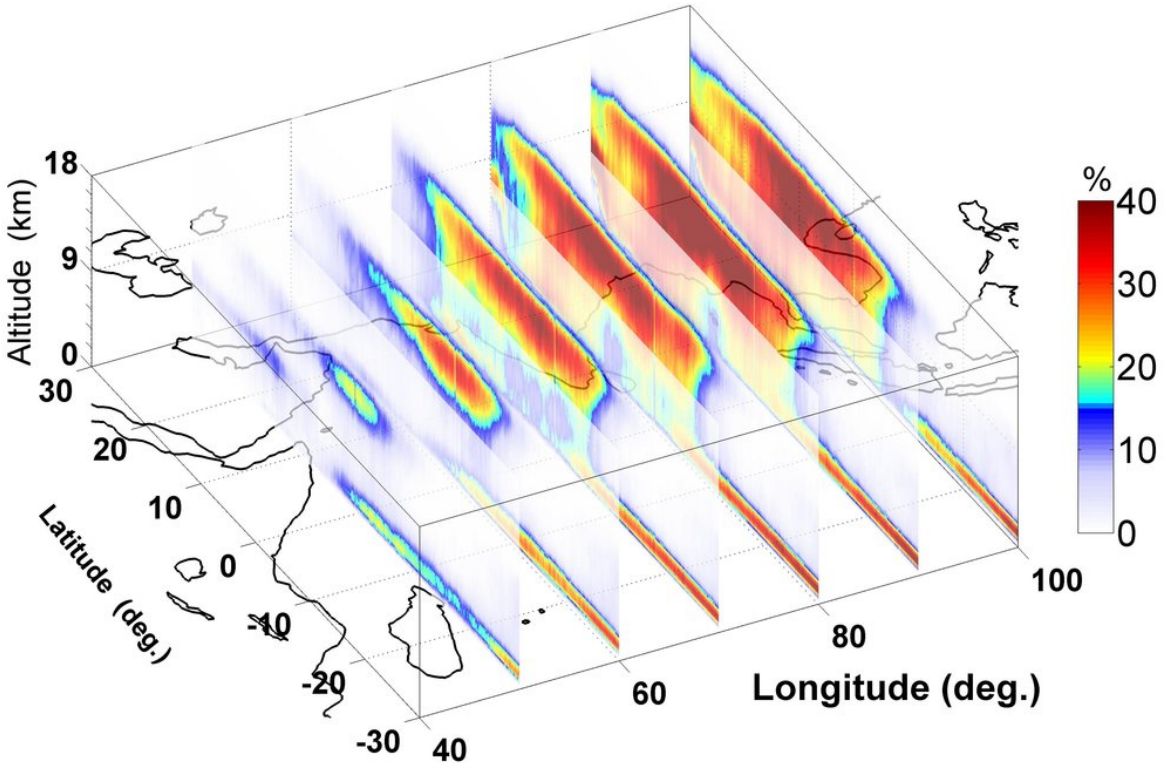

Figure 3.15: Same as Figure 3.14, but for a better graphical representation to depict the westward transport of clouds.

Association between the latitude variations of the vertical distribution of clouds and atmospheric circulation is examined using the meridional circulation shown in Figure 3.17, which depicts the vector plots of the longitudinally averaged meridional and vertical winds obtained from MERRA as a function of latitude and altitude. The predominant deep convection in the 90 - 100°E longitude band over the Bay of Bengal which extend above ∼150 hPa level is clearly discernible in Figure 3.17. This convection is strongest between the latitudes of 10°N to 22°N. The altitude of largest updraft increases towards the south (which appear as the southward lilt in the convective core in Figure 3.17). Correspondingly, the altitude of largest cloudiness also shows a southward tilt in this longitude band (Figure 3.14). The updraft at south of the equator (0 to 5°S) is considerably weaker than that in the northern hemisphere, resulting in the weaker vertical development of clouds at 0 to 5°S. The meridional outflow from the northern hemisphere and the equatorial trough is limited to a few degrees at south of the equatorial trough (Figure 3.17), which results in the relatively small spatial extent of the outflow clouds observed in the upper troposphere over the southern hemispheric Indian Ocean (Figures 3.14 and 3.16). Strong downdraft associated with the Hadley circulation prevails in the middle and upper troposphere at south of ∼5°S. However, the core of this downdraft is located at south of ∼25°S. In general, the convection in this region is highly inhibited and the cloudiness at the south Indian Ocean are mainly

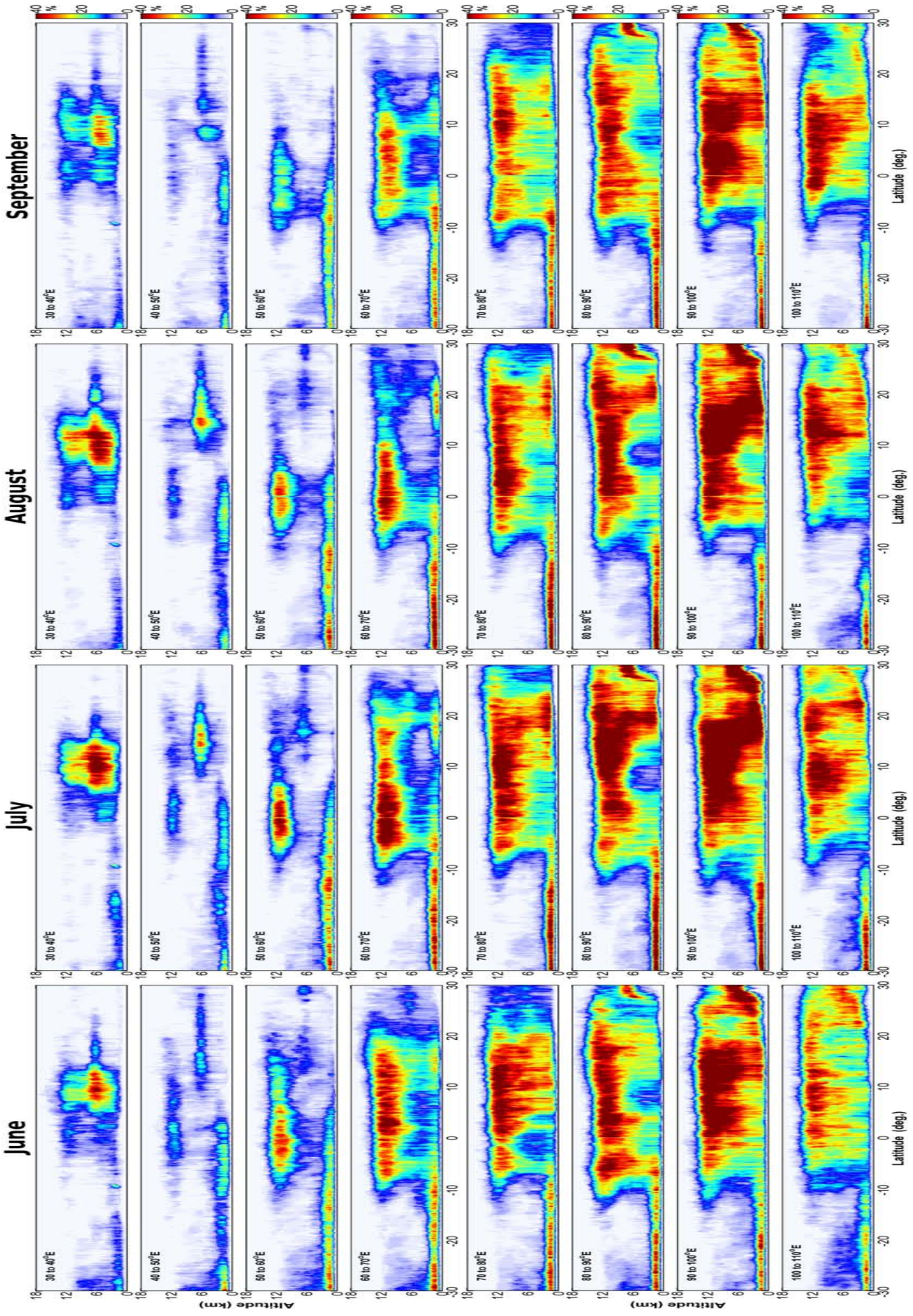

Figure 3.16: Multi-year (2006 to 2010) monthly mean latitude-altitude cross sections of the frequency of occurrence of clouds averaged for different longitude bands of 10° width (30 to 40°E, 40 to 50°E,..., 100 to 110°E) over the Indian subcontinent and the surrounding oceanic regions during June, July, August and September.

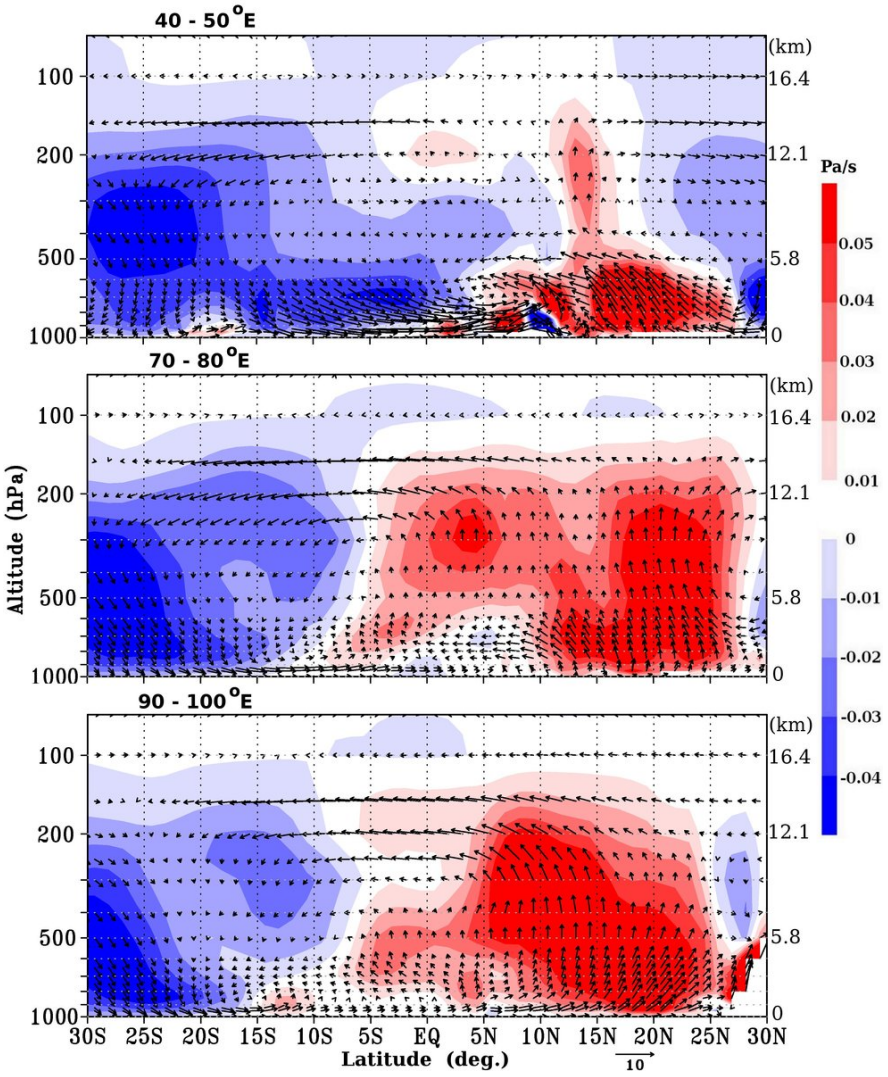

Figure 3.17: Longitudinally averaged seasonal mean meridional circulation during the summer monsoon season, shown by vector plots of the average meridional and vertical winds in the longitude bands of 40 to 50°E, 70 to 80°E and 90 to 100°E as a function of altitude and latitude. The vertical winds are multiplied by 50 for clearly representing the circulation pattern. Blue shade indicates downdraft and red shade indicates updraft.

confined to <3 km altitude.

Figure 3.17 shows that strong updraft, right from the lower troposphere to ∼150 hPa level, prevails in the latitude band of 10 to 25°N over the Indian region (70 to 80°E). This convection is strongest towards the northern latitudes, especially at north of 15°N. Mid- and upper tropospheric convection prevails above 550 hPa level at south of this deep convective region. Convection at the Equatorial Trough is seen at the north of 5°S, but is weaker than the northern hemispheric convection over the Indian region. Strong downdraft prevails at south of the Equatorial Trough, especially at south of 10°S. The vertical distribution of clouds in this longitude band is in agreement with

this pattern of the meridional circulation.

Except for a weak convection prevailing over the relatively dry land areas in east Africa and Arabia in the northern hemisphere, downdraft prevails over the eastern longitude band of 40 to 50°E. Strong downdraft is present over all latitudes in the southern hemisphere in this longitude band, where the cloudiness is extremely weak. The shallow clouds below ∼3 km altitude, which usually prevail in the southern hemisphere, extends up to ∼3°N. A mid-tropospheric band of cloudiness prevails between 5 to 7 km altitude in this longitude band, which is an extension of a similar feature in the longitude band of 30 to 40°E.

3.5.3.2 Altitude-longitude cross sections of cloud distribution and atmospheric circulation

Figure 3.18 shows the multi-year (2006 to 2011) seasonal mean longitude-altitude cross sections of F_{ALT} averaged for different latitude bands during the Asian summer monsoon season. East-west cross section of the zonal circulation, averaged at 10° latitude bands are shown in Figure 3.19 for investigating the effect of zonal circulation on cloudiness. Strong vertical development of clouds over the north and northeast Bay of Bengal is clearly seen in the 10 to 20°N latitude band, with maximum cloudiness at 95 to 100°E. Another region of strong vertical cloud development, though less prominent, is observed at 72 to 76°E, which is the region at west of the Western Ghats. This is in agreement with the zonal circulation which shows largest updraft at east of 90°E and a relatively weaker updraft at west of 76°E. Most importantly, strong easterly winds of average magnitude >10 ms^{-1} prevails in the upper troposphere in this latitude band, which causes a pronounced westward transport of clouds and moisture from the deep convective region of the Bay of Bengal. This westward outflow of convective anvils is seen in Figure 3.18. Almost similar features are observed at the 0 to 10°N latitude band as well, though the updrafts at 90 to 100°E and 70 to 76°E are considerably less than those at the 10 to 20°N latitude band. However, the westward spreading of the deep convective outflow is more prominent in this latitude as the average tropical easterly wind speed is larger here than at 10 to 20°N. Notably, this outflow extends upto ∼55°E, which is ∼15° away from the convection at east Arabian Sea and 35° away from the deep convective region in the east Bay of Bengal. It is very likely that the outflow from deep convective regions of the east Bay of Bengal gets added with the outflow from convection at the east Arabian Sea, which eventually spreads up to ∼55°E. Notwithstanding this, the westward transport of >15° from the deep convective region is quite large and is primarily aided by the strong easterly winds associated with the tropical easterly jet stream (TEJ) prevailing in this region. This is in agreement with the conclusions drawn by *Sathiyamoorthy et al.* [2004] based on

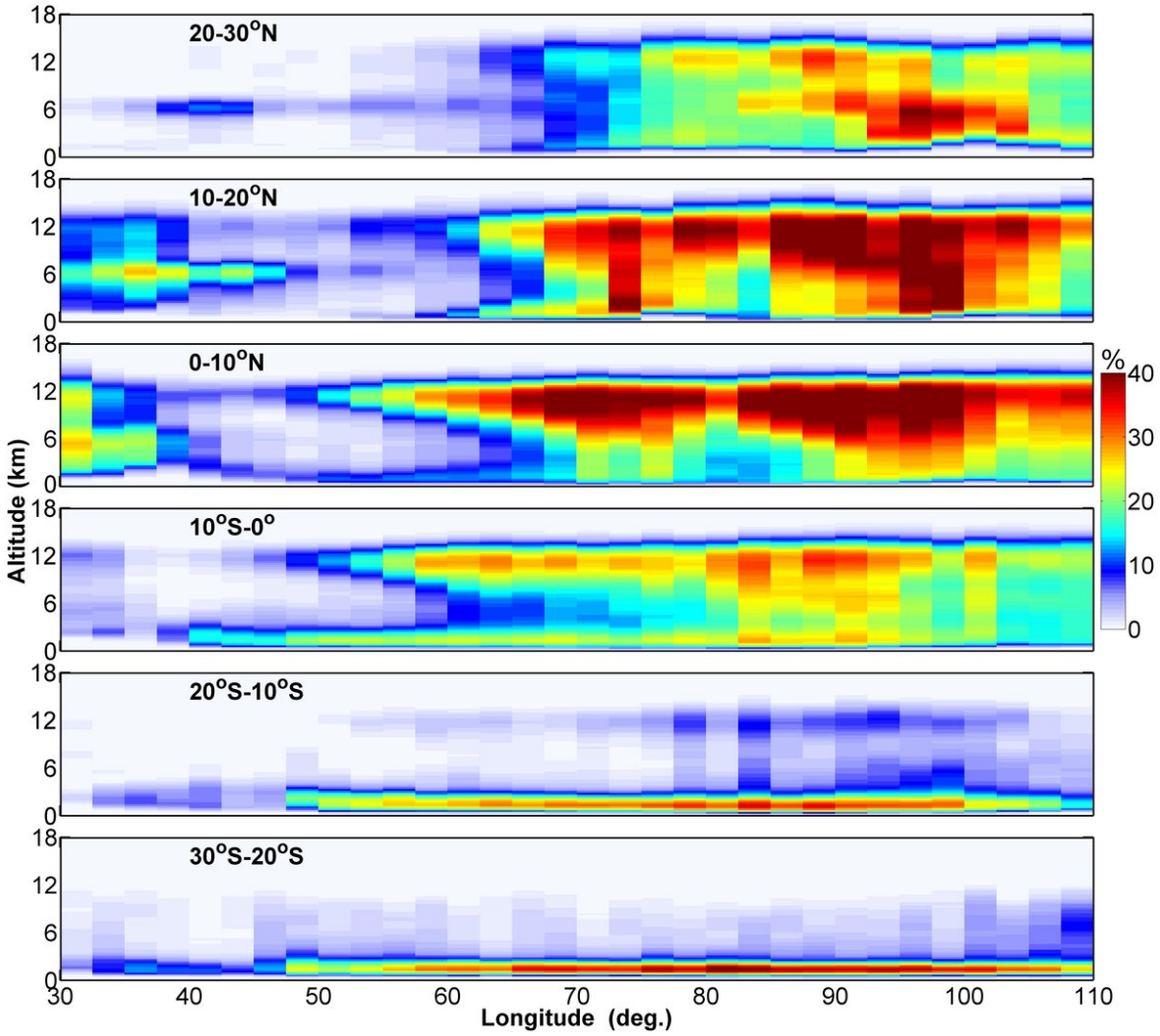

Figure 3.18: Multi-year (2006 to 2011) seasonal mean longitude-altitude cross sections of the frequency of occurrence of clouds averaged for different latitude bands of 10° width (20 to 30°N, 10 to 20°N,..., 30°S to 20°S) over the Indian subcontinent and the surrounding oceanic regions during the Asian summer monsoon season.

the spatial distribution of total cloudiness. A better graphical representation of this is shown in Figure 3.15, which clearly depicts the westward spreading of clouds from the deep convective areas of the Bay of Bengal and east Arabian Sea. As seen in the zonal circulation (Figure 3.19, strong downdraft prevails at 45 to 60°E longitude band in all the latitudes (both in the northern and southern hemisphere), which inhibits further westward propagation of the outflows as well as any in situ generation of convection.

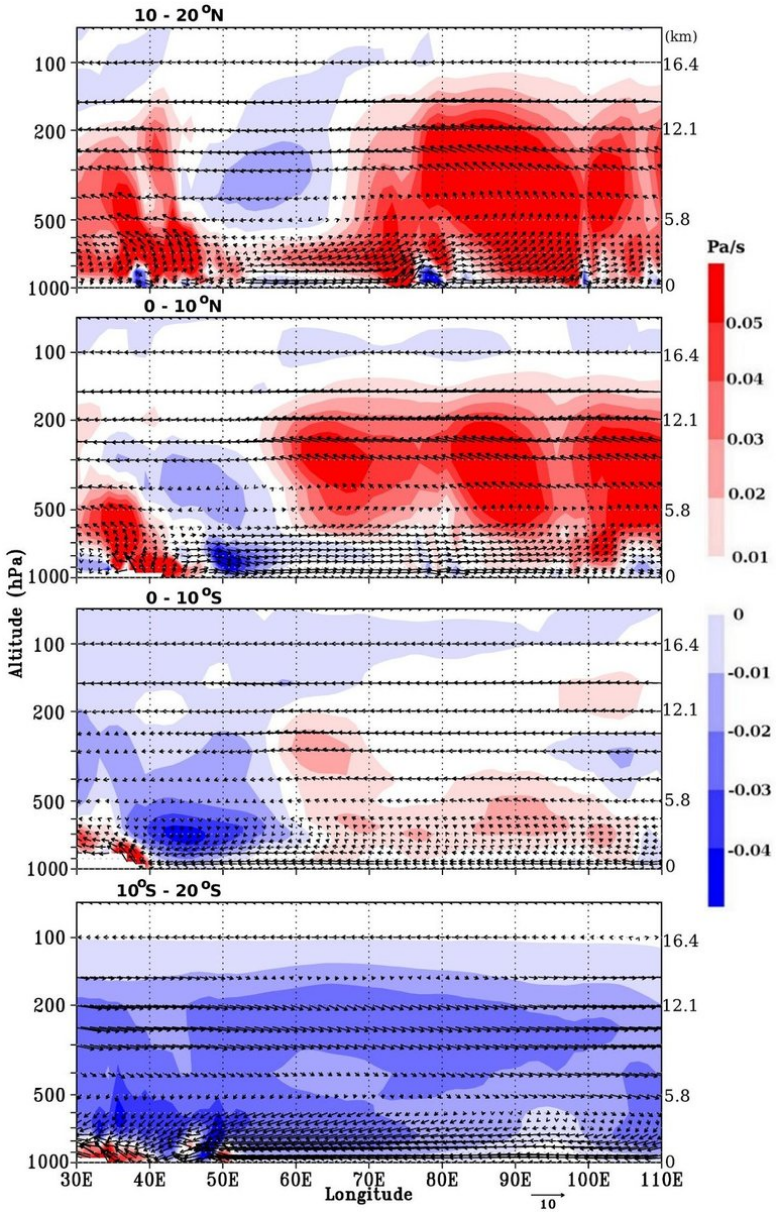

Figure 3.19: Latitudinally averaged seasonal mean zonal circulation during the summer monsoon season, shown by vector plots of the average zonal and vertical winds in the latitude bands of 10 to 20°N, 0 to 10°N, 0 to 10°S and 10°S to 20°S as a function of altitude and longitude. The vertical winds are multiplied by 50 for clearly representing the circulation pattern. Blue shade indicates downdraft and red shade indicates updraft.

3.5.4 Post-monsoon Season

3.5.4.1 Altitude-latitude cross sections of cloud distribution and atmospheric circulation

Seasonal mean (2006 to 2010) latitude-altitude cross sections of F_{ALT} averaged for different longitude bands over the study region during the post-monsoon season are

shown in Figure 3.20 and the corresponding monthly mean variations of F_{ALT} during October and November are shown in Figure 3.21. Most intense cloudiness over the east equatorial Indian Ocean occurs during this season. Significant vertical development of clouds (with F_{ALT} >20% at all altitudes) occurs right from the lower troposphere to the upper troposphere within the latitudes of 10°S and 10°N in the 90 to 100°E longitude band, which is the ITCZ. The values of F_{ALT} maximizes in this longitude band within about 5° on either side of the equator where the upper tropospheric cloudiness is >40% in the altitude band of 10 to 13 km. Drastic reduction of F_{ALT} occurs above ∼13.5 km. Despite the intense vertical development of clouds in this region, the upper altitude of large cloudiness as well as the frequency of occurrence of clouds is lesser than the corresponding values observed over the northeast Bay of Bengal during the Asian summer monsoon season. Cirrus outflows from the convective cells extend up to ∼5 to 8° from the northern and southern boundaries of the ITCZ. The mean latitudinal positions of the ITCZ at all longitude bands during this season are centered around the equator, though their strength decreases westward of 90°E.

Associated with the descending limb of the Hadley cell, the cloudiness rapidly decreases towards south and north of the ITCZ. This reduction in cloudiness at south of the ITCZ is considerably larger than that at the north in the longitude band of 80 to 110°E. The cloudiness shows an increases at north of ∼20 to 25°N in the sub-Himalayan region. Similar to the other seasons, large amount of lower tropospheric clouds prevail below ∼3 km altitude in the south Indian Ocean where the descending limb of the Hadley cell appears. These clouds have the maximum frequency of occurrence in the altitude range of 1 to 1.5 km. Their amount is largest between 70 to 90°E where the values of F_{ALT} is >30% at the peak altitude of occurrence. Their occurrence is rather insignificant at 40 to 50°E, especially at north of ∼25°S. As in the other seasons, such a cloud band does not appear in the northern hemisphere.

The east-west asymmetry in cloudiness associated with the ITCZ over the equatorial region is highly prominent during this season. Vertical development of clouds as well as their frequency of occurrence in the equatorial region decreases systematically towards the west. The lowest values of F_{ALT} at all altitudes occur in the longitude band of 40 to 50°E where their values are mostly <10%. These results are in agreement with the spatial distribution of total cloudiness derived from the NOAA-AVHRR data (Figure 3.3) and indicate that the Walker cell is very strong during this season.

Effect of the atmospheric circulation on the vertical distribution of clouds is examined using Figure 3.22 which shows the seasonal mean meridional circulation in the longitude bands of 40 to 50°E, 70 to 80°E and 90 to 100°E during the post-monsoon season. Strong updraft in the ITCZ which is almost symmetric around the equator at the central and east equatorial Indian Ocean is clearly manifested in this figure.

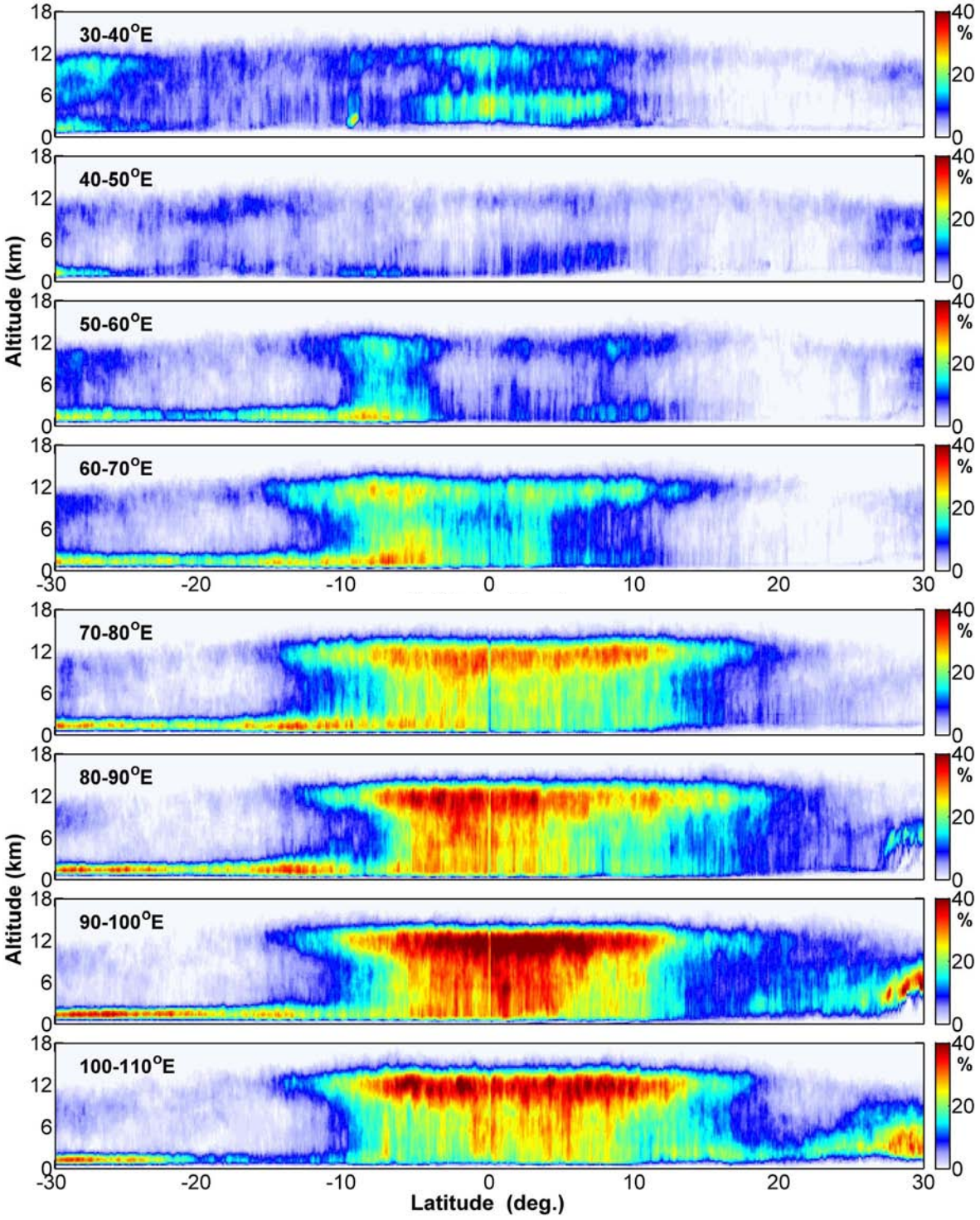

Figure 3.20: Multi-year (2006 to 2010) seasonal mean latitude-altitude cross sections of the frequency of occurrence of clouds averaged for different longitude bands of 10° width (30 to 40°E, 40 to 50°E, ..., 100 to 110°E) over the Indian subcontinent and the surrounding oceanic regions during the post-monsoon season (ON).

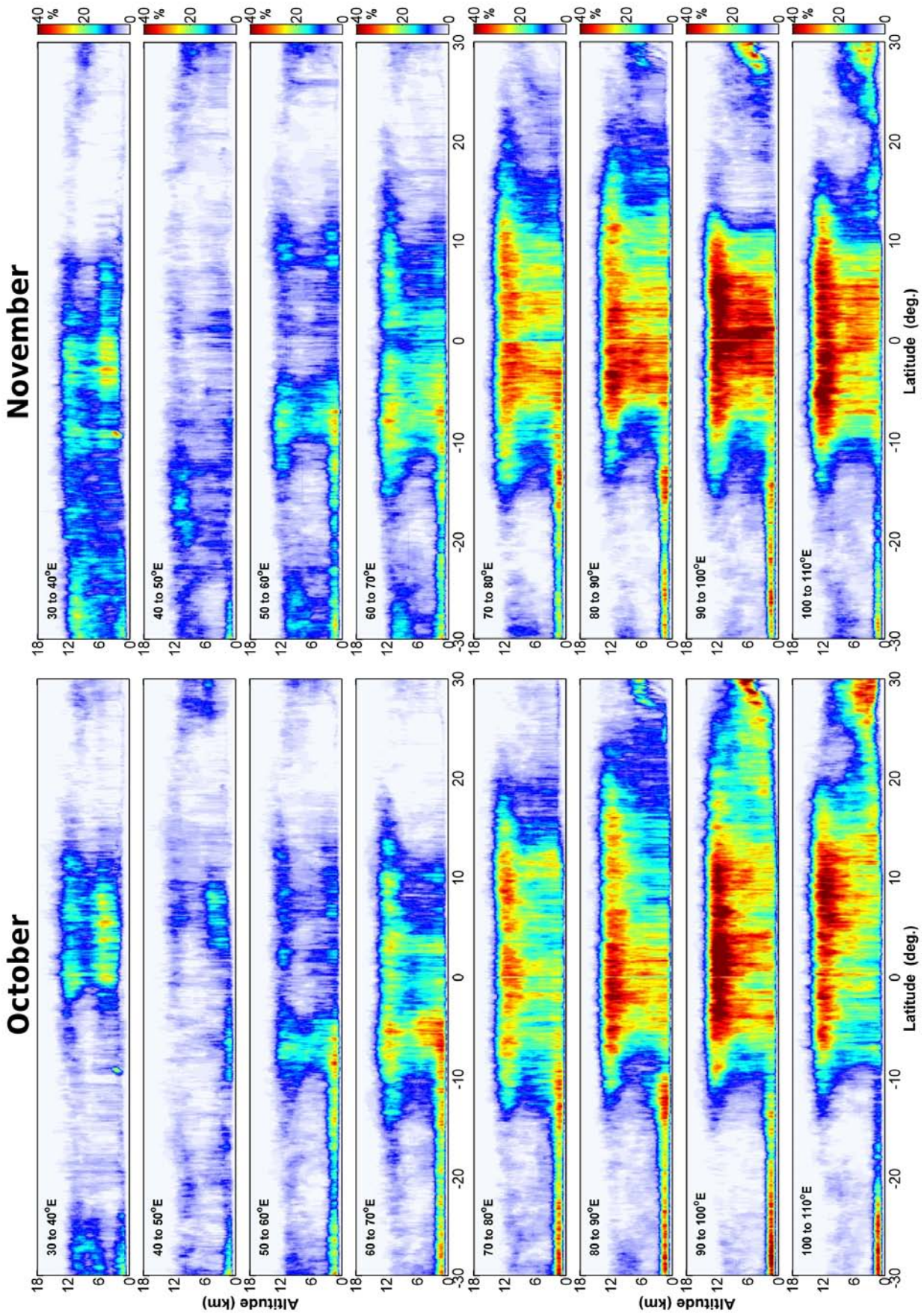

Figure 3.21: Multi-year (2006 to 2010) monthly mean latitude-altitude cross sections of the frequency of occurrence of clouds averaged for different longitude bands of 10° width (30 to 40°E, 40 to 50°E,..., 100 to 110°E) over the Indian subcontinent and the surrounding oceanic regions during October and November.

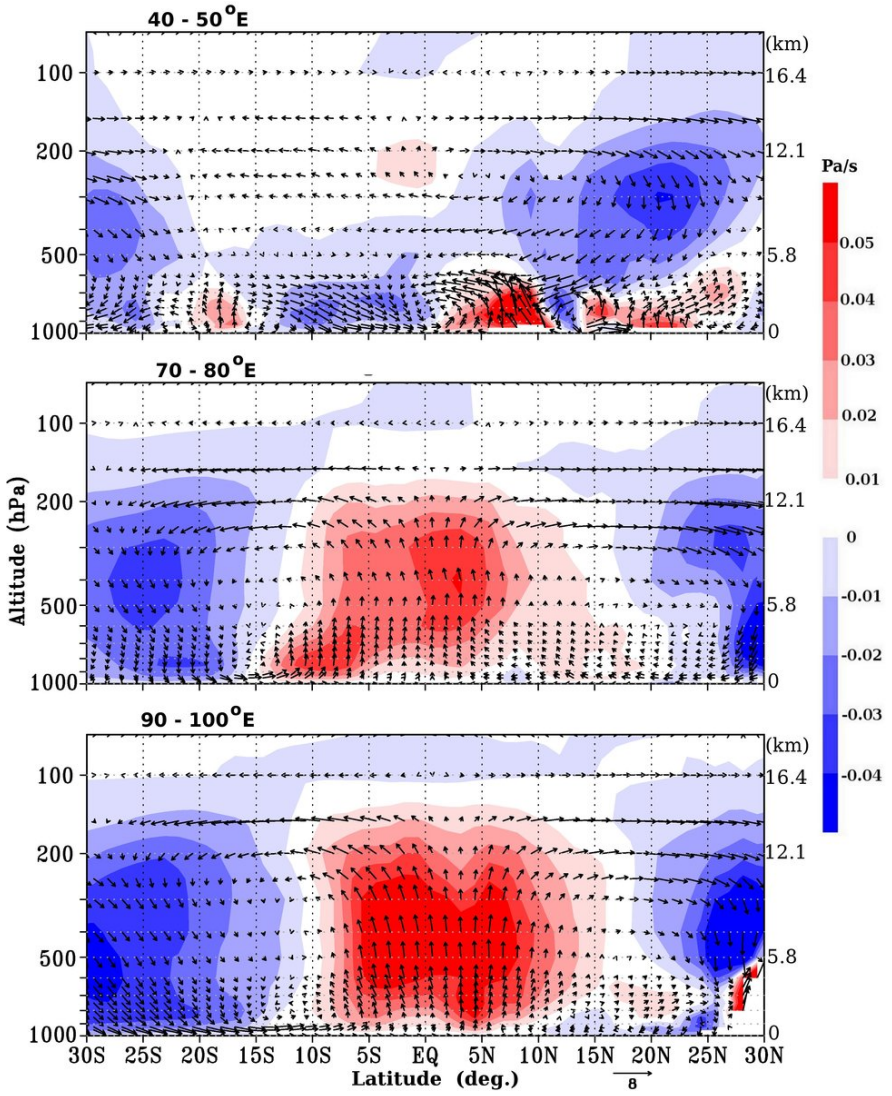

Figure 3.22: Longitudinally averaged seasonal mean meridional circulation during the post-monsoon season, shown by vector plots of the average meridional and vertical winds in the longitude bands of 40 to 50°E, 70 to 80°E and 90 to 100°E as a function of altitude and latitude. The vertical winds are multiplied by 50 for clearly representing the circulation pattern. Blue shade indicates downdraft and red shade indicates updraft.

Updraft in the ITCZ at the east equatorial Indian Ocean (90 to 100°E) prevails in the latitude band of 8°S to 10°N, with largest convection around the equator. Though the updrafts prevail up to ∼150 hPa level in this longitude band, their magnitude decreases above ∼250 hPa level, leading to the divergence of winds above this level. Associated with the Hadley cell, strong downdrafts prevail at south of 10°S and north of ∼20°N latitudes over the east equatorial Indian Ocean; subsidence at the southern branch is stronger than that at the north. The vertical distribution of clouds over this region is in agreement with the MERRA-derived meridional circulation. The updraft in the sub-Himalayan region extending up to ∼600 to 500 hPa level, which is capped

by downdraft above, is clearly manifested in the meridional circulation in the longitude band of 90 to 100°E. Though this feature is observed in the vertical development of clouds as well, they show cloudiness extending up to ∼6 to 7 km, which is well above the region of updraft in the sub-Himalayan region. These features on the cloudiness at the sub-Himalayan region and their genesis though the orographic influence are manifested in all seasons, though with varying degree. Difference between the observed vertical extent of clouds and updraft in the reanalysis data might have been caused by the deficiency of MERRA in the orographically dominated regions.

Strength of the updraft in the ITCZ at the Indian longitude sector of 70 to 80°E is weaker than that over the east Indian Ocean region. This results in rather weaker cloudiness over the ITCZ in this longitude band (Figures 3.20 and 3.21). However, strength of the subsidence at descending limbs of the Hadley cell in this longitude band is comparable in both hemispheres. This results in the nearly symmetrical vertical distribution of clouds with respect to the equator in this longitude band (Figures 3.20 and 3.21). Subsidence prevails at almost all latitudes in the 40 to 50°E longitude band. The near-absence of updraft associated with the ITCZ in this longitude band is caused by the strong subsidence associated with the Walker cell. This leads to the negligible vertical development of clouds as observed in (Figures 3.20 and 3.21). However, strength of the subsidence at the south Indian Ocean and northern hemisphere is substantially weaker than that at the descending limbs of the Hadley cell observed at other longitude bands. Such weak subsidence cannot effectively trap the moisture to the lower atmosphere. This might have been one of the main reasons for the large reduction in the occurrence of low-altitude clouds in this longitude band over the south Indian Ocean.

3.5.4.2 Altitude-longitude cross sections of cloud distribution and atmospheric circulation

Figure 3.23 shows the multi-year (2006 to 2010) seasonal mean longitude-altitude cross sections of F_{ALT} averaged for different latitude bands (30°S to 20°S, 20°S to 10°S, ... 20 to 30°N) over the study region during the post-monsoon season. The corresponding latitudinally averaged zonal circulations around the equator are depicted in Figure 3.24. The longitude-altitude cross sections of cloudiness and the zonal circulation in the latitude bands of 0 to 10°N and 0 to 10°S represent their zonal cross sections at the ITCZ region. These figures clearly show the Walker circulation cell with large deep convection and cloudiness at the east equatorial Indian Ocean and the subsidence at east of 55°E longitude. Cloudiness generated by the deep convection over the east equatorial Indian Ocean extends from the lower troposphere to ∼13.5 km altitude, while the corresponding top altitude is ∼0.5 to 1 km smaller at ∼60 to 70°E.

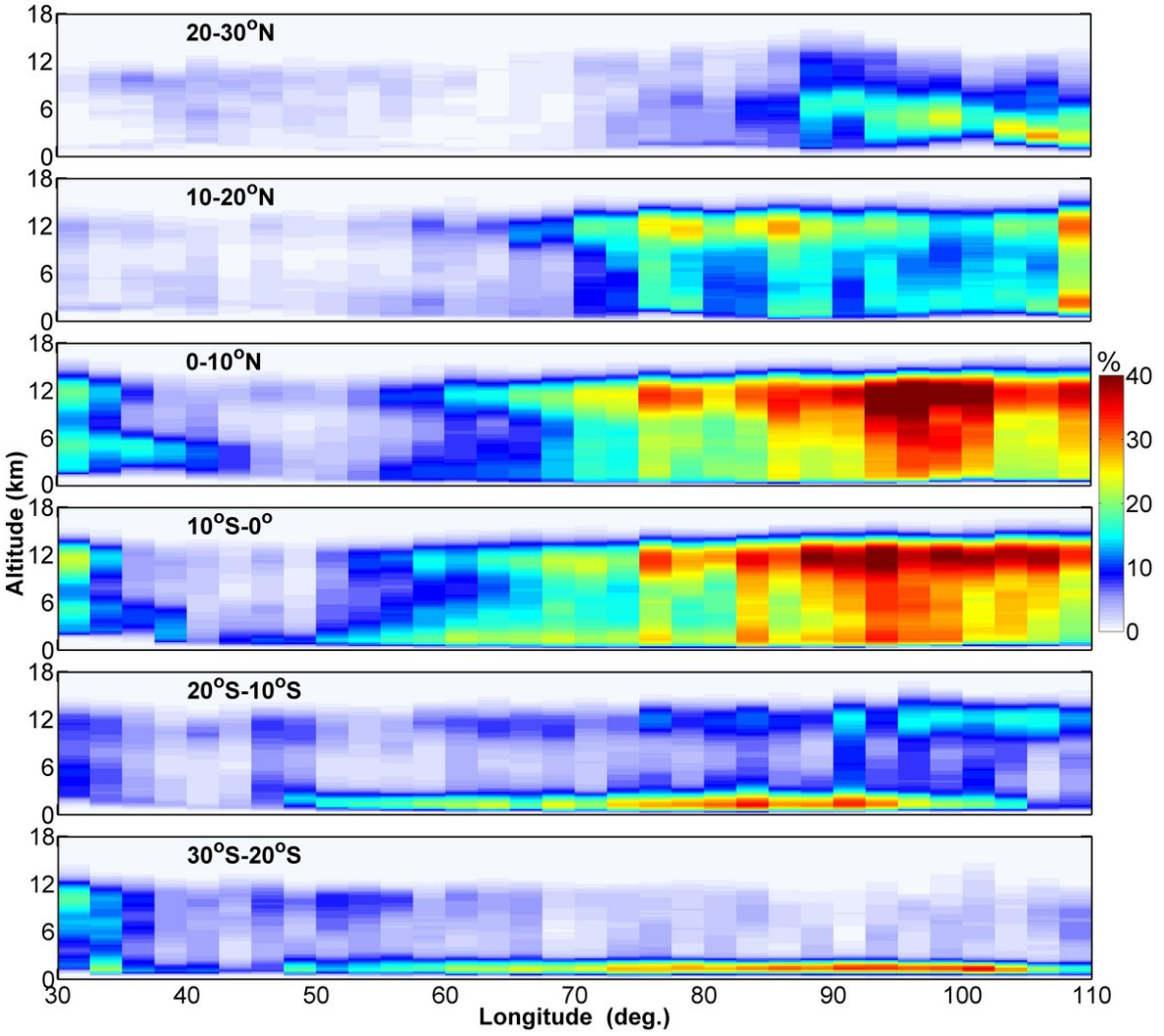

Figure 3.23: Multi-year (2006 to 2011) seasonal mean longitude-altitude cross sections of the frequency of occurrence of clouds averaged for different latitude bands of 10° width (20 to 30°N, 10 to 20°N,..., 30°S to 20°S) over the Indian subcontinent and the surrounding oceanic regions during the post-monsoon season.

These are in agreement with the zonal cross section of the circulation obtained from MERRA data. On average, over the central and east equatorial Indian Ocean, the updraft attains maximum strength between the isobaric levels of ∼600 and ∼250 hPa. The winds are diverging above ∼250 hPa level, though updrafts still prevail up to ∼150 hPa, especially over the east equatorial Indian Ocean. This limits the convection mostly to <13.5 km altitude, as seen in the vertical structure of cloud distribution. The upper tropospheric zonal winds over the equatorial Indian Ocean during this season is substantially weaker than that during the summer monsoon season. This has resulted in the weak zonal convective outflow of cirrus anvils from the deep convective regions at the east and central equatorial Indian Ocean to the western parts.

The updraft at west of ∼40°E in the equatorial region manifested in the MERRA

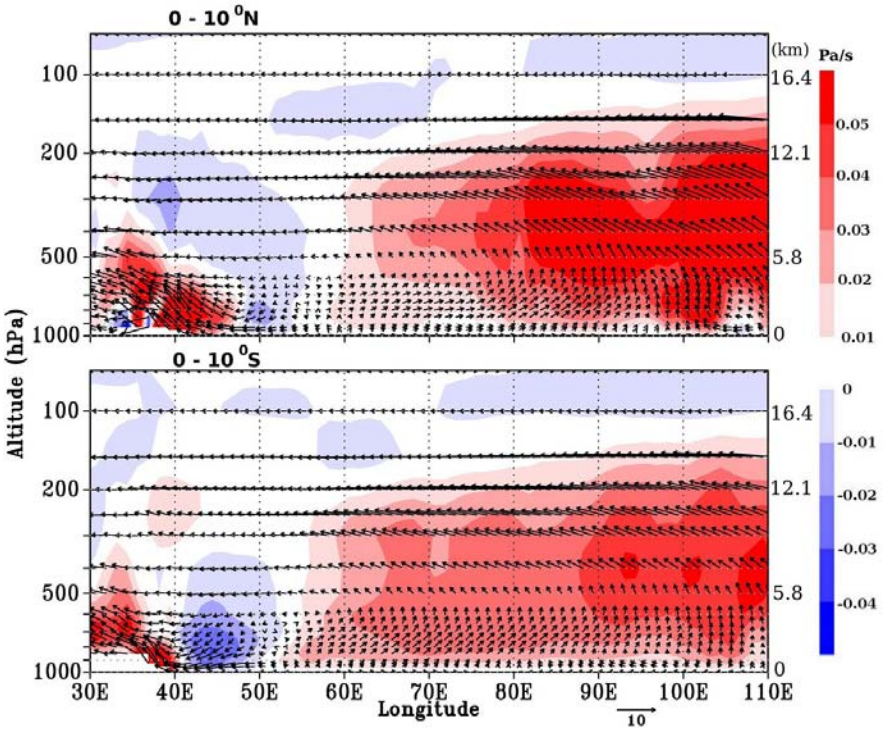

Figure 3.24: Latitudinally averaged seasonal mean zonal circulation during the post-monsoon season, shown by vector plots of the average zonal and vertical winds in the latitude bands of 0 to 10°S and 0 to 10°N as a function of altitude and longitude. The vertical winds are multiplied by 50 for clearly representing the circulation pattern. Blue shade indicates downdraft and red shade indicates updraft.

data is collocated with the convective clouds observed using CloudSat data. Both the updraft and cloudiness are weaker in this region compared to that over the east equatorial Indian Ocean. In the sub-Himalayan region (20 to 30°N), vertical development of clouds shows an enhancement in the upper altitude from 105°E to 90°E; this cloud structure is absent at west of 85°E. Frequency of occurrence of the low-altitude clouds observed at the south Indian Ocean is larger in the 10°S to 20°S (F_{ALT} >40% at the peak altitude) compared to that at 20°S to 30°S latitude band (F_{ALT} <30%). Further, these clouds are prominent only in the longitude band of 50 to 105°E.

3.6 Interannual variations of the vertical distribution of clouds

The relatively short period of observation (June 2006 to February 2011) as well as the smaller frequency of observation (due to the profiling limited to the sub-satellite track in the 16-day orbit cycle) do not permit an exhaustive investigation on the inter-annual variations in the vertical distribution of clouds. Hence, this section is mainly limited to the examination of the reproducibility of the seasonal mean latitude-altitude

cross sections of F_{ALT} during different years. Figure 3.25(a-d) shows the seasonal mean latitude-altitude cross sections of F_{ALT} in the longitude band of 80 to 90°E (the Bay of Bengal sector) during the winter, pre-monsoon, summer monsoon and post-monsoon seasons of the individual years.

3.6.1 Winter season

CloudSat data during 07 December 2009 to 16 January 2010 and 01 January to 06 February 2011 were not released by CloudSat data processinng centre due to technical reasons and hence could not be included in the present analysis. Excluding the winter period of 2010 and 2011 due to the above reason, the cloud distribution during all years during the winter period are consistent. The following are the major differences during the individual years.

1. The amount of cirrus clouds over the south Indian Ocean during 2007 is larger than that during the other years.
2. Location of the deep convective clouds associated with the ITCZ during 2008 extends up to ∼12°S, which is at least 3° southward compared to the other seasons.
3. Cloudiness at the descending limb of the Hadley cell in the northern hemisphere during 2008 is ∼10% while the corresponding values are ∼5% or less during the other years.

3.6.2 Pre-monsoon season

Overall, cloud distribution during the pre-monsoon season of the individual years are similar, except for the following differences.

1. The mid- and upper tropospheric cloudiness over the south Indian Ocean (descending limb of the Hadley cell) during 2007 is distinctly larger than that during the other years when this region is almost cloud-free.
2. The amount of clouds at the ITCZ region and the cirrus clouds at the outflow region are distinctly larger during 2008 compared to the other years.
3. The amount of lower-tropospheric clouds (at <3 km altitude) at the south Indian Ocean (at the descending limb of Hadley cell) is relatively smaller during 2008 compared to the other years.
4. Cirrus clouds usually seen at south of 25°S is absent during 2010.

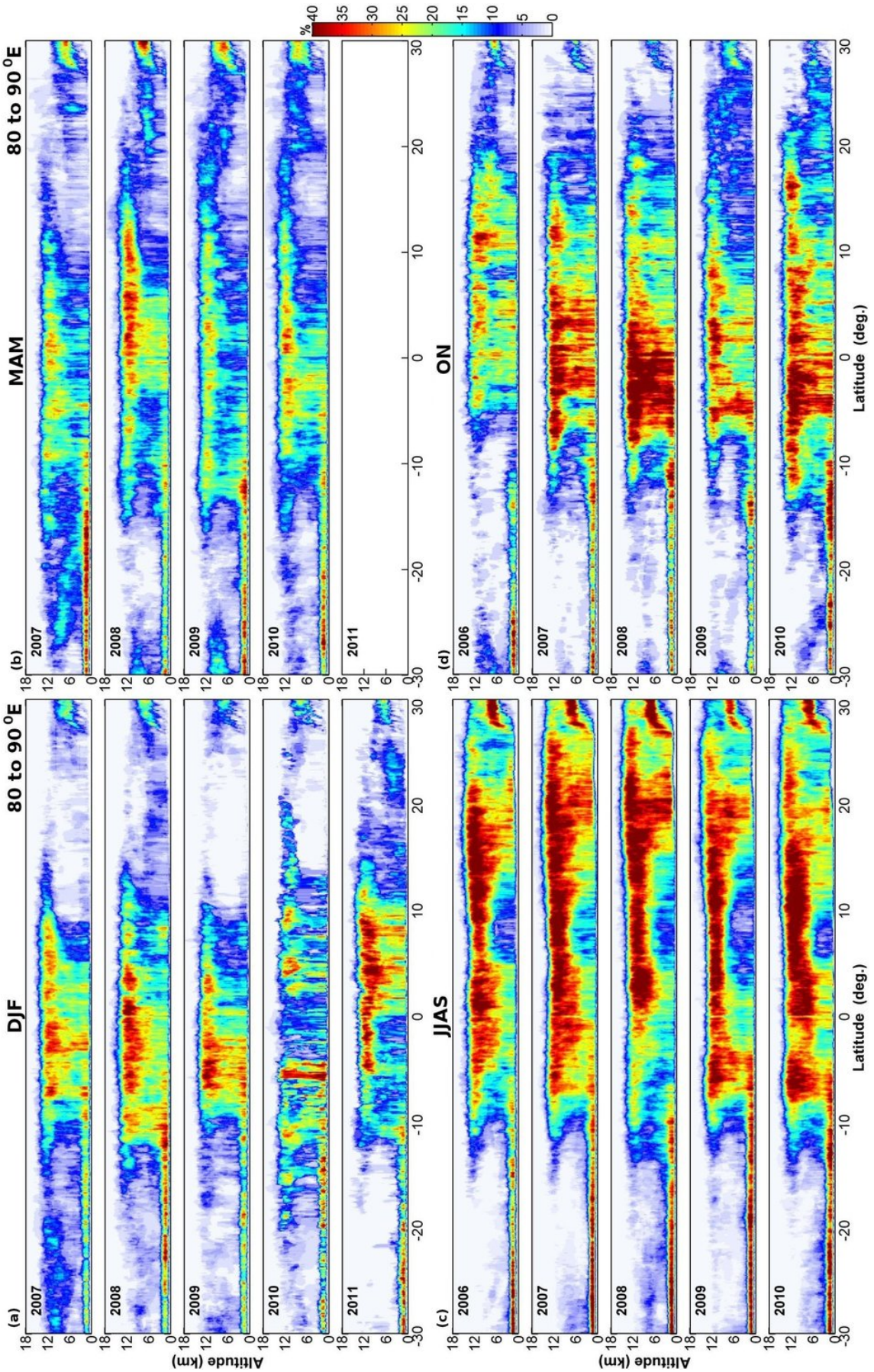

Figure 3.25: (a–d) Seasonal mean latitude-altitude cross sections of F_{ALT} in the longitude band of 80 to 90°E (the Bay of Bengal sector) during the winter, pre-monsoon, summer monsoon and post-monsoon seasons of the individual years.

3.6.3 Summer monsoon season

On average, the vertical distribution of clouds and its spatial variations have similar structures during all years. However, the intensity of cloudiness as well as the characteristics of certain features had significant year-to-year variations. The most prominent among them are the following.

1. Magnitude of cloudiness and the location of maximum cloudiness at the deep convective region of the Bay of Bengal: The values of F_{ALT} in this region are largest during 2007 and 2008 and least during 2009 and 2010.

2. Cloudiness at the equatorial trough shows maximum convection and cloudiness during 2009 and 2010; however, during these years, its location has been shifted by ∼3 to 5° towards the south of its position during the other years.

3. Spatial extent of 'the pool of inhibited cloudiness' over the southwest Bay of Bengal is largest and the values of F_{ALT} below ∼7 km altitude in this region are the least during 2009. In contrast, spatial extent of the pool is the least and cloudiness at the pool is largest during 2007, 2008 and 2010.

Variations in the vertical development of clouds can have an important role in governing rainfall over the Indian region.

3.6.3.1 Vertical distribution of clouds during the drought year – 2009

It may be noted that the all-India rainfall was 698 mm during the summer monsoon season of 2009 as against the long-term seasonal average of 892.2 mm, resulting in a seasonal rainfall deficit of 21.8%. The largest deficit occurred in June (-47.2%), followed by August (-26.5%), September (-20.2%) and July (-4.3%) [Source: Summary of Rainfall characteristics by the India Meteorological Department]. In contrast, the All-India rainfall during ASM of other years during the 2006 to 2010 period were normal and within -1.7% to +5.7% of the long-term average. The seasonal mean vertical distribution of clouds during 2009 clearly shows weakening of convection and vertical development of clouds over the Bay of Bengal longitude sector in the latitude band of 18 to 22°N where intense convection usually takes place during the ASM. While the values of F_{ALT} in this region is larger than 35% during the ASM of normal years (e.g., 2007, 2008), its values were generally ∼30% or less during 2009. The weaker convection over the north Bay of Bengal led to a vast region over the Bay of Bengal to be devoid of large-scale cloudiness during 2009: as a result, the spatial extent of 'the pool of inhibited cloudiness' over the southwest Bay of Bengal has increased

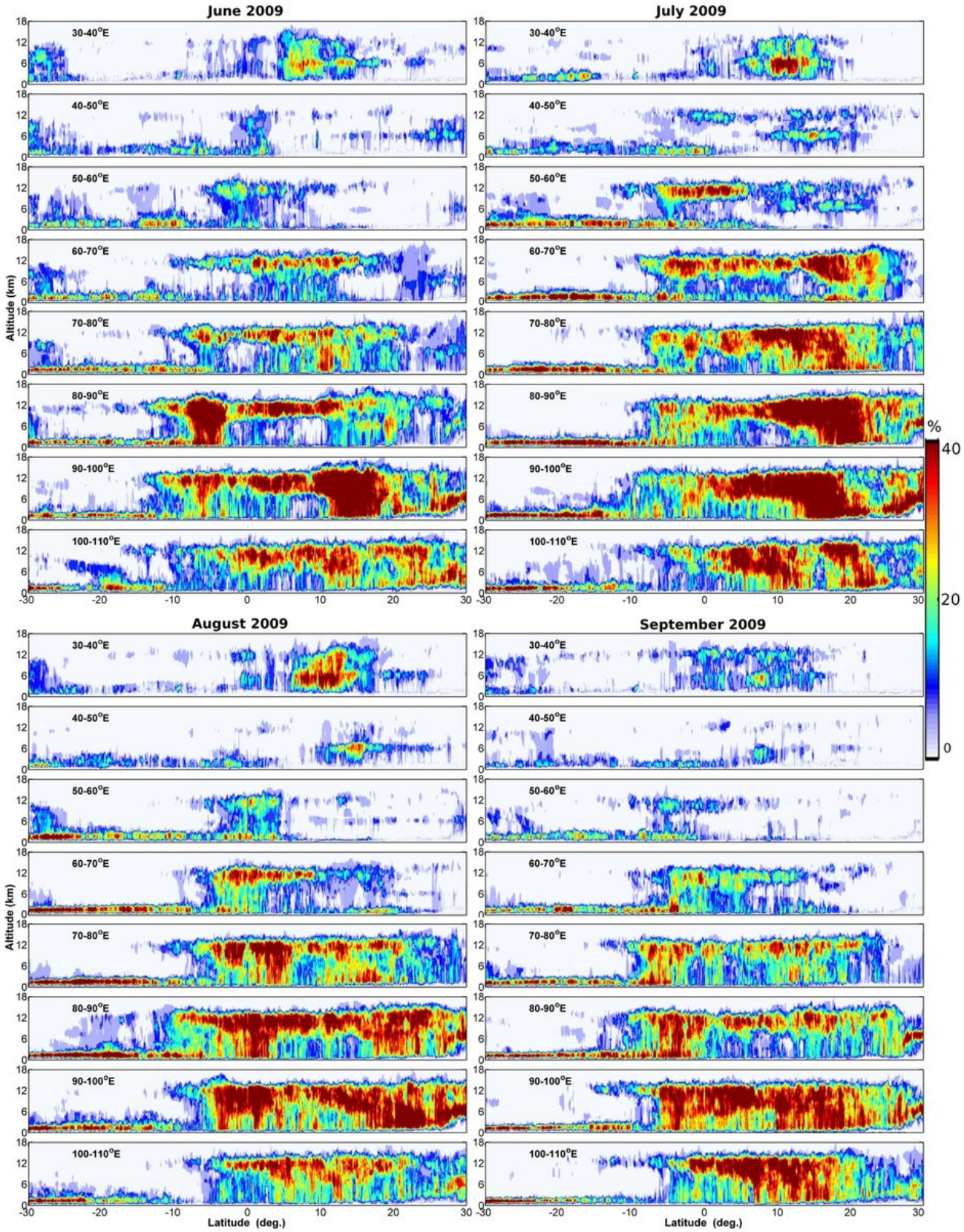

Figure 3.26: Latitude-altitude cross sections of F_{ALT} at different longitude bands during June, July, August and September of 2009.

significantly. Further a large area in the 'pool of inhibited cloudiness' during 2009 had F_{ALT} <5% at altitudes below ~7 km.

As 2009 had large deficit in summer monsoon rainfall, the vertical distribution of cloudiness during this year is examined in detail. The latitude-altitude cross sections of F_{ALT} at different longitude bands during June, July, August and September of 2009 are shown in Figure 3.26. Comparison of this figure with the multi-year monthly mean cloud distribution depicted in Figure 3.16 shows the following features.

1. During June 2009, the vertical development of clouds over the Indian region and the west Bay of Bengal (70 to 90°E) is considerably weaker compared to the multi-year mean. As a result, amount of cirrus clouds at the east Arabian Sea sector (60 to 70°E) also is weak. In contrast, the vertical development of clouds over the northeast Bay of Bengal (90 to 100°E) and the equatorial trough region have enhanced substantially. A distinct increase in the top altitude of convective clouds over the northeast Bay of Bengal (90 to 100°E, 10 to 20°N) is also observed. Spatial extent of the 'pool of inhibited cloudiness' over the southwest Bay of Bengal during June 2009 is considerably larger.

2. Vertical distribution of clouds and its spatial variations during July 2009 are comparable to those in the corresponding multi-year monthly mean variations during July. Large-scale convection over the north Bay of Bengal and the Indian landmass is seen during July 2009. Anomalous convection at the equatorial trough observed in the longitude band of 80 to 100°E is weakened.

3. Vertical development of clouds over the whole region is somewhat weaker during August 2009 compared to the corresponding multi-year mean. This deficit is most pronounced in the Indian region (70 to 80°E; 10 to 25°N) followed by the north Bay of Bengal (80 to 90°E). On the contrary, convection at the equatorial trough region in the longitude band of 70 to 100°E strengthens during August 2009.

4. The vertical development of clouds over the Indian and the west Bay of Bengal sectors continues to be weaker during September 2009. The equatorial trough also continues to be stronger with positive anomaly in the vertical development of clouds, especially in the longitude band of 80 to 100°E.

Monthly variations of the vertical distribution of clouds observed using CloudSat are in agreement with the corresponding variations in rainfall distribution described above. Most importantly, the anomalous weakening of convection and vertical development of clouds over the Indian region and the west Bay of Bengal occurs together

with an anomalous strengthening of the equatorial trough region, especially at the east equatorial Indian Ocean. In general, intensification of convection and cloudiness over the northeast Bay of Bengal is also observed during the anomalous weakening of convection over the Indian region.

3.6.4 Post-monsoon season

Though broad features of the vertical distribution of clouds are similar during the individual years, the absolute magnitude of the vertical development of clouds undergoes considerable year to year variations, as listed below:

1. The values of F_{ALT} at the ITCZ are the least during 2006 when their values are generally <25% in most of the regions. In contrast, the corresponding values are >35% during 2007, 2008 and 2010 – the largest values observed being in 2008 (F_{ALT} ~40%).

2. The outflow of cirrus clouds from the deep convective regions of the ITCZ (especially at the southern hemisphere) is the least during 2006.

3. Cloudiness between 5 to 12°S is the least during 2006. This is especially the case with the lower-tropospheric clouds below the altitude of 3 km, which are present in this region during all other years.

3.7 Summary and conclusions

Vertical distribution of the monthly and seasonal mean frequency of clouds and their spatial variations over the Indian subcontinent and the surrounding oceanic regions in the geographical region between 30°S and 30°N and 30 to 110°E derived from multi-year (2006 to 2011) observations using spaceborne Cloud Profiling Radar onboard the polar orbiting CloudSat are presented in this chapter. Characteristics of the spatial distribution of clouds are compared with their long-term horizontal distribution derived from imager (NOAA-AVHRR) data. CloudSat can provide the vertical distribution of all optically thick clouds (except the semitransparent clouds), and is the only such satellite to monitor the altitude profiles of clouds around the globe as of now. Notwithstanding the uniqueness of CloudSat data in terms of the high-resolution vertical profiling of clouds, these observations are limited to the sub-satellite track for a 16-day orbit cycle. Due to this limitation, the monthly and seasonal mean latitude-altitude cross sections of F_{ALT} are averaged for different longitude bands of 10° width. Similarly, the longitude-altitude cross sections are estimated for latitude bands of 10° width. These zonal and meridional cross sections provide a 3-dimensional distribution of the seasonal and monthly mean cloudiness. However, structures having spatial

scales of the order of a few degrees may not be detectable in this analysis. The observations using passive radiometer imagers (such as NOAA-AVHRR) can provide only the horizontal distribution of total cloudiness and are biased to the high altitude clouds. Role of the atmospheric circulation and SST in governing the horizontal and vertical distribution of clouds are investigated using the SST derived from TRMM Microwave Imager and atmospheric circulation obtained from MERRA. Main accomplishments of this study are: (a) it provides a quantitative estimate of multi-year monthly and seasonal mean vertical distribution of clouds and its spatial variations over the Indian subcontinent and the surrounding oceans, and (b) assessment of the influence of atmospheric circulation on the horizontal and vertical distribution of clouds. Features of the cloud distribution and atmospheric circulation presented in this chapter also provide the necessary background information for the following chapters. Some of the important features observed in this study are further investigated and are presented in the subsequent chapters.

Structure of the Hadley and Walker circulation cells are well discernible in the horizontal and vertical distribution of clouds. Meridional and zonal structure of the vertical distribution of clouds at the ITCZ (the ascending limb of the Hadley cell), the descending limb of the Hadley cell and the east-west asymmetry in the zonal distribution of clouds at the equatorial region caused by the Walker circulation are compared with the corresponding dynamical structures inferred from the MERRA data; the former can be used to indirectly verify the latter.

During all seasons, CloudSat observations show that the vertical distribution of clouds over the ITCZ is marked by large values of F_{ALT} at all altitudes in the troposphere below ∼13 to 15 km. Cloudiness in the upper troposphere in the deep convective regions increases with altitude to attain peak occurrence in the altitude band of ∼9 to ∼13 km. This is primarily because of the occurrence of thick cirrus clouds, most which are formed from the outflow of deep convective clouds as anvils or might be the remnants of deep convective clouds after precipitation. The relatively long atmospheric residence time of cirrus clouds (several hours to 2 days) compared to the low- and middle-level clouds (few minutes to few hours) also lead to increased amount of cirrus clouds in the upper troposphere. As a result of the strong outflow from the deep convective clouds, meridional cross section of the vertical distribution of clouds shows well-developed anvils on either side of the ITCZ. Depending on the strength of the Hadley circulation cell and the resulting upper tropospheric wind divergence (which vary with longitude and season), these cirrus outflows are found prominently up to ∼4 to ∼10° (approx. 440 to 1100 km) meridionally from the northern and southern boundaries of the ITCZ core. Though these cirrus outflows in the meridional direction get weakened further poleward, their presence could be traced well up to the sinking

zones of the Hadley cell on both hemispheres (up to ∼10 to 20° meridionally from the boundaries of the ITCZ). Thickness of these anvil structures is ∼4 to 5 km near the ITCZ boundaries and decreases monotonically with increase in distance. This is mainly because of the increase in base altitude while the top altitude remains almost the same. This increase in the base altitude of the cirrus anvils might have been mainly contributed by: (i) increase in meridional wind with altitude and (ii) radiative heating of the cirrus cloud base due to absorption of IR radiation from the cloud-free or low-level cloud regions below and subsequent evaporation of the cirrus from the base. In contrast, the IR radiative cooling from the cirrus top would help its sustenance for a longer period, till the cloud becomes very thin. These cirrus clouds would be prominent in modulating the radiation budget of the earth-atmosphere system and thermal structure of the upper troposphere, which need to be further investigated.

One of the most important features of the vertical distribution of clouds during the Asian summer monsoon season (ASM) is the occurrence of deepest convection over the entire study domain and among the deepest global convective regions at the north and northeast Bay of Bengal. Though these features prevail throughout the ASM, they are more intense during July-August. The zone of intense convection is centered around 16 to 22°N and 80 to 90°E (the north Bay of Bengal adjoining the east coast of Peninsular India) and around 12 to 20°N and 90 to 100°E (the northeast Bay of Bengal) the latter is stronger than the former. The altitude of largest cloud occurrence over both these deep convective zones tends to shift southward. A large fraction of the deep convective clouds reach up to ∼15 km altitude in these regions. In contrast, the occurrence of deep convective clouds almost ceases at the altitude of ∼13 to 14 km over all other regions during the ASM as well as the other seasons. This clearly shows that the top altitudes of deep convective clouds over the north/northeast Bay of Bengal extends at least 1 to 2 km above that over the other deep convective regions. Though less intense compared to the north/northeast Bay of Bengal, deep convective clouds are also prominent over the monsoon trough, the equatorial trough and the southeast Arabian Sea. The tropical easterly jetstream (TEJ) causes westward transport of large amount of cirrus outflows from the deep convective regions in the Bay of Bengal up to the central Arabian Sea. Eastward extent of this cirrus spreading is ∼30 to 40° from the deep convective regions in the Bay of Bengal and is further aided by the outflow from the southeast Arabian Sea. Another major feature observed during the ASM is the persistence of a 'pool of inhibited cloudiness' with negligible cloudiness below ∼7 km altitude in the region encompassed between ∼5 to 12°N and ∼80 to 90°E. This is one of the least explored aspects of the Asian summer monsoon and is further investigated in detail in Chapter 4.

During all seasons, the meridional cross section of the vertical distribution of clouds

shows minimum cloudiness at the descending limbs of the Hadley cell in both hemispheres. Strength of the ITCZ as inferred from the vertical development of clouds is largest at the east equatorial Indian Ocean and minimum at the west (mainly ∼40 to 50°E). This east-west asymmetry prevails during all seasons and is caused by the Walker circulation which has its ascending limb at the east equatorial Indian Ocean (and the western Pacific) and descending limb at the west equatorial Indian Ocean. In general, this east-west asymmetry in the vertical development of clouds in the equatorial region is most prominent during October-November and April-May periods. As seen from the meridional cross sections of the frequency of occurrence of clouds in the lower to upper troposphere and their spatial gradients, the latitudinal width of the ITCZ is found to be largest (∼10 to 16°) at the east equatorial Indian Ocean and least (¡10°) at the western Indian Ocean where the ITCZ is rather weak and less organized. Structure of the ITCZ and the Hadley and the Walker cells observed using the zonal and meridional cross sections of the vertical distribution of clouds are well in agreement with those inferred from the atmospheric circulation obtained from the reanalysis data.

CloudSat observations show persistent occurrence of low-level clouds throughout the south Indian Ocean (at south of the ITCZ) at the descending limb of the Hadley cell during all seasons. These clouds are very shallow and occur mostly in the altitude band of 1 to 3 km, with the largest frequency of occurrence of ∼30 to 40% at ∼1.5 km. The cold SST at the south Indian Ocean (SST in the range of 25 to 27°C) cannot provide sufficient moisture flux to the atmosphere for generating the observed persistent cloudiness. It is likely that the lower tropospheric moisture required for the observed cloud development might have been produced mainly by the sea surfing caused by the strong surface winds in this region. The moisture produced through evaporation of sea spray gets mixed in the atmospheric boundary layer by the turbulence generated by the wind shears. The moisture is trapped in the lower troposphere by the strong downdraft at the descending limb of the Hadley cell which effectively prevents their upward transport from the lower troposphere. This leads to accumulation of moisture in the lower troposphere and subsequent development of shallow clouds in this region. In contrast, a similar feature is almost completely absent in the northern hemisphere. Compared to the southern hemispheric Indian Ocean, the surface wind speeds, sea agitation and wind shears are rather weak in the northern hemisphere. Further, the prevailing dry winds from the continents would further decrease the water vapour mixing ratio generated by the evaporation from ocean surface at this region. In contrast, the south Indian Ocean is considerably vast and the influence of dry winds from the continents is negligible over most of the regions. A combination of the above mechanisms might prevent significant development of lower tropospheric clouds over the Arabian Sea region while the south Indian Ocean can have larger moisture accumulation and cloudiness in the lower troposphere. However, this hypothesis needs to be further ascertained using

observations of moisture and atmospheric thermo-dynamics in this region.

Overall, the seasonal mean vertical distribution of clouds and their spatial variations are more or less similar during the individual years. However, remarkable differences were observed in these features during the summer monsoon season of 2009, which was a drought year with a seasonal mean all-India rainfall deficit of 21.8%. The seasonal mean vertical distribution of clouds during 2009 clearly shows weakening the vertical development of clouds over the Indian landmass and the north Bay of Bengal where intense convection usually take place during the ASM. While the values of F_{ALT} in this region is larger than 35% during the ASM of normal years (e.g., 2007, 2008), its values are ∼30% or less during 2009. The weaker convection over the north Bay of Bengal led to a vast region over the Bay of Bengal to be devoid of large-scale cloudiness during 2009: as a result, the spatial extent of 'the pool of inhibited cloudiness' over the southwest Bay of Bengal has increased significantly. During June 2009, the vertical development of clouds over the Indian region and the west Bay of Bengal (70 to 90°E longitude) is considerably weaker compared to the corresponding multi-year mean. In contrast, the vertical development of clouds over the northeast Bay of Bengal (90 to 100°E) and the equatorial trough region have enhanced substantially. However, the vertical distribution of clouds and its spatial variations during July 2009 are comparable to those in the corresponding multi-year monthly mean. Vertical development of clouds over the Indian and Bay of Bengal regions are somewhat weaker during August and September 2009 compared to the corresponding multi-year mean. This deficit is most pronounced in the Indian region (70 to 80°E; 10 to 25°N) followed by the north Bay of Bengal (80 to 90°E). Monthly variations of the vertical distribution of clouds observed using CloudSat are in agreement with the corresponding variations in rainfall distribution. Most importantly, the anomalous weakening of convection and vertical development of clouds over the Indian region and the north Bay of Bengal occurs together with an anomalous strengthening of convection at the equatorial trough region and the east Bay of Bengal.

Chapter 4

'Pool of Inhibited Cloudiness' over the Southwest Bay of Bengal during Asian Summer Monsoon season: Characteristics and Potential Genesis Mechanism

4.1 Introduction

Spaceborne observations and experimental campaigns during the past few decades have made significant advancements in the understanding of the Asian summer monsoon (ASM: June to September). However, knowledge of several monsoon features and the underlying physical processes are still inadequate, because of which the modelling and long-range forecast of ASM remain elusive. Distribution of clouds over the Indian subcontinent and the surrounding regions during ASM has several important features. For example, the highest cloud top altitudes [*Meenu et al.*, 2010] and integrated latent heat release [*Zuluaga et al.*, 2010] over the planet occur over the Bay of Bengal (BoB) during ASM. In contrast to the near-cancellation of the longwave and shortwave cloud radiative forcing at the top-of-atmosphere over the tropics, net cloud radiative forcing over a vast region in the Indian subcontinent and the surrounding oceans is negative during ASM [*Rajeevan and Srinivasan*, 2000; *Roca et al.*, 2005]. As seen in Chapter 3, the spatial and vertical distribution of clouds derived from long term satellite data clearly shows a predominant reduction in cloudiness over the southwest Bay of Bengal during the ASM. This 'pool' of inhibited cloudiness covers an area of >1 million Km^2 and is a persistent feature during all years. This 'pool' is geographically separated from

the rain shadow region of the Western Ghats which extent all along the western coast of peninsular India between ~7°N to 20°N. Though the existence of this feature is seen in the regional distributions of clouds, precipitation and outgoing longwave radiation (OLR) reported in the literature [e.g., *Goswami et al.*, 1999; *Meenu et al.*, 2007, 2010], its characteristics and potential genesis mechanism were not explored till *Nair et al.* [2011]. This is primarily because of the limitation of space-borne passive radiometric observations, which could not clearly bring out the distribution of clouds as they are generally biased towards high-altitude clouds. In contrast to this, the active remote sensing of hydrometeors using CloudSat have enabled the detection of clouds occurring below optically thick high-altitude clouds [*Haynes and Stephens*, 2007], which elucidate certain unique features of their vertical distribution in the 'pool'. The characteristics and genesis of this 'pool' have been explained for the first time by *Nair et al.* [2011]. This chapter presents the detailed analysis of cloudiness of this 'pool' based on long-term space borne observations of the vertical and spatial distributions of clouds and precipitation. The observed characteristics of cloud distribution together with the observations of atmospheric energetics and surface wind divergence and atmospheric circulation obtained from reanalysis data are used to explore the potential generation mechanism for this 'pool' and its impact on the summer monsoon circulation.

4.1.1 Objectives of the study

The main objectives of this study are:

1. Detailed analysis of the characteristics of the 'pool of inhibited cloudiness' in terms of spatial and vertical distribution of clouds,

2. Investigation of the generation mechanism of the 'pool' by combining the observed 3-dimensional structure of cloud distribution, spatial variation in atmospheric energetics and surface wind divergence as well as the atmospheric circulation obtained from reanalysis data.

4.2 Data

Long term spatial distribution of clouds (1996 to 2010) is derived on a daily basis by analyzing the data obtained from the Advanced Very High Resolution Radiometer (AVHRR; Global Area Coverage–GAC) onboard NOAA-14/16/18 satellites. This data has daily coverage over the entire study region considered here. Pixel resolution of AVHRR-GAC data is 4 km at nadir. Brightness temperature observed in the thermal infrared bands are used to identify the cloudy pixels based on the method described in Chapter 2. Pixel-level cloudiness derived from each satellite pass is transformed into a

uniform geographical grid of size 0.25°. The monthly mean frequency of occurrence of clouds (F_C) in each grid is obtained by averaging the observed daily mean cloudiness in the respective grids for each month. Entire AVHRR data during the 1996 to 2010 period are used in this analysis.

Vertical distribution of clouds is obtained using CloudSat data. The Cloud Profiling Radar (CPR) operating at 94 GHz provides the altitude profiles of backscattered radar signal from hydrometeors with a vertical resolution of 240 m along the sub-satellite track [*Haynes and Stephens*, 2007]. Details of CloudSat data and its analysis are presented in Chapters 2 and 3. The footprint size of a single profile is 1.7 km along track by 1.4 km across track. The CloudSat orbits have a repetivity of 16 days. This study utilizes the cloud geometrical profile product, 2B-GEOPROF (Version-4) which provides the cloud mask containing the information on cloud layers and their top and base altitudes for the individual profiles along the satellite orbit [*Mace et al.*, 2007]. These data are used to estimate the monthly and seasonal mean altitude profiles of the frequency of occurrence of clouds (F_{ALT}) and their zonal and meridional variations during the June to September period of 2006 to 2010.

Long-term seasonal mean spatial distribution of precipitation over the study domain is obtained from the Global Precipitation Climatology Project (GPCP Version 2.1) data [*Adler et al.*, 2003], which has a geographical resolution of 2.5°. Monthly and seasonal mean values of SST are examined using the TMI-SST data which has a pixel resolution of 0.25° and accuracy of 0.5°C. The surface wind divergence (SWD) during 1996 to 2009 are obtained from the spaceborne scatterometer observations (European Remote Sensing Satellite – ERS 1 and 2, and QuikScat satellite of NASA), which have a spatial resolution of 0.5° (QuikScat) and 1° (ERS) [*Liu*, 2002]. The atmospheric circulation data during the above period are obtained from MERRA.

4.3 Detailed analysis of cloud distribution of the 'pool'

4.3.1 Spatial distribution of clouds

Figure 4.1 depicts the long-term (1996 to 2010) seasonal mean distribution of the frequency of occurrence of clouds (F_C) over the Indian subcontinent and the surrounding oceanic regions during ASM derived from AVHRR data, which clearly shows the presence of a large 'pool of inhibited cloudiness' over the southwest Bay of Bengal (BoB) centred around 8°N, 82°E adjoining SriLanka. Seasonal mean values of F_C in the 'pool' are <50% while those over the surrounding regions are ~70 to 90%. It may be stated here that the features of cloud distribution, including characteristics of the

'pool' region, observed using AVHRR data during 2006 to 2010 are similar to that for 1996 to 2010 shown in Figure 4.1. Figures 4.2(a–d) depict the long-term (1996 to 2010) monthly mean spatial distribution of F_C during June, July, August and September; which show that the 'pool' appears throughout the ASM. However, the 'pool' is most prominent during June to August and weakens in September. The corresponding long-term monthly mean latitude and longitude variations of F_C averaged along 80 to 85° E and 5 to 10°N, respectively, during June, July, August and September are depicted in Figure 4.2(e) and (f), which show the persistence of the 'pool' throughout the ASM, though its prominence is maximum during July to August. Similar features are also seen in the regional distribution of clouds reported by *Meenu et al.* [2007, 2010]. As clearly identified from the latitudinal and longitudinal variations of F_C (Figure 4.2(e),(f)), the 'pool' extends from 77 to 90°E and 3 to 13°N, which are remarkably similar during all the above months.

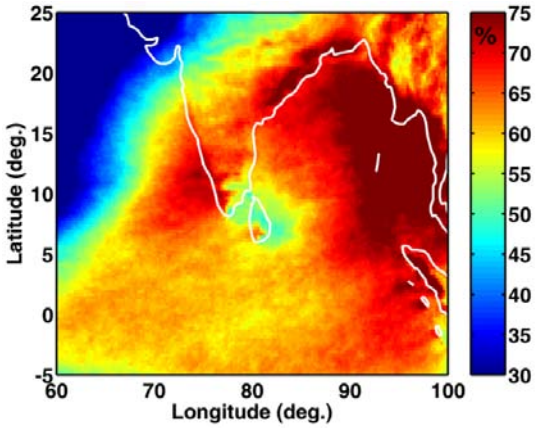

Figure 4.1: Long term (1996 to 2010) seasonal mean spatial distribution of the frequency of occurrence of clouds (F_C) during ASM (JJAS). Note the 'pool of inhibited cloudiness' where F_C is lesser at the southwest Bay of Bengal.

4.3.2 Vertical distribution of clouds

The seasonal mean latitude-altitude cross section of altitude profiles of the frequency of occurrence of clouds (F_{ALT}) during the ASM of 2006 to 2010 derived from 2B-GEOPROF, averaged along the 80 to 85°E longitude band is represented in Figure 4.4(a). The corresponding longitude-altitude cross section of F_{ALT} averaged for the 5 to 10°N latitude band is depicted in Figure 4.3 (b). For better identification of the geographical location of the 'pool', the latitude-altitude cross sections of F_{ALT} described in Figure 4.3(a) is shown in Figure 4.4 along with the geographical map. The most remarkable feature observed in Figure 4.3 is the drastic decrease or near-absence of clouds in the lower and middle troposhere in the 'pool' region, which appears as a *vault* whose location and boundaries match well with those derived from Figure 4.1.

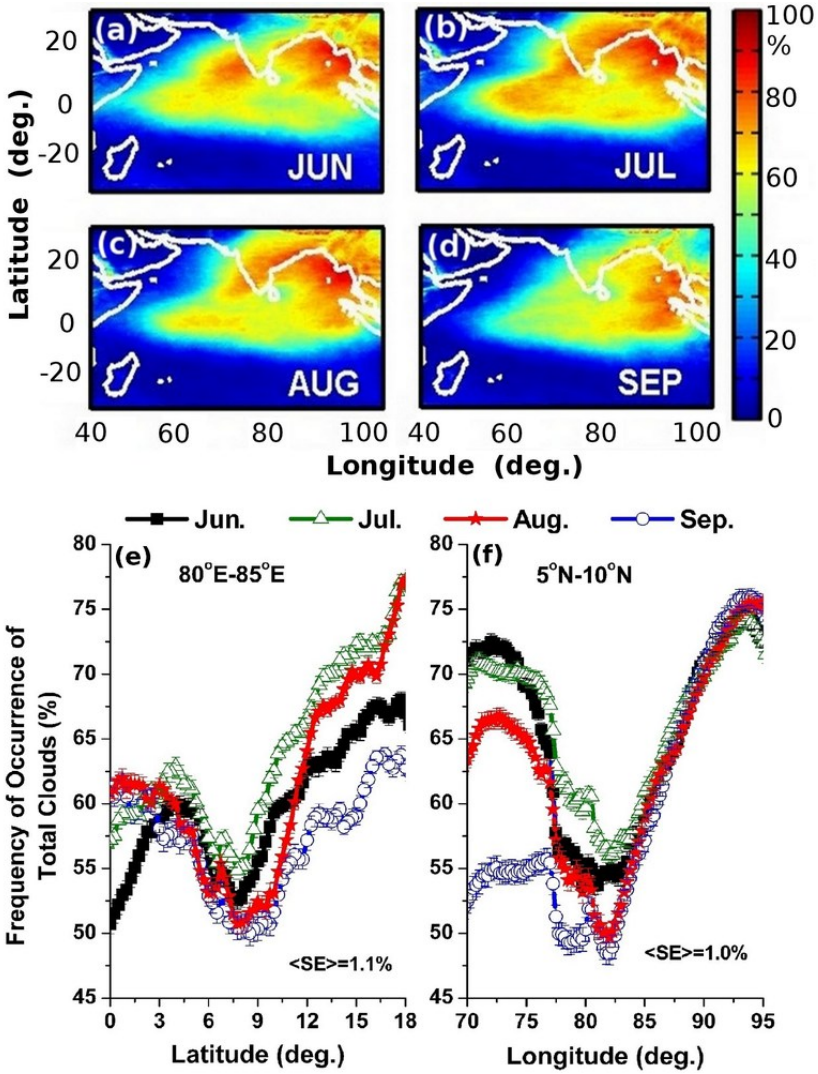

Figure 4.2: Monthly mean spatial distribution of F_C during (a) June, (b) July, (c) August and (d) September (averaged for 1996 to 2010). (e) Monthly mean latitude variation of F_C averaged along 80 to 85°E longitude band during June, July, August and September (average for 1996 to 2010). (f) Same as (e) but for the longitude variation averaged in the latitude band of 5 to 10°N.

Peak altitude of the vault occurs at ∼9°N with a near uniform decrease in the top altitude towards south and north (Figure 4.3(a)). The vault like structure vanishes at south of ∼3°N and north for ∼13°N. The longitude-altitude cross section of F_{ALT} (Figure 4.3(b)) reveal that the vault is confined between about 76 to 87°E; the western part is manifested by the deep convection at west of ∼76°E (mainly the east Arabian Sea) while the eastern border is associated with the deep convection prevailing over the east BOB. Interestingly, the base of the thick clouds which appear at top of the vault increases towards the west from 87 E to 76°E. Thus, this 'vault' is sandwiched between the deep convective regions in the north BoB and equatorial trough region at south of ∼3°N. The value of F_{ALT} below ∼7 km at the centre of the 'pool' is generally

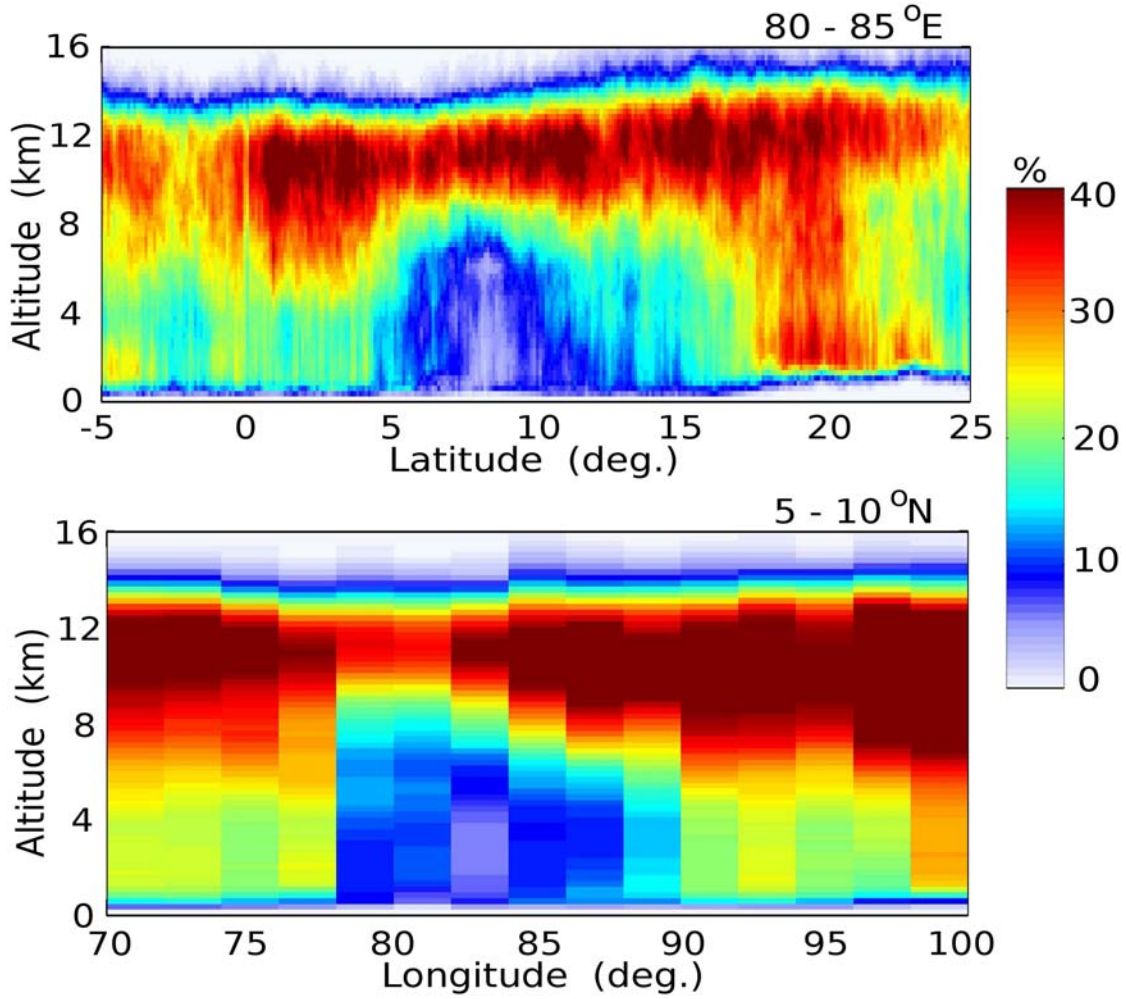

Figure 4.3: (a) Average (2006 to 2010) seasonal mean latitude-altitude cross-section of the frequency of occurrence of clouds (F_{ALT}, expressed in percentage) during ASM along 80 to 85°E. (b) Same as (a) but for the longitude-altitude cross-section averaged along 5 to 10°N.

<10%, which is markedly lower than that over the surrounding regions (F_{ALT} ~25 to 35%) where the deep convective clouds are present from <1 km and extend up to ~13 km. However, F_{ALT} increases considerably above ~7 km and its spatial gradient almost vanishes in the altitude band of ~10 to 13 km where F_{ALT} is >40% over a vast region.

Most of the high-altitude clouds observed over the 'pool' region might be cirrus clouds generated by westward spreading of outflows from the deep convective systems situated at the eastern BoB by the strong upper tropospheric easterly winds (see Figure 4.5), which is a characteristic feature of ASM [e.g., *Sathiyamoorthy et al.*, 2004]. This is also evident from the shifting of top of the vault to higher altitudes from the eastern part to western part of the 'pool' (Figure 4.3(b)).

While the AVHRR data provide the spatial distribution of the total frequency of

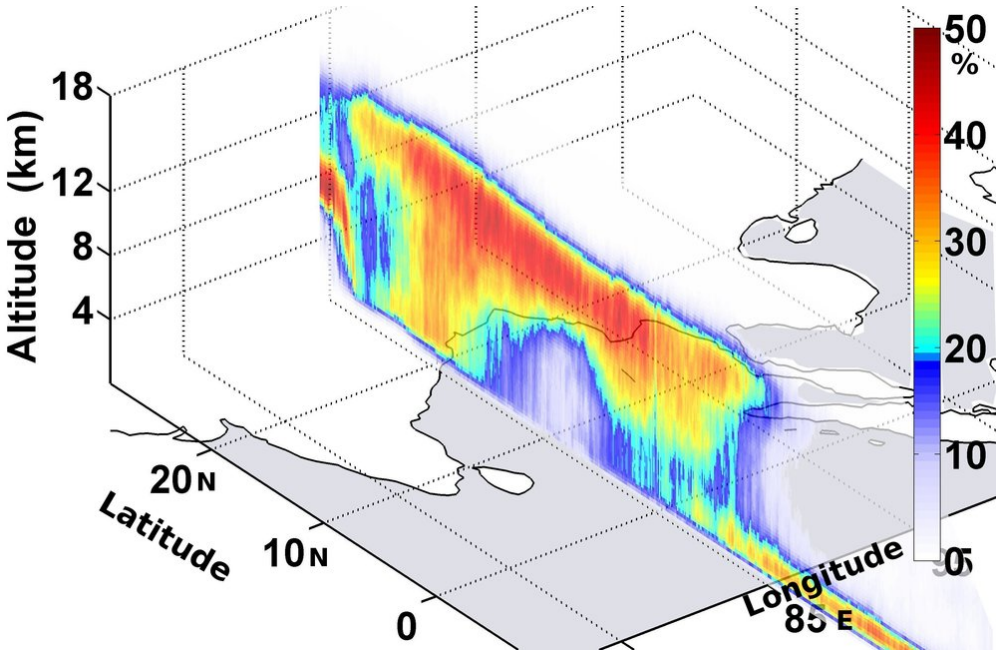

Figure 4.4: Seasonal mean latitude-altitude cross-sectionof F_{ALT} during the ASM (JJAS) for the longitude band of 80 to 90°E. Same as Figure 4.3(a), but projected on the geographical map.

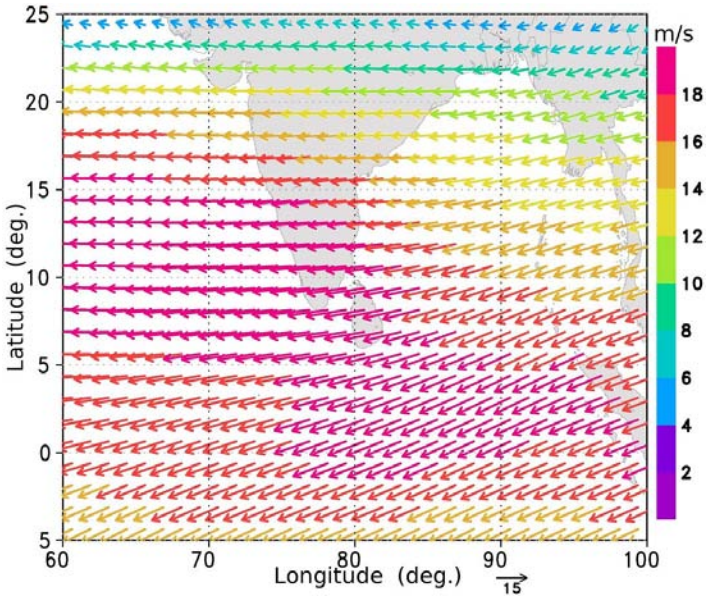

Figure 4.5: Seasonal mean wind speed and direction during ASM (JJAS) of 2006 to 2010 at 200 hPa level (obtained from) MERRA data.

occurrence of clouds (total clouds occurring at all altitudes), it cannot provide the longitudinal slices of cloud occurrence at different altitudes. The latter is estimated using CloudSat data and is presented in Figure 4.6 which depict horizontal slices of this frequency of occurrence of clouds at 1 km, 5 km and 12 km as contour maps. The 'pool' with smaller values of F_{ALT} is clear in the horizontal slices at 1 and 5 km. The horizontal

slice of cloud occurrence at 12 km which is above the vault structure of the 'pool', is manifested by high values of cloud occurrence over the entire BoB, south peninsular India and east Arabian Sea. A rapid reduction in cloud occurrence occurs towards the central and western part of Arabian Sea. As seen from Figures 4.3, 4.4 and 4.6, the vertical development of clouds below ∼7 km altitude is completely inhibited in the 'pool' and hence it is named here as the 'pool of inhibited cloudiness'. However, the 'pool' region is fully covered with cirrus clouds caused by the deep convective outflows originating in the east BoB.

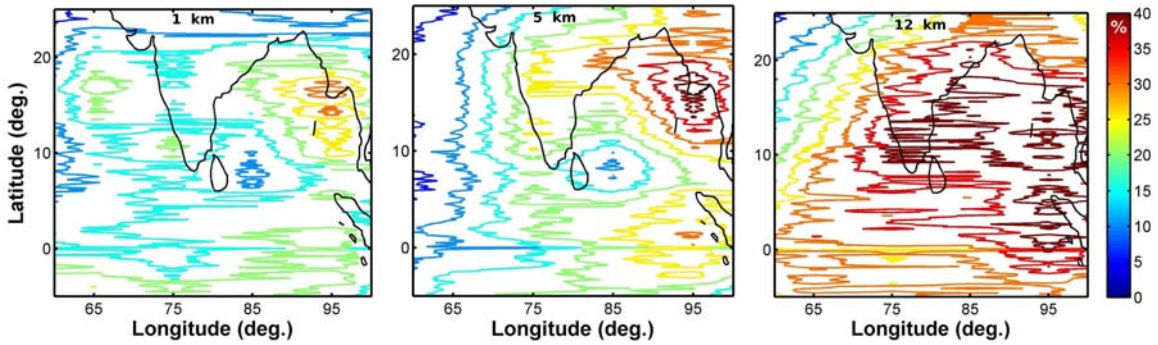

Figure 4.6: Horizontal slices of the seasonal mean frequency of occurrence of clouds at 1 km, 5 km and 12 km during ASM (JJAS) of 2006 to 2010 derived from CloudSat data.

4.3.2.1 Monthly variation of F_C and F_{ALT}

Monthly mean structure of the 'pool' during the course of the summer monsoon season is shown in Figure 4.7 which depicts the multi year (2006 to 2010) mean latitude-altitude cross-sections of F_{ALT} in the longitudinal belt of 80 to 90°E during June, July, August and September. As seen in Figure 4.7 the 'pool' is present at the same location throughout the ASM. However, the strength of the 'pool' (as manifested in

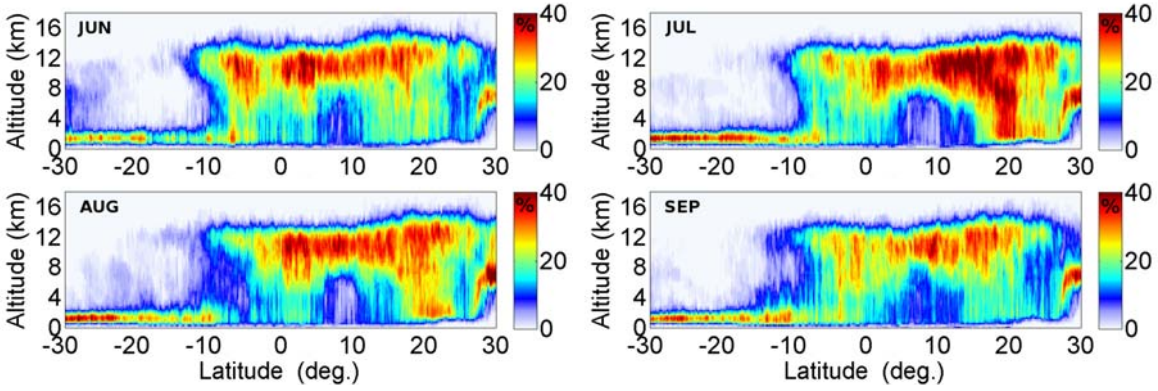

Figure 4.7: Same as Figure 4.3(a), but for the multi-year mean F_{ALT} (averaged in the longitude band of 80 to 90°E) during June, July, August and September months (average for 2006 to 2010).

the width/height and reduced cloudiness) is largest during July to August and weakest in September. The monthly variations of F_{ALT} observed in Figure 4.7 is in agreement with the spatial distribution of F_C observed in Figure 4.2. Remarkably, the 'pool' is most prominent (July–August) when the deep convection over the Bay of Bengal and the Arabian Sea are well developed.

One of the obvious questions that arises here is the characteristics of the 'pool' during active and break cycles of summer monsoon. However, it is to be noted that the appearance of the inhibited cloudiness in the imager (AVHRR) data is often marred by the frequent occurrence of cirrus clouds. Analysis of AVHRR data did not clearly bring out significant difference in the characteristics of the 'pool' during active break cycles of ASM. The limitation in the frequency of observation due to poor repeativity of CloudSat (16 day repeativity) does not permit discerning the differences in the characteristics of the 'pool' during active and weak phases. Though this is an important aspect, it is not presented in this thesis due to the limitation of CloudSat and AVHRR data.

4.4 Manifestation of the 'pool' in precipitation and outgoing longwave radiation

The analysis of clouds presented in Section 4.3 clearly shows the absence of deep convective clouds (or near absence of low and middle level clouds) in the 'pool' region. Obviously, this will result in reduction of precipitation and increase in the Outgoing Longwave Radiation (OLR) over the 'pool' compared to its surroundings. This aspect is shown in Figures 4.8(a) and (b) which depict the longterm (1996 to 2010) average of the seasonal mean precipitation rate (obtained from GPCP data) and OLR (obtained from NOAA) respectively over the study region.

Precipitation rate over the 'pool' region is substantially less (seasonal mean precipitation rate of <3 mm day^{-1}) compared to the surrounding regions of deep convection, especially over the east Arabian Sea and the north Bay of Bengal where the precipitation rates are in the range of 8 to 14 mm day^{-1}. The precipitation rates over the east and central equatorial Indian Ocean are also quite large (>6 mm day^{-1}).

The OLR is >220 Wm^{-2} over the pool region while the corresponding values over the surrounding regions is ∼10 to 25 Wm^{-2} smaller. This is the result of the thin (cirrus) clouds over the pool region which allows partial penetration of the terrestrial radiation emitted from the lower atmosphere or surface to pass through them. In contrast, the thick convective clouds over the surrounding regions (especially over the northeast BoB and the southeast Arabian Sea are fully opaque to the terrestrial radiation from below and hence the OLR actually emanates from the cold cloud top in

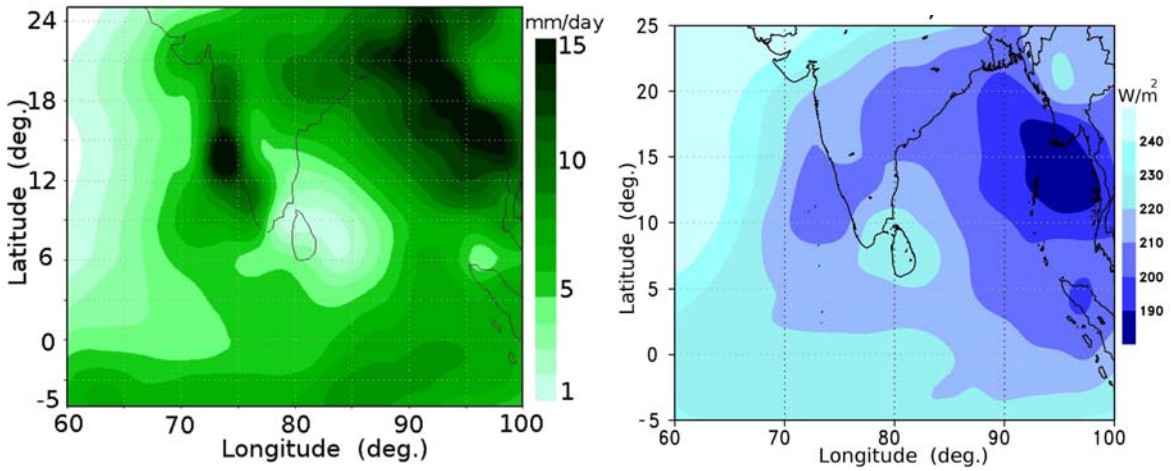

Figure 4.8: Long-term (1996 to 2010) average of (a) seasonal mean precipitation rate (GPCP data) and (b) OLR during the Asian summer monsoon season.

these regions. This results in OLR values of <200 Wm^{-2} .

4.5 Investigation on the genesis of the 'pool'

The role played by the SST, surface wind divergence, atmospheric circulation, latent heating, lower tropospheric stability and CAPE are investigated to explore the genesis and maintenance of the 'pool of inhibited cloudiness'.

4.5.1 Role of Sea Surface Temperature

Role of Sea Surface Temperature (SST) on the genesis of the 'pool' is examined using the long-term (1996 to 2010) seasonal mean spatial distribution of SST depicted in Figure 4.9 (a). It shows a cold tongue originating off the southern tip of India (STI) and extending up to the south central BoB. This cold tongue [*Joseph et al.*, 2005] arises from the ocean upwelling caused by the prevailing surface wind and its eastward spreading by the summer monsoon current into the BoB [*Rao et al.*, 2006]. However, the cold tongue has significantly large eastward extension than the 'pool', while the latter extends farther to the north compared to the former. The locations of minima in SST and cloudiness are also different: F_C at the west coast of Sri Lanka is significantly larger than that at the east, though SST at the former region is ∼1°C lesser than that at the latter. Furthermore, SST is >28.4°C at most part of the 'pool', which is sufficiently high for the development of convection and clouds (results presented in Chapter 5).

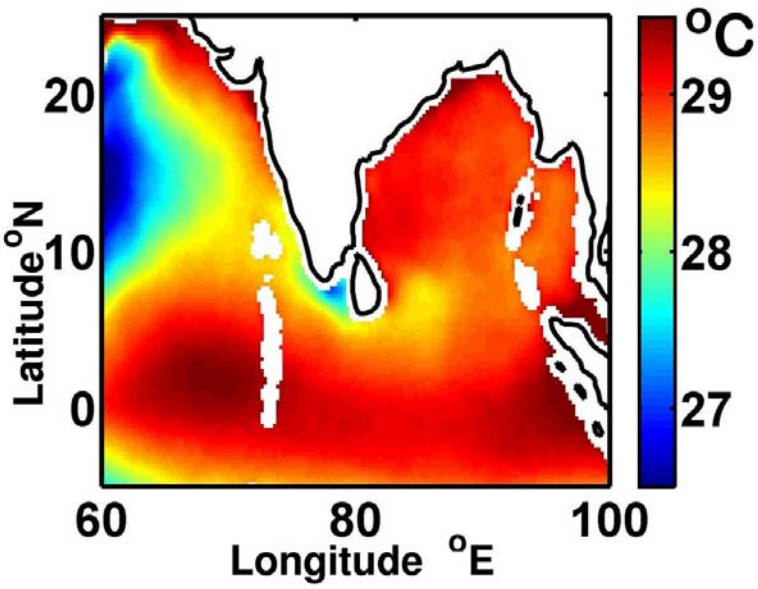

Figure 4.9: Spatial variation in the seasonal mean Sea Surface Temperature during ASM (average of 2006 to 2010) at the study region.

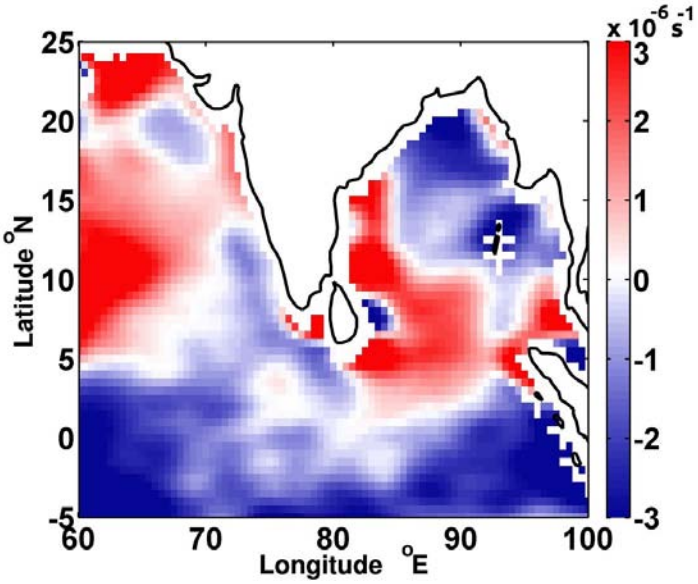

Figure 4.10: Spatial variation in the seasonal mean Surface Wind Divergence during ASM (average of 2006 to 2009) over the study region observed using spaceborne scatterometers during ASM.

4.5.2 Role of surface wind divergence

Figure 4.10 (b) shows the long-term (1996 to 2009) seasonal mean surface wind divergence (SWD) observed using spaceborne scatterometers during ASM. Except for a small converging area present in the the surface wind wake region of Sri Lanka, the surface winds are significantly diverging at the 'pool' and converging outside the

'pool'. Over the 'pool' region, this would produce a moisture divergence at the surface. This divergence of surface wind must be replenished by subsidence from above, which would inhibit the cloud formation. Closure of the above surface wind field suggests the existence of a regional scale atmospheric circulation cell with subsidence at the 'pool' and convection at its surroundings. This inference is well supported by the horizontal and vertical distribution of clouds depicted in Figures 4.1 and 4.3. This mini-circulation might be the potential mechanism for the inhibition of cloudiness and precipitation at the 'pool'. The proposed mini- circulation is explained in Section 4.6.

4.5.3 Role of vertical wind

Evidence for such a mini-circulation is examined using MERRA data. Figure 4.11 depicts the latitudinal and longitudinal cross sections of the altitude profiles of long-term seasonal mean vertical wind (in Pa s^{-1}), sliced through the centre of the 'pool', which shows a strong subsidence below ~700 hPa (~3 km) at/near the 'pool' region and convection at its surroundings. The strong convection at the north BoB and relatively weaker circulation at the equatorial trough are clearly discernible in Figure 4.11. Similarly, the convection is very strong near the east BoB and the east Arabian Sea. These convective regions are manifested in Figure 4.1 to 4.7 as the regions with deep convective clouds. The area within the above regions with strong updraft are manifested by down draft and almost coincides with the observed 'pool'. However, the spatial distribution of the subsidence and convection obtained from MERRA does not exactly match with that inferred from Figures 4.1 to 4.4. Note that the cloud-free region in the 'pool' extends up to ~7 km and up to the east BoB, while the downdraft seen in Figure 4.11 is significantly limited in altitude and its eastward extent. This shows that the actual structure and magnitude of the mini-circulation is underestimated in the reanalysis data.

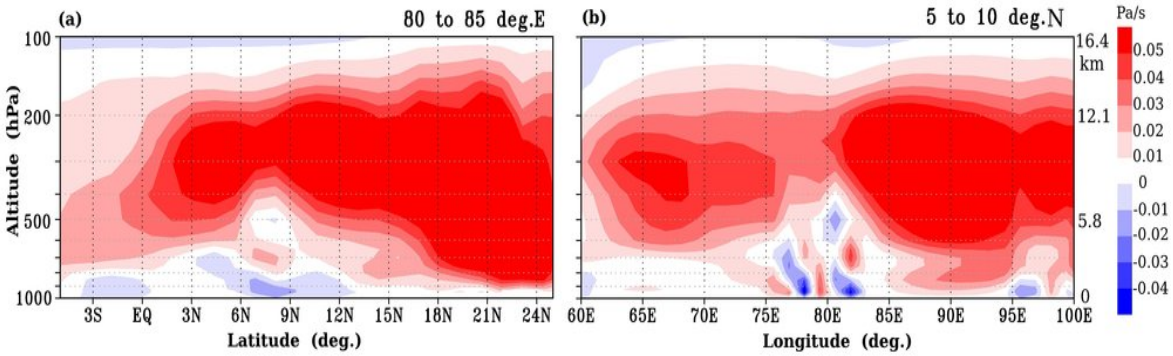

Figure 4.11: (a) Latitude-altitude cross-section of vertical wind during JJAS (1996 to 2010) averaged along 80 to 85°E. The vertical wind is taken from MERRA. Altitude shown is in pressure coordinates. (b) Same as (a), but for longitude–altitude cross-section averaged for 5 to 10°N during JJAS.

4.5.4 Role of latent heat release

The above mentioned mini-circulation cell, embedded in the synoptic-scale monsoon circulation and responsible for the genesis of the 'pool', might be triggered by the considerable spatial gradient of latent heating in the troposphere over the geographically fixed zones of large-scale cloudiness and precipitation at the east and equatorial Indian Ocean, the north and east BoB, the southeast Arabian Sea and Indian landmass. Figure 4.12 shows the altitude profiles of the regionally averaged latent heating rate over the 'pool' and surrounding deep convective regions at the centre, west, northwest, northeast and southeast and south of the pool. The largest seasonal mean values of Latent Heating rate (LHR) in the above deep convective regions occur between 3 to 10 km altitude where it is typically in the range of 0.06 to 0.20 K/h (1.4 to 4.8 K day^{-1}), while the corresponding values of LHR in the 'pool' are mostly around 0.03 K/h ($\sim$0.7 K day^{-1}). Figure 4.13 shows the altitude variation of seasonal mean latent heating rate (LHR) due to precipitating clouds (derived from TRMM-PR data during 2006 to 2010) in the zonal and meridional planes, cutting across the 'pool' region. Large spatial gradient of LHR along the latitude and longitudinal planes across the 'pool' is clearly seen in this figure. This spatial gradient of LHR is quite large in the altitude band of 1 to 12 km. Such high and persistent spatial gradient in LHR with large atmospheric heating at the regions surrounding the 'pool' will cause a circulation whereby the heat is transported to the 'pool' region through advection. Such a circulation is possible only through the mini-circulation. Thus, it is proposed here that the 'pool' is maintained by the mini-circulation (embedded in the large scale monsoon circulation) which is driven by the differential heating of the atmosphere associated with latent heating by deep convection in the surrounding regions.

4.5.5 Role of lower tropospheric stability and CAPE

Lower tropospheric stability (LTS) is a measure of the atmospheric stability and is computed as the difference between the potential temperature at 700 hPa and 1000 hPa. Smaller the values, higher is the instability. Figure 4.14(a) shows the spatial variation of LTS during JJAS months determined from Reanalysis data. In the 'pool' region, LTS is larger than $\sim$13 K indicating larger lower tropospheric stability over the pool, while its value at the north and east of the 'pool' are relatively smaller indicating larger instability. The larger LTS over the 'pool' compared to the surrounding regions is an indicator of subsidence over the 'pool'.

Convective Available Potential Energy (CAPE) is a measure of the energy available in the atmosphere for convection to grow. Figure 4.14(b) shows that the largest values of CAPE are observed in the north Bay of Bengal compared to the 'pool'; the values of

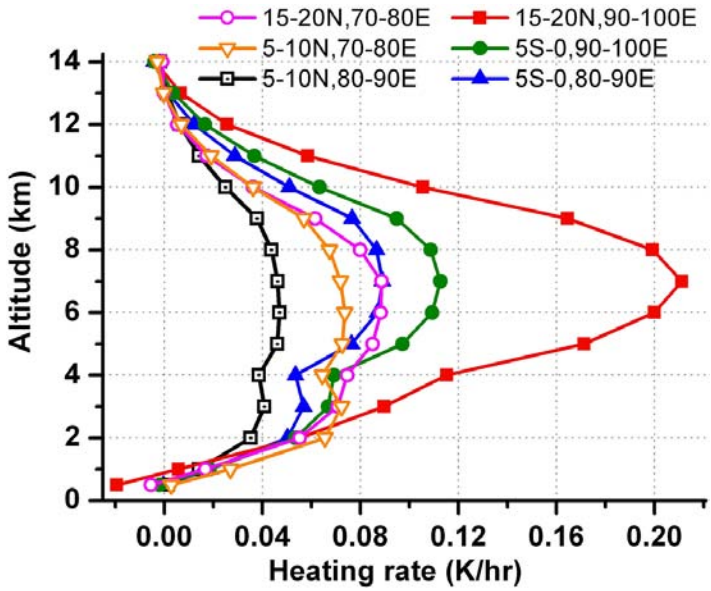

Figure 4.12: Seasonal mean altitude profiles of regionally averaged latent heating rate (K/h) released by precipitating clouds during JJAS (estimated from TRMM-PR). The regions represent the 'pool' (5 to 10°N, 80 to 90°E), and the regions to the west (5 to 10°N, 70 to 80°E), northwest (15 to 20°N, 70 to 80°E), northeast (15 to 20°N, 90 to 100°E), southeast (5°S to 0°, 90 to 100°E) and south (5°S to 0°, 80 to 90°E) of the 'pool'.

CAPE are more than double in regions adjoining the 'pool' which further corroborates the inferences derived from LTS that the 'pool' region is rather stable compared to its surroundings and hence is a region of inhibited convection.

4.6 Integrated analysis of the 'pool of inhibited cloudiness' and potential effects on summer monsoon

Various pieces of evidences and inferences obtained from the above analysis of clouds, SST and atmospheric thermo-dynamics are integrated below to bring out a robust mechanism for the genesis of the 'pool' through a 'mini-circulation'.

The above analysis clearly shows the following observed facts:

1. Large deep convection exists in the region surrounding the 'pool' while the lower and middle level clouds are almost absent below 7 km altitude in the 'pool' region.

2. Large amount of latent heat is liberated in the deep convective regions surrounding the 'pool' while that in the 'pool' is negligible, which causes a large spatial gradient in latent heating at all altitudes between 1 to 10 km across the 'pool'.

3. Scatterometer observations shows that the surface winds are highly diverging at

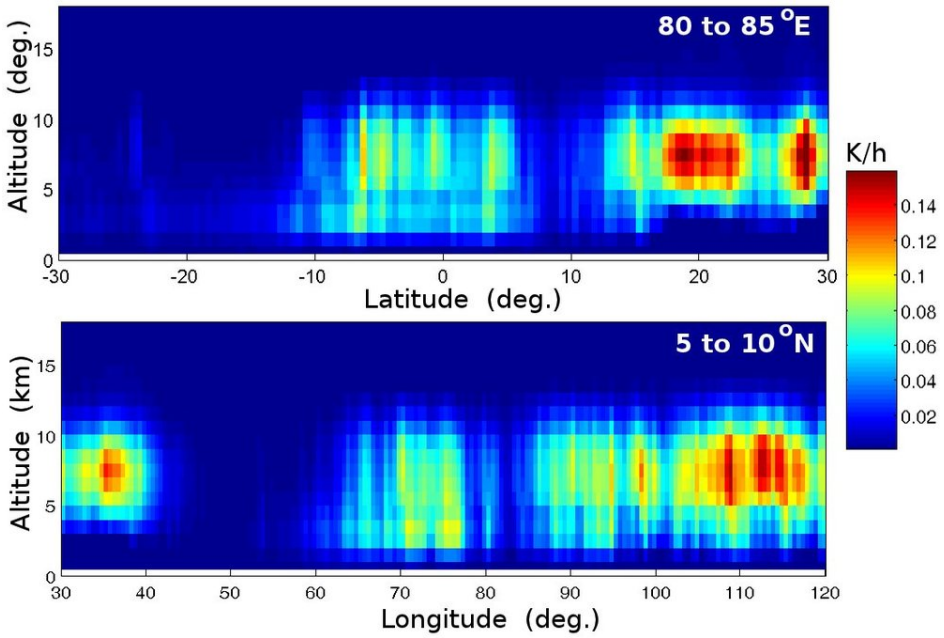

Figure 4.13: (a) Latitude-altitude cross section of latent heat rate (K/h) released into the atmosphere by precipitating clouds (estimated from TRMM-PR data) during JJAS (2006 to 2010), averaged in the longitude band of 80 to 85°E. (b) same as (a) but for the longitude-altitude cross section averaged in the latitude band of 5 to 10°N.

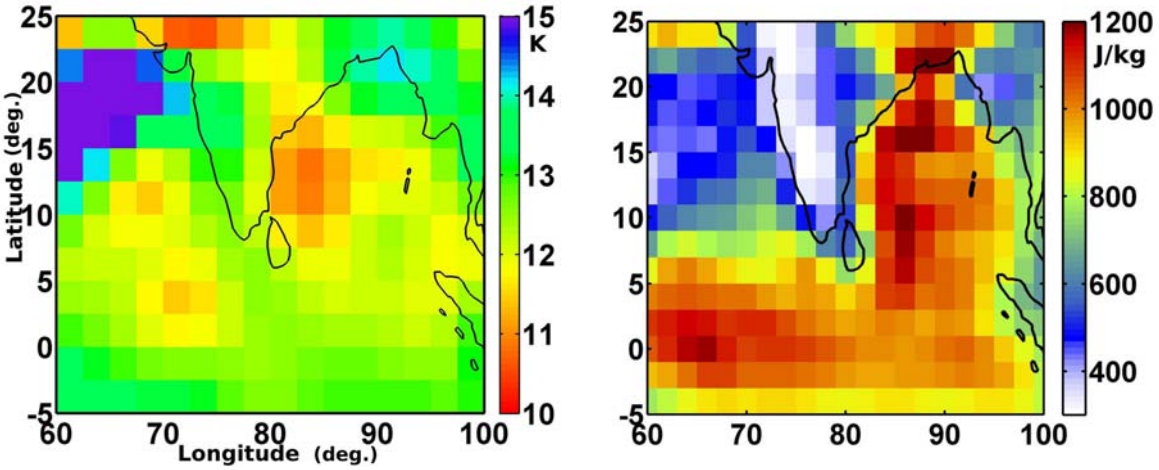

Figure 4.14: Long term (2006 to 2010) seasonal mean spatial variations of (a) Lower Tropospheric Stability (K) and (b) CAPE (J/kg) during JJAS, obtained from Reanalysis data.

the 'pool' while they are highly converging at the surrounding regions of the deep convection.

4. Widespread cirrus clouds occurs over the 'pool' and hence the spatial gradient of clouds at altitudes >∼10 km is absent.

All the above aspects points to the existence of a mini circulation with large scale

ascending of tropospheric air at the deep convective regions surrounding the 'pool' and strong descending of air in the lower and middle atmosphere in the 'pool' region. It is important, to note that only a small fraction of ascending circulation from the deep convective regions would be sinking over the 'pool'. The closure of ascending air mass is mainly completed by the descending at the subsidence zones in the subtropical high regions (eg. at south of ∼15°S) associated with the Hadley circulation cell, which is the main driver for the monsoon circulation. All the above aspects and the proposed mini circulation embedded in the large scale monsoon circulation are schematically presented in Figure 4.15; the zonal and meridional cross-section of the altitude variation of F_{ALT} are also shown in Figure 4.15.

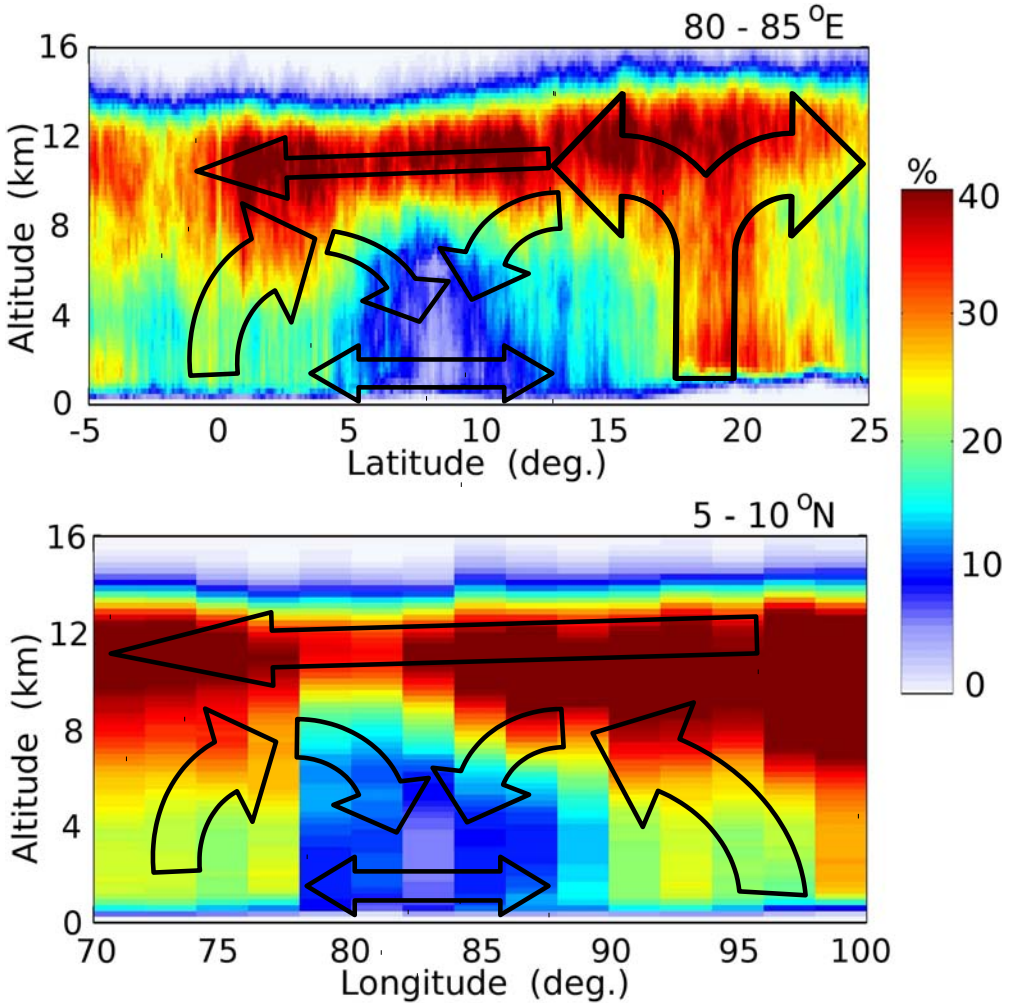

Figure 4.15: Schematic of the proposed mini-circulation embedded in the large scale summer monsoon circulation. The schematic is superimposed on the latitudinal and longitudinal cross-sections of altitude variations of F_{ALT}.

The MERRA data (or any similar data set such as ERA or NCEP) do show a descending of the airmass in the lower troposphere over the peninsular Indian longitude and the east BoB during the ASM. However, the descending zone is not exactly

collocated with the 'pool' but rather more shifted towards east. Further, the 'pool' region is clearly manifested by absolutely cloud free region upto ∼7 km (at the centre of the 'pool') while the descending of air mass in the reanalysis is confined to lower troposphere (<3 km). This shows that the 'embedded mini-circulation cell' proposed in this study, which is essential to interpret the observed features of the vertical distribution of clouds, is of larger magnitude than the small-scale feature manifested in the reanalysis data. This aspect need to be investigated further using atmospheric modelling, which would reproduce the observed magnitudes and gradient in the latent heating of the atmosphere. Not withstanding this, the reanalysis data do reproduce a small scale circulation in the vicinity of the 'pool'. In line with the above, the spatial variations of CAPE and lower tropospheric stability derived from the reanalysis data also shows the larger stability and weaker convective potential energy at the 'pool'.

Notwithstanding the larger solar heating of the surface due to less cloudiness, the 'pool' region is able to maintain relatively lower SST compared to the largely cloudy regions at its surroundings. This shows that, in addition to the contribution from the spreading of cold waters from southern tip of india [*Rao et al.*, 2006], the cold SST at the 'pool' might also be driven by the ocean upwelling caused by the surface wind divergence associated with the mini-circulation described above. The mini-circulation described above would also contribute to the maintenance of large-scale convection at the regions surrounding the 'pool' and hence would be an important component of the ASM. Through the deep convection in the BoB, the Arabian Sea and equatorial trough are mainly driven by the large-scale monsoon circulation, warmer SST and orographic effects, the descending of air mass at the 'pool' would further strengthen this convection by providing better ventilation for the convected air. Surface wind divergence at the 'pool' would further strengthen the convergence of surface air mass and convection at the convective regions surrounding the 'pool'. Thus the proposed circulation superposed on the large-scale monsoon circulation might be important in further strengthening deep convection at the regions surrounding the 'pool'.

4.7 Summary and conclusions

Using long-term satellite observations of clouds, this study clearly shows the persistence of a 'pool of inhibited cloudiness' over the southwest Bay of Bengal throughout the Asian summer monsoon season. Frequency of occurrence of clouds in this 'pool' is 20 to 40% less than the surroundings. Seasonal mean precipitation rate over the 'pool' is <3 mm day^{-1} while that over the surrounding regions is mostly in the range of 6 to 14 mm day^{-1} . Though this 'pool' is observable in the regional distributions of clouds, precipitation, and OLR reported earlier, it received little attention so far and the contribution of low-, middle- and high-level clouds in its manifestation could not

be deciphered unambigously. This information is essential for identifying the genesis of the 'pool'. This study, mainly based on multi-year vertical distribution of clouds observed using CloudSat, reveals that the 'pool' is almost completely contributed by a drastic reduction or near-absence of clouds below ∼7 km that appear as a vault-like structure in the zonal and meridional cross section of the vertical distribution of clouds. In contrast, spatial gradient of high-altitude clouds over the entire region is negligible. The geographical location of this pool is remarkably consistent during the June to September period and occurs between 77 to 90°E in longitude and 3 to 13°N in latitude, which is surrounded by regions having large-scale convective clouds.

Putting together the pieces of observation of the structure of the 'pool' (in terms of cloudiness), surface wind divergence and differential latent heating of the atmosphere, the physical mechanism for the genesis of the 'pool' is proposed to stem from the existence of a mini-circulation in the lower and middle troposphere with significant divergence of surface wind at the 'pool' and subsidence above, which is closed by the surface wind convergence and updraft in the troposphere over the surrounding deep convective regions. This mini-circulation is embedded in the large-scale monsoon circulation and might be a dynamical response of the atmosphere to the considerable spatial gradient of latent heating caused by the geographically fixed convective regions surrounding the 'pool'. The subsidence and surface wind divergence of air at the 'pool' will be at least partly responsible for closure of the strong updraft at the surrounding deep convective regions and hence might be an important component of the ASM. Genesis and maintenance of the 'pool' might be further influenced by orography of the region, the low-level jet and the relatively low SST at the south BoB. It is also likely that, at least part of the reduction in SST observed in the 'pool' is contributed by the surface wind divergence. However, significant differences exist in the mini-circulation features derived from the reanalysis of atmospheric circulation and that inferred from the spaceborne observations of surface wind divergence and cloud distribution. The observed mini-circulation might play an important role in the monsoon dynamics as well as in the active-break spells of ASM, which needs to be explored further.

Chapter 5

Role of SST and Atmospheric Thermo-dynamics in Regulating Vertical Distribution of Clouds

5.1 Introduction

Development of clouds are governed by a host of processes and parameters, the most prominent among them being the moist static energy near the surface, water vapour content in the troposphere, atmospheric thermodynamical instability and circulation systems controlling the atmospheric convergence/ divergence and vertical winds [*Zhang*, 1993; *Bony et al.*, 1997; *Tompkins*, 2001; *Rondanelli and Lindzen*, 2008; *Zelinka and Hartmann*, 2011]. Over the oceanic regions, most of the above controlling parameters are substantially influenced by the sea surface temperature (SST) [*Gadgil et al.*, 1984; *Lindzen and Nigam*, 1987; *Cho et al.*, 2012; *Meenu et al.*, 2012; *Sabin et al.*, 2012], while the SST itself is regulated through cloud feedback processes, especially through modification of net radiative fluxes at the surface [*Ramanathan and Collins*, 1991; *Waliser*, 1996; *Sud et al.*, 1999]. Larger values of SST generally yield higher equivalent potential temperature (and hence higher moist static energy) in the atmospheric boundary layer, and can trigger local convection through thermodynamical changes within the atmospheric column [*Bony et al.*, 1997]. On the contrary, the spatial gradient of SST, rather than the local SST, is important in driving large-scale circulation, which transport heat and moisture and affect thermodynamical stability of the atmosphere in large spatial scales [*Lindzen and Nigam*, 1987; *Waliser*, 1996; *Bony et al.*, 1997] and in turn regulate the cloud occurrence and the associated radiative forcing [e.g. *Yuan et al.*, 2008].

Investigations on the variations of cloudiness with SST and large-scale atmospheric

circulation and the underlying physics have been carried out extensively during the past few decades [*Gadgil et al.*, 1984; *Graham and Barnett*, 1987; *Zhang*, 1993; *Waliser*, 1996; *Tompkins*, 2001; *Rondanelli and Lindzen*, 2008; *Zelinka and Hartmann*, 2011; *Meenu et al.*, 2012; *Sabin et al.*, 2012]. These studies showed a general pattern of consistent increase in cloudiness with SST in the range of ∼26 to 28°C and peak cloud occurrence at SST∼28.5 to 29.5°C. Most of them showed a decrease in cloudiness with further increase in SST above ∼29.5°C [*Gadgil et al.*, 1984; *Graham and Barnett*, 1987; *Waliser*, 1996] while such reduction was not clearly discernible in all regions or during all seasons [*Lau et al.*, 1997; *Meenu et al.*, 2012]. The SST threshold for convection corresponds to the minimum SST that can generate large convective available potential energy (CAPE) through a deep tropospheric layer [*Bhat et al.*, 1996]. *Lau et al.* [1997] argued that the critical SST threshold (e.g., >27°C) required for convection to occur does not have any fundamental microphysical or thermodynamical importance, but arises from the fact that this regime represents a transition between stable and convective atmospheric conditions. They further suggested that the reduction of cloudiness at high SSTs might be due to the influence of large-scale subsidence forced through nearby or remotely generated deep convection. Studies using cloud resolving models showed that the dependence of convective activity on SST could result from an organized positive feedback by which the occurrence of convection aids future convection likely to occur in the same location [*Tompkins*, 2001]. *Meenu et al.* [2012] showed that significant seasonal and spatial variations occur in the SST-dependence of cloudiness, and that the regions of the warmest SST, maximum surface wind convergence, and the largest cloudiness are generally not collocated. *Hartmann and Michelsen* [1993] showed that the shortwave cloud radiative forcing is better related to upper-tropospheric divergence than SST, which further reinforce the importance of remote forcing of cloud generation through large-scale dynamics.

The role of clouds in decreasing the SST through feedback processes [e.g. *Ramanathan and Collins*, 1991; *Pierrehumbert*, 1996; *Fu et al.*, 2002] as well as the increase in SST associated with global warming (and the potential changes in convection associated with it) have further enhanced the importance of the investigations on SST-cloudiness relationship [e.g. *Sud et al.*, 2008; *Johnson and Xie*, 2010]. *Waliser and Graham* [1993] showed that the high SSTs eventually lead to increase in deep convection that cool the sea surface through enhanced cloudiness and turbulent heat exchange. The 'thermostat effect' of highly reflective cirrus clouds [*Ramanathan and Collins*, 1991], by which the increase in cloudiness tends to decrease the shortwave radiative heating of the surface, was proposed as a potential mechanism for limiting the maximum SST to less than ∼32°C. However, several studies have questioned the generalization of this proposal under all conditions [e.g. *Wallace*, 1992; *Arking and Ziskin*, 1994; *Waliser*, 1996; *Lau et al.*, 1997]. Model simulations showed that, associated with

global warming, the threshold SST required for convection to occur (~27°C) might also increase, thereby limiting any anomalous increase in cloudiness that can be expected from the observed SST-cloudiness relationship due to increase in SST [e.g. *Sud et al.*, 2008]. *Johnson and Xie* [2010] detected a parallel upward trend of 0.1°C/decade over 3 decades (1980 to 2009) in both the convection threshold and tropical mean SST. *Rajendran et al.* [2012] have observed a strong relationship between the variations of rainfall and SST across a threshold value.

5.1.1 Limitations of previous studies

Most importantly, observations of the SST-cloudiness relationship are influenced by the methods used to determine cloudiness: the passive radiometer observations, on which all the previous studies were based, have two major limitations.

1. They cannot provide the actual vertical distribution of clouds (except for broadly classifying them as low-, middle-, high- or deep-convective cloud based on the observed cloud top brightness temperature) and hence their dependence on SST.

2. As the passive radiometers observe only the emitted (IR) or reflected (shortwave band) radiations, they cannot discriminate between deep convective clouds and optically thick cirrus clouds. Though those satellite sensors incorporating the water vapour band can discriminate thin semitransparent cirrus, they will yield same cloud top brightness temperature for optically thick cirrus as well as deep convective clouds [*Rajeev et al.*, 2008]. While the deep convective clouds could be generated through convection driven by the local warm SST, the cirrus might originate from the outflows of deep convection. Thus, if the cloud information is derived from the imager data, it would lead to unrealistic SST-convection-cloudiness relationship.

It may be noted that (as explained in section 5.3), the SST over the regions of cirrus outflow can be different from the SST at the deep convective regions. Thus the former are not affected by the local SST. The vertical distribution of clouds observed using the spaceborne radar CloudSat and spaceborne lidar CALIPSO provide a unique solution to this enigma. While the CloudSat can detect optically thick clouds and their altitude distributions, the optically thin clouds can be detected using CALIPSO. The synergy of the capabilities of CloudSat and CALIPSO are utilized in this study to accurately determine the SST-dependence of the vertical distribution of clouds.

5.1.2 Objectives and uniqueness of the present study

Main objectives of this study are:

1. To examine the variations in the vertical distribution of clouds with SST in the tropical Indian Ocean, the Bay of Bengal and the Arabian Sea.

2. To investigate the potential influence of spatial gradient of SST and parameters that govern atmospheric stability and circulation in modyfing the observed SST–cloudiness relationship.

This study utilises about 4.5 years (June 2006 to February 2011) of the CloudSat and CALIPSO observations of the vertical distribution of clouds and the corresponding values of SST as well as SST gradient, surface wind divergence, upper tropospheric divergence, CAPE and lower tropospheric stability. This study provide the first of such observations on the dependence of cloud vertical distribution on SST and would contribute to improvements in the understanding of the SST-convection-cloudiness relationship, which is especially important for reducing the over-sensitivity of cloudiness/precipitation to SST in atmospheric models [e.g. *Martin and Schumacher*, 2012].

5.2 Data and methodology

The vertical distribution of clouds is obtained from a combined analysis of the data obtained from the polar sunsynchronous CloudSat and CALIPSO satellites along their sub-satellite tracks. As explained in Chapter 2, both these satellites are part of the A-Train constellation of satellites, which follow the same satellite orbits with an equatorial crossing time around 01:30 local time (separated by a few minutes). These satellite orbits have a 16-day repeativity cycle and the longitude separation between adjacent orbits is $\sim$1.6° at the equator. The CloudSat has a Cloud Profiling Radar (CPR) operating at 94 GHz and provides the altitude profiles of backscattered radar signal from hydrometeors with a vertical resolution of 240 m and along-track resolution of 1.7 km [*Haynes and Stephens*, 2007]. The Cloud Aerosol Lidar with Orthogonal Polarization (CALIOP) onboard the CALIPSO provides the altitude profiles of lidar backscatter signals (parallel and perpendicular polarized signals at 532 nm and total backscattered signal at 1064 nm) with a vertical resolution of 30 to 60 m and along-track spatial resolution of 333 m, which can provide the vertical profiles of clouds and aerosols and their optical properties [*Winker et al.*, 2007]. The CPR can detect optically thick cloud layers and are less sensitive to optically thin clouds such as semitransparent cirrus. In contrast, the CALIPSO can detect even very thin cirrus clouds with visible band cloud optical depth as low as 0.03 [e.g. *Meenu et al.*, 2011], but cannot probe the cloud layers located beneath optically thick clouds. Retrievals of cloud properties from the backscattered Radar and Lidar signals along the sub-satellite track observed using CloudSat and CALIPSO respectively were carried out by the Data Processing Centre at NASA.

This study utilizes the 2B-GEOPROF-LIDAR data (Version 003) during the period of June 2006 to February 2011, provided by the CloudSat data processing centre which utilizes the synergy of the observational capabilities of CloudSat and CALIPSO [*Mace et al.*, 2009]. The 2B-GEOPROF-LIDAR data provide optimally merged analysis of the data from CloudSat and CALIPSO and give the best picture of the vertical distribution of cloud occurrence as has been compiled so far. Details of the 2B-GEOPROF-LIDAR dataset, methodology for the combined analysis to derive the cloud mask, the complexities involved while combining the information derived from instruments with different observational capabilities and spatial resolutions and the uncertainties are extensively discussed in *Mace et al.* [2009] and the Algorithm Theoretical Basis Document (available online from `http://www.cloudsat.cira.colostate.edu`). The 2B-GEOPROF-LIDAR dataset provide information on up to 5 cloud layers (their altitudes of occurrence) with a vertical resolution of 240 m and along track resolution of 1 km.

The SST data are obtained from the TRMM Microwave Imager (TMI) that utilizes the observations at 10.7 GHz which are nearly transparent to clouds [*Reynolds et al.*, 2010]. This data is advantageous over the infrared SST observations that require a cloud-free field of view. The TMI-SST provides daily observations covering the global region extending from 40°S to 40°N at a pixel resolution of 0.25°. Comparison of the TMI-SST with insitu observations using buoys shows that, on average, the former is accurate to better than 0.5°C. The mean SST for the period from June 2006 to February 2011 is represented in Figure 3.2 in (Chapter 3 and that for different seasons are shown in Figure 5.1.

The atmospheric circulation and thermodynamical data are obtained from the NCEP-NCAR reanalysis which integrate the data from a variety of observing systems with numerical models to produce a temporally and spatially consistent synthesis of observations and analyses of variables with spatial resolution of 2.5° [*Kalnay et al.*, 1996]. The surface wind divergence (SWD) during this period are obtained from the spaceborne scatterometer observations from QuikScat satellite of NASA, which have a spatial resolution of 0.5° [*Liu*, 2002].

All the above data sets have different spatial resolutions. Collocation of the above data is done on the spatial resolution of 2B-GEOPROF-LIDAR data (1 km), which is better than that of TMI-SST (0.25°). Thus there will be ∼25 numbers of 2B-GEOPROF-LIDAR data points within a geographical grid of the SST data and the spatial variations of SST at scales smaller than 0.25° are neglected. Though the study is made using the high-resolution profiles obtained from 2B-GEOPROF-LIDAR on an orbit-by-orbit basis, this study focusses only on the seasonal and long-term mean SST-cloudiness relationship. The above daily data over the tropical Indian Ocean, the

Bay of Bengal, and the Arabian Sea, encompassed between 15°S to 25°N and 30°E to 110°E are used in this study. This region covers a wide range of SST (∼24 to 32°C) and convective conditions required for the study within a limited geographical box of size 80° in longitude and 40° in latitude in the tropics.

5.3 Spatio-temporal variations of SST

Figure 3.2 (Chapter 3) depicts spatial variations of the monthly mean SST (averaged during 2006 to 2011) over the oceanic regions surrounding the Indian subcontinent, which shows that the study region is characterized by a wide range of SSTs. The warmest SSTs (∼31°C) over the study region is observed over the south-central Arabian Sea (around 53 to 70°E and 0 to 10°N) during April and May (the 'Arabian Sea Warm Pool') [*Sijikumar and Rajeev*, 2012]. The lowest SSTs (22 to 26°C) are observed at the south Indian Ocean (south of ∼15°S, almost throughout the year) and the north Arabian Sea (during December to March). Most regions of the equatorial Indian Ocean, the Arabian Sea and the Bay of Bengal are relatively warmer throughout the year with SSTs generally ranging from 28 to 29°C. During the summer monsoon months, the SST is largest over the equatorial Indian Ocean (equatorial trough, with SST>29°C). In October, the largest SST is observed over the north Bay of Bengal and around 60°E to 70°E over the equatorial Indian Ocean. Over the western Indian Ocean (including that near Madagascar), the SST increases by more than 1.5°C in a wider region from February to March-April. The east equatorial Indian Ocean is warmest during April and May.

Figure 5.1 shows the seasonal mean SSTs over the study region during winter (DJF), pre-monsoon (MAM), summer monsoon (JJAS) and post-monsoon (ON) seasons (averaged during 2006 to 2011). Figure 5.2 shows the corresponding seasonal mean vertical distributions of clouds at different longitude sectors, observed using CloudSat data, which is similar to the results presented in Chapter 3. A comparison of Figures 5.1 and 5.2 shows the following:

1. The regions of cold SSTs (<26°C) in the southern hemisphere Indian Ocean (especially south of ∼12°S) are manifested by shallow cloud layers which are limited to <2.5 km altitude.

2. Similar is the case with the north Arabian Sea, especially during winter, where the clouds are generally limited to <3 km over the regions of cold SSTs.

3. In general, the deep convective regions are always associated with relatively warmer SSTs (SST>28°C). However, the largest cloudiness (or deep convection) need not be always associated with the warmest SSTs. For example, the warmest

SSTs over the study region are observed at the tropical Indian Ocean during the pre-monsoon season, while the frequency of occurrence of clouds is largest (especially over the north Bay of Bengal) during the Asian summer monsoon season though the SSTs are smaller by 1 to 2°C.

4. Strong cirrus outflows (fully detached from the lower or middle level clouds) originating from the top of the deep convective regions are present throughout the year. Top altitude of the outflows and deep convective clouds are comparable.

As seen in Figures 5.1, 5.2 and 5.3, the cirrus outflows often extend far from the deep convective regions (as far as ∼5 to 8° geographically) where the local SSTs are considerably smaller than the deep convective regions. However the physical thickness of these cirrus outflow layers are generally larger (vary from 2 to 5 km) and hence are expected to be optically thicker. This aspect is better represented in Figure 5.3, which shows the meridional variations of the vertical distribution of clouds and SST, averaged in the longitude band of 80 to 90°E during the winter season. The well-defined cirrus outflows (fully detached from the lower or middle level clouds) arising from the deep convective region are clearly discernible at north and south of the deep convection. The SSTs at these cirrus outflow regions are ∼1 to 3°C smaller than that at the deep convective regions (e.g., 10 to 20°S). However, top altitudes of the outflows and deep convective clouds are comparable. Hence, the passive radiometer techniques (involving IR observations) would observe the same cloud top brightness temperatures for both these cloud types [*Rajeev et al.*, 2008] and hence cannot discriminate between the deep convective clouds extending from the lower or middle troposphere up to the upper troposphere and the optically thick cirrus outflows whose cloud top is similar to that of the deep convective clouds. This will lead to misinterpretation of the SST-cloudiness relationship when the SSTs are collocated with the cloud properties observed using passive imager data, and is a major limitation of similar studies that are reported in the literature.

5.3.1 Number of observation points

Figure 5.4 depicts the histograms of the number of collocated 2B-GEOPROF-LIDAR data points as a function of SST during different seasons and the entire period (2006 to 2011). Maxima in all the histograms occur in the range of 28 to 29°C, where the total number of observations over the entire period exceeds 1 million (per 0.3°C SST interval). Though the number of collocated points decreases considerably for SST>29°C, their number (per 0.3°C SST interval) for the long-term analysis is more than 0.25 million for all SSTs in range of 24 to 30.5°C. At SST>31°C, the number of collocated points decrease rapidly below ∼60,000. Due to this reason, this study

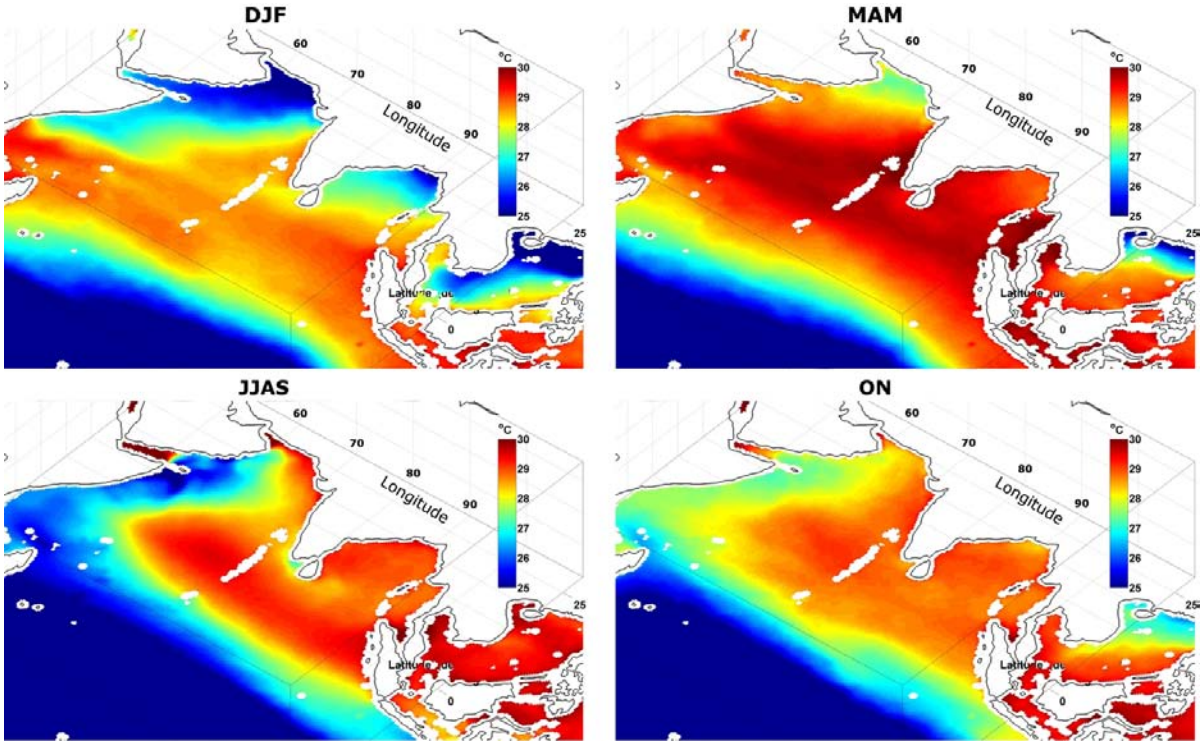

Figure 5.1: Multi-year (2006 to 2011) seasonal mean SST during winter (DJF), pre-monsoon (MAM), summer monsoon (JJAS) and post-monsoon (ON).

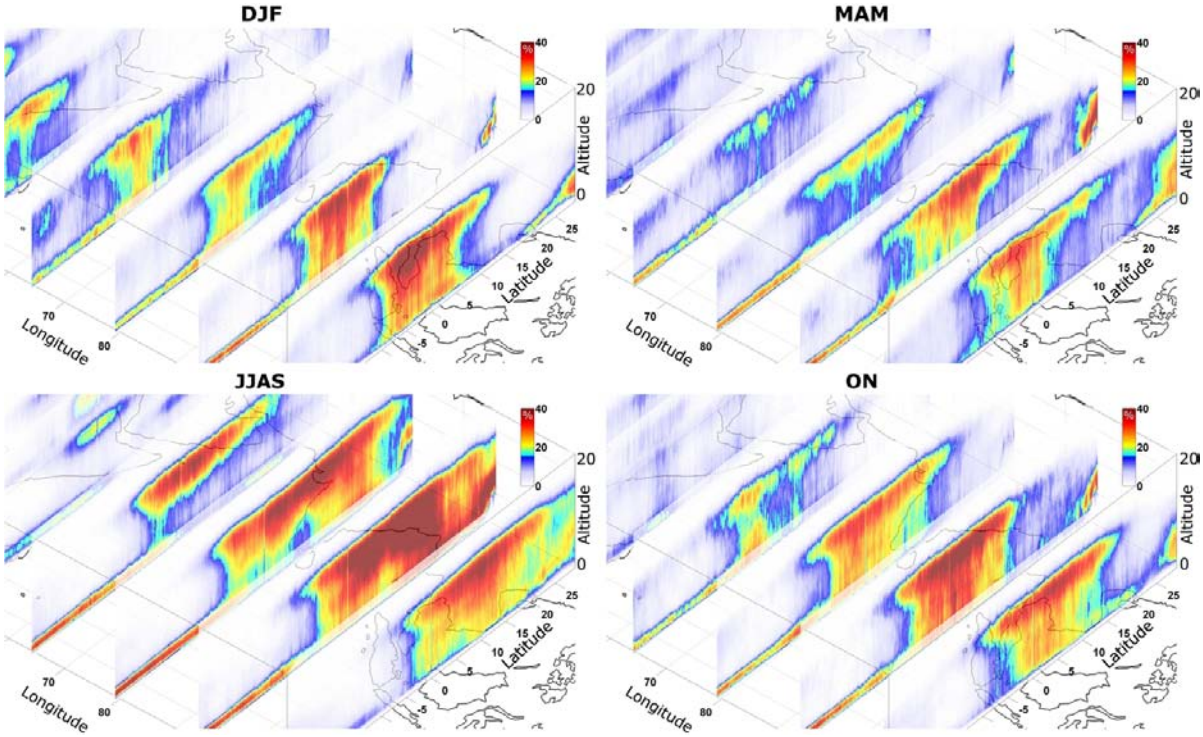

Figure 5.2: Multi-year (2006 to 2011) seasonal mean vertical distribution of clouds (frequency of occurrence in percentage) in different longitudinal slices during winter, pre-monsoon, summer monsoon and post-monsoon seasons.

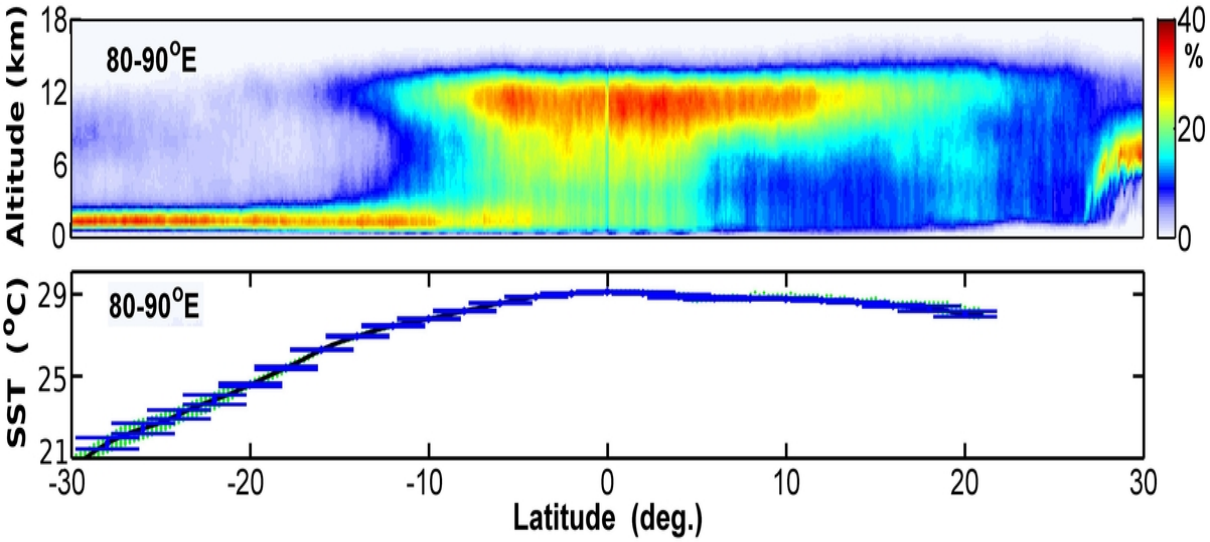

Figure 5.3: Long term mean (a) Latitude-altitude distribution of the frequency of occurrence of clouds in the longitude belt of 80 to 90°E, and (b) corresponding SST. The vertical bars represent standard deviations.

focusses here on the variations in cloudiness in the SST range of 24 to 30.5°C where the total number of observations are quite large. However, at SST ∼31°C, there are still ∼60,000 collocated points; hence a quantitative outlook on the SST dependence at SST>30.5°C is provided wherever required/important.

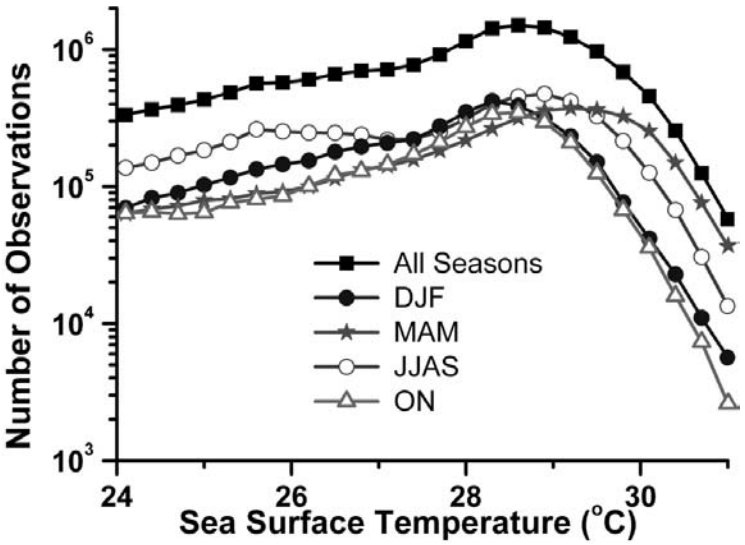

Figure 5.4: Number of collocated observations of 2BGEOPROF-LIDAR data as a function of TMI-SST at SST interval of 0.3°C for the total period of June 2006 to February 2011 and for different seasons during the period: winter (DJF), pre-monsoon (MAM), summer monsoon (JJAS) and post-monsoon (ON).

5.3.2 Variation of cloud vertical distribution with SST

Figure 5.5 shows the frequency of occurrence of clouds (FOC) as a function of altitude and SST, obtained by combining the whole data (2006 to 2011) over the study region. Based on the altitude variation of cloud occurrence, three distinct regimes of SSTs are discernible in Figure 5.5, (i) SST<27.5°C; (ii) 27.5°C⩽SST<29°C; and (iii) SST⩾29°C.

1. At SST<27.5°C, the convection is extremely weak that most of the total cloudiness is limited to <2 km altitude with peak occurrence at 1 to 1.5 km. This appearance is akin to the cloud distribution in the high-pressure areas due to trapping of airmass in the lower troposphere by downdraft from above. In this regime, frequency of occurrence of the low-altitude marine clouds consistently decreases at larger SSTs. At the altitude of their peak occurrence (∼1 to 1.5 km), the cloudiness decreases typically from ∼40% at 24°C to ∼25% at 27.5°C. Occurrence of clouds above these low-level clouds is very rare, though a building up of upper level clouds in the altitude band of ∼10 to 15 km is observed with increase in SST. However, these upper layer clouds are completely detached from the lower-level clouds.

2. In the SST range of 27.5°C<SST<29°C, FOC in the altitude band of ∼3 to 10 km increases with SST, presumably indicating an increase in the convective activity. However, significant increase in this vertical development of clouds is seen only above SST ∼28°C. Though the occurrence of low-altitude clouds decreases with SST in this regime as well, it is less significant compared to that for SST<27.5°C. The prominent peak in FOC observed in the altitude of ∼1 to 1.5 km at SST<27.5°C substantially diminishes with increase in SST. This shows that the increase in convection and vertical development of clouds with SST might have led to the increase in cloudiness at altitudes above 3 km.

3. FOC in the altitude region of about 3 to 12 km attains its peak value in the SST range of 29 to 30.5°C, where the SST-dependence of FOC is negligible at all altitudes.

Figure 5.5 shows that the FOC rapidly increases above the altitude of ∼8 km and maximizes in the altitude band of 13 to 16 km. The occurrence of high-altitude clouds increases with SST right from ∼25 to 26°C and the largest occurrence is observed at 14 to 16 km altitude in the SST range of 29.5 to 30.5°C. In addition to the deep convective clouds that originate right from the lower troposphere, the increase in cloudiness at higher altitudes might have been contributed by an increase in cirrus clouds also,

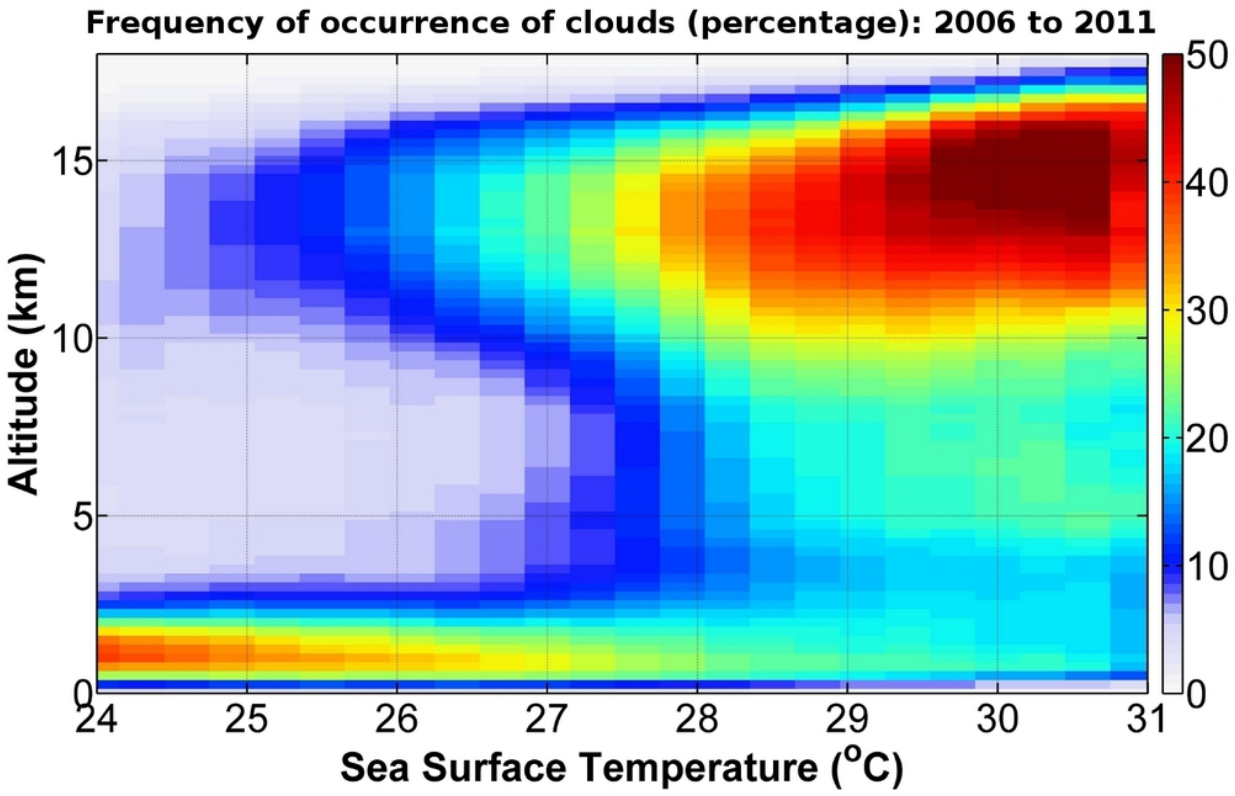

Figure 5.5: Altitude distribution of the frequency of occurrence of clouds (in percentage) as a function of SST during 2006 to 2011.

as they can be produced from the anvils or remnants of convective clouds and have larger lifetime compared to the deep convective clouds. The cirrus production also may be expected to be larger at higher SSTs (SST>29°C) where the deep convection is more prominent. At SSTs <27.5°C, the occurrence of high-altitude clouds is fully detached from the clouds originating in the lower altitudes, while the continuity in their occurrence at the lower, middle and upper levels are quite evident for SST>28°C. These manifestations clearly show that the occurrence of high-altitude clouds for SST<28°C is predominantly caused by the outflow from deep convective systems occurring in the nearby warmer oceanic regions. Another important feature observed in Figure 5.5 is the systematic increase in the penetration of deep convective clouds to higher altitudes (as high as ∼17 km) as well as the frequency of occurrence of clouds in the upper-troposphere (above 13 km) with increase in SST, which are evident even up to SST ∼30.5°C. In the altitude band of 16 to 17 km, the frequency of occurrence of clouds is ∼25 to 40% at SST∼30.5°C.

The season-wise altitude variations in the FOC with SST during the winter (December to February), pre-monsoon (March to May), summer monsoon (June to September) and post-monsoon (October to November) seasons are shown in Figure 5.6. Overall, the SST-cloudiness relationships observed during different seasons are consistent and

are similar to that observed using the long-term mean variations illustrated in Figure 5.5. However, significant variations are observed in the absolute values of the FOC. For example, the increase in FOC in the altitude range of 3 to 8 km observed for SST>27.5°C as well as the cloud occurrence in the SST range of 28 to 30°C are considerably smaller during the pre-monsoon season (Figure 5.6(b)) compared to the other seasons. In contrast, the frequency of cloud occurrence at SST∼31°C during this season is quite large. these high SSTs are observed at the Arabian Sea warm pool region. These observations are consistent with the total frequency of occurrence of clouds at all altitudes observed over the study region during the pre-monsoon season using imager data (NOAA-AVHRR) [*Meenu et al.*, 2012] and arises mainly from the large-scale descending of airmass in the western tropical Indian Ocean associated with the Walker circulation cell, which inhibit the vertical development of clouds, despite warmer SSTs (∼28 to 29°C) over this region. Similarly, though most of the north Arabian Sea is considerably warmer (SST∼28 to 30°C) during this season, the large-scale sinking of tropospheric airmass in this region associated with the descending limb of the Hadley circulation cell inhibits the vertical development of clouds. These aspects on the linkages between atmospheric circulation and cloudiness are described in Chapter 3. These features indicate the role of large-scale atmospheric dynamics in significantly modulating the vertical distribution of clouds. The large value of FOC at SST>30°C observed during the pre-monsoon season are associated with the relatively larger cloudiness at the eastern part of the Arabian Sea warm pool, especially during May (with SST>30°C).

As seen from Figures 5.5 and 5.6, the SST-dependences of cloudiness have distinctly different variations in the altitude bands of <2 km, 2 to 8 km and >8 km. For a more quantitative study, variations in the average frequency of occurrence of clouds in the above altitude bands as a function of SST are shown in Figure 5.7. Figure 5.7(c) shows that, in the 2 to 8 km altitude band, the average cloud occurrence frequency is ∼7% at SST<27°C. Its increase with SST is prominent only above ∼27.5°C and maximises in the SST range of 29 to 30.5°C where it remains steady with an average occurrence of ∼20%. As shown by the standard deviations (vertical bars in Figure 5.7), variability in the frequency of occurrence of clouds in the 2 to 8 km altitude band is considerably smaller at SST>28°C compared to the lower SSTs. Under the influence of outflow from the deep convective regions, the occurrence of high-altitude clouds (>8 km altitude) consistently increases for SST>25°C (Figure 5.7(b)). The magnitude of this increase is also larger than that of the clouds in the 2 to 8 km altitude band. As indicated by the standard deviation, the mean FOC in the upper troposphere shows larger variability at higher SSTs. Figure 5.7(a) depicts the average FOC in the altitude band of 16 to 17 km, which is close to the altitude of cold point tropopause (∼16.5 to 17.5 km) in this region [*Meenu et al.*, 2010]. In contrast to the SST-dependence of average cloudiness

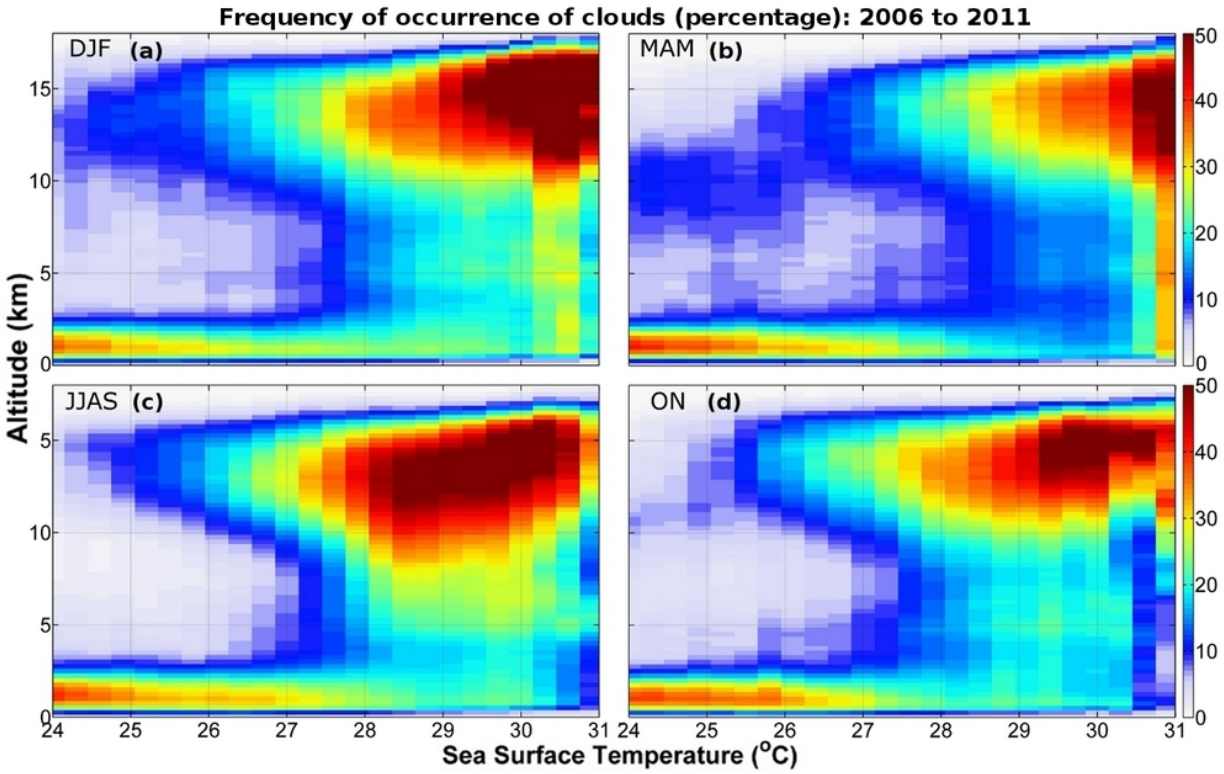

Figure 5.6: Altitude distribution of the frequency of occurrence of clouds (in percentage) as a function of SST during 2006 to 2011 for different seasons (a) Winter (DJF), (b) Premonsoon (MAM), (c) Summer Monsoon (JJAS) and (d) Postmonsoon (ON).

in the middle and upper troposphere (Figs. 5.7(b),(c),(d)), FOC in the 16-17 km altitude region rapidly increases above ∼28.5°C and continues to increase till ∼30.5°C. This clearly shows that, on average, the penetration of deep convection just below the cold point tropopause significantly increases with SST even up to ∼30.5°C. A weak decreasing trend is observed in FOC at SST>30.8°C at all altitudes >2 km.

The SST-dependences of the seasonal and long-term mean total frequency of occurrence of clouds derived from the above observations at all altitudes are shown in Figure 5.8. In this analysis, a pixel is considered as cloudy if cloud appears at any altitude. In principle, they are similar to the frequency of occurrence of clouds that would be observed using the imager data (e.g., NOAA-AVHRR), which is extensively reported in the literature. Figure 5.8 shows that the long-term mean occurrence of total cloudiness shows a consistent increase with SST for SST>26°C. During the summer monsoon season, this increase in cloudiness is more rapid and tends to saturate at SST>28.5°C. In contrast, during the winter and pre-monsoon seasons, the increase in cloudiness occurs only over warmer regions with SST>27°C. The threshold SST of ∼26 to 27°C, above which the total cloudiness increases with SST (Figure 5.8), is distinctly smaller than the threshold SST of ∼27.5 to 28°C observed in Figure 5.7(c) for the vertically developing clouds, indicated by the cloudiness in the 2 to 8 km altitude

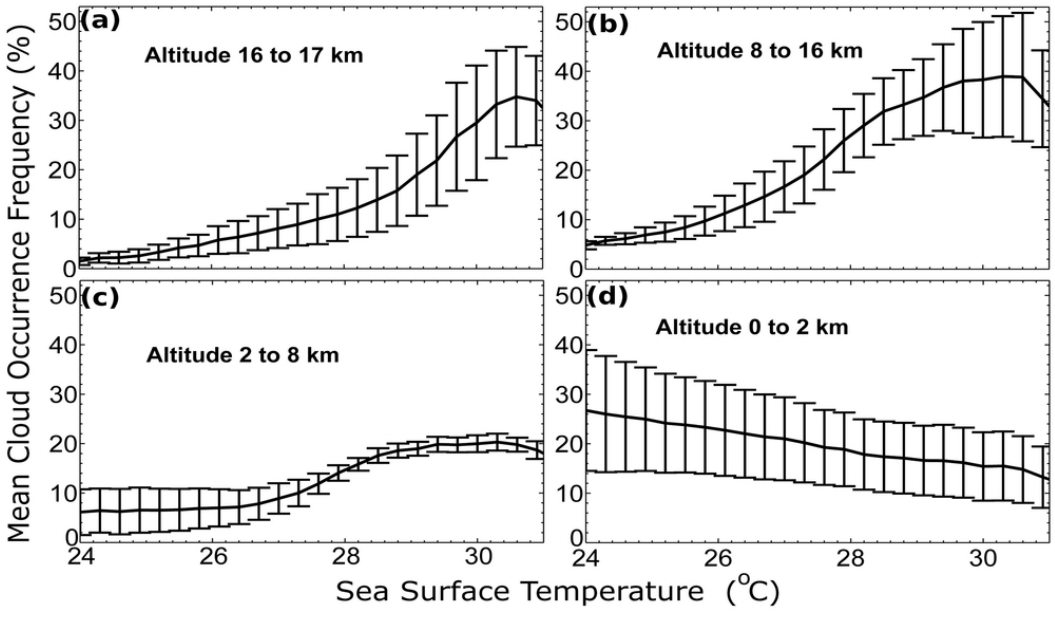

[h]

Figure 5.7: Average frequency of occurrence of clouds for different altitude bands as a function of SST. Standard deviation is represented by the vertical bars.

band. Clearly, this difference is associated with the increase in cirrus clouds generated from deep convective outflows which significantly contributes to the total cloudiness at SST<27.5°C.

The SST-dependences of total cloudiness reported in the literature using imager data [e.g., *Meenu et al.*, 2012] are similar to those shown in Figure 5.8, especially for SST<29.5°C. As explained earlier, this similarity is expected because the imager data will not be able to discriminate locally produced convective clouds originating from the lower troposphere from the thick cirrus clouds generated by deep convective outflows. However, Figure 5.8 shows that, above the threshold SST, the total cloudiness increase with SST even upto ∼30.5°C (or saturates at SST>28.5°C and remains steady even upto ∼30.5°C during the summer monsoon season). This result differs from those reported earlier using imager data where the total cloudiness is generally found to decrease with increase in SST above ∼29.5°C. [e.g., *Gadgil et al.*, 1984; *Graham and Barnett*, 1987; *Lau et al.*, 1997; *Bony et al.*, 1997]. This is an important difference and might be mainly due to the exclusion of a fraction of thin cirrus clouds which would be underestimated or undetected by the conventional imagers (in which clouds are detected based on the thermal IR radiation emitted from the clouds) [e.g., *Rajeev et al.*, 2008]. On the other hand, these thin clouds will be detectable using CALIPSO and a combination of CloudSat and CALIPSO, would detect clouds of all opacity.

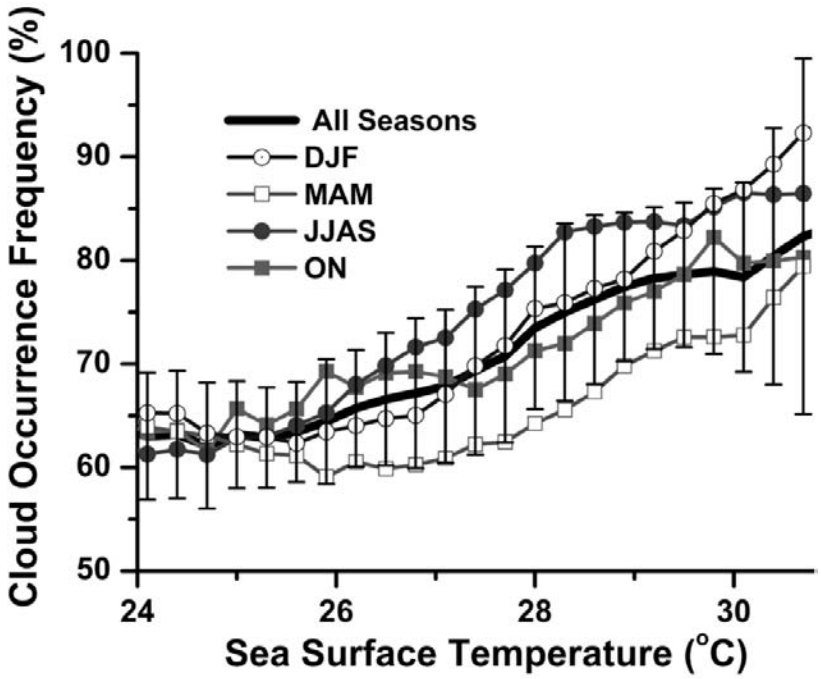

Figure 5.8: Variations in the mean frequency of occurrence of clouds with SST for the period of study (2006 to 2011) and for different seasons. Standard deviations for all seasons are represented by vertical bars. Standard deviations for individual seasons are comparable to that for the whole period.

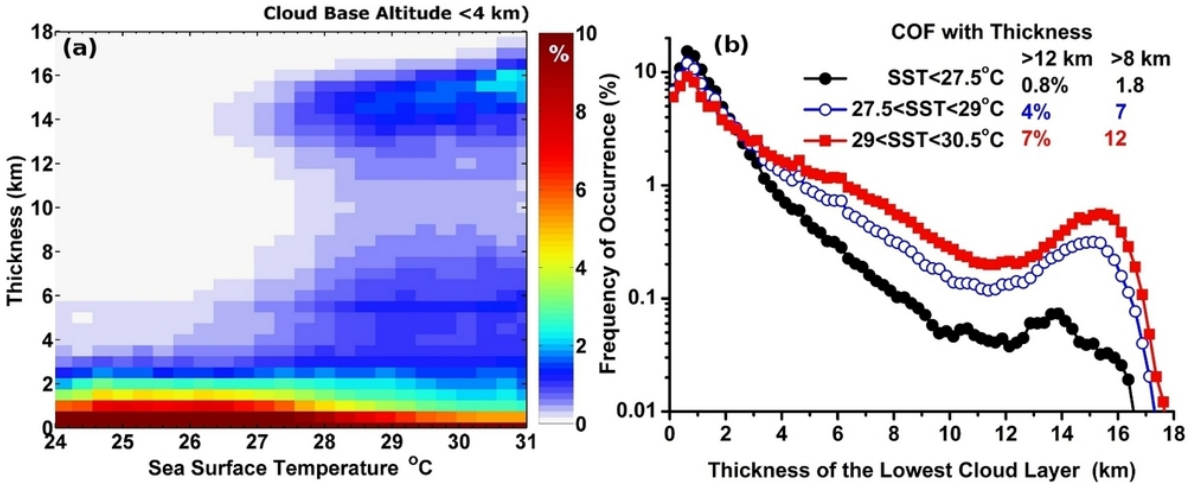

Figure 5.9: (a) Probability distribution function of cloud thickness as a function of SST for clouds having base altitude <4 km. (b) Frequency of occurrence of clouds as a function of cloud thickness (for clouds with base altitude <4 km) for three regimes of SST: SST<27.5°C, 27.5<SST<29°C, and 29<SST<30.5°C.

5.3.3 Variation of cloud thickness with SST

The SST-dependence of cloud thickness is shown in Figure 5.9(a), which depicts the long-term (2006 to 2011: all seasons) mean frequency distribution of cloud thickness (at

thickness intervals of 0.25 km) as a function of SST. Figure 5.9(b) shows the average frequency of occurrence of clouds as a function of cloud thickness for different SST ranges: <27.5°C, 27.5 to 29°C and >29°C. Hence, only those clouds having their base altitude occurring below 4 km are included in this analysis. Figures 5.9(a,b) shows that, in all SSTs, the probability of occurrence is largest for thin clouds and the occurrence frequency decreases with increase in cloud thickness up to ∼10 to 11 km. The rate of this decrease is rapid for lower SSTs (SST<27.5°C) and smaller for warmer SSTs. One of the most striking features seen in Figure 5.9(a,b) is the increase in the probability of occurrence of clouds with thickness greater than ∼10 to 11 km. The magnitude of this secondary peak increases significantly with SST and is prominent even up to SST∼30.5°C (5.9(a)). The average frequency of occurrence of clouds with thickness >12 km is 0.8%, 4% and 7% for SST<27.5°C, 27.5<SST<29°C and SST>29°C respectively. Furthermore, the cloud thickness at which this secondary maximum occurs systematically increases with SST from ∼13 km for SST<27.5°C to ∼15 km for 27.5<SST<29°C and 15.5 km for SST>29°C.

5.4 Role of atmospheric thermo-dynamics in modulating the observed SST–cloudiness relationship

As discussed earlier, in addition to SST, the convection and cloudiness over a given region is significantly regulated by the spatial gradient of SST (which has significant influence on the large-scale atmospheric circulation) and atmospheric dynamical factors such as surface wind convergence, lower tropospheric stability, upper tropospheric divergence and convective available potential energy (CAPE), all of which are crucial in determining the vertical wind velocity and formation of convective clouds.

5.4.1 Role of SST gradient

Figure 5.10 shows the probability distribution function for the magnitude of the spatial gradient of SST as a function of SST, derived from the TMI-SST dataset over the study region during 2006 to 2011. The features are very similar for different seasons and hence are not shown separately. The spatial gradients of SST are generally larger for SST<27.5°C, where the gradient values are mostly in the range of 0 to 0.8°C/deg. The mean SST gradient is largest in the SST range of 26.5 to 27.5°C, where the gradient values are generally in the range of 0.1 to 0.5°C/deg. On the contrary, the SST gradients are remarkably smaller for higher values of SST, especially at SST>28.5°C where the gradients are generally <0.2°C/deg and mostly <0.1°C/deg. As seen in Figs.5.5 to

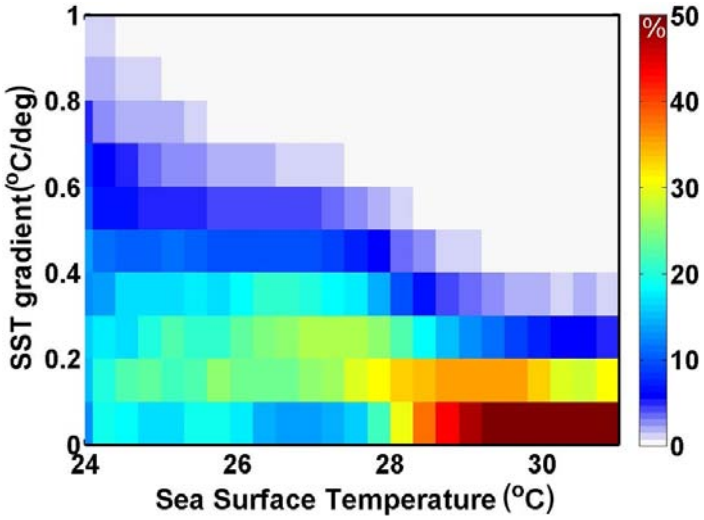

Figure 5.10: Probability distribution function of SST gradient as a function of SST.

5.7, the occurrence of convective clouds increases with SST above ∼27.5°C, where the SST gradient is largest. However, the maximum cloudiness occurs at SST ∼29 to 30.5°C where the SST gradients are substantially smaller. Figure 5.10 together with Figs.5.5 to 5.7 clearly shows that both SST and its spatial gradient are important in determining the vertical development of clouds. However, their prominence differ at different ranges of SST. At relatively lower SST of ∼27.5°C, the convection appears to be regulated by the SST gradient. The decrease in the magnitude of SST gradient slows down the rate of increase in convection with SST, especially for SST>29°C.

5.4.2 Role of surface wind divergence

The probability distributions function of surface wind divergence (SWD, observed using Scatterometer data) as a function of TMI-SST is depicted in Figure 5.11(a). The surface winds are mostly diverging (positive values of SWD) at SST<26°C, which will inhibit large scale convection in the lower troposphere and vertical development of clouds. The SWD decreases, albeit weakly, with increase in SST. At SST∼27.5°C, the probabilities for the occurrence of surface wind convergence is comparable to that for divergence. On average, the surface winds have a larger probability for convergence at SST of ∼28 to 29°C, while at higher SSTs, the probability for convergence is again comparable to that for divergence. Thus, occurrence of convective clouds caused by the surface wind convergence will be largest at SST∼28 to 29°C, which is also the SST range at which the occurrence of convective clouds shows rapid increase with SST (Figs. 5.5 and 5.6).

5.4.3 Role of upper level wind divergence

The probability distribution function of the upper tropospheric wind divergence at 150 hPa level as a function of TMI-SST is depicted in Figure 5.11(b). This analysis is carried out using the monthly mean NCEP-analysis data and coloacted monthly mean TMI-SST data. Figure 5.11(b) shows that the upper level winds are strongly converging at SST<27.5°C. This will cause downdraft of upper tropospheric airmass and inhibit convection at the lower levels. However, the average magnitude and probability for upper tropospheric convergence decrease with further increase in SST. The 150 hPa level winds are mostly diverging at SST>28°C and the average divergence increases up to SST∼29°C, above which the average magnitude of the wind divergence does not significantly vary with SST. The ventilation provided by the upper level divergence aids convection from the lower altitudes, thereby increasing the occurrence of convective clouds. The variations in the upper-level divergence with SST are in tandem with the corresponding variations in the vertical distribution of clouds in the middle- and upper troposphere. Though the upper-level divergence does not increase with SST for SST>29°C, these winds are still considerably diverging, which enable the convergence from below. However, the occurrence of convective clouds cannot further increase through this process at SST>29°C and might have contributed to the observed weakening of the rate of increase in the frequency of occurrence of convective clouds for SST>29°C.

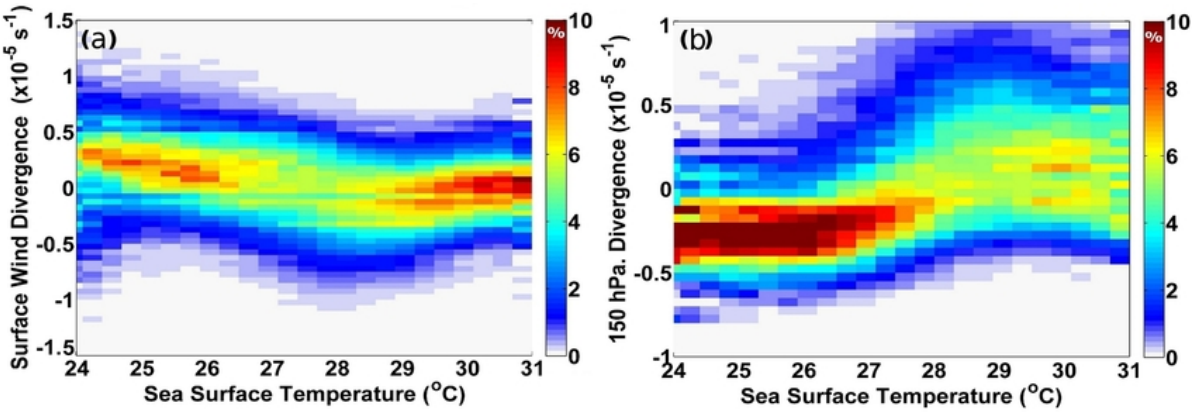

Figure 5.11: Probability distribution function of (a) surface wind divergence and (b) wind divergence at 150 hPa as a function of SST.

5.4.4 Role of Lower Tropospheric Stability (LTS)

The potential temperature at 700 hPa. level minus that at 1000 hPa. provides an index of the stability of the lower troposphere [*Klein and Hartmann*, 1993]. Figure 5.12(a) shows the probability distribution function of the lower tropospheric stability

(LTS) as a function of SST. Larger the value of LTS, more stable is the lower troposphere. Figure 5.12(a) shows that the LTS is quite high and rather steady (mean value of ∼15 K) at SST<26.5°C and systematically decreases with further increase in SST. The LTS is distinctly smaller and remains almost steady (mean value ∼12 K) for 29<SST<30.5°C. The decrease in lower tropospheric stability would trigger convection in the lower troposphere and this effect systematically increases with SST. Thus, the convection arising from the reduction in lower tropospheric stability might contribute to the observed rapid increase in convective clouds in the SST range of 27.5 to 29°C and weaken further increase in their occurrence at SST>29°C.

5.4.5 Role of Convective Available Potential Energy (CAPE)

Figure 5.12(b) shows the probability distribution function for the convective available potential energy (CAPE) as a function of SST, the pattern of which is strikingly similar to the SST-dependence of the vertical distribution of cloud occurrence observed in Figs.5.5 to 5.7. (Figure 5.12(b) is derived from the monthly mean value of CAPE and SST and hence has resulted in the relatively lower magnitude of CAPE. This is because, though the CAPE value on an individual convective cell can be quite large (even exceeding 4000 J/kg) but the average value over a month at a given location will be smaller as shown in Figure 5.12(b)). The average CAPE remains almost steady (mean value <300 J/kg) for SST<27°C and thereafter steadily increases with SST till ∼29.5°C to attain the peak (mean value ∼1200 J/kg). Further increase of CAPE with SST is negligible. The increase in CAPE would increase convection and frequency of occurrence of clouds in the middle and upper troposphere. As the CAPE does not significantly increase with SST at SST>29.5°C, the occurrence of deep convective cloudiness would be large but almost steady in this SST range.

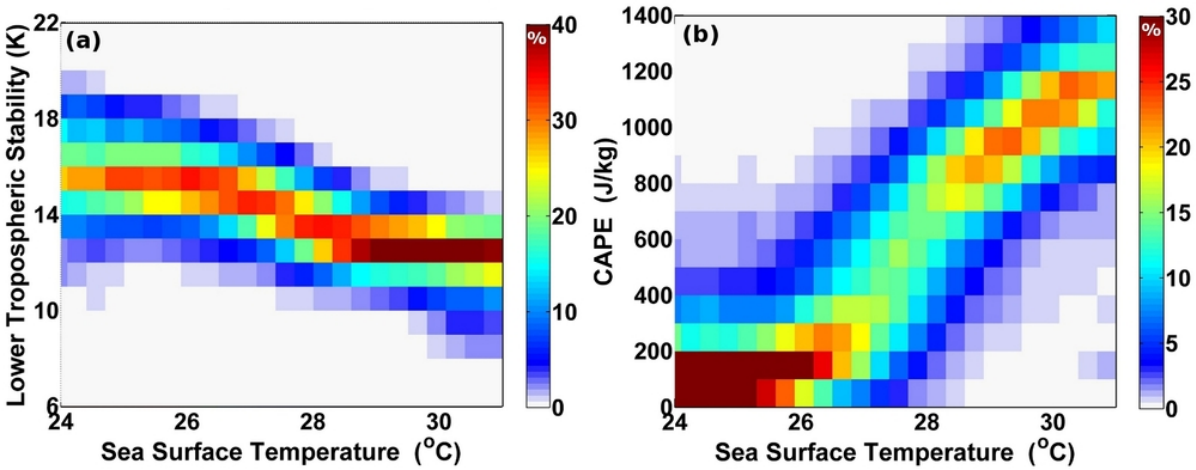

Figure 5.12: Probability distribution function of (a) lower tropospheric stability and (b) CAPE as a function of SST.

5.5 Integrated picture of the relationship among SST, atmospheric thermo-dynamics and vertical distribution of clouds

This study clearly shows that, the frequency of occurrence of clouds in the middle and upper troposphere, apparently produced by deep convection, increases significantly only for SST>27.5°C and attain the maximum cloudiness at SST ∼29 to 30.5°C. Most importantly, the frequency of occurrence of clouds does not decrease with increase in SST, at least till ∼30.5°C. These results significantly differ from the SST-dependence of total cloudiness derived using imager data that is reported in the literature, in which the total cloudiness is found to increase with SST above ∼26 to 27°C to attain a peak value at ∼29.5°C and decrease with further increase in SST. The present study clearly reveals that main cause for these differences between the results reported in the literature based on imager data and the present observations stems from the fact that the imager observations could not isolate the effect of cirrus clouds generated by the outflows from deep convection.

The present study also shows that the frequency of occurrence of lower tropospheric clouds decreases with increase in SST, especially in the SST range of 24 to 27°C. This is in agreement with the observations of *Bony et al.* [1997] showing a decrease in cloud fraction and optical depth with increase in SST for SST<27°C. These regions of smaller SST in the tropics are generally characterized by large-scale subsidence driven by the remotely generated convection at warmer oceanic regions [e.g., *Waliser and Graham*, 1993] and favours the occurrence of low-level clouds. In the study region, the cold SSTs generally occur over the southwest Indian Ocean during the Asian summer monsoon season and the north Arabian Sea during winter and are manifested by the descending limb of Hadley or Walker circulation cells, as discussed in Chapter 3. Both these conditions are associated with divergence of the lower tropospheric winds, which cause trapping of air (and moisture) in the atmospheric boundary layer or lower troposphere and prevent vertical development of clouds. This observed decrease in the lower tropospheric cloudiness with increase in SST might be due to the fact that the warmer SSTs cause vertical transport of moisture from the lower troposphere by convection to the middle and upper troposphere where they cause cloud formation.

While SST controls the moist static energy available at the surface, which is crucial for local convection, the updraft in the atmosphere is also influenced by remote forcing of tropospheric circulation driven by the large-scale spatial gradient of SST. The atmospheric convection is further modified by a variety of strongly interlinked atmospheric dynamical/ thermodynamical parameters such as lower tropospheric stability

and convergence, upper tropospheric divergence and CAPE. The observed variations in the SST-dependence of the vertical distribution of cloudiness are explainable based on the variations in the above parameters. Among them, the variations of CAPE and upper level divergence with SST are strikingly similar to the corresponding variations in the vertical distribution of clouds with SST, especially the rapid development of convection above 28°C and little variations in the vertical distribution of clouds in the SST band of 29 to 30.5°C.

One of the striking features observed in Figs.5.5 to 5.7 is the increase in the cloud top altitude up to which significant convection takes place, even for SST>29.5°C where the spatial gradient of SST as well as the increase in upper-level divergence are negligible. This might have been primarily caused by (i) an increase in CAPE, though weak, in the SST range of 29 to 30°C, and (ii) increase in the moist static energy available at the surface through increase in SST. The present observations confirm the inferences made by *Meenu et al.* [2012], who showed that the cloud top brightness temperature decreases (indicating an increase in cloud top altitude) with increase in SST throughout the observed SST regime of 25 to 30°C, immaterial of the SST-dependence of the frequency of occurrence of clouds. The observed increase in the top altitude of deep convective clouds with SST might increase the convective tropopause altitude and significantly affect the thermodynamics and structure of the tropical tropopause layer (TTL) [*Gettelman and Forster*, 2002], which need to be investigated in detail.

The frequency of occurrence of upper level clouds, especially above ∼10 km altitude, is found to increase substantially with altitude (Figs.5.5 to 5.6). This increase is most prominent in the SST range of 29.5 to 30.5°C. It is primarily due to the increase in cirrus clouds, which have longer lifetime compared to the deep convective clouds in the middle and upper troposphere. Another important feature observed in the present study is the increase in the probability of occurrence of deep convective clouds having thickness >12 km. Prominence of this secondary peak increases with SST. The probability of occurrence of clouds as a function of cloud thickness in this secondary peak is explainable based on the potential temperature lapse rate. Altitude variation of potential temperature shows that, on average, the lapse rate of potential temperature (LRPT= $d\theta/dz$) is minimum near the convective tropical tropopause altitude, which is the base of the TTL [*Gettelman and Forster*, 2002]. Over the study region, the LRPT is generally largest in the lower and middle troposphere and decreases above ∼10 km altitude to attain a minimum value in the convective tropopause around 12 to 15 km [e.g., *Mehta et al.*, 2008; *Meenu et al.*, 2010]. Under highly convective conditions, the LRPT can be very close to zero or sometimes even negative [*Mehta et al.*, 2008]. This means that, for a convection having sufficient energy to reach in the vicinity of the convective tropopause, it requires only little more energy to be pushed up by another

couple of kilometres or be naturally pushed up due to the instability (LRPT<0°C/km) in the vicinity of the convective tropopause. *Hartmann* [2002] proposed that the most active convection will be limited to the altitude range where radiative cooling is efficient: this occurs only below ∼200 hPa level as water vapour amount is considerably smaller in the colder regions above. Based on this, they argued that the tropical convective clouds might detrain preferentially near 200 hPa. level. The above mechanisms might be mainly responsible for the secondary peak observed in the probability of occurrence of clouds as a function of cloud thickness.

5.6 Summary and conclusions

First observations of the SST-dependence of the vertical distribution of clouds have been presented in this chapter. This further refines the extensively-investigated SST-dependence of total cloudiness reported in the literature using imager data and explains the potential causes for the observed differences.

Some of the salient results of the study are:

1. Variations in the altitude distribution of clouds with SST show three distinct regimes: SST<27.5°C, 27.5°C<SST<29°C and SST>29°C.

2. At SST<27.5°C, the convection is extremely weak that most of the clouds are limited to <2 km altitude with peak occurrence at 1 to 1.5 km.

3. Frequency of occurrence of the low-altitude clouds as well as the prominence of the peak at 1.5 km consistently decreases for SST>24°C.

4. Vertical development of clouds through the 3 to 12 km altitude region increases for SST>27.5°C to achieve maximum cloud occurrence in the SST range of 29 to 30.5°C, where the SST-dependence of cloud occurrence is negligible.

5. Penetration of the deep convective clouds to altitudes >15 km and their frequency of occurrence increase with SST till ∼30°C.

6. These observations reveal two major differences with the SST-dependence of total cloudiness reported earlier using imager data:

   (a) the increase in cloudiness at SST >26 to 27°C observed using the imager data is found to be an artifact due to increase in cirrus clouds generated by deep convective outflows and are not directly driven by the local SST, and

   (b) the total cloudiness does not decrease for SST>29°C, but rather remains steady.

7. Role of the spatial gradient of SST and atmospheric dynamical parameters in modulating the observed SST-dependence of cloudiness at different SST regimes has been unambigiously brought out.

Chapter 6

Vertical Distribution of Cirrus Clouds and their Descending Nature

6.1 Introduction

Cirrus clouds constitute the largest fraction of upper tropospheric clouds [*Corti et al.*, 2006; *Wang and Dessler*, 2006]. They play an important role in regulating the moisture content and thermal structure of the tropical tropopause layer (TTL) and climate of the earth-atmosphere system [*Stephens et al.*, 1990; *Ramanathan and Collins*, 1991; *Hartmann et al.*, 2001; *Gettelman et al.*, 2002]. Their spatial extent can range from less than a kilometre to several hundreds of kilometres. In general, the horizontal extent and lifetime of tropical cirrus are significantly larger than any other cloud types and hence can persist even for more than a day [*Taylor et al.*, 2011]. With very cold cloud top temperature, they are highly influential in governing the climate, and act as a thermal blanket by trapping the outgoing terrestrial (IR) radiation, efficiency of which depends on the cloud fraction, altitude and optical depth. Effectiveness of cirrus clouds in reflecting the incoming solar radiation back to space depends on the cloud optical depth (COD). In general, the optical depth of cirrus clouds is rather small (typically <1) and hence are semi-transparent to the shortwave radiation from the Sun. Trapping of terrestrial radiation (causing a warming of the earth's surface) and reflection of incoming solar radiation (causing a cooling of the earth's surface) determines the net effect of cirrus clouds on the earth-atmosphere system. The former is called longwave cloud radiative forcing and the latter is called shortwave cloud radiative forcing, and are highly sensitive to physical and micro-physical properties of cirrus [*Stephens et al.*, 1990]. Due to their low optical depth and occurrence in the cold upper troposphere, the

longwave radiative forcing of the tropical cirrus clouds often exceeds the corresponding shortwave forcing, resulting in a net warming of the earth's surface [*Choi and Ho*, 2006]. However, due to large variations in their spatial distribution, altitude of occurrence, atmospheric residence time, microphysical and radiative properties and morphology, absolute magnitudes of the impact of cirrus clouds on radiation, atmospheric thermal structure and moisture budget are highly variable in space and time and are poorly understood [*Stubenrauch et al.*, 2007]. The representation of cirrus clouds in climate models needs to be improved significantly [*Mitchell et al.*, 2008]. Understanding of the macro- and micro-physical properties of cirrus clouds, their formation and maintenance are essential for cirrus parametrization and their incorporation into models.

Extensive studies on the spatial distribution of cirrus are reported in the literature, mostly using satellite remote sensing techniques [e.g., *Wang et al.*, 1996; *Winker and Trepte*, 1998; *Wang and Dessler*, 2006; *Nazaryan et al.*, 2008], airborne observations [e.g., *McFarquhar et al.*, 2000; *Whiteway et al.*, 2004] and ground-based observations at few geographical locations [e.g., *Sassen and Chow*, 1992; *Parameswaran et al.*, 2003; *Immler et al.*, 2007]. Globally, a wide tropical region covering the Bay of Bengal, the tropical Indian Ocean, the western Pacific, and southeast Asia has the largest frequency of occurrence of cirrus clouds over the entire globe [*Wang et al.*, 1996; *Wang and Dessler*, 2006; *Fu et al.*, 2007], a significant fraction of them being optically and physically thin [*Meenu et al.*, 2011]. Vertical distribution of cirrus clouds over Gadanki (13.5°N, 79.2°E) has been extensively investigated using Lidar observations [e.g. *Bhavani Kumar et al.*, 2001; *Parameswaran et al.*, 2003; *SunilKumar et al.*, 2003; *Sivakumar et al.*, 2003; *Sunilkumar et al.*, 2008; *Sunilkumar and Parameswaran*, 2005; *Thampi et al.*, 2009], which have clearly brought out the monthly, annual and interannual variations in their altitude and frequency of occurrence and cloud optical depth. Combination of these lidar observations with spaceborne observations using SAGE-II and Kalpana-1-VHRR have further improved the understanding on the genesis of cirrus clouds and classifying the properties of insitu produced and those transported from the deep convective outflows [e.g. *Rajeev et al.*, 2008; *Sunilkumar et al.*, 2010; *Thampi et al.*, 2012]. Similar studies have been carried out from a few other tropical locations as well [e.g. *Sassen and Chow*, 1992; *Immler et al.*, 2007; *Seifert et al.*, 2007; *Das et al.*, 2009].

Detailed studies on the monthly mean spatial distribution of semi-transparent cirrus clouds (STC) (frequency and altitude of occurrence, geometrical thickness and cloud optical depth and their annual and inter-annual variations over the Indian region and the surrounding oceans have been carried out using CALIPSO data [*Meenu et al.*, 2011]). The above observations using ground based Lidar, SAGE-II, CALIPSO, Kalpana-I-VHRR and other satellites revealed that, on average, cirrus occurrence peaks

in the altitude band of ∼14 to 16 km. About <6% of cirrus clouds were found to occur above the cold point tropopause [*Meenu et al.*, 2011]. Over the Indian region, their occurrence is largest during the summer monsoon season. Though the cloud optical depths are found to vary over a wide range, most of them have COD values between 0.03 to 0.3 (and are classified as thick cirrus).

Gravitational settling of ice particles in cirrus clouds or downward movement of these ice crystals due to subsidence of upper tropospheric airmass associated with atmospheric waves, general circulation or other processes results in the descending of cirrus clouds with time [e.g., *Heymsfield and Iaquinta*, 2000; *Mitchell et al.*, 2008]. Descending of cirrus has the potential to influence the moisture and radiation budget of the upper troposphere [e.g., *Jakob*, 2002; *Jensen et al.*, 2011]. Sedimentation of ice particles from cirrus clouds [*Mitchell et al.*, 2008] is one of the important mechanisms responsible for the dehydration of the upper troposphere and lower stratosphere (UTLS) region. Sublimation of ice particles during descending increases water vapour content in the altitudes to which they subside [*Jensen et al.*, 2011], and might reduce the cirrus lifetime. For a change in the ice particle terminal velocity in the range 0.1 to 2 ms^{-1}, the cirrus radiative forcing can change by as large as 20 Wm^{-2} [*Jakob*, 2002]. Parameterisation of ice particle sedimentation in large-scale circulation models is important for defining their overall impact, including cirrus cloud ice water path and longwave forcing [e.g., *Mitchell et al.*, 2008].

Though the observations using CALIPSO and SAGE-II provided global vertical distribution of cirrus clouds, the frequency of observation at a given location by these satellites is very poor and cannot be used to study any cirrus feature that varies at relatively shorter time scales, such as time evolution of their physical and optical properties during their life cycle. Though the observations using geostationary satellites such as Kalpana-1-VHRR provide near continuous observations (at ∼30 min intervals), they cannot provide the vertical structure of clouds. Studies on the time evolution of cirrus clouds (including their altitude structure) can be carried out only using continuous observations using Lidar. This chapter presents the vertical distribution of cirrus clouds, their monthly and annual variations and short-term evolution during the lifetime of cirrus clouds based on multi-year (March 2008 to May 2011) dual polarization micro pulse Lidar observation carried out at Thiruvananthapuram (8.5°N, 77°E), a tropical station located in the southwest Indian peninsula.

Note that the local convective conditions and proximity to the northeast Bay of Bengal (where the largest deep convection and cirrus clouds occur over the entire globe) at Thiruvananthapuram are quite different from those at Gadanki, where extensive lidar-based studies on cirrus clouds were carried out earlier. Thus, the present observations on cirrus characteristics at Thiruvananthapuram further add to improving

the understanding on cirrus clouds over the Indian subcontinent. More importantly, the time evolution of cirrus clouds at short time scales was not investigated extensively in the earlier studies. One of the unique aspects of the time evolution of cirrus is their descending nature associated with sedimentation and atmospheric dynamics. This chapter extensively investigates the descending nature of tropical cirrus clouds and associated changes in their physical and optical properties, and provides the most detailed characterization of the descending nature of tropical cirrus clouds reported till date [*Nair et al.*, 2012]. Potential impact of cirrus descending on the cloud radiative forcing is also investigated.

6.1.1 Objectives of the present study

Main objectives of this study are:

1. Investigation of the monthly mean vertical distribution of cirrus clouds and their properties (frequency of occurrence, cloud optical depth, physical thickness, linear depolarization ratio) and their seasonal and annual variations over Thiruvananthapuram (85°N, 77°E), a tropical station located in the southwest coast of peninsular India.

2. Detailed exploration of the short term evolution of cirrus clouds during their life cycle and quantification of the descending nature of tropical cirrus and associated changes in their properties.

3. Model estimation of the impact of descending in changing cirrus cloud radiative forcing at top of the atmosphere.

These objectives are realized using the systematic long-duration micropulse lidar (MPL) observations carried out at Thiruvananthapuram during 2008 to 2011. Such regular long-duration lidar observations from a fixed location are sparse, but crucial for understanding the morphology and descending characteristics of cirrus clouds. This study is motivated by the dearth of observations on the descending of cirrus clouds and would be useful in understanding the sedimentation of tropical cirrus clouds and their role in regulating the moisture and radiation budget of the tropical tropopause layer (TTL) layer. Characteristics of the descending cirrus layers and their potential impact on the cloud radiative forcing at top-of-the-atmosphere (TOA) are presented.

6.2 Micropulse Lidar data and method of analysis

Long duration observations carried out using a dual-polarization Micropulse Lidar (MPL) at Thiruvananthapuram during the period of March 2008 to May 2011 com-

prising of 513 days of observations are used in this study. The MPL operates at the wavelength of 532 nm with a pulse repetition frequency of 2500 Hz and maximum pulse energy of 8 μJ. A Maksutov-Cassegrain type telescope having diameter of 178 mm is used for transmitting the laser beam and receiving the backscattered radiation. Detailed specifications of the MPL system are given in Chapter 2.

The MPL observations are made with a vertical resolution of 30 m and time integration of 60 s, and are used to derive the altitude profile of backscatter coefficient and linear depolarization ratio [*Rajeev et al.*, 2010; *Mishra et al.*, 2010]. The linear depolarization ratio (LDR) is a measure of the non-sphericity of the scatterers: larger non-sphericity leads to high value of LDR [*Rajeev et al.*, 2010]. Cirrus clouds, which are dominated by highly non-spherical ice crystals, are best discriminated from the high value of LDR (mostly between 0.1 to 0.4). These values of LDR are larger than that caused by aerosols in the upper troposphere [e.g. *Rajeev et al.*, 2010; *Mishra et al.*, 2010]. During non-precipitating conditions, observations using MPL were carried out almost continuously for about 60 h per week, albeit with short breaks. Sharp cloud boundaries, larger short-term variabilities of cirrus and their occurrence at the upper troposphere as ice crystals (high values of LDR) further enables the unambigious identification of cirrus clouds using dual polarization MPL observations. Ground based Lidar observations of cirrus clouds are hampered in the presence of optically thick clouds present below the cirrus clouds. This is a major limitation of the ground based Lidar systems, and hence data during such cloud conditions cannot be used to investigate the cirrus clouds occurring above optically thick clouds. Notwithstanding this limitation, Lidars can observe cirrus clouds formed from the outflow of convection formed elsewhere if the outflow region is away from the convection and overcast lower/middle level clouds. More importantly, the high sensitivity as well as dual polarization capability of the present system equips it to observe even very thin cirrus clouds at the tropopause altitudes.

6.2.1 Cirrus clouds as observed by Micropulse Lidar

Figure 6.1 shows a typical time-altitude cross section of the attennuated backscattered lidar signal (ABS, which is the range-corrected lidar signal) in the co- and cross-polarized channels observed during 03 to 05 February 2009. The X-axis shows time, expressed as fraction of the day. The vertical white bands represent data gap period during which MPL was temporarily shut down. White grains are because of poor signal-to-noise ratio (SNR) on account of daytime solar background noise. The corresponding image of LDR is depicted in Figure 6.1(c). The band having large values of attennuated lidar signal and very low LDR observed below $\sim$2 km is mainly caused by aerosols in the lower troposphere. Figure 6.2 is a vertically zoomed version of Fig-

ure 6.1. An almost continuous band of cirrus cloud around 15 km with thickness of ∼1.7 km, is manifested in Figures 6.1 and 6.2 as a distinct band having large values of ABS in both the Co- and Cross-polarized channels and is more prominent in LDR. Though its presence is not well discernible during the daytime due to the large solar background noise, the continuity in its appearance indicates that the entire cirrus band may be part of the same system. Notably, the cloud system shows significant time variations in its structure, as indicated by the variations in ABS and LDR. This might be because of the presence of individual patches in this cirrus cloud system. (It is important to note that a cirrus system originating from the source might compose of closely packed patches). Notwithstanding this, the altitude band of its appearance is remarkably stable (14 to 16 km) during the entire period displayed in Figure 6.1 which last for ∼43 hours. This example shows that a cirrus cloud system can persist for several hours to more than a day [*Taylor et al.*, 2011]. All the three days of observation is associated with near-absence of low- and middle level clouds except for a short duration of boundary layer clouds at ∼1.5 km altitude during the afternoon of 04 February 2009, above which the backscattered lidar signal is considerably weak. This results in the cirrus present around 15 km to become undetectable temporarily.

The values of ABS in the cross-polarised channel (Figure 6.1)), are distinctively larger for cirrus clouds while more spherical particles like water clouds (the boundary layer clouds in the afternoon of 04 February) have very small values. This is because of the larger nonsphericity of ice crystals in cirrus clouds and hence larger values of LDR compared to water droplets in low level clouds. The LDR values of cirrus clouds depicted in Figure 6.1 are generally in the range of 0.3 to 0.4 while those of aerosols are less than 0.1. This distinctiveness provide another handle for unambigiously identifying cirrus clouds.

6.2.2 Cirrus identification

Cirrus clouds are identified from the backscattered lidar signals in the co- and cross-polarized channels using the following conditions [*Nair et al.*, 2012]:

1. Base of the cirrus layer should be above 8 km at the beginning of its occurrence.
2. Base and top altitudes of cirrus clouds are determined from the altitude gradients of range-corrected lidar signal and LDR which should be at least 2 times more than the corresponding gradients observed outside the cloud boundaries.
3. Value of LDR within the cirrus layer should be at least 0.05 greater than the values observed above and below the cirrus layer, with a minimum absolute value of 0.06. (This value is selected based on extensive visual examination of the MPL data for a variety of cirrus layers in the upper troposphere).

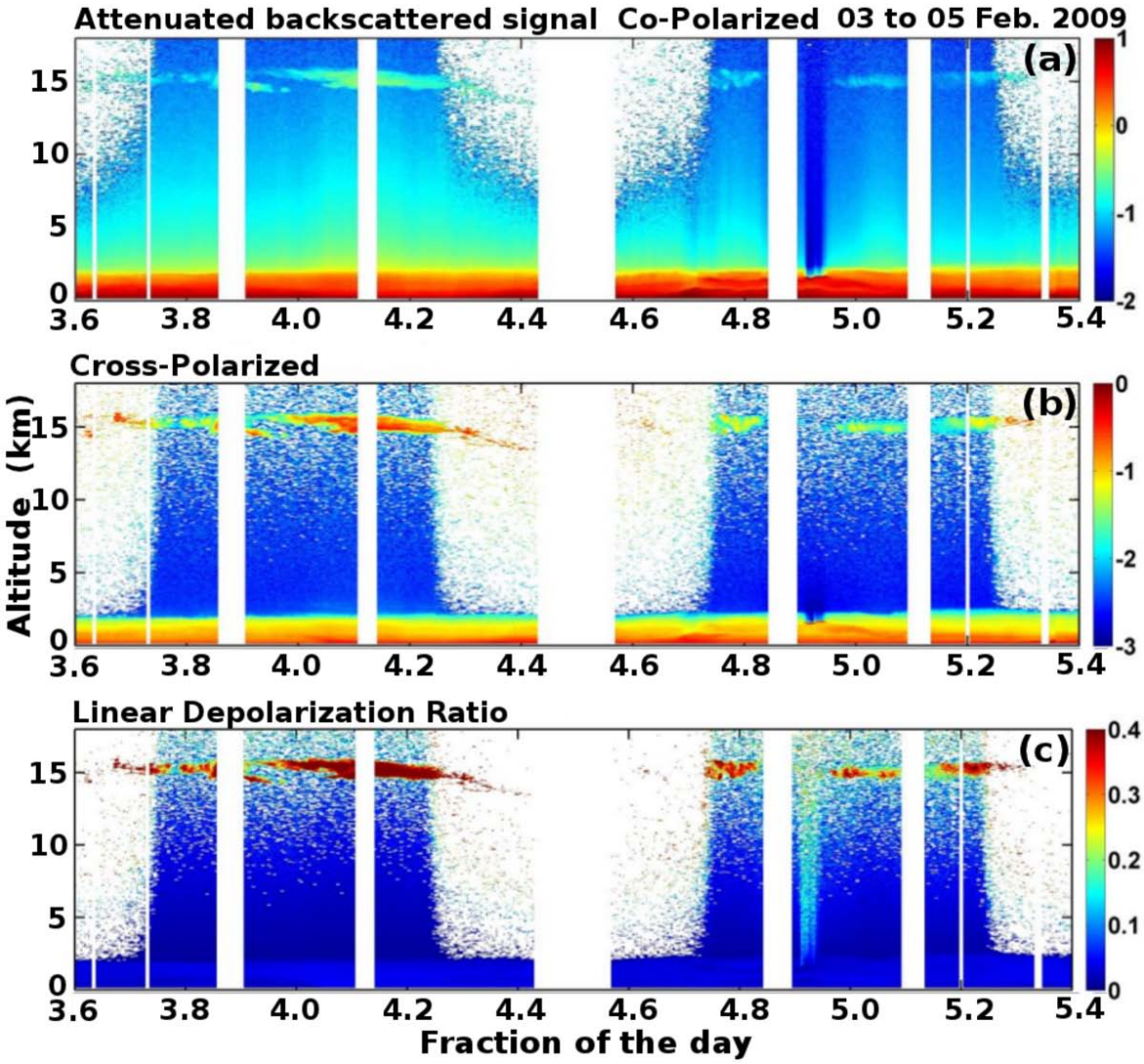

Figure 6.1: Time-altitude cross sections of the attenuated backscattered signal (ABS) during 15:00 IST on 3 February to 10:00 IST on 5 February 2009 in (a) Co-Polarizaed (b) Cross-Polarized channels. (c) shows the corresponding image of Linear Depolarization Ratio. Co- and Cross-polarisation observations are having units: counts.km^2.μs^{-1}.μJ^{-1}. White bands indicate the duration when the system was not operational.

4. Cirrus cloud detected using the above criteria should extend for at least 3 consecutive altitude bins (i.e., a minimum cirrus thickness of 90 m) and last for at least 6 successive time bins (i.e., a minimum duration of 6 minutes).

The last condition is enforced mainly to avoid spurious detection of cirrus clouds due to noise. The above criteria used to identify cirrus layers are consistent with that reported in the literature for lidar data analysis [e.g., *Sassen and Chow*, 1992]. Even thin cirrus clouds can be discriminated using the MPL data during night. However, due to the interference of background solar radiation (low SNR), optically thin cirrus clouds are

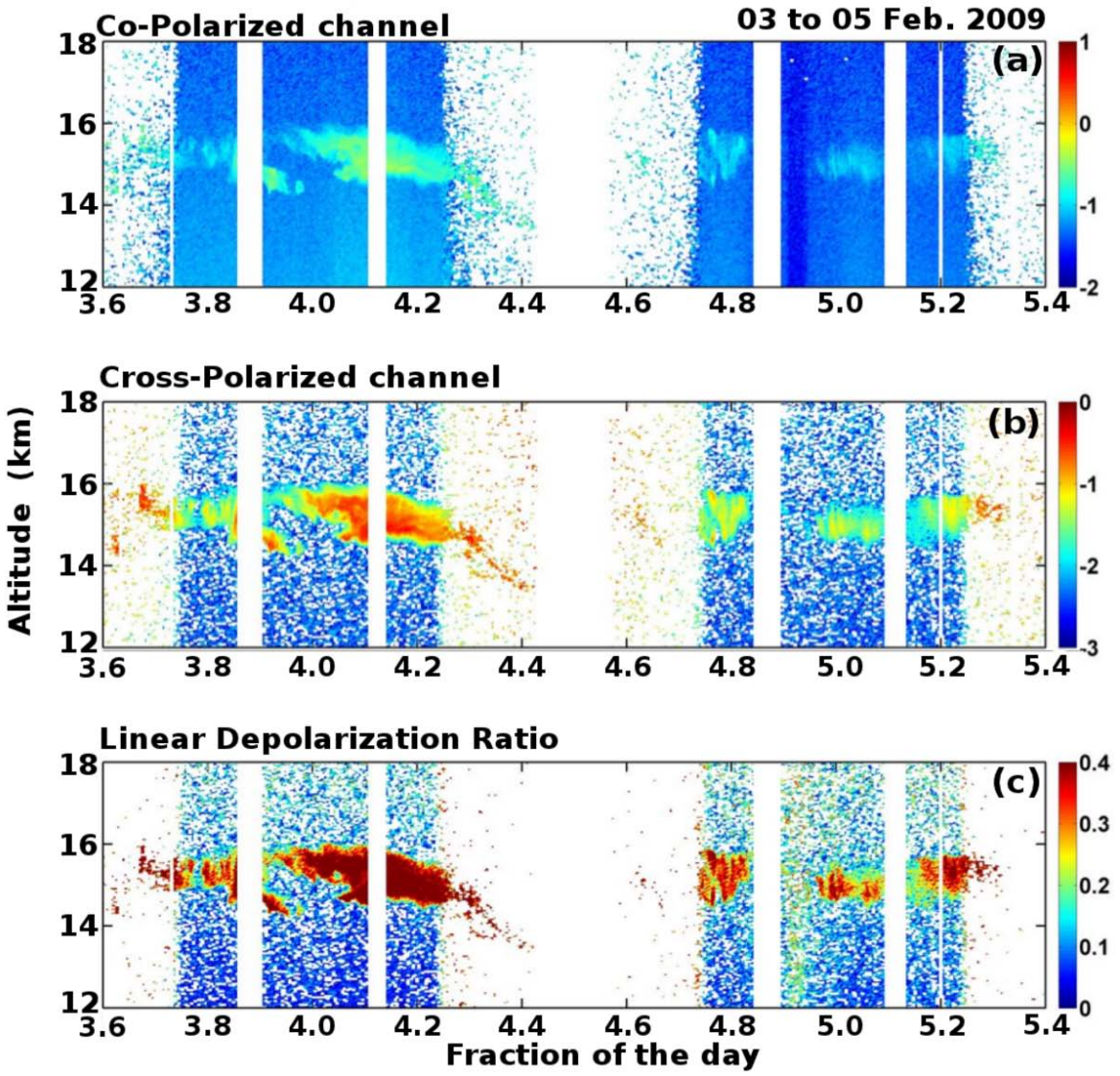

Figure 6.2: Same as Figure 6.1 but zoomed to the altitude range of 12 to 18 km.

not unambiguously discernible during daytime. Because of this day-night difference in cirrus detection, no attempt is made in this study to investigate the or diurnal variations in cirrus occurrence and their properties. As the occurrence of descending cirrus is not highly frequent, all unambiguous cirrus detections during both day and night are used in the present study to improve the statistics.

6.2.3 Identification of descending cirrus

One of the main features observed in the time evolution of cirrus clouds is their descending or ascending nature with time. Such persistent vertical movements are observed very frequently and can be caused by atmospheric waves or buoyancy effects. Figure 6.3 shows typical examples of cirrus clouds descending with time. However,

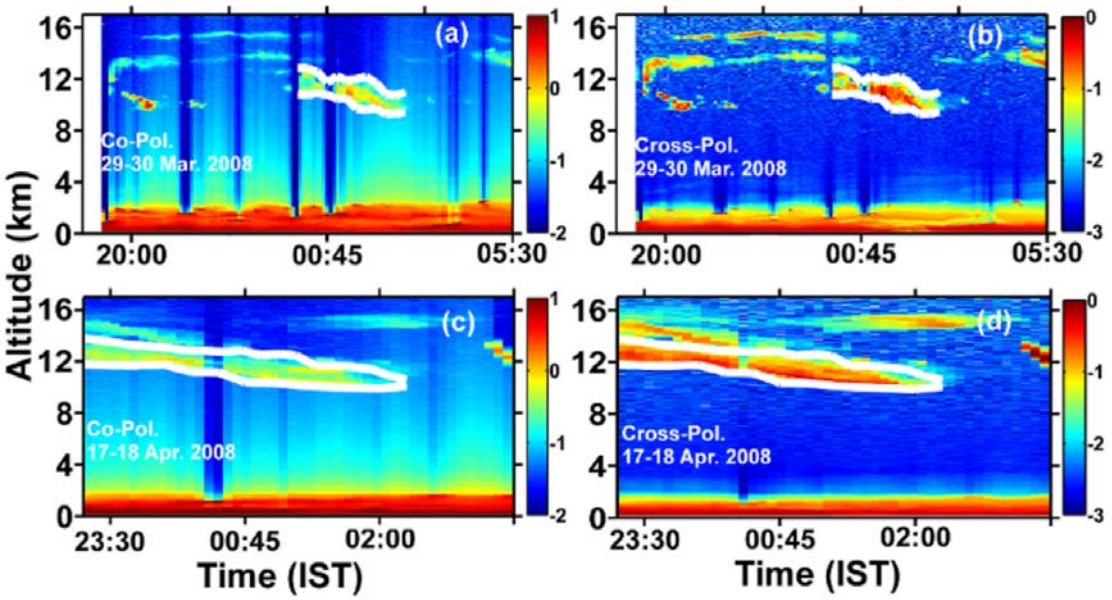

Figure 6.3: Time-altitude cross-sections of the attenuated backscattered lidar signal (ABS) in the co-polarised (left) and cross-polarised (right) channels on the nights of 29 March 2008 (top) and 17 April 2008 (bottom). The thick white lines indicate the top and base of the descending cirrus clouds detected using the criteria described in Sections 6.2.2 and 6.2.3.

the descending of cirrus clouds needs to be identified unambiguously and structural variations in a single cloud should not be misinterpreted for descending/ascending.

In the present study, a cirrus layer is identified as a descending cirrus only when the cloud base shows a consistent decrease for >30 min from the start, with a minimum vertical displacement of 300 m. Start of the descending cloud is marked as the time at which base of the cloud starts descending (in almost all cases this coincides with the first appearance of the cirrus). Similarly, end of a descending cloud is marked by the time when the base no longer descends (mostly, this coincides with the time when the cloud itself disappears). It is important to note that cirrus uncinus clouds have a characteristic 'hook-like' structure (with 'head' having a size less than 1 to 2 km) [*Ludlam*, 1956; *Heymsfield*, 1975; *Sassen*, 2002] and might appear as a descending structure when the cloud moves across the field of view of the lidar. However, the above criterion of minimum duration of cirrus descent (>30 min) would prevent this erroneous detection of cirrus uncinus as descending cirrus, as the spatial scale of the cirrus uncinus 'head (and hence its duration for passage over the site) is short.

6.2.4 Determination of cirrus properties

6.2.4.1 Physical properties

The physical properties of cirrus clouds (cloud base, cloud top, cloud thickness, duration) are determined quantitatively using the criteria described in Section 6.2.2. Descending cirrus is identified using the criteria given in Section 6.2.3. The speed of descending of the top (or base) of cirrus is determined by dividing the vertical displacement of the top (or base) with the duration of descending. The speed of descending of the top and base are calculated separately as the ice crystals of different size/shape/orientation need not have uniform fall velocity. In principle, cirrus cloud with an ensemble of ice particles having different sizes can have a slow descending of the top (as the smaller particles fall slowly compared to the larger ones, due to air drag) compared to the bottom. However, any vertical movement of airmass (associated with the mean circulation or atmospheric waves) can significantly hamper such a clear structure.

Typical examples of the time-altitude cross-sections of ABS received in the co-polarized and cross-polarized channels (of MPL) during the nights of 29 March and 17 April 2008 are shown in Figure 6.3. Multiple cirrus layers persisting for ∼2 to 4 hours were observed between 9 and 16 km during both these days. All the observed cirrus layers are semitransparent, as the lidar backscattered signal obtained from altitude regions are well discernible. In both these days, some of the lower cirrus layers appearing between 9 and 15 km show downward slanting structure, lasting for about 2 to 4 hours and descending by ∼2 km. Base and top altitudes of the descending cirrus layers determined using the criteria discussed above are marked with thick white lines. Other cirrus layers are also determined using the above method. Radiosonde observations show wind speeds of about 6 to 8 ms^{-1} persisting in this altitude region during the above days. The observed descending duration of 2 to 4 hours under such wind condition indicates that these descending cirrus structures might have horizontal dimensions in the range of ∼40 to 120 km. Strikingly, most of the upper cirrus layers which are ∼1 to 4 km above these descending layers have stable vertical structures. Proximity of such stable cirrus layer rules out the possibility of a strong downdraft in the upper troposphere or atmospheric waves as the causative mechanism for the descending cirrus. Physical and optical thickness of these descending cirrus layers are larger than the stable cirrus layers above. This shows that the descend of the above cirrus layers is likely to be associated with sedimentation of cloud particles.

6.2.4.2 Cloud Optical Depth (COD)

Optical depth of cirrus can be determined either by inverting the altitude profile of lidar backscattered signal using Fernald's or Klett's method [*Fernald*, 1984; *Klett*, 1985], or using the two-way transmittance computed from the attenuation of the Lidar backscattered signal as the laser beam pass through the cloud [*Young*, 1995]. Klett's and Fernald's methods require apriori information on the extinction-to-backscatter ratio of clouds, which in principle can vary over a wide range (typically 20 to 80). The two-way transmittance method [*Young*, 1995] does not require any assumption on the extinct-to-backscatter ratio or system constant.

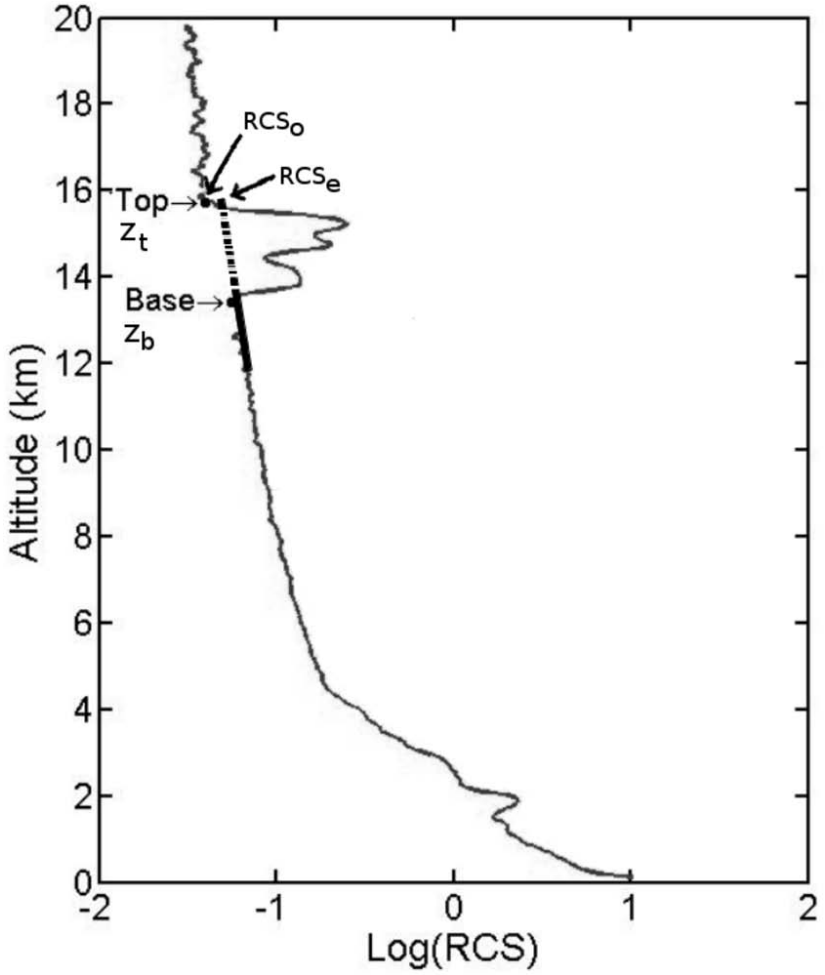

Figure 6.4: Altitude profile of range corrected lidar signal (RCS) in logarithmic scale. The cloud base and top altitudes are denoted by Z_b and Z_t respectively. The RCS values extrapolated from below the cloud base is indicated by the dashed line.

The COD presented in this chapter are obtained using the method suggested by *Young* [1995]. Figure 6.4 shows typical example of the altitude profile of range corrected lidar signal (RCS) when a cirrus cloud is present. Note that the extrapolated signal (RCS_e), obtained by regressing the RCS for a small altitude region below the cloud

layer (indicated by the dashed line in Figure 6.4) is the expected value of RCS if the cloud layer was not present between the altitudes, Z_b to Z_t. The two-way transmittance associated with the cloud layer has reduced the signal to RCS_o just above Z_t. Hence, RCS_e ans RCS_o are related as:

$$RCS_o = RCS_e e^{-2\tau} \tag{6.1}$$

i.e.,

$$\tau = \frac{1}{2} ln(\frac{RCS_e}{RCS_o}) \tag{6.2}$$

τ is the optical depth of the layer between Z_b and Z_t. The factor 2τ is because of the 2-way transmittance of the laser beam through the cloud. The value of τ is contributed by COD, molecular and aerosol optical depths within the layer between Z_b and Z_t.

However, as the cirrus clouds occur mostly above 8 km, the above contributions due to aerosols and molecules are very small compared to that of cirrus clouds [e.g., *Young*, 1995; *Rajeev et al.*, 2010]. Molecular optical depth between the altitude of Z_b and Z_t is estimated using the monthly mean profiles of atmospheric density obtained from atmospheric model based on long-term radiosonde observations over the site [*Sasi and Gupta*, 1986]. The aerosol contribution to COD is neglected. Only night time profiles are used for determining COD, mainly to avoid the errors due to low SNR conditions during the day. In order to increase the SNR (and reduce the errors), the backscattered lidar signal is integrated for a minimum period of 10 minutes for determining the COD. This integration may go up to 20 minutes for improving the SNR; COD will not be determined if the SNR is so poor that the boundaries of the cloud are not well discernible. The mean COD for the cloud (average of all CODs determined during the cloud duration) only is presented here. Sensitivity analysis shows that the maximum uncertainty in COD derived using this method is less than 20%. The mean optical depth of the descending cirrus (depicted in Figure 6.3) on the night of 29 March 2008 is 0.44 ± 0.12 and that of 17 April 2008 night is 0.29 ± 0.09.

6.2.4.3 Linear Depolarization Ratio (LDR)

The linear depolarization ratio (LDR) is determined using the method proposed by *Flynn et al.* [2007] for the configuration of the dual polarization MPL (described in Chapter 2). Using the co-polarized and depolarized lidar signals, the depolarization ratio, δ_{MPL}, and hence the linear depolarization ratio (LDR, denoted by the symbol δ_L) are estimated [*Flynn et al.*, 2007] as:

$$\delta_{MPL} = \frac{|P_0|}{|P_{\pi/2}|} \tag{6.3}$$

and

$$\delta_L = \frac{\delta_{MPL}}{\delta_{MPL} + 1} \tag{6.4}$$

where P_0 is the lidar backscattered signal received when the Liquid Crystal Retarder (LCR) in MPL is operated with zero retardation (cross polarized channel for MPL configuration) and $P_{\pi/2}$ is when the LCR is operated with a quarter wave retardation (co-polarization channel for MPL configuration). As explained earlier, LDR is an indicator of the extent of non-sphericity associated with the scatterers [*Sakai et al.*, 2000; *Rajeev et al.*, 2010; *Mishra et al.*, 2010]. The larger the value of LDR, the higher is the non-sphericity of scatterers (ice crystals in the present case).

6.2.4.4 Frequency of occurrence of cirrus

The daily mean frequency of occurrence of cirrus at a given altitude is determined by dividing the number of profiles in which cirrus is present at that altitude during this day by the total number of profiles that cover up to this altitude in this day. The total frequency of occurrence of cirrus on a given day (immaterial of the altitude of occurrence) is determined by dividing the number of profiles in which cirrus is present in any altitude bin on that day by the total number of profiles on that day. Profiles that are contaminated by the obscuration caused by low altitude clouds are excluded from this analysis. The monthly mean frequency of occurrence of clouds during a month is determined by averaging the daily mean frequency of occurrence of clouds during that month. Similarly, the monthly mean altitude profile of the frequency of occurrence of cirrus in a month is determined by averaging the daily mean altitude profiles of the frequency of occurrence of cirrus during that month.

The daily mean cloud optical depth is obtained by averaging all the cloud optical depths observed during that day. Daily mean altitude profiles of LDR of cirrus are determined by averaging the cirrus LDR at each altitude in which cirrus is present during that day. The monthly mean values of COD, and LDR are determined by averaging the daily CODs and LDRs during the days in which clouds are present.

For descending cirrus layers, the vertical displacement of top and base of the clouds, duration and speed of descending are also determined. Using the above methods, various features of cirrus such as the altitude of cloud top and cloud base, mean COD and LDR are determined for further analysis.

6.3 Characteristics of cirrus clouds

6.3.1 Total frequency of occurrence of cirrus

Monthly mean frequency of occurrence of cirrus clouds (total, independent of their altitude of occurrence) observed using MPL, averaged during 2008 to 2011, is depicted in Figure 6.5, which shows a highly prominent annual variation with minimum occurrence (∼30%) during January to March and peak (∼75% to 85%) occurrence during June to August. The occurrence shows a systematic increase from March to May during the pre-monsoon season and continues to increase till July-August period of the summer monsoon season. A rapid reduction in cirrus occurrence is observed from August to September. A secondary maximum in cirrus occurrence is observed in November, followed by a decrease to the annual minimum by January-February.

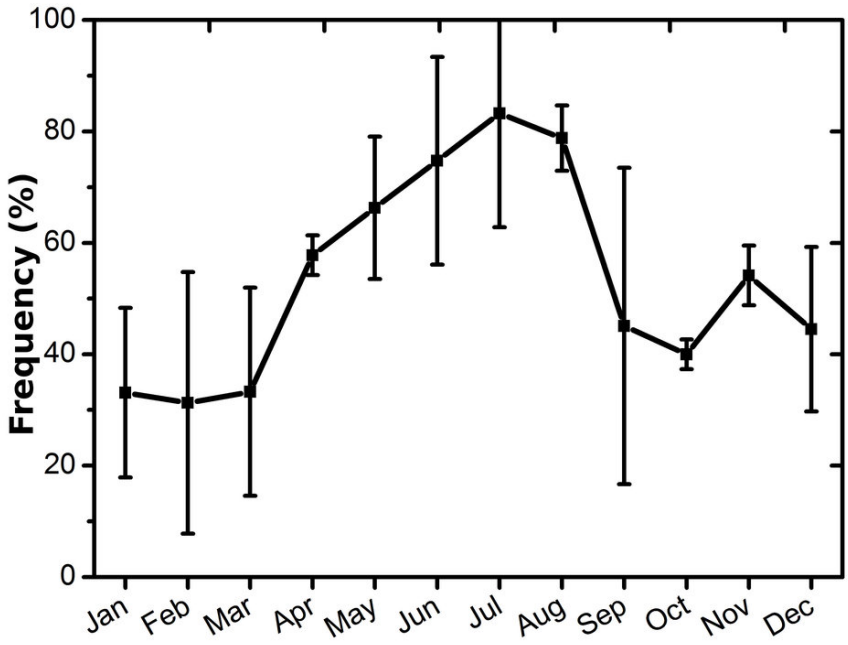

Figure 6.5: Multi-year (2008 to 2011) monthly mean frequency of occurrence (%) of cirrus over Thiruvananthapuram. Vertical bars indicate standard deviations.

As shown in Chapter 3, the winter season is characterized by a strong descending limb of Hadley circulation over the Indian region. During this season, Thiruvananthapuram is at the southern boundary of this descending limb, where convection is highly inhibited. In the absence of deep convective outflows, which is one of the main sources of cirrus clouds, the cirrus occurrence is mainly limited to those generated in situ. This leads to the lowest frequency of occurrence of cirrus clouds during the winter season. Over Thiruvananthapuram convection starts picking up from March and increases during April to May. This results in the increased availability of upper tropo-

spheric moisture and convective outflows, both of which increases the cirrus occurrence as seen in Figure 6.5. The largest occurrence of cirrus clouds observed during June to August is the result of intense deep convection taking place over the Bay of Bengal and the strong westward transport of moisture and cirrus outflows from these regions by the large upper tropospheric easterlies prevailing during the summer monsoon seasons [*Rajeev et al.*, 2008; *Sunilkumar et al.*, 2010]. This long range transport of moisture and cirrus clouds from the Bay of Bengal to the Indian subcontinent and the east Arabian sea by the tropical easterly jet stream (TEJ) is well discernible from the satellite observations of cirrus clouds determined using INSAT and KALPANA-1-VHRR data [*Sathiyamoorthy et al.*, 2004; *Rajeev et al.*, 2008; *Sunilkumar et al.*, 2010] and CALIPSO data [*Meenu et al.*, 2011]. This process weakens considerably from August to September leading to substantial reduction in cirrus occurrence. The secondary maximum observed in cirrus occurrence during November is due to the increase in the locally generated deep convection during this season, which is associated with northeast monsoon. The efficiency of this process diminishes in December. On a seasonal basis, the frequency of occurrence of cirrus is ∼36%, 52%, 70% and 47% during the winter, pre-monsoon, summer monsoon and post-monsoon season respectively (see Figure 6.9). Overall, the annual variation in the frequency of occurrence of cirrus clouds observed over Thiruvananthapuram is well in agreement with the regional distribution of cirrus observed using Kalpana-1-VHRR data [*Rajeev et al.*, 2008; *Sunilkumar et al.*, 2010], and is explainable on the basis of large scale atmospheric circulation as discussed above. Overall, the annual variations of cirrus occurrence depicted in Figure 6.5 is similar to that observed over Gadanki (13.5°N, 79.2°E) [*Parameswaran et al.*, 2003; *SunilKumar et al.*, 2003].

6.3.2 Altitude variation of the frequency of occurrence of cirrus (FOC)

Figure 6.6(a) shows the multi year (2008 to 2011) annual and seasonal mean altitude variations of the frequency of occurrence of cirrus (FOC)in the altitude range of 8 to 18 km. Notably, frequency of occurrence of cirrus below 9 km altitude is <6% during all seasons and shows a rapid increase above. Winter season is marked by a near absence of cirrus below ∼9 km. In general, the largest values of FOC occurs in the altitude band of 11 to 15 km during all seasons. Compared to other seasons the values of FOC are minimum at all altitudes below 15 km during winter. A weak increase in FOC is observed in the altitude band of 13 to 15.5 km during winter, above which it monotonically decreases to ∼5% at 16.5 km. During the pre-monsoon season, the peak occurrence of cirrus is observed between 11 to 15.5 km (FOC ∼15%) followed by a systematic decrease above. The cirrus occurrence during summer monsoon is

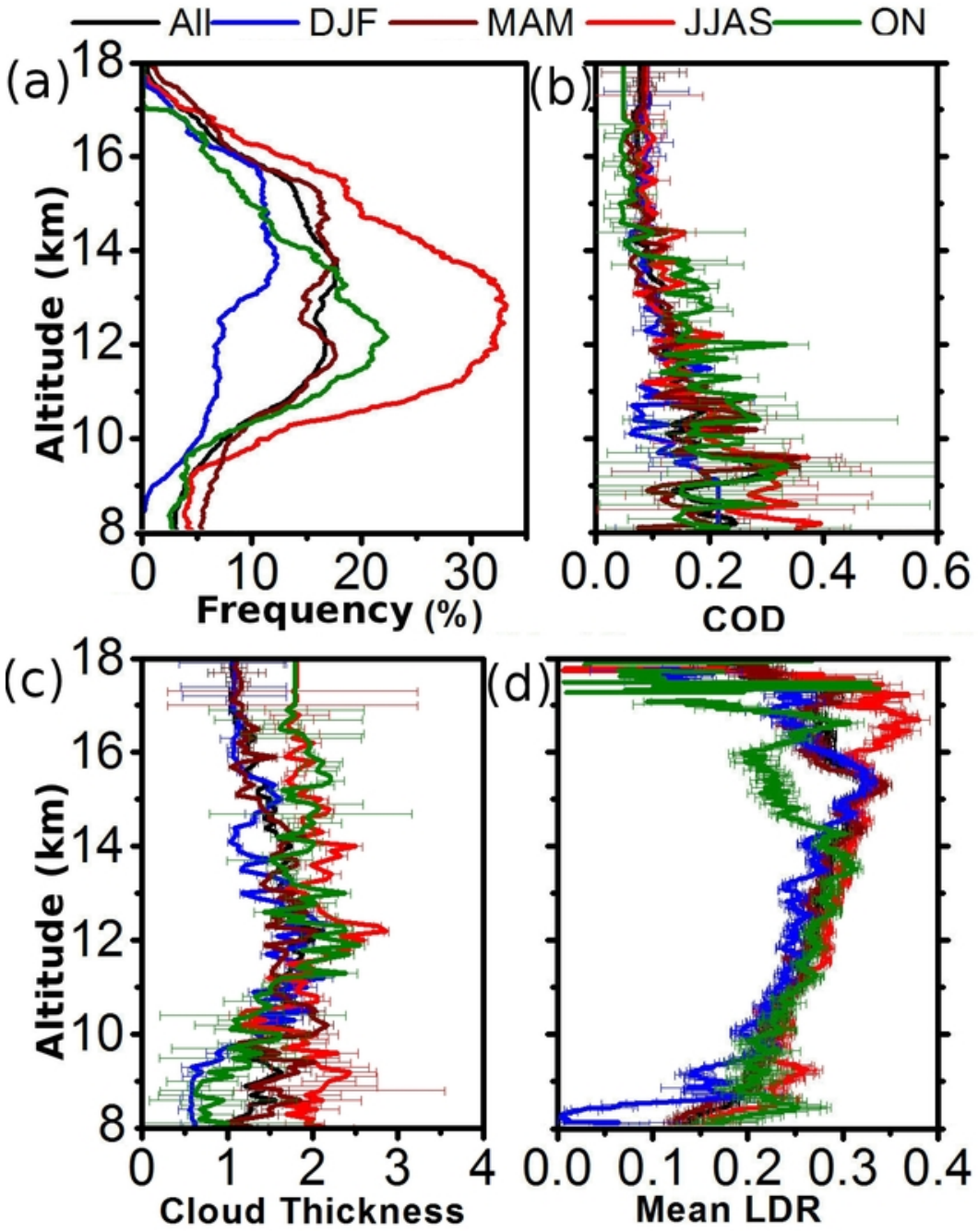

Figure 6.6: Multi-year (2008 to 2011) annual and seasonal mean (Winter-DJF, Pre-monsoon-MAM, Summer monsoon-JJAS, Post-monsoon-ON) altitude profiles of (a) frequency of occurrence of cirrus, (b) cloud optical depth, (c) cloud thickness and (d) LDR.

substantially larger than the other seasons in the altitude band of ∼10 to 16 km. The peak occurrence during this season is observed in the altitude range of 11 to 13.5 km where the FOC is >30%. The profiles of FOC during the post-monsoon season shows a relatively narrow peak between 11 to 13.5 km, above which its values monotonically decreases with altitude. The value of FOC above ∼16.5 km are comparable during all

seasons (<8%) and shows a monotonic decrease to ~3 to 6% above 17 km. Though very small (~2 to 4%) cirrus clouds do occur above ~17.5 km and are almost absent above 18 km. In this context, it is important to note that the mean cold point tropopause during all seasons appear in the altitude range of ~16.5 km (summer monsoon) to ~17.5 km (winter) [e.g. *Meenu et al.*, 2010]. The convective tropopause over the study region is generally in the range of 12 to 14 km [*Meenu et al.*, 2010; *Mehta et al.*, 2008; *Sunilkumar et al.*, 2012]. Thus the peak frequency of occurrence of cirrus occurs near the convective tropopause and ~2 to 4 km below the cold point tropopause layer (TTL). (The tropical tropopause region is defined as the altitude region between the convective tropopause and cold point tropopause). This clearly shows that the peak occurrence of cirrus as well as its rapid reduction above occurs in the TTL region. This is expected as the base of TTL is represented by the convective tropopause altitude above which the convection from below give way to large scale divergence and hence horizontal spreading of cirrus anvils.

6.3.3 Altitude variation of cloud optical depth

Figure 6.6(b) depicts the multi year (2008 to 2011) seasonal and annual mean variations of COD as a function of geometric centre altitude of the cloud layer. Geometric centre altitude represents the mid altitude of the cloud, obtained by taking the average of the base and top altitudes of the cloud. In general, COD decreases almost linearly with altitude during all seasons. At the altitude of ~8 km, the seasonal and annual mean CODs are in the range of 0.10 to 0.4 while the corresponding values at ~15 km ~0.05 to 0.12. Above ~15 km altitude, the altitude variations of COD are negligible and the absolute values of COD (~0.1) are comparable during all seasons. Though seasonal changes in the altitude variation of COD are not very large, the COD values in the lower altitudes (<10 km) are larger during the summer monsoon season compared to the other seasons. As indicated by the standard deviations, variability in COD is largest below ~10 km and considerably smaller at higher altitudes, especially above ~15 km.

6.3.4 Altitude variation of physical thickness of clouds

The multi-year (2008 to 2011) seasonal and annual mean altitude profiles of physical thickness of cirrus clouds (top minus base altitudes) as a function of the geometrical centre of the cloud are shown in Figure 6.6(c). In general, the cloud thickness (CT) shows an increase between the altitudes of 8 to ~12 km. On average the mean values of CT are in the range of 0.5 to 2 km at 8 km while the corresponding values at ~12 km are in the range of 1.5 to 2.5 km. During winter and pre-monsoon seasons, CT shows a weak decrease with increase in altitude, especially above 13 km. The mean

value of CT is ∼1 km in the altitude band of 15 to 18 km during these seasons. On the contrary, cloud thickness does not show any pronounced altitude variation above ∼12 km during summer monsoon and post-monsoon seasons. This seasonal contrast in cloud thickness is well discernable in the altitude band of 15 to 18 km in this region: the mean value of CT during summer monsoon and post-monsoon seasons is ∼1.8 km while the corresponding values is ∼1 km during winter and pre-monsoon season.

6.3.5 Linear Depolarization Ratio

The multi-year (2008 to 2011) seasonal and annual mean altitude variations of cirrus LDR are depicted in Figure 6.6(d), which clearly shows a systematic increase in LDR with altitude between 8 to 15.5 km altitudes. The absolute values of LDR as well as its altitude variation during all seasons are remarkably consistent in the altitude range of 10 to 14 km. The seasonal mean values of LDR are in the range of 0.2 to 0.25 at ∼10 km altitude and increases to ∼0.25 to 0.32 at 14 km. This shows that the non-sphericity associated with cirrus crystals systematically increases with altitude. This variation might be associated with corresponding variation in the ice crystal shape/non-sphericity with decrease in temperature [e.g. *Heymsfield et al.*, 2003]. Except during the post-monsoon season, LDR values continues to increase up to ∼15.5 km (winter and pre-monsoon) and ∼16.5 km (summer monsoon season). Remarkably, the values of LDR decreases rapidly above this peak altitude. Their values are generally in the range of 0.1 to 0.2 at ∼17.5 km altitude, which are distinctly smaller than their corresponding seasonal mean values observed at ∼15 to 17 km. Note that this decrease in LDR occurs very near to cold point tropopause or just above it. As seen in Figure 6.6(a) the frequency of occurrence of cirrus is very small at these altitudes. Furthermore, the COD as well as the physical thickness of clouds are also smaller in this region. These properties suggest that the cirrus clouds in this very cold environment (with small moisture content, especially above the cold point tropopause) might have been formed in situ and are rather small and/or relatively less asymetrical in shape. This inference is further supported by the limited observations of the varieties of the size and shape of cirrus with altitude and cloud temperature using aircraft sampling carried out at limited geographical locations [*Heymsfield et al.*, 2003].

6.3.6 Classification of clouds using COD

An important classification of cirrus clouds is based on COD as: (i) sub-visual (COD$\leqslant$0.03), (ii) thick (0.03$<$COD$\leqslant$0.3) and (iii) dense (COD$>$0.3) cirrus. Radiative effects of cirrus clouds increases from sub-visual to dense cirrus. The most potential mechanism for the generation of sub-visual cirrus is in situ production while that of dense cirrus is from convective outflows. Table 6.1 shows the frequency of occur-

rence of cirrus clouds (in percentage) under the above three classes during different seasons. During all seasons, the probability of occurrence is largest for thick cirrus (0.03<COD<0.3). About 64 to 73% of clouds are under this category. In contrast, the percentage occurrence of sub-visual cirrus is 18 to 24% and that of dense cirrus is 3 to 17%. The largest occurrences sub-visual and thick cirrus are observed during winter (24 and 73% respectively), while that of dense cirrus is the least (<3%) during this season. This is expected as the moisture availability in the upper troposphere as well as the probability of occurrence of cirrus from deep convective outflow (both which can lead to dense cirrus) are the least during winter. The occurrence of dense cloud is largest during post-monsoon season (17%). The distribution of sub-visual, thick and dense cirrus during the summer monsoon and post-monsoon seasons are somewhat similar. The occurrence of sub-visual cirrus is smaller and that of thick and dense cirrus are larger during these seasons.

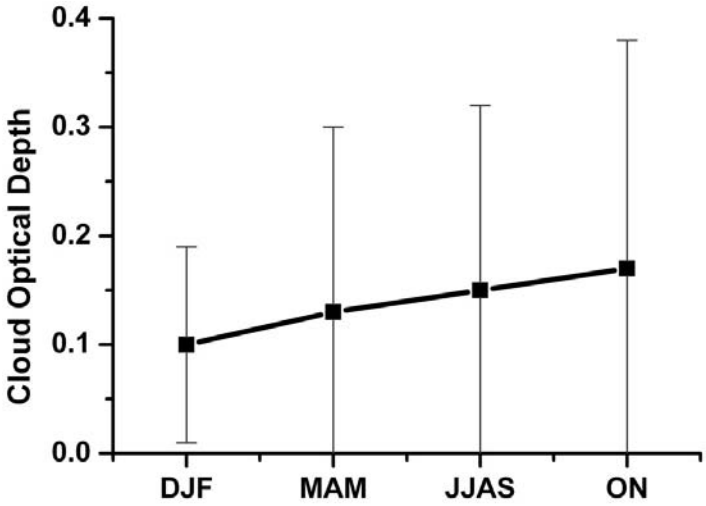

Figure 6.7: Seasonal mean variation of COD. Standard deviations are represented by the vertical bars.

Figure 6.7 depicts the seasonal mean variations of COD during the four seasons. The seasonal mean COD during winter is ∼0.10 while the corresponding values during the summer monsoon and post-monsoon seasons are >0.15. This is mainly because of highly infrequent occurrence dense cirrus during winter (Table 6.1). The annual mean values of COD observed over Thiruvananthapuram is 0.14 ± 0.16. In general, the seasonal variations in COD and the frequency of occurrence of sub-visual, thick and dense cirrus clouds observed over Gadanki are comparable to those reported here [*Sunilkumar and Parameswaran*, 2005; *Sunilkumar et al.*, 2008]. However, the frequency of occurrence of sub-visual clouds over Gadanki [e.g. *Sunilkumar and Parameswaran*, 2005] is generally larger than those observed during all seasons.

Table 6.1: Frequency of occurrence of cirrus (%): classification based on COD.

COD Season	<0.03 sub-visual	0.03 to 0.3 thin	>0.3 thick
DJF	24	73	3
MAM	24	65	11
JJAS	18	68	14
ON	19	64	17

6.3.7 Relationship among COD, CT and LDR

In principle, the physical and optical thickness of clouds might be related as the thicker clouds are expected to have larger values of COD. This correlation will be significant if the cloud extinction coefficient is constant for different clouds. Relationship between the physical and optical thickness of clouds during different seasons is explored using the scatter plot shown in Figure 6.8(a). Large scatter is observed in Figure 6.8(a), indicating that these two parameters are not highly correlated. The primary reason for the large scatter in Figure 6.8(a) is that the cloud extinction coefficient has large cloud-to-cloud variations. The correlation between CT and COD is extremely poor in winter. Notwithstanding this, a better positive correlation between CT and COD is observed during other seasons, especially at CT>2 km. Note that the cirrus clouds during winter is primarily generated through in situ production while those during the other seasons have larger contribution from convective outflows (pre- and post-monsoon seasons) and long-range transport (summer monsoon season). Figure 6.8(b) depicts the scatter plot of COD versus LDR, which shows a clear inter-dependence during all seasons. The range of variation of LDR consistently increases with COD. In general, for clouds with COD<0.2 the values of LDR can be in the range of <0.1 to ∼0.5. On the contrary, the range of LDR for COD>0.3 is about 0.2 to 0.4. This shows that while the optically thin clouds can have a large variation in non-sphericity, the dense clouds mostly comprise of highly non-spherical ice crystals; the relatively spherical ice crystals are almost absent in the dense cirrus clouds. The interdependence of COD and LDR is less prominent during winter (when COD values are rather small) and prominent during the other seasons. One of the reasons for this could be the highly infrequent occurrence of cirrus with COD>0.3 during winter.

6.4 Characteristics of descending cirrus

The long duration observations using MPL clearly revealed the descending nature of cirrus clouds in all seasons. Characteristics of the descending nature of cirrus clouds are presented in this section.

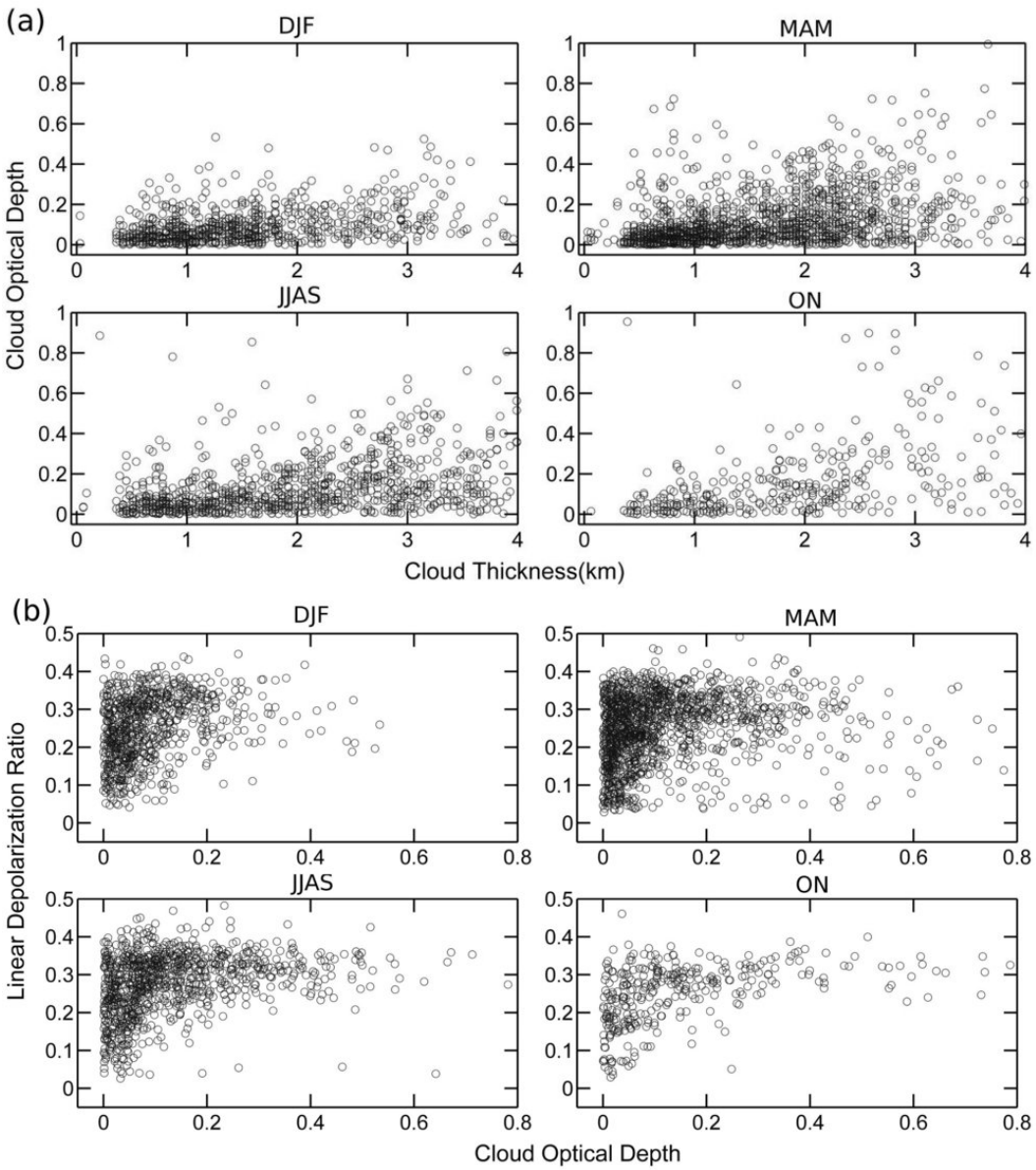

Figure 6.8: Scatter plots showing (a) CT versus COD and (b) COD versus LDR during different seasons.

6.4.1 Seasonal variation of the occurrence of descending and ascending cirrus

Descending structures similar to those shown in Figure 6.3 were observed on several days/nights throughout the year. Out of the 513 days of MPL observation during the study period (March 2008 to May 2011), cirrus clouds were present on 291 days and descending cirrus layers were clearly discernible on 103 days. The seasonal mean frequency of occurrence of cirrus clouds (with at least one cirrus layer) and descending cirrus clouds (in percentages) during the winter, pre-monsoon, summer monsoon and post-monsoon seasons are shown in Figure 6.9. The frequency of occurrence of cirrus

clouds that are ascending (detected by applying the same criteria as that applied for descending cirrus, but for the upward movement of the cloud base) are also shown in Figure 6.9 for comparison. The seasonal variation in the mean frequency of occurrence of cirrus clouds is also shown in Figure 6.9. The occurrence of descending cirrus is the largest during the pre- and post-monsoon seasons (∼23 to 24%) and least during winter (∼15%). It may be noted that multiple cirrus layer can occur during a given day. The fraction of the cirrus clouds that are descending out of the total cirrus occurrence could not be accurately estimated due to the highly frequent occurrence of multiple cirrus layers simultaneously, with variable overlapping time (see Figure 6.3). However, a basic estimate of this descending cirrus fraction can be obtained by taking the ratio of the frequency of occurrence of descending cirrus to that of the total cirrus, which turns out to be ∼42, 45, 26, and 49% during DJF, MAM, JJAS, and ON respectively. Remarkably, the fraction of cirrus clouds that are descending is the least during summer monsoon season when the occurrence of cirrus is the largest. During all seasons, the frequency of occurrence of ascending cirrus (<5%) is substantially smaller than those descending, which further confirms that the descending clouds mainly arise from ice crystal sedimentation. The ascending movement of cirrus clouds might have been the result of upper tropospheric updraft or atmospheric waves.

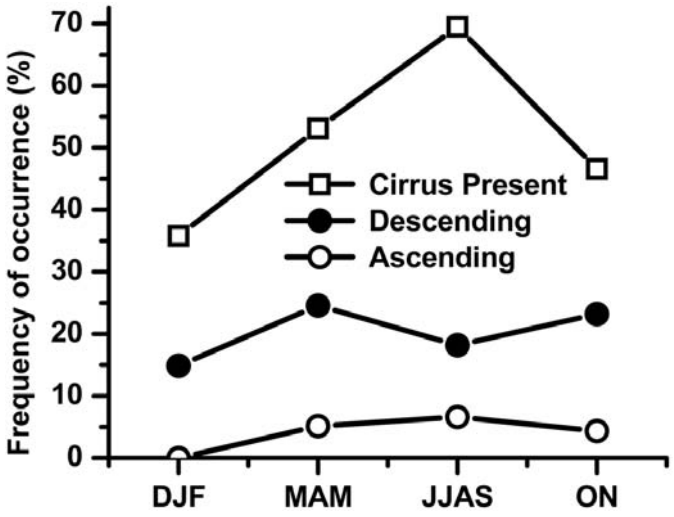

Figure 6.9: Seasonal mean frequency of occurrence (%) of total, descending and ascending cirrus clouds during winter (DJF), pre-monsoon (MAM), summer monsoon (JJAS) and post-monsoon (ON) seasons.

As the frequency of occurrence of ascending cirrus is very small, this study focuses only on the characteristics of descending cirrus clouds. During the pre- and post-monsoon seasons and winter, the upper tropospheric winds over the site are rather small (typically 5 to 10 ms^{-1}), while the summer monsoon season is manifested by strong upper tropospheric winds (with typical easterly wind speeds of 10 to 20 ms^{-1}). It is likely that the lowest occurrence of descending cirrus during the summer monsoon

season might be, at least partly, due to the rapid horizontal movement of cirrus clouds (caused by high-speed zonal winds), because of which the descending of cirrus clouds (observed as a function of time over a given location) will be minimum. This proposition is further supported by the occurrence of significant fraction of descending cirrus during the other seasons when the upper tropospheric winds are weak (because of which the cirrus clouds spend more time over a given location). However, this proposition needs to be further verified based on observations of the altitude profiles of vertical velocities in the troposphere and microphysical properties (especially size) of cirrus ice crystals, both of which can cause changes in descent rates of cirrus.

6.4.2 Altitude distribution of descending cirrus

As the season-wise number of descending cirrus observed are rather small to conduct a detailed statistical analysis of their seasonal mean characteristics, the remaining part of this chapter is based on the analysis by combining all of them for the entire study period and provide the multi-year annual mean picture of the characteristics of descending cirrus. The frequencies of occurrence of cloud top and base before and after descent are depicted in Figure 6.10 (a) (for cloud base) and Figure 6.10 (b) (for cloud top). In majority of cases, the cloud top is between 12 and 16 km before descent and between 9 and 14 km after descent. Similarly, in most of the cases, the cloud base is between 11 to 15 km before descent and between 8 and 13 km after descent. The peak of the distribution of cloud top, which is ∼14.5 km before descent, decreases to ∼11.5 km after descent. Similarly, the peak of the distribution of cloud base decreases from ∼13.5 km before descent to ∼11.5 km after descent. Over this study region, the annual variation of cold point tropopause is in the range of 16.5 to 17.5 km and the base of the TTL is around 11 to 14 km [e.g. *Meenu et al.*, 2010]. Thus, most of the cirrus clouds before descent occur around the TTL base and ∼2 to 4 km below the cold point tropopause. The frequency of occurrence of descending clouds above 15 km is considerably small. At end of descent, majority of these clouds reach altitudes that are up to 4 km below the mean TTL base. Based on the mean temperature profile derived from radiosonde observations at Thiruvananthapuram, average temperature of the most probable cloud top increases from ∼201 ± 2 K before descent to ∼216 ± 2 K after descent, yielding a mean enhancement of ∼15 K in the cloud top temperature. Probability distribution functions (PDF) of the cloud base and top altitudes before and after the descending are depicted in Figures 6.10 (c) and 6.10 (d). Although these plots show considerable spread in the PDF, the mean vertical displacement appears to be nearly uniform at all altitudes. The most probable downward displacements of cloud top and base are in the range of ∼1.5 to 2.5 km.

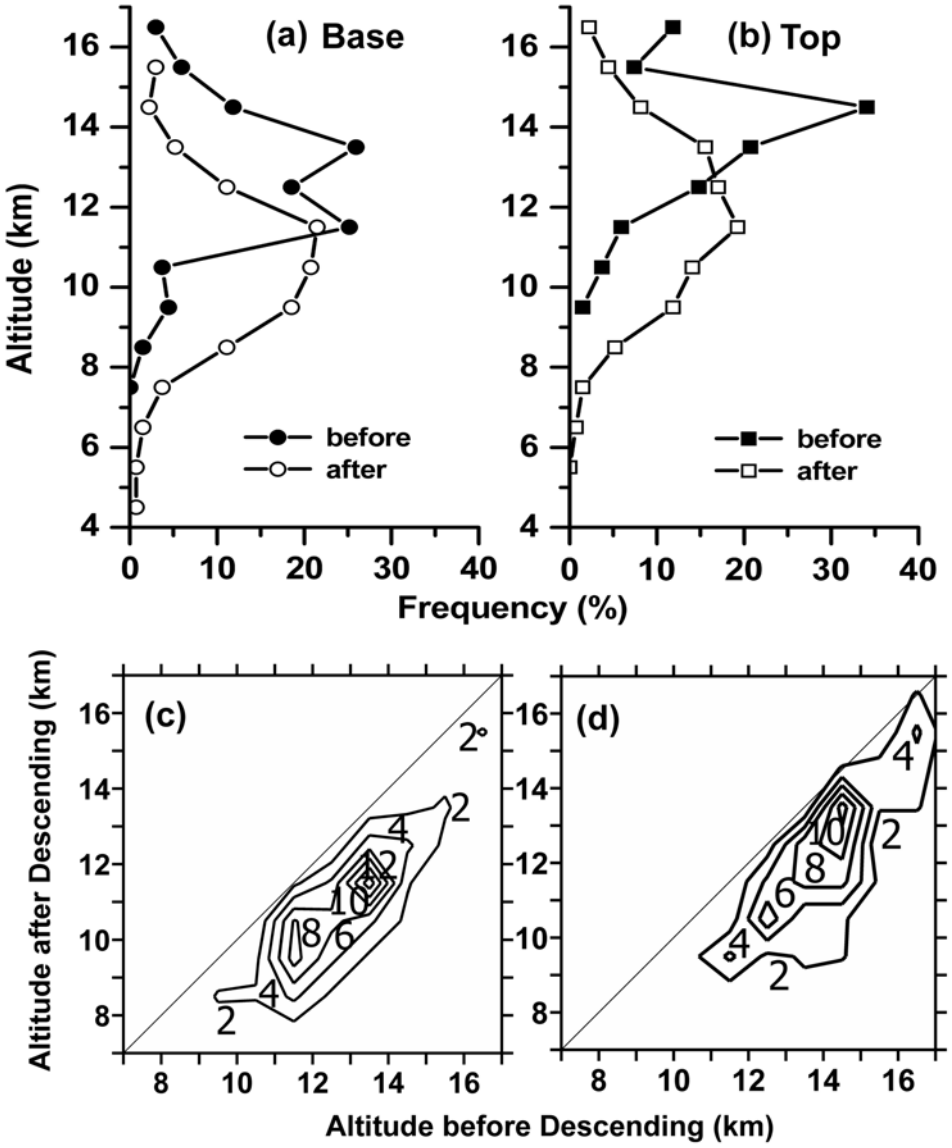

Figure 6.10: Distribution of the frequency of occurrence of the altitude of (a) cirrus-base and (b) cirrus-top before and after descent. Probability distribution function (PDF) for altitude before descent of the cirrus clouds versus altitude after descent for (c) cloud-base and (d) cloud top.

6.4.3 Displacement of cloud base and top

Figure 6.11(a) depicts the PDF of the vertical displacements of cloud top versus that of the cloud base which shows that, on average, the vertical displacements of the top and base generally have a one-to-one relationship. However, considering that the mean displacements of the base and top of the clouds are 2.07 ± 1.24 km and 2.01 ± 1.30 km respectively, spread in the PDFs shown in Figure 6.11(a) is significant. Difference between the vertical displacements of the top and base of cloud is maximum for displacements in the range of 1 to 3 km. Any non-uniform descending would result

in physical thinning (when top descends more than base) or thickening of the cloud (when base descends more than top). On average, the percentage of clouds that are thickening or thinning by >300 m during descending are almost equal (∼23% each), while the thickening/thinning of the remaining 54% is <300 m. The detailed analysis shows that, in >75% of the cases, vertical displacement of the cloud top and base is <3 km. In a few cases (∼2%), the cloud top and base have descended by >5 km.

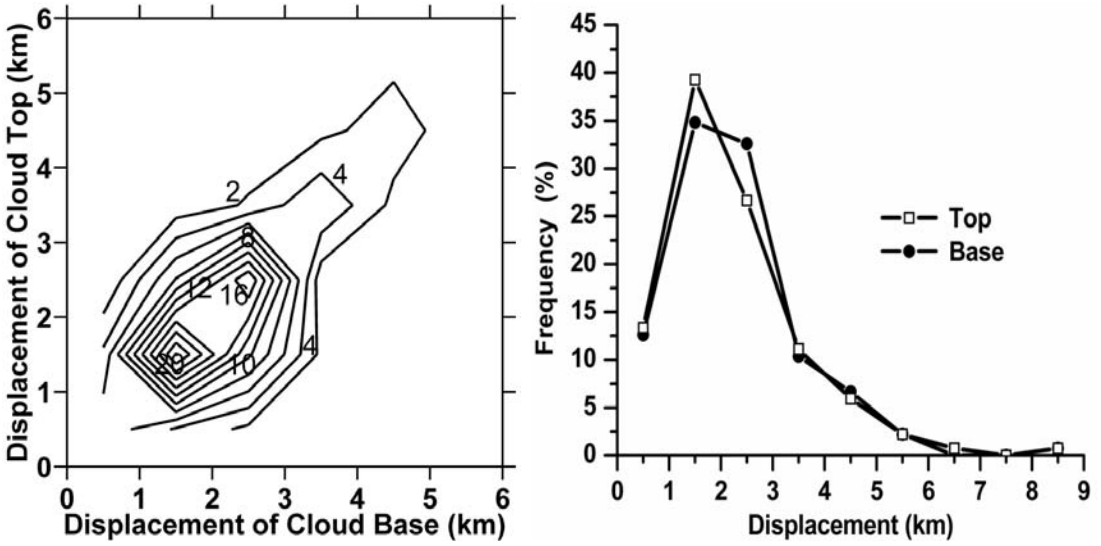

Figure 6.11: (a) Probability distribution function for downward displacement of cloud base versus that for cloud top for descending cirrus clouds. (b) Frequency distribution of displacement of cloud base and top.

6.4.4 Duration of descend

As evident from the histogram of frequency distribution of duration of the descend (Figure 6.12), the most preferred descent duration is between 1 and 2 hours. Probability of occurrence of descending clouds is found to decrease with increase in the descent duration. Out of the 136 cases of descending cirrus, 53% lasted for less than 2 hour. In about 8% cases the duration was less than 1 hour. Nearly 40% of cirrus had descent duration between 2 to 5 hour. Only in 7% cases did the descent duration exceed 5 hour. Some of the cases where duration was less than 1 hour min may be because of cirrus uncinus type of clouds where the cloud itself may be of 'hooked' shape. They usually have horizontal dimension of few kilometres. In the presence of strong upper tropospheric winds, the individual cells drift quickly.

6.4.5 Relation between duration and descending speed

The PDFs of the descent speed versus duration of descending for the top and base of cirrus clouds are depicted in Figure 6.13, which shows that the descent speed is

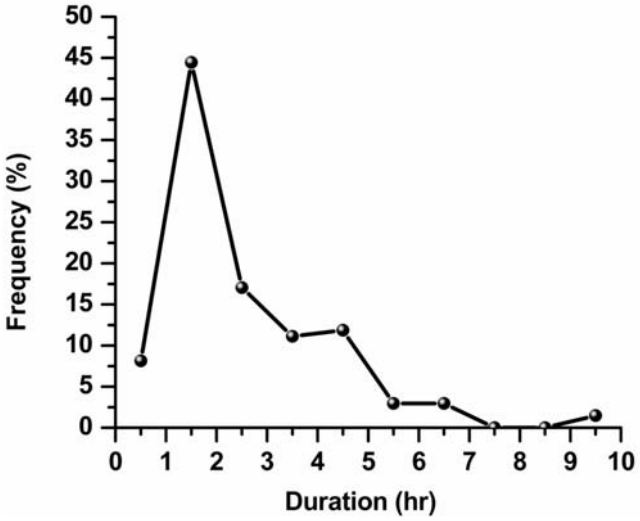

Figure 6.12: Histogram of duration of descend.

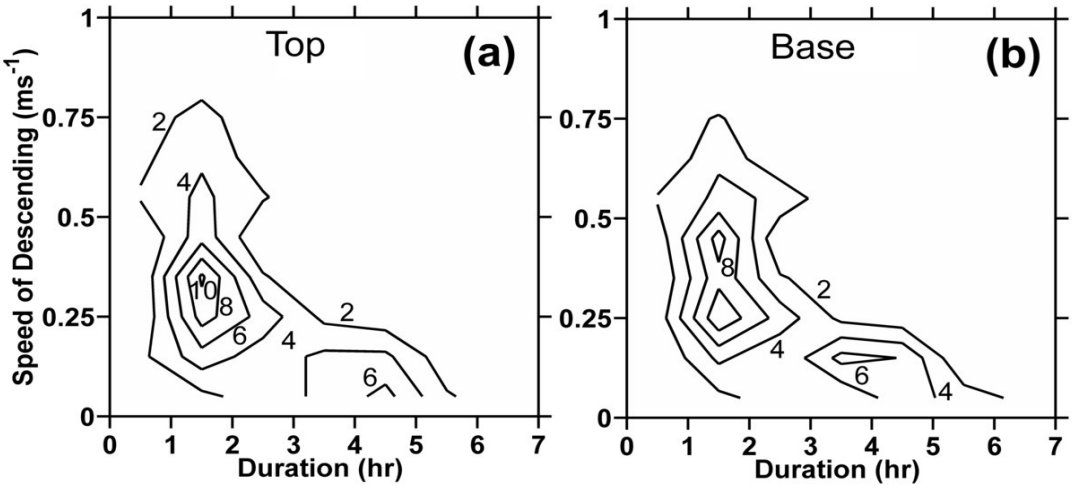

Figure 6.13: Probability distribution function for duration of descending versus speed of descending for (a) cloud top and (b) cloud base.

inversely proportional to the duration. Clouds having duration of <2 h have descent speeds varying over a wide range of ∼0.1 to 0.7 ms^{-1}, though most of them have descent rates of 0.2 to 0.5 ms^{-1}. In contrast, all cirrus layers lasting for >3 h have descent speeds of <0.28 ms^{-1}. This shows that, on average, the rapidly descending cirrus clouds dissipate faster than the gradually descending ones. Radiative heating at the cloud base and sublimation arising from sedimentation to sub-saturated regions are among the major dissipation processes for cirrus clouds [e.g., *Mace et al.*, 2006; *Jensen et al.*, 2011]. Considering this, the above relationship between the descent speed and duration is expected, since the slowly descending cirrus layers would take more time to reach the sub-saturated regions beneath. Furthermore, radiative cooling at the top of cirrus layers might decrease the cloud top temperature, thus maintaining higher

relative humidity with respect to ice and hence lesser dissipation compared to the fast descending ones.

Histograms of the speed of descending of both the cloud top and base (figure not shown) are similar and exhibit a monotonic decrease in the frequency of occurrence with increasing descent speed. About 69% of cloud top and 66% of cloud base have descent speeds <0.4 ms^{-1}, and 95% have descent speeds of <0.8 ms^{-1}. The average cirrus cloud sedimentation rates (average for both top and base) is 0.33 ms^{-1}, which is comparable to the mean cirrus sedimentation rates of 0.3 to 0.5 ms^{-1} reported by *Deng and Mace* [2008].

6.4.6 Relation between COD and duration of descend

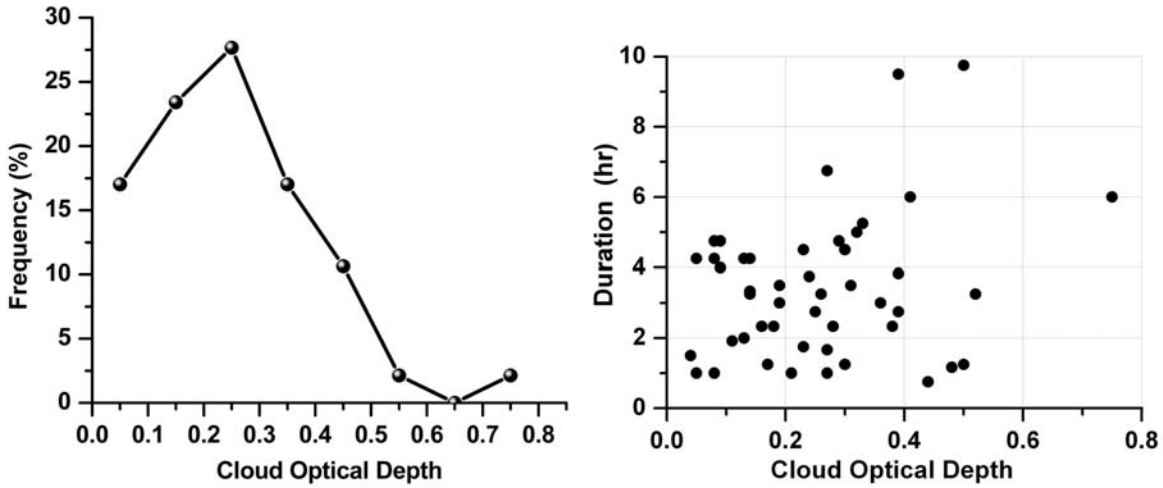

Figure 6.14: (a) Histogram of the cloud optical depth for descending cirrus clouds. (b) Probability distribution of cloud optical depth (COD) versus duration for clouds which descend.

Figure 6.14 (a) shows the histogram of the mean COD observed for the descending layers. In general, the mean COD ranges from 0.05 to 0.75, with a peak ∼0.25. Around 80% of descending cirrus have COD in the range 0.2 to 0.5. Statistically, around 68% of descending cirrus are thin cirrus (0.03 < COD < 0.3) and 32% are dense cirrus (COD >0.3). The seasonal mean CODs of descending cirrus are 0.16 ± 0.10, 0.27 ± 0.12, 0.30 ± 0.16, 0.30 ± 0.20 during DJF, MAM, JJAS, and ON respectively, which are larger than the corresponding mean cirrus cloud optical depths (all cirrus included) of 0.10 ± 0.09, 0.13 ± 0.17, 0.15 ± 0.17, 0.17 ± 0.21 during the above seasons. On average, descending cirrus has a larger optical thickness than typically observed in cirrus clouds. None of the descending cirrus is of sub-visual cirrus type (with COD <0.03). Note that, larger the value of COD, larger might be the ice water content [e.g., *Heymsfield et al.*, 2003]. It is likely that the sizes of ice crystals might

be small in clouds with very small ice water content (or COD); absolute magnitudes of cirrus sedimentation may be quite small to be observable in the lidar observations of descending cirrus. This could probably be responsible for the fact that none of the observed SVCs are of descending type. A significant part of the tropical cirrus clouds formed in the TTL layer, especially near cold point tropopause, have low values of COD (mean COD <0.1; see Figure 6.6(b). Figure 6.14(b) shows the PDF of COD versus duration of descending. Though the optically thicker clouds might be expected to have longer duration (as they might take more time to dissipate), Figure 6.14 (b) shows that the duration of descending does not show any prominent variation with COD. However, the longest durations are observed for the largest COD. The PDF of COD versus vertical displacement (figure not shown) also shows considerable spread, similar to that seen in Figure 6.14 (b).

6.4.7 Relation between COD and speed of descend

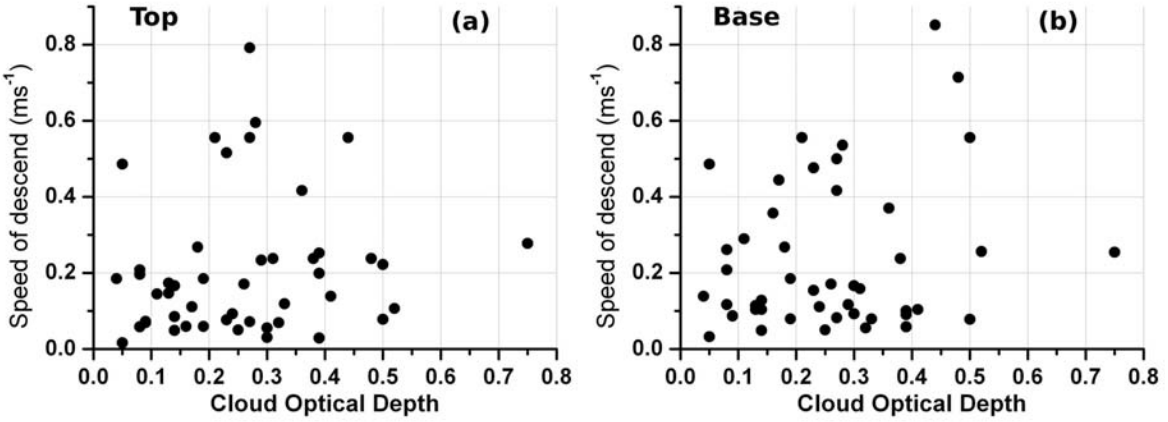

Figure 6.15: Probability distribution for cloud optical depth versus speed of descending for (a) cloud top, and (b) cloud base.

Figure 6.15 shows the PDF for COD versus descent speed for (a) cloud top and (b) cloud base. Though the mean descent speed and its range of variations are generally larger for optically thicker clouds, the relationship is rather far from robust. This might be due to the following reasons: (i) COD and ice crystal sizes might be poorly correlated, and (ii) the descent speed of cirrus might be significantly influenced by factors such as upper tropospheric vertical wind (which can alter the fall speed [*Lin et al.*, 2005; *Mace et al.*, 2006] and size, shape and orientation of the ice particles (the shape and its orientation might influence the air drag as the crystals sediments). The above observations (Figures 6.11(a), 6.13 and 6.15) indicate that, on average, both cloud top and cloud base descend with comparable rates with no significant thickening or thinning of the clouds. On the contrary, the cirrus clouds descending due to gravitational settling alone are expected to thicken with time as the cirrus might

contain a spectrum of ice crystals over a broad size range [e.g., *Frey et al.*, 2011] and therefore have different terminal velocities. At the cloud top, small ice crystals might remain, whereas the large ice crystals would fall and thus form a new cloud base. This spreading (rather separation of the sizes by gravity) should lead to (i) a broadening of the layer and (ii) different descent rates for top and base of the cloud. However, in general, the present observations indicate a significantly different behavior. This might be due to the dominance of the uplift (or downdraft) provided by vertical winds over the gravitational settling rates of ice particles (at least in majority of cases), which could significantly alter the actual descent rates of cirrus clouds. This suggests that the size of ice particles estimated from cirrus descent speeds (attributing it as arising only from sedimentation due to weight of the ice particles [*Das et al.*, 2010]) could be considerably different from their actual sizes. However, a robust physical explanation for the absence of cirrus broadening due to descending will require simultaneous measurements of vertical winds and cloud microphysical properties.

Main limitations of the present study are the absence of collocated observations of the altitude profiles of vertical wind, temperature, and humidity, which would have provided insight into the maintenance of cirrus layers by the upper tropospheric vertical winds, inferences on the actual sedimentation rates (and hence sizes) of cirrus ice particles, and the potential impact of cirrus descent on the thermodynamics and moisture content of the TTL. However, altogether, the results presented here clearly show that the descent speed of cirrus clouds is not merely governed by the sedimentation rate associated with the mass of the ice particles alone. This inference is in agreement with those reported by *Lin et al.* [2005] and *Mace et al.* [2006] who suggested that large scale vertical motions are important in maintaining the cirrus systems against particle sedimentation. More than 20% of the observed descending cirrus clouds have vertical displacements of >3 km and in few cases (∼2%) the cloud layers have descended by 5 to 8.5 km. About ∼7% of the descending cirrus layers have lasted for >5 h. These observations support the findings of *Heymsfield and Donner* [1990] that cirrus particles could fall through sub-saturated air for several kilometers, before fully sublimating. Neglecting the vertical wind in the upper troposphere and following the relationships between the fall speed and crystal size for different shapes [*Mitchell et al.*, 1996; *Das et al.*, 2010], the maximum dimension of ice crystals estimated from the present observations of descent rates are mostly in the range of 200 to 400 μm. However, in a background atmosphere with weak ascending motion, the cloud ice particle sizes inferred above could be an overestimate.

6.5 Change in cloud radiative forcing due to descending cirrus

Potential impact of the descending of cirrus on cloud radiative forcing (CRF) is investigated using radiative transfer model computations described by *Corti and Peter* [2009]. This is a simple model for estimating the long-wave and short-wave cloud radiative forcing (SWCRF and LWCRF respectively), and is based on parameterization for CRF that is estimated from detailed radiative transfer computations covering a global range of realistic atmospheric conditions, cloud properties, surface reflectance, and atmospheric profiles of temperature, ozone and water vapor. *Corti and Peter* [2009] have made extensive comparisons of this model with the CRF estimated from other models, which show that the accuracy of this semiquantitative parameterization is better than 20%. The LWCRF at top-of-atmosphere (TOA) for various combinations of COD and cloud top temperatures (which correspond to the cloud top altitudes being considered here and are obtained from the annual mean altitude profiles of atmospheric temperature over the site) are carried out using this model. The effect of descending of cirrus on the LWCRF is estimated by differencing the LWCRF for different cloud top altitudes from that for a reference altitude of 15 km, which is the typical cirrus cloud top altitude before descent, observed in the present study (Figure 6.16 (a)). Any variations in COD during descending are not considered here. The SWCRF at TOA due to cirrus descending is negligible. Thus, in effect, the change in LWCRF estimated here as a result of cirrus descending will be same as the change in net CRF due to descending.

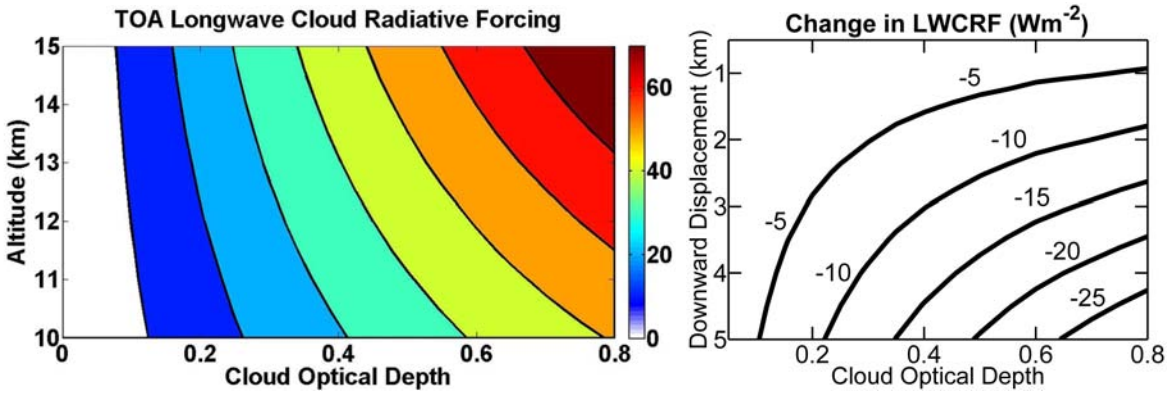

Figure 6.16: (a) Top of the atmosphere (TOA) longwave cloud radiative forcing (LWCRF in Wm^{-2}) at different altitude ranges (b) Change in LWCRF due to descending of cirrus having cloud top altitude of 15 km before descent, plotted as a function of cloud optical depth versus downward displacement. COD is assumed to be invariant during descending.

Figure 6.16 (b) shows contours of the change in LWCRF at TOA due to cirrus

descending, as a function of COD and downward displacement, for a cloud having cloud top altitude of 15 km before descent. As expected, the change in LWCRF at TOA is negative, indicating that the descending of cirrus decreases the LWCRF at TOA. The typical vertical displacements and CODs observed in the present study are in the range of 1.0 to 3.5 km and 0.1 to 0.4 respectively. This would result in a decrease of 1 to 12.9 Wm^{-2} in the LWCRF at the TOA due to descending of cirrus. For the observed mean COD of 0.26 and mean cloud top descending of 2.0 km, the reduction in LWCRF is 4.2 Wm^{-2}. Though rare, large descending (>4 km) of optically thicker clouds (COD >0.5) can decrease the LWCRF at TOA by more than 16 Wm^{-2}.

6.6 Summary and conclusions

Lidar observations of tropical cirrus clouds over Thiruvananthapuram, a coastal station located in the southwest peninsular India during March 2008 to May 2011 reveal a pronounced annual variation in the frequency of occurrence of cirrus, with minimum occurrence during winter months (especially January-February FOC ∼30%) and largest occurrence during the summer monsoon months of June to August (FOC ∼75 to 85%). While the cirrus occurring above the site during the summer monsoon season might be mainly advected from the deep convection outflows from the Bay of Bengal by the tropical easterly jet stream, those during winter might mostly be produced in situ. During pre-monsoon and post-monsoon seasons, localised convective outflows might generate cirrus. The largest frequency of occurrence of cirrus is observed in the altitude range of 11 to 15 km, irrespective of season. The peak occurrence of cirrus is observed near the base of the TTL layer. Majority of the cirrus clouds (64 to 73%) have COD in the range of 0.03 to 0.3 and are classified as thick cirrus. The frequency of occurrence of sub-visual cirrus (COD<0.03) is ∼18 to 24%. The non-sphericity of the the ice crystals is observed to increase substantially with altitude, upto ∼14.5 to 16.5 km. This is followed by a rapid decrease in LDR, especially above ∼16 to 17 km, indicating a corresponding change in their genesis. It is highly likely that the cirrus with low values of LDR observed near the cold point tropopause are formed in situ.

MPL observations have revealed significant occurrence of descending cirrus layers throughout the year. The duration of cirrus descending is so large that it cannot be attributed to the manifestation of cirrus uncinus. Probability of occurrence of descending cirrus is larger during pre-monsoon and post-monsoon seasons (about 23 to 24%) and least during winter (15%). Though the frequency of occurrence of cirrus clouds is largest (69%) during the summer monsoon season, the fraction of cirrus clouds that are descending is the least (<26%) during this season. The fractions of descending cirrus during the other seasons are ∼41 to 49%. The smaller fraction of descending

cirrus observed during the summer monsoon season might be due to the high-speed upper tropospheric easterlies prevailing during this season, which are responsible for the long-range transport of cirrus and moisture from the Bay of Bengal region. The most probable base (top) altitudes of descending cirrus layers are in the range of 11 to 15 km (12 to 16 km) before descent and 8 to 13 km (9 to 14 km) after descent. Most of the descending cirrus clouds form very close to the TTL base (around 14 to 15 km) and settle downward. The frequency of occurrence and vertical displacement of descending cirrus layers occurring within 2 km below the cold point tropopause is considerably smaller than those occurring at or below the TTL base. On average, the vertical displacements of the top and base of cirrus layers show almost a one-to-one relationship; the most probable vertical displacements are in the range of 1.5 to 2.5 km. The percentage of cirrus that are thickening or thinning by >300 m during descending are almost equal (∼23% each), while the thickening/thinning of the remaining 54% is <300 m. In >20% of the cases, the vertical displacement of the cloud top and base is >3 km. Most probable duration of the descending cirrus layers is 1 to 2 h (frequency of occurrence of ∼45%). However, nearly 40% of the descending cirrus lasted for 2 to 5 h. The frequency of occurrence of descending cirrus layers that last for <1 h or >5 h is very small (∼7 to 8%). The descent speed is inversely proportional to the cloud duration. All cirrus layers lasting for >3 h have descent speeds of <0.28 ms^{-1}. Around 95% of descending cirrus clouds have settling speed less than 0.8 ms^{-1} and none of these clouds are of sub-visual type (COD <0.03). Most probable value of COD for descending cirrus is between 0.2 and 0.3. On average, descending increases the cloud top temperature from ∼201 ± 2 K (before descent) to ∼216 ± 2 K (after descent), yielding a mean enhancement of ∼15 K in cloud top temperature. Radiative transfer calculations show that the descending of cirrus clouds would cause a typical reduction of ∼1 to 12.9 Wm^{-2} in the long-wave CRF at TOA (for vertical displacements and CODs in the ranges of 1.0 to 3.5 km and 0.1 to 0.4 respectively).

The results presented in this chapter would be useful for incorporating cirrus characteristics in general circulation models. The potential impact of vertical winds, atmospheric circulation and properties of ice particles on the descent speeds needs to be investigated in detail. Further, the impact of descending on the moisture budget of the upper troposphere needs to be ascertained based on collocated observations of descending cirrus layers with altitude profiles of temperature and humidity.

Chapter 7

Role of Clouds on the Energetics of the Earth-Atmosphere System

7.1 Introduction

Radiation budget and energetics of the earth-atmosphere system are strongly controlled by the ubiquitous clouds through several mechanisms, the most prominent among them being the latent heat release and cloud-radiation interactions. On average, the net radiation balance at the Earth's surface (balance between the incoming solar radiation absorbed at the Earth's surface and the terrestrial radiation emitted from the Earth's surface) is positive at the tropics. Transport of this 'excess energy' to the atmosphere (which has a negative net radiation balance) takes place through the sensible and latent heat fluxes [e.g., *Trenberth et al.*, 2009]. Latent heat liberated in the atmosphere during cloud droplet formation is the most effective mechanism for the transfer of this 'excess energy', which heat the atmosphere and modulate its thermal structure [*Houze*, 1982; *Trenberth et al.*, 2009]. The latent heating of the tropical atmosphere is estimated to account for about 75% of the total atmospheric heating [e.g., *Riehl and Simpson*, 1979; *Zuluaga et al.*, 2010], which would play a fundamental role in driving the tropical weather with scale sizes ranging from meso-scale to synoptic- and planetary scales [e.g., *Nigam et al.*, 2000]. Estimation of the altitude profiles of cloud latent heating of the atmosphere requires the altitude profiles of liquid and ice water content in the clouds. While the integrated values of liquid and ice water content in the atmosphere can be determined through microwave remote sensing techniques, accurate observations of their altitude profiles is highly limited. This is especially the case of non-precipitating clouds, which form the largest fraction of all the clouds present in the atmosphere. Due to these factors, quantitative studies on the role of clouds on the latent heating of the atmosphere are rather limited.

The term 'cloud radiative forcing' (CRF) denotes the influence of clouds on the radiation budget of the earth-atmosphere system [*Ramanathan et al.*, 1989; *Li and Trishchenko*, 2001]. Reflection of the incoming solar radiation by clouds reduces the amount of shortwave flux (SWF) reaching the earth's surface, and hence causes a net cooling at the surface. At the same time, this causes an increase in the upwelling SWF at the top-of-the-atmosphere (TOA). This is termed as the shortwave cloud radiative forcing (SWCRF) and is estimated by subtracting the shortwave radiative fluxes during clear-sky condition from that during 'any cloud condition' on a given day over the same region for identical solar zenith angle. At the TOA, this can be written as:

$$SWCRF = -(SWF - SWF_{clear}) \tag{7.1}$$

where SWF represent the shortwave flux on any given day over a given location and Local Time (LT) and SWF_{clear} represent the shortwave flux under clear-sky conditions over the same location and LT. The negative sign indicates that this radiative flux is lost from the earth-atmosphere system. Obviously, and as given by the above equation, the SWCRF=0 for cloud-free conditions. In general, the SWF under cloudy condition is greater than SWF_{clear} (except over highly reflecting surfaces like ice at low solar elevation angles), leading to generally negative values for the SWCRF. The value of SWCRF is governed by the reflectivity of the cloud, which primarily depends on the cloud properties such as optical depth, droplet size distribution and phase. On the contrary, the long-wave terrestrial radiation emitted from the earth's surface is absorbed by clouds and is in turn re-emitted at the ambient cloud temperature, which is lesser than the earth's surface temperature. As this emission takes place in all directions, part of the re-emitted radiation goes to space and the remaining to the earth. Effectively, this causes a trapping of the terrestrial IR radiation, which warms the earth's surface. This is called longwave cloud radiative forcing (LWCRF) and, as in the case of SWCRF at the TOA, it is expressed as:

$$LWCRF = -(LWF - LWF_{clear}) \tag{7.2}$$

where LWF represents the longwave flux at TOA at a location on a given day and local time under (under all conditions of cloud occurrence) and LWF_{clear} is the corresponding longwave flux over the same location and local time under clear-sky condition. Magnitude of the LWCRF depends on the top altitude (or temperature), optical depth (or transmittance) and emissivity of the cloud. As the cloud top temperature is generally colder than the surface temperature, the LWF_{clear} is larger than LWF under cloudy conditions and hence, the LWCRF is generally positive. The net effect of clouds (cooling or warming the earth-atmosphere system) will be determined by the net cloud radiative forcing (NCRF), which is the sum of SWCRF and LWCRF.

Satellite-based observations using the Earth Radiation Budget Experiment (ERBE) have provided the first direct quantitative assessment of the global variations in cloud radiative forcing (CRF), which gave new insights into the role of clouds on the climate system [*Ramanathan et al.*, 1989; *Harrison et al.*, 1990]. These observations showed that, on average, clouds cool the Earth-atmosphere system [*Ramanathan et al.*, 1989], magnitude of which were found to vary in the range of 14 to 21 Wm^{-2} between April 1985 and January 1986 [*Harrison et al.*, 1990]. Furthermore, the ERBE data showed that clouds have considerable effect on the spatial gradient of atmospheric and surface radiative heating. Effectively, the CRF leads to a reduction in the equator-to-pole radiative heating gradient of the planet [*Harrison et al.*, 1990]. In general, clouds are also found to reduce the seasonal changes in the net radiative heating of the earth-atmosphere system. In the winter hemisphere, the longwave and shortwave cloud forcing were found to nearly cancel each other, while in the summer the negative shortwave cloud forcing had significantly larger magnitude than the positive longwave cloud forcing, producing a strong cooling of the earth-atmosphere system [*Harrison et al.*, 1990]. In the tropics, the LWCRF and SWCRF attain their peak values over the regions of strong convection and tend to nearly cancel each other [*Kiehl*, 1994]. Large magnitudes and near-cancellation of the shortwave and longwave CRF in the tropical convective regions imply that clouds have a considerable influence on the vertical distribution of radiative heating between the atmosphere and the surface.

Based on the long-term data from ERBE and CERES instruments, *Wielicki et al.* [2002] showed that the tropical mean (20°N to 20°S) earth radiation budget have significantly changed during the late 1980s and the 1990s. The magnitudes of the global mean shortwave and longwave components of CRF are expected to be several times larger than that for the doubling of CO_2 [*Hansen et al.*, 1984]. Hence, small changes in the cloud radiative forcing can significantly affect the climate through feedback mechanisms. Changes in CRF were found to occur in response to cloud development and the conditions favouring them, especially the sea surface temperature and the large-scale vertical motion in the troposphere [*Yuan et al.*, 2008]. Averaged over the whole tropics, the ratio of shortwave to longwave cloud forcing is about 1.2 in the regions of upward motion, and increases to about 1.9 in the regions of strong subsidence [*Yuan et al.*, 2008]. In contrast to the near-cancellation of the average SWCRF and LWCRF over deep convective regions in the tropics [*Kiehl*, 1994], the net cloud radiative forcing at the TOA is negative over the Indian region during the Asian summer monsoon season: magnitude of the cooling by NCRF exceeds 30 Wm^{-2} over a quarter of the Asian summer monsoon region [*Rajeevan and Srinivasan*, 2000]. This large negative NCRF has been attributed to the presence of large amount of high-altitude optically thick clouds [*Rajeevan and Srinivasan*, 2000]. Spreading of cirrus clouds from the deep convective areas of the Bay of Bengal into the Peninsular India and the Arabian

Sea are also responsible for the enhanced cloud radiative forcing over these regions [*Sathiyamoorthy et al.*, 2004]. These aspects of cloud radiative forcing are unique over the Indian region. Notwithstanding the fundamental science contributions from the above studies using ERBE data, it is important to note the ERBE observations were basically using the data from radiometers onboard the polar Sun-synchronous satellites (observations limited to almost same local time of the day) and hence have limitations in studying the diurnal variation of CRF.

The main objectives of the studies reported in this chapter are:

1. Estimate the seasonal variations of cloud radiative forcing and their mean diurnal variations during the summer monsoon and post-monsoon seasons, and
2. Estimate the altitude variations of the seasonal mean latent heating of the atmosphere released by precipitating clouds over the Indian region.

The CRF is estimated from the data obtained from ScaRaB flown onboard the Megha-Tropiques satellite. This study is limited to July to November period of 2012, during which the ScaRaB data was released. Though the length of the ScaRaB data used here is rather limited compared to the other data sets used in this thesis, it provides an opportunity to explore certain important features which were not investigated in detail in the earlier studies using ERBE data. The latent heating of the atmosphere by precipitating clouds are studied using the data obtained from the Precipitation Radar (PR) onboard the TRMM satellite during 2006 to 2011.

7.2 Data and method of analysis

7.2.1 Megha-Tropiques ScaRaB data

The instantaneous shortwave and longwave fluxes at the TOA derived from the observations using the ScaRaB flown onboad the Megha-Tropiques (MT) satellite are used for estimating the cloud radiative forcing during July-November period of 2012. Details of the orbital characteristics of MT satellite and measurement of shortwave and longwave radiance at TOA using ScaRaB are given in Chapter 2. The conversion of the SW and LW radiance to the corresponding fluxes at TOA and the sources of uncertainty are also explained in Chapter 2 (section 2.4). Table 2.8 summarizes the spectral channels and characteristics of the ScaRaB instrument. As explained in Chapter 2, the Megha-Tropiques satellite revolves around the earth in a low-inclination orbit (inclination of 20°) with respect to the equatorial plane. As its orbital period is ~101.93 minutes, it makes 14 complete orbits per day.

The low inclination of the MT satellite provides better temporal coverage of the tropics. On average, a given location in the tropics will be covered up to a maximum of 6 times in a day, each observation corresponding to different local time. However, it is important to note that the frequency of observation of a location varies considerably during the precessing MT orbital cycle of 51 days: a given location may not be observed at a given local time for several days consecutively. The spatial resolution of ScaRaB is 40 km at nadir. The number of pixels per scan line is 51 and the total swath is ∼2200 km. As explained in Chapter 2, the radiance observed by ScaRaB in the shortwave and longwave bands are converted to the shortwave and longwave fluxes at TOA using ERBE-like Angular Distribution Models (ERBE-ADMs).

Comparisons of the ScaRaB-derived instantaneous fluxes with those from CERES for the same sun-pixel-satellite geometry were carried out by the instrument team [*Chomette et al.*, 2012; *Sathiyamoorthy et al.*, 2013]. These studies showed a constant bias error of ∼19 Wm^{-2} in the ScaRaB-derived shortwave fluxes. After correcting for this bias error, the instantaneous SW fluxes were found to follow a 1:1 relationship with the CERES data, with an RMS error of <26 Wm^{-2}. The longwave fluxes do not show any significant bias errors: the intercomparison showed an RMS error of ∼8 Wm^{-2}.

7.2.2 Estimation of SWCRF, LWCRF and NCRF from ScaRaB data

As explained earlier, the shortwave and longwave cloud radiative forcing are estimated as:

$$SWCRF = -(SWF - SWF_{clear}) \tag{7.3}$$

$$LWCRF = -(LWF - LWF_{clear}) \tag{7.4}$$

It is important to note that the above CRFs and fluxes are for a given pixel and Local Time. The local time variation of longwave flux depends on the surface and cloud properties. In addition to the cloud properties, the shortwave flux is also a strong function of the solar zenith angle (and hence local time of the day). The values of SWF_{clear} at a given geographical location and local time can be obtained through different ways: model estimates, reference data sets of clear sky fluxes from other sources, or direct observations using ScaRaB itself. The last method is followed here as it has the advantage of automatically eliminating the errors in the estimated values of SWCRF and LWCRF arising from the instrumental biases (the bias errors are same for clear-sky and cloudy pixels). This is especially advantageous as the instrumental

bias in ScaRaB-derived SWF is significant [*Chomette et al.*, 2012; *Sathiyamoorthy et al.*, 2013]. However, this method has an important limitation: a given geographical location should be devoid of clouds in each local time bin (of, say, 1 hour interval) during a month for generating the reference clear-sky fluxes as a function of latitude, longitude and local time. Further, though the ScaRaB observes a given geographical location up to 6 times a day, this location need not be observed at a given local time for several consecutive days. (Note that this is the advantage of a Sun synchronous satellite in which the observations are available at the same local time everyday notwithstanding the non-availability of observations at other times of the day). Due to the above reasons, the analysis is carried out here for an 'equivalent day' by combining all the observations at a given geographical location at 1-hourly time bins during a month. Though decreasing the time interval to less than 1 hour is more advantages, it leaves with large data-gaps, especially in SWF_{clear} and LWF_{clear}.

In the present study, the first step involved in the processing of the ScaRaB data is to segregate it into cloud-free and cloudy pixels and estimate the reference clear-sky fluxes. The Level-2 data contain information on the surface type and cloud condition (Note that the ERBE-like inversion of radiance to fluxes at TOA requires knowledge of the surface type and cloud condition). The surface type for a given geographical latitude and longitude is taken from the standard reference library, while the cloud condition of the pixel at the time of observation is determined from the narrowband radiances observed in the visible band and atmospheric window channels (channels 1 and 4) of ScaRaB and from collocated high-resolution observations using geostationary satellites). The clear-sky shortwave and longwave flux data (which are in pixel coordinate system) are then gridded to a uniform geographical grid with a latitude-longitude resolution of $1^\circ \times 1^\circ$ for a fixed local time interval of 1 hour by averaging all the pixel-level fluxes observed within the geographical grid and local time bin. It is most important to note that the time binning (1 hourly bin) must be done as a function of Local Time (LT) at the pixel and not as a function of UTC or any other standard time. This is because the radiative fluxes at a given location vary as a function of Local Time of the location. This analysis provides a 3-dimensional array of average clear-sky shortwave and longwave radiative fluxes as function of latitude, longitude and local time, for an 'equivalent day' for each month.

In the second step, the instantaneous cloud radiative forcing is estimated by differencing the clear-sky shortwave and longwave radiative fluxes (obtained using the method described above) from the pixel-level radiative fluxes, considering the latitude, longitude, and local time of observation of the pixel. The instantaneous cloud radiative forcing thus estimated are averaged to a uniform geographical grid with a spatial resolution of $1^\circ \times 1^\circ$ at local time bins of 1 hour by averaging all the pixel-level instan-

taneous CRFs estimated within the geographical grid and time bin during a month. This analysis provides the 'equivalent day' diurnal variation of SWCRF and LWCRF (at 1-hourly time bins) over a given geographical grid. The NCRF for a given geographical grid and local time bin is obtained by summing the corresponding SWCRF and LWCRF. As explained earlier, the estimated CRFs at 1 hour time bins have gaps over certain cloudy regions due to the non-availability of reference clear-sky pixels at that particular time on a given month. In order to minimize such data gaps, the estimated CRFs during the 'equivalent day' are further averaged at 3 hourly bins. The diurnally varying SWCRF, LWCRF and NCRF are integrated to obtain the diurnal mean SWCRF, LWCRF, and NCRF for the geographical grid during the month. The monthly mean values of SWCRF, LWCRF and NCRF are averaged to obtain the seasonal mean values of cloud radiative forcing.

7.2.3 Latent Heating Rates (LHR) from TRMM-Precipitation Radar data

The Precipitation Radar (PR) onboard the TRMM satellite provided the first-ever estimate of the vertical profile of the latent heat that is released by the precipitating clouds. The TRMM is a low-inclination (35°) satellite. The Precipitation Radar is a scanning radar operating at 13.8 GHz and detects the altitude-resolved radar signal scattered/reflected from precipitating clouds, which in turn is used to derive the radar reflectivity of these clouds. Details of the latent heating rates estimated from the TRMM-PR data are given in Chapter 2 (Section 2.5). Horizontal resolution of the TRMM-PR is 4.3 km at nadir, the range resolution is 250 m and the scanning swath width is 220 km. The radar reflectivity observed by PR can define the layer depth of the precipitation and provide information about the rainfall reaching the surface. Estimates of the rainfall (R) are carried out using the altitude profiles of radar reflectivity (Z) observed by the PR radar, employing the Z-R relationship [*Tao et al.*, 2006]. The estimated rain rates are used to derive the altitude profiles of latent heating of the atmosphere by the convective and stratiform precipitating clouds. Methodologies for estimating latent heating based on precipitation-rate profile retrievals obtained from TRMM measurements are described in *Tao et al.* [2006].

The present study employs the TRMM-PR-Level-3 product - the monthly mean convective and stratiform latent heating (CSH) - which has a spatial resolution of 0.5°×0.5° at 19 vertical levels from the surface to a height of 18 km. The CSH-LH data during 2006 to 2011 are used in the present study. This period also covers the duration of CloudSat observations used in this thesis (Chapter 3) to study the vertical distribution of clouds. The main drawback of this data set is that the CSH algorithm does not estimate the LHR in the absence of surface rainfall. however, on a large-scale,

the net LHR in the absence of surface precipitation is very small [*Zuluaga et al.*, 2010]. The CSH latent heat estimates had been evaluated using those estimated from in situ ground-based rainfall measurements and were found to be in agreement for different regions of the tropics [e.g., *Tao et al.*, 2001]. The spatial structure of the rainfall distribution and its temporal evolution (especially on monthly and seasonal scales) derived from TRMM-PR were found to be in agreement with that inferred from insitu observations [*Mitra et al.*, 2009]. Overall, the uncertainty in the instantaneous values of LHR estimated from TRMM-PR is expected to be quite large. However, the spatial and temporal averaging will reduce the overall uncertainty of the seasonal mean LHR to less than 30%.

7.3 Results and Discussion

7.3.1 Cloud Radiative Forcing at TOA

The mean shortwave and longwave cloud radiative forcing at the TOA during the summer monsoon and post-monsoon seasons are estimated from the radiative fluxes derived from the MT-ScaRaB data during July to November 2012, using the methodology explained in Section 7.2.2. The results obtained from this study are presented below.

7.3.1.1 CRF during summer monsoon season

Figure 7.1 shows regional distribution of the seasonal mean longwave, shortwave and net cloud radiative forcing (diurnally averaged) over the Indian subcontinent and the surrounding oceans during July-September period of 2012. The patches indicate the regions where the CRF could not be estimated due to want of clear-sky pixels. Note that the estimation of diurnal mean CRF based on the method followed in the present study require fluxes estimated from the clear-sky pixels in all the time bins; the absence of this information even for a single local time bin can result in the data gap in the diurnal mean CRF. However, it is important to note that the absence of clear-sky pixels in the ScaRaB data does not necessarily mean that the region is overcast throughout the period but that it is cloudy whenever the satellite overpass took place. This means, the absence of clear-sky pixels occurs over regions of large-scale cloudiness, but does not necessarily mean that this region has the largest frequency of occurrence of clouds.

The mean LWCRF during the summer monsoon is largest over the northeast Bay of Bengal, where its value is greater than 100 Wm^{-2}. The spatial variation of LWCRF in this region is remarkably large, especially towards the land areas. The CloudSat

and NOAA-AVHRR observations (presented in Chapter 3) show that this region has the largest frequency of occurrence of clouds, with the tallest cloud top altitudes. On average, the seasonal mean top altitude of optically thick clouds is greater than 14 km over this region. The seasonal mean LWCRF is in the range of 60 to 80 Wm^{-2} over the Indian land mass while it ranges from 40 to 70 Wm^{-2} over the east Arabian Sea and the equatorial trough region in the Indian Ocean. The LWCRF shows large spatial gradients towards the west Arabian Sea: a region of substantially small LWCRF (LWCRF<20 Wm^{-2}) is observed in the west Arabian Sea and the adjoining landmass. A region of enhanced LWCRF (with values between 40 to 70 Wm^{-2}) is observed over the central African region. The LWCRF is <25 Wm^{-2} over almost the entire southern hemispheric Indian Ocean at south of the equatorial trough. The lowest values of LWCRF (typically <15 Wm^{-2}) are observed over the Arabian landmass, the southwest Indian Ocean near Madagascar and adjoining parts of South Africa and the southeast Indian Ocean off the Sumatra coast.

The SWCRF is negative in all the regions. Similar to the LWCRF, the seasonal mean SWCRF is also largest over the northeast Bay of Bengal where its magnitude is 100 to 160 Wm^{-2}. The SWCRF has larger magnitudes (>90 Wm^{-2}) over the central African region as well. The lowest magnitudes of SWCRF are observed over the west Arabian Sea, Arabia and southeast Indian Ocean off the coast of Sumatra. Notwithstanding the above similarities between LWCRF and SWCRF, the following distinct differences are observed in their spatial variations. The magnitude of SWCRF is considerably large (>120 Wm^{-2}) over the northern parts of India, and is associated with the mean location of the monsoon trough. High values of the SWCRF are also observed along the west coast of Indian Peninsula, associated with the clouds occurring over the western side of the Western Ghats. Note that the magnitude of SWCRF depends mainly on the cloud albedo (cloud optical depth) while that of LWCRF depends on the cloud top temperature (cloud top altitude) as well as cloud optical depth. This shows that the clouds occurring over the Monsoon trough region as well as off the Western Ghats have albedo comparable to those occurring over the north Bay of Bengal, yielding comparable values of SWCRF over these regions. However, the top altitudes of optically thick clouds are largest over the north Bay of Bengal compared to the other regions, which explains the large differences in the values of LWCRF at these regions. These results are also in agreement with the spatial and vertical distribution of clouds presented in Chapter 3. Though the magnitudes of SWCRF over the equatorial trough region are significant (in the range of 40 to 80 Wm^{-2}), they are less prominent compared to the corresponding values at most of the other locations. This might be because of the relatively lower albedo of clouds occurring in this region.

One of the most remarkable features of SWCRF is its significant magnitude (20 to

40 Wm^{-2}) over the entire south Indian Ocean. Note that the corresponding values of LWCRF over this region are negligible. This is primarily because of the presence of large amount of low-altitude clouds which occur below ~2 to 3 km altitude. As shown in Chapter 3, top altitudes of the clouds occurring over the Southern Hemispheric Indian Ocean are generally <3 km. Hence the difference between the cloud top temperature and the temperature of the ocean surface would not be significant. This relatively small difference in cloud and surface temperatures explains the very small values of the estimated LWCRF over the south Indian Ocean. On the contrary, magnitudes of the SWCRF of these clouds are quite significant, indicating that their albedos are considerably large.

In almost all the regions, values of the NCRF are negative, indicating that the net effect of clouds is cooling. This net cooling occurs because the cooling produced by the SWCRF exceeds the warming produced by the LWCRF. Magnitudes of the NCRF are largest (>40 Wm^{-2}) over the Indian landmass especially over the monsoon trough region and off the Western Ghats. The NCRF are less prominent over the northeast Bay of Bengal which witnessed the largest magnitudes of SWCRF and LWCRF in the study region. The NCRF shows large cooling over the south Indian Ocean, the north Arabian Sea and most parts of the African region (including the coastal Africa), where the magnitude of the NCRF is >25 Wm^{-2}. This is primarily because of the weak warming produce by the LWCRF, which is far below the cooling produced by the SWCRF. Over most parts of the equatorial trough region in the Indian Ocean, the south and central Arabian Sea and the south Bay of Bengal, the warming produced by the LWCRF almost cancels the cooling produced by the SWCRF, yielding a nearly zero NCRF. These results clearly shows the significantly large net cooling effect over the regions dominated by the low-altitude clouds. In contrast, some of the regions of large-scale cloudiness and convection have negligible cooling effect (the equatorial Indian Ocean and the south-central Arabian Sea). However, the NCRF has a net cooling effect over the deep convective regions of the north Bay of Bengal as well as over parts of the Indian landmass covering the monsoon trough region and west of the Western Ghats. Large negative values of NCRF (-30 to -65 Wm^{-2}) are also observed over the northeast India and most parts of east Asia.

Most of the above described features, the absolute magnitudes of the LWCRF, SWCRF and NCRF as well as their spatial variations are similar to those reported by *Rajeevan and Srinivasan* [2000] based on the ERBE data during June to September period of 1985 to 1988. The values of NCRF at the regions of deep convection over the north Bay of Bengal, the northern parts of India and off the western Ghats and the regions of east Asia reported by *Rajeevan and Srinivasan* [2000] are in the range of -20 to -60 Wm^{-2}. The corresponding values observed in the present study are in the

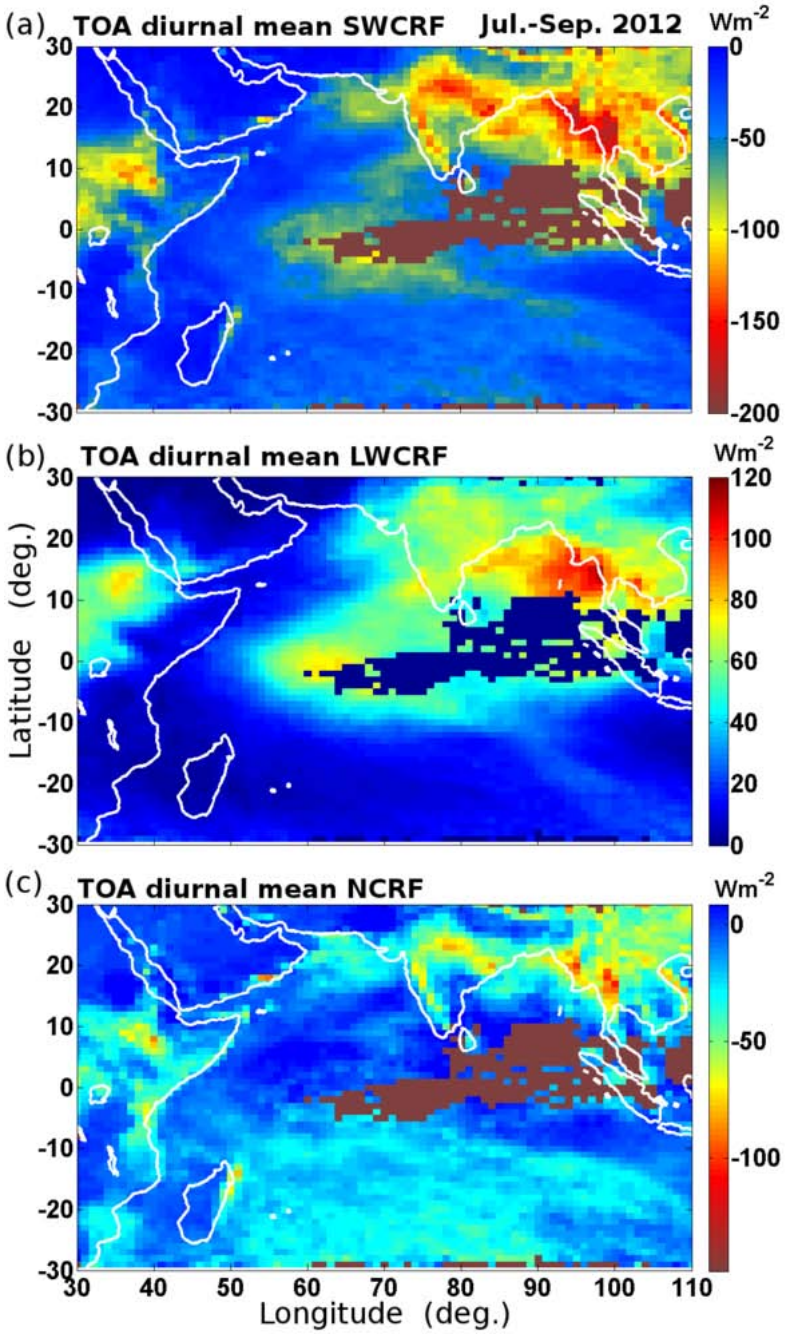

Figure 7.1: Regional distribution of seasonal mean LWCRF, SWCRF and NCRF at TOA (diurnally averaged) over the Indian subcontinent and the surrounding oceans during July to September period of 2012. The patches indicates the region where the CRF could not be estimated due to want of clear-sky pixels in all time bins.

range of -25 to -65 Wm^{-2}, and are in agreement with the values reported by *Rajeevan and Srinivasan* [2000], within the uncertainty limits. The cooling effect of NCRF over most parts of the central and east coast of Africa and the near-cancellation of SWCRF and LWCRF over the Indian Ocean and the south-central Arabian Sea are also in agreement in both these studies. Over most parts of the south Indian Ocean, *Rajeevan*

and Srinivasan [2000] shows that the NCRF is in the range of -10 to -20 Wm^{-2} while the present study shows that this value is mostly in the range of -20 to -25 Wm^{-2}.

7.3.1.2 Diurnal variation of LWCRF during summer monsoon season

Due to the absence of solar radiation, the SWCRF is zero during night. On the contrary, the LWCRF exists throughout the day and provides insight into the diurnal evolution of clouds and their radiative impact. Figure 7.2 depicts the diurnal variation of LWCRF derived from the ScaRaB data, by averaging the seasonal mean LWCRF at 3 hourly intervals for the 'equivalent day' of the summer monsoon season. A systematic diurnal variation is observed in LWCRF. The magnitude of this diurnal variation is largest over the deep convective regions of the northeast Bay of Bengal, where the LWCRF maximizes during 21 to 03 LT (LWCRF 100 to 110 Wm^{-2}) and minimizes during 09 to 15 LT (LWCRF 70 to 105 Wm^{-2}). Though the phase of the diurnal variation of LWCRF varies regionally, over most of the regions (including the continental regions and the Southern Hemispheric Indian Ocean), their values are minimum during the daytime (especially during the forenoon hours of 06 to 12 LT) and largest during the night or late evening. Figure 7.2 also shows that the LWCRF could not be estimated over certain regions during the night-time while it could be estimated over almost all regions during the daytime. The inability to estimate LWCRF at some locations during certain periods in the night – due to the unavailability of reference clear-sky pixels –has resulted in the data gaps shown in Figures 7.1 and 7.2.

In order to further quantify the day-night changes observed in Figure 7.2, the seasonal mean values of LWCRF averaged during the daytime (08 to 16 LT) and night time (20 to 04 LT) are presented in Figure 7.3. The difference between the daytime and night time values of LWCRF is also shown in this figure. The period around the morning and evening are avoided to get a clear picture of the day-night difference. Figure 7.3 shows that, over most regions having significant cloudiness, the LWCRF during the night time exceeds that during daytime by >10 Wm^{-2}. This is the case over the north Bay of Bengal, the east Arabian Sea, and the continental regions of India and central Africa (African monsoon region). Over the deep convective regions, the night time value exceeds the daytime LWCRF by >20 Wm^{-2}. Strikingly, the night time values of LWCRF are also larger over the southern hemispheric Indian Ocean which is dominated by shallow clouds limited to less than ∼3 km altitude. On the other hand, the daytime values of LWCRF are larger mainly over the coastal regions of east Africa where the overall cloud amount is rather small.

Note that the LWCRF can increase with decrease in cloud top temperature (usually associated with the vertical development of clouds and increase in cloud top altitude), increase in cloud amount, transition from optically thinner clouds to thicker clouds or a

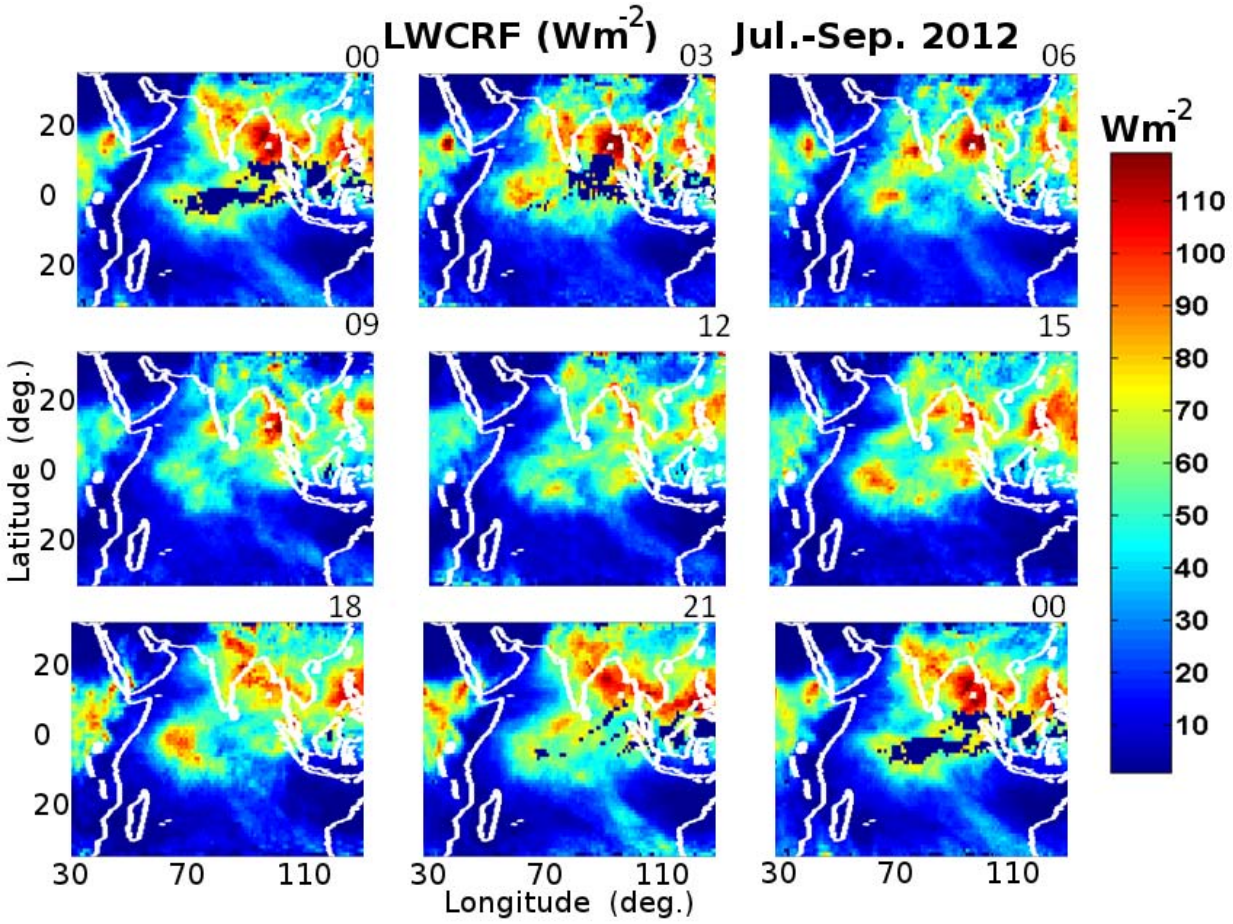

Figure 7.2: Seasonal mean diurnal variation of LWCRF obtained by avearaging the seasonal mean LWCRF at 3 hourly intervals (local time indicated at the top of each figure) for the 'equivalent day' of the summer monsoon season. The patches indicate data gaps in the estimated LWCRF due to the absence of clear-sky reference pixels.

combination of the above. It can also increase if the surface temperature increases but the cloud top temperature remains the same. The last mechanism, together with the daytime development of clouds forced by the shortwave heating of land surface, might have triggered the increase in daytime LWCRF over the coastal regions of Africa. However, it cannot explain the increase in the high night time values of LWCRF (increase of >10 Wm^{-2}) over the land as the land surface temperatures are larger during the daytime than during night. Over the oceanic regions, though the SSTs generally maximize in the night time, the diurnal variation in surface temperature is less than 2°C. The observed change in clear-sky LW radiative fluxes at TOA over the oceanic regions (due to change in surface temperature) is typically <5 Wm^{-2} and cannot explain the large increase (10 to 30 Wm^{-2}) in the observed night time LWCRF. Several studies have reported that the strength of organized convection and cloudiness maximizes during the night time, especially over the oceans [*Chen and R*, 1997; *Hall and Vonder Haar*, 1999; *Soden*, 2000; *Machado et al.*, 2002; *Slingo et al.*, 2004; *Tian et al.*, 2004; *Chung et al.*,

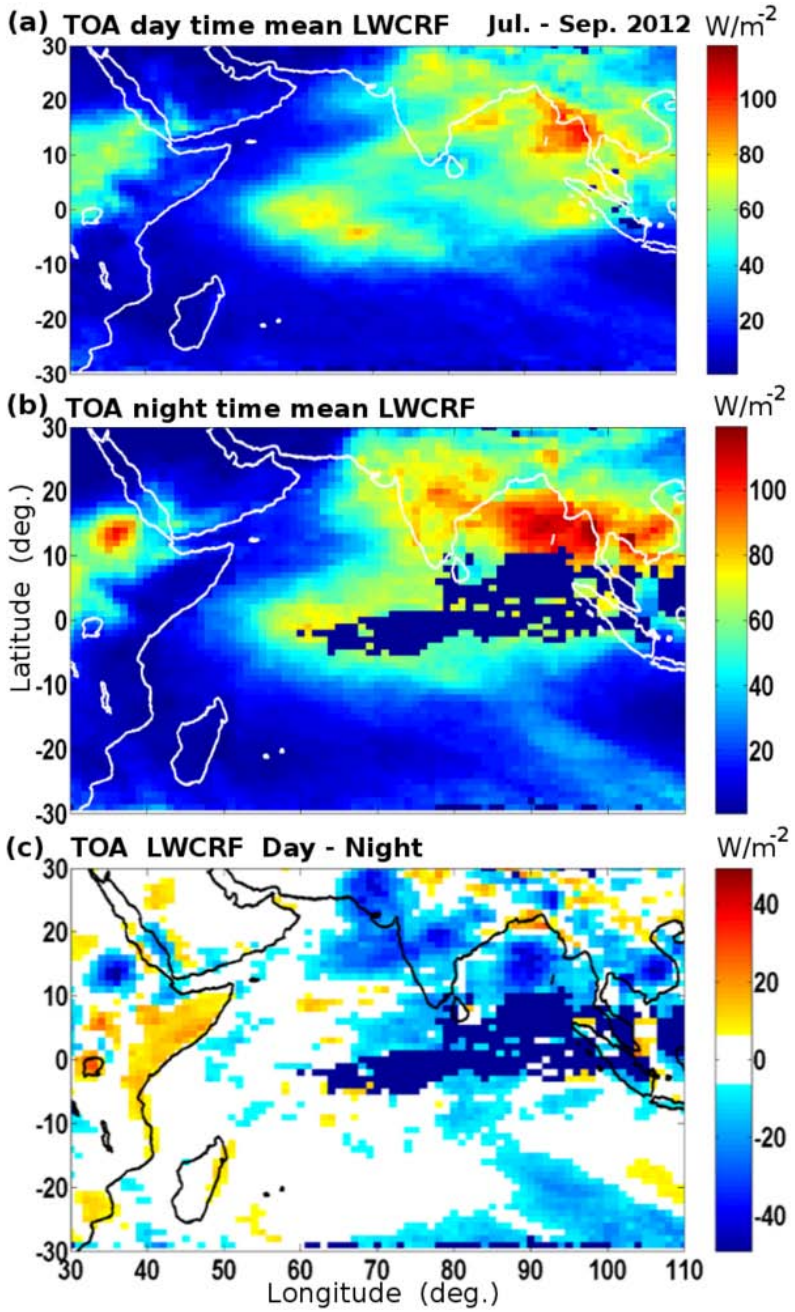

Figure 7.3: Seasonal mean LWCRF averaged during (a) day time (08 to 16 LT) and (b) nighttime (20 to 04 LT) of the summer monsoon season. (c) The difference between daytime and night time values of LWCRF ($LWCRF_{Day}$ – $LWCRF_{Night}$)

2007; *Hong et al.*, 2008]. The observed increase in the LWCRF might have resulted from this strengthening, which would result in the increased vertical development of clouds and their higher frequency of occurrence during the night-time.

7.3.1.3 Day-night variations in the NCRF during summer monsoon season

As explained earlier, the SWCRF is zero during the night-time, while it has a cooling effect (negative values of SWCRF) during the daytime. On the contrary, the warming due to LWCRF exists throughout the day. Figure 7.4 depicts the spatial variations in the NCRF during the daytime (08 to 16 LT) and night-time (20 to 04 LT), which shows that the net effect of clouds during the daytime is to produce a cooling effect. Magnitude of this daytime cooling is largest over the north Bay of Bengal, the Indian landmass encompassing the monsoon trough and off the Western Ghats, and the central African region, where the NCRF varies in the range of -100 to -200 Wm^{-2}. The daytime NCRF over the southern hemispheric Indian Ocean is in the range of -50 to -100 Wm^{-2}. On the contrary, the night time values of NCRF are always positive (warming) due to the absence of the cooling due to SWCRF. This night time warming effect is largest over the north Bay of Bengal, equatorial trough region of the Indian Ocean, the Indian landmass and the central African region, where the values of NCRF are in the range of 50 to 100 Wm^{-2}. In contrast, the night time NCRF over the southern hemispheric Indian Ocean is nearly zero and hence the day-night differences of NCRF is <100 Wm^{-2} in this region. The above analysis shows that the day-night differences in NCRF is as large as 250 Wm^{-2} over the north Bay of Bengal, equatorial trough region, Indian landmass and central African region. This day-night change in the NCRF is quite large and would be a prominent component in determining the diurnal variation of the energy budget of the earth-atmosphere system.

7.3.1.4 CRF during post-monsoon season

Figure 7.5 shows spatial variations of the seasonal mean LWCRF, SWCRF and NCRF (diurnally averaged) over the Indian subcontinent and the surrounding oceans during the post-monsoon season (October-November) of 2012. As seen in Chapter 3, the ITCZ during this season is located in the equatorial region. The diurnal mean CRF could not be estimated over part of this region due to the non-availability of clear-sky reference pixels for all time bins. In general, the seasonal mean LWCRF is in the range of 60 to 110 Wm^{-2} over most of the ITCZ region, while its value decreases rapidly to less than 10 Wm^{-2} at central India and the Southern Hemispheric Indian Ocean, both of which are occupied by the descending limb of the Hadley Cell. Similarly, a strong east-west asymmetry is observed in the equatorial Indian Ocean: eastern part of the equatorial Indian Ocean is occupied by the ascending limb of the Walker Cell with LWCRF exceeding 100 Wm^{-2} while the descending limb of the Walker Cell occupies the western equatorial Indian Ocean manifested by LWCRF <10 Wm^{-2}. The seasonal mean values of LWCRF over the east coast of Africa are similar to that over the adjoining oceanic regions, with LWCRF <10 Wm^{-2}. However, the central and south-

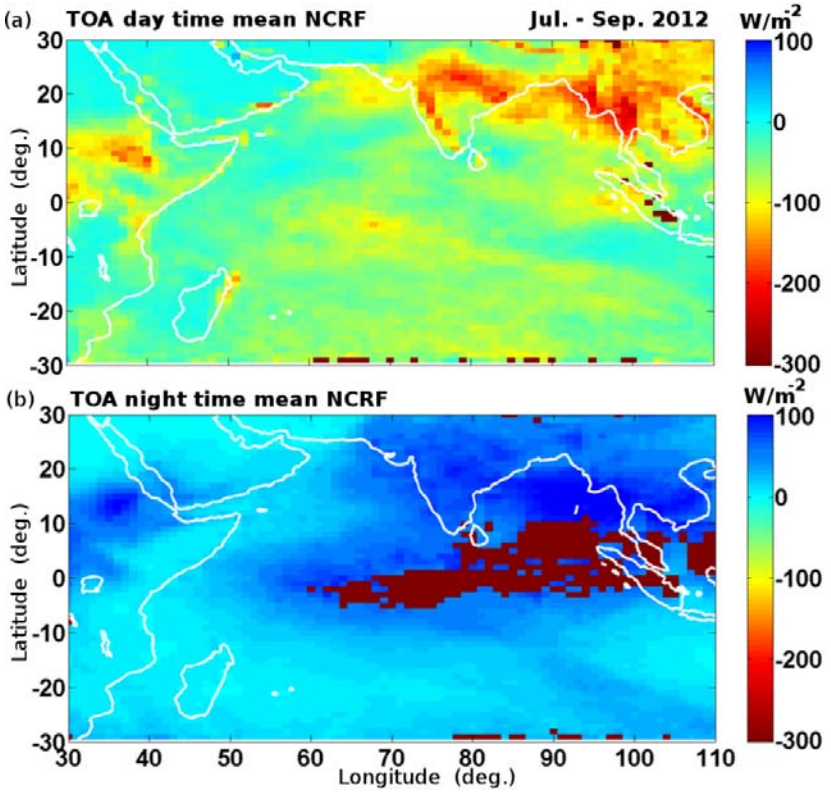

Figure 7.4: Variations in the NCRF during the daytime (08 to 16 LT) and night time (20 to 04 LT) during the summer monsoon season of 2012.

central Africa in the equatorial region and southern hemisphere have LWCRF in the range of 40 to 60 Wm^{-2}.

Overall pattern of the spatial distribution of the seasonal mean SWCRF is similar to that of the LWCRF: regions having larger magnitudes of SWCRF are usually characterized by larger values of LWCRF. In the ITCZ region, the SWCRF is generally in the range of -50 to -100 Wm^{-2}. However, the SWCRF is remarkably significant (-50 to -100 Wm^{-2}) over the southern hemispheric Indian Ocean, especially at south of ∼20°S, where the LWCRF is the least (<10 Wm^{-2}). As revealed by the CloudSat observations (Chapter 3), this region is dominated by the low-altitude clouds whose cloud top altitudes are generally <3 km. The smaller difference between the temperatures at the sea surface and cloud top gives rise to the weak seasonal mean LWCRF while the highly reflecting nature of these clouds produces significantly high values of the SWCRF. Similar features are also seen over east Asia and north east India at north of the ITCZ band.

The seasonal mean NCRF is nearly zero or negative in all the regions. Over most of the ITCZ region, the SWCRF almost cancels the LWCRF, yielding nearly zero NCRF. However, over the regions at the southern hemispheric Indian Ocean and east Asia, which are dominated by the low-altitude clouds, the NCRF is negative, with most of

the values in the range of -30 to -60 Wm^{-2}. Significantly negative values of NCRF (-30 to -50 Wm^{-2}) are also observed over most of the African region (including the east coast of Africa, where the LWCRF is negligible). On average, the observed NCRF has a systematic latitude variation: large cooling at the southern hemisphere Indian Ocean and almost zero NCRF at the equatorial region and northern hemisphere. Clearly, this latitude gradient in NCRF will result in a corresponding gradient in the atmospheric and surface energetics and would modulate the general circulation of the atmosphere.

7.3.1.5 Diurnal variation of LWCRF during post-monsoon season

Figure 7.6 depicts the 3-hourly seasonal mean LWCRF obtained from the 'equivalent day analysis' carried out during the post-monsoon season. On average, the LWCRF over the ITCZ and the deep convective zones in Central Africa maximizes during the night and early morning hours and minimizes during the daytime. For example, the LWCRF over the central African region is maximum during 18 to 03 LT while it is minimum during 09 to 12 LT. Almost similar is the case at the ITCZ region as well. These observations are similar to those during the Asian summer monsoon season, which clearly show that the deep convective regions have peak cloud top altitude and/or largest cloudiness during the night-time. Figure 7.7 shows the average seasonal mean LWCRF during the daytime and night-time and their differences during the post-monsoon season. As seen in Figure 7.6, the reference clear-sky pixels were absent in certain regions in the ITCZ during some time bins in the night, whereas these data are available in all regions during the daytime. Hence, in Figure 7.8, the data gap in the estimated values of LWCRF occurs only during the night-time. Figure 7.8 shows that the mean LWCRF during the night-time exceeds that over the daytime by 10 to 30 Wm^{-2} over the ITCZ. The deep convective region over Central Africa also displays similar feature, though the day-night difference is less significant (typically 10 Wm^{-2}). In contrast, the daytime values are larger over the continental regions (including northeast India, east Asia and the east coast of Africa) as well as some part of the southwestern Indian Ocean, where the LWCRF during the daytime is larger than the corresponding night-time values by 10 to 20 Wm^{-2}.

7.3.1.6 Day-night variations in the NCRF during the post-monsoon season

The seasonal mean NCRF in the daytime (08 to 16 hrs LT) and night-time (20 to 04 hrs LT) during the post-monsoon season of 2012 are depicted in Figure 7.8, which clearly shows that the NCRF is negative (cooling) during the daytime and positive (warming) during the night-time at all locations. The daytime cooling effect of NCRF is largest (-90 to -150 Wm^{-2}) over most of the ITCZ and the southern hemispheric Indian Ocean. The daytime cooling of comparable magnitude is also observed over

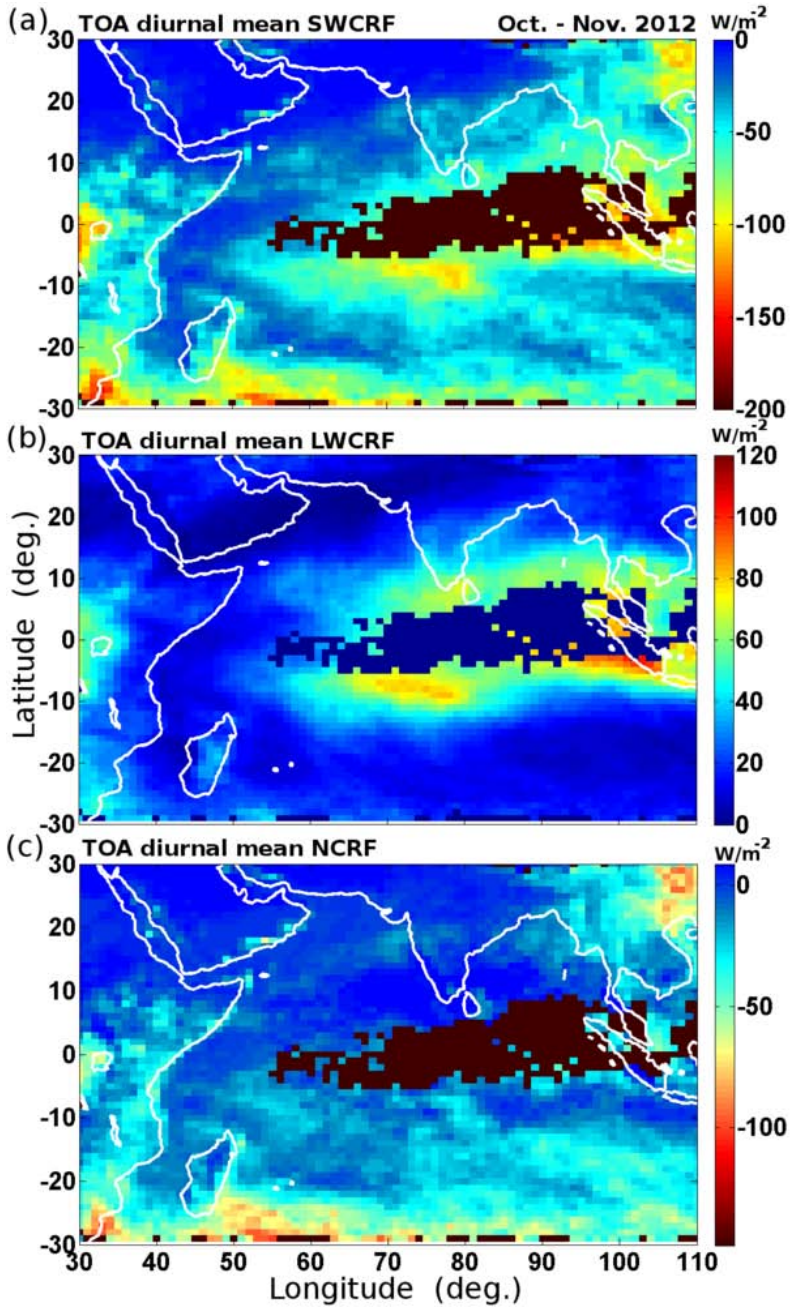

Figure 7.5: Spatial distributions of the seasonal mean LWCRF, SWCRF and NCRF (diurnally averaged) over the Indian subcontinent and the surrounding oceans during the post-monsoon season (October and November) of 2012. Patches indicate the regions where the CRF could not be estimated due to the absence of clear-sky pixels in all time bins.

the east Asia, east China as well as the central African region. The minimum cooling effect of the NCRF is observed over the Arabian Sea and the Arabian Desert regions which are mostly devoid of clouds during this season. On the other hand, the night-time warming effect of NCRF is largest over the ITCZ band (50 to 100 Wm^{-2}) as well as the central parts of the African continent (20 to 60 Wm^{-2}). The night-time

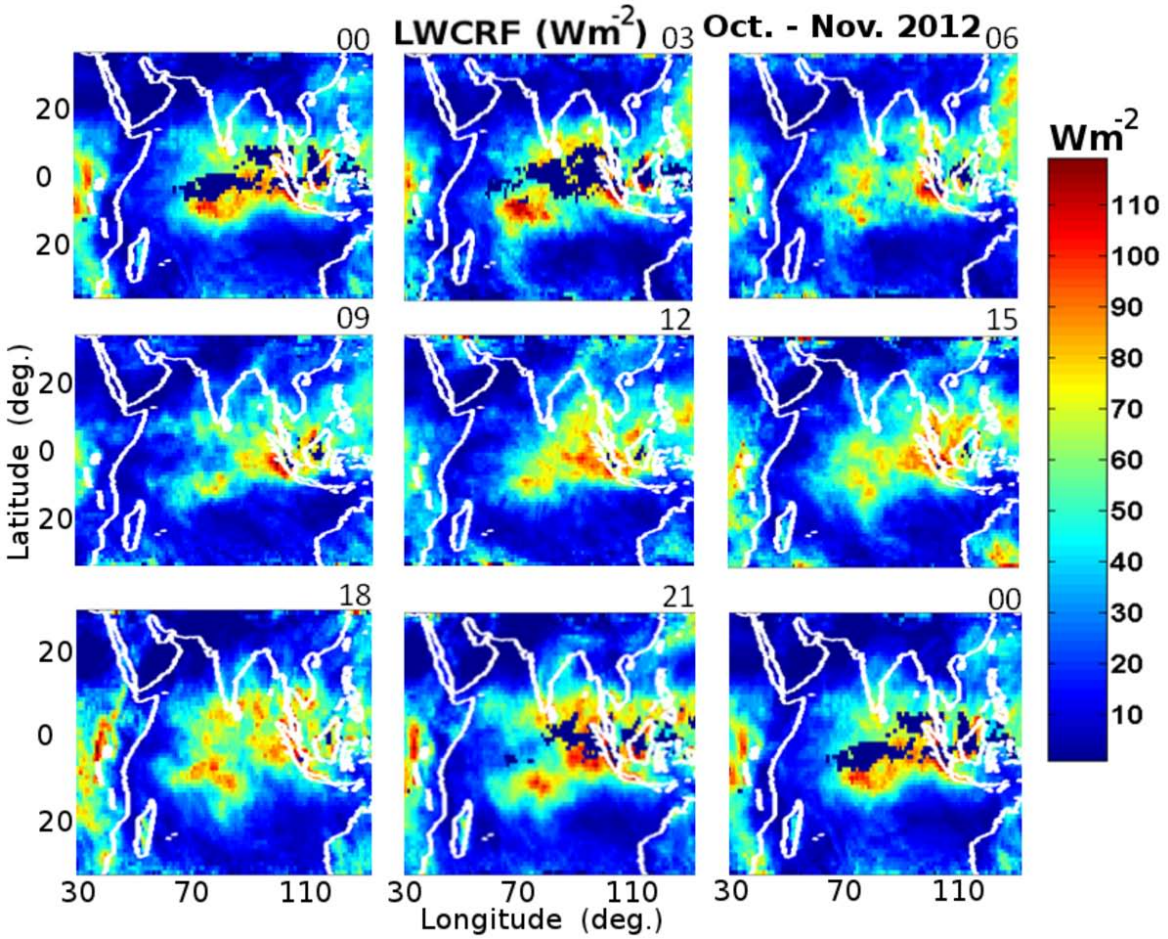

Figure 7.6: 3-hourly seasonal mean LWCRF obtained from the 'equivalent day' analysis during the post-monsoon season of 2012.

warming effect is negligible over the other regions. Thus, the diurnal variation of the NCRF is largest over the ITCZ band (typically varying from -100 Wm^{-2} during the daytime to 100 Wm^{-2} during the night) and the Central African regions (generally varying from -100 Wm^{-2} during the daytime to 60 Wm^{-2} in the night-time). This large variation in NCRF would significantly modulate the diurnal variation of the surface and atmospheric energetics and atmospheric circulation.

7.3.2 Latent heating of the atmosphere by precipitating clouds

7.3.2.1 Winter season

As explained in Section 7.2.3, the latent heating rates (LHR) in the atmosphere caused by precipitating clouds are estimated using the TRMM-Precipitation Radar data. Figure 7.9 shows the multi-year (2006 to 2011) seasonal mean latitude-altitude cross sections of LHR (in units of K/h) during winter (DJF). These images represent the meridional mean variations of LHR, averaged at longitude bands of 10° width, between

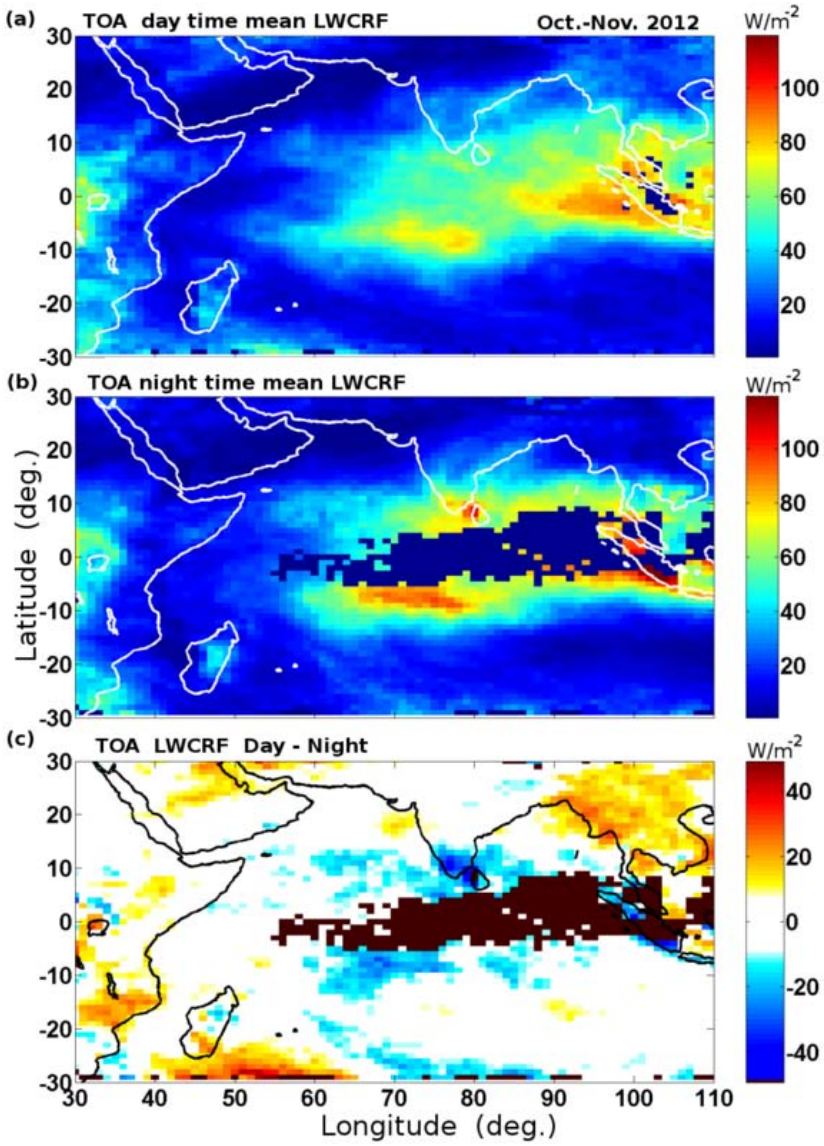

Figure 7.7: Seasonal mean LWCRF during the daytime (08 to 16 LT) and nighttime (20 to 04 LT) and the day-night differences during the post-monsoon season.

30°E to 110°E. The latent heating undergoes substantial spatial variations, both along the latitude and longitude. Though the geographical locations having significantly high values of LHR coincide with those of cloud occurrence (see the meridional cross-sections of the altitude distribution of clouds observed using CloudSat, presented in Chapter 3), their altitudes of peak occurrence as well as the spatial gradients are considerably different. In general, the largest values of LHR are observed in the altitude band of 5 to 10 km in all latitudes and longitude sectors. On the contrary, the largest occurrence of clouds is generally observed in the altitude bands of 10 to 13 km and <3 km (Chapter 3). A large fraction of the clouds that occur in the altitude band of 10 to 13 km are cirrus clouds, which does not precipitate. Similar is the case of the low-altitude cumuli form or stratocumulus clouds that dominate the cloud occurrence below 3 km

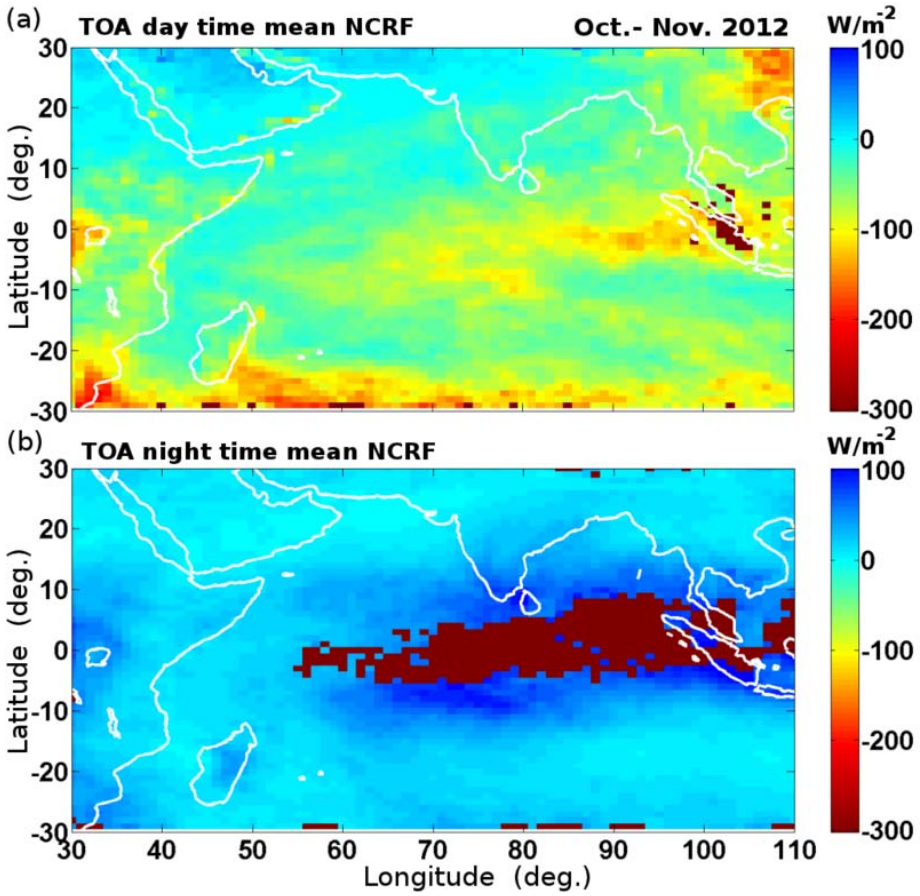

Figure 7.8: Seasonal mean NCRF during the daytime (08 to 16 LT) and nighttime (20 to 04 LT) for the post-monsoon season of 2012.

in the southern hemisphere Indian Ocean. Significant difference observed between the altitudes of largest LHR and cloud occurrence arises from the non-precipitating nature of majority of the clouds.

On average, the largest values of LHR are observed over the south African region in the longitude band of 30 to 40°E between 20°S to 5°S, where the seasonal mean LHR is in the range of 0.1 to 0.18 K/h in the 5 to 10 km altitude region. The latitude gradient of LHR is highly remarkable, especially at the north of this intensely heating band, where the LHR decreases from 0.1 K/h around the equator to <0.02 K/h at north of 3°N. Such rapid latitude gradients are observed in the variations of cloud occurrence as well. The values of LHR are <0.02 K/h at all altitudes in the arid regions at the north. Though the absolute magnitudes of LHR are different, somewhat similar latitude variations, with high values of LHR in the southern hemisphere and negligible latent heating in the northern hemisphere are observed in all the longitude sectors, especially between 50 to 70°E. This is because of the large-scale moisture convergence and convection in the ITCZ band whose seasonal mean location (core) varies between ∼15°S to 5°S in the above longitude band during winter. The near-absence of precipi-

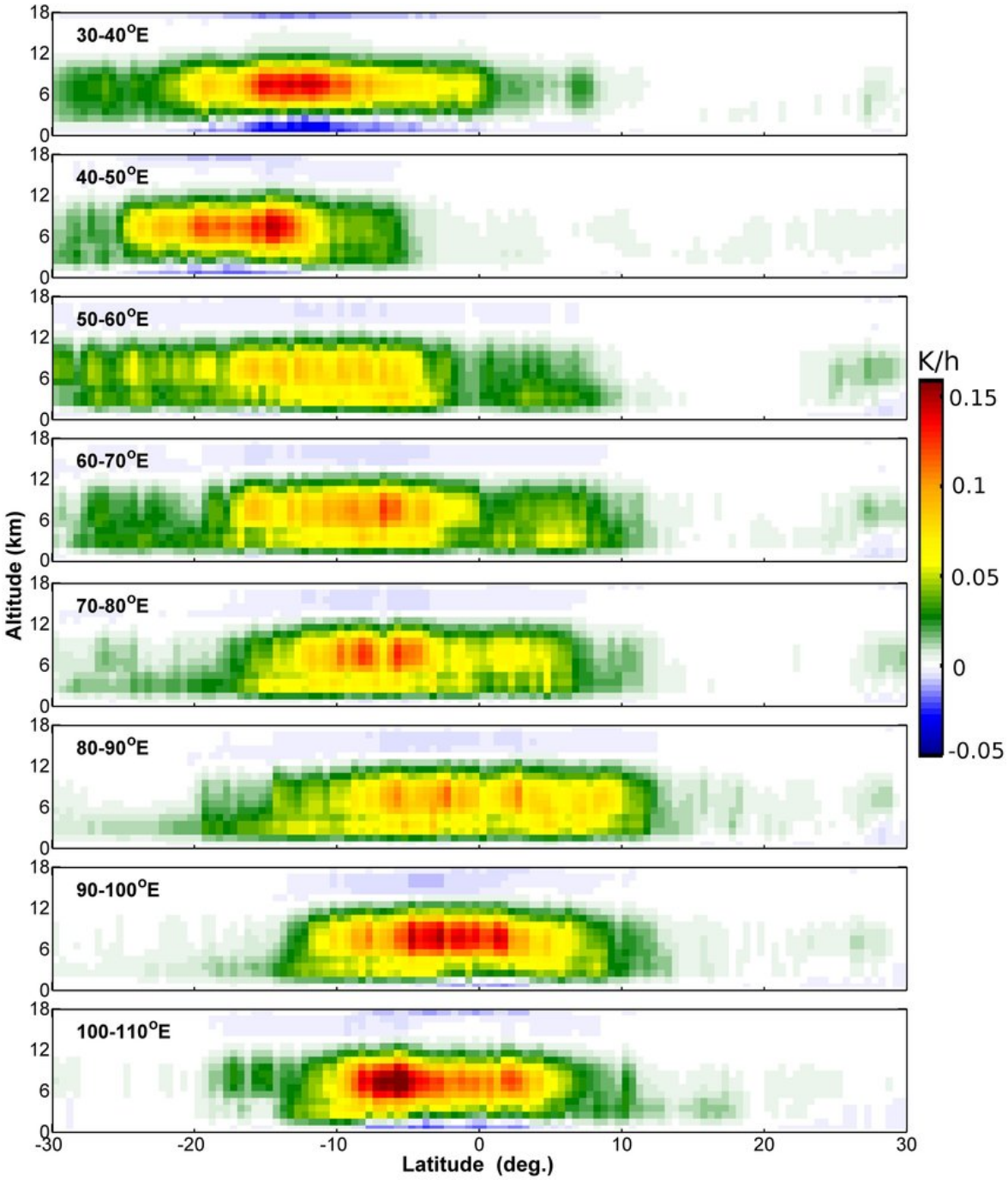

Figure 7.9: Long-term (2006 to 2011) seasonal mean latitude-altitude cross sections of the latent heating rate (LHR, in units of K/h) by precipitating clouds during the winter season. The latitude variations of LHR are averaged at 10° longitude bands, from 30°E to 110°E.

tating clouds in the descending limb of Hadley Cell results in negligible values of LHR in the northern hemisphere. Zonally, the minimum values of LHR are observed in the 50 to 60°E longitude band, where the cloudiness is rather small. On average, the LHR systematically increases eastwards from the longitude of 50 to 100°E; this is also associated with the northward shifting of the latitude of maximum LHR. The above features are consistent with the strengthening and northward tilting of the ITCZ towards the east equatorial Indian Ocean during the winter season. The LHR exceeds 0.14 K/h over a wide region of the east equatorial Indian Ocean and Sumatra/Indonesia in the longitude band of 90 to 110°E. However, this band is confined between 10°S and 5°N and has large latitude gradients towards the north and south. Note that this is the seat of the ascending limb of Walker Cell where the cloud occurrence is the largest. It is interesting note that the cloudiness is largest over the east equatorial Indian Ocean while the latent heating is largest in the 30 to 40°E longitude band in the South African region. This indicates the large amount of cirrus and other non-precipitating clouds in the east equatorial Indonesian region compared to the South African region. Further, though the frequency of occurrence of shallow clouds at <3 km is quite large over the southern hemispheric Indian Ocean, especially between 60 to 100°E longitudes, the LHR associated with this cloud band is <0.02 K/h.

7.3.2.2 Pre-monsoon season

Figure 7.10 depicts the seasonal mean latitude-altitude cross sections of LHR for different longitude bands during the pre-monsoon season (MAM). As in the winter season, the LHR is largest between 5 to 10 km altitudes over most regions. The largest values of LHR during this season are observed at the east equatorial Indian Ocean in the longitude band of 90 to 110°E, where the seasonal mean LHR generally exceeds 0.1 K/h. Similar to the cloud distribution, the LHR also shows substantially large east-west asymmetry during this season. On average, the seasonal mean values of LHR is <0.07 K/h in all the regions at west of 80°E longitude. The smaller values of LHR over the western hemispheric Indian Ocean are associated with the increased strength of the descending limb of the Walker Cell during this season. Compared to winter, magnitude of the spatial variations of LHR is also small during this season. In the longitude band of 40 to 60°E, the LHR is almost insignificant in the northern hemisphere. On the contrary, significant values of LHR (0.04 to 0.06 K/h) are seen over most of the southern hemispheric Indian Ocean in the above longitude band. The LHR shows a systematic increase towards the east of 80°E, and is closely associated with a corresponding increase in cloudiness (Chapter 3). The latitude variation of LHR in this longitude band is largest at across 15°S; despite the large occurrence of low-level clouds at <3 km altitude, south of 15°S is marked by insignificant latent heating of the

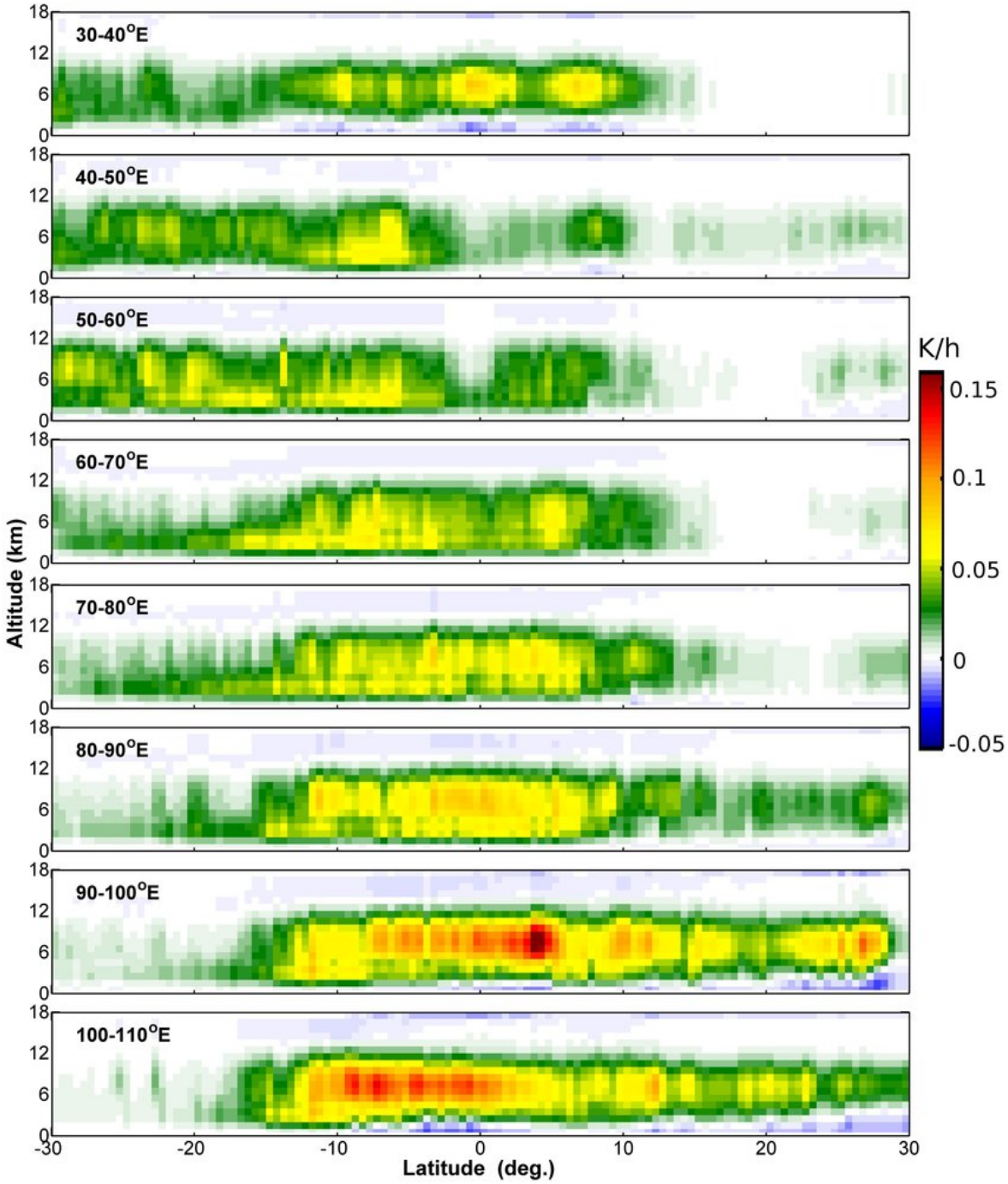

Figure 7.10: Same as Figure 7.9, but for the pre-monsoon season.

atmosphere. Over the Bay of Bengal sector, the latitude gradient of LHR is relatively small in the northern hemisphere. This is because of the occurrence of large-scale cloudiness over the northeast India and east Asia during this season, especially in May. A region of relatively weak cloudiness at ∼20°N and a northward increase in cloudiness are observed in the longitude band of 90 to 110°E (Chapter 3). The LHR also shows similar behaviour.

7.3.2.3 Summer monsoon season

The largest frequency of occurrence of clouds and highest cloud top over the entire globe occurs over the Bay of Bengal during the Asian summer monsoon season [*Meenu et al.*, 2010; *Nair et al.*, 2011]. The multi-year (2006 to 2010) seasonal mean latitude-altitude cross sections of LHR for different longitude bands during the summer monsoon season (JJAS) are depicted in Figure 7.11. As in the winter and pre-monsoon seasons, the LHR is largest between 5 to 10 km altitudes over most regions. On average, the spatial variations of clouds and LHR are similar. Associated with the African Monsoon, the latent heating rate over the Central African region in the longitude band of 30 to 40°E is mostly in the range of 0.1 to 0.15 K/h. The east-west asymmetry in cloudiness with considerably small cloudiness in the west Arabian Sea and the western Indian Ocean and substantially large amount of clouds in the east Bay of Bengal and the east equatorial Indian Ocean are well-reproduced in the spatial distribution of LHR as well. The lowest values of LHR are observed in the 40 to 60°E longitude band where its values are <0.02 K/h in most of the latitudes. At east of 60°E, the eastward increase in LHR at north of 10°S is closely associated with a corresponding increase in cloudiness (Chapter 3). The latitude gradient of LHR in this region is quite large across ∼10°S, with LHR<0.02 K/h at south of 10°S. Over most regions at east of ∼70°E, the meridional gradient of LHR is rather small in the northern hemisphere, except over the northeast Bay of Bengal. The largest values of LHR are observed over the northeast Bay of Bengal in the geographical region encompassed between 10 to 22°N and 90 to 100°E, where the seasonal mean LHR is >0.20 K/h. Note that this encompasses the region of largest rainfall over the study domain with a seasonal mean rainfall amount of >14 mm/day (see the seasonal mean rainfall map presented in Figure 4.8(b) of Chapter 4). The large meridional gradient of LHR - caused by the weak LHR over the southern hemisphere Indian Ocean and large values of LHR in the northern hemisphere over the Indian landmass, east Asia and the Bay of Bengal - would play a pivotal role in the energetics, thermodynamical structure, and general circulation of the atmosphere in this region.

One of the most remarkable features of the vertical distribution of LHR over the deep convective regions of the northeast Bay of Bengal is that the latent heating liberated by the precipitating clouds is >0.1 K/h between 3 to 12 km altitude. Over all other regions and seasons, the upper altitude of significant latent heating is limited to a maximum of 10 km. However, the peak values of LHR are observed in the altitude band of 5 to 10 km over the northeast Bay of Bengal, where the LHR is >0.15 K/h. Thus, the latent heating of the atmosphere is most intense and deepest over the northeast Bay of Bengal during the Asian summer monsoon season. Though the values of LHR over some parts of the east equatorial Indian Ocean (which is the annual mean location

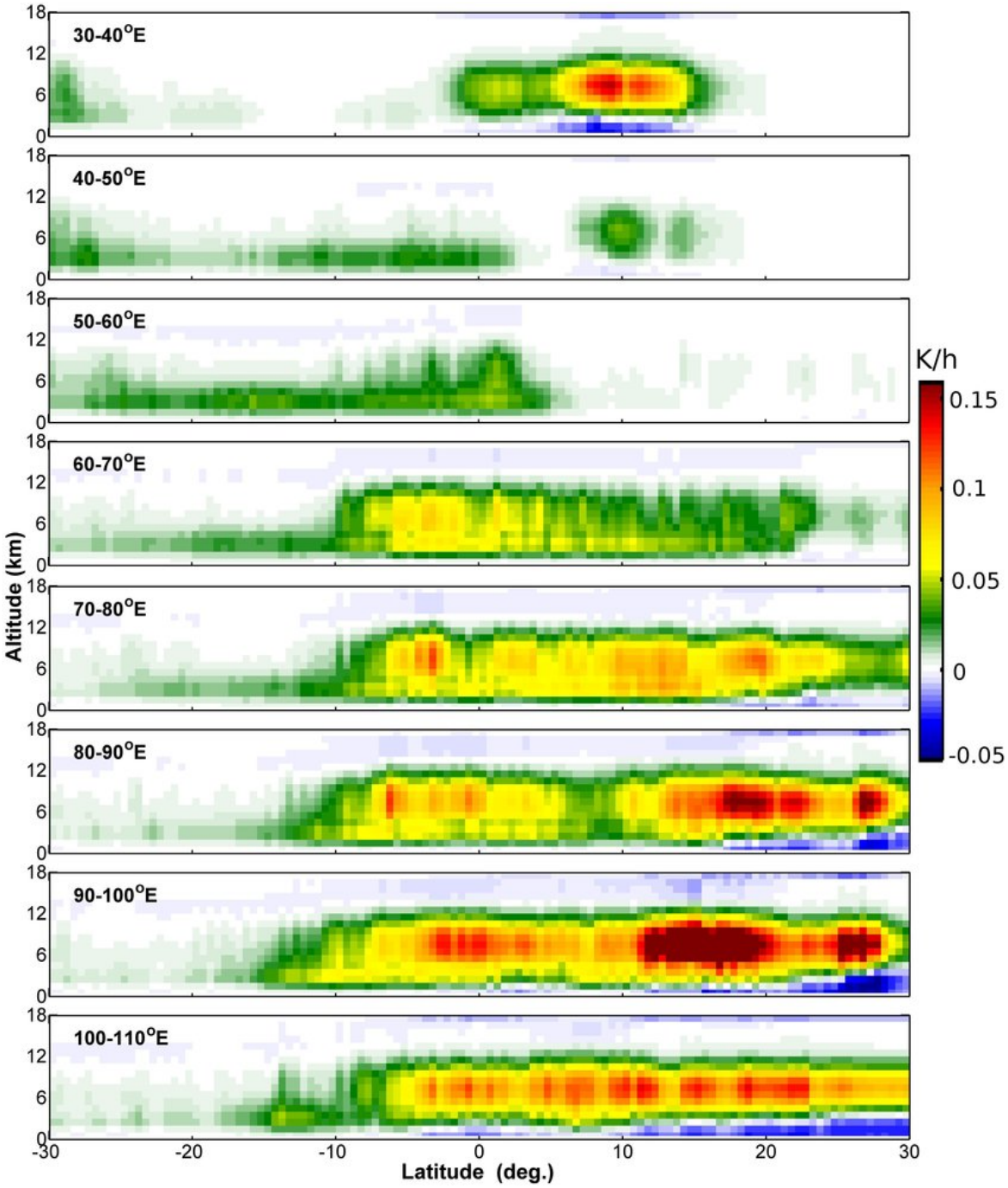

Figure 7.11: Same as Figure 7.9, but for the summer monsoon season.

of the ascending limb of the Walker circulation cell) exceed 0.15 K/h, intensity and depth of atmospheric latent heating is largest over the northeast Bay of Bengal during the summer monsoon season. Another prominent feature observed in Figure 7.11 is the zone of distinctly smaller values of LHR observed around 5 to 12°N and 80 to 90°E, which is surrounded by the regions of intense latent heat release. This is associated with the near-absence of precipitating clouds in the 'pool of inhibited convection'

located in the southwest Bay of Bengal. Such sharp gradients in LHR would cause differential heating of the atmosphere, triggering a mini-circulation with convergence of middle tropospheric air above the 'pool' and divergence at the lower-troposphere, which might play a fundamental role in the genesis of the 'pool' [*Nair et al.*, 2011]. This aspect is discussed in detail in Chapter 4.

7.3.2.4 Post-monsoon season

The seasonal mean latitude-altitude cross sections of LHR during the post-monsoon season (ON) are shown in Figure 7.12. As in all other seasons, the LHR is largest in the altitude band of 5 to 10 km. The east-west asymmetry is highly prominent in LHR, with substantially lower values of LHR in the western Indian Ocean and the Arabian Sea compared to the eastern Indian Ocean and the Bay of Bengal. The lowest values of LHR are observed in the longitude zone of 40 to 50°E. Unlike the summer monsoon season, the regions of large-scale convection and cloudiness are rather confined to smaller latitude bands and are associated with the ITCZ. This results in rather rapid meridional variations of LHR, especially in the geographical region at east of 60°E. The lowest values of LHR are observed at south of 10°S and north of 12°N in the Arabian Sea sector, and south of 10°S and north of 15°N in the Bay of Bengal and Indian longitude sectors. The low-altitude cloud bands occurring in the southern hemisphere Indian Ocean do not produce significant latent heating of the atmosphere.

The largest values of LHR are observed over the east equatorial Indian Ocean in the geographical region from 90 to 110°E longitude and 8°S to 8°N latitude, with seasonal mean LHR varying between 0.12 to 0.16 K/h. On average, this is the largest magnitude of LHR over the east equatorial Indian Ocean during any season. The latitude gradient of LHR is remarkably high across the southern boundary of this zone at 8°S. Note that the cloudiness, precipitation and LHR over this zone attain their annual peak values during this season. Though weaker than that over the northeast Bay of Bengal during the summer monsoon season, the latent heating is quite deep and intense over this zone.

7.3.2.5 Regional differences in the seasonal mean LHR

As seen in the previous section, the LHR undergoes large regional variations during all seasons. Obviously, the most prominent factor that controls this regional difference will be the amount of cloudiness and their vertical distribution. While the large-scale convergence in the ITCZ produces intense convection and high values of LHR, the regions of large-scale descending have negligible values of LHR. Even within the ITCZ region, spatial variations in LHR are quite significant. A quantitative assessment of these regional variations is important for addressing the regional mean heating gradi-

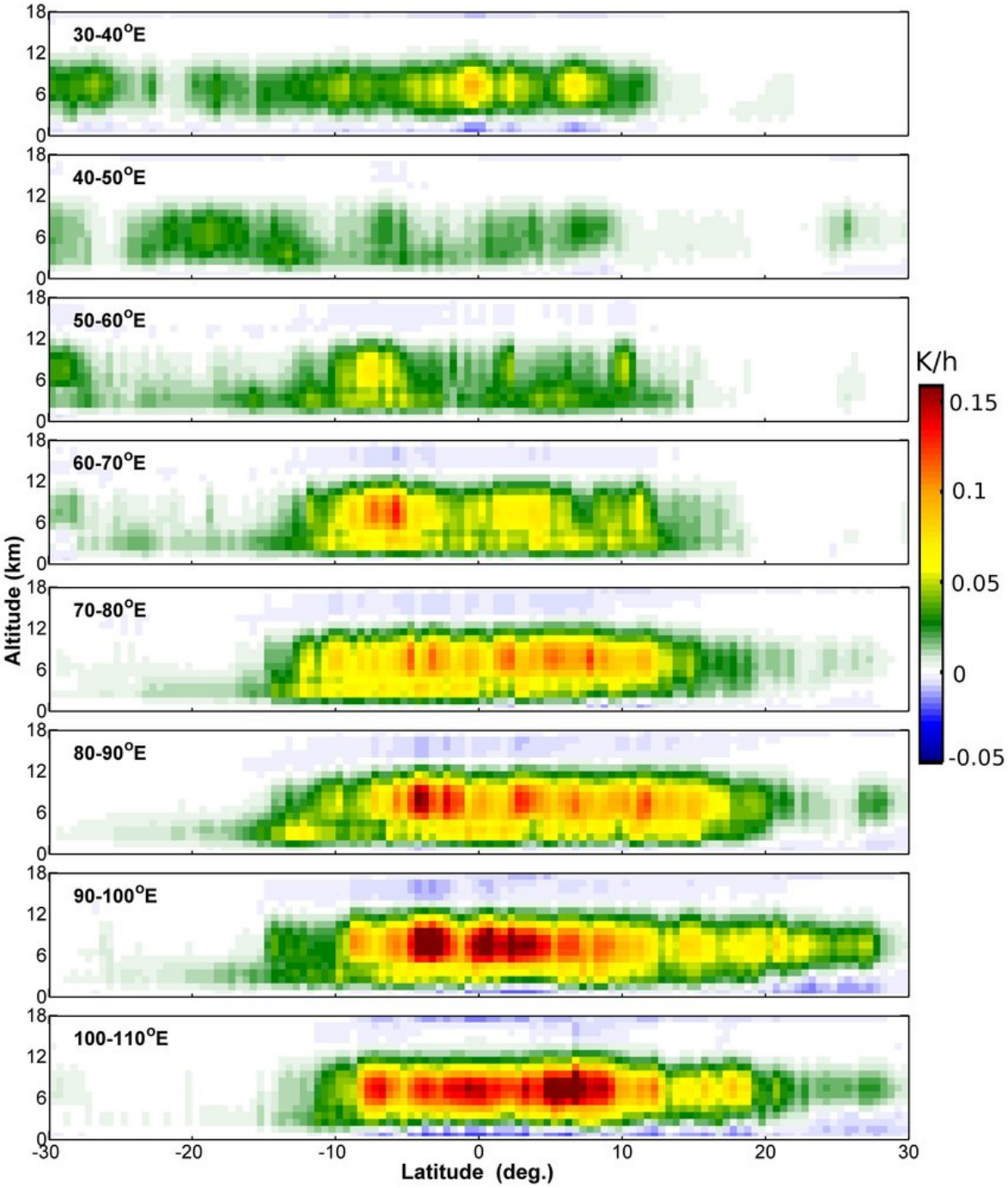

Figure 7.12: Same as Figure 7.9, but for the post-monsoon season.

ents and their potential influence on atmospheric circulation.

Figure 7.13 shows the altitude profiles of the regional mean LHR at selected regions during the contrasting seasons of winter and summer monsoon. The regions in each season are selected based on the frequency of occurrence of clouds and the atmospheric dynamical characteristics. The seasonal mean spatial distribution of the frequency of occurrence of clouds is also shown in Figure 7.13 for comparison. The regions marked

as W_1, W_2, W_3 represent 3 adjacent zones with varying cloudiness located along the ITCZ during the winter season. The boxes marked as W_4, W_5 and W_6 represent the zones located at the descending limb of Hadley circulation in the northern hemisphere, with markedly less cloudiness, and are located along the same meridian of W_1, W_2 and W_3. Similarly, W_7 and W_8 represent the regions located in the descending limb of Hadley Cell in the southern hemisphere, with clouds appearing only below $\sim$ 3 km altitude and are in the same longitudes as W_1 and W_3.

Altitude profiles of the regional mean LHR shows a broad peak, mostly appearing in the altitude band of 5 to 9 km and a rather narrow secondary peak around 2 to 3 km altitude. Even along the ITCZ, the mean LHR shows considerable spatial variations, which is especially large at the broad peak around 5 to 9 km altitude. In this altitude band, the seasonal mean heating rates change from 0.07 K/h to 0.10 K/h within about 20° longitude. The meridional gradient of regional mean LHR between the ascending and descending limbs of Hadley Cell is the largest: in the 5 to 9 km altitude band, the regional mean LHR varies from 0.07 to 0.10 K/h at the ITCZ to nearly zero values at the northern and southern hemispheric descending zones located within 10 to 20° latitude from the ITCZ band. This might be crucial in determining the atmospheric thermal structure and positively feeding back to the maintenance of the meridional circulation to enable the heat transfer from the warm ITCZ regions to the colder subtropics. It is important to note that this heating rate is almost negligible above $\sim$12 km. Interestingly, below $\sim$3 km altitude, the heating rate at the southern hemispheric Indian Ocean is around 0.01 to 0.02 K/h, which is larger than their corresponding values in the northern hemisphere. This effect, produced by the low-altitude clouds in the southern hemisphere, suppresses the meridional gradient of LHR below $\sim$3 km altitude in the southern hemisphere compared to the corresponding gradient in the northern hemisphere. The enhanced values of LHR ($\sim$0.02 K/h) at the altitudes below 10 km in the southwest Indian Ocean (60 to 70°E; 25 to 30°S) are due to the proximity to the convective clouds over the Madagascar region.

During the summer monsoon season, which is characterized by deep convective clouds over the Bay of Bengal and large-scale cloudiness over a vast region, the seasonal mean altitude profiles of regionally averaged LHR for the following zones are displayed in Figure 7.13. The region S_1 represents the largest deep convective region in the northeast Bay of Bengal and adjoining land, while S_2 represents the east equatorial Indian Ocean with significant cloudiness, and S_3 represents the high-pressure region where large-scale descending of tropospheric airmass occurs. These zones, S_1, S_2 and S_3 are along the same longitude band. The regions S_4 and S_5 represent the regions of large-scale cloudiness over the southeast Arabian Sea and east coast of Peninsular India, while S_6 represents the descending branch of Hadley Cell located along the same

longitude band. The box marked as S_7 represents the subtropical high-pressure region (the Mascarene High) during the summer monsoon season.

On average, the structure of the altitude profiles of LHR at the deep convective and high-pressure regions are generally similar to those during the winter season. Altitude profiles of the regional mean LHR show a broad peak, mostly appearing in the altitude band of 5 to 9 km, and a narrow secondary peak around 2 to 3 km altitude. In the altitude band of 5 to 9 km, the regional mean LHR over the northeast Bay of Bengal varies from 0.15 to 0.22 K/h, which is almost double of the corresponding values over the east Arabian Sea and the adjoining peninsular India. The mean LHR in the above altitude band over the east equatorial Indian Ocean (LHR$\sim$0.12 K/h) is also substantially smaller than that over the northeast Bay of Bengal. Over the southern hemispheric Indian Ocean, the mean LHR is negligible in the middle and upper troposphere and $<$0.02 K/h below $\sim$3 km. The above analysis clearly brings out the substantially large regional variations of LHR over the Indian subcontinent and adjoining oceanic regions during the summer monsoon season compared to the winter season. Such large regional differences would contribute to the high winds associated with the strong summer monsoon circulation. The negative values of LHR observed below $\sim$1 km altitude over the northeast Bay of Bengal might be because of the evaporation of precipitation in the sub-cloud region.

7.4 Summary and conclusions

The energetics and radiation budget of the earth-atmosphere system are strongly modulated by clouds. This chapter presents:

1. The seasonal mean shortwave, longwave and net cloud radiative forcing at the top of the atmosphere and their diurnal variations during the summer monsoon and post-monsoon seasons estimated using the data obtained from ScaRaB onboard the recently launched Megha-Tropiques satellite, and

2. Spatial variations of the seasonal mean altitude profiles of the latent heating rate in the atmosphere by precipitating clouds using the data obtained from Precipitation Radar (PR) onboard the TRMM satellite during 2006 to 2011, over the Indian region and the surrounding oceans.

Low-inclination of the Megha-Tropiques satellite orbit yields frequent observations of the tropical regions at different local time of the day. The ScaRaB observations of the radiances in the broad shortwave and longwave bands (which in turn are used to estimate the corresponding shortwave and longwave radiative fluxes at the TOA) enable the estimation of diurnal variations in cloud radiative forcing, which are then integrated

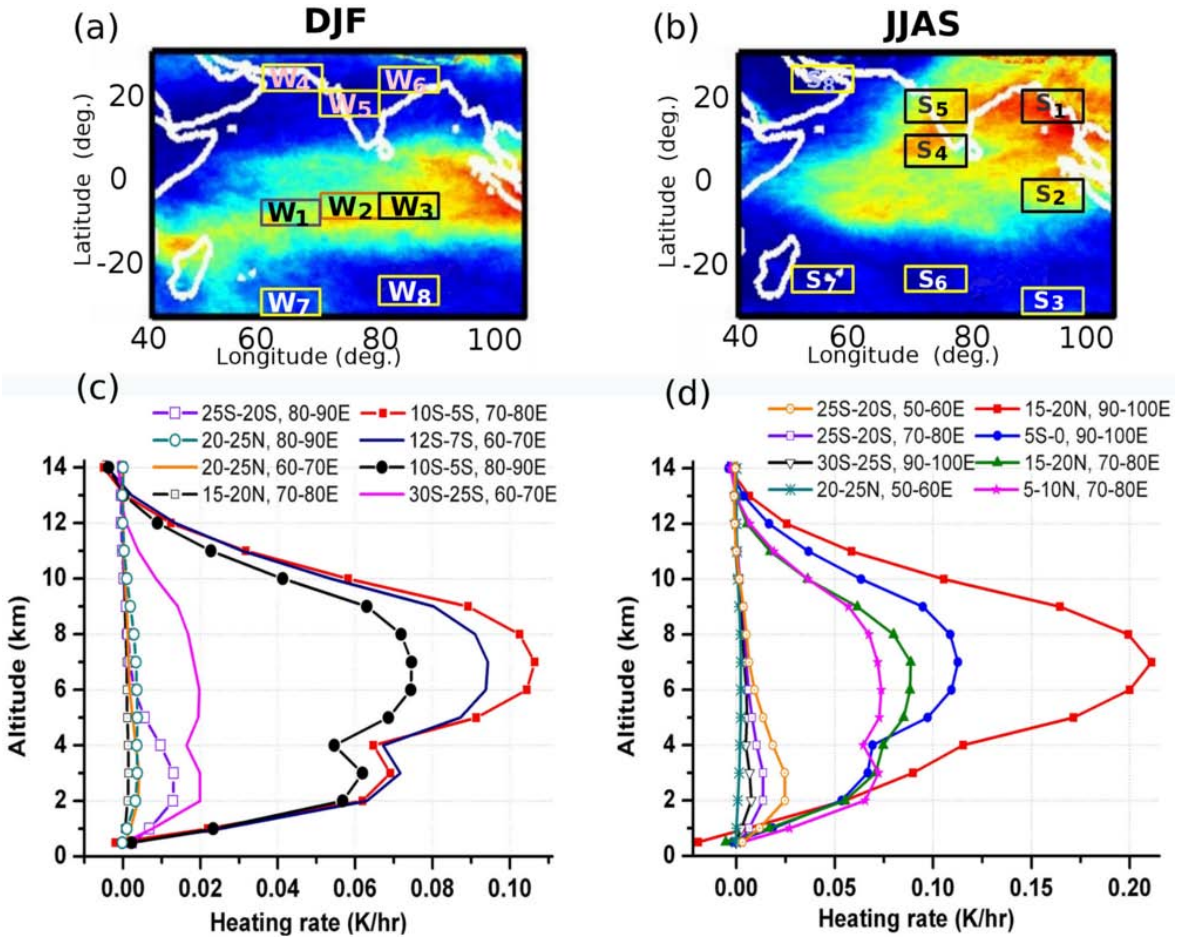

Figure 7.13: (a,b) Spatial variation of the long-term seasonal mean cloudiness during winter season and summer monsoon seasons. The selected regions for which the altitude profiles are given in (c) and (d) are indicated in (a) and (b). Altitude profiles of the regional mean LHR at selected regions during (c) winter season and (d) summer monsoon seasons.

to estimate the seasonal mean cloud radiative forcing. Analysis of the ScaRaB data shows that the LWCRF is always positive (warming of the earth-atmosphere system) while the SWCRF is negative (cooling). Mean values of the LWCRF and SWCRF during the summer monsoon are largest over the northeast Bay of Bengal, where LWCRF is generally greater than 100 Wm^{-2} while SWCRF is in the range of -100 to -160 Wm^{-2}. This yields a negative (cooling) net cloud radiative forcing of -10 to -60 Wm^{-2} during the Asian summer monsoon season over the northeast Bay of Bengal, which is characterized by the deepest convection and optically thick clouds over the entire globe. The minimum values of LWCRF and SWCRF during the summer monsoon season are observed at the west Arabian Sea and the adjoining Arabian Desert, where their magnitudes are <20 Wm^{-2} and the NCRF is nearly zero. Notwithstanding the similarities observed in the spatial variations of LWCRF and SWCRF, they show certain distinct differences:

1. Magnitude of SWCRF is considerably large (>120 Wm^{-2}) over the northern parts of India (the mean location of the monsoon trough) and along the west coast of Indian Peninsula, while the mean LWCRF over these locations is <80 Wm^{-2}. This suggests that the clouds occurring over the monsoon trough region as well as off the Western Ghats have albedo comparable to those occurring over the north Bay of Bengal, yielding comparable values of SWCRF over these regions. However, the top altitudes of optically thick clouds are largest over the north Bay of Bengal compared to the above regions, which explains the large differences in the values of LWCRF at these regions.

2. One of the most remarkable features of SWCRF is its significant magnitude (20 to 40 Wm^{-2}) over the entire south Indian Ocean, while the corresponding values of LWCRF over this region are negligible. This is primarily because of the presence of large amount of significantly reflecting low-altitude clouds which occur below ∼2 to 3 km altitude. The difference between the temperatures of the ocean surface and cloud top is rather small, resulting in negligible values of LWCRF. The NCRF in this region is to produce a net cooling of -20 to -40 Wm^{-2}.

Diurnal variation of the LWCRF is largest over the deep convective regions of the northeast Bay of Bengal, where the LWCRF maximizes during 21 to 03 LT (LWCRF ∼100 to 110 Wm^{-2}) and minimizes during 09 to 15 LT (LWCRF ∼70 to 105 Wm^{-2}). Over most of the regions, their values are minimum during the daytime (especially the forenoon hours of 06 to 12 LT) and largest during the night or late evening. Over the deep convective regions, the night-time value exceeds the daytime LWCRF by >20 Wm^{-2}. The night-time values of LWCRF are also larger over the southern hemispheric Indian Ocean which is dominated by low-altitude clouds. The net effect of clouds during the daytime is to produce a cooling effect. Magnitude of this daytime cooling is largest over the north Bay of Bengal, the Indian landmass encompassing the monsoon trough and off the Western Ghats, and the central African region, where the NCRF varies in the range of -100 to -200 Wm^{-2}. The NCRF over the southern hemispheric Indian Ocean is in the range of -50 to -100 Wm^{-2}. The night-time values of NCRF are always positive (warming) due to the absence of the cooling due to SWCRF. This night-time warming effect is largest over the north Bay of Bengal, equatorial trough region of the Indian Ocean, the Indian landmass and the central African region, where the values of NCRF are in the range of 50 to 100 Wm^{-2}. The night-time NCRF over the southern hemispheric Indian Ocean is nearly zero and the day-night differences of NCRF is <100 Wm^{-2} in this region.

During the post-monsoon season, the seasonal mean LWCRF is largest (60 to 110 Wm^{-2}) over the ITCZ, while its value decreases rapidly to less than 10 Wm^{-2}

at central India and the Southern Hemispheric Indian Ocean, both of which are occupied by the descending limb of the Hadley Cell. In the ITCZ region, the SWCRF is generally in the range of -50 to -100 Wm^{-2}. However, the SWCRF is remarkably significant (-50 to -100 Wm^{-2}) over the southern hemispheric Indian Ocean, especially at south of ∼20°S, where the LWCRF is the least (<20 Wm^{-2}). Over most of the ITCZ region, the SWCRF almost cancels the LWCRF, yielding nearly zero NCRF. However, over the regions at the southern hemispheric Indian Ocean and east Asia, which are dominated by the low-altitude clouds, the NCRF is negative, with most of the values in the range of -30 to -60 Wm^{-2}.

The TRMM-PR observations show that, though the geographical locations having significantly high values of LHR coincide with those of cloud occurrence, their altitudes of peak occurrence as well as the spatial gradients are considerably different. The largest values of LHR are generally observed in the altitude band of 5 to 10 km in all latitudes and longitude sectors. On the contrary, the largest occurrence of clouds is generally observed in the altitude bands of 10 to 13 km and <3 km. This major difference stems from the fact that a large fraction of clouds that occur in the altitude band of 10 to 13 km are cirrus clouds, which does not precipitate. Similar is the case of the low-altitude cumuli form or stratocumulus clouds that dominate the southern hemisphere Indian Ocean. During the winter season, the largest values of LHR are observed over the south African region in the longitude band of 30 to 40°E between 20°S to 5°S, where the seasonal mean LHR is in the range of 0.1 to 0.18 K/h in the 5 to 10 km altitude region. At the north of this intensely heating band, the LHR decreases to <0.02 K/h at north of 3°N, producing a large spatial gradient in the atmospheric heating rates. Zonally, the minimum values of LHR are observed in the 50 to 60°E longitude band, where the cloudiness is rather small. On average, the LHR systematically increases eastwards from the longitude of 50 to 100°E and it exceeds 0.14 K/h over a wide region of the east equatorial Indian Ocean and Sumatra/Indonesia in the longitude band of 90 to 110°E. During the summer monsoon season, the largest values of LHR are observed over the northeast Bay of Bengal in the geographical region encompassed between 10 to 22°N and 90 to 100°E, where the seasonal mean LHR is >0.20 K/h. This season is marked by large meridional gradient of LHR - caused by the weak LHR over the southern hemisphere Indian Ocean and large values of LHR in the northern hemisphere over the Indian landmass, east Asia and the Bay of Bengal.

As seen above, the radiative effect of clouds is to cause a net cooling during the daytime and warming during the night time. This will modulate the total radiative flux available at the surface, leading to a reduction in the diurnal variation of the net radiative flux at the surface. This in turn would reduce the diurnal variation in radiative heating (and hence temperature) of the surface. Similarly, the large spatial

variations in the net cloud radiative forcing would modulate the horizontal variations in heating/cooling of the earth-atmosphere system. The atmospheric heating is also strongly modulated by the latent heating, producing substantial spatial gradients in atmospheric heating rates. All these would play a pivotal role in the energetics, thermodynamical structure, and general circulation of the atmosphere in this region, which needs to be examined further.

Chapter 8

Summary and Future Scope

Knowledge of the three-dimensional distribution of clouds and their properties is of fundamental importance for understanding a host of processes involving clouds, including the cloud development and feedback processes, role on the energetics, thermodynamics, moisture budget and hydrological cycle of the earth-atmosphere system and their eventual parameterization into the weather and climate models. This is also important for investigating the aerosol-cloud interaction as well as the radiative impact of aerosols under cloudy conditions. Major gaps in the accurate knowledge of cloud properties and their spatio-temporal variations as well as the atmospheric processes involving clouds (which are highly non-linear) are among the root causes for the uncertainties in the prediction of weather and climate. Spatial distribution of clouds, their temporal evolution and impact on the energetics of the earth-atmosphere system over the Indian subcontinent and the surrounding oceans have certain distinctive features, which include: (i) substantial, but systematic, annual variation in the distribution and properties of clouds associated with the massive monsoon circulation caused by the largest annual migration of ITCZ over the entire globe, (ii) occurrence of the highest cloud tops over the entire globe over the north and east Bay of Bengal during the June to August period, (iii) ubiquitous presence of semitransparent cirrus clouds during the Asian summer monsoon (ASM) season, most of which are transported into the Indian landmass and the Arabian Sea from the deep convective outflows in the northeast Bay of Bengal, (iv) Significant lifting of the convective tropopause and thinning of the TTL by the intense deep convective clouds over the north Bay of Bengal during the ASM, (v) the strongest ascending limb of the Walker circulation located in the east equatorial Indian Ocean and the western Pacific and its descending limb at the west equatorial Indian Ocean/east Africa leading to substantial zonal variations in convection, cloudiness and associated radiative forcing over the equatorial Indian Ocean, (vi) large spatial variations in SST from $<24^{\circ}$C to $>30^{\circ}$C and the associated changes in cloud development, and (vii) significantly large negative net cloud radiative forcing over

the Indian region (<-30 Wm^{-2}) during the ASM, which is distinctly different from the near-zero net CRF over the tropics. Immense effect of the Asian summer monsoon on the socio-economical conditions of billions of people in the region further emphasizes the necessity for improved understanding and prediction of regional weather, which, in turn, requires significant improvements in the understanding of the regional cloud properties and feedback mechanisms. The horizontal distribution of clouds (total as well as the high-altitude clouds) and their temporal evolution over the Indian subcontinent and surrounding oceans are well explored in the past using satellite data. Spatial distribution of cirrus clouds was also investigated extensively. However, barring a few studies, investigations on the vertical distribution of clouds over the entire troposphere and their spatial variations (providing the 3-dimensional distribution of clouds) over the Indian region are extremely limited. As the cloud occurrence is intertwined with the atmospheric dynamics, the 3-dimensional distribution of clouds also acts as tracer for some of the atmospheric dynamical phenomena which are hitherto not well understood. Role of SST and atmospheric thermo-dynamical parameters on the vertical development of clouds as well as the impact of clouds on the energetics of the earth-atmosphere system is least understood. Main motivation for the present study is to improve the scientific understanding to fill the above prominent gap areas. The study is focused on the Indian subcontinent and the surrounding oceans bound within the latitude-longitude bands of 30°S to 30°N and 30°E to 110°E. Main objectives of this thesis are to:

1. Estimate the monthly and seasonal mean vertical distribution of clouds and their spatial variations (which provide a monthly and seasonal mean 3-dimensional distribution of clouds) using multi-year satellite data and to investigate their association with the general circulation of the atmosphere.

2. Investigate the characteristics of the 'pool of inhibited cloudiness' that appear over the southwest Bay of Bengal during the Asian summer monsoon season (revealed by the 3-dimensional distribution of clouds) and identify the potential mechanisms for its genesis.

3. Investigate the role of SST and atmospheric thermo-dynamical parameters in regulating the vertical development and distribution of clouds, which is a proxy for atmospheric convection.

4. Investigate the vertical distribution of tropical cirrus clouds and time evolution of their vertical structure (especially the descending nature) using lidar observations at Thiruvananthapuram (8.5°N, 77°E), a tropical coastal station at the southwest Peninsular India.

5. Assessment of the impact of clouds on the energetics of the earth-atmosphere system, by estimating the regional distribution of the seasonal mean cloud radiative forcing at top-of-the-atmosphere and latent heating of the atmosphere by precipitating clouds using satellite data.

This chapter presents the summary of the major results and conclusions derived from this study and the scope for future research based them.

8.1 Summary of the major results and conclusions

Chapter 1

Background information on the generation of clouds and their classification, physics of cloud formation, in situ and remote sensing techniques for investigating cloud properties and radiative forcing, global and regional distribution of clouds and their association with atmospheric general circulation, effect of clouds on the radiation budget and atmospheric energetics, importance and uniqueness of cloud studies over the Indian subcontinent and the surrounding oceans and scope of the present study are presented in Chapter 1.

Chapter 2

Details of the satellite data from different platforms, experimental details of the Micropulse lidar system, and methods used for the data analyses employed in this thesis are presented in Chapter 2. This study is mainly based on about 4.5 years (June 2006 to February 2011) of observations carried out using the Cloud Profiling Radar onboard CloudSat satellite (CloudSat 2B-GEOPROF Version-4 data) for investigating the vertical profiles of clouds and their spatial variations, long-term horizontal distribution of clouds derived from about 12 years of NOAA-AVHRR data (1996 to 2010), combined analysis of CloudSat and CALIPSO data (2006 to 2010) to derive the vertical distribution of semitransparent clouds and optically thick clouds, TRMM-Precipitation Radar data (2006 to 2011) to derive the atmospheric latent heating by precipitating clouds, the Megha-Tropiques-ScaRaB data (July to November 2012) to derive the seasonal mean shortwave, longwave and net cloud radiative forcing during the summer monsoon and post-monsoon seasons of 2012, and the TMI-derived SST (2006 to 2011). Time evolution of the vertical structure of tropical cirrus clouds are investigated using the micropulse lidar observations carried out at Thiruvananthapuram during March 2008 to May 2011. The atmospheric thermo-dynamical parameters are obtained from the reanalysis data (MERRA) and surface wind divergence are derived

from spaceborne Scatterometers. Advantages and limitations of each of these data sets and potential sources of errors and uncertainty limits are also presented in Chapter 2.

Chapter 3

A quantitative estimate of the multi-year (2006 to 2011) monthly and seasonal mean vertical distribution of clouds and its spatial variations (providing a monthly and seasonal mean 3-dimensional cloud distribution) over the Indian subcontinent and the surrounding oceans and the influence of atmospheric general circulation - especially the ITCZ and the Hadley and Walker circulation cells - on the observed mean three-dimensional distribution of clouds and its seasonal evolution are presented in Chapter-3. The monthly and seasonal mean latitude-altitude cross sections of the frequency of occurrence of clouds (F_{ALT}) are averaged for different longitude bands of 10° width. Similarly, the longitude-altitude cross sections are estimated for latitude bands of 10° width. Features of the cloud distribution and atmospheric circulation presented in this chapter also provide the necessary background information for the succeeding chapters. Some of the important features observed in this study are further investigated and are presented in the subsequent chapters. Notwithstanding the temporal and spatial sampling limitations of CloudSat, the horizontal distribution of clouds obtained using CloudSat data are found to be well in agreement with the long-term horizontal cloud distribution derived from imager (NOAA-AVHRR) data. Structure of the Hadley and Walker circulation cells are well discernible in the horizontal and vertical distribution of clouds.

During all seasons, the meridional cross sections of the vertical distribution of clouds show minimum cloudiness at the descending limbs of the Hadley cell in both hemispheres. Strength of the ITCZ as inferred from the vertical development of clouds is largest at the east equatorial Indian Ocean (east of ∼90°E) and minimum at the west (mainly ∼40 to 50°E). This east-west asymmetry prevails during all seasons and is caused by the Walker circulation that has its ascending limb at the east equatorial Indian Ocean (and the western Pacific) and descending limb at the west equatorial Indian Ocean. This feature is most prominent during October-November and April-May periods. As seen from the meridional cross sections of F_{ALT}, the latitudinal width of the ITCZ is found to be largest (∼10 to 16°) at the east equatorial Indian Ocean and least (<10°) at the western Indian Ocean where the ITCZ is rather weak and less organized. Structure of the ITCZ shows a small, but persistent northward tilt from the west Indian Ocean to the east during January to March. Characteristics of the ITCZ and the Hadley and Walker cells observed using the meridional and zonal cross sections of F_{ALT} are well in agreement with those inferred from the atmospheric circulation obtained from the reanalysis data (MERRA).

As a result of the strong outflow from the deep convective clouds, meridional cross section of the vertical distribution of clouds shows well-developed anvils on either side of the ITCZ. Depending on the strength of the Hadley circulation cell and the resulting upper tropospheric wind divergence, these cirrus outflows are found to be prominent up to ∼4 to ∼10° meridionally from the northern and southern boundaries of the ITCZ core. Though these cirrus outflows in the meridional direction get weakened further poleward, their presence could be traced well up to the sinking zones of the Hadley cell on both hemispheres (up to ∼10 to 20° meridionally from the boundaries of the ITCZ). Thickness of these anvil structures is ∼4 to 5 km near the ITCZ boundaries and decreases monotonically with increase in distance. This is mainly because of the increase in base altitude while the top altitude remains almost the same. Increase in the base altitude of the cirrus anvils might have been caused by the IR radiative heating of the cirrus cloud base due to absorption of IR radiation emitted from the cloud-free or low-level cloud regions below and subsequent evaporation of the cirrus from the base. In contrast, the IR radiative cooling from the cirrus top would help its sustenance for a longer period, till the cloud becomes very thin.

Over the deep convective regions, frequency of occurrence of clouds in the upper troposphere increases with altitude to attain peak occurrence in the altitude band of ∼9 to ∼13 km. In addition to the deep convective clouds, this increase is significantly contributed by the occurrence of thick cirrus clouds, most of which are formed from the outflow of deep convective clouds as anvils or the remnants of deep convective clouds after precipitation. The relatively long atmospheric residence time of cirrus clouds (several hours to ∼2 days) compared to the low- and middle-level clouds (few minutes to few hours) also contributes to increased amount of cirrus clouds observed in the upper troposphere.

The vertical distribution of clouds during the ASM shows several striking features. The north and northeast Bay of Bengal witness the deepest convection over the entire study domain - and among the deepest global convective regions–during this season, with a large fraction of the deep convective clouds reaching up to ∼15 km altitude. This feature is most intense during July-August. The zone of intense convection is centered around 16 to 22°N and 80 to 90°E (the north Bay of Bengal adjoining the east coast of Peninsular India) and around 12 to 20°N and 90 to 100°E (the northeast Bay of Bengal) - the latter is stronger than the former. In contrast, the occurrence of deep convective clouds almost ceases at the altitude of ∼13 to 14 km over all other regions during the ASM as well as the other seasons. This clearly shows that the top altitudes of deep convective clouds over the north/northeast Bay of Bengal extends at least 1 to 2 km above that over the other deep convective regions. Though less intense compared to the north/northeast Bay of Bengal, the deep convective clouds are also

prominent over the monsoon trough, the equatorial trough and the southeast Arabian Sea. The tropical easterly jetstream (TEJ) causes westward transport of large amount of cirrus outflows from the deep convective regions in the Bay of Bengal up to the central Arabian Sea. Eastward extent of this cirrus spreading is ∼30 to 40° from the deep convective regions in the Bay of Bengal and is further aided by the outflow from the southeast Arabian Sea.

Descending limb of the Hadley cell at the south Indian Ocean (at south of the ITCZ) is manifested by the persistent occurrence of low-altitude clouds and near-absence of convective clouds in the middle and upper troposphere during all seasons. The low-altitude clouds are very shallow and mostly occur in the altitude band of 1 to 3 km, with the largest frequency of occurrence of ∼30 to 40% at ∼1.5 km. In contrast, a similar feature is almost completely absent in the descending limb of the Hadley cell in the northern hemisphere. As the cold SST at the south Indian Ocean (SST <26°C) cannot provide sufficient moisture flux to the atmosphere for generating the highly persistent cloudiness, it is most likely that the lower tropospheric moisture required for the observed cloud development might have been produced mainly by the sea surfing caused by the strong surface winds in this region and its trapping below the strong trade-wind inversion. The moisture produced through evaporation of sea spray gets mixed in the atmospheric boundary layer by the turbulence generated by the strong wind shears. The moisture is trapped in the lower troposphere by the strong down-draft at the descending limb of the Hadley cell, which effectively prevents their upward transport from the lower troposphere. This leads to accumulation of moisture in the lower troposphere and subsequent development of shallow clouds in this region. Compared to the southern hemispheric Indian Ocean, the surface wind speeds, and sea agitation are rather weak in the northern hemisphere. The prevailing dry winds from the continents to the Arabian Sea and the Bay of Bengal would further decrease the water vapour mixing ratio generated by the evaporation from ocean surface at these oceanic regions. A combination of the above mechanisms might prevent significant development of lower tropospheric clouds over the Arabian Sea region while the south Indian Ocean can have larger moisture accumulation and cloudiness in the lower troposphere. However, this hypothesis needs to be further ascertained using observations of moisture and atmospheric thermo-dynamics in this region.

In general, the seasonal mean vertical distribution of clouds and their spatial variations are more or less similar during the individual years. However, considerable differences were observed in these features during the summer monsoon season of 2009, which was a drought year with a seasonal mean all-India rainfall deficit of 21.8%. Compared to the corresponding multi-year mean, the vertical development of clouds over the Indian region and the north Bay of Bengal (70 to 90°E longitude) is considerably

subdued while those over the northeast Bay of Bengal (90 to 100°E) and the equatorial trough region have substantially enhanced during the ASM of 2009. The above differences are most prominent during August and September - with the most pronounced deficit in the Indian region (70 to 80°E; 10 to 25°N) followed by the north Bay of Bengal (80 to 90°E), while the differences are negligible during July 2009. Monthly variations of the vertical distribution of clouds observed using CloudSat are in agreement with the corresponding variations in rainfall distribution. This study clearly shows that the anomalous weakening of convection and vertical development of clouds over the Indian region and the north Bay of Bengal occurs together with an anomalous strengthening of convection at the equatorial trough region and the east Bay of Bengal.

Chapter 4

One of the most remarkable features observed in the monthly and seasonal mean three-dimensional distribution of clouds is the persistent occurrence of a 'pool of inhibited cloudiness' over the southwest Bay of Bengal during the Asian summer monsoon season. Characteristics of this 'pool' and the potential mechanisms for its genesis are presented in Chapter 4. Frequency of occurrence of clouds in this 'pool' is 20 to 40% less than that of the surroundings. Seasonal mean precipitation rate over the 'pool' is <3 mm day^{-1} while that over the surrounding regions is mostly in the range of 6 to 14 mm day^{-1}. CloudSat observations clearly show that the 'pool' is almost completely contributed by a drastic reduction or near-absence of clouds below $\sim$7 km altitude that appear as a 'vault-like structure' in the zonal and meridional cross sections of the vertical distribution of clouds. In contrast, spatial gradient of high-altitude clouds above $\sim$8 km altitude over the entire region is negligible. The geographical location of this pool is remarkably consistent during the June to September period and occurs between 77 to 90°E in longitude and 3 to 13°N in latitude, which is surrounded by regions having large-scale convective clouds.

Putting together the pieces of observations of the structure of the 'pool' (in terms of cloudiness), surface wind divergence and differential latent heating of the atmosphere estimated from TRMM-PR data, the genesis of the 'pool' is proposed to stem from the existence of a mini-circulation in the lower and middle troposphere with significant divergence of surface wind at the 'pool' and subsidence in the middle troposphere, which is closed by the surface wind convergence and updraft in the troposphere over the surrounding deep convective regions. This mini-circulation is embedded in the large-scale monsoon circulation and might be a dynamical response of the atmosphere to the considerable spatial gradient of latent heating caused by the geographically fixed convective regions surrounding the 'pool'. The subsidence and surface wind divergence of air at the 'pool' will be at least partly responsible for the strong updraft at the

surrounding deep convective regions and hence might be an important component of the ASM. Genesis and maintenance of the 'pool' might be further influenced by orography of the region, the low-level jet and the relatively low SST at the south Bay of Bengal. It is also likely that, at least part of the reduction in SST observed in the 'pool' is contributed by the surface wind divergence associated with the proposed mini-circulation. However, significant differences exist in the circulation features derived from the reanalysis of atmospheric circulation at the 'pool' and that inferred from the spaceborne observations of surface wind divergence and cloud distribution.

Chapter 5

Extensive studies on the SST-dependence of cloudiness carried out in the past based on the total and high-altitude clouds observed using imager data showed that the total cloudiness increases with local SST above ∼26.5°C to attain a peak value at ∼29.5°C and decrease with further increase in SST. However, the 3-dimensional distribution of clouds derived from CloudSat data clearly shows the long-range transport of optically thick cirrus clouds considerably away from their source regions. Imager data cannot discriminate between these optically thick cirrus clouds and the deep convective clouds of local origin. While the latter might be triggered by local SST, the former is not, and hence, the SST-cloudiness relationship derived from imager data would be contaminated.

Utilizing the synergy of the capabilities of CloudSat and CALIPSO and ∼4.5 years of their observations, the role of SST and its spatial gradient and atmospheric thermodynamical parameters such as the lower tropospheric stability, convective available potential energy (CAPE), and wind convergence on the vertical distribution and development of clouds are investigated, as presented in Chapter-5. Direct observations on the dependence of the vertical development of clouds on SST and other atmospheric thermo-dynamic variables are least (if not never) explored, though improvements in these aspects are essential to quantify the effect of clouds and their potential feedback mechanisms.

Variations in the vertical distribution of clouds with SST show three distinct regimes: SST$<$27.5°C, 27.5°C$\leqslant$SST$<$29°C and SST$\geqslant$29°C. At SST$<$27.5°C, the convection is extremely weak that most of the clouds are limited to $<$2 km altitude with peak occurrence at ∼1 to 1.5 km. Frequency of occurrence of the low-altitude clouds as well as the prominence of the peak at ∼1.5 km consistently decreases for SST$>$24°C. Vertical development of clouds through the 3 to 12 km altitude region increases for SST$>$27.5°C to achieve maximum cloud occurrence in the SST range of 29 to 30.5°C. Penetration of the deep convective clouds to altitudes $>$15 km and their frequency of occurrence increase with SST till ∼30°C. These observations reveal two major differences with

the SST-dependence of total cloudiness reported earlier using imager data: (i) the increase in cloudiness at SST >26 to 27°C observed using the imager data is found to be an artifact due to increase in cirrus clouds generated by deep convective outflows and are not directly driven by the local SST, and (ii) the total cloudiness does not decrease for SST>29.5°C as showed by the imager data, but rather remains steady, at least till ∼30.5°C. Main cause for these differences between the results reported in the literature based on imager data and the present observations is that the imager observations could not isolate the effect of cirrus clouds generated by the outflows from deep convection. This causes biases in the SST-cloudiness relationship derived from the imager data, especially when the deep convection is generated in a region having large spatial gradient of SST.

The frequency of occurrence of lower tropospheric clouds decreases with increase in SST, especially in the SST range of 24 to 27°C. These regions of smaller SST in the tropics are generally characterized by large-scale subsidence driven by the remotely generated convection at warmer oceanic regions and favour the occurrence of low-level clouds. In the study region, the cold SSTs generally occur at the south Indian Ocean and are manifested by the descending limb of Hadley cell, which causes trapping of moisture in the lower troposphere and prevent vertical development of clouds. The observed decrease in the lower tropospheric cloudiness with increase in SST might be due to the fact that the warmer SSTs cause vertical transport of moisture from the lower troposphere by convection to the middle and upper troposphere where they cause cloud formation.

While the local SST regulates the moist static energy available at the surface, which is crucial for local convection, the updraft in the atmosphere is also influenced by remote forcing of tropospheric circulation driven by the large-scale spatial gradient of SST. The observed variations in the SST-dependence of the vertical distribution of cloudiness are explainable based on variations in the above parameters. Among them, the variations of CAPE and upper level divergence with SST are strikingly similar to the corresponding variations in the vertical distribution of clouds with SST, especially the rapid development of convection above 28°C and little variations in the vertical distribution of clouds in the SST band of 29 to 30.5°C. One of the striking features observed is the increase in the cloud top altitude up to which significant convection takes place, even for SST>29.5°C where the spatial gradient of SST as well as the increase in upper-level divergence are negligible. This is primarily caused by (i) an increase in CAPE, though weak, in the SST range of 29 to 30°C, and (ii) increase in the moist static energy available at the surface through increase in SST.

Another important feature observed is the increase in the probability of occurrence of deep convective clouds having vertical extent of >12 km. Prominence of this sec-

ondary peak increases with SST. The probability of occurrence of clouds as a function of cloud thickness in this secondary peak is explainable based on the potential temperature lapse rate. Over the study region, the convective tropopause, marked by a minimum in the potential temperature lapse rate (LRPT), is located around 12 to 15 km. Under highly convective conditions, the LRPT can be very close to zero or sometimes even negative. This means that, for a convective system having sufficient energy to reach in the vicinity of the convective tropopause, it requires only little more energy to be pushed up by another couple of kilometres or be naturally pushed up due to the instability (LRPT<0°C/km) in the vicinity of the convective tropopause.

Chapter 6

Studies carried out in the past using satellite data and ground-based lidar observations have provided a wealth of information on the monthly mean regional distribution of semi-transparent cirrus clouds (STC) and their characteristics over the Indian region and the surrounding oceans. However, investigations on the time evolution of the vertical structure of cirrus clouds requires observations at very short time intervals which cannot be carried out using satellite data. More importantly, as the descending of cirrus clouds is one of the potential mechanisms for their dissipation, investigations on the time evolution of the vertical structure of cirrus clouds is extremely important. This is one of the least explored aspects on cirrus clouds. Detailed characteristics of tropical cirrus clouds and time evolution of their vertical structure over Thiruvananthapuram (8.5° N, 77° E), a station located at the southwest coast of Peninsular India, are investigated using multi-year (2008 to 2011) observations carried out using Micropulse Lidar (MPL). Potential impact of cirrus descending on the cloud radiative forcing is also investigated.

The MPL observations reveal a pronounced annual variation in the frequency of occurrence of cirrus (FOC), with minimum occurrence during winter months (especially January-February, with FOC ∼30%) and largest occurrence during the summer monsoon months, especially of June to August (FOC ∼75 to 85%). While the cirrus occurring over Thiruvananthapuram during the summer monsoon months might have originated from the deep convective outflows from the Bay of Bengal advected by the tropical easterly jet stream, those during winter might mostly be produced in situ. During the pre-monsoon and post-monsoon seasons, localized convective outflows might generate cirrus. The largest frequency of occurrence of cirrus is observed in the altitude range of 11 to 15 km, irrespective of the season. The peak occurrence of cirrus is near the base of the TTL layer. Majority of the cirrus clouds (64 to 73%) have COD in the range of 0.03 to 0.3. The frequency of occurrence of sub-visual cirrus (COD<0.03) is ∼18 to 24%. Non-sphericity of the ice crystals (inferred from the linear

depolarization ratio, LDR) is observed to increase substantially with altitude, up to ∼14.5 to 16.5 km. This is followed by a rapid decrease in LDR, especially above ∼16 to 17 km altitude, indicating a corresponding change in the genesis of cirrus near the cold point tropopause. It is highly likely that the cirrus with low values of LDR observed near the cold point tropopause are formed in situ.

In large number of cases, time evolution of the vertical structure of cirrus clouds (observed using the vertical profiles of lidar signal at high temporal and vertical resolution) shows a pronounced descending structure, indicating the significant occurrence of descending cirrus layers. This feature is observed throughout the year. The duration of cirrus descending is so large that it cannot be attributed to the manifestation of cirrus uncinus. Probability of occurrence of descending cirrus is larger during pre-monsoon and post-monsoon seasons (about 23 to 24%) and least during winter (15%). Though the frequency of occurrence of cirrus clouds is largest (69%) during ASM, the fraction of cirrus clouds that are descending is the least (<26%) during this season. The fractions of descending cirrus during the other seasons are ∼41 to 49%. Reduction in the frequency of occurrence of descending cirrus observed during the ASM might be due to the high-speed upper tropospheric easterlies prevailing during this season, which are responsible for the long-range transport of cirrus and moisture from the Bay of Bengal region.

The most probable base (top) altitudes of descending cirrus layers are in the range of 11 to 15 km (12 to 16 km) before descent and 8 to 13 km (9 to 14 km) after descent. Most of the descending cirrus clouds form very close to the TTL base (around 14 to 15 km) and settle downward. The frequency of occurrence and vertical displacement of descending cirrus layers occurring within 2 km below the cold point tropopause is considerably smaller than those occurring at or below the TTL base. On average, the vertical displacements of the top and base of cirrus layers show almost a one-to-one relationship; the most probable vertical displacements are in the range of 1.5 to 2.5 km. The percentage of cirrus that are thickening or thinning by >300 m during descending are almost equal (∼23% each), while the thickening/thinning of the remaining 54% is <300 m. In >20% of the cases, vertical displacement of the cloud top and base is >3 km. Most probable duration of the descending cirrus layers is 1 to 2 h (frequency of occurrence of ∼45%). However, nearly 40% of the descending cirrus lasted for 2 to 5 h. The frequency of occurrence of descending cirrus layers that last for <1 h or >5 h is very small (∼7 to 8%). The descent speed is inversely proportional to the cloud duration. All cirrus layers lasting for >3 h have descent speeds of <0.28 ms^{-1}. Around 95% of descending cirrus clouds have settling speed less than 0.8 ms^{-1} and none of these clouds are of sub-visual type (COD <0.03). Most probable value of COD for descending cirrus is between 0.2 and 0.3. On average, descending increases the

cloud top temperature from ∼201± 2 K (before descent) to ∼216±2 K (after descent), yielding a mean enhancement of ∼15 K in cloud top temperature. Radiative transfer calculations show that the descending of cirrus clouds would cause a typical reduction of ∼1 to ∼12.9 Wm^{-2} in the long-wave CRF at TOA (for vertical displacements and CODs in the ranges of 1.0 to 3.5 km and 0.1 to 0.4 respectively).

Chapter 7

Impact of clouds on the energetics of the earth-atmosphere system is investigated using the satellite-based estimations of clouds radiative forcing (CRF) at top-of-the-atmosphere (TOA) and latent heating of the atmosphere by precipitating clouds. The seasonal mean shortwave, longwave and net cloud radiative forcing at the top of the atmosphere (TOA) and their diurnal variations during the summer monsoon and post-monsoon seasons are estimated using the data obtained from ScaRaB onboard Megha-Tropiques (MT) satellite during July to November 2012. Spatial variations of the seasonal mean altitude profiles of the latent heating rate (LHR) in the atmosphere by precipitating clouds are investigated using the data obtained from the Precipitation Radar (PR) onboard the TRMM satellite over the Indian region and the surrounding oceans during 2006 to 2011.

Low-inclination orbit of the Megha-Tropiques enables frequent observations of a location in the tropical region at different local time of the day. The ScaRaB observations of shortwave and longwave radiative fluxes at the TOA enable the estimation of diurnal variations in cloud radiative forcing. However, as the frequency of observation at a location varies considerably during the precessing MT orbital cycle of 51 days, data for long period should be used for estimating the diurnal variation of CRF based on an 'equivalent-day' analysis during the period. Hence, this study reports only the seasonal mean diurnal variations of shortwave, longwave and net CRF at the TOA. The longwave cloud radiative forcing (LWCRF) is found to be always positive (warming of the earth-atmosphere system) while the shortwave CRF (SWCRF) is always negative (cooling). Mean values of the LWCRF and SWCRF during the ASM are largest over the northeast Bay of Bengal, where LWCRF is generally greater than 100 Wm^{-2} while SWCRF is in the range of -100 to -160 Wm^{-2}. This yield a negative (cooling) net cloud radiative forcing (NCRF) of -10 to -60 Wm^{-2} during the ASM over the north-east Bay of Bengal, which is characterized by the deepest convection and optically thick clouds. The minimum values of LWCRF and SWCRF during the ASM are observed over the west Arabian Sea and the adjoining Arabian Desert, where their magnitudes are <20 Wm^{-2} and the NCRF is nearly zero.

Notwithstanding the similarities observed in the spatial variations of LWCRF and SWCRF, they show certain distinct differences: (i) Magnitude of the mean SWCRF

is considerably large (>120 Wm^{-2}) over the northern parts of India (along the mean location of the Monsoon Trough) and along the west coast of Indian Peninsula, while the mean LWCRF over these locations is <80 Wm^{-2}. This suggests that the clouds occurring over the Monsoon Trough region as well as off the Western Ghats have albedo comparable to those occurring over the north Bay of Bengal, yielding comparable values of SWCRF over these regions. However, the top altitudes of optically thick clouds are largest over the north Bay of Bengal compared to the above regions, which explains the large differences in the values of LWCRF at these regions. (ii) One of the most remarkable features of SWCRF is its significant magnitude (-20 to -40 Wm^{-2}) over the entire south Indian Ocean, while the corresponding values of LWCRF over this region are negligible. This is primarily because of the presence of large amount of significantly reflecting low-altitude clouds which occur below ∼2 to 3 km altitude. The difference between the temperatures of the ocean surface and cloud top is rather small, resulting in negligible values of LWCRF. The NCRF in this region is to produce a net cooling of -20 to -40 Wm^{-2}.

Diurnal variation of the LWCRF is largest over the deep convective regions of the northeast Bay of Bengal, where the LWCRF maximizes during 21 to 03 Local Time (LT) (LWCRF ∼100 to 110 Wm^{-2}) and minimizes during 09 to 15 LT (LWCRF ∼70 to 105 Wm^{-2}). Over most of the regions, their values are minimum during the daytime (especially the forenoon hours of 06 to 12 LT) and largest during the night or late evening. Over the deep convective regions, the nighttime value exceeds the daytime LWCRF by >20 Wm^{-2}. The nighttime values of LWCRF are also larger over the southern hemispheric Indian Ocean which is dominated by low-altitude clouds. The net effect of clouds during the daytime is to produce a cooling effect. Magnitude of this daytime cooling is largest over the north Bay of Bengal, the Indian landmass encompassing the monsoon trough and off the Western Ghats, and the central African region, where the daytime NCRF varies in the range of -100 to -200 Wm^{-2}. The NCRF over the southern hemispheric Indian Ocean is in the range of -50 to -100 Wm^{-2}. The nighttime values of NCRF are always positive (warming) because of the absence of cooling due to SWCRF. This nighttime warming effect is largest over the north Bay of Bengal, equatorial trough region of the Indian Ocean, the Indian landmass and the central African region, where the values of NCRF are in the range of 50 to 100 Wm^{-2}. The nighttime NCRF over the southern hemispheric Indian Ocean is quite small and the day-night differences of NCRF is <100 Wm^{-2} in this region.

During the post-monsoon season, the seasonal mean LWCRF is largest (60 to 110 Wm^{-2}) over the ITCZ, while its value decreases rapidly to less than 10 Wm^{-2} at central India and the Southern Hemispheric Indian Ocean, both of which are occupied by the descending limb of the Hadley Cell. In the ITCZ region, the SWCRF

is generally in the range of -50 to -100 Wm^{-2}. However, the SWCRF is remarkably significant (-50 to -100 Wm^{-2}) over the southern hemispheric Indian Ocean, especially at south of ∼20°S, where the LWCRF is the least (<10 Wm^{-2}). Over most of the ITCZ region, the SWCRF almost cancels the LWCRF, yielding nearly zero NCRF. However, over the regions at the southern hemispheric Indian Ocean and east Asia, which are dominated by the low-altitude clouds, the NCRF is negative, with most of the values in the range of -30 to -60 Wm^{-2}.

The latent heating rates estimated from the TRMM-PR observations show that, though the geographical locations having significantly high values of LHR coincide with those of cloud occurrence, their altitudes of peak occurrence as well as the spatial gradients are considerably different. The largest values of LHR are generally observed in the altitude band of 5 to 10 km in all regions. On the contrary, the largest occurrence of clouds is generally observed in the altitude bands of 10 to 13 km and <3 km. This major difference is because a large fraction of clouds that occur in the altitude band of 10 to 13 km are cirrus clouds, which do not precipitate. Similar is the case of the low-altitude cumuli or stratocumulus clouds that dominate the Southern Hemisphere Indian Ocean. During the winter season, the largest values of LHR are observed over the southern Africa in the longitude band of 30 to 40°E between 20°S to 5°S, where the seasonal mean LHR is in the range of 0.1 to 0.18 K/h in the 5 to 10 km altitude region. At the north of this intensely heating band, the LHR decreases to <0.02 K/h at north of 3°N, producing a large spatial gradient in the atmospheric heating rates. Zonally, the minimum values of LHR are observed in the 50 to 60°E longitude band, where the cloudiness is rather small. On average, the LHR systematically increases eastwards from the longitude of 50°E to 100°E and it exceeds 0.14 K/h over a wide region of the east equatorial Indian Ocean and Sumatra/Indonesia in the longitude band of 90 to 110°E. During the summer monsoon season, the largest values of LHR are observed over the northeast Bay of Bengal in the geographical region encompassed between 10 to 22°N and 90 to 100°E, where the seasonal mean LHR is >0.20 K/h. This season is marked by large meridional gradient of LHR caused by the small values of LHR over the southern hemisphere Indian Ocean and large values in the northern hemisphere over the Indian landmass, east Asia and the Bay of Bengal.

8.2 Future Scope

The above studies have brought out the monthly and seasonal mean 3-dimensional distribution of clouds, their regulation by the large-scale atmospheric circulation, SST and atmospheric thermo-dynamics. Impact of clouds on the energetics of the earth-atmosphere system has also been estimated. Some of the important scientific aspects that need to be explored, in the light of the results obtained from the present study,

are listed below:

1. The radiative effect of clouds is to found to cause a net cooling of the earth-atmosphere system during the daytime and warming during the nighttime. This will correspondingly modulate the total radiative flux available at the surface, leading to a reduction in the diurnal variation of the net radiative flux and heating at the surface. Similarly, the large spatial variations in the net cloud radiative forcing would modulate the horizontal variations in heating/cooling of the earth-atmosphere system and hence the atmospheric dynamics. This would play a major factor in the cloud feedback processes. Two important aspects that need to be explored are: (i) the role of cloud radiative forcing on the diurnal variation of the surface heating and subsequent change in atmospheric dynamics, and (ii) the effect of cloud radiative forcing on the reduction of differential heating of the surface and atmosphere.

2. The present study is limited to the latent heating of the atmosphere by precipitating clouds. On average, a substantially large portion (typically 90%) of the total clouds are non-precipitating. The latent heat released by these clouds during cloud formation is quite large, but largely unexplored. This is primarily because of the absence of information on the altitude profiles of cloud water content. The altitude profiles of radar reflectivity observed using CloudSat have the potential to provide this information (albeit with relatively large uncertainty). Exploration of the latent heating by clouds is essential for quantitative assessment of the impact of clouds on the energetics of the atmosphere and to understand the cloud feedback processes.

3. The present study clearly brings out the characteristics of the 'pool of inhibited cloudiness'. Its potential genesis mechanism from a mini-circulation, embedded in the large-scale monsoon circulation, is proposed based on the available observations. This needs to be explored further, especially using coupled atmospheric circulation models. Further, the characteristics and role this 'pool' during the active and break cycles of the summer monsoon, and vice versa, need to be investigated.

4. The SST-dependence of the vertical distribution of clouds reported here further refines the extensively investigated SST-dependence of total cloudiness reported in the literature using imager data and explains the potential causes for the observed differences. However, the present study does not address the variations in cloudiness with SST for SST$>$30.5°C and the factors that limit the maximum SST to less than $\sim$32°C. The cloud information derived from the CALIPSO and CloudSat data over the warm pool regions, together with the energetics of the

ocean and atmospheric processes, have the potential to address this fundamental science question.

5. Physical and optical characteristics of the descending tropical cirrus layers are presented here. The observed features clearly show the importance of mechanisms other than sedimentation of ice crystals in regulating the descending of cirrus clouds. The most important candidate among them is the atmospheric downdraft. The potential impact of atmospheric circulation and waves (especially through the vertical winds) in this regulation needs to be addressed. Further, the impact of descending of the cirrus clouds is among the potential mechanisms responsible for causing dehydration and altering the thermo-dynamic properties of the upper troposphere and lower stratosphere (UTLS). This needs to be ascertained based on collocated observations of descending cirrus layers with altitude profiles of temperature and humidity at the UTLS region.

References

Ackerman, A. S. (2000), Reduction of Tropical Cloudiness by Soot, *Science*, *288*(5468), 1042–1047, doi:10.1126/science.288.5468.1042.

Adler, R. F., et al. (2003), The Version-2 Global Precipitation Climatology Project (GPCP) monthly precipitation analysis (1979 – present), *J. Hydrometeor.*, *4*, 1147–1167.

Albrecht, B. A. (1989), Aerosols, cloud microphysics, and fractional cloudiness., *Science*, *245*(4923), 1227–30, doi:10.1126/science.245.4923.1227.

Andreae, M. O., and D. Rosenfeld (2008), Aerosol-cloud-precipitation interactions. Part 1. The nature and sources of cloud-active particles, *Earth Sci. Rev.*, *89*, 13–41.

Arking, A., and D. Ziskin (1994), Relationship between Clouds and Sea Surface Temperatures in the Western Tropical Pacific, *J. Clim.*, *7*(6), 988–1000, doi:10.1175/1520-0442(1994)007⟨0988:RBCASS⟩2.0.CO;2.

Ashok, K., Z. Guan, and T. Yamagata (2001), Impact of the Indian Ocean dipole on the relationship between the Indian monsoon rainfall and ENSO, *Geophys. Res. Lett.*, *28*(23), 4499–4502, doi:10.1029/2001GL013294.

Ashok, K., Z. Guan, N. H. Saji, and T. Yamagata (2004), Individual and Combined Influences of ENSO and the Indian Ocean Dipole on the Indian Summer Monsoon, *J. Clim.*, *17*(16), 3141–3155, doi:10.1175/1520-0442(2004)017⟨3141:IACIOE⟩2.0.CO;2.

Babu, S. S. (2004), Aerosol black carbon over Arabian Sea during intermonsoon and summer monsoon seasons, *Geophys. Res. Lett.*, *31*(6), L06,104, doi:10.1029/2003GL018716.

Battan, L. J. (2003), *Cloud Physics-A Popular Illustration to Appplied Meteorology*, Dover Publications, New York, USA.

Baum, B. A., A. J. Heymsfield, P. Yang, and S. T. Bedka (2005), Bulk Scattering Properties for the Remote Sensing of Ice Clouds. Part I: Microphysical Data and Models, *J. Appl. Meteorol.*, *44*(12), 1885–1895, doi:10.1175/JAM2308.1.

Behera, S. K., R. Krishnan, and T. Yamagata (1999), Unusual ocean-atmosphere conditions in the tropical Indian Ocean during 1994, *Geophys. Res. Lett.*, *26*(19), 3001–3004, doi:10.1029/1999GL010434.

Bentamy, A., Y. Quilfen, F. Gohin, N. Grima, M. Lenaour, and J. Servain (1996), Determination and validation of average wind fields from ERS-1 scatterometer measurements, *Global Atmos. Ocean Syst.*, *4*, 1–29.

Bhat, G. S., J. Srinivasan, and S. Gadgil (1996), Tropical deep convection, convective available potential energy and sea surface temperature, *J. Meteor. Soc. Jpn.*, *74*, 155–166.

Bhavani Kumar, Y., V. S. Siva Kumar, A. R. Jain, and P. B. Rao (2001), MST radar

and polarization lidar observations of tropical cirrus, *Ann. Geophys.*, *19*(8), 873–882, doi:10.5194/angeo-19-873-2001.

Bony, S., K.-M. Lau, and Y. C. Sud (1997), Sea Surface Temperature and Large-Scale Circulation Influences on Tropical Greenhouse Effect and Cloud Radiative Forcing, *J. Clim.*, *10*(8), 2055–2077, doi:10.1175/1520-0442(1997)010⟨2055:SSTALS⟩2.0.CO;2.

Bony, S., W. D. Collins, and D. W. Fillmore (2000), Indian Ocean Low Clouds during the Winter Monsoon, *J. Clim.*, *13*(12), 2028–2043, doi:10.1175/1520-0442(2000)013⟨2028:IOLCDT⟩2.0.CO;2.

Bréon, F.-M., and M. Doutriaux-Boucher (2005), A comparison of cloud droplet radii measured from space, *IEEE Transactions on Geoscience and Remote Sensing*, *43*(8), 1796–1805, doi:10.1109/TGRS.2005.852838.

Campbell, J. R., D. L. Hlavka, E. J. Welton, C. J. Flynn, D. D. Turner, J. D. Spinhirne, V. S. Scott, and I. H. Hwang (2002), Full-Time, Eye-Safe Cloud and Aerosol Lidar Observation at Atmospheric Radiation Measurement Program Sites: Instruments and Data Processing, *J. Atmos. Oceanic Technol.*, *19*(4), 431–442, doi:10.1175/1520-0426(2002)019⟨0431:FTESCA⟩2.0.CO;2.

Cess, R. D., et al. (1990), Intercomparison and interpretation of climate feedback processes in 19 atmospheric general circulation models, *J. Geophys. Res.*, *95*(D10), 16,601, doi:10.1029/JD095iD10p16601.

Cetrone, J., and R. A. Houze (2009), Anvil clouds of tropical mesoscale convective systems in monsoon regions, *Q. J. R. Meteorol. Soc.*, *135*(639), 305–317, doi:10.1002/qj.389.

Chang, F.-L., and Z. Li (2005), A New Method for Detection of Cirrus Overlapping Water Clouds and Determination of Their Optical Properties, *J. Atmos. Sci.*, *62*(11), 3993–4009, doi:10.1175/JAS3578.1.

Charlson, R. J., S. E. Schwartz, J. M. Hales, R. D. Cess, J. A. Coakley, J. E. Hansen, and D. J. Hofmann (1992), Climate forcing by anthropogenic aerosols., *Science*, *255*(5043), 423–30, doi:10.1126/science.255.5043.423.

Chen, S. S., and A. H. J. R (1997), Diurnal variation and life-cycle of deep convective systems over the tropical Pacific warm pool, *Q. J. R. Meteorol. Soc.*, *123*, 357 – 388.

Cho, H., C.-H. Ho, and Y.-S. Choi (2012), The observed variation in cloud-induced longwave radiation in response to sea surface temperature over the Pacific warm pool from MTSAT-1R imagery, *Geophys. Res. Lett.*, *39*(18), doi:10.1029/2012GL052700.

Choi, Y. S., and C. H. Ho (2006), Radiative effects of cirrus with different optical properties over the tropics in MODIS and CERES observations, *Geophys. Res. Lett.*, *33*, L21,811, doi:10.1029/2006GL027403.

Chomette, O., P. Raberanto, N. Gif, M. Capderou, and R. Rica (2012), ScaRaB onboard MeghaTropiques, in *IndoFrench Woprkshop on MeghaTropiques*, ISRO-CNES.

Chung, E. S., B. J. Sohn, J. Schmetz, and M. Koenig (2007), Diurnal variation of upper tropospheric humidity and its relations to convective activities over tropical Africa, *Atmos. Chem. Phys.*, *7*, 2489 – 2502.

Clothiaux, E. E., et al. (1999), The Atmospheric Radiation Measurement Program Cloud Radars: Operational Modes, *J. Atmos. Oceanic Technol.*, *16*(7), 819–827, doi:10.1175/1520-0426(1999)016⟨0819:TARMPC⟩2.0.CO;2.

Coakley, J. A., and F. P. Bretherton (1982), Cloud cover from high-resolution scanner

data: Detecting and allowing for partially filled fields of view, *J. Geophys. Res.*, *87*(C7), 4917, doi:10.1029/JC087iC07p04917.

Comstock, J. M. (2004), Evidence of high ice supersaturation in cirrus clouds using ARM Raman lidar measurements, *Geophys. Res. Lett.*, *31*(11), L11,106, doi:10.1029/2004GL019705.

Comstock, J. M., and K. Sassen (2001), Retrieval of Cirrus Cloud Radiative and Backscattering Properties Using Combined Lidar and Infrared Radiometer (LIRAD) Measurements, *J. Atmos. Oceanic Technol.*, *18*(10), 1658–1673, doi:10.1175/1520-0426(2001)018⟨1658:ROCCRA⟩2.0.CO;2.

Corti, T., and T. Peter (2009), A simple model for cloud radiative forcing, *Atmos. Chem. Phys.*, *9*, 5751–5758, doi:10.5194/acp-9-5751-2009.

Corti, T., B. P. Luo, Q. Fu, H. Vomel, and T. Peter (2006), The impact of cirrus clouds on tropical troposphere-to-stratosphere transport, *Atmos. Chem. Phys.*, *6*, 2539–2547, doi:10.5194/acpd-6-1725-2006.

Das, P. K. (1968), *Monsoons*, vol. 613, 1–254 pp., National Book Trust, New Delhi.

Das, S. K., C.-W. Chiang, and J.-B. Nee (2009), Characteristics of cirrus clouds and its radiative properties based on lidar observation over Chung-Li, Taiwan, *Atmos. Res.*, *93*(4), 723–735, doi:10.1016/j.atmosres.2009.02.008.

Das, S. K., J. B. Nee, and C. W. Chiang (2010), A LiDAR study of the effective size of cirrus ice crystals over Chung-Li, Taiwan, *J. Atmos. Sol. Terr. Phys.*, *72*(9–10), 781–788, doi:10.1016/j.jastp.2010.03.024.

de Reus, M., et al. (2009), Evidence for ice particles in the tropical stratosphere from in-situ measurements, *Atmos. Chem. Phys.*, *9*(18), 6775–6792, doi:10.5194/acp-9-6775-2009.

Decker, M., M. A. Brunke, Z. Wang, K. Sakaguchi, X. Zeng, and M. G. Bosilovich (2012), Evaluation of the Reanalysis Products from GSFC, NCEP, and ECMWF Using Flux Tower Observations, *J. Clim.*, *25*(6), 1916–1944, doi:10.1175/JCLI-D-11-00004.1.

Deirmendjian, D. (1969), *Electromagnetic Scattering on Spherical Polydisperions*, 316 pp., Elsevier, California.

Deng, M., and G. D. Mace (2008), Cirrus cloud microphysical properties and air motion statistics using cloud radar Doppler moments: Water content, particle size, and sedimentation relationships, *Geophys. Res. Lett.*, *35*(L17808), doi:10.1029/2008GL035054.

Derrien, M., B. Farki, L. Harang, H. LeGléau, A. Noyalet, D. Pochic, and A. Sairouni (1993), Automatic cloud detection applied to NOAA-11 /AVHRR imagery, *Remote Sens. Environ.*, *46*(3), 246–267, doi:10.1016/0034-4257(93)90046-Z.

Dessler, A. E., and P. Yang (2003), The Distribution of Tropical Thin Cirrus Clouds Inferred from Terra MODIS Data, *J. Clim.*, *16*(8), 1241–1247, doi:10.1175/1520-0442(2003)16⟨1241:TDOTTC⟩2.0.CO;2.

Devasthale, A., and H. Grassl (2009), A daytime climatological distribution of high opaque ice cloud classes over the Indian summer monsoon region observed from 25-year AVHRR data, *Atmos. Chem. Phys.*, *9*(1), 23–58, doi:10.5194/acpd-9-23-2009.

Dowling, D. R., and L. F. Radke (1990), A Summary of the Physical Properties of Cirrus Clouds, *J. Appl. Meteorol.*, *29*(9), 970–978, doi:10.1175/1520-0450(1990)029⟨0970:ASOTPP⟩2.0.CO;2.

Durden, S., and R. Boain (2004), Orbit and Transmit Characteristics of the CloudSat Cloud Profiling Radar (CPR), *Tech. rep.*, Jet Propulsion Laboratory, California Institute of Technology, Pasadena, CA 91109.

Durkee, P., F. Pfeil, E. Frost, and R. Shema (1991), Global analysis of aerosol particle characteristics, *Atmos. Environ.*, *25*(11), 2457–2471, doi:10.1016/0960-1686(91)90163-2.

Ellis, T. D., T. L'Ecuyer, J. M. Haynes, and G. L. Stephens (2009), How often does it rain over the global oceans? The perspective from CloudSat, *Geophys. Res. Lett.*, *36*(3), L03,815, doi:10.1029/2008GL036728.

Fernald, F. G. (1984), Analysis of atmospheric lidar observations: Some comments, *Appl. Opt.*, *23*, 652–653, doi:10.1364/AO.23.000652.

Flynn, C. J., A. Mendoza, Y. Zheng, and S. Mathur (2007), Novel polarization-sensitive micropulse lidar measurement technique., *Opt. Exp.*, *15*(6), 2785–90.

Fox, N. I., and A. J. Illingworth (1997), The Retrieval of Stratocumulus Cloud Properties by Ground-Based Cloud Radar, *J. Appl. Meteorol.*, *36*(5), 485–492, doi:10.1175/1520-0450(1997)036⟨0485:TROSCP⟩2.0.CO;2.

Franya, G. B., and A. P. Cracknell (1995), A simple cloud masking approach using NOAA AVHRR daytime data for tropical areas, *Int. J. Remote Sensing*, *16*(9), 1697–1705, doi:10.1080/01431169508954506.

Frey, W., et al. (2011), In situ measurements of tropical cloud properties in the West African Monsoon: Upper tropospheric ice clouds, Mesoscale Convective System outflow, and subvisual cirrus, *Atmos. Chem. Phys.*, *11*, 5569–5590, doi:10.5194/acp-11-5569-2011.

Fu, Q., M. Baker, and D. L. Hartmann (2002), Tropical cirrus and water vapor: an effective Earth infrared iris feedback?, *Atmos. Chem. Phys.*, *2*(1), 31–37, doi:10.5194/acp-2-31-2002.

Fu, Q., Y. Hu, and Q. Yang (2007), Identifying the top of the tropical tropopause layer from vertical mass flux analysis and CALIPSO lidar cloud observations, *Geophys. Res. Lett.*, *34*, L14,813, doi:10.1029/2007GL030099.

Fu, R., A. D. Del Genio, and W. B. Rossow (1990), Behavior of Deep Convective Clouds in the Tropical Pacific Deduced from ISCCP Radiances, *J. Clim.*, *3*(10), 1129–1152, doi:10.1175/1520-0442(1990)003⟨1129:BODCCI⟩2.0.CO;2.

Fu, R., A. D. Del Genio, and W. B. Rossow (1994), Influence of Ocean Surface Conditions on Atmospheric Vertical Thermodynamic Structure and Deep Convection, *J. Clim.*, *7*(7), 1092–1108, doi:10.1175/1520-0442(1994)007⟨1092:IOOSCO⟩2.0.CO;2.

Gadgil, S., P. V. Joseph, and N. V. Joshi (1984), Ocean-atmosphere coupling over monsoon regions, *Nature*, *312*, 141–143.

Gambheer, A. V., and G. S. Bhat (2000), Life Cycle Characteristics of Deep Cloud Systems over the Indian Region Using INSAT-1B Pixel Data, *Mon. Weather Rev.*, *128*(12), 4071–4083, doi:10.1175/1520-0493(2000)129⟨4071:LCCODC⟩2.0.CO;2.

Gambheer, A. V., and G. S. Bhat (2001), Diurnal variation of deep cloud systems over the Indian region using INSAT-1B pixel data, *Meteorol. Atmos. Phys.*, *78*(3-4), 215–225, doi:10.1007/s703-001-8175-4.

Garrett, T. J., et al. (2005), Evolution of a Florida Cirrus Anvil, *J. Atmos. Sci.*, *62*(7), 2352–2372, doi:10.1175/JAS3495.1.

Gerber, H., B. Arends, and A. Ackerman (1994), New microphysics sensor for aircraft use, *Atmos. Res.*, *31*(4), 235–252, doi:10.1016/0169-8095(94)90001-9.

Gettelman, A., and d. P. M. Forster (2002), A climatology of the tropical tropopause layer, *J. Meteor. Soc. Jpn.*, *80*, 911–924.

Gettelman, A., W. J. Randel, F. Wu, and S. T. Massie (2002), Transport of water vapor in the tropical tropopause layer, *Geophys. Res. Lett.*, *29*(01), 1009, doi:10.1029/2001GL013818.

Goswami, B. N., V. Krishnamurthy, and H. Annamali (1999), A broad scale circulation index for the interannual variability of the Indian summer monsoon, *Q. J. R. Meteorol. Soc.*, *125*, 611–633, doi:10.1029/2007GL029335.

Graham, N. E., and T. P. Barnett (1987), Sea Surface Temperature, Surface Wind Divergence, and Convection over Tropical Oceans., *Science*, *238*(4827), 657–9, doi:10.1126/science.238.4827.657.

Grossman, R. L., and O. Garcia (1990), The Distribution of Deep Convection over Ocean and Land during the Asian Summer Monsoon, *J. Clim.*, *3*(9), 1032–1044, doi:10.1175/1520-0442(1990)003⟨1032:TDODCO⟩2.0.CO;2.

Gruber, A., X. Su, M. Kanamitsu, and J. Schemm (2000), The Comparison of Two Merged Rain Gauge-Satellite Precipitation Datasets, *Bull. Am. Meteorol. Soc.*, *81*(11), 2631–2644, doi:10.1175/1520-0477(2000)081⟨2631:TCOTMR⟩2.3.CO;2.

Guimond, S. R., M. A. Bourassa, and P. D. Reasor (2011), A Latent Heat Retrieval and Its Effects on the Intensity and Structure Change of Hurricane Guillermo (1997). Part I: The Algorithm and Observations, *J. Atmos. Sci.*, *68*(8), 1549 – 1567.

Gupta, S. K., A. C. Wilber, W. L. DarnellL, and J. T. Suttles (1993), Longwave surface radiation over the globe from satellite data: An error analysis, *Int. J. Remote Sensing*, *14*(1), 95–114, doi:10.1080/01431169308904323.

Hahn, C. J., S. G. Warren, and J. London (1996), Edited synoptic cloud reports from ships and land stations over the globe, 1982–1991, pp. 1982–1991.

Haladay, T., and G. Stephens (2009), Characteristics of tropical thin cirrus clouds deduced from joint CloudSat and CALIPSO observations, *J. Geophys. Res.*, *114*, D00A25, doi:10.1029/2008JD010675.

Hall, T. J., and T. H. Vonder Haar (1999), The Diurnal Cycle of West Pacific Deep Convection and Its Relation to the Spatial and Temporal Variation of Tropical MCSs, *J. Atmos. Sci.*, *56*(19), 3401–3415, doi:10.1175/1520-0469(1999)056⟨3401:TDCOWP⟩2.0.CO;2.

Hansen, J., A. Lacis, D. Rind, G. Russell, P. Stone, I. Fung, J. Lerner, and R. Ruedy (1984), *Climate sensitivity: Analysis of feedback mechanisms. Climate Processes and Climate Sensitivity*, pp. 130 – 163, AGU.

Hanson, H. P., P. Cornillon, G. R. Halliwell, and V. Halliwell (1991), Climatological perspectives, oceanographic and meteorological, on variability in the subtropical convergence zone in the northwestern Atlantic, *J. Geophys. Res.*, *96*(C5), 8517, doi:10.1029/90JC02487.

Harrison, E. F., P. Minnis, B. R. Barkstrom, V. Ramanathan, R. D. Cess, and G. G. Gibson (1990), Seasonal variation of cloud radiative forcing derived from the Earth Radiation Budget Experiment, *J. Geophys. Res.*, *95*(D11), 18,687, doi:10.1029/JD095iD11p18687.

Hartmann, D. L. (2002), An important constraint on tropical cloud - climate feedback, *Geophys. Res. Lett.*, *29*(20), 1951, doi:10.1029/2002GL015835.

Hartmann, D. L., and M. L. Michelsen (1993), Large-Scale Effects on the Regulation of Tropical Sea Surface Temperature, *J. Clim.*, *6*(11), 2049–2062, doi:10.1175/1520-0442(1993)006⟨2049:LSEOTR⟩2.0.CO;2.

Hartmann, D. L., and D. A. Short (1980), On the Use of Earth Radiation Budget Statistics for Studies of Clouds and Climate, *J. Atmos. Sci.*, *37*(6), 1233–1250, doi:10.1175/1520-0469(1980)037⟨1233:OTUOER⟩2.0.CO;2.

Hartmann, D. L., M. E. Ockert-Bell, and M. L. Michelsen (1992), The Effect of Cloud Type on Earth's Energy Balance: Global Analysis, *J. Clim.*, *5*(11), 1281–1304, doi:10.1175/1520-0442(1992)005⟨1281:TEOCTO⟩2.0.CO;2.

Hartmann, D. L., J. R. Holton, and Q. Fu (2001), The heat balance of the tropical tropopause, cirrus, and stratospheric dehydration, *Geophys. Res. Lett.*, *28*(10), 1969–1972, doi:10.1029/2000GL012833.

Haynes, J. M., and G. L. Stephens (2007), Tropical oceanic cloudiness and the incidence of precipitation: Early results from CloudSat, *Geophys. Res. Lett.*, *34*(L09811), doi:10.1029/2007GL029335.

Hegg, D. A., and P. V. Hobbs (1992), Cloud condensation nuclei in the marine atmosphere: A review, *Nucleation and Atmospheric Aerosol*, pp. 181–192.

Hess, M., P. Koepke, and I. Schult (1998), Optical Properties of Aerosols and Clouds: The Software Package OPAC, *Bull. Am. Meteorol. Soc.*, *79*(5), 831–844, doi:10.1175/1520-0477(1998)079⟨0831:OPOAAC⟩2.0.CO;2.

Heymsfield, A. (1975), Cirrus Uncinus Generating Cells and the Evolution of Cirriform Clouds. Part I: Aircraft Observations of the Growth of the Ice Phase, *J. Atmos. Sci.*, *32*(4), 799–808, doi:10.1175/1520-0469(1975)032⟨0799:CUGCAT⟩2.0.CO;2.

Heymsfield, A. J. (1986), Ice Particles Observed in a Cirriform Cloud at 83C and Implications for Polar Stratospheric Clouds, *J. Atmos. Sci.*, *43*(8), 851–855, doi:10.1175/1520-0469(1986)043⟨0851:IPOIAC⟩2.0.CO;2.

Heymsfield, A. J. (2007), On measurements of small ice particles in clouds, *Geophys. Res. Lett.*, *34*(23), n/a–n/a, doi:10.1029/2007GL030951.

Heymsfield, A. J., and L. J. Donner (1990), A Scheme for Parameterizing Ice-Cloud Water Content in General Circulation Models, *J. Atmos. Sci.*, *47*, 1865–1877, doi:10.1175/1520-0469(1990)047⟨1865:ASFPIC⟩2.0.CO;2.

Heymsfield, A. J., and R. G. Knollenberg (1972), Properties of cirrus generating cells., *J. Atmos. Sci.*, *29*, 1358–1366.

Heymsfield, A. J., and G. M. McFarquhar (1996), High Albedos of Cirrus in the Tropical Pacific Warm Pool: Microphysical Interpretations from CEPEX and from Kwajalein, Marshall Islands, *J. Atmos. Sci.*, *53*(17), 2424–2451, doi:10.1175/1520-0469(1996)053⟨2424:HAOCIT⟩2.0.CO;2.

Heymsfield, A. J., and C. M. R. Platt (1984), A Parameterization of the Particle Size Spectrum of Ice Clouds in Terms of the Ambient Temperature and the Ice Water Content, *J. Atmos. Sci.*, *41*(5), 846–855, doi:10.1175/1520-0469(1984)041⟨0846:APOTPS⟩2.0.CO;2.

Heymsfield, A. J., S. Matrosov, and B. Baum (2003), Ice water path-optical depth relationships for cirrus and deep stratiform ice cloud layers, *J. Appl. Meteorol.*, *42*, 1369–1390.

Heymsfield, J. A., and J. Iaquinta (2000), Cirrus Crystal Terminal Velocities, *J. Atmos. Sci.*, *57*, 916–938.

Hobbs, P. V. (1993), *Aerosol.Cloud Interactions, In Aerosol-Cloud-Climate Interactions*, 33–73 pp., Academic Press, Inc., San Diego,California.

Hogan, R. J., and A. J. Illingworth (2000), Deriving cloud overlap statistics from radar, *Q. J. R. Meteorol. Soc.*, *126*(569), 2903–2909, doi:10.1002/qj.49712656914.

Holton, J. R., and A. Gettelman (2001), Horizontal transport and the dehydration of the stratosphere, *Geophys. Res. Lett.*, *28*(14), 2799–2802, doi:10.1029/2001GL013148.

Hong, G., P. Yang, B.-C. Gao, B. A. Baum, Y. X. Hu, M. D. King, and S. Platnick (2007), High Cloud Properties from Three Years of MODIS Terra and Aqua Collection-4 Data over the Tropics, *J. Appl. Meteorol.*, *46*(11), 1840–1856, doi: 10.1175/2007JAMC1583.1.

Hong, G., G. Heygster, J. Notholt, and S. A. Buehler (2008), Interannual to Diurnal Variations in Tropical and Subtropical Deep Convective Clouds and Convective Overshooting from Seven Years of AMSU-B Measurements, *J. Clim.*, *21*, 4168 – 4189, doi:10.1175/2008JCLI1911.1.

Houze, R. A. (1982), Cloud clusters and large-scale vertical motions in the tropics, *J. Meteor. Soc. Jpn.*, *60*, 396 – 410.

Houze, R. A. (2004), Mesoscale convective systems, *Rev. Geophys.*, *42*(4), RG4003, doi:10.1029/2004RG000150.

Huffman, G. J., et al. (1997), The Global Precipitation Climatology Project (GPCP) Combined Precipitation Dataset, *Bull. Am. Meteorol. Soc.*, *78*(1), 5–20, doi:10.1175/1520-0477(1997)078⟨0005:TGPCPG⟩2.0.CO;2.

Immler, F., K. Krüger, S. Tegtmeier, M. Fujiwara, P. Fortuin, G. Verver, and O. Schrems (2007), Cirrus clouds, humidity, and dehydration in the tropical tropopause layer observed at Paramaribo, Suriname (5.8N, 55.2W), *J. Geophys. Res.*, *112*(D3), D03,209, doi:10.1029/2006JD007440.

IPCC (2007), *Climate Change 2007: The Physical Science Basis*, pp. 19–91, Cambridge University Press.

Ivanova, D., D. L. Mitchell, W. Arnott, and M. Poellot (2001), A GCM parameterization for bimodal size spectra and ice mass removal rates in mid-latitude cirrus clouds, *Atmos. Res.*, *59-60*, 89–113, doi:10.1016/S0169-8095(01)00111-9.

Jakob, C. (2002), *Ice clouds in numerical weather prediction models: Progress, problems and prospects*, 327–345 pp., Oxford University Press.

Jayaraman, A., H. Gadhavi, D. Ganguly, A. Misra, S. Ramachandran, and T. Rajesh (2006), Spatial variations in aerosol characteristics and regional radiative forcing over India: Measurements and modeling of 2004 road campaign experiment, *Atmos. Environ.*, *40*(34), 6504–6515, doi:10.1016/j.atmosenv.2006.01.034.

Jensen, E. J., L. Pfister, A. S. Ackerman, A. Tabazadeh, and O. B. Toon (2001), A conceptual model of the dehydration of air due to freeze-drying by optically thin, laminar cirrus rising slowly across the tropical tropopause, *J. Geophys. Res.*, *106*(D15), 17,237, doi:10.1029/2000JD900649.

Jensen, E. J., et al. (2009), On the importance of small ice crystals in tropical anvil cirrus, *Atmos. Chem. Phys.*, *9*(15), 5519–5537, doi:10.5194/acp-9-5519-2009.

Jensen, E. J., L. Pfister, and O. B. Toon (2011), Impact of radiative heating, wind shear, temperature variability, and microphysical processes on the structure and evolution

of thin cirrus in the tropical tropopause layer, *J. Geophys. Res.*, *116*, D12,209, doi: 10.1029/2010JD015417.

Jiang, X., et al. (2011), Vertical Diabatic Heating Structure of the MJO: Intercomparison between Recent Reanalyses and TRMM Estimates, *Mon. Weather Rev.*, *139*(10), 3208–3223, doi:10.1175/2011MWR3636.1.

Jish Prakash, P., and P. Pradeep Kumar (2010), Laboratory experiments on the effect of organic acids and metals on the charge transfer during ice crystal – graupel collision under the conditions similar to stratiform clouds, *Atmos. Chem. Phys. Discuss.*, *10*(1), 245–280, doi:10.5194/acpd-10-245-2010.

Johnson, N. C., and S.-P. Xie (2010), Changes in the sea surface temperature threshold for tropical convection, *Nature Geo.*, *3*(12), 842–845, doi:10.1038/ngeo1008.

Joseph, P. V., and T. P. Sabin (2008), An ocean–atmosphere interaction mechanism for the active break cycle of the Asian summer monsoon, *Clim. Dyn.*, *30*(6), 553–566, doi:10.1007/s00382-007-0305-2.

Joseph, P. V., K. P. Sooraj, C. A. Babu, and T. P. Sabin (2005), A cold pool in the Bay of Bengal and its interaction with the active-break cycle of the monsoon, in *CLIVAR Exchanges*, vol. 34, pp. 10–12, Southampton, UK.

Kalnay, E., et al. (1996), The NCEP/NCAR 40-Year Reanalysis Project, *Bull. Am. Meteorol. Soc.*, *77*(3), 437–471, doi:10.1175/1520-0477(1996)077⟨0437:TNYRP⟩2.0.CO;2.

Kandel, R., et al. (1998), The ScaRaB Earth Radiation Budget Dataset, *Bull. Am. Meteorol. Soc.*, *79*(5), 765–783, doi:10.1175/1520-0477(1998)079⟨0765:TSERBD⟩2.0.CO;2.

Kärcher, B., and S. Solomon (1999), On the composition and optical extinction of particles in the tropopause region, *J. Geophys. Res.*, *104*(D22), 27,441, doi: 10.1029/1999JD900838.

Kent, G. S., E. R. Williams, P.-H. Wang, M. P. McCormick, and K. M. Skeens (1995), Surface Temperature Related Variations in Tropical Cirrus Cloud as Measured by SAGE II, *J. Clim.*, *8*(11), 2577–2594, doi:10.1175/1520-0442(1995)008⟨2577:STRVIT⟩2.0.CO;2.

Kidwell, K. B. (1998), NOAA Polar Orbiter Data Users Guide.

Kiehl, J. T. (1994), On the Observed Near Cancellation between Longwave and Shortwave Cloud Forcing in Tropical Regions, *J. Clim.*, *7*(4), 559–565, doi:10.1175/1520-0442(1994)007⟨0559:OTONCB⟩2.0.CO;2.

Kiehl, J. T., and K. E. Trenberth (1997), Earth's Annual Global Mean Energy Budget, *Bull. Am. Meteorol. Soc.*, *78*(2), 197–208, doi:10.1175/1520-0477(1997)078⟨0197:EAGMEB⟩2.0.CO;2.

Klein, S. A., and D. L. Hartmann (1993), The Seasonal Cycle of Low Stratiform Clouds, *J. Clim.*, *6*(8), 1587–1606, doi:10.1175/1520-0442(1993)006⟨1587:TSCOLS⟩2.0.CO;2.

Klett, J. D. (1985), Lidar inversion with variable backscatter/extinction ratios, *Appl. Opt.*, *24*(11), 1638, doi:10.1364/AO.24.001638.

Knollenberg, R. G., K. Kelly, and J. C. Wilson (1993), Measurements of high number densities of ice crystals in the tops of tropical cumulonimbus, *J. Geophys. Res.*, *98*(D5), 8639, doi:10.1029/92JD02525.

Koren, I. (2004), Measurement of the Effect of Amazon Smoke on Inhibition of Cloud Formation, *Science*, *303*(5662), 1342–1345, doi:10.1126/science.1089424.

Krall, G. M., and W. R. Cottom (2012), Potential indirect effects of aerosol on tropical cyclone intensity: convective fluxes and cold-pool activity, *Atmos. Chem. Phys. Discuss.*, *12*(1), 351–385, doi:10.5194/acpd-12-351-2012.

Kummerow, C. (1998), Beamfilling Errors in Passive Microwave Rainfall Retrievals, *J. Appl. Meteorol.*, *37*(4), 356–370, doi:10.1175/1520-0450(1998)037⟨0356:BEIPMR⟩2.0.CO;2.

Laing, A. G., and J. M. Fritsch (1993), Mesoscale Convective Complexes over the Indian Monsoon Region, *J. Clim.*, *6*(5), 911–919, doi:10.1175/1520-0442(1993)006⟨0911:MCCOTI⟩2.0.CO;2.

Lau, K.-M., and H.-T. Wu (2010), Characteristics of Precipitation, Cloud, and Latent Heating Associated with the Madden-Julian Oscillation, *J. Clim.*, *23*(3), 504 – 518.

Lau, K. M., T. Nakazawa, and C. H. Sui (1991), Observations of cloud cluster hierarchies over the tropical western Pacific, *J. Geophys. Res.*, *96*(S01), 3197, doi:10.1029/90JD01830.

Lau, K.-M., H.-T. Wu, and S. Bony (1997), The Role of Large-Scale Atmospheric Circulation in the Relationship between Tropical Convection and Sea Surface Temperature, *J. Clim.*, *10*(3), 381–392, doi:10.1175/1520-0442(1997)010⟨0381:TROLSA⟩2.0.CO;2.

Lawrence, M. G., and J. Lelieveld (2010), Atmospheric pollutant outflow from southern Asia: a review, *Atmos. Chem. Phys.*, *10*(22), 11,017–11,096, doi:10.5194/acp-10-11017-2010.

Lawson, R. P., B. Baker, B. Pilson, and Q. Mo (2006), In Situ Observations of the Microphysical Properties of Wave, Cirrus, and Anvil Clouds. Part II: Cirrus Clouds, *J. Atmos. Sci.*, *63*(12), 3186–3203, doi:10.1175/JAS3803.1.

Li, J., H.-L. Huang, C.-Y. Liu, P. Yang, T. J. Schmit, H. Wei, E. Weisz, L. Guan, and W. P. Menzel (2005), Retrieval of Cloud Microphysical Properties from MODIS and AIRS, *J. Appl. Meteorol.*, *44*(10), 1526–1543, doi:10.1175/JAM2281.1.

Li, L., S. M. Sekelsky, G. A. Sadowy, S. C. Reising, S. L. Durden, S. J. Dindardo, and F. K. Li (1999), Attenuation and Rain Rate Estimation from Airborne and Combined Airborne and Ground-Based Millimeter Cloud Radar Measurements, in *Ninth ARM Science Team Meeting Proceedings*, pp. 1–9, San Antonio, Texas,.

Li, Z., and A. P. Trishchenko (2001), Quantifying Uncertainties in Determining SW Cloud Radiative Forcing and Cloud Absorption due to Variability in Atmospheric Conditions, *J. Atmos. Sci.*, *58*(4), 376–389, doi:10.1175/1520-0469(2001)058⟨0376:QUIDSC⟩2.0.CO;2.

Liebmann, B., and D. L. Hartmann (1982), Interannual Variations of Outgoing IR Associated with Tropical Circulation Changes During 1974–78, *J. Atmos. Sci.*, *39*(5), 1153 – 1162, doi:10.1175/1520-0469(1982)039⟨1153:IVOOIA⟩2.0.CO;2.

Liebmann, B., and C. A. Smith (1996), Description of a complete (interpolated) outgoing longwave radiation dataset, *Bull. Am. Meteorol. Soc.*, *77*, 1275–1277.

Lin, B., P. Minnis, B. Wielicki, D. R. Doelling, R. Palikonda, D. F. Young, and T. Uttal (1998), Estimation of water cloud properties from satellite microwave, infrared and visible measurements in oceanic environments 2. Results, *J. Geophys. Res.*, *103*(D4), 3887–3905, doi:10.1029/97JD02817.

Lin, B., P. Minnis, A. Fan, J. A. Curry, and H. Gerber (2001), Comparison of

cloud liquid water paths derived from in situ and microwave radiometer data taken during the SHEBA/FIREACE, *Geophys. Res. Lett.*, *28*(6), 975–978, doi: 10.1029/2000GL012386.

Lin, R. F., D. O. C. Starr, J. Reichardt, and P. J. DeMott (2005), Nucleation in synoptically forced cirrostratus, *J. Geophys. Res.*, *110*, D08,208, doi:10.1029/2004JD005362.

Lindzen, R. S., and S. Nigam (1987), On the Role of Sea Surface Temperature Gradients in Forcing Low-Level Winds and Convergence in the Tropics, *J. Atmos. Sci.*, *44*(17), 2418–2436, doi:10.1175/1520-0469(1987)044⟨2418:OTROSS⟩2.0.CO;2.

Ling, J., and C. Zhang (2011), Structural Evolution in Heating Profiles of the MJO in Global Reanalyses and TRMM Retrievals, *J. Clim.*, *24*(3), 825 – 842.

Liou, K.-N. (1986), Influence of Cirrus Clouds on Weather and Climate Processes: A Global Perspective, *Mon. Weather Rev.*, *114*(6), 1167–1199, doi:10.1175/1520-0493(1986)114⟨1167:IOCCOW⟩2.0.CO;2.

Liu, C., E. J. Zipser, and S. W. Nesbitt (2007), Global Distribution of Tropical Deep Convection: Different Perspectives from TRMM Infrared and Radar Data, *J. Clim.*, *20*(3), 489–503, doi:10.1175/JCLI4023.1.

Liu, G., J. A. Curry, and R.-S. Sheu (1995), Classification of clouds over the western equatorial Pacific Ocean using combined infrared and microwave satellite data, *J. Geophys. Res.*, *100*(D7), 13,811, doi:10.1029/95JD00823.

Liu, W. T. (2002), Progress in scatterometer application, *J. Oceanogr.*, *58*, 121–136.

Ludlam, F. (1956), The forms of ice clouds, II, *Q. J. R. Meteorol. Soc.*, *82*, 257–265.

Luo, Z., and W. B. Rossow (2004), Characterizing Tropical Cirrus Life Cycle, Evolution, and Interaction with Upper-Tropospheric Water Vapor Using Lagrangian Trajectory Analysis of Satellite Observations, *J. Clim.*, *17*(23), 4541–4563, doi:10.1175/3222.1.

Mace, G. (2007), Level 2 GEOPROF Product Process Description and Interface Control Document Algorithm version 5.3, *Tech. rep.*, Cooperative Institute for Research in the Atmosphere ,Colorado State University, Fort Collins, CO 80523.

Mace, G. G., S. Benson, and E. Vernon (2006), Cirrus clouds and the large-scale atmospheric state: Relationships revealed by six years of ground-based data, *J. Clim.*, *19*, 3257–3278, doi:10.1175/JCLI3786.1.

Mace, G. G., R. Marchand, Q. Zhang, and G. Stephens (2007), Global hydrometeor occurrence as observed by CloudSat: Initial observations from summer 2006, *Geophys. Res. Lett.*, *34*(L09808), doi:10.1029/2006GL029017.

Mace, G. G., Q. Q. Zhang, M. Vaughan, R. Marchand, G. Stephens, C. Trepte, and D. Winker (2009), A description of hydrometeor layer occurrence statistics derived from the first year of merged Cloudsat and CALIPSO data, *J. Geophys. Res.*, *114*, doi:D00a2610.1029/2007jd009755.

Machado, L. A. T., W. B. Rossow, R. L. Guedes, and A. W. Walker (1998), Life Cycle Variations of Mesoscale Convective Systems over the Americas, *Mon. Weather Rev.*, *126*(6), 1630–1654, doi:10.1175/1520-0493(1998)126⟨1630:LCVOMC⟩2.0.CO;2.

Machado, L. A. T., H. Laurent, and A. A. Lima (2002), Diurnal march of the convection observed during TRMM-WETAMC/LBA, *J. Geophys. Res.*, *107*, doi: 10.1029/2001JD000338.

Magagi, R., and A. P. Barros (2004), Estimation of Latent Heating of Rainfall during the Onset of the Indian Monsoon Using TRMM PR and Radiosonde Data, *J. Appl. Meteorol.*, *43*(2), 328–349.

Mapes, B. E., and R. A. Houze (1993), Cloud Clusters and Superclusters over the Oceanic Warm Pool, *Mon. Weather Rev.*, *121*(5), 1398–1416, doi:10.1175/1520-0493(1993)121⟨1398:CCASOT⟩2.0.CO;2.

Marchand, R., G. G. Mace, T. Ackerman, and G. Stephens (2008), Hydrometeor Detection Using Cloudsat An Earth-Orbiting 94-GHz Cloud Radar, *J. Atmos. Oceanic Technol.*, *25*(4), 519–533, doi:10.1175/2007JTECHA1006.1.

Marchand, R., J. Haynes, G. G. Mace, T. Ackerman, and G. Stephens (2009), A comparison of simulated cloud radar output from the multiscale modeling framework global climate model with CloudSat cloud radar observations, *Journal of Geophysical Research-Atmospheres*, *114*, doi:D00a2010.1029/2008jd009790.

Martin, E. R., and C. Schumacher (2012), The Relationship between Tropical Warm Pool Precipitation, Sea Surface Temperature, and Large-Scale Vertical Motion in IPCC AR4 Models, *J. Atmos. Sci.*, *69*(1), 185–194, doi:10.1175/JAS-D-11-0104.1.

Masunaga, H. (2002), Physical properties of maritime low clouds as retrieved by combined use of Tropical Rainfall Measurement Mission Microwave Imager and Visible/Infrared Scanner: Algorithm, *J. Geophys. Res.*, *107*(D10), 4083, doi:10.1029/2001JD000743.

McFarlane, S. A., and W. W. Grabowski (2007), Optical properties of shallow tropical cumuli derived from ARM ground-based remote sensing, *Geophys. Res. Lett.*, *34*(6), L06,808, doi:10.1029/2006GL028767.

McFarquhar, G. M., and A. J. Heymsfield (1996), Microphysical Characteristics of Three Anvils Sampled during the Central Equatorial Pacific Experiment, *J. Atmos. Sci.*, *53*(17), 2401–2423, doi:10.1175/1520-0469(1996)053⟨2401:MCOTAS⟩2.0.CO;2.

McFarquhar, G. M., A. J. Heymsfield, J. Spinhirne, and B. Hart (2000), Thin and subvisual tropopause tropical cirrus: Observations and radiative impacts, *J. Atmos. Sci.*, *57*, 1841–1852.

McGill, M., D. Hlavka, W. Hart, V. S. Scott, J. Spinhirne, and B. Schmid (2002), Cloud Physics Lidar: Instrument Description and Initial Measurement Results, *Appl. Opt.*, *41*(18), 3725, doi:10.1364/AO.41.003725.

Meenu, S. (2010), Studies on the regional distribution of clouds over the Indian region (30°S-30°S; 40°E-105°E) and its association with the atmospheric dynamical features using remote sensing data, Ph.D. thesis, University of Kerala.

Meenu, S., K. Rajeev, K. Parameswaran, and C. S. Raju (2007), Characteristics of double ITCZ over the tropical Indian Ocean, *J. Geophys. Res.*, *112*(D11106), doi:10.1029/2006JD007950.

Meenu, S., K. Rajeev, K. Parameswaran, and A. K. M. Nair (2010), Regional distribution of deep clouds and cloud top altitudes over the Indian subcontinent and the surrounding oceans, *J. Geophys. Res.*, *115*, D05,205, doi:10.1029/2009JD011802.

Meenu, S., K. Rajeev, and K. Parameswaran (2011), Regional and vertical distribution of semitransparent cirrus clouds over the tropical Indian region derived from CALIPSO data, *J. Atmos. Sol. Terr. Phys.*, *73*, 1967–1979, doi:10.1016/j.jastp.2011.06.007.

Meenu, S., K. Parameswaran, and K. Rajeev (2012), Role of sea surface temperature and wind convergence in regulating convection over the tropical Indian Ocean, *J. Geophys. Res.*, *117*(D14), 1–12, doi:10.1029/2011JD016947.

Mehta, S. K., B. V. K. Murthy, D. N. Rao, M. V. Ratnam, K. Parameswaran, K. Rajeev, C. S. Raju, and K. G. Rao (2008), Identification of tropical convective tropopause

and its association with cold point tropopause, *J. Geophys. Res.*, *113*, D00B04, doi: 10.1029/2007JD009625.

Menon, H. B., N. Sangekar, A. Lotliker, K. Krishna Moorthy, and P. Vethamony (2011), Aerosol optical thickness and spatial variability along coastal and offshore waters of the eastern Arabian Sea, *ICES J. Mar. Sci.*, *68*(4), 745–750, doi:10.1093/icesjms/fsq191.

Metz, B., O. R. Davidson, P. R. Bosch, R. Dave, and L. A. Meyer (2007), *Climate Change 2007: Mitigation*, chap. chapters 3, Cambridge University Press.

Mishra, M. K., K. Rajeev, B. V. Thampi, K. Parameswaran, and A. K. M. Nair (2010), Micro pulse lidar observations of mineral dust layer in the lower troposphere over the southwest coast of Peninsular India during the Asian summer monsoon season, *J. Atmos. Sol. Terr. Phys.*, *72*, 1251–1259, doi:10.1016/j.jastp.2010.08.012.

Mishra, M. K., K. Rajeev, A. K. M. Nair, K. Krishna Moorthy, and K. Parameswaran (2012), Impact of a noon-time annular solar eclipse on the mixing layer height and vertical distribution of aerosols in the atmospheric boundary layer, *J. Atmos. Sol. Terr. Phys.*, *74*, 232–237, doi:10.1016/j.jastp.2011.10.012.

Mitchell, D. L., S. K. Chai, Y. Liu, A. J. Heymsfield, and Y. Dong (1996), Modeling cirrus clouds. Part I: Treatment of bimodal size spectra and case study analysis, *J. Atmos. Sci.*, *53*, 2952–2966.

Mitchell, D. L., P. Rasch, D. Ivanova, G. McFarquhar, and T. Nousiainen (2008), Impact of small ice crystal assumptions on ice sedimentation rates in cirrus clouds and GCM simulations, *Geophys. Res. Lett.*, *35*, L09,806, doi:10.1029/2008GL033552.

Mitra, A. K., A. K. Bohra, M. N. Rajeevan, and T. N. Krishnamurthi (2009), Daily Indian Precipitation Analysis Formed from a Merge of Rain-Gauge Data with the TRMM TMPA Satellite-Derived Rainfall Estimates, *J. Meteor. Soc. Jpn.*, *87A*, 265–279, doi:10.2151/jmsj.87A.265.

Monge, J. L., R. S. Kandel, L. A. Pakhomov, and V. I. Adasko (1991), ScaRaB Earth radiation budget scanning radiometer, *Metrologia*, *28*, 261 – 284.

Moore, B. I., W. L. Gates, L. J. Mata, A. Underdal, and R. J. Stouffer (2001), *Advancing our understanding. Climate Change 2001: The Scientific Basis*, 769–785 pp., Cambridge University Press.

Moorthy, K., S. Suresh Babu, M. R. Manoj, and S. K. Satheesh (2013), Buildup of aerosols over the Indian Region, *Geophys. Res. Lett.*, *40*(5), 1011–1014, doi:10.1002/grl.50165.

Moorthy, K. K., S. K. Satheesh, and B. V. K. Murthy (1997), Investigations of marine aerosols over the tropical Indian Ocean, *J. Geophys. Res.*, *102*(D15), 18,827, doi: 10.1029/97JD01121.

Moran, K. P., B. E. Martner, M. J. Post, R. A. Kropfli, D. C. Welsh, and K. B. Widener (1998), An Unattended Cloud-Profiling Radar for Use in Climate Research, *Bull. Am. Meteorol. Soc.*, *79*(3), 443–455, doi:10.1175/1520-0477(1998)079⟨0443:AUCPRF⟩2.0.CO;2.

Nair, A. K. M., K. Rajeev, S. Sijikumar, and S. Meenu (2011), Characteristics of a persistent "pool of inhibited cloudiness" and its genesis over the Bay of Bengal associated with the Asian summer monsoon, *Ann. Geophys.*, *29*(7), 1247–1252, doi: 10.5194/angeo-29-1247-2011.

Nair, A. K. M., K. Rajeev, M. K. Mishra, B. V. Thampi, and K. Parameswaran (2012),

Multiyear lidar observations of the descending nature of tropical cirrus clouds, *J. Geophys. Res.*, *117*(D18), 1–9, doi:10.1029/2011JD017406.

Nair, S. K., K. Parameswaran, and K. Rajeev (2005), Seven year satellite observations of the mean structures and variabilities in the regional aerosol distribution over the oceanic areas around the Indian subcontinent, *Ann. Geophys.*, *23*(6), 2011–2030, doi:10.5194/angeo-23-2011-2005.

Nair, V. S., S. S. Babu, and K. K. Moorthy (2008), Aerosol characteristics in the marine atmospheric boundary layer over the Bay of Bengal and Arabian Sea during ICARB: Spatial distribution and latitudinal and longitudinal gradients, *J. Geophys. Res.*, *113*(D15), D15,208, doi:10.1029/2008JD009823.

Nakazawa, T. (1988), Tropical super clusters within intraseasonal variations over the western Pacific., *J. Meteor. Soc. Jpn.*, *66*, 823–839.

Nazaryan, H., M. P. McCormick, and W. P. Menzel (2008), Global characterization of cirrus clouds using CALIPSO data, *J. Geophys. Res.*, *113*, D16,211, doi:10.1029/2007JD009481.

Newell, R. E., and S. Gould-Stewart (1981), A Stratospheric Fountain?, *J. Atmos. Sci.*, *38*(12), 2789–2796, doi:10.1175/1520-0469(1981)038⟨2789:ASF⟩2.0.CO;2.

Nigam, S., C. Chung, and E. DeWeaver (2000), ENSO diabatic heating in ECMWF and NCEP-NCARreanalyses, and NCAR CCM3 simulation, *J. Clim.*, *13*, 3152 – 3171.

Niranjan, K., B. L. Madhavan, and V. Sreekanth (2007), Micro pulse lidar observation of high altitude aerosol layers at Visakhapatnam located on the east coast of India, *Geophys. Res. Lett.*, *34*(3), L03,815, doi:10.1029/2006GL028199.

Norris, J. R. (1998a), Low Cloud Type over the Ocean from Surface Observations. Part I: Relationship to Surface Meteorology and the Vertical Distribution of Temperature and Moisture, *J. Clim.*, *11*(3), 369–382, doi:10.1175/1520-0442(1998)011⟨0369:LCTOTO⟩2.0.CO;2.

Norris, J. R. (1998b), Low Cloud Type over the Ocean from Surface Observations. Part II: Geographical and Seasonal Variations, *J. Clim.*, *11*(3), 383–403, doi:10.1175/1520-0442(1998)011⟨0383:LCTOTO⟩2.0.CO;2.

Pai, D. S., and M. Rajeevan (1998), Clouds and cloud radiative forcing over tropical Indian ocean and their relationship with sea surface temperature, *Curr. Sci.*, *75*, 372–381.

Pandithurai, G., S. Dipu, T. V. Prabha, R. S. Maheskumar, J. R. Kulkarni, and B. N. Goswami (2012), Aerosol effect on droplet spectral dispersion in warm continental cumuli, *J. Geophys. Res.*, *117*(D16), D16,202, doi:10.1029/2011JD016532.

Parameswaran, K., K. Rajeev, and K. Sen Gupta (1997), An observational study of night time aerosol concentrations in the lower atmosphere at a tropical coastal station, *J. Atmos. Sol. Terr. Phys.*, *59*(14), 1727–1737, doi:10.1016/S1364-6826(97)00013-8.

Parameswaran, K., S. SunilKumar, B. Krishna Murthy, K. Satheesan, Y. Bhavani Kumar, M. Krishnaiah, and P. R. Nair (2003), Lidar observations of cirrus cloud near the tropical tropopause: temporal variations and association with tropospheric turbulence, *Atmos. Res.*, *69*(1-2), 29–49, doi:10.1016/j.atmosres.2003.08.002.

Park, M.-S., and R. L. Elsberry (2013), Latent Heating and Cooling Rates in Developing and Nondeveloping Tropical Disturbances during TCS-08: TRMM PR versus ELDORA Retrievals, *J. Atmos. Sci.*, *70*, 15 – 35.

Patil, S., and R. Yadav (2005), Large-scale changes in the cloud radiative forcing over the

Indian region, *Atmos. Environ.*, *39*(26), 4609–4618, doi:10.1016/j.atmosenv.2005.03.051.

Peter, T., et al. (2003), Ultrathin Tropical Tropopause Clouds (UTTCs): I. Cloud morphology and occurrence, *Atmos. Chem. Phys.*, *3*(4), 1083–1091, doi:10.5194/acp-3-1083-2003.

Pierrehumbert, R. T. (1996), Some remarks on mechanisms for the regulation of tropical sea surface temperature, in *Clouds, Chemistry and Climate*, nato asi series ed., p. 260, Springer, Berlin.

Pincus, R., S. A. McFarlane, and S. A. Klein (1999), Albedo bias and the horizontal variability of clouds in subtropical marine boundary layers: Observations from ships and satellites, *J. Geophys. Res.*, *104*(D6), 6183, doi:10.1029/1998JD200125.

Platt, C. M. R. (1973), Lidar and Radioinetric Observations of Cirrus Clouds, *J. Atmos. Sci.*, *30*(6), 1191–1204, doi:10.1175/1520-0469(1973)030⟨1191:LAROOC⟩2.0.CO;2.

Platt, C. M. R. (1978), Lidar Backscatter from Horizontal Ice Crystal Plates, *J. Appl. Meteorol.*, *17*(4), 482–488, doi:10.1175/1520-0450(1978)017⟨0482:LBFHIC⟩2.0.CO;2.

Platt, C. M. R., S. C. Scott, and A. C. Dilley (1987), Remote Sounding of High Clouds. Part VI: Optical Properties of Midlatitude and Tropical Cirrus, *J. Atmos. Sci.*, *44*(4), 729–747, doi:10.1175/1520-0469(1987)044⟨0729:RSOHCP⟩2.0.CO;2.

Platt, C. M. R., J. D. Spinhirne, and W. D. Hart (1989), Optical and microphysical properties of a cold cirrus cloud: Evidence for regions of small ice particles, *J. Geophys. Res.*, *94*(D8), 11,151, doi:10.1029/JD094iD08p11151.

Pradeep Kumar, P., K. Broekhuizen, and J. P. D. Abbatt (2003), Organic acids as cloud condensation nuclei: Laboratory studies of highly soluble and insoluble species, *Atmos. Chem. Phys.*, *3*(3), 509–520, doi:10.5194/acp-3-509-2003.

Prospero, J. M., R. J. Charlson, V. Mohnen, R. Jaenicke, A. C. Delany, J. Moyers, W. Zoller, and K. Rahn (1983), The atmospheric aerosol system: An overview, *Rev. Geophys.*, *21*(7), 1607, doi:10.1029/RG021i007p01607.

Pruppacher, H. R., and J. D. Klett (1980), Microphysics of Clouds and Precipitation, *18*, doi:10.1007/0-306-48100-6.

Puranik, D. M., and R. N. Karekar (2006), *Precursors to Convection over Peninsular India during March–May in AMSU-B Data*, vol. 21, 781–801 pp., doi:10.1175/WAF945.1.

Quante, M., and D. O. Starr (2002), *Dynamical process in cirrus clouds: A Review of observational results.*, 346–374 pp., Oxford University Press.

Quilfen, Y. (1993), ERS-1 scatterometer off-line products: calibration/validation results and case studies, in *Proceedings of IGARSS '93 - IEEE International Geoscience and Remote Sensing Symposium*, vol. 1993, pp. 1750–1752, Proceedings of International Geoscience and Remote Sensing, IEEE, doi:10.1109/IGARSS.1993.322422.

Rajeev, K., and V. Ramanathan (2001), Direct observations of clear-sky aerosol radiative forcing from space during the Indian Ocean Experiment, *J. Geophys. Res.*, *106*(D15), 17,221, doi:10.1029/2000JD900723.

Rajeev, K., et al. (2008), Observational assessment of the potential of satellite-based water vapor and thermal IR brightness temperatures in detecting semitransparent cirrus., *Geophys. Res. Lett.*, *35*(L08808), doi:10.1029/2008GL033393.

Rajeev, K., K. Parameswaran, B. V. Thampi, M. K. Mishra, A. K. M. Nair, and S. Meenu

(2010), Altitude distribution of aerosols over Southeast Arabian Sea coast during pre-monsoon season: Elevated layers, long-range transport and atmospheric radiative heating, *Atmos. Environ.*, *44*, 2597–2604, doi:10.1016/j.atmosenv.2010.04.014.

Rajeevan, M., and J. Srinivasan (2000), Net cloud radiative forcing at the top of the atmosphere in the Asian monsoon region, *J. Clim.*, *13*, 650–657.

Rajeevan, M., P. Rohini, K. Niranjan Kumar, J. Srinivasan, and C. K. Unnikrishnan (2012), A study of vertical cloud structure of the Indian summer monsoon using CloudSat data, *Clim. Dyn.*, *40*(3-4), 637–650, doi:10.1007/s00382-012-1374-4.

Rajendran, K., R. S. Nanjundiah, S. Gadgil, and J. Srinivasan (2012), How good are the simulations of tropical SST – rainfall relationship by IPCC AR4 atmospheric and coupled models ?, *J. Earth Syst. Sci.*, *121*(3), 595–610.

Ramage, C. (1971), Monsoon Meteorology, in *International Geophysical Series, Vol. 15*, p. 296, Academic Press, San Diego,California.

Ramanathan, V., and W. Collins (1991), Thermodynamic regulation of ocean warming by cirrus clouds deduced from observations of the 1987 El Niño, *Nature*, *351*(6321), 27–32, doi:10.1038/351027a0.

Ramanathan, V., R. D. Cess, E. F. Harrison, P. Minnis, B. R. Barkstrom, E. Ahmad, and D. Hartmann (1989), Cloud-radiative forcing and climate: results from the Earth radiation budget experiment., *Science*, *243*(4887), 57–63, doi:10.1126/science.243.4887.57.

Ramanathan, V., et al. (2001), Indian Ocean Experiment: An integrated analysis of the climate forcing and effects of the great Indo-Asian haze, *J. Geophys. Res.*, *106*, 28,371–28,398 ST – Indian Ocean Experiment: An inte.

Ramesh Kumar, M. R., A. K. Babu, and C. Reason (2009), On the role of convective systems over the northwest Pacific and monsoon activity over the Indian subcontinent, *Meteorol. Appli.*, *16*(3), 353–360, doi:10.1002/met.131.

RameshKumar, M. R., A. Devasthale, G. Levy, S. Sankar, S. Bakan, and H. Grassl (2012), A multi-sensor climatological view of double ITCZs over the Indian Ocean, *Int. J. Remote Sensing*, *33*(9), 2925–2936, doi:10.1080/01431161.2011.625056.

Rangno, A. L., and P. V. Hobbs (1991), Ice particle concentrations and precipitation development in small polar maritime cumuliform clouds, *Q. J. R. Meteorol. Soc.*, *117*(497), 207–241, doi:10.1002/qj.49711749710.

Rao, C. R. N., and J. Chen (1995), Inter-satellite calibration linkages for the visible and near-infrared channels of the Advanced Very High Resolution Radiometer on the NOAA-7, -9 and11 spacecraft, *Int. J. Remote Sensing*, *16*, 1931 – 1942.

Rao, C. R. N., and J. Chen (1999), Revised post launch calibration of the visible and near infrared channels of the advanced very high resolution radiometer (AVHRR) on the NOAA-14 space craft, *Int. J. Remote Sensing*, *20*, 3485 – 3491.

Rao, R. R., Kumar, M. S. G, Ravichandran, M, Samala, B. K, Anitha, and G (2006), Observed intra-seasonal variability of mini-cold pool off the southern tip of India and its intrusion into the south central Bay of Bengal during summer monsoon season, *Geophys. Res. Lett.*, *33*(L15606), doi:10.1029/2006GL026086.

Rao, Y. P. (1976), Southwest Monsoon, *Tech. Rep. 1/1976*, New Delhi.

Reynolds, R. W., C. L. Gentemann, and G. K. Corlett (2010), Evaluation of AATSR and TMI Satellite SST Data, *J. Clim.*, *23*(1), 152–165, doi:10.1175/2009JCLI3252.1.

Riehl, H., and J. Simpson (1979), The heat balance of the equatorial trough zone, revisited, *Atmos. Phys.*, *52*, 287 – 304.

Rienecker, M. M., et al. (2011), MERRA: NASAs Modern-Era Retrospective Analysis for Research and Applications, *J. Clim.*, *24*(14), 3624–3648, doi:10.1175/JCLI-D-11-00015.1.

Ringer, M. A., and K. P. Shine (1997), Sensitivity of the Earth's radiation budget to interannual variations in cloud amount, *13*(3), 213–222, doi:10.1007/s003820050161.

Roberts, J. B., F. R. Robertson, C. A. Clayson, and M. G. Bosilovich (2012), Characterization of Turbulent Latent and Sensible Heat Flux Exchange between the Atmosphere and Ocean in MERRA, *J. Clim.*, *25*(3), 821–838, doi:10.1175/JCLI-D-11-00029.1.

Roca, R., and V. Ramanathan (2000), Scale Dependence of Monsoonal Convective Systems over the Indian Ocean, *J. Clim.*, *13*(7), 1286–1298, doi:10.1175/1520-0442(2000)013⟨1286:SDOMCS⟩2.0.CO;2.

Roca, R., M. Viollier, L. Picon, and M. Desbois (2002), A multisatellite analysis of deep convection and its moist environment over the Indian Ocean during the winter monsoon, *J. Geophys. Res.*, *107*(D19), doi:10.1029/2000JD000040.

Roca, R., S. Louvet, L. Picon, and M. Desbois (2005), A study of convective systems, water vapor and top of the atmosphere cloud radiative forcing over the Indian Ocean using INSAT-1B and ERBE data, *Meteorol. Atmos. Phys.*, *90*, 49–65, doi:10.1007/s00703-004-0098-3.

Rogers, R. R., and M. Yau (1979), *A short course in cloud physics*, vol. 2, 304 pp., Butterworth-Heinemann, Oxford UK.

Rondanelli, R., and R. S. Lindzen (2008), Observed variations in convective precipitation fraction and stratiform area with sea surface temperature, *J. Geophys. Res.*, *113*(D16), D16,119, doi:10.1029/2008JD010064.

Rosenfeld, D., W. L. Woodley, D. Axisa, E. Freud, J. G. Hudson, and A. Givati (2008), Aircraft measurements of the impacts of pollution aerosols on clouds and precipitation over the Sierra Nevada, *J. Geophys. Res.*, *113*(D15), D15,203, doi:10.1029/2007JD009544.

Rosenfeld, D., W. L. Woodley, A. Khain, W. R. Cotton, G. Carrió, I. Ginis, and J. H. Golden (2012), Aerosol Effects on Microstructure and Intensity of Tropical Cyclones, *Bull. Am. Meteorol. Soc.*, *93*(7), 987–1001, doi:10.1175/BAMS-D-11-00147.1.

Rossow, W., et al. (1985), ISCCP cloud analysis algorithm intercomparison, *Adv. Space Res.*, *5*(6), 185, doi:10.1016/0273-1177(85)90319-9.

Rossow, W. B. (1989), Measuring Cloud Properties from Space: A Review, *J. Clim.*, *2*(3), 201–213, doi:10.1175/1520-0442(1989)002⟨0201:MCPFSA⟩2.0.CO;2.

Rossow, W. B., and L. C. Garder (1993), Validation of ISCCP Cloud Detections, *J. Clim.*, *6*(12), 2370–2393, doi:10.1175/1520-0442(1993)006⟨2370:VOICD⟩2.0.CO;2.

Rossow, W. B., and A. A. Lacis (1990), Global, Seasonal Cloud Variations from Satellite Radiance Measurements. Part II. Cloud Properties and Radiative Effects, *J. Clim.*, *3*(11), 1204–1253, doi:10.1175/1520-0442(1990)003⟨1204:GSCVFS⟩2.0.CO;2.

Rossow, W. B., and C. Pearl (2007), 22-Year survey of tropical convection penetrating into the lower stratosphere, *Geophys. Res. Lett.*, *34*(4), L04,803, doi:10.1029/2006GL028635.

Rossow, W. B., and R. A. Schiffer (1991), ISCCP Cloud Data Products, *Bull. Am. Meteorol. Soc.*, *72*(1), 2–20, doi:10.1175/1520-0477(1991)072⟨0002:ICDP⟩2.0.CO;2.

Rossow, W. B., and R. A. Schiffer (1999), Advances in Understanding Clouds from ISCCP, *Bull. Am. Meteorol. Soc.*, *80*(11), 2261–2287, doi:10.1175/1520-0477(1999)080⟨2261:AIUCFI⟩2.0.CO;2.

Sabin, T. P., C. A. Babu, and P. V. Joseph (2012), SST-convection relation over tropical oceans, *Int. J. Climatol.*, doi:10.1002/joc.3522.

Saha, K. (1971), Mean cloud distributions over tropical oceans, *Tellus*, *23*(2), 183–195.

Saha, K. (1972), The double Intertropical Convergence Zone in the Indian Ocean: Fact or fiction?, *J. Mar. Bio. Assoc.India*, *14*, 758–766.

Saji, N. H., B. N. Goswami, P. N. Vinayachandran, and T. Yamagata (1999), A dipole mode in the tropical Indian Ocean, *Nature*, *401*, 360–363.

Sakai, T., T. Shibata, S.-a. Kwon, Y.-s. Kim, K. Tamura, and Y. Iwasaka (2000), Free tropospheric aerosol backscatter, depolarization ratio, and relative humidity measured with the Raman lidar at Nagoya in 1994-1997: contributions of aerosols from the Asian Continent and the Pacific Ocean, *Atmos. Environ.*, *34*, 431–442.

Samala, B. K., and R. Krishnan (2008), Cloud-radiative impacts on the tropical Indian Ocean associated with the evolution of monsoon breaks, *Int. J. Climatol.*, *28*(2), 205–217, doi:10.1002/joc.1518.

Sasi, M. N., and K. S. Gupta (1986), A reference atmosphere for the Indian equatorial zone from surface to 80 km, *Sci. Rep.*, *006*, 85.

Sassen, K. (2000), LIDAR backscatter depolarization technique for cloud and aerosol research, *Light Scattering by Nonspherical Particles: Theory, Measurements, and Geophysical Applications*, pp. 393–416.

Sassen, K. (2002), *Cirrus*, chap. Cirrus clouds: A modern perspective, pp. 11–40, Oxford University Press.

Sassen, K., and J. R. Campbell (2001), A Midlatitude Cirrus Cloud Climatology from the Facility for Atmospheric Remote Sensing. Part I: Macrophysical and Synoptic Properties, *J. Atmos. Sci.*, *58*(5), 481–496, doi:10.1175/1520-0469(2001)058⟨0481:AMCCCF⟩2.0.CO;2.

Sassen, K., and B. S. Chow (1992), Subvisual-thin cirrus lidar dataset for satellite verification and climatological research, *J. Appl. Meteorol.*, *31*, 1275–1285.

Sassen, K., M. K. Griffin, and G. C. Dodd (1989), Optical Scattering and Microphysical Properties of Subvisual Cirrus Clouds, and Climatic Implications, *J. Appl. Meteorol.*, *28*(2), 91–98, doi:10.1175/1520-0450(1989)028⟨0091:OSAMPO⟩2.0.CO;2.

Sassen, K., Z. Wang, and D. Liu (2009), Cirrus clouds and deep convection in the tropics: Insights from CALIPSO and CloudSat, *J. Geophys. Res.*, *114*, doi:10.1029/2009JD011916.

Satheesh, S., and K. Krishna Moorthy (2005), Radiative effects of natural aerosols: A review, *Atmos. Environ.*, *39*(11), 2089–2110, doi:10.1016/j.atmosenv.2004.12.029.

Satheesh, S. K., K. K. Moorthy, and B. V. K. Murthy (1998), Spatial Gradients in Aerosol Characteristics over the Arabian Sea and Indian Ocean, *J. Geophys. Res.*, *103*(D20), 26,183, doi:10.1029/98JD00803.

Sathiyamoorthy, V., P. K. Pal, and P. C. Joshi (2004), Influence of the upper-

tropospheric wind shear upon cloud radiative forcing in the Asian monsoon region, *J. Clim.*, *17*, 2725–2735.

Sathiyamoorthy, V., B.P.Shukla, R.Sikhakolli, S.Chaurasia, B. Simon, B. S., Pal, and G. P. K. (2013), Top of atmosphere flux from the Megha-Tropiques ScaRaB, *Curr. Sci.*, *104*.

Saunders, R. W., and K. T. Kriebel (1988), An improved method for detecting clear sky and cloudy radiances from AVHRR data, *Int. J. Remote Sensing*, *9*(1), 123–150, doi:10.1080/01431168808954841.

Schiffer, R. A., and W. B. Rossow (1983), The International Satellite Cloud Climatology Project (ISCCP) – The First Project of the World Climate Research Program, *Bull. Am. Meteorol. Soc.*, *64*, 779–784.

Seifert, P., A. Ansmann, D. Müller, U. Wandinger, D. Althausen, A. J. Heymsfield, S. T. Massie, and C. Schmitt (2007), Cirrus optical properties observed with lidar, radiosonde, and satellite over the tropical Indian Ocean during the aerosol-polluted northeast and clean maritime southwest monsoon, *J. Geophys. Res.*, *112*(D17), D17,205, doi:10.1029/2006JD008352.

Seinfeld, J. H., and S. N. Pandis (1997), Atmospheric Chemistry and Physics: From Air Pollution to Climate Change.

Sèze, G., and H. Pawlowska (2001), Cloud cover analysis with METEOSAT-5 during INDOEX, *J. Geophys. Res.*, *106*(D22), 28,415, doi:10.1029/2001JD900097.

Sherwood, S. C., and A. E. Dessler (2001), A Model for Transport across the Tropical Tropopause, *J. Atmos. Sci.*, *58*(7), 765–779, doi:10.1175/1520-0469(2001)058⟨0765:AMFTAT⟩2.0.CO;2.

Siingh, D., V. Gopalakrishnan, R. Singh, A. Kamra, S. Singh, V. Pant, R. Singh, and A. Singh (2007), The atmospheric global electric circuit: An overview, *Atmos. Res.*, *84*(2), 91–110, doi:10.1016/j.atmosres.2006.05.005.

Sijikumar, S., and K. Rajeev (2012), Role of the Arabian Sea Warm Pool on the Precipitation Characteristics during the Monsoon Onset Period, *J. Clim.*, *25*(6), 1890–1899, doi:10.1175/JCLI-D-11-00286.1.

Sikka, D. R., and S. Gadgil (1980), On the maximum cloud zone and the ITCZ over India longitude during the southwest monsoon, *Mon. Weather Rev.*, *108*, 1840–1853.

Simon, A., C. K. Rajan, and T. N. Krishnamurti (2006), Space-time variability of low frequency oscillations and Asian summer monsoon precipitation, *Meteorol. Atmos. Phys.*, *93*(3-4), 177–199, doi:10.1007/s00703-005-0141-z.

Singh, P., and P. S. Salvekar (2004), *Simulation of Tropical Indian Ocean Surface Circulation Using a Free Surface Sigma Coordinate Model*, 106 pp., Indian Institute of Tropical Meteorology, Pune.

Sivakumar, V., Y. Bhavanikumar, P. B. Rao, K. Mizutani, T. Aoki, M. Yasui, and T. Itabe (2003), Lidar observed characteristics of the tropical cirrus clouds, *Radio Sci.*, *38*(6), 1–9, doi:10.1029/2002RS002719.

Slingo, A., and J. M. Slingo (1988), The response of a general circulation model to cloud longwave radiative forcing. I: Introduction and initial experiments, *Q. J. R. Meteorol. Soc.*, *114*, 1027 – 1062.

Slingo, A., K. I. Hodges, and G. J. Robinson (2004), Simulation of the diurnal cycle in a climate model and its evaluation using data from Meteosat 7, *Q. J. R. Meteorol. Soc.*, *130*, 1449 – 1467.

Smith, G. L., R. N. Green, E. Raschke, L. M. Avis, J. T. Suttles, B. A. Wielicki, and R. Davies (1986), Inversion methods for satellite studies of the Earth's Radiation Budget: Development of algorithms for the ERBE Mission, *Rev. Geophys.*, *24*(2), 407, doi:10.1029/RG024i002p00407.

Soden, B. J. (2000), The diurnal cycle of convection, clouds, and water vapor in the tropical upper troposphere, *Geophys. Res. Lett.*, *27*, 2173 – 2176.

Spinhirne, J. D., and W. D. Hart (1990), Cirrus Structure and Radiative Parameters from Airborne Lidar and Spectral Radiometer Observations: The 28 October 1986 FIRE Study, *Mon. Weather Rev.*, *118*(11), 2329–2343, doi:10.1175/1520-0493(1990)118⟨2329:CSARPF⟩2.0.CO;2.

Srinivasan, J., and P. C. Joshi (2007), What have we learned about the Indian monsoon from satellite data?, *Curr. Sci.*, *93*, 165–172.

Srinivasan, J., and G. L. Smith (1996), The Role of Heat Fluxes and Moist Static Energy in Tropical Convergence Zones, *Mon. Weather Rev.*, *124*(10), 2089–2099, doi:10.1175/1520-0493(1996)124⟨2089:TROHFA⟩2.0.CO;2.

Stephens, G. L. (1988), Radiative transfer through arbitrarily shaped media. Part II: Group theory and closures, *J. Atmos. Sci.*, *45*, 1836–1848.

Stephens, G. L., S.-C. Tsay, P. W. Stackhouse, and P. J. Flatau (1990), The Relevance of the Microphysical and Radiative Properties of Cirrus Clouds to Climate and Climatic Feedback, *J. Atmos. Sci.*, *47*(14), 1742–1754, doi:10.1175/1520-0469(1990)047⟨1742:TROTMA⟩2.0.CO;2.

Stephens, G. L., R. J. Engelen, M. Vaughan, and T. L. Anderson (2001), Toward retrieving properties of the tenuous atmosphere using space-based lidar measurements, *J. Geophys. Res.*, *106*(D22), 28,143, doi:10.1029/2001JD000632.

Stephens, G. L., et al. (2008), CloudSat mission: Performance and early science after the first year of operation, *J. Geophys. Res.*, *113*, D00A18, doi:10.1029/2008JD009982.

Stith, J. L., J. E. Dye, A. Bansemer, A. J. Heymsfield, C. A. Grainger, W. A. Petersen, and R. Cifelli (2002), Microphysical Observations of Tropical Clouds, *J. Appl. Meteorol.*, *41*(2), 97–117, doi:10.1175/1520-0450(2002)041⟨0097:MOOTC⟩2.0.CO;2.

Ström, J., B. Strauss, T. Anderson, F. Schröder, J. Heintzenberg, and P. Wendling (1997), In Situ Observations of the Microphysical Properties of Young Cirrus Clouds**, *J. Atmos. Sci.*, *54*(21), 2542–2553, doi:10.1175/1520-0469(1997)054⟨2542:ISOOTM⟩2.0.CO;2.

Stubenrauch, C. J., and U. Schumann (2005), Impact of air traffic on cirrus coverage, *Geophys. Res. Lett.*, *32*(14), n/a–n/a, doi:10.1029/2005GL022707.

Stubenrauch, C. J., F. Eddounia, J. M. Edwards, and A. Macke (2007), Evaluation of Cirrus Parameterizations for Radiative Flux Computations in Climate Models Using TOVS-ScaRaB Satellite Observations, *J. Clim.*, *20*, 4459–4475, doi:10.1175/JCLI4251.1.

Sud, Y. C., G. K. Walker, and K. M. Lau (1999), Mechanisms regulating sea-surface temperatures and deep convection in the tropics, *Geophys. Res. Lett.*, *26*(8), 1019, doi:10.1029/1999GL900197.

Sud, Y. C., G. K. Walker, Y. P. Zhou, Schmidt, G. A., K. M. Lau, and R. F. Cahalan (2008), Effects of doubled CO 2 on tropical sea surface temperatures (SSTs) for onset of deep convection and maximum SST: Simulations based inferences, *Geophys. Res. Lett.*, *35*(12), L12,707, doi:10.1029/2008GL033872.

SunilKumar, S., K. Parameswaran, and B. Krishna Murthy (2003), Lidar observations of cirrus cloud near the tropical tropopause: general features, *Atmos. Res.*, *66*(3), 203–227, doi:10.1016/S0169-8095(02)00159-X.

Sunilkumar, S. V., and K. Parameswaran (2005), Temperature dependence of tropical cirrus properties and radiative effects, *J. Geophys. Res.*, *110*(D13), doi:10.1029/2004JD005426.

Sunilkumar, S. V., K. Parameswaran, and B. V. Thampi (2008), Interdependence of tropical cirrus properties and their variability, *Ann. Geophys.*, *26*(3), 413–429, doi:10.5194/angeo-26-413-2008.

Sunilkumar, S. V., K. Parameswaran, K. Rajeev, B. V. K. Murthy, S. Meenu, S. K. Mehta, and A. Babu (2010), Semitransparent cirrus clouds in the tropical tropopause layer during two contrasting seasons, *J. Atmos. Sol. Terr. Phys.*, *72*(9–10), 745–762, doi:10.1016/j.jastp.2010.03.020.

Sunilkumar, S. V., A. Babu, and K. Parameswaran (2012), Mean structure of the tropical tropopause and its variability over the Indian longitude sector, doi:10.1007/s00382-012-1496-8.

Suttles, J. T., et al. (1988), Angular Radiation Models for Earth-Atmosphere System, Vol. 1, Shortwave Radiation, *Tech. Rep. 1184*, Langley Res. Cent., Hampton, Va.

Suttles, J. T., R. N. Green, G. L. Smith, B. A. Wielicki, I. J. Walker, V. R. Taylor, and L. L. Stowe (1989), Angular Radiation Models for the Earth-Atmosphere System (LW radiation), *Tech. Rep. 1184*, NASA RP.

Tahnk, W. R., and J. A. Coakley (2002), Aerosol optical depth and direct radiative forcing for INDOEX derived from AVHRR: Observations, January–March 1996–2000, *J. Geophys. Res.*, *107*(D19), 8010, doi:10.1029/2000JD000183.

Takano, Y., and K. N. Liou (1995), Radiative Transfer in Cirrus Clouds. Part III: Light Scattering by Irregular Ice Crystals, *J. Atmos. Sci.*, *52*(7), 818–837, doi:10.1175/1520-0469(1995)052⟨0818:RTICCP⟩2.0.CO;2.

Tao, W.-K., S. Lang, W. S. Olson, R. Meneghini, S. Yang, J. Simpson, C. Kummerow, E. Smith, and J. Halverson (2001), Retrieved Vertical Profiles of Latent Heat Release Using TRMM Rainfall Products for February 1998 **, *J. Appl. Meteorol.*, *40*(6), 957–982, doi:10.1175/1520-0450(2001)040⟨0957:RVPOLH⟩2.0.CO;2.

Tao, W.-K., et al. (2006), Retrieval of Latent Heating from TRMM Measurements, *Bull. Am. Meteorol. Soc.*, *87*(11), 1555–1572, doi:10.1175/BAMS-87-11-1555.

Tao, W.-K., S. Lang, X. Zeng, S. Shige, and Y. Takayabu (2010), Relating Convective and Stratiform Rain to Latent Heating, *J. Clim.*, *23*(7), 1874 – 1893.

Taylor, J. R., W. J. Randel, and E. J. Jensen (2011), Cirrus cloud-temperature interactions in the tropical tropopause layer: A case study, *Atmos. Chem. Phys.*, *11*, 10,085–10,095, doi:10.5194/acp-11-10085-2011.

Thampi, B. V., S. V. Sunilkumar, and K. Parameswaran (2009), Lidar studies of particulates in the UTLS region at a tropical station over the Indian subcontinent, *J. Geophys. Res.*, *114*(D8), doi:10.1029/2008JD010556.

Thampi, B. V., K. Parameswaran, and S. Sunilkumar (2012), Semitransparent cirrus clouds in the upper troposphere and their contribution to the particulate scattering in the tropical UTLS region, *J. Atmos. Sol. Terr. Phys.*, *74*, 1–10, doi:10.1016/j.jastp.2011.09.005.

Thomas, A. (2002), In situ measurements of background aerosol and subvisible cirrus

in the tropical tropopause region, *J. Geophys. Res.*, *107*(D24), 4763, doi:10.1029/2001JD001385.

Tian, B., B. J. Soden, and X. Wu (2004), Diurnal cycle of convection, clouds, and water vapor in the tropical upper troposphere: Satellites versus a general circulation model, *J. Geophys. Res.*, *109*(D10101), doi:10.1029/2003JD004117.

Tompkins, A. M. (2001), On the Relationship between Tropical Convection and Sea Surface Temperature, *J. Clim.*, *14*(5), 633–637, doi:10.1175/1520-0442(2001)014⟨0633:OTRBTC⟩2.0.CO;2.

Trenberth, K. E., J. T. Fasullo, and J. Kiehl (2009), Earth's Global Energy Budget, *Bull. Am. Meteorol. Soc.*, *90*(3), 311–323, doi:10.1175/2008BAMS2634.1.

Turner, D. D., et al. (2007), Thin Liquid Water Clouds: Their Importance and Our Challenge, *Bull. Am. Meteorol. Soc.*, *88*(2), 177–190, doi:10.1175/BAMS-88-2-177.

Turner, F. M., and L. F. Radke (1973), The Design and Evaluation of an Airborne Optical Ice Particle Counter, *J. Appl. Meteorol.*, *12*(8), 1309–1318, doi:10.1175/1520-0450(1973)012⟨1309:TDAEOA⟩2.0.CO;2.

Twomey, S. (1977), The Influence of Pollution on the Shortwave Albedo of Clouds, *J. Atmos. Sci.*, *34*(7), 1149–1152, doi:10.1175/1520-0469(1977)034⟨1149:TIOPOT⟩2.0.CO;2.

Varikoden, H., R. Harikumar, V. S. K. S. M. Das, S. Sampath, and G. M. Kumar (2009), Properties of cloud base height during southwest monsoon period over a tropical station, Thiruvananthapuram, *Curr. Sci.*, *96*, 562–568.

Viollier, M., and P. Raberanto (2010), Radiometric and Spectral Characteristics of the ScaRaB-3 Instrument on Megha-Tropiques: Comparisons with ERBE, CERES, and GERB, *J. Atmos. Oceanic Technol.*, *27*, 428 – 442.

Waliser, D. E. (1996), Formation and Limiting Mechanisms for Very High Sea Surface Temperature: Linking the Dynamics and the Thermodynamics, *J. Clim.*, *9*(1), 161–188, doi:10.1175/1520-0442(1996)009⟨0161:FALMFV⟩2.0.CO;2.

Waliser, D. E., and N. E. Graham (1993), Convective cloud systems and warm-pool sea surface temperatures: Coupled interactions and self-regulation, *J. Geophys. Res.*, *98*(D7), 12,881, doi:10.1029/93JD00872.

Wallace, J. M. (1992), Effect of deep convection on the regulation of tropical sea surface temperature, *Nature*, *357*(6375), 230–231, doi:10.1038/357230a0.

Wallace, J. M., and P. V. Hobbs (1977), *Atmospheric Science an introductory survey*, 483 pp., Academic Press, San Diego.

Wang, J., and W. B. Rossow (1998), Effects of Cloud Vertical Structure on Atmospheric Circulation in the GISS GCM, *J. Clim.*, *11*(11), 3010–3029, doi:10.1175/1520-0442(1998)011⟨3010:EOCVSO⟩2.0.CO;2.

Wang, L., and A. E. Dessler (2006), Instantaneous cloud overlap statistics in the tropical area revealed by ICESat/GLAS data, *Geophys. Res. Lett.*, *33*, L15,804, doi:10.1029/2005GL024350.

Wang, P. H., P. Minnis, M. P. McCormick, G. S. Kent, and K. M. Skeens (1996), A 6-year climatology of cloud occurrence frequency from Stratospheric Aerosol and Gas Experiment II observations (1985–1990), *J. Geophys. Res.*, *101*(29), 407–429, doi:10.1029/96JD01780.

Wang, Z., and K. Sassen (2001), Cloud Type and Macrophysical Property Retrieval

Using Multiple Remote Sensors, *J. Appl. Meteorol.*, *40*(10), 1665–1682, doi:10.1175/1520-0450(2001)040⟨1665:CTAMPR⟩2.0.CO;2.

Welton, E. J. (2002), Measurements of aerosol vertical profiles and optical properties during INDOEX 1999 using micropulse lidars, *J. Geophys. Res.*, *107*(D19), doi:10.1029/2000JD000038.

Wentz, F. J., and T. Meissner (2000), Algorithm Theoretical Basis Document (ATBD) Version-2: AMSR Ocean Algorithm, RSS Technical Proposal, *Tech. Rep. 121599A-1*.

Whiteway, J., et al. (2004), Anatomy of cirrus clouds: Results from the Emerald airborne campaigns, *Geophys. Res. Lett.*, *31*, L24,102, doi:10.1029/2004GL021201.

Wielicki, B. A., and R. N. Green (1989), Cloud Identification for ERBE Radiative Flux Retrieval, *J. Appl. Meteorol.*, *28*(11), 1133–1146, doi:10.1175/1520-0450(1989)028⟨1133:CIFERF⟩2.0.CO;2.

Wielicki, B. A., and L. Parker (1992), On the determination of cloud cover from satellite sensors: The effect of sensor spatial resolution, *J. Geophys. Res.*, *97*(D12), 12,799, doi:10.1029/92JD01061.

Wielicki, B. A., B. R. Barkstrom, E. F. Harrison, R. B. Lee, G. Louis Smith, and J. E. Cooper (1996), Clouds and the Earth's Radiant Energy System (CERES): An Earth Observing System Experiment, *Bull. Am. Meteorol. Soc.*, *77*(5), 853–868, doi:10.1175/1520-0477(1996)077⟨0853:CATERE⟩2.0.CO;2.

Wielicki, B. A., et al. (1998), Clouds and the Earths Radiant Energy System (CERES): Algorithm overview, *IEEE Trans. Geosci. Remote Sens.*, *36*, 1127 – 1140.

Wielicki, B. A., et al. (2002), Evidence for large decadal variability in the tropical mean radiative energy budget., *Science*, *295*(5556), 841–4, doi:10.1126/science.1065837.

Wielicki, B. A., K. Priestley, N. L. P. Minnis, D. Kratz, T. Charlock, D. Doelling, and D. Young (2006), CERES radiation budget accuracy overview, in *12th Conf. Atmospheric Radiation*, Amer. Meteor. Soc, Madison, WI,.

Wilcox, E. M., and V. Ramanathan (2001), Scale Dependence of the Thermodynamic Forcing of Tropical Monsoon Clouds: Results from TRMM Observations, *J. Clim.*, *14*(7), 1511–1524, doi:10.1175/1520-0442(2001)014⟨1511:SDOTTF⟩2.0.CO;2.

Winker, D., and T. C. Trepte (1998), Laminar cirrus observed near the tropical tropopause by LITE, *Geophys. Res. Lett.*, *25*, 3351–3354.

Winker, D., R. Couch, and M. McCormick (1996), An overview of LITE: NASA's Lidar In-space Technology Experiment, *Proceedings of the IEEE*, *84*(2), 164–180, doi:10.1109/5.482227.

Winker, D. M., W. H. Hunt, and M. J. McGill (2007), Initial performance assessment of CALIOP, *Geophys. Res. Lett.*, *34*(19), L19,803, doi:10.1029/2007GL030135.

Wonsick, M. M., R. T. Pinker, and Y. Govaerts (2009), Cloud Variability over the Indian Monsoon Region as Observed from Satellites, *J. Appl. Meteorol.*, *48*(9), 1803–1821, doi:10.1175/2009JAMC2027.1.

Wylie, D., D. L. Jackson, W. P. Menzel, and J. J. Bates (2005), Trends in Global Cloud Cover in Two Decades of HIRS Observations, *J. Clim.*, *18*(15), 3021–3031, doi:10.1175/JCLI3461.1.

Wylie, D. P., and W. P. Menzel (1999), Eight Years of High Cloud Statistics Using HIRS, *J. Clim.*, *12*, 170–184.

Wylie, D. P., W. P. Menzel, H. M. Woolf, and K. I. Strabala (1994), Four Years of

Global Cirrus Cloud Statistics Using HIRS, *J. Clim.*, *7*(12), 1972–1986, doi:10.1175/1520-0442(1994)007⟨1972:FYOGCC⟩2.0.CO;2.

Xie, S., et al. (2009), Climatology of Warm Rain and Associated Latent Heating Derived from TRMM PR Observations, *J. Clim.*, *22*(18), 4908 – 4929.

Yang, Y., et al. (2008), Retrievals of Thick Cloud Optical Depth from the Geoscience Laser Altimeter System (GLAS) by Calibration of Solar Background Signal, *J. Atmos. Sci.*, *65*(11), 3513–3526, doi:10.1175/2008JAS2744.1.

Young, S. A. (1995), Lidar analysis of lidar backscatter profiles in optically thin clouds, *Appl. Opt.*, *34*, 7019–7031.

Yuan, J., D. L. Hartmann, and R. Wood (2008), Dynamic Effects on the Tropical Cloud Radiative Forcing and Radiation Budget, *J. Clim.*, *21*(11), 2337–2351, doi:10.1175/2007JCLI1857.1.

Yue, Q., and K. N. Liou (2009), Cirrus cloud optical and microphysical properties determined from AIRS infrared spectra, *Geophys. Res. Lett.*, *36*(5), L05,810, doi:10.1029/2008GL036502.

Zelinka, M. D., and D. L. Hartmann (2011), The observed sensitivity of high clouds to mean surface temperature anomalies in the tropics, *J. Geophys. Res.*, *116*(D23), 1–16, doi:10.1029/2011JD016459.

Zhang, C. (1993), Large-Scale Variability of Atmospheric Deep Convection in Relation to Sea Surface Temperature in the Tropics, *J. Clim.*, *6*(10), 1898–1913, doi:10.1175/1520-0442(1993)006⟨1898:LSVOAD⟩2.0.CO;2.

Zhang, C., et al. (2010), MJO Signals in Latent Heating: Results from TRMM Retrievals, *J. Atmos. Sci.*, *67*(11), 3488 – 3508.

Zhang, H., G. M. McFarquhar, W. R. Cotton, and Y. Deng (2009), Direct and indirect impacts of Saharan dust acting as cloud condensation nuclei on tropical cyclone eyewall development, *Geophys. Res. Lett.*, *36*(6), L06,802, doi:10.1029/2009GL037276.

Zuidema, P. (2003), Convective Clouds over the Bay of Bengal, *Mon. Weather Rev.*, *131*(5), 780–798, doi:10.1175/1520-0493(2003)131⟨0780:CCOTBO⟩2.0.CO;2.

Zuluaga, M. D., C. D. Hoyos, and P. J. Webster (2010), Spatial and temporal distribution of latent heating in the south Asian monsoon region, *J. Clim.*, *23*, 2010–2029, doi:10.1175/2009JCLI3026.1.

Appendix A

Journal Publications

1. **Nair,A.K.M.**, K.Rajeev, M.K.Mishra, B.V.Thampi, and K.Parameswaran (2012), Multi-year Lidar observations of the descending nature of tropical cirrus clouds, *J. Geophys. Res.*, 117, D18201, doi:10.1029/2011JD017406.
2. Mishra,M.K., K.Rajeev, **A.K.M. Nair**, K.Krishna Moorthy and K. Parameswaran (2012), Impact of a noon-time annular solar eclipse on the mixing layer height and vertical distribution of aerosols in the atmospheric boundary layer, *J. Atmos. Sol. Terr. Phys.*, 74, 232-237, doi:10.1016/j.jastp.2011.10.012.
3. **Nair,A.K.M**, K. Rajeev, S. Sijikumar, and S. Meenu (2011), Characteristics of a persistent 'pool of inhibited cloudiness' and its genesis over the Bay of Bengal associated with the Asian summer monsoon, *Ann. Geophys.*, 29, 12471252, doi:10.5194/angeo-29-1247-2011.
4. Mishra,M.K., K. Rajeev, B.V.Thampi, K.Parameswaran, and **A.K.M.Nair** (2010), Micropulse Lidar observations of the dust layer in the lower troposphere over the southwest coast of Peninsular India during the Asian Summer Monsoon, *J. Atmos. Sol. Terr. Phys.*, 72, 12511259, doi:10.1016/j.jastp.2010.08.012.
5. K. Rajeev, K. Parameswaran, B.V. Thampi, M.K. Mishra, **A.K.M.Nair** and S. Meenu (2010), Altitude distribution of aerosols over Southeast Arabian Sea coast during pre-monsoon season: Elevated layers, long-range transport and atmospheric radiative heating, *Atmos. Environ.*, 44, 2122, 2597-2604, doi:10.1016/j.atmosenv.2010.04.014.
6. Meenu, S., K. Rajeev, K. Parameswaran, and **A.K.M.Nair** (2010), Regional distribution of deep clouds and cloud top altitudes over the Indian subcontinent and the surrounding oceans, *J.Geophys.Res.*, 115, D05205, doi:10.1029/2009JD011802.

JOURNAL OF GEOPHYSICAL RESEARCH, VOL. 117, D18201, doi:10.1029/2011JD017406, 2012

Multiyear lidar observations of the descending nature of tropical cirrus clouds

Anish Kumar M. Nair,[1] K. Rajeev,[1] Manoj Kumar Mishra,[1] Bijoy V. Thampi,[1,2] and K. Parameswaran[1]

Received 30 December 2011; revised 11 July 2012; accepted 8 August 2012; published 18 September 2012.

[1] Sedimentation of ice particles from cirrus clouds is one of the main processes responsible for dehydration of the upper troposphere. Multiyear-long-duration lidar observations of tropical cirrus over Thiruvananthapuram (8.5°N, 77°E) show the descending nature of these clouds throughout the year, with a mean frequency of occurrence of ∼20%. Majority of these descending cirrus occur near the base of tropical tropopause layer (TTL), while their frequency of occurrence and vertical extent of descent near the cold point tropopause are considerably less. On average, vertical displacement of the top and base of cirrus is almost similar. The most probable vertical displacement of cirrus is 1.5 – 2.5 km with descent duration of 1–2 h. However, in >20% of the cases, the vertical displacement is >3 km and ∼40% of the descending cirrus layers last for 2–5 h. Around 95% of descending cirrus clouds have a settling speed <0.8 ms^{-1}. On average, the percentage of clouds that are thickening or thinning by >300 m during descent are almost equal (∼23% each), while the thickening/thinning of the remaining 54% is <300 m. About 79% of these descending cirrus layers have cloud optical depth (COD) between 0.1 to 0.5. None of these clouds are of sub-visual type (COD <0.03). For the typical range of vertical displacements and CODs observed in the present study, the descending of cirrus clouds are estimated to decrease the longwave cloud radiative forcing at top of the atmosphere by 1 to 12.9 Wm^{-2}.

Citation: Nair, A. K. M., K. Rajeev, M. K. Mishra, B. V. Thampi, and K. Parameswaran (2012), Multiyear lidar observations of the descending nature of tropical cirrus clouds, *J. Geophys. Res.*, *117*, D18201, doi:10.1029/2011JD017406.

1. Introduction

[2] Cirrus clouds, constituting the largest fraction of upper tropospheric clouds [*Corti et al.*, 2006; *Wang and Dessler*, 2006], play an important role in regulating the moisture content and thermal structure of the tropical tropopause layer (TTL) [*Hartmann et al.*, 2001; *Gettelman et al.*, 2002]. In general, horizontal extent and lifetime of tropical cirrus are significantly larger than any other cloud types and hence can persist for more than a day [*Taylor et al.*, 2011]. Extensive studies on the spatial distribution of cirrus are reported in the literature, mostly based on satellite remote sensing [e.g., *Wang et al.*, 1996; *Winker and Trepte*, 1998; *Wang and Dessler*, 2006; *Nazaryan et al.*, 2008], airborne observations [e.g., *McFarquhar et al.*, 2000; *Whiteway et al.*, 2004] and ground-based observations at few geographical locations [e.g., *Sassen and Cho*, 1992; *Parameswaran et al.*, 2004; *Immler et al.*, 2007]. Globally, a wide tropical region encompassing the Bay of Bengal, the tropical Indian Ocean, the western Pacific, and Southeast Asia has the largest frequency of occurrence of cirrus clouds [*Wang et al.*, 1996; *Fu et al.*, 2007], a significant fraction of them being optically and physically thin [*Meenu et al.*, 2011]. Due to their low optical depth and occurrence in the cold upper troposphere, the longwave radiative forcing of the tropical cirrus clouds often exceeds the corresponding shortwave forcing, resulting in a net warming of the earth's surface [*Choi and Ho*, 2006]. However, due to large variations in their spatial distribution, altitude of occurrence, atmospheric residence time, microphysical and radiative properties, and morphology absolute magnitudes of the impact of cirrus clouds on radiation, thermal structure and moisture budget of the atmosphere are highly variable in space and time and poorly understood [*Stubenrauch et al.*, 2007].

[3] Gravitational settling of ice particles in cirrus clouds or downward movement of these ice crystals due to subsidence of upper tropospheric air mass associated with atmospheric waves, general circulation or other processes results in descending of cirrus clouds with time [e.g., *Heymsfield and Iaquinta*, 2000; *Mitchell et al.*, 2008]. Cirrus descent has the potential to influence the moisture and radiation budget of the upper troposphere [e.g., *Jakob*, 2002; *Jensen et al.*, 2011]. Sedimentation of ice particles from cirrus clouds

[1]Space Physics Laboratory, Vikram Sarabhai Space Centre, Thiruvananthapuram, India.
[2]Now at Laboratoire de Météorologie Dynamique/IPSL, UPMC-Jussieu, Paris, France.

Corresponding author: K. Rajeev, Space Physics Laboratory, Vikram Sarabhai Space Centre, Thiruvananthapuram 695022, India. (k_rajeev@vssc.gov.in)

0148-0227/12/2011JD017406

[*Mitchell et al.*, 2008] is one of the important mechanisms responsible for the dehydration of the upper troposphere and lower stratosphere (UTLS) region. Sublimation of ice particles during descending increases water vapor content in the altitudes to which they subside [*Jensen et al.*, 2011], and might reduce the cirrus lifetime. For a change in the ice particle terminal velocity in the range 0.1–2 ms^{-1}, the cirrus radiative forcing can change by as large as $\sim$20 Wm^{-2} [*Jakob*, 2002]. Parameterization of ice particle sedimentation in large-scale circulation models is important for defining their overall impact, including cirrus cloud ice water path and longwave forcing [e.g., *Mitchell et al.*, 2008].

[4] Main objective of the present study is to investigate the descending nature of cirrus clouds based on systematic long-duration lidar observations carried out at Thiruvananthapuram (8.5°N, 77°E), a tropical station located in the southwest Peninsular India, during 2008 – 2011. Such regular long-duration lidar observations from a fixed location are sparse, but crucial for understanding the morphology and characteristics of descending cirrus clouds. This study is motivated by the dearth of observations on the descending of cirrus clouds and would be useful in understanding the cirrus sedimentation of tropical cirrus clouds and their role in regulating the moisture and radiation budget of the TTL layer. Characteristics of the descending cirrus layers and their potential impact on the cloud radiative forcing at top-of-the-atmosphere (TOA) are presented in this paper.

2. Data and Method of Analysis

2.1. Instrument Setup

[5] Long duration observations carried out using a co-axial dual-polarization Micropulse Lidar (MPL) at Thiruvananthapuram during the period of March 2008 – May 2011 are used in this study. The MPL operates at the wavelength of 532 nm with a pulse repetition frequency of 2500 Hz and maximum pulse energy of 8 μJ. A Maksutov-Cassegrain type telescope having diameter of 178 mm is used for transmitting the laser beam and receiving the backscattered radiation. The observations are made with a vertical resolution of 30 m and time integration of 60 s. The lidar system alternates between the co-polarization and cross-polarization modes at an interval of 60 s. Data received during the two successive complimentary modes of operation are used to derive the altitude profile of attenuated backscatter coefficient and linear depolarization ratio [*Rajeev et al.*, 2010]. The linear depolarization ratio (LDR) is a measure of the non-sphericity of scatterers: larger non-sphericity leads to high value of LDR [*Rajeev et al.*, 2010]. Cirrus clouds, which are dominated by highly non-spherical ice crystals, are best discriminated from the high value of LDR (mostly between 0.1 to 0.4). During non-precipitating conditions, observations using MPL were carried out almost continuously for about 60 h per week, albeit with short breaks.

2.2. Cirrus Identification

[6] Cirrus clouds are identified from the backscattered lidar signals in the co- and cross-polarized channels using the following conditions: (i) Base of the cirrus layer should be above 8 km in the beginning of its occurrence (this condition is not imposed after the initial occurrence since the objective here is to investigate descending cirrus), (ii) Base and top altitudes of cirrus clouds are determined from the altitude gradients of range-corrected lidar signal and LDR which should be at least 2 times more than the corresponding gradients observed outside the cloud boundaries, (iii) Value of LDR within the cirrus layer should be at least 0.05 greater than the values observed above and below the cirrus layer, with a minimum absolute value of 0.08. (This value is selected based on extensive visual examination of the MPL data for a variety of cirrus layers and aerosols in the upper troposphere), (iv) Cirrus cloud detected using the above criteria should extend for at least 3 consecutive altitude bins (i.e., a minimum cirrus thickness of 90 m) and last for at least 3 successive time bins. The last condition is enforced mainly to avoid spurious detection of cirrus clouds due to noise. The above criteria used to identify cirrus layers are consistent with that reported in the literature for lidar data analysis [e.g., *Sassen and Cho*, 1992]. Further to this, cirrus layer is identified as a descending cirrus only when the cloud base shows a consistent decrease for >30 min from the start, with a minimum vertical displacement of 300 m. Start of the descending cloud is marked as the time at which base of the cloud starts descending (in almost all cases this coincides with the first appearance of the cirrus). Similarly, end of a descending cloud is marked by the time when the base no longer descends (mostly, this coincides with the time when the cloud itself disappears). It is important to note that cirrus uncinus clouds have a characteristic 'hook like' structure (with size of the 'head' less than 1–2 km) [*Sassen*, 2002] and might appear as a descending structure when the cloud moves across the field of view of the lidar. However, the above criterion of minimum duration of cirrus descent (>30 min) would prevent this erroneous detection of cirrus uncinus as descending cirrus, as the spatial scale of the cirrus uncinus 'head' (and hence its duration for passage over the site) is short.

[7] Even thin cirrus clouds can be discriminated from the MPL data during night. However, due to the interference of background solar radiation (low signal-to-noise ratio, SNR), optically thin cirrus clouds are not unambiguously discernible during daytime. Because of this day-night bias in cirrus detection, no attempt is made in this study to investigate the day-night differences or diurnal variations in cirrus occurrence and their properties. However, as the occurrence of descending cirrus is not highly frequent, all unambiguous cirrus detections during both day and night are used in the present study to improve the statistics.

2.3. Determination of Cirrus Properties

[8] Cloud optical depth (COD) of cirrus (whose base and top are clearly identifiable from the lidar backscattered signal) is derived from the two-way transmittance computed from the attenuation of the lidar backscattered signal as it passes through the cloud. Details of this method are described in *Young* [1995]. The COD is estimated as half of the logarithm of the ratio of range-corrected lidar backscattered signals (RCS) just below the cloud base to that immediately above the cloud top, after correcting for the molecular and aerosol contributions to the altitude variation of RCS. This method of determining COD does not require knowledge of the lidar system constant. Molecular contribution to RCS (as a function of altitude) is estimated using the monthly mean profiles of atmospheric density obtained

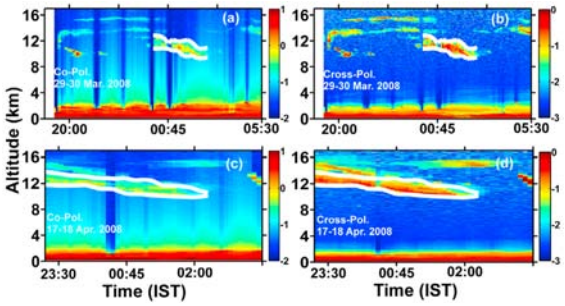

Figure 1. Time series of the altitude structure of attenuated backscattered lidar signal (ABS) received in the (left) co-polarized and (right) cross-polarized channels of MPL at Thiruvananthapuram on the nights of (top) 29 March 2008 and (bottom) 17 April 2008. The thick white lines indicate the detected top and base of the descending cirrus clouds.

from atmospheric model (based on long-term radiosonde observations over the site). Similarly, the seasonal mean altitude profiles of aerosol extinction coefficient derived from MPL observations over the site are used to determine the aerosol contribution to RCS [*Rajeev et al.*, 2010; *Mishra et al.*, 2010]. As the cirrus clouds occur mostly above 8 km, the above contributions due to aerosols and molecules are very small compared to that of cirrus clouds [e.g., *Young*, 1995]. Only nighttime profiles are used for determining COD, mainly to avoid the errors due to low SNR conditions during the day. In order to increase the SNR (and reduce the errors), the backscattered lidar signal is integrated for a minimum period of 10 min for determining the COD. This integration may be up to 20 min for improving the SNR; COD will not be determined if the SNR is so poor that the boundaries of the cloud are not well discernible. The mean COD for the cloud (average of all CODs determined during the cloud duration) only is presented here. Sensitivity analysis shows that the maximum uncertainty in COD derived using this method is less than 20%.

[9] Using the presented methodology, various features of descending cirrus such as the altitude of cloud top and cloud base at the beginning and end of descending (as explained earlier, downward shifting of the cloud base is used for identifying cirrus descent), duration of descending, vertical displacement, speed of descending and mean COD are determined for further analysis. Typical examples of the time-altitude cross-sections of ABS received in the co-polarized and cross-polarized channels (of MPL) during the nights of 29 March and 17 April 2008 are shown in Figure 1. Multiple cirrus layers persisting for ~2–4 h were observed between 9 and 16 km during both these days. All the observed cirrus layers are semitransparent, as the atmosphere above the clouds are well discernible. In both these days, some of the lower cirrus layers appearing between 9 and 15 km show downward slanting structure, lasting for about 2–4 h and descending by ~2 km. Base and top altitudes of the descending cirrus layers observed during these days are marked with thick white lines. Considering the atmospheric wind speeds of about 6–8 ms^{-1} persisting in this altitude region during the above days (based on radiosonde observations), these descending cirrus structures might have horizontal dimensions in the range of ~40–120 km. The mean optical depth of the descending cirrus on the night of 29 March 2008 is 0.44 ± 0.12 and that of 17 April 2008 night is 0.29 ± 0.09. Strikingly, most of the upper cirrus layers which are ~1–4 km above these descending layers have stable vertical structures. Proximity of such stable cirrus layer rules out the possibility of a strong downdraft in the upper troposphere or atmospheric waves as the causative mechanism for the descending cirrus. Physical and optical thicknesses of these descending cirrus layers are larger than the stable cirrus layers above. Hence, descent of the cirrus is likely to be associated with sedimentation of cloud particles. It is also interesting to note that the contrast in cirrus clouds in the cross-polarized channel is better than that in the co-polarized channel. This is due to a large relative increase in the strength of the lidar backscattered signal from cirrus clouds in the cross-polarized channel compared to that in the co-polarized channel (because of a significant increase in LDR within the cirrus due to large non-sphericity of ice crystals).

3. Results and Discussion

[10] Descending structures similar to those shown in Figure 1 are observed on several days/nights throughout the year. Out of the 513 days of MPL observation during the study period (March 2008 to May 2011), cirrus clouds were present on 291 days and descending cirrus layers were clearly discernible on 103 days. The seasonal mean frequency of occurrence of cirrus clouds (with at least one cirrus layer) and descending cirrus clouds (in percentages) during the winter (December – February: DJF), pre-monsoon (March – May: MAM), summer monsoon (June – September: JJAS) and post-monsoon (October – November: ON) seasons are shown in Figure 2. The frequency of occurrence of cirrus clouds that are ascending (detected by applying the same criteria as that applied for descending cirrus, but for the upward movement of the cloud base) are also shown in Figure 2 for comparison. The frequency of occurrence of cirrus clouds is the largest during summer monsoon season (~69%) and the least during winter (~36%). The occurrence of descending cirrus is the largest during the pre- and post-monsoon seasons (~23–24%) and least during winter

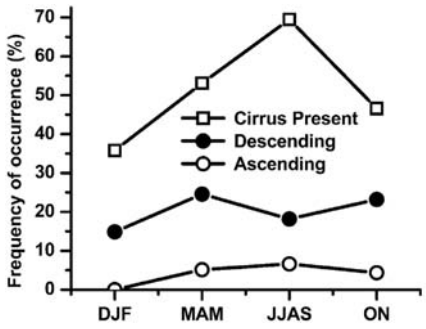

Figure 2. Seasonal mean frequency of occurrence (in %) of total, descending and ascending cirrus clouds during winter (DJF), pre-monsoon (MAM), summer monsoon (JJAS) and post-monsoon (ON) seasons.

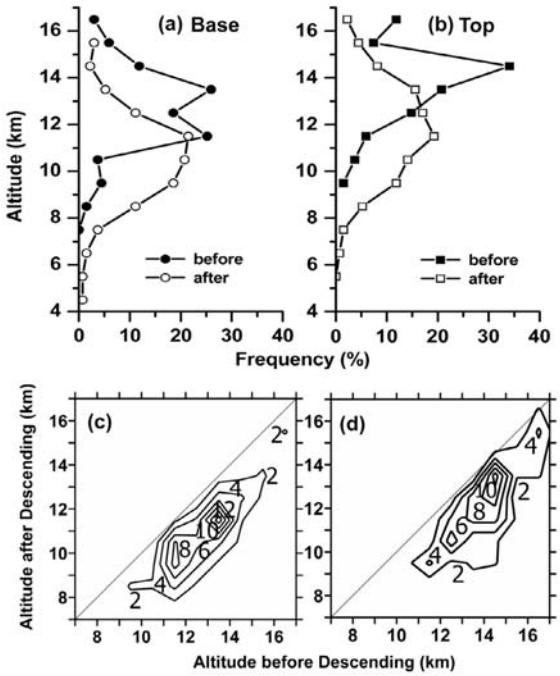

Figure 3. Distribution of the frequency of occurrence of the altitude of (a) cirrus-base and (b) cirrus-top before and after descent. Probability distribution function (PDF) for altitude before descent of the cirrus clouds versus altitude after descent for (c) cloud base and (d) cloud top.

(∼15%). Fraction of the cirrus clouds that are descending out of the total cirrus occurrence could not be accurately estimated due to the highly frequent occurrence of multiple cirrus layers simultaneously, with variable overlapping time (see Figure 1). However, a basic estimate of this descending cirrus fraction can be obtained by taking the ratio of the frequency of occurrence of descending cirrus to that of the total cirrus, which turns out to be ∼42, 45, 26, and 49% during DJF, MAM, JJAS, and ON respectively. Remarkably, the fraction of cirrus clouds that are descending is the least during summer monsoon season when the occurrence of cirrus is the largest. During all seasons, the frequency of occurrence of ascending cirrus (<5%) is substantially smaller than those descending, which further confirms that the descending clouds mainly arise from ice crystal sedimentation. The ascending movement of cirrus clouds might have been the result of upper tropospheric updraft or atmospheric waves. Hereafter, we focus only on the characteristics of descending cirrus clouds.

[11] Seasonal variations of the observed frequency of occurrence of cirrus clouds are in agreement with that reported earlier based on the satellite and lidar observations over the Peninsular India, which showed wide-spread occurrence of cirrus over the Indian region during the summer monsoon season associated with the long-range westward transport of water vapor and anvils from the deep convective regions over the Bay of Bengal [*Rajeev et al.*, 2008; *Meenu et al.*, 2010; *Sunilkumar et al.*, 2010]. Satellite observations suggest that significant cirrus occurrence over Peninsular India during the other seasons might be of local origin [*Sunilkumar et al.*, 2010]. Cirrus occurrence over Peninsular India is the least during winter, when the middle and upper tropospheric subsidence associated with the descending limb of Hadley circulation cell is prominent over the central and Peninsular Indian region [*Rajeev et al.*, 2008; *Sunilkumar et al.*, 2010]. A significant fraction of cirrus clouds over the site, especially during the pre- and post-monsoon seasons, might be linked to anvils from the locally originating deep convective clouds, which tend to maximize during the afternoon hours. Of all the descending clouds observed during 18:00–06:00 IST (Indian Standard Time) (when cirrus detection can be carried out without significant bias from background solar radiation), descending was initiated between 18:00–24:00 IST in ∼71% of the cases while ∼29% started descent between 00:00–06:00 IST.

[12] During the pre- and post-monsoon seasons and winter, the upper tropospheric winds over the site are small (typically 5–10 ms^{-1}), while the summer monsoon season is manifested by strong upper tropospheric winds (with typical easterly wind speeds of 10–20 ms^{-1}). It is likely that the lowest occurrence of descending cirrus during the summer monsoon season might be, at least partly, due to the rapid horizontal movement of cirrus clouds (caused by high-speed zonal winds) because of which the descending of cirrus clouds (observed as a function of time over a given location) will be minimum. This proposition is further supported by the occurrence of significant fraction of descending cirrus during the other seasons when the upper tropospheric winds are weak (because of which the cirrus clouds spend more time over a given location). However, this proposition needs to be further verified based on observations of the altitude profiles of vertical velocities in the troposphere and microphysical properties (especially size) of cirrus ice crystals, both of which can cause changes in descent rates of cirrus clouds.

[13] As the season-wise number of descending cirrus observed are rather small to conduct a detailed statistical analysis of their seasonal mean characteristics, the remaining part of this paper is based on the analysis by combining all of them for the entire study period. The frequencies of occurrence of cloud top and base before and after descent are depicted in Figure 3a (for cloud base) and Figure 3b (for cloud top). In majority of cases, the cloud top is between 12 and 16 km before descent and between 9 and 14 km after descent. Similarly, in most of the cases, the cloud base is between 11 to 15 km before descent and between 8 and 13 km after descent. The peak of the distribution of cloud top, which is ∼14.5 km before descent, decreases to ∼11.5 km after descent. Similarly, the peak of the distribution of cloud base decreases from ∼13.5 km before descent to ∼11.5 km after descent. Over this study region, the annual variation of cold point tropopause is in the range of 16.5 – 17.5 km and the base of the TTL is around 11–14 km [*Meenu et al.*, 2010]. (Here the TTL is referred as the altitude band between the cold point tropopause and the altitude of minimum potential temperature lapse rate, the latter being an indicator of the convective tropopause). Thus, most of the cirrus clouds before descent occur around the TTL base and ∼2–4 km below the cold point tropopause.

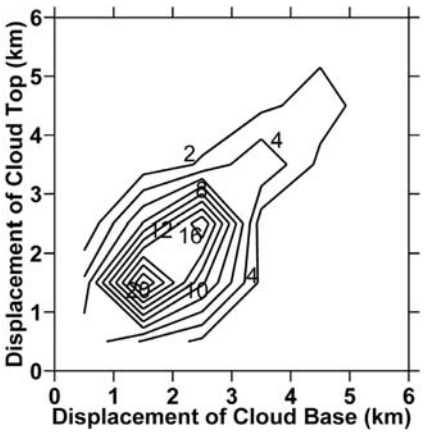

Figure 4. Probability distribution function for downward displacement of cloud base versus that for cloud top for descending cirrus clouds.

The frequency of occurrence of descending clouds above 15 km is considerably small. At end of descent, majority of these clouds reach altitudes that are up to 4 km below the mean TTL base. Based on the mean temperature profile derived from radiosonde observations at Thiruvananthapuram, average temperature of the most probable cloud top increases from ~201 ± 2 K before descent to ~216 ± 2 K after descent, yielding a mean enhancement of ~15 K in the cloud top temperature. Probability distribution functions (PDF) of the cloud base and top altitudes before and after the descending are depicted in Figures 3c and 3d. Although these plots show considerable spread in the PDF, the mean vertical displacement appears to be nearly uniform at all altitudes. The most probable downward displacements of cloud top and base are in the range of ~1.5 – 2.5 km.

[14] Figure 4 depicts the PDF of the vertical displacements of cloud top versus that of the cloud base which shows that, on average, the vertical displacements of the top and base generally have a one-to-one relationship. However, considering that the mean displacements of the base and top of the clouds are 2.07 ± 1.24 km and 2.01 ± 1.30 km respectively, spread in the PDFs shown in Figure 4 is significant. Difference between the vertical displacements of the top and base of cloud is a maximum for displacements in the range of 1–3 km. Any non-uniform descending would result in physical thinning (when top descends more than base) or thickening of the cloud (when base descends more than top). On average, the percentage of clouds that are thickening or thinning by >300 m during descending are almost equal (~23% each), while the thickening/thinning of the remaining 54% is <300 m. The detailed analysis shows that, in >75% of the cases, vertical displacement of the cloud top and base is <3 km. In few cases (~2%), the cloud top and base have descended by >5 km.

[15] The PDFs of the descent speed versus duration of descending for the top and base of cirrus clouds are depicted in Figure 5, which shows that the descent speed is inversely proportional to the duration. Clouds having duration of <2 h have descent speeds varying over a wide range of ~0.1–0.7 ms^{-1}, though most of them have descent rates of 0.2–0.5 ms^{-1}. In contrast, all cirrus layers lasting for >3 h have descent speeds of <0.28 ms^{-1}. This shows that, on average, the rapidly descending cirrus clouds dissipate faster than the gradually descending ones. Radiative heating at the cloud base and sublimation arising from sedimentation to sub-saturated regions are among the major dissipation processes for cirrus clouds [e.g., *Mace et al.*, 2006; *Jensen et al.*, 2011]. Considering this, the above relationship between the descent speed and duration is expected, since the slowly descending cirrus layers would take more time to reach the sub-saturated regions beneath. Furthermore, radiative cooling at the top of cirrus layers might decrease the cloud top temperature, thus maintaining higher relative humidity with respect to ice and hence lesser dissipation compared to the fast descending ones.

[16] As evident from Figure 5, the most preferred descent duration is 1.5 h. Probability of occurrence of descending clouds is found to decrease with increase in the descent duration. Out of the 136 cases of descending cirrus, 53% lasted for less than 2 h. In about 8% cases the duration was less than 1 h. Nearly 40% of cirrus had descent duration between 2 to 5 h. Only in 7% cases did the descent duration exceed 5 h. Histograms of the speed of descending of both the cloud top and base (figure not shown) are similar and exhibit a monotonic decrease in the frequency of occurrence with increasing descent speed. About 69% of cloud top and 66% of

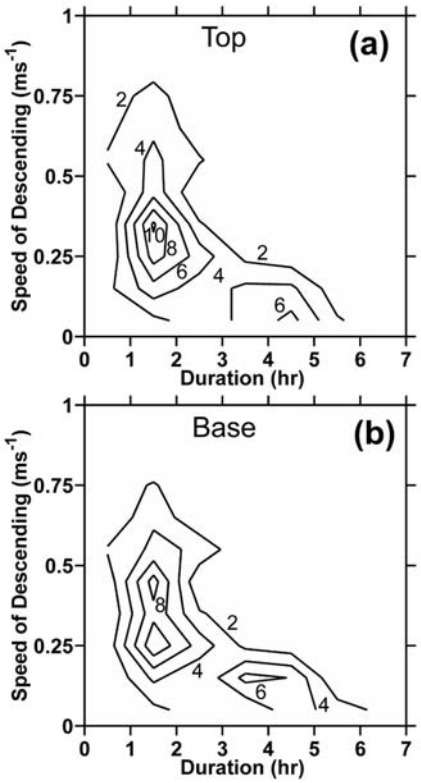

Figure 5. Probability distribution functions for duration of descending versus speed of descending for (a) cloud top and (b) cloud base.

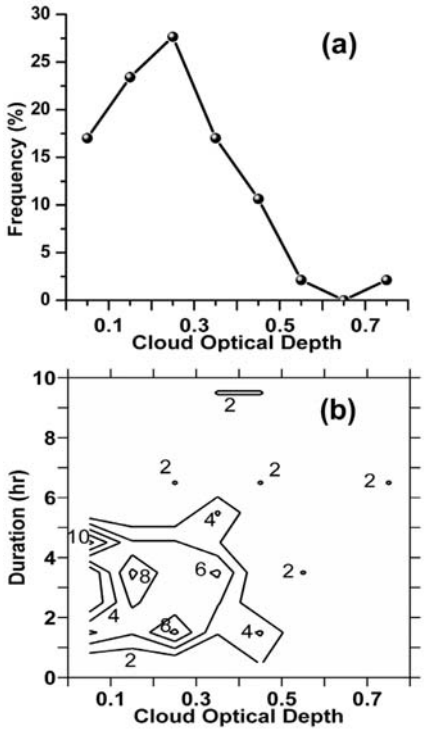

Figure 6. (a) Histogram of the cloud optical depth for descending cirrus clouds. (b) Probability distribution function for cloud optical depth versus duration for descending cirrus clouds.

cloud base have descent speeds <0.4 ms^{-1}, and 95% have descent speeds of <0.8 ms^{-1}. The average cirrus cloud sedimentation rates (average for both top and base) is 0.33 ms^{-1}, which is comparable to the mean cirrus sedimentation rates of 0.3–0.5 ms^{-1} reported by *Deng and Mace* [2008].

[17] Figure 6a shows the histogram of the mean COD observed for the descending layers. In general, the mean COD ranges from 0.05 to 0.75, with a peak ~0.25. Around 80% of descending cirrus have COD in the range 0.2 to 0.5. Statistically, around 68% of descending cirrus are thin cirrus (0.03 < COD < 0.3) and 32% are dense cirrus (COD >0.3). The seasonal mean CODs of descending cirrus are 0.16 ± 0.10, 0.27 ± 0.12, 0.30 ± 0.16, 0.30 ± 0.20 during DJF, MAM, JJAS, and ON respectively, which are larger than the corresponding mean cirrus cloud optical depths (all cirrus included) of 0.10 ± 0.09, 0.13 ± 0.17, 0.15 ± 0.17, 0.17 ± 0.21 during the above seasons. Thus, on average, descending cirrus has a larger optical thickness than typically observed in cirrus clouds. None of the descending cirrus is of subvisual cirrus (SVC) type (with COD <0.03).

[18] Note that, larger the value of COD, larger might be the ice water content [e.g., *Heymsfield et al.*, 2003]. It is likely that the sizes of ice crystals might be small in clouds with very small ice water content (or COD); absolute magnitudes of cirrus sedimentation may be quite small to be observable in the lidar observations of descending cirrus. This could probably be responsible for the fact that none of the observed SVCs are of descending type. CALIPSO observations, however, showed that substantial part of the tropical cirrus clouds formed in the TTL layer, especially near cold point tropopause, are SVCs [*Meenu et al.*, 2011]. Figure 6b shows the PDF of COD versus duration of descending. Though the optically thicker clouds might be expected to have longer duration (as they might take more time to dissipate), Figure 6b shows that the duration of descending does not show any prominent variation with COD. However, the longest durations are observed for the largest COD. The PDF of COD versus vertical displacement (figure not shown) also shows considerable spread, similar to that seen in Figure 6b.

[19] Figure 7 shows the PDF for COD versus descent speed for (a) cloud top and (b) cloud base. Though the mean descent speed and its range of variations are generally larger for optically thicker clouds, the relationship is rather far from robust. This might be due to the following reasons: (i) COD and ice crystal sizes might be poorly correlated, and (ii) the descent speed of cirrus might be significantly influenced by factors such as upper tropospheric vertical wind (which can alter the fall speed [*Lin et al.*, 2005; *Mace et al.*, 2006]) and size, shape and orientation of the ice particles (the shape and its orientation might influence the air drag as the crystals sediments). The above observations (Figures 4, 5 and 7) indicate that, on average, both cloud top and cloud base

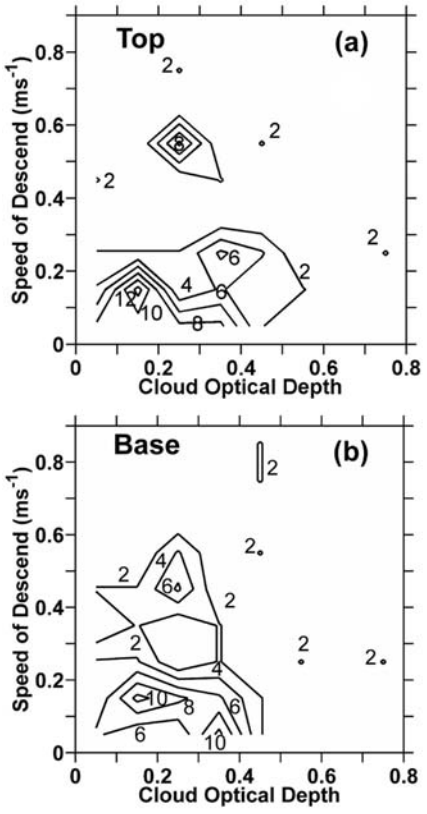

Figure 7. Probability distribution functions for cloud optical depth versus speed of descending for (a) cloud top and (b) cloud base.

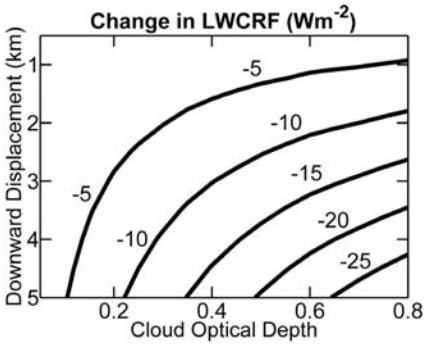

Figure 8. Change in longwave cloud radiative forcing (LWCRF) due to descending of cirrus having cloud top altitude of 15 km before descent, plotted as a function of cloud optical depth versus downward displacement. COD is assumed to be invariant during descending.

descend with comparable rates with no significant thickening or thinning of the clouds. On the contrary, the cirrus clouds descending due to gravitational settling alone are expected to thicken with time as the cirrus might contain a spectrum of ice crystals over a broad size range [e.g., *Frey et al.*, 2011] and therefore have different terminal velocities. At the cloud top, small ice crystals might remain, whereas the large ice crystals would fall and thus form a new cloud base. This spreading (rather separation of the sizes by gravity) should lead to (i) a broadening of the layer and (ii) different descent rates for top and base of the cloud. However, in general, the present observations indicate a significantly different behavior. This might be due to the dominance of the uplift (or downdraft) provided by vertical winds over the gravitational settling rates of ice particles (at least in majority of cases), which could significantly alter the actual descent rates of cirrus clouds. This suggests that the size of ice particles estimated from cirrus descent speeds (attributing it as arising only from sedimentation due to weight of the ice particles [*Das et al.*, 2010]) could be considerably different from their actual sizes. However, a robust physical explanation for the absence of cirrus broadening due to descending will require simultaneous measurements of vertical winds and cloud microphysical properties.

[20] Potential impact of the descending of cirrus on cloud radiative forcing (CRF) is investigated using radiative transfer model computations described by *Corti and Peter* [2009] (http://www.iac.ethz.ch/url/crf). This is a simple model for estimating the long-wave and short-wave cloud radiative forcing (SWCRF and LWCRF respectively), and is based on parameterization for CRF that is estimated from detailed radiative transfer computations covering a global range of realistic atmospheric conditions, cloud properties, surface reflectance, and atmospheric profiles of temperature, ozone and water vapor. *Corti and Peter* [2009] have made extensive comparisons of this model with the CRF estimated from other models, which show that the accuracy of this semiquantitative parameterization is better than 20%. We used this model to estimate the LWCRF at top-of-atmosphere (TOA) for various combinations of COD and cloud top temperatures (which correspond to the cloud top altitudes being considered here and are obtained from the annual mean altitude profiles of atmospheric temperature over the site). The effect of descending of cirrus on the LWCRF is estimated by differencing the LWCRF for different cloud top altitudes from that for a reference altitude of 15 km, which is the typical cirrus cloud top altitude before descent, observed in the present study. Any variations in COD during descending are not considered here. The SWCRF at TOA due to cirrus descending is negligible. Thus, in effect, the change in LWCRF estimated here as a result of cirrus descending will be same as the change in net CRF due to descending.

[21] Figure 8 shows contours of the change in LWCRF at TOA due to cirrus descending, as a function of COD and downward displacement, for a cloud having cloud top altitude of 15 km before descent. As expected, the change in LWCRF at TOA shown in Figure 8 is negative, indicating that the descending of cirrus decreases the LWCRF at TOA. The typical vertical displacements and CODs observed in the present study are in the range of 1.0–3.5 km and 0.1–0.4 respectively. This would result in a decrease of 1 to 12.9 Wm^{-2} in the LWCRF at the TOA due to descending of cirrus. For the observed mean COD of 0.26 and mean cloud top descending of 2.0 km, the reduction in LWCRF is 4.2 Wm^{-2}. Though rare, large descending (>4 km) of optically thicker clouds (COD >0.5) can decrease the LWCRF at TOA by more than 16 Wm^{-2}.

[22] Main limitations of the present study are the absence of collocated observations of the altitude profiles of vertical wind, temperature, and humidity, which would have provided insight into the maintenance of cirrus layers by the upper tropospheric vertical winds, inferences on the actual sedimentation rates (and hence sizes) of cirrus ice particles, and the potential impact of cirrus descent on the thermodynamics and moisture content of the TTL. However, altogether, the results presented here clearly show that the descent speed of cirrus clouds is not merely governed by the sedimentation rate associated with the mass of the ice particles alone. This inference is in agreement with those reported by *Lin et al.* [2005] and *Mace et al.* [2006] who suggested that large scale vertical motions are important in maintaining the cirrus systems against particle sedimentation. More than 20% of the observed descending cirrus clouds have vertical displacements of >3 km and in few cases (~2%) the cloud layers have descended by 5 to 8.5 km. About ~7% of the descending cirrus layers have lasted for >5 h. These observations support the findings of *Heymsfield and Donner* [1990] that cirrus particles could fall through sub-saturated air for several kilometers, before fully sublimating. Neglecting the vertical wind in the upper troposphere and following the relationships between the fall speed and crystal size for different shapes *[Mitchell et al.*, 1996; *Das et al.*, 2010], the maximum dimension of ice crystals estimated from the present observations of descent rates are mostly in the range of 200–400 μm. However, in a background atmosphere with weak ascending motion, the cloud ice particle sizes inferred above could be an overestimate.

4. Conclusions

[23] Lidar observations of cirrus clouds over the tropical Indian station, Thiruvananthapuram, during March 2008 to

May 2011 reveal significant occurrences of descending cirrus layers throughout the year. The duration of cirrus descending is so large that it cannot be attributed to the manifestation of cirrus uncinus. Probability of occurrence of descending cirrus is larger during pre-monsoon and post-monsoon seasons (about 23–24%) and least during winter (15%). Though the frequency of occurrence of cirrus clouds is largest (69%) during the summer monsoon season, the fraction of cirrus clouds that are descending is the least (<26%) during this season. The fractions of descending cirrus during the other seasons are ∼41–49%. The smaller fraction of descending cirrus observed during the summer monsoon season might be due to the high-speed upper tropospheric easterlies prevailing during this season, which are responsible for the long-range transport of cirrus and moisture from the Bay of Bengal region. The most probable base (top) altitudes of descending cirrus layers are in the range of 11–15 km (12–16 km) before descent and 8–13 km (9–14 km) after descent. Most of the descending cirrus clouds form very close to the TTL base (around 14–15 km) and settle downward. The frequency of occurrence and vertical displacement of descending cirrus layers occurring within 2 km below the cold point tropopause is considerably smaller than those occurring at or below the TTL base. On average, the vertical displacements of the top and base of cirrus layers show almost a one-to-one relationship; the most probable vertical displacements are in the range of 1.5–2.5 km. The percentage of cirrus that are thickening or thinning by >300 m during descending are almost equal (∼23% each), while the thickening/thinning of the remaining 54% is <300 m. In >20% of the cases, the vertical displacement of the cloud top and base is >3 km. Most probable duration of the descending cirrus layers is 1–2 h (frequency of occurrence of ∼45%). However, nearly 40% of the descending cirrus lasted for 2–5 h. The frequency of occurrence of descending cirrus layers that last for <1 h or >5 h is very small (∼7–8%). The descent speed is inversely proportional to the cloud duration. All cirrus layers lasting for >3 h have descent speeds of <0.28 ms^{-1}. Around 95% of descending cirrus clouds have settling speed less than 0.8 ms^{-1} and none of these clouds are of sub-visual type (COD <0.03). Most probable value of COD for descending cirrus is between 0.2 and 0.3. On average, descending increases the cloud top temperature from ∼201 ± 2 K (before descent) to ∼216 ± 2 K (after descent), yielding a mean enhancement of ∼15 K in cloud top temperature. Radiative transfer calculations show that the descending of cirrus clouds would cause a typical reduction of ∼1 to 12.9 Wm^{-2} in the long-wave CRF at TOA (for vertical displacements and CODs in the ranges of 1.0–3.5 km and 0.1–0.4 respectively).

[24] The results presented here would be useful for incorporating cirrus characteristics in atmospheric circulation models. The potential impact of vertical winds, atmospheric circulation and properties of ice particles on the descent speeds needs to be investigated in detail. Further, the impact of descending on the moisture budget of the upper troposphere needs to be ascertained based on collocated observations of descending cirrus layers with altitude profiles of temperature and humidity.

[25] **Acknowledgments.** K. Parameswaran acknowledges CSIR for providing grant under the Emeritus Scientist Scheme. A. K. M. Nair acknowledges ISRO for Research Fellowship. We thank the anonymous reviewers for their highly constructive suggestions, which helped us to improve the scientific content and quality of this paper.

References

Choi, Y. S., and C. H. Ho (2006), Radiative effects of cirrus with different optical properties over the tropics in MODIS and CERES observations, *Geophys. Res. Lett.*, *33*, L21811, doi:10.1029/2006GL027403.

Corti, T., and T. Peter (2009), A simple model for cloud radiative forcing, *Atmos. Chem. Phys.*, *9*, 5751–5758, doi:10.5194/acp-9-5751-2009.

Corti, T., B. P. Luo, Q. Fu, H. Vomel, and T. Peter (2006), The impact of cirrus clouds on tropical troposphere-to-stratosphere transport, *Atmos. Chem. Phys.*, *6*, 2539–2547, doi:10.5194/acp-6-2539-2006.

Das, S. K., J. B. Nee, and C. W. Chiang (2010), A LiDAR study of the effective size of cirrus ice crystals over Chung-Li, Taiwan, *J. Atmos. Terr. Phys.*, *72*(9–10), 781–788, doi:10.1016/j.jastp.2010.03.024.

Deng, M., and G. G. Mace (2008), Cirrus cloud microphysical properties and air motion statistics using cloud radar Doppler moments: Water content, particle size, and sedimentation relationships, *Geophys. Res. Lett.*, *35*, L17808, doi:10.1029/2008GL035054.

Frey, W., et al. (2011), In situ measurements of tropical cloud properties in the West African Monsoon: Upper tropospheric ice clouds, Mesoscale Convective System outflow, and subvisual cirrus, *Atmos. Chem. Phys.*, *11*, 5569–5590, doi:10.5194/acp-11-5569-2011.

Fu, Q., Y. Hu, and Q. Yang (2007), Identifying the top of the tropical tropopause layer from vertical mass flux analysis and CALIPSO lidar cloud observations, *Geophys. Res. Lett.*, *34*, L14813, doi:10.1029/2007GL030099.

Gettelman, A., W. J. Randel, F. Wu, and S. T. Massie (2002), Transport of water vapor in the tropical tropopause layer, *Geophys. Res. Lett.*, *29*(1), 1009, doi:10.1029/2001GL013818.

Hartmann, D. L., J. R. Holton, and Q. Fu (2001), The heat balance of the tropical tropopause, cirrus, and stratospheric dehydration, *Geophys. Res. Lett.*, *28*(10), 1969–1972, doi:10.1029/2000GL012833.

Heymsfield, A. J., and L. J. Donner (1990), A scheme for parameterizing ice-cloud water content in general circulation models, *J. Atmos. Sci.*, *47*, 1865–1877, doi:10.1175/1520-0469(1990)047<1865:ASFPIC>2.0.CO;2.

Heymsfield, A. J., and J. Iaquinta (2000), Cirrus crystal terminal velocities, *J. Atmos. Sci.*, *57*, 916–938, doi:10.1175/1520-0469(2000)057<0916:CCTV>2.0.CO;2.

Heymsfield, A. J., S. Matrosov, and B. Baum (2003), Ice water path–optical depth relationships for cirrus and deep stratiform ice cloud layers, *J. Appl. Meteorol.*, *42*, 1369–1390, doi:10.1175/1520-0450(2003)042<1369:IWPDRF>2.0.CO;2.

Immler, F., K. Kruger, S. Tegtmeier, M. Fujiwara, P. Fortuin, G. Verver, and O. Schrems (2007), Cirrus clouds, humidity, and dehydration in the tropical tropopause layer observed at Paramaribo, Suriname (5.81°N, 55.21°W), *J. Geophys. Res.*, *112*, D03209, doi:10.1029/2006JD007440.

Jakob, C. (2002), Ice clouds in numerical weather prediction models: Progress, problems and prospects, in *Cirrus*, edited by D. Lynch et al., pp. 327–345, Oxford Univ. Press, Oxford U. K.

Jensen, E. J., L. Pfister, and O. B. Toon (2011), Impact of radiative heating, wind shear, temperature variability, and microphysical processes on the structure and evolution of thin cirrus in the tropical tropopause layer, *J. Geophys. Res.*, *116*, D12209, doi:10.1029/2010JD015417.

Lin, R. F., D. O. C. Starr, J. Reichardt, and P. J. DeMott (2005), Nucleation in synoptically forced cirrostratus, *J. Geophys. Res.*, *110*, D08208, doi:10.1029/2004JD005362.

Mace, G. G., S. Benson, and E. Vernon (2006), Cirrus clouds and the large-scale atmospheric state: Relationships revealed by six years of ground-based data, *J. Clim.*, *19*, 3257–3278, doi:10.1175/JCLI3786.1.

McFarquhar, G. M., A. J. Heymsfield, J. Spinhirne, and B. Hart (2000), Thin and subvisual tropopause tropical cirrus: Observations and radiative impacts, *J. Atmos. Sci.*, *57*, 1841–1853, doi:10.1175/1520-0469(2000)057<1841:TASTTC>2.0.CO;2.

Meenu, S., K. Rajeev, K. Parameswaran, and A. K. M. Nair (2010), Regional distribution of deep clouds and cloud top altitudes over the Indian subcontinent and the surrounding oceans, *J. Geophys. Res.*, *115*, D05205, doi:10.1029/2009JD011802.

Meenu, S., K. Rajeev, and K. Parameswaran (2011), Regional and vertical distribution of semitransparent cirrus clouds over the tropical Indian region derived from CALIPSO data, *J. Atmos. Terr. Phys.*, *73*, 1967–1979, doi:10.1016/j.jastp.2011.06.007.

Mishra, M. K., K. Rajeev, B. V. Thampi, K. Parameswaran, and A. K. M. Nair (2010), Micro pulse lidar observations of mineral dust layer in the lower troposphere over the southwest coast of Peninsular India during the Asian summer monsoon season, *J. Atmos. Terr. Phys.*, *72*, 1251–1259, doi:10.1016/j.jastp.2010.08.012.

Mitchell, D. L., S. K. Chai, Y. Liu, A. J. Heymsfield, and Y. Dong (1996), Modeling cirrus clouds. Part I: Treatment of bimodal size spectra and case study analysis, *J. Atmos. Sci.*, *53*, 2952–2966, doi:10.1175/1520-0469(1996)053<2952:MCCPIT>2.0.CO;2.

Mitchell, D. L., P. Rasch, D. Ivanova, G. McFarquhar, and T. Nousiainen (2008), Impact of small ice crystal assumptions on ice sedimentation rates in cirrus clouds and GCM simulations, *Geophys. Res. Lett.*, *35*, L09806, doi:10.1029/2008GL033552.

Nazaryan, H., M. P. McCormick, and W. P. Menzel (2008), Global characterization of cirrus clouds using CALIPSO data, *J. Geophys. Res.*, *113*, D16211, doi:10.1029/2007JD009481.

Parameswaran, K., S. V. Sunilkumar, B. V. Krishna Murthy, and K. Satheeshan (2004), Lidar observations of high altitude cirrus clouds near the tropical tropopause, *Adv. Space Res.*, *34*, 845–850, doi:10.1016/j.asr.2003.08.064.

Rajeev, K., et al. (2008), Observational assessment of the potential of satellite-based water vapor and thermal IR brightness temperatures in detecting semitransparent cirrus, *Geophys. Res. Lett.*, *35*, L08808, doi:10.1029/2008GL033393.

Rajeev, K., K. Parameswaran, B. V. Thampi, M. K. Mishra, A. K. M. Nair, and S. Meenu (2010), Altitude distribution of aerosols over southeast Arabian Sea coast during pre-monsoon season: Elevated layers, long-range transport and atmospheric radiative heating, *Atmos. Environ.*, *44*, 2597–2604. doi:10.1016/j.atmosenv.2010.04.014.

Sassen, K. (2002), Cirrus clouds: A modern perspective, in *Cirrus*, edited by D. Lynch et al., pp. 11–40, Oxford Univ. Press, Oxford, U. K.

Sassen, K., and B. S. Cho (1992), Subvisual-thin cirrus lidar dataset for satellite verification and climatological research, *J. Appl. Meteorol.*, *31*, 1275–1285, doi:10.1175/1520-0450(1992)031<1275:STCLDF>2.0.CO;2.

Stubenrauch, C. J., F. Eddounia, J. M. Edwards, and A. Macke (2007), Evaluation of cirrus parameterizations for radiative flux computations in climate models using TOVS–ScaRaB satellite observations, *J. Clim.*, *20*, 4459–4475, doi:10.1175/JCLI4251.1.

Sunilkumar, S. V., K. Parameswaran, K. Rajeev, B. V. Krishna Murthy, S. Meenu, S. K. Mehta, and A. Babu (2010), Semitransparent cirrus clouds in the tropical tropopause layer during two contrasting seasons, *J. Atmos. Terr. Phys.*, *72*(9–10), 745–762, doi:10.1016/j.jastp.2010.03.020.

Taylor, J. R., W. J. Randel, and E. J. Jensen (2011), Cirrus cloud-temperature interactions in the tropical tropopause layer: A case study, *Atmos. Chem. Phys.*, *11*, 10,085–10,095, doi:10.5194/acp-11-10085-2011.

Wang, L., and A. E. Dessler (2006), Instantaneous cloud overlap statistics in the tropical area revealed by ICESat/GLAS data, *Geophys. Res. Lett.*, *33*, L15804, doi:10.1029/2005GL024350.

Wang, P. H., P. Minnis, M. P. McCormick, G. S. Kent, and K. M. Skeens (1996), A 6-year climatology of cloud occurrence frequency from Stratospheric Aerosol and Gas Experiment II observations (1985–1990), *J. Geophys. Res.*, *101*, 29,407–29,429, doi:10.1029/96JD01780.

Whiteway, J., et al. (2004), Anatomy of cirrus clouds: Results from the Emerald airborne campaigns, *Geophys. Res. Lett.*, *31*, L24102, doi:10.1029/2004GL021201.

Winker, D., and C. Trepte (1998), Laminar cirrus observed near the tropical tropopause by LITE, *Geophys. Res. Lett.*, *25*, 3351–3354, doi:10.1029/98GL01292.

Young, S. A. (1995), Lidar analysis of lidar backscatter profiles in optically thin clouds, *Appl. Opt.*, *34*, 7019–7031, doi:10.1364/AO.34.007019.

Journal of Atmospheric and Solar-Terrestrial Physics 74 (2012) 232–237

Contents lists available at SciVerse ScienceDirect

Journal of Atmospheric and Solar-Terrestrial Physics

journal homepage: www.elsevier.com/locate/jastp

Short Communication

Impact of a noon-time annular solar eclipse on the mixing layer height and vertical distribution of aerosols in the atmospheric boundary layer

Manoj Kumar Mishra, K. Rajeev*, Anish Kumar M. Nair, K. Krishna Moorthy, K. Parameswaran

Space Physics Laboratory, Vikram Sarabhai Space Centre, Thiruvananthapuram 695022, India

ARTICLE INFO

Article history:
Received 9 April 2011
Received in revised form
7 October 2011
Accepted 12 October 2011
Available online 29 October 2011

Keywords:
Annular solar eclipse
Atmospheric boundary layer
Aerosols
Mixing layer height

ABSTRACT

Impact of the long duration noontime annular solar eclipse on 15 January 2010 on the vertical distribution of aerosols and mixing layer height (H_M) in a well-developed convective atmospheric boundary layer (ABL) has been investigated using continuous Lidar observations over a tropical coastal station, Thumba (8.5°N, 76.9°E). This study shows that H_M has decreased from its peak value of ~1800 m at 12:00 h to ~1000 m following the annular phase of the eclipse (13:17 h), while the corresponding decrease in the total aerosol abundance of ABL is ~29%. The post-eclipse increase of H_M is rapid compared to that during forenoon.

1. Introduction

One of the main features of atmospheric boundary layer (ABL) is the mixing layer height (H_M), below, which aerosols are nearly well mixed by the turbulence generated because of thermal instabilities and wind shears (Stull, 1988). Temporal evolution of H_M is a potential tool for characterizing the ABL. The mixing layer height undergoes a strong diurnal variation, primarily driven by a corresponding variation in the vertical flux of energy and momentum caused by the balance between the heating of earth's surface by the incoming solar radiation and radiative cooling of the surface. Under cloud-free conditions, the mixing layer can continue to grow for few hours even after the surface virtual potential temperature flux has reached its maximum, since the energy is still substantial even with low solar zenith angle (Yi et al., 2001). Knowledge of the mixing layer height and its temporal evolution are of substantial importance for understanding the dispersion of pollutants and modeling of ABL (e.g. Kunhikrishnan et al., 1993; Parameswaran et al., 1997).

The noontime annular solar eclipse on 15 January 2010 provided a unique opportunity to investigate the responses of the boundary layer processes, vertical distribution of pollutants in ABL and the mixing layer height, to the rapid but systematic variations in the incoming solar radiation, which is one of the primary driving forces that regulates the surface heating and convection. This noontime event is expected to produce significant impact on the ABL since it has occurred at the time when the maximum solar heating of the surface takes place. During the annular solar eclipse, the moon geometrically hides the solar disk, so that the solar radiation reaching the earth is rather quickly switched off and on. The effect of such an event will be considerably different from that associated with the diurnal variation of solar radiation intensity, which is rather slow and accompanied by the time-dependent changes in the atmospheric features. Though studies dealing with the ABL characteristcs during the solar eclipse events are reported in the literature (e.g., Sethuraman, 1982; Eaton et al., 1997; Dolas et al., 2002; Krishnan et al., 2004; Ratnam et al., 2010; Subrahamanyam and Anurose, 2011), investigations on the impact of solar eclipse on the vertical distribution of aerosols is highly limited (Kolev et al., 2005; Amiridis et al., 2007; Babu et al., 2011).

Main objective of the present study i's to investigate the impact of the noontime annular solar eclipse on 15 January 2010 on the vertical distribution of aerosols and mixing layer height over a tropical coastal station using continuous lidar observations of the altitude profiles of aerosol backscatter coefficient during the eclipse and adjacent control days having similar meteorological conditions. Importance of this event is further enhanced by the calm and cloud-free wintertime conditions that prevailed during this event, which provided ideal environment for driving the daytime evolution of ABL through the solar heating of surface and its identification without any significant influence of prominent weather systems and clouds.

2. Experimental setup, data and method of analysis

Details of the annular solar eclipse event on 15 January 2010 are given in Table 1. The path of maximum obscuration during

* Corresponding author. Tel.: +91 471 2563886.
E-mail address: k_rajeev@vssc.gov.in (K. Rajeev).

1364-6826/$ - see front matter © 2011 Elsevier Ltd. All rights reserved.
doi:10.1016/j.jastp.2011.10.012

Table 1
Details of the annular solar eclipse event on 15 January 2010 over Thumba.

First contact	05:35 UTC 11:05 IST
Second contact	07: 40 UTC 13:10 IST
Maximum contact	07:44 UTC 13:14 IST
Third contact	07:47 UTC 13:17 IST
Fourth contact	09:35 UTC 15:05 IST
Umbral Duration	07 min 16 s.
Obscuration at maximum contact	84.3%
Magnitude of the eclipse	91.8%

this eclipse passed through Thumba (8.5°N, 76.9°E), a coastal station located in the southwest Peninsular India at ~500 m inland from the Arabian Sea. At Thumba, first contact of the eclipse occurred at 11:05 Indian Standard Time (IST), attained annularity during 13:10 to 13:17 IST (second to third contacts, lasting for 7.2 min) with a maximum magnitude of ~91.8% (~84.3% obscuration) and ended at 15:05 IST (fourth contact).

A Micropulse Lidar (MPL) with dual polarization capability (model: MPL-4B of Sigma Space Corporation, USA) was operated almost continuously during 14, 15, 16 January 2010 (except for short breaks of <1 h duration at approximately 6 hourly intervals) for studying the altitude distribution of aerosols and its time evolution. This system consists of a diode-pumped frequency-doubled solid state Nd:YAG laser transmitter emitting laser pulses at the wavelength of 532 nm having a pulse width of 7 ns at a pulse repetition frequency of 2500 Hz and maximum pulse energy of 8 μJ. During this experiment, the MPL observations were carried out with a range resolution of 30 m and time integration of 60 s. A Maksutov–Cassegrain type telescope having diameter of 178 mm is used for transmitting the laser beam as well as receiving the backscattered lidar signal. The receiver channel incorporates two identical narrow band interference filters (having spectral width of 0.14 nm) to minimize the background radiation, which enables the daytime observations using MPL. The detector is a Silicon Avalanche Photodiode (Si-APD) operated in photon counting mode. The lidar system alternates between two states of polarization (co-polarized and cross-polarized) at an interval of 60 s.

The MPL system uses same telescope as both transmitter and receiver and hence the lidar signals are obtained from a reasonably short range of 90 m onwards. The raw data are subsequently corrected for the detector noise and dead-time (Rajeev et al., 2010). In addition to these corrections, lidar signals from the near field also require a range-dependent geometrical correction factor (Welton et al., 2002). This geometrical correction factor $g(r)$ ('r' being the range) was determined experimentally by sending the laser beam horizontally from top of a 30 m tall building on a hill (close to the coast) and observing the lidar signal at 30 m range resolution. In order to reduce the effect of atmospheric inhomogeneity, the observations were carried out in six different directions (all into the sea) for about 15 min in each direction. The range compensated signal $\Phi(r)$ ($=r^2P(r)$, where $P(r)$ is the lidar signal after background subtraction) exponentially increases with range up to about 1 km followed by a relatively weak exponential decrease. The atmospheric extinction coefficient is estimated using the slope method over the range of 1500–2000 m (which is significantly more than 1 km). Assuming the horizontal homogeneity, the values of $\Phi(r)$ for each profile are corrected for the two-way atmospheric transmittance using the value of extinction coefficient derived for that profile. The above parameter normalized with respect to its peak value (the peak value is observed at 1080 m in all directions) directly provides the geometric correction factor. The value of $g(r)$ increases up to a range of 1080 m and is very close to unity (within 2%) beyond this. The dispersion in the values of $g(r)$ derived from observations taken at different directions is significantly small ($<3\%$), which indicates the reliability of the experimentally derived value of geometrical correction factor. The average values of $g(r)$ obtained in different directions are used for the geometric correction of the lidar data up to a range of 1080 m, beyond, which $g(r)=1$. By applying this correction, useful information can be derived from MPL for altitudes above 135 m.

For each altitude profile of lidar signal, the average photon count observed between the altitudes of 50–60 km is considered as the background, which is subtracted from the measured signal to estimate the true backscattered signal. The altitude profiles of aerosol backscatter coefficient (β_a) are derived using Fernald's method (Fernald, 1984), assuming a mean value of 40 Sr for the extinction-to-backscatter ratio (S). Altitude profiles of the linear depolarization ratio (LDR) are estimated from the co- and cross-polarized backscattered lidar signals following the method described by Flynn et al. (2007). The linear depolarization ratio is an indicator of sphericity of aerosols: LDR increases with non-sphericity of aerosols and is very low ($\mathrm{LDR}<0.02$) for highly spherical aerosols. Further details of the MPL system, method of data processing, estimation of β_a and LDR, sources of errors and the uncertainty limits are described elsewhere (Mishra et al., 2010; Rajeev et al., 2010). Sensitivity analysis (for typical variations in the assumed value of S, and the boundary condition of β_a at the reference altitude) shows a typical uncertainty of ~20% in β_a and ~40% in LDR below 5 km.

A quantitative analysis of H_M is carried out using the vertical gradient and temporal variations of the attenuated backscatter coefficient (ABC, which is the range corrected lidar signal after incorporating the necessary corrections and subtracting the background noise) derived from lidar data. The altitude at which the filtered first order derivative of ABC with respect to altitude [d(ABC)/dz] turns negative is considered as the base of the entrainment zone and H_M (Flamant et al., 1997; Menut et al., 1999; Amiridis et al., 2007). However, because of the variations in signal-to-noise ratio as well as presence of transient layers, it is essential that H_M determined using the above method is further verified using the time variation of ABC at each altitude [d(ABC)/dt], in which ABC is identified as the altitude where sudden change in the time variation of ABC occurs. The value of ABC determined using the above two methods during the present observation period are found to be in agreement within ± 60 m.

A Sunphotometer (Microtop-II, Solar Light Co.) was used to observe the aerosol optical depths (AOD) at the wavelengths of 440, 500, 675 and 1020 nm during cloud-free daytime conditions. Uncertainty in the AOD is less than ± 0.04. Aerosol optical depth at the MPL wavelength of 532 nm is estimated by fitting a power law type variation of AOD (Angstrom relation) to the above measurements. Altitude profiles of the aerosol backscatter and extinction coefficients, obtained by inverting the MPL data, are weighed by the ratio of AOD observed using Sunphotometer to that of the column integrated extinction coefficient derived from MPL data. This ensures that the integrated extinction coefficient derived from MPL is equal to the AOD observed using Sunphotometer, which further reduces the uncertainty of the altitude profiles of aerosol backscatter and extinction coefficients derived from MPL (Rajeev et al., 2010).

Spectral measurements of the direct solar radiation in the wavelength band of 350–2200 nm were carried out using a calibrated spectroradiometer (Model: FieldSpec3, of Analytical Spectral Devices, USA). It employs a cosine corrected receptor (RCR) in the fore-optics for the collection of the irradiance, which is fed to the detector through a fiber optic cable. A direct irradiance attachment having a field-of-view of 2.5° is fitted to the RCR for making measurements of the direct solar irradiance. Radiometric calibration of this system is carried out at subsystem

level as well as in the integrating mode, which enables the measurement of absolute spectral radiance with a maximum uncertainty of 5%.

3. Results and discussion

Thumba and the surrounding regions were free from any major weather systems during the experiment, though scattered low-level clouds (cumulus) occurred almost throughout the daytime on 14 January 2010. However, cloud amount on this day had decreased considerably by the evening and was generally cloud-free after the midnight. In contrast, the ambient meteorological conditions during 15–16 January were generally similar. The amount of low- and middle-level clouds were considerably smaller during both these days, except for the occurrence of isolated thin boundary layer clouds during the evolution of ABL, which make them ideal for investigating the evolution of ABL characteristics using lidar. However, MPL observations showed the occurrence of thin cirrus clouds on 16 January while such clouds were absent on 15th. Considering the above conditions, 16 January is considered as the control day against which temporal variations of the aerosol profiles during the eclipse day are compared for quantifying the impact of solar eclipse on the aerosol distribution.

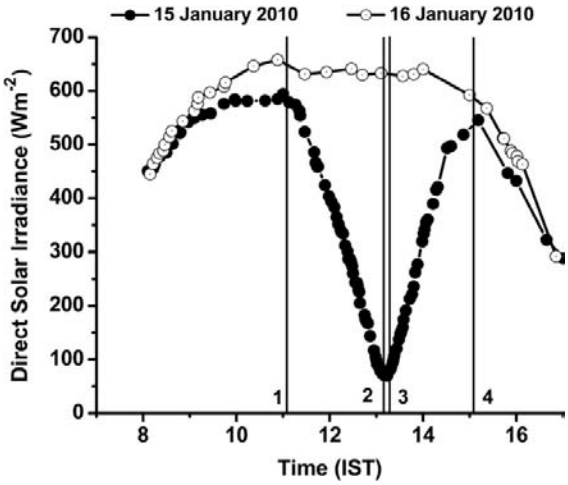

Fig. 1. Time variations of the direct solar irradiance (integrated in the spectral band of 350–2200 nm) during 15 and 16 January 2010. The vertical lines indicate the 1st, 2nd, 3rd, and 4th contacts of the annular solar eclipse (marked as 1, 2, 3 and 4, respectively).

Time variations of the direct solar irradiance (F_d, integrated in the spectral band of 350–2200 nm) at the earth's surface during 15 and 16 January 2010 obtained using spectroradiometer are depicted in Fig. 1, which show a systematic decrease of F_d after the first contact of the eclipse. At the peak of the eclipse (between the second and third contacts) F_d is only ~11% of the corresponding value observed during the control day. This is followed by an increase in F_d up to the fourth contact. Before and after the eclipse period, the values of F_d during 15 January are very similar to that during the control day. In response to the reduction in solar radiation associated with this eclipse, the soil surface temperature has decreased from 40.6 °C at 12:00 IST to 38.5 °C at 14:00 IST, which is followed by an increase up to 42 °C at 16:00 IST.

Time-altitude cross sections of ABC and LDR derived from MPL observations in the altitude band of 135–2000 m during 15 and 16 January 2010 are shown in Fig. 2(a,b). The solid lines in these figures indicate time variations of H_M identified using the filtered first order derivative of ABC with respect to altitude. During the early morning of 16 January (control day), an elevated layer of aerosols was clearly discernible between 500 and 1000 m with its centroid located at ~700 m. This structure, though with varying magnitude, was present since 00:00 IST and continued up to

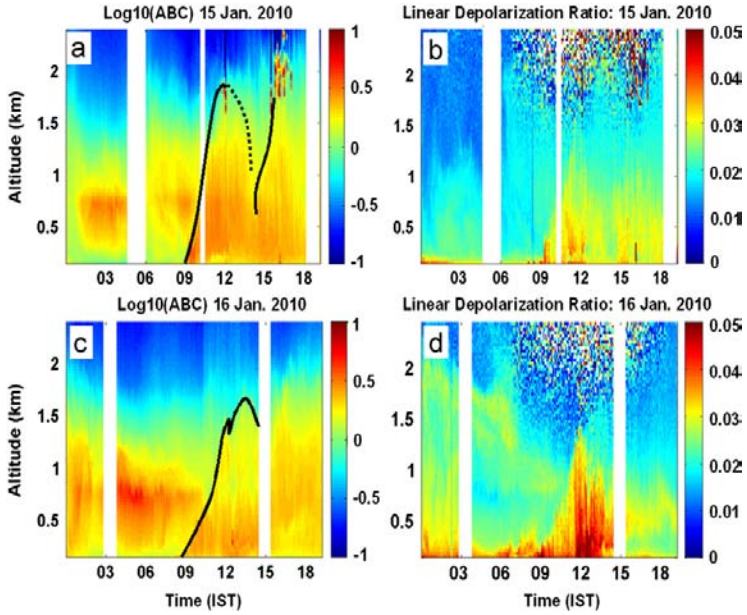

Fig. 2. Time-altitude cross-sections of (a) attenuated backscatter coefficient plotted in Log scale (arbitrary unit) and (b) linear depolarization ratio on 15 January 2010. (c) and (d) are same as (a) and (b), respectively, but for 16 January 2010.

~10:30 IST. Notwithstanding this, Fig. 2 clearly shows the diurnal evolution of the ABL, notably the upward movement of the convective boundary layer height after ~09:00 IST during the control day. Development of the daytime ABL and the accompanying changes in vertical transport of aerosols are well discernible on this day during 09:00–12:00 IST in both ABC and LDR. The mixed layer height increases monotonically from ~200 m at 09:00 IST to ~1600 m at 13:00 IST, which is followed by a quasi-steady state of H_M during the afternoon period. The temporal variations of ABC above H_M are considerably smaller than that below. The magnitude of LDR and its spatio-temporal variations are only in the range of 0.02–0.04, which is significantly less than the corresponding values of 0.1–0.3 observed for mineral dust (e.g., Mishra et al., 2010; Rajeev et al., 2010). This shows that the aerosols observed in the ABL during this period are more-or-less spherical in nature. Notwithstanding this, the evolution of ABL is clearly discernible from the altitude-time variations of LDR, which shows the vertical transport of relatively non-spherical aerosols (LDR~0.04), particularly during the forenoon period. Though very small, the increase in sphericity of aerosols in the upper part of ABL and during the afternoon period might be associated with the hygroscopic growth of aerosols in these altitudes due to increase in humidity of the vertically transported air because of adiabatic cooling. Due to this reason, the spatio-temporal variations of LDR shown in Fig. 2 cannot clearly represent the evolution of ABL and H_M at higher altitudes and afternoon period.

Spatio-temporal variations of the vertical distribution of aerosols during the eclipse day are generally consistent with that during the control day. The elevated aerosol layer observed in the nocturnal ABL during the control day is observed during the eclipse day as well, with ABC showing a broad peak between ~400–1000 m during 00:00–10:00 IST. Evolution of the convective ABL is clearly observed in the time-altitude cross sections of ABC and LDR during 09:00–12:00 IST. The value of H_M has increased from ~200 m at 09:00 IST to ~1800 m at 12:00 IST during the eclipse day. Fig. 2a shows the occurrence of isolated and thin boundary layer clouds between 1600–1800 m during 11:30–12:30 IST. This is a characteristic feature of the daytime convective ABL [Stull, 1988], with the cloud bottom representing the top of the convective ABL and base of the entrainment zone. This further confirms the estimated value of H_M and its time evolution derived from the vertical and temporal variations of ABC. Remarkably, Fig. 2a shows a small but well-discernible decrease in the values of ABC after attaining the peak value of H_M around 12:00 IST. This depletion initially occurs at ~1500–1800 m and spreads to the lower altitudes up to ~1000 m at ~14:00 IST. Note that the aerosols transported to the ABL by the convective eddies during the forenoon period cannot be removed significantly by the abatement of convection (e.g., Parameswaran et al., 1997). This has resulted in the relatively small vertical and temporal variations of aerosols after 12:00 IST compared to that during the evolution of convective ABL. Notwithstanding this, the reduction of ABC is discernible in the altitude band of 1000–1800 m during 12:00–14:00 IST. Upper boundary of this region where the values of ABC decrease with time is indicated by the dashed line in Fig. 2a and represents shrinking of the mixing layer during the eclipse. Clearly, this has been primarily driven by the decrease in surface heating (indicated by a reduction of ~2.1 °C in soil temperature) and convection due to the reduction in solar irradiance caused by the eclipse. An overall depletion in aerosol concentration is observed for ~1 h around 13:30 IST over the entire ABL. This also suggests that H_M might have lowered to even below ~1000 m after the annular eclipse period, though this could not be quantitatively estimated from the time-altitude cross section of ABC due to its considerably small variation with time and altitude. It is highly likely that the weakening of convection in ABL might strengthen the subsidence of the stable air aloft through a process opposite to that operating during the evolution of convective boundary layer seen during the forenoon period. This also might contribute to the decrease in H_M observed during the eclipse period.

Upward transport of aerosols in the lower part of ABL (below ~500 m) after the third contact is seen in Fig. 2a, indicating the regeneration of thermals after the annular phase of the eclipse. Increase of H_M after ~14:00 IST is clearly identifiable in Fig. 2a and is indicated by the solid line (values of H_M below ~500 m are not shown here since they could not be determined unambiguously). Interestingly, increase in H_M after the annular phase of the eclipse is more rapid than that during the forenoon period. This might be because of the prevailing thermodynamic state of ABL after the eclipse, which is significantly modified by the almost fully developed convective ABL before the beginning of the eclipse. This condition would be significantly different from that during the forenoon convective evolution of ABL from the stable nocturnal boundary layer. The post-eclipse increase in aerosol concentration above ~1000 m occurs only ~40 min after that observed in the lower part of ABL. Post-eclipse evolution of ABL eventually led to the formation of isolated low-level clouds in the altitude band of 1500–2200 m during 15:00–16:30 IST (Fig. 2). This feature further confirms the post-eclipse enhancement of H_M to >1800 m. Remarkably, a small but persistent reduction in LDR occurs almost throughout the ABL for more than 1 h after the second contact of the eclipse, which might be associated with the increased hygroscopic growth of aerosols.

The lidar signals were inverted using Fernald's method to derive the altitude profiles of aerosol backscatter coefficient (β_a), which provides more quantitative information on the aerosol loading compared to ABC. However, in order to improve the signal-to-noise ratio and accuracy of the retrieved profiles of β_a, particularly at higher altitudes around the noontime, the lidar data were integrated for 30 min before carrying out the Fernald's inversion. Because of this, the temporal resolution of the profiles of β_a is less than that of ABC. Fig. 3 shows the time-altitude cross-sections of β_a during the eclipse and control days. During both

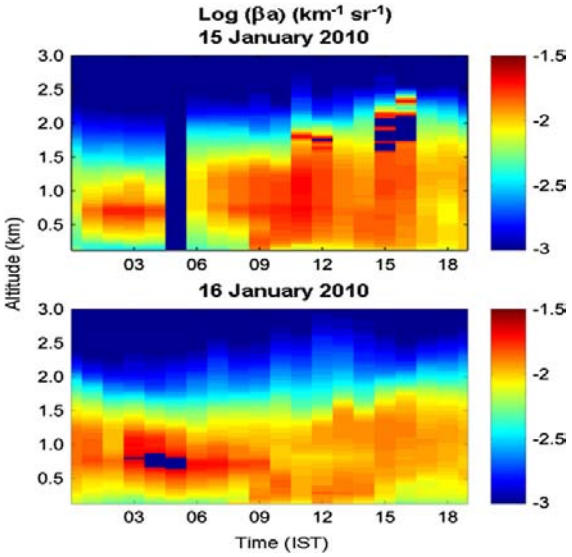

Fig. 3. Time-altitude cross-sections of aerosol backscatter coefficient (plotted in Log scale, $km^{-1}\,sr^{-1}$) during the eclipse (top panel) and control (bottom panel) days.

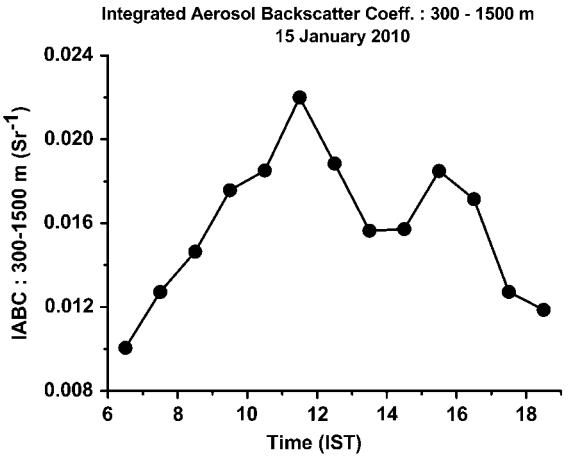

Fig. 4. Time variation of the integrated aerosol backscatter coefficient (IABC) in the altitude band of 300–1500 m during 15 January 2010.

these days, the value of β_a below ~300 m peaks around 09:00 IST, which is followed by lifting up of aerosols to higher altitudes with the evolution of ABL. Increase in aerosol amount below ~1800 m altitude during the convective evolution of ABL before the eclipse and reduction in aerosol abundance during the eclipse are clearly discernible in Fig. 3. The increase in aerosol amount in the lower part of ABL after the annular phase of the eclipse also is clearly seen. The above variations in the vertical distribution of aerosols during and immediately after the solar eclipse are distinctly different from those observed during the control day.

A quantitative assessment of the effect of solar eclipse on the total aerosol loading of ABL is investigated based on temporal variations of the integrated aerosol backscatter coefficient (IABC) in the altitude band of 300–1500 m during the eclipse day and is shown in Fig. 4. Though the mixing height has increased up to ~1600–1800 m during the afternoon, the values of β_a in the altitude range of 300–1500 m only are used for estimating IABC to avoid any influence of low altitude clouds, which were present above ~1500 m for a while during the evolution of the ABL, as seen in Fig. 2. Fig. 4 shows a consistent increase of IABC during the forenoon period; its value has increased by ~50% from 08:30 to 11:30 IST and is due to the vertical mixing of aerosols during the evolution of ABL. This is followed by a decrease of IABC, which attains a minimum value during 13:30–14:30 IST and is clearly linked to the abatement of convection and vertical transport of aerosols caused by the solar eclipse. The depletion of aerosol concentration from its peak (at 11:30 IST) to trough (13:30–14:30 IST) is ~29%. The convective development of ABL following the annular phase of eclipse enhances the value of IABC by ~18% during 14:30–15:30 IST. Timings of the peaks and troughs in the temporal evolution of IABC are in agreement with those expected from the variations in the surface heating and associated convection inferred from the meteorological observations.

4. Conclusions

At the peak of the eclipse, direct component of the surface-reaching solar irradiance in the spectral band of 350–2200 nm is only ~11% of the corresponding value observed on the control day. This has resulted in the decrease of surface temperature by ~2 °C during the eclipse and consequent abatement of atmospheric convection. Time-altitude cross-sections of the aerosol backscatter coefficient and linear depolarization ratio clearly depict differences in the evolution of convective ABL during the eclipse and control days. During both these days, the aerosol concentration in the residual layer peaked in the altitude band of 600–1200 m during the post-midnight and morning hours. Notwithstanding this, upward movement of the mixing layer height from ~200 m at ~09:00 IST to reach a peak altitude of ~1600–1800 m around the noontime is discernible during both the days. During the eclipse day, the aerosol backscatter coefficient and H_M show a decrease after attaining their peak values around the noon. This depletion initially occurs at ~1500–1800 m and spreads to the lower altitudes with time. Driven by the decrease in surface heating and weakening of convection during the eclipse event, the mixing layer height has decreased from ~1800 m at 12:00 IST to ~1000 m after the third contact. Vertical transport of aerosols caused by the increase in convection after the annular eclipse is observed in the lower part of ABL after the third contact, while increase in aerosol concentration in the upper part of ABL occurs only ~40 min later. The mixing layer height increases to >1800 m during the post-eclipse period. This increase is more rapid than that during the forenoon convective evolution of ABL. Eclipse-induced abatement of convection has decreased the integrated aerosol backscatter coefficient in the altitude band of 300–1500 m by ~29% from its peak value observed before the eclipse. In contrast, the post-eclipse development of ABL has enhanced the integrated aerosol backscatter coefficient in the above altitude band by ~18%. A small but persistent reduction in linear depolarization ratio occurs almost throughout the ABL for more than 1 h after the second contact of the eclipse (13:10 IST).

This study clearly shows the impact of the noontime annular solar eclipse event in bringing about changes in the vertical transport of pollutants over a coastal location. In addition to providing a better understanding of the response time of aerosols in the convective boundary layer, the results presented here offer a test case for the atmospheric models.

Acknowledgments

We are thankful to Prof. R. Sridharan, former Director of SPL, for the overall coordination and planning of the Solar Eclipse Experiment. We thank the reviewers for their valuable suggestions. K. Parameswaran is Emeritus Scientist supported by CSIR grant.

References

Amiridis, V., Melas, D., Balis, D.S., Papayannis, A., Founda, D., Katragkou, E., Giannakaki, E., Mamouri, R.E., Gerasopoulos, E., Zerefos, C., 2007. Aerosol lidar observations and model calculations of the planetary boundary layer evolution over Greece, during the March 2006 total solar eclipse. Atmospheric Chemistry and Physics 7, 6181–6189.

Babu, S.S., Sreekanth, V., Moorthy, K.K., Mohan, M., Kirankumar, N.V.P., Subrahamanyam, D.B., Gogoi, M.M., Kompalli, S.K., Beegum, N., Chaubey, J.P., Kumar, V.H.A., Manchanda, R.K., 2011. Vertical profiles of aerosol black carbon in the atmospheric boundary layer over a tropical coastal station: perturbations during an annular solar eclipse. Atmospheric Research 99, 471–478. doi:10.1016/j.atmosres.2010.11.019.

Dolas, P.M., Ramachandran, R., Sen Gupta, K., Patil, S.M., Jadhav, P.N., 2002. Atmospheric surface layer processes during the total solar eclipse of 11 August 1999. Boundary Layer Meteorology 104, 445–461.

Eaton, F.D., Hines, J.R., Hatch, W.H., Cionco, R.M., Byers, J., Garvey, D., 1997. Solar eclipse effects observed in the planetary boundary layer over a desert. Boundary Layer Meteorology 83, 331–346.

Flamant, C., Pelon, J., Flamant, P., Durand, P., 1997. Lidar determination of the entrainment zone thickness at the top of the unstable marine atmospheric boundary layer. Boundary Layer Meteorology 83, 247–284.

Fernald, F.G., 1984. Analysis of atmospheric lidar observations: some comments. Applied Optics 23, 652–653.

Flynn, C.J., Mendoza, A., Zheng, Y., Mathur, S., 2007. Novel polarization-sensitive micropulse lidar measurement technique. Optics Express 15 (6), 2785–2790.

Kolev, N., Tatarov, B., Grigorieva, V., Donev, E., Simenonov, P., Umlensky, V., Kaprielov, B., Kolev, I., 2005. Aerosol Lidar and in situ ozone observations of the planetary boundary layer over Bulgaria during the solar eclipse of 11 August 1999. International Journal of Remote Sensing 26, 3567–3584.

Krishnan, P., Kunhikrishnan, P.K., Ravindran Sudha, Ramachandran Radhika, Subrahamanyam D.B. and Ramana M.V., 2004. Observation of the Atmospheric surface layer parameters over a semi arid region during the solar eclipse of August 11, 1999.In: Proceedings of the Indian Academy Sd (Earth and Planetary Science), vol. 113, pp. 353–363.

Kunhikrishnan, P.K., Gupta, K.S., Radhika, R., Prakash, J.W.J., Nair, K.N., 1993. Study on thermal internal boundary layer structure over Thumba, India. Annual Geophysics 11, 52–60.

Menut, L., Flamant, C., Pelon, J., Flamant, P., 1999. Urban boundary layer height determination from lidar measurements over the Paris area. Applied Optics 38, 945–954.

Mishra, M.K., Rajeev, K., Thampi, B.V., Parameswaran, K., Nair, A.K.M., 2010. Micro pulse lidar observations of mineral dust layer in the lower troposphere over the southwest coast of Peninsular India during the Asian summer monsoon season. J. Atmos. Sol. Terr. Phys. 72, 1251–1259.

Parameswaran, K., Rajeev, K., Sen Gupta, K., 1997. An observational study of night time aerosol concentration in the lower atmosphere at a tropical coastal station. J. Atmos. Solar Terr. Phys. 59, 1727–1737.

Rajeev, K., Parameswaran, K., Thampi, B.V., Mishra, M.K., Nair, A.K.M., Meenu, S., 2010. Altitude distribution of aerosols over Southeast Arabian Sea coast during pre-monsoon season: elevated layers, long-range transport and atmospheric radiative heating. Atmospheric Environment 44, 2597–2604.

Ratnam, V.M., Shravan Kumar, M., Basha, G., Anandan, V.K., Jayaraman, A., 2010. Effect of the annular solar eclipse of 15 January 2010 on the lower atmospheric boundary layer over a tropical rural station. J. Atmos. Sol Terr. Phys. 72, 1393–1400.

Sethuraman, S., 1982. Dynamics of the atmospheric boundary layer during the 1980 total solar eclipse. Proceedings of INSA 48, 187–195.

Stull, R.B., 1988. An Introduction to Boundary Layer Meteorology. Kluwer Academic Publishers, Dordrecht, The Netherlands.

Subrahamanyam, D.B., and Anurose, T.J., 2011. Solar eclipse induced impacts on sea/land breeze circulation over Thumba: a case study, Journal of Atmospheric and Solar Terrestrial Physics., 10.1016/j.jastp.2011.01.002.

Welton, E.J., Voss, K.J., Quinn, P.K., Flatau, P.J., Markowicz, K., Campbell, J.R., Spinhirne, J.D., Gordon, H.R., Johnson, J.E., 2002. Measurements of aerosol vertical profiles and otical properties during INDOEX 1999 using micropulse lidars. Journal of Geophysical Research 107, 8019. doi:10.1029/2000JD000038.

Yi, C., Davis, K.J., Berger, B.W., 2001. Long-term observations of the dynamics of the continental planetary boundary layer. Journal of Atmospheric Science 58, 1288–1299.

Ann. Geophys., 29, 1247–1252, 2011
www.ann-geophys.net/29/1247/2011/
doi:10.5194/angeo-29-1247-2011

Annales Geophysicae

Characteristics of a persistent "pool of inhibited cloudiness" and its genesis over the Bay of Bengal associated with the Asian summer monsoon

Anish Kumar M. Nair, K. Rajeev, S. Sijikumar, and S. Meenu

Space Physics Laboratory, Vikram Sarabhai Space Centre, Thiruvananthapuram 695 022, India

Received: 25 February 2011 – Revised: 2 June 2011 – Accepted: 20 June 2011 – Published: 13 July 2011

Abstract. Using spatial and vertical distributions of clouds derived from multi-year spaceborne observations, this paper presents the characteristics of a significant "pool of inhibited cloudiness" covering an area of $>10^6$ km^2 between 3–13° N and 77–90° E over the Bay of Bengal (BoB), persisting throughout the Asian summer monsoon season (ASM). Seasonal mean precipitation rate over the "pool" is <3 mm day^{-1} while that over the surrounding regions is mostly in the range of 6–14 mm day^{-1}. Frequency of occurrence of clouds in this "pool" is ∼20–40 % less than that over the surrounding deep convective regions. Zonal and meridional cross sections of the altitude distribution of clouds derived from CloudSat data reveal a vault-like structure at the "pool" with little cloudiness below ∼7 km, indicating that this "pool" is almost fully contributed by the substantially reduced or near-absence of low- and middle-level clouds. This suggest the absence of convection in the "pool" region. Spaceborne scatterometer observations show divergence of surface wind at the "pool" and convergence at its surroundings, suggesting the existence of a mini-circulation embedded in the large-scale monsoon circulation. Reanalysis data shows a mini-circulation extending between the surface and ∼3 km altitude, but its spatial structure does not match well with that inferred from the above observations. Sea surface at the south BoB during ASM is sufficiently warm to trigger convection, but is inhibited by the subsidence associated with the mini-circulation, resulting in the "pool". This mini-circulation might be a dynamical response of the atmosphere to the substantial spatial gradient of latent heating by large-scale cloudiness and precipitation at the vast and geographically fixed convective zones surrounding the "pool". Subsidence at the "pool" might contribute to the maintenance of convection at the above zones and be an important component of ASM that is overlooked hitherto.

Correspondence to: K. Rajeev
(k_rajeev@vssc.gov.in)

Keywords. Atmospheric composition and structure (Cloud physics and chemistry) – Meteorology and atmospheric dynamics (Climatology; Tropical meteorology)

1 Introduction

Spaceborne observations and experimental campaigns during the past few decades have made significant advancements in the understanding of the Asian summer monsoon (ASM). However, knowledge of several monsoon features and the underlying physical processes are still inadequate, because of which the modeling and long-range forecast of ASM remain elusive. Distribution of clouds over the Indian subcontinent and the surrounding regions during ASM (June–September period) has several important features. For example, the highest cloud top altitudes (Meenu et al., 2010) and integrated latent heat release (Zuluaga et al., 2010) over the planet occur over the Bay of Bengal (BoB) during ASM. In contrast to the near-cancellation of the longwave and shortwave cloud radiative forcing at the top-of-atmosphere over the tropics, net cloud radiative forcing over a vast region in the Indian subcontinent and the surrounding oceans is negative during ASM (Rajeevan and Srinivasan, 2000; Roca et al., 2005). Using long-term spaceborne observations of cloud characteristics over south Asia and the adjoining oceanic regions, this paper brings out the occurrence, characteristics and potential genesis mechanism of a "pool of inhibited cloudiness" covering an area of more than 1 million km^2 over the south BoB during the ASM. Though the existence of this feature is seen in the regional distributions of clouds, precipitation and outgoing longwave radiation (OLR) reported in the literature (e.g., Goswami et al., 1999; Meenu et al., 2007, 2010), the contribution of low-, middle- and high-level clouds in its manifestation could not be deciphered unambigously. This is primarily because of the limitation of spaceborne passive radiometric observations, which are generally biased towards high-altitude clouds due to the absorption of

Published by Copernicus Publications on behalf of the European Geosciences Union.

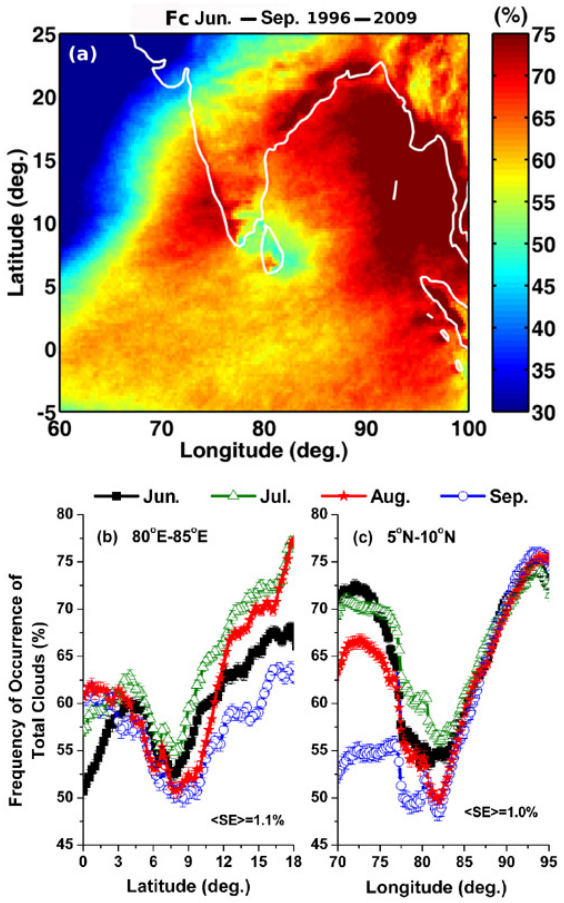

Fig. 1. **(a)** Long-term (1996–2009) seasonal mean spatial distribution of the frequency of occurrence of clouds (F_c, expressed in percentage) observed during ASM. **(b)** Long-term monthly mean latitudinal variations of the frequency of occurrence of clouds, averaged along in 80–85° E during June, July, August and September. **(c)** Same as **(b)** but for the longitudinal variation averaged along 5–10° N. The vertical lines indicate the standard errors of F_c and <SE> represents average error.

radiation emitted from lower cloud layers by the cloud layer above them. In contrast to this, the active remote sensing of hydrometeors using CloudSat have enabled the detection of clouds occurring below optically thick high-altitude clouds (Haynes and Stephens, 2007), which elucidate certain unique features of their vertical distribution in the "pool". Potential mechanisms for the genesis of the "pool" are identified by analysing the sea surface temperature (SST), atmospheric circulation and spaceborne observations of surface wind divergence.

2 Data

Spatial distribution of clouds during 1996–2009 is derived on a daily basis by analyzing the data obtained from the Advanced Very High Resolution Radiometer (AVHRR; Global Area Coverage – GAC) onboard NOAA-14/16/18 satellites. This data has daily coverage over the entire study region considered here. Pixel resolution of AVHRR-GAC data is 4 km at nadir. Brightness temperature observed in the thermal infrared bands are used to identify the cloudy pixels based on the method described in Meenu et al. (2010). Pixel-level cloudiness derived from each satellite pass is transformed into a uniform geographical grid of size 0.25°. The monthly mean frequency of occurrence of clouds (F_c) in each grid is obtained by averaging the observed daily mean cloudiness in the respective grids for each month. Entire AVHRR data during the 1996–2009 period is used in this analysis.

Vertical distribution of clouds are obtained from the polar orbiting sun-synchronous satellite, CloudSat, having a Cloud Profiling Radar (CPR) operating at 94 GHz, which provides the altitude profiles of backscattered radar signal from hydrometeors with a vertical resolution of 240 m along the subsatellite track (Haynes and Stephens, 2007). The footprint size of a single profile is 1.7 km along track by 1.4 km across track. The CloudSat orbits have a repetivity of 16 days. The raw data is processed at the CloudSat data processing centre to derive different science data products. This study utilizes the cloud geometrical profile product, 2B-GEOPROF (Version-4) which provides the cloud mask containing the information on cloud layers and their top and base altitudes for the individual profiles along the satellite orbit (Mace et al., 2007). This data are used to estimate the monthly and seasonal mean altitude profiles of the frequency of occurrence of clouds (F_{ALT}) and their zonal and meridional distributions during the June–September period of 2006–2009.

Long-term seasonal mean spatial distribution of precipitation over the study domain are obtained from the Global Precipittion Climatology Project (GPCP Version 2.1) data (Adler et al., 2003), which has a geographical resolution of 2.5°. Long term (1996–2009) monthly and seasonal mean values of SST are examined using the NOAA optimum interpolated SST (OI–SST). The surface wind divergence (SWD) during this period are obtained from the spaceborne scatterometer observations (European Remote Sensing Satellite – ERS 1 and 2, and QuikScat satellite of NASA), which have a spatial resolution of 0.5° (QuikScat) and 1° (ERS) (Liu, 2002). The atmospheric circulation data during the above period are obtained from ECMWF ERA-Interim reanalysis.

3 Results and discussion

Figure 1a shows the long-term (1996–2009) seasonal mean distribution of F_c over the Indian subcontinent and the surrounding oceanic regions during ASM derived from AVHRR

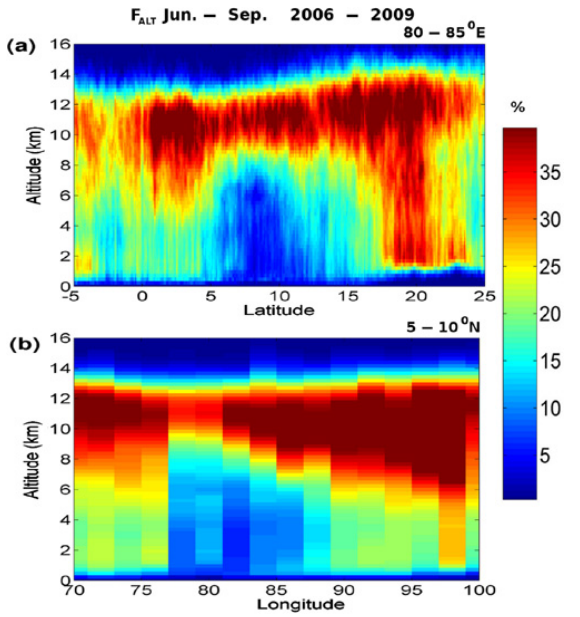

Fig. 2. **(a)** Four-year (2006–2009) average seaonal mean latitude-altitude cross section of the frequency of occurrence of clouds (F_{ALT}, expressed in percentage) during ASM along 80–85° E. **(b)** Same as **(a)** but for the longitude-altitude cross section averaged along 5–10° N.

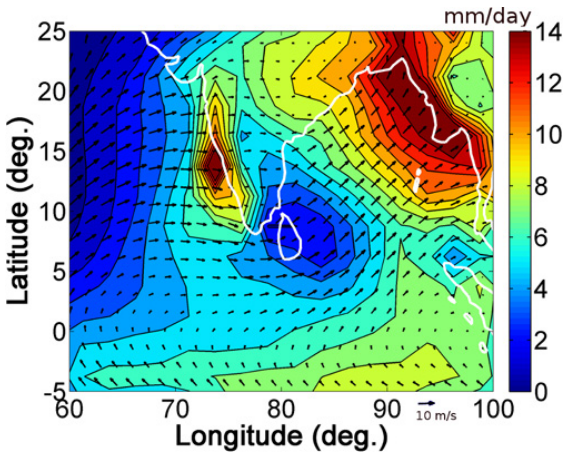

Fig. 3. Long-term (1996–2009) seasonal mean regional distribution of precipitation rate (mm day^{-1}) during ASM. The vectors represent the corresponding long-term seasonal mean winds at 1000 hpa level during this season.

data, which clearly shows the presence of a large "pool of inhibited cloudness" over the southwest BoB centred around 8° N, 82° E adjoining Sri Lanka. Seasonal mean values of F_{c} in the "pool" are <50 % while those over the surrounding regions are ∼70–90 %. The corresponding long-term monthly mean latitude and longitude variations of F_{c} averaged along 80–85° E and 5–10° N, respectively, during June, July, August and September are depicted in Fig. 1b, c, which show the persistence of the "pool" throughout the ASM, though its prominence is maximum during July–August. Similar features are also seen in the regional distribution of clouds reported by Meenu et al. (2007, 2010). As identified from the well shaped latitudinal and longitudinal variations of F_{c} (Fig. 1b, c), the "pool" extends from 77 to 90° E and 3 to 13° N, which are remarkably similar during all the above months. Though not depicted here, this "pool" is also clearly observable in the monthly and seasonal mean images of the outgoing longwave radiation (with an enhancement of ∼10 to 25 W m^{-2} over the pool compared to its surroundings) and is manifested by remarkably less precipitation. Such a "pool" is absent during other seasons.

The seasonal mean latitude-altitude cross section of F_{ALT} during the ASM of 2006–2009 derived from 2B-GEOPROF, averaged along the 80–85° E longitude band is shown in Fig. 2a. The corresponding longitude-altitude cross section of F_{ALT} averaged for the 5–10° N latitude band is depicted in Fig. 2b. The most remarkable feature observed in Fig. 2a, b is the drastic decrease or near-absence of clouds in the lower and middle troposhere in the "pool" region, which appears as a vault whose location and boundaries match with those derived from Fig. 1. (It may be stated here that the features of cloud distribution, including characteristics of the "pool" region, observed using AVHRR data during 2006–2009 are similar to that for 1996–2009 shown in Fig. 1). The value of F_{ALT} below ∼7 km at the centre of the "pool" is generally <10 %, which is markedly lower than that over the surrounding regions (F_{ALT} ∼ 25–35 %) where the deep convective clouds are present from <1 km and extend up to ∼13 km. However, F_{ALT} increases considerably above ∼7 km and its spatial gradient almost vanishes in the altitude band of ∼10–13 km where F_{ALT} is >40 % over a vast region. This might be the reason for the absence of the pool of inhibited cloudiness in the regional distribution of semitransparent cirrus clouds reported by Sunilkumar et al. (2010). Similar to F_{c}, the considerably less value of F_{ALT} observed below ∼7 km in the "pool" is most prominent in July–August. Most of the high-altitude clouds observed over the "pool" region might be cirrus clouds generated by westward spreading of outflows from the deep convective systems situated at the eastern BoB by the strong upper tropospheric easterly winds, which is a characteristic feature of ASM (e.g., Sathiyamoorthy et al., 2004).

Since the "pool" is characterized by weak occurrence or near-absence of low- and middle-level clouds, it might be manifested in precipitation as well. This is shown in Fig. 3, which depicts the long-term (1996–2009) seasonal mean precipitation rate (in mm day^{-1}) over the study area during

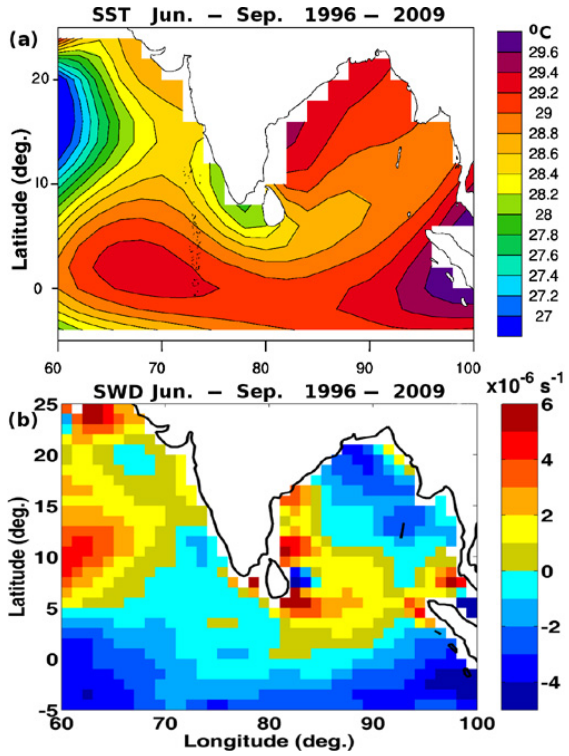

Fig. 4. Long-term (1996–2009) seasonal mean distribution of **(a)** SST and **(b)** surface wind divergence (s^{-1}) during ASM.

ASM, obtained from the GPCP data. Long-term seasonal mean winds at 1000 hpa level obtained from ECMWF-ERA are also shown in this figure. Precipitation rate over the "pool" region is substantially less (seasonal mean precipitation rate of $<3\,mm\,day^{-1}$) compared to the surrounding regions of deep convection, especially over the east Arabian Sea and north Bay of Bengal where the precipitation rates are in the range of 8–14 mm day^{-1}. The precipitation rates over the east and central equatorial Indian Ocean are also quite large ($>6\,mm\,day^{-1}$). As inferred from the vector winds at 1000 hpa level, the large-scale convection and precipitation at the Bay of Bengal and east Arabian Sea might have been caused by strong convergence of surface wind, aided by orographic lifting.

Role of SST on the genesis of the "pool" is examined using the long-term (1996–2009) seasonal mean spatial distribution of SST depicted in Fig. 4a. It shows a cold tongue originating off the southern tip of India (STI) and extending up to the south central BoB. This cold tongue (Joseph et al., 2005) arises from the ocean upwelling caused by the prevailing surface wind and its eastward spreading by the summer monsoon current into the BoB (Rao et al., 2006). However, the cold tongue has significantly large eastward extension than the "pool", while the latter extends farther to the north compared to the former. The locations of minima in SST and cloudiness are also different: F_c at the west coast of Sri Lanka is significantly larger than that at the east, though SST at the former region is ∼1 °C lesser than that at the latter. Furthermore, SST is ≥28.4 °C at most part of the "pool", which is sufficiently high for the development of convection and clouds (e.g., Gadgil et al., 1984). Figure 4b shows the long-term seasonal mean surface wind divergence observed using spaceborne scatterometers during ASM. In general, the surface wind is significantly diverging at the "pool" and converging outside this region. Over the "pool" region, this would produce a moisture divergence at the surface and subsidence from above, which would inhibit the cloud formation. Closure of the above surface wind field suggests the existence of a regional scale atmospheric circulation cell with subsidence at the "pool" and convection at its surroundings. This inference is well supported by the horizontal and vertical distribution of clouds depicted in Figs. 1 and 2. This mini-circulation might be the potential mechanism for the inhibition of cloudiness and precipitation at the "pool".

Evidence for such a mini-circulation is examined using ERA data. Figure 5 depicts the latitudinal and longitudinal cross sections of the altitude profiles of long-term seasonal mean vertical wind (in Pa s^{-1}), sliced through the centre of the "pool", which shows a strong subsidence below ∼700 hPa (∼3 km) at/near the "pool" region and convection at its surroundings. However, the spatial distribution of the subsidence and convection are not well matched with that inferred from Figs. 1–4: note that the cloud-free region extends up to ∼7 km and up to the east BoB, while the downdraft seen in Fig. 5 is significantly limited in altitude and its eastward extent. This shows that the actual structure and magnitude of the mini-circulation might have been underestimated by the reanalysis data.

The above mini-circulation cell, embedded in the synoptic-scale monsoon circulation and responsible for the genesis of the "pool", might be triggered by the considerable spatial gradient of latent heating (LH) in the troposphere over the geographically fixed zones of large-scale cloudiness and precipitation at the east and equatorial Indian Ocean, north and east BoB, southeast Arabian Sea and Indian land-mass, as a result of the modulation of summer monsoon circulation by SST, orography and land-sea contrast. The largest monthly mean values of LH over the above deep convective regions (though having considerable spatio-temporal variations) occur between 3–7 km altitude where it is typically in the range of 1.4 to 4.0 K day^{-1}, while the corresponding values of LH over the "pool" are negligible (Zuluaga et al., 2010). Whereas the synoptic-scale monsoon circulation provides the main closure mechanism for the updraft at the fixed zones of deep convection, this study shows that the mini-circulation described above also contributes significantly to the maintenance of large-scale convection at the

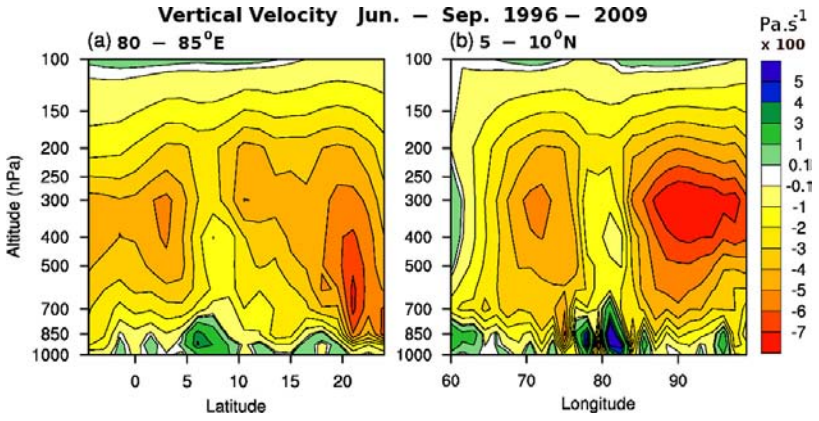

Fig. 5. **(a)** Long-term (1996–2009) seaonal mean latitude-altitude cross section of the pressure vertical velocity ($\mathrm{Pa\,s^{-1}} \times 100$) averaged along 80–85° E, obtained from ERA. **(b)** Same as **(a)** but for the longitude-altitude cross section averaged along 5–10° N. The vertical velocities are multiplied by 100 in the above figures for better visualisation.

above zones and hence would be an important component of the ASM. However, the strength of the "pool" and the mini-circulation might be modulated by the active and break spells of the monsoon (or vice versa), which is not investigated here. Notwithstanding the larger solar heating of the surface due to less cloudiness, the "pool" region is able to maintain low SST compared to the largely cloudy regions at its surroundings. This shows that, in addition to the contribution from the spreading of cold waters from STI (Rao et al., 2006), the cold SST at the "pool" might also be driven by the ocean upwelling caused by the surface wind divergence associated with the mini-circulation described above (Fig. 4b).

4 Conclusions

Using long-term satellite observations of clouds, this study clearly shows the persistence of a "pool of inhibited cloudiness" over the southwest Bay of Bengal throughout the Asian summer monsoon season. Frequency of occurrence of clouds in this "pool" is 20–40 % less than the surroundings. Seasonal mean precipitation rate over the "pool" is $<3\,\mathrm{mm\,day^{-1}}$ while that over the surrounding regions is mostly in the range of 6–14 $\mathrm{mm\,day^{-1}}$. Though this "pool" is observed in the regional distributions of clouds, precipitation, and OLR reported earlier, the contribution of low-, middle- and high-level clouds in its manifestation could not be deciphered unambigously. This information is essential for identifying the genesis of the "pool". This study, based on the vertical distribution of clouds observed using CloudSat, reveals that the "pool" is almost completely contributed by a drastic reduction or near-absence of clouds below $\sim$7 km that appear as a vault-like structure in the zonal and meridional cross section of the vertical distribution of clouds. In contrast, spatial gradient of high-altitude clouds over the entire region is negligible. The geographical location of this pool is remarkably consistent during the June–September period and occurs between 77–90° E in longitude and 3–13° N in latitude, which is surrounded by regions having large-scale convective clouds. This study shows that the physical mechanism for the genesis of the "pool" might, most likely, stem from the existence of a mini-circulation in the lower troposphere with significant divergence of surface wind at the "pool" and subsidence above, which is closed by the surface wind convergence and updraft in the troposphere over the surrounding deep convective regions. This mini-circulation is embedded in the large-scale monsoon circulation and might be a dynamical response of the atmosphere to the considerable spatial gradient of latent heating caused by the geographically fixed convective regions surrounding the "pool". The subsidence and surface wind divergence of air at the "pool" will be at least partly responsible for closure of the strong updraft at the surrounding deep convective regions and hence might be an important component of the ASM. Genesis and maintenance of the "pool" might be further influenced by orography of the region, the low-level jet and the relatively low SST at the south BoB. It is also likely that, at least part of the reduction in SST observed in the "pool" is contributed by the surface wind divergence. However, significant differences exist in the mini-circulation features derived from the reanalysis of atmospheric circulation and that inferred from the spaceborne observations of surface wind divergence and cloud distribution. The observed mini-circulation might play an important role in the monsoon dynamics as well as in the active-break spells of ASM, which needs to be explored further.

Acknowledgements. CloudSat 2BGeoProf data was obtained from http://cloudsat.cira.colostate.edu. AVHRR data was obtained from http://www.class.noaa.gov. ERA-40 data was provided by

ECMWF. NOAA OI-SST was obtained from NOAA-CIRES Climate Diagnostics Center, Boulder, Colorado. The ERS-1/2 and QuikSCAT scatterometer data were taken from CERSAT, at IFREMER, Plouzané (France). The GPCP combined precipitation data were developed and computed by the NASA/Goddard Space Flight Center’s Laboratory for Atmospheres as a contribution to the GEWEX Global Precipitation Climatology Project. A. K. M. Nair and S. Meenu are supported by ISRO through Research Fellowship and Research Associateship respectively.

Topical Editor P. Drobinski thanks one anonymous referee for her/his help in evaluating this paper.

References

Adler, R. F., Huffman, G. J., Chang, A., Ferraro, R., Xie, P. P., Janowiak, J., Rudolf, B., Schneider, U., Curtis, S., Bolvin, D., Gruber, A., Susskind, J., Arkin, P., and Nelkin, E.: The Version-2 Global Precipitation Climatology Project (GPCP) monthly precipitation analysis (1979–present), J. Hydrometeor., 4, 1147–1167, 2003.

Gadgil, S., Joseph, P. V., and Joshi, N. V.: Ocean-atmosphere coupling over monsoon regions, Nature, 312, 141–143, 1984.

Goswami, B. N., Krishnamurthy, V., and Annamali, H.: A broad-scale circulation index for the interannual variability of the Indian summer monsoon, Q. J. Roy. Meteorol. Soc., 125, 611–633, 1999.

Haynes, J. M. and Stephens, G. L.: Tropical oceanic cloudiness and the incidence of precipitation: Early results from CloudSat, Geophys. Res. Lett., 34, L09811, doi:10.1029/2007GL029335, 2007.

Joseph, P. V., Sooraj, K. P., Babu, C. A., and Sabin, T. P.: A cold pool in the Bay of Bengal and its interaction with the active-break cycle of the monsoon, CLIVAR Exchanges 34, Southampton, UK, 10 10–12, 2005.

Liu, W. T.: Progress in scatterometer application, J. Oceanogr., 58, 121–136, 2002.

Mace, G. G., Marchand, R., Zhang, Q., and Stephens, G.: Global hydrometeor occurrence as observed by CloudSat: Initial observations from summer 2006, Geophys. Res. Lett., 34, L09808, doi:10.1029/2006GL029017, 2007.

Meenu, S., Rajeev, K., Parameswaran, K., and Raju, C. S.: Characteristics of double ITCZ over the tropical Indian Ocean, J. Geophys. Res., 112, D11106, doi:10.1029/2006JD007950, 2007.

Meenu, S., Rajeev, K., Parameswaran, K., and Nair, A. K. M.: Regional distribution of deep clouds and cloud top altitudes over the Indian subcontinent and the surrounding oceans, J. Geophys. Res., 115, D05205, doi:10.1029/2009JD011802, 2010.

Rajeevan, M. and Srinivasan, J.: Net cloud radiative forcing at the top of the atmosphere in the Asian monsoon region, J. Climate, 13, 650–657, 2000.

Rao, R. R, Kumar, M. S. G., Ravichandran, M., Samala, B. K., and Anitha, G.: Observed intra-seasonal variability of mini-cold pool off the southern tip of India and its intrusion into the south central Bay of Bengal during summer monsoon season, Geophys. Res. Lett., 33, L15606, doi:10.1029/2006GL026086, 2006.

Roca, R., Louvet, S., Picon, L., and Desbois, M.: A study of convective systems, water vapor and top of the atmosphere cloud radiative forcing over the Indian Ocean using INSAT-1B and ERBE data, Meteorol. Atmos. Phys., 90, 49–65, doi:10.1007/s00703-004-0098-3, 2005.

Sathiyamoorthy, V., Pal, P. K., and Joshi, P. C.: Influence of the upper-tropospheric wind shear upon cloud radiative forcing in the Asian monsoon region, J. Climate, 17, 2725–2735, 2004.

Sunilkumar, S. V., Parameswaran, K., Rajeev, K., Krishna Murthy, B. V., Meenu, S., Mehta, Sk. K., and Babu, A.: Semitransparent cirrus clouds in the Tropical Tropopause Layer during two contrasting seasons, J. Atmos. Solar Terr. Phys. 72, 745–762, doi:10.1016/j.jastp.2010.03.020, 2010.

Zuluaga, M. D., Hoyos, C. D., and Webster, P. J.: Spatial and temporal distribution of latent heating in the south Asian monsoon region, J. Climate, 23, 2010–2029, doi:10.1175/2009JCLI3026.1, 2010.

Journal of Atmospheric and Solar-Terrestrial Physics 72 (2010) 1251–1259

Contents lists available at ScienceDirect

Journal of Atmospheric and Solar-Terrestrial Physics

journal homepage: www.elsevier.com/locate/jastp

Micro pulse lidar observations of mineral dust layer in the lower troposphere over the southwest coast of Peninsular India during the Asian summer monsoon season

Manoj Kumar Mishra, K. Rajeev*, Bijoy V. Thampi, K. Parameswaran, Anish Kumar M. Nair

Space Physics Laboratory, Vikram Sarabhai Space Centre, Thiruvananthapuram 695022, India

ARTICLE INFO

Article history:
Received 12 April 2010
Received in revised form
14 August 2010
Accepted 16 August 2010
Available online 22 August 2010

Keywords:
Aerosol transport
Mineral dust
Lidar
Asian summer monsoon
Indian region

ABSTRACT

A large aerosol plume with optical depth exceeding 0.7 engulfs most parts of the Arabian Sea during the Asian summer monsoon season. Based on Micro Pulse Lidar observations during the June–September period of 2008 and 2009, the present study depicts, for the first time, the existence of an elevated dust layer occurring very frequently in the altitude band of 1–3.5 km over the west coast of peninsular India with relatively large values of linear depolarization ratio (δ_L). Large values of δ_L indicate the dominance of significantly non-spherical aerosols. The aerosol optical depth of this layer (0.2) is comparable to that of the entire atmospheric column during dust-free days. Back-trajectory analysis clearly shows the advection of airmass from the arid regions of Arabia and the west Arabian Sea, through the altitude region centered around 3 km. This is in contrast to the airmass below 1 km originating from the pristine Indian Ocean region which contains relatively spherical aerosols of marine origin with δ_L generally <0.05.

1. Introduction

Atmospheric aerosols play a significant role in the radiation budget and climate of the earth-atmosphere system (Forster et al., 2007). During the Asian summer monsoon season (June–September), the strong westerly winds (5–20 m/s) in the lower and middle troposphere causes significant long-range transport of Arabian dust over to the north Arabian Sea while the large sea surface winds produce considerable amounts of sea salt aerosols. Aerosols from these two sources lead to the manifestation of an intense aerosol plume over the entire north Arabian Sea with visible band aerosol optical depth (AOD) often exceeding 0.7 (Zhu et al., 2007; Remer et al., 2008). However, southerly wind in the lower troposphere over the south Arabian Sea brings dust-free airmass from the pristine Indian Ocean into these regions leading to a strong latitude gradient in AOD around ~8–10°N (Nair et al., 2005). Strong precipitation over the eastern Arabian Sea, which implies wet-removal of aerosols, further increases the spatial gradient in AOD over this region.

Regional distribution of aerosols over the Arabian Sea during the Asian summer monsoon season has been extensively studied using satellite observations (e.g., Husar et al., 2001; Li and Ramanathan, 2002; Rajeev et al., 2004; Nair et al., 2005; Zhu et al., 2007; Remer et al., 2008); these studies show the predominance of dust aerosol plume over the Arabian Sea during this season, with peak values of AOD occurring in July. Dominance of the dust plume in this region is also evident from the ground based observations of spectral AOD at Minicoy (8.5N° and 73°E), an island location in the equatorial Indian Ocean (Moorthy and Satheesh, 2000). This aerosol plume is dominated by coarse mode particles (Remer et al., 2008) and the estimated contribution of non-sea salt aerosols is at least three times larger than sea salt aerosols produced by the prevailing high wind speed over these oceanic regions (Parameswaran et al., 2007).

The amount of dust over to the east Arabian Sea region could be significantly reduced by the large-scale precipitation prevailing in this season. However, the observational data on aerosol optical depth over the east Arabian Sea is rather limited mainly because of the large frequency of occurrence of clouds over this region (Nair et al., 2005; Meenu et al., 2010). The regional mean aerosol radiative forcing at the surface during June–August period over the Arabian Sea is estimated to be about -17.8 W/m^2 and the corresponding value of the aerosol radiative heating of the atmosphere is approximately 10.8 W/m^2 (Zhu et al., 2007). Altitude distribution of aerosols using CALIOP (Cloud-Aerosol Lidar with Orthogonal Polarization) onboard the Cloud-Aerosol Lidar and Infrared Pathfinder Satellite Observation (CALIPSO) showed the presence of dust layers over the Arabian region extending up to ~5 km in altitude, during the June–August period. The frequency of occurrence of such dust events are reported to be >78% (Liu et al., 2008). Altitude distribution of aerosols over Maldives (4.1°N and 73.3°E) observed using a ground based Lidar also showed the presence of an elevated aerosol layer (Muller et al., 2001). Except for

* Corresponding author. Tel.: +91 471 2563886.
E-mail address: k_rajeev@vssc.gov.in (K. Rajeev).

1364-6826/$ - see front matter © 2010 Elsevier Ltd. All rights reserved.
doi:10.1016/j.jastp.2010.08.012

these, observations of the altitude distribution of aerosols over the Arabian Sea and over the west coast of peninsular India during the Asian summer monsoon season are sparse. Such observations are essential for determining the pathways of aerosol transport, radiative heating of the atmosphere, and the potential role of aerosols in modulating cloud properties. Unlike satellite or ground based sun-photometer observations, ground based Lidars have the potential to provide altitude profile of aerosols even in the presence of dense high altitude clouds, a scenario often observed over the east Arabian Sea region. In this paper, the altitude distribution of aerosols during the Asian summer monsoon season (June–September) of 2008 and 2009 are investigated using the Micro Pulse Lidar at Trivandrum (8.5°N and 77°E), a station located in the Arabian Sea coast of south peninsular India. Lidar observations of the linear depolarization ratio are used to characterize the dust layers. The role of long range transport and percentage contribution of the dust layer to the columnar AOD is also investigated.

2. Data and method of analysis

Altitude profiles of aerosol backscatter coefficient (β_a) and linear depolarization ratio (δ_L) obtained using the Micro Pulse Lidar (Model: MPL-4B-532/POL-SW of Sigma Space Corporation, USA) during June–September period of 2008 and 2009 are used for the present study. This Lidar employs a frequency doubled diode pumped solid state Nd:YAG laser delivering optical pulses at 532 nm wavelength at a rate of 2.5 kHz and pulse width of 7 ns. The maximum pulse energy is 8 μJ. A Maksutov–Cassegrain type telescope (diameter of 178 mm) is used for transmitting the laser beam and receiving the backscattered signal. Two identical interference filters (each having a bandwidth of 0.14 nm and out-of-band rejection of 10^5) are used in cascade to limit the background. This makes the MPL suitable for daytime operation also. The detector is a Silicon Avalanche Photodiode (Si-APD) operated in photon counting mode.

In MPL, the polarization sensitive detection of backscattered light is achieved by activating a liquid crystal retarder (LCR) such that it alternately transmits linearly (when no retarding potential is applied) and circularly (when a quarter-wave retarding potential is applied) polarized light. The backscattered radiation is received in both cases through a polarizing beam splitter, which directs the co-polarized and depolarized signals (in the two cases, respectively) to the detector. The details of the polarization sensitive Lidar measurements and determination of the linear depolarization ratio are given by Flynn et al. (2007). Using the co-polarized and depolarized lidar signals, the depolarization ratio, δ_{MPL}, and hence the linear depolarization ratio (δ_L) are estimated (Flynn et al., 2007) as

$$\delta_{MPL} = \frac{|P(0)|}{|P(\pi/2)|} \tag{1}$$

and

$$\delta_L = \frac{\delta_{MPL}}{\delta_{MPL}+1} \tag{2}$$

where $P(0)$ is the received power when the LCR is operated with zero retardation and $P(\pi/2)$ that when the LCR is operated with a quarter wave retardation. The value of δ_L is an indicator of the extent of non-sphericity associated with the scatterers (Sakai et al., 2000). The larger the value of δ_L, the higher is the non-sphericity of aerosols. The value of δ_L is used as a potential tool for differentiating different aerosol types (Rajeev et al., 2010).

The lidar system alternates between the two states of polarization at an interval of 1 min. The co-polarized and depolarized lidar backscattered signals are collected alternately with a range resolution of 30 m and time integration for 1 min. The total lidar backscattered signal power (Flynn et al., 2007) is estimated as

$$P = 2P(0)+P(\pi/2) \tag{3}$$

The range-dependent lidar geometrical correction factor $g(r)$ ('r' being the range) is obtained by operating the lidar horizontally from an elevated location, following the method described by Welton et al. (2002) assuming a horizontally stratified atmosphere. The dead-time correction of the APD detector is carried out based on the calibration curve provided by the manufacturer. For each profile, the average photon count observed between the altitudes of 50 and 60 km is considered as the background, which is subtracted from the measured signal to estimate the true backscattered signal. Extreme care is taken to avoid cloud-contamination. The Lidar data when clear sky condition prevails at least up to an altitude of 6 km, for a minimum period of 30 min continuously, only are used to derive the altitude profile of β_a by inverting the lidar backscattered signal using Fernald's algorithm (Fernald, 1984), assuming an aerosol extinction-to-backscatter ratio (S) of 30 Steradian (Sr). The molecular backscattering and extinction coefficients are derived from the monthly mean standard atmospheric model of pressure (P) and temperature (T) for Trivandrum.

For inverting the lidar data, the reference altitude Z_R is assumed to be 20 km (up to which signal-to-noise ratio is fairly good during night), where the aerosol backscatter coefficient is assumed to be zero. However, during the daytime (as the signal-to-noise ratio is good only up to 6–10 km) or when optically thick high altitude clouds are present above 6 km, the reference altitude also is correspondingly reduced. The aerosol backscatter at this reference level is taken from the closest nighttime inverted altitude profile of β_a, for which good signal-to-noise ratio is achievable up to 20 km.

Sensitivity analysis (for the variations in the assumed value of S, and the boundary condition of β_a at Z_R) is carried out to ascertain the accuracy of the lidar-derived β_a, which shows that the uncertainty associated with the estimated value of β_a is approximately 30%. Utilization of the same telescope and detector system for the measurement of co- and cross-polarized signal reduces the uncertainty in δ_L, which is typically about 40%. However, above $\sim$5 km, the strength of the cross-polarized lidar signal due to scattering by aerosols is very weak, and the uncertainty in δ_L will be $>$50%. The columnar aerosol optical depth (τ) is measured during cloud-free conditions using a sun-photometer (Microtops-II, Solar Light Co.) which provides AOD at 5 wavelengths: 440, 500, 675, 936, and 1020 nm. In order to minimize the uncertainty in the lidar inverted profile, the aerosol backscatter and extinction profiles derived from MPL data are weighted by the AOD obtained using the sun-photometer on the same day. Regional distribution of AOD (τ at 550 nm) over the Arabian Sea is extracted from the data obtained from MODIS (Moderate Resolution Imaging Spectroradiometer: MOD08_D3.005 product) onboard the Aqua satellite. The standard error associated with this AOD is $0.03 \pm 0.05\tau$ over the ocean.

3. Results and discussion

3.1. Altitude structure of β_a and δ_L

Fig. 1 shows the altitude–time cross section of the attenuated lidar backscatter signal ($P_N = z^2P(z)$, where z is the altitude and $P(z)$ is the backscattered power from z) in the co-polarized channel along with δ_L obtained from MPL data during 11–12 June and 02–03 September 2008 as two typical examples. For a comparison of aerosol loading over the Arabian Sea on these days,

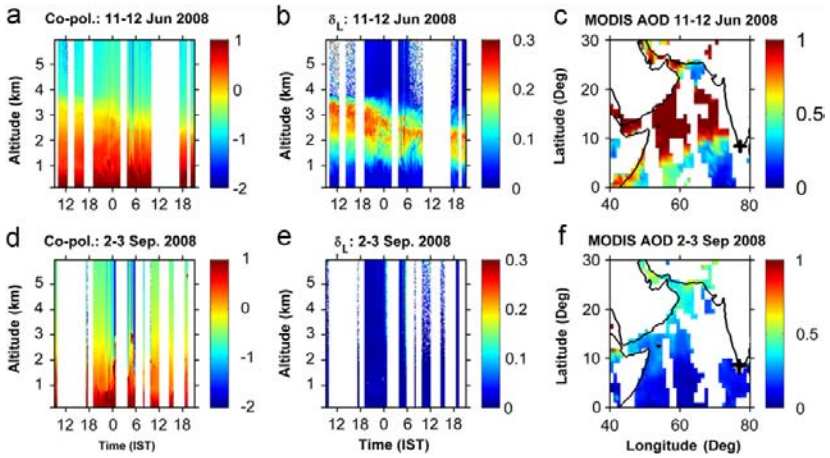

Fig. 1. Time–altitude variations of (a) range-compensated attenuated lidar backscatter signal (P_N, co-polarized component) and (b) linear depolarization ratio (δ_L) during 11–12 June 2008, (c) Spatial distribution of average AOD during 11–12 June 2008 derived from MODIS data. (d, e, f) are same as (a, b, c), respectively that for 02–03 September 2008. The location of Trivandrum is indicated by a '+' sign in (c) and (f).

the regional distribution of AOD (at 550 nm) obtained from MODIS at 13:30 local time (averaged for the respective two consecutive days) is also shown in this figure. During the night of 11 June 2008 (Fig.1a) the attenuated backscatter signal is maximum near the surface and decreases with increase in altitude. A relatively large decrease in the values of P_N above 3 km is worth noting. The corresponding time–altitude variation of δ_L (Fig. 1b) shows a prominent aerosol layer with significantly large value of δ_L (in the range 0.1–0.25) between 1 and 3.5 km, while its value below 1 km is considerably small (<0.05). This clearly indicates that the layer at 1–3.5 km is dominated by highly non-spherical aerosols, while those below 1 km are relatively more spherical. Remarkably, the upper boundary of the elevated layer (observed in P_N and δ_L) descends from 3.5 km to less than 3 km during the course of this night. The spatial distribution of AOD in Fig.1c shows high values over the Arabian Sea, extending from the northwest Arabian Sea up to the west coast of peninsular India with a pronounced latitude gradient across $\sim 8^{\circ}$N.

In contrast, the time–altitude cross-sections of P_N and δ_L during 2–3 September 2008 (Fig. 1d and e) do not show any prominent elevated layer. The values of δ_L are generally <0.03 showing the dominance of nearly spherical aerosols throughout the altitude. The regional distribution of AOD during 2–3 September (Fig. 1f) shows substantially low values of AOD over the east Arabian Sea compared to that during 11–12 June 2008. The high values of AOD and the dust plume during these days are rather confined to the west Arabian Sea. This is in agreement with the MPL observations (Fig. 1d and e) showing the absence of any dust layer over Trivandrum during this day.

Isolated low level clouds are observed on 2–3 September 2008 as seen in Fig. 1d, manifested by the intermittent spikes below the altitude of ~ 3 km, which are followed by large reduction in the value of P_N above the altitude of their occurrence. The absence of Lidar signal above the clouds is because of their large optical depth. The values of δ_L at the altitude of cloud occurrence (in the lower troposphere) are generally small (<0.01). Similar observations of small value of δ_L associated with low-level clouds are found throughout the year (not shown in figure). This clearly shows that particles associated with these clouds are mostly small water droplets which are fairly homogeneous and spherical in nature and the enhancement in δ_L observed around 3 km is not caused by the presence of such

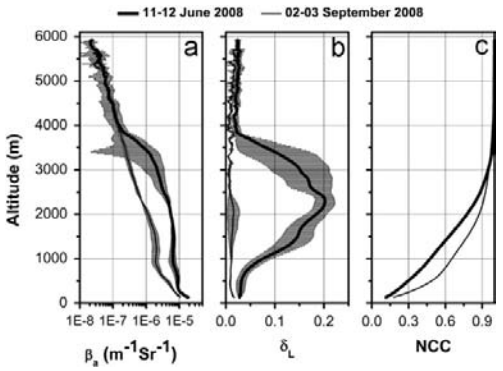

Fig. 2. Mean profile of (a) aerosol backscatter coefficient (β_a, shown in log-scale), (b) linear depolarization ratio (δ_L), and (c) normalized columnar contribution to AOD for the cases shown in Fig. 1.

low-level clouds. As explained earlier, the cloudy data are eliminated from the subsequent analysis to derive altitude profiles of β_a and δ_L.

Mean altitude profiles of β_a and δ_L during 11–12 June and 2–3 September 2008 are shown in Fig. 2. The altitude gradient of β_a during 11–12 June is considerably small up to ~ 3 km, followed by a rapid decrease above. The altitude profile of δ_L also shows a distinct layer between 1 and 3.3 km, with mean value of δ_L in the range 0.1–0.2. In contrast, the altitude profile of β_a on 2–3 September shows a steady decrease with increase in altitude right from the surface, even though the rate of decrease varies with altitude. Note that the values of δ_L for the entire altitude region are less than 0.02 during these days. The mean value of β_a between 700 m and 3 km on 02–03 September is smaller than that on 11–12 June by a factor of 2, while the values of β_a above ~ 4 km are comparable.

The normalized cumulative contribution of aerosols (NCC) at different altitudes to the total atmospheric aerosol loading is estimated by integrating β_a from the surface up to a particular altitude, z, and normalizing it with the column integrated aerosol backscatter coefficient. This parameter provides a quantitative assessment of the percentage contribution of aerosols from

different altitudes to the total columnar aerosol loading and AOD. The altitude variations of NCC during the above periods are presented in Fig. 2c. While the mean AOD during 11–12 June is 0.38, the layer integrated AOD of the dust layer on this day between 1 and 3.5 km is 0.21. This figure also shows that, while the contribution of aerosols in the altitude region above 1 km to the AOD is ~55% on 11–12 June, the corresponding value is only 38% during 2–3 September.

3.2. Month-to-month variation in the mean altitude structure of β_a, δ_L, and NCC: influence of dust layer

It is observed that the dust layer persists for long time (even for few days) when the value of δ_L is very high (typically >0.12), while it is intermittent when δ_L is relatively less. The values of δ_L are <0.05 when the dust layer is not discernible in the time–altitude cross sections of δ_L. Based on the altitude profiles of δ_L, the lidar data are grouped into three different categories: (1) days with no dust layer ($\delta_L<0.05$ throughout the profile or $\delta_L \geq 0.05$ for an altitude extent of <0.5 km), (2) days with weak/moderate dust layer ($0.05 \leq \delta_L < 0.12$ for an altitude extent of ≥ 0.5 km), and (3) days with prominent dust layer ($\delta_L \geq 0.12$ for an altitude extent of ≥ 0.5 km). However, this classification is rather arbitrary. Histograms of the frequency of occurrence of different values of δ_L in the altitude range 1–3.5 km (the typical altitude of occurrence of the dust layer) under different conditions are shown in Fig.3. The general characteristics of the histograms are similar during 2008 and 2009. Whenever the dust layer is strong, the values of δ_L in the above altitude band vary over a wide range 0.01–0.24 with a broad peak in the range 0.08–0.15. The frequency distribution of δ_L during the occurrence of weak layers is narrower and less skewed compared to that during the occurrence of strong layers, and is centered around 0.06. The value of δ_L never exceeds 0.05 when the dust layer is absent (note that, based on the criteria for classification of dust layers, the values of $\delta_L \geq 0.05$ which is limited to an altitude extent of <0.5 km are classified as profiles with no dust layer). Fig. 3 substantiates the arbitrary criteria followed in the classification of the dust layers.

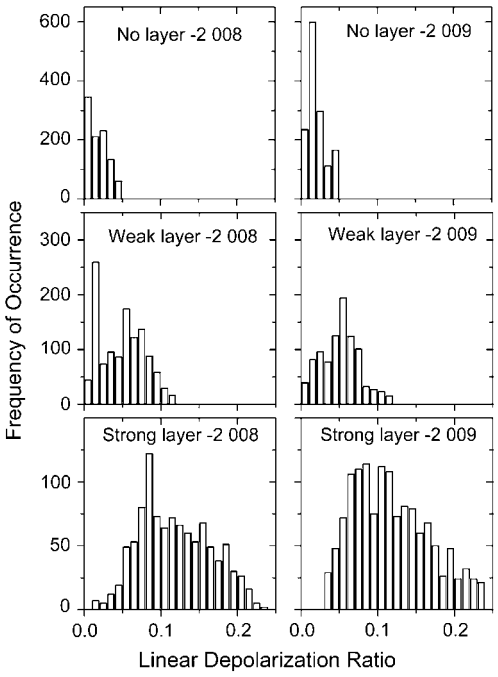

Fig. 3. Histograms of the frequency of occurrence of different values of δ_L in the altitude range 1–3.5 km under different types of dust layer.

Table 1 shows the frequency of occurrence of profiles in each of the above categories for June–September in years 2008 and 2009, obtained by dividing the number of daily mean profiles in each category with the total number for the respective month. Note that altitude profiles of β_a are obtained only for cloud-free conditions. Large frequency of occurrence of low and middle level clouds and precipitation over the site during the Asian summer monsoon season significantly limits the total number of days of useful observations. (Usual date of onset of the summer monsoon over Trivandrum is 1 June.) Table 1 shows that the frequency of occurrence of dust layers is maximum during July (when moderate or strong dust layers occurred on all the days of observation during 2008 and 2009), which is followed by August (when the moderate or strong dust layers occurred during 70% and 64% of the days in 2008 and 2009). The frequency of occurrence of dust layer is minimum in June and September with a large variability from 2008 to 2009. Earlier satellite observations showed that, in general, the mineral dust plume over the Arabian Sea maximizes during June–July period (e.g., Nair et al., 2005). However, the large frequency of occurrence of clouds over the east Arabian Sea significantly impedes the number of cloud-free pixels observed by the satellites from which the AOD can be retrieved (e.g., Meenu et al., 2010). Notwithstanding this, the largest values of MODIS-derived AOD (as shown latter in Fig. 8) over the southeastern Arabian Sea (near the coast of Trivandrum) during the present study period occur in June–July 2008 and July 2009. In contrast, the AOD values over the Arabian Sea as a whole and southeast Arabian Sea in particular are very small in June 2009. This is in agreement with the MPL observations of the frequency of occurrence of the dust layer, which shows that the dust layer is absent in June 2009 while strong dust layers are present in June 2008.

Table 1
Frequency of occurrence of weak/moderate and strong dust layers and dust-free days during June–September period of 2008 and 2009.

Months	Number of days when β_a, δ_{MPL} could be estimated	Frequency of occurrence of strong elevated aerosol layer (%)	Frequency of occurrence of weak/moderate aerosol layer (%)	Frequency of occurrence of dust-free days (%)
June 2008	9	45	22	33
July 2008	3	100	0	0
August 2008	10	50	20	30
September 2008	15	0	60	40
June 2009	12	0	16	84
July 2009	16	50	50	0
August 2009	14	57	7	36
September 2009	6	0	17	83

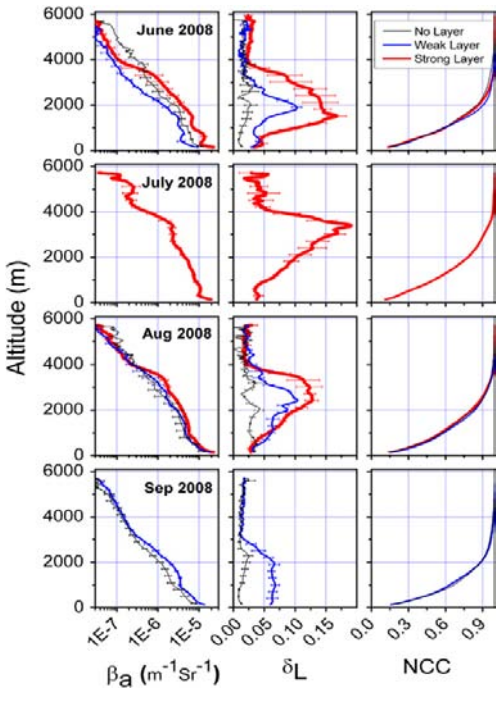

Fig. 4. Monthly mean altitude profiles of aerosol backscatter coefficient (β_a, shown in the left panel), linear depolarization ratio (δ_L, shown in the middle panel) and normalized columnar contribution to AOD (NCC, shown in the right panel) during June–September of 2008.

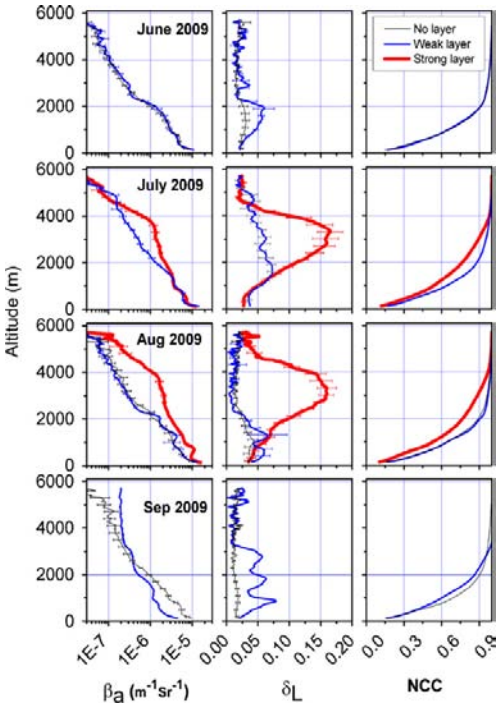

Fig. 5. Same as Fig. 3 but for 2009.

Altitude profiles of mean β_a, δ_L, and NCC for the above three classes in June–September are presented in Figs. 4 and 5, respectively, for years 2008 and 2009. It is interesting to note that the mean values of β_a are significantly large in the altitude region of 1–3.5 km when the dust layer is strong. Rapid decrease in β_a above ~3.5 km is particularly notable during days in which the dust layer is strong. The average value of β_a in the altitude region of 1–3.5 km is maximum during July and August. In the altitude band of 0–3.5 km, the mean aerosol scale height (altitude extent over which β_a decreases to e^{-1} of its value at the base altitude) is 1.4 ± 0.1 km during the strong-dust days while its value is ~1 km during the other days.

The mean value of δ_L in the altitude region of 1–3.5 km during the occurrence of a weak/moderate or strong dust layer is found to be significantly larger than that during the dust-free days. The peak value of δ_L often exceeds 0.15 during strong dust days. In all the three classes, the value of δ_L is generally less than 0.05 below ~1 km and above ~4 km. This, together with the rapid decrease of β_a above 3.5 km clearly shows that the dust layer is fairly confined to an altitude region of 1–3.5 km. High value of β_a and low value of δ_L below 1 km suggests significant contribution of nearly spherical aerosols in this region. The hygroscopic growth of sea salt aerosols (with RH > 90% below 1 km) leads to the formation of nearly spherical aerosols, for which the value of δ_L is relatively small. Note that, strong wet-removal of aerosols prevailing during this period leads to a rapid decrease in aerosol concentration (including dust) within the atmospheric boundary layer (ABL). This process also might significantly contribute to the observed decrease in β_a in this region (< ~1 km).

Altitude variation of NCC shows that the elevated aerosol layer contributes more than 50% of the AOD during the strong dust days. The mean AOD on such days is significantly larger than that during the other days. Weighting the altitude profiles of NCC with the value of AOD on that day provide the mean layer integrated optical depth of the dust layer between 1 and 3.5 km, which is 0.2. Note that, this value is comparable to the total column integrated AOD on the non-dusty days during this period. This shows the importance of the elevated dust layer in modulating the AOD during the Asian summer monsoon season. Altitude profile of NCC shows that the contribution of aerosols above 1 km to AOD is rather small during September (~35%) compared to the June–August period.

3.3. Sources of aerosols at different altitudes

As seen from the above analysis, the optical properties of aerosols in the elevated layer can be different from those below. In order to identify the sources of these particles, we have examined the 7-day air back-trajectories at different altitudes in the lower troposphere ending at this location for all the days during the study period using the NOAA ARL HYSPLIT model obtained through their website (http://www.arl.noaa.gov/ready).

The air trajectories ending at 1 km over Trivandrum on different days in June–September during 2008 and 2009 are presented in Fig. 6 and those ending at 3 km in Fig. 7. In all these months, most of the air trajectories ending at 1 km above the surface originate from the Indian Ocean and the South Arabian Sea and take a curve near the Horn of Africa (the Somali jet region) to reach Trivandrum. None of them originate from the northern side. However, in August and September, these trajectories mostly traverse the central Arabian Sea. It is quite interesting to note that significant number of trajectories ending at 3 km originate from Arabian landmass and traverse the west Arabian Sea to reach Trivandrum. During this period the Arabian

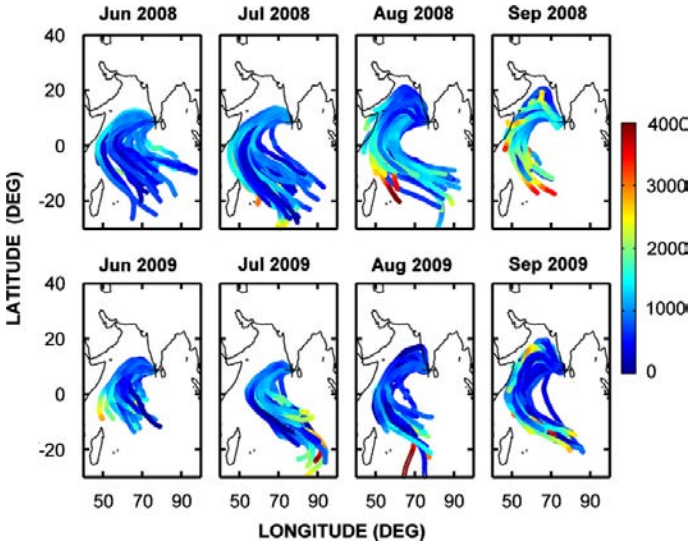

Fig. 6. Air back-trajectories ending at 1 km over Trivandrum on all the days of the month during June–September 2008 and 2009.

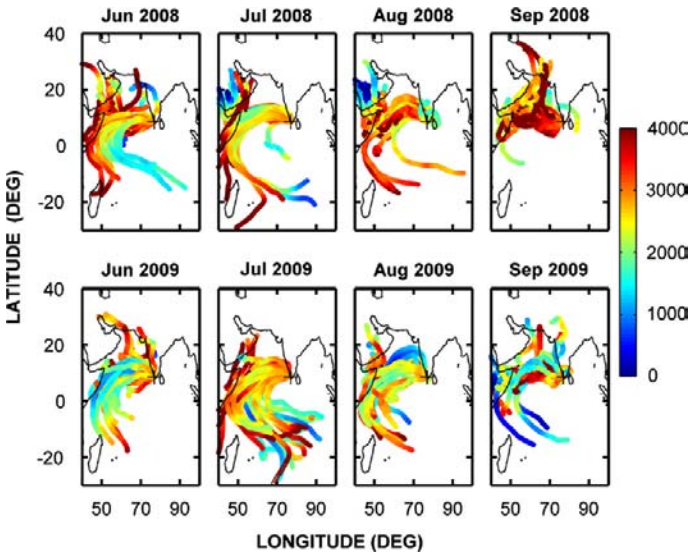

Fig. 7. Same as Fig. 5, but for the air back-trajectories ending at 3 km over Trivandrum.

landmass is heated to its maximum (boreal summer) and is also a location of strong surface winds. Dust storm is very common over Arabia during this period. Increase in convective activity is also favourable for the uplift of mineral dust originating from the arid surface. On examining the air trajectories ending at 3 km (almost middle of the observed dust layer over Trivandrum) it can be seen that in July, August and September significant fraction of the trajectories have passed through the north of 10°N including the western parts of Arabian Sea, the Horn of Africa or the Arabian region. The back-trajectories between 2 and 4 km (not shown here) are almost similar to that at 3 km. The back-trajectories ending at <1 km (not shown here) are similar to those at 1 km (Fig. 6) but shows larger contribution of airmass from the south Arabian Sea and Indian Ocean. This clearly shows that the airmass below 1 km is distinctly different and originates from the pristine Indian Ocean region, while the airmass above contains significant contribution from the west Arabian Sea or Arabia. Pronounced increase in δ_L around 1–3.5 km and the significant decrease in the value of δ_L (0.02–0.05) below 1 km are in agreement with the proposed transport derived from airmass trajectories. Although the trajectories ending at 1 km traverse the central Arabian Sea during August and September, the AOD over this region is lower compared to that in July (as shown in Fig. 8).

The Potential of long-range transport in bringing mineral dust over Trivandrum is further examined using the regional distribution of AOD (at 550 nm) observed by MODIS (Remer et al., 2008) during June–September period of 2008 and 2009. The spatial distribution of AOD thus obtained over the Arabian Sea region is

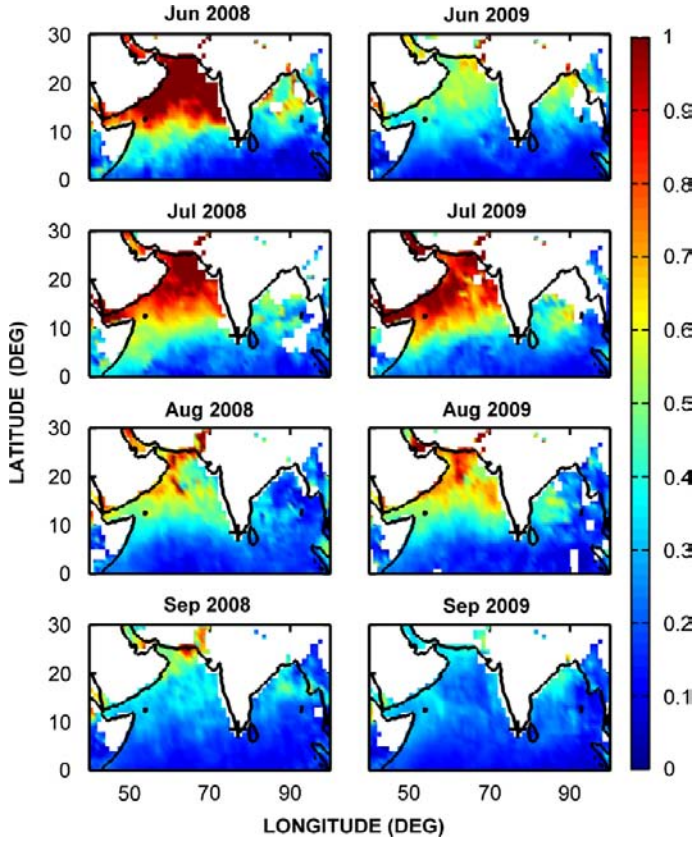

Fig. 8. Monthly mean regional distribution of AOD over the Arabian Sea region during June–September months of 2008 and 2009. The location of Trivandrum is indicated by a '+' sign.

depicted in Fig. 8. High values of AOD over the Arabian Sea, with its peak in the northwestern parts, can be seen in all these months. This peak value and the southward extension of the region of high AOD increases from June to July and subsequently decreases. In September, the region of high AOD shrinks significantly to remain fairly confined to the northwestern parts. Trivandrum is located in the southern boundary of the region of this enhanced AOD. Daily maps of AOD (e.g., Fig. 1) clearly depict the spatial extent the dust plume, which often engulf a large region up to Trivandrum. However, the strong influx of airmass from the Tropical Indian Ocean over the Arabian Sea limits the southward extension of the dust plume to a great extent which leads to a large latitude gradient around 10°N. Note that, the air back-trajectories around 2–3 km (Fig. 7) are mostly oriented along 8–12°N, which indicate that the southward advection of the dust plume might be rather weak. The frequency of occurrence of dust layers over Trivandrum is maximum in July (Table 1), when the southern boundary of the dust plume often reaches up to ~8°N (Fig. 8). Fig. 6 also shows that the back-trajectories ending at 1 km over Trivandrum during August and September mostly traverse the central and northeast Arabian Sea, where the value of AOD is relatively small in August compared to July. Hence, the airmass from the central and northeast Arabian Sea during August may be less efficient in transporting dust over to Trivandrum. This is further confirmed by the low values of δ_L observed in the ABL (Figs. 4 and 5).

As can be seen from Fig. 7, the number of air trajectories originating from Arabia and ending at 3 km over Trivandrum is significantly less in June and July 2009 compared to that in year 2008. The relatively lower values of δ_L during June and July 2009 indicate that the elevated dust layer is weaker compared to that during the corresponding periods of 2008. It is also interesting in this context to note that the values of AOD over the east Arabian Sea during June–July 2009 are also less compared to that in 2008. These features lead to the inference that the observed difference in the altitude structure of aerosols (and the dust layers) in these two consecutive years is mainly due to corresponding changes in synoptic circulation. The absence of strong dust days over Trivandrum in June 2009 also is consistent with the observed weak southward extension of the region of high AOD over the Arabian Sea.

Though the long-term satellite observations have revealed the transport of dust over the Arabian Sea during the Asian summer monsoon season (e.g., Remer et al., 2008; Nair et al., 2005), these inferences were based on a limited amount of data in each year as the occurrence of clouds are very frequent over the eastern Arabian Sea (Nair et al., 2005; Meenu et al., 2010) during this period. Strong sea surface winds (often exceeding >10 m/s) during this season generate abundant sea salt aerosols from the sea surface over the Arabian Sea, which also is added to the transported Arabian dust. A thin layer of widespread cirrus over the east Arabian Sea during this season (Rajeev et al., 2008) further complicates the discrimination of dust from satellite or in situ measured AOD. Note that both the dust and the sea spray aerosols are relatively large in size and they cannot be discriminated based on AOD data alone. Observations using

CALIPSO, however, have revealed the significant depolarization property of aerosols over the Arabian Sea (Liu et al., 2008), which could mainly be attributed to the dust aerosols transported from Arabia, as the locally generated sea-salt aerosols tend to be nearly spherical with low values of δ_L. However, due to the low frequency of observation by CALIPSO (orbit repeatability of 16 days) and high frequency of occurrence of optically thick high-altitude clouds, the amount of aerosol data collected from CALIPSO over the Arabian Sea during the summer monsoon is considerably small. The present dual polarization lidar observations of aerosols over Trivandrum, during most of the days in which clear sky conditions prevailed at least up to 6 km, show that the transport of dust over the east Arabian Sea and west coast of India occur mostly during the July–August period through the altitude region of 1–3.5 km. This, however, is consistent with the satellite observations which show that the southern boundary of the dust plume reaches only up to $\sim 8^{\circ}$N during this period. Though the integrated extinction coefficient of the dust layer is relatively small (~ 0.2 even when the dust layer is strong) compared to the AOD observed at the northwestern parts of the Arabian Sea during July–August (mean AOD at 550 nm is ~ 0.8 over this region; see Fig. 8), it is comparable to the total AOD observed during the dust-free days over Trivandrum. Persistent transport of pristine airmass from the Tropical Indian Ocean (with column AOD < 0.15 observed during the dust-free days) significantly impedes large scale spreading of the dust plume over to the southern Arabian Sea and Indian Ocean.

4. Conclusion

Earlier studies based on satellite data revealed that the northern part of the Arabian Sea is significantly influenced by the large-scale transport of dust from the Arabian Desert during the Asian summer monsoon season (June–September). However, the high frequency of occurrence of dense clouds over the eastern parts of the Arabian Sea during this season had considerably reduced the frequency of observations of AOD using satellite and ground-based radiometers. A first-time observation on the altitude distribution of aerosol backscatter coefficient and linear depolarization ratio (an indicator of the non-sphericity of aerosols) over the west coast of Peninsular India (Trivandrum) during the Asian summer monsoon season (June–September) in the two consecutive years, 2008 and 2009, is carried out using a Micro Pulse Lidar. These observations are further supported by regional distribution of MODIS AOD and HYSPLIT air back-trajectory analyses. The lidar observations revealed the existence of an elevated layer of highly non-spherical aerosols in the altitude region of 1–3.5 km (just above the ABL), which is very common during the July–August period. The appearance of this layer starts in June, with the arrival of monsoon over the west coast of India, and subsequently intensifies with the advancement of monsoon further northwards. This layer, which is most prominent in July–August, starts weakening by September. The observed increase in δ_L within the elevated layer suggests that the particles constituting this layer are relatively non-spherical compared to those above and below. This elevated layer contributes $> 55\%$ of the column integrated backscatter coefficient and AOD during the strong dust days. The optical depth of this layer is ~ 0.20 which is similar to the total columnar AOD observed during dust-free days. Low values of δ_L below this layer (within ABL) indicate that the particles in this altitude region are nearly spherical in nature.

The day-to-day and monthly variations observed in the satellite derived AOD over the southeast Arabian Sea are in agreement with those of the altitude structure of lidar-derived aerosol backscatter coefficient at Trivandrum. Satellite observations of the regional distribution of AOD show a pronounced latitude gradient across 8–12°N, which encompasses the present observation site. This leads to large day-to-day variability in the strength of the dust layer at this location, depending strongly on the prevailing lower-tropospheric circulation. The back trajectory analysis shows that, over Trivandrum, while the advection of airmass from the pristine Indian Ocean dominates below 1 km, the airmass around 3 km (the peak altitude of the dust layer) has a significant contribution from the dust-laden air from the Arabian landmass and the western Arabian Sea. These observations along with the values of δ_L at different altitudes unambiguously show that the elevated layer composed of highly non-spherical particles, formed as a consequence of a long-range transport of mineral dust from the arid regions of Arabia, while those below 1 km are mostly produced at the sea surface.

Acknowledgement

The authors gratefully acknowledge the NOAA Air Resources Laboratory (ARL) for the provision of the HYSPLIT transport and dispersion model and READY website (http://www.arl.noaa.gov/ready.html) used in this publication. The authors would like to acknowledge the MODIS Science Team for the Science Algorithms, the Processing Team for producing MODIS data, and the GES DAAC tools for accessing Aqua MODIS data. One of the authors, Dr. K. Parameswaran would like to acknowledge CSIR for providing grant through the Emeritus Scientist scheme.

References

Fernald, F.G., 1984. Analysis of atmospheric lidar observations: some comments. Applied Optics 23, 652–653.
Flynn, C.J., Mendoza, A., Zheng, Y., Mathur, S., 2007. Novel polarization-sensitive micropulse lidar measurement technique. Optics Express 15 (6), 2785–2790.
Forster, P., Ramaswamy, V., Artaxo, P., Berntsen, T., Betts, R., Fahey, D.W., Haywood, J., Lean, J., Lowe, D.C., Myhre, G., Nganga, J., Prinn, R., Raga, G., Schulz, M., Van Dorland, R., 2007. Changes in atmospheric constituents and in radiative forcing. In: Solomon, S., Qin, D., Manning, M., Chen, Z., Marquis, M., Averyt, K.B., Tignor, M., Miller, H.L. (Eds.), Climate Change 2007: The Physical Science Basis. Contribution of Working Group I to the Fourth Assessment Report of the Intergovernmental Panel on Climate Change. Cambridge University Press, Cambridge, United Kingdom; New York NY, USA.
Husar, R.B., et al., 2001. Asian dust events of April 1998. Journal of Geophysical Research 106 (D16), 18,317–18,330.
Li, F., Ramanathan, V., 2002. Winter to summer monsoon variation of aerosol optical depth over the tropical Indian Ocean. Journal of Geophysical Research 107 (D16), 4284. doi:10.1029/2001JD000949.
Liu, D., Wang, Z., Liu, Z., Winker, D., Trepte, C., 2008. A height resolved global view of dust aerosols from the first year CALIPSO lidar measurements. Journal of Geophysical Research 113, D16214. doi:10.1029/2007JD009776.
Meenu, S., Rajeev, K., Parameswaran, K., Nair, A.K.M., 2010. Regional distribution of deep clouds and cloud top altitudes over the Indian subcontinent and the surrounding oceans. Journal of Geophysical Research 115, D05205. doi:10.1029/2009JD011802.
Moorthy, K.K., Satheesh, S.K., 2000. Characteristics of aerosols over a remote island, Minicoy in the Arabian Sea: optical properties and retrieved size distributions. Quarterly Journal of the Royal Meteorological Society 126, 81–109.
Muller, D., Franke, K., Wagner, F., Althausen, D., Ansmann, A., Heintzenberg, J., 2001. Vertical profiling of optical and physical particle properties over the tropical Indian Ocean with six wavelength lidar 1, seasonal cycle. Journal of Geophysical Research 106, 28,567–28,575.
Nair, S.K., Parameswaran, K., Rajeev, K., 2005. Seven-years satellite observations of the mean structure and variabilities in the regional aerosol distribution over the oceanic areas around the Indian subcontinent. Annales Geophysicae 23, 2011–2030.
Parameswaran, K., Nair, S.K., Rajeev, K., 2007. Spatial distribution of sea-salt and non-sea-salt aerosol optical depths over the oceanic regions around the Indian subcontinent from space borne measurements. Journal of Marine Atmospheric Research 3, 64–82.
Rajeev, K., Nair, S.K., Parameswaran, K., Suresh Raju, C., 2004. Satellite observations of the regional aerosol distribution and transport over the Arabian Sea, Bay of Bengal, and Indian Ocean. Indian Journal of Marine Research 33, 11–29.
Rajeev, K., Parameswaran, K., Meenu, S., Sunilkumar, S.V., Thampi, B.V., Raju, C.S, Murthy, B.V.K., Jagannath, K.S., Mehta, S.K., Rao, D.N., Rao, K.G., 2008.

Observational assessment of the potential of satellite-based water vapor and thermal IR brightness temperatures in detecting semitransparent cirrus. Geophysical Research Letters 35, L08808. doi:10.1029/2008GL033393.

Rajeev, K., Parameswaran, K., Thampi, B.V., Mishra, M.K., Nair, A.K.M., Meenu, S., 2010. Altitude distribution of aerosols over Southeast Arabian Sea coast during pre-monsoon season: elevated layers, long-range transport and atmospheric radiative heating. Atmospheric Environment 44, 2597–2604. doi:10.1016/j.atmosenv.2010.04.014.

Remer, L.A., Kleidman, R.G., Levy, R.C., Kaufman, Y.J., Tanré, D., Mattoo, S., Martins, J.V., Ichoku, C., Koren, I., Yu, H., Holben, B.N., 2008. Global aerosol climatology from the MODIS satellite sensors. Journal of Geophysical Research 113, D14S07. doi:10.1029/2007JD009661.

Sakai, T., Shibata, T., Kwon, S.-A., Kim, Y.-S, Tamura, K., Iwasaka, Y., 2000. Free tropospheric aerosol backscatter, depolarization ratio, and relative humidity measured with the Raman lidar at Nagoya in 1994–1997: contributions of aerosols from the Asian Continent and the Pacific Ocean. Atmospheric Environment 34 (3), 431–442.

Welton, E.J., Voss, K.J., Quinn, P.K., Flatau, P.J., Markowicz, K., Campbell, J.R., Spinhirne, J.D., Gordon, H.R., Johnson, J.E., 2002. Measurements of aerosol vertical profiles and optical properties during INDOEX 1999 using micropulse lidars. Journal of Geophysical Research 107, 8019. doi:10.1029/2000JD000038.

Zhu, A., Ramanathan, V., Li, F., Kim, D., 2007. Dust plumes over the Pacific, Indian, and Atlantic oceans: climatology and radiative impact. Journal of Geophysical Research 112, D16208. doi:10.1029/2007JD008427.

Atmospheric Environment 44 (2010) 2597–2604

Contents lists available at ScienceDirect

Atmospheric Environment

journal homepage: www.elsevier.com/locate/atmosenv

Altitude distribution of aerosols over Southeast Arabian Sea coast during pre-monsoon season: Elevated layers, long-range transport and atmospheric radiative heating

K. Rajeev*, K. Parameswaran, Bijoy V. Thampi, Manoj Kumar Mishra, Anish Kumar M. Nair, S. Meenu

Space Physics Laboratory, Vikram Sarabhai Space Centre, Thiruvananthapuram 695 022, India

ARTICLE INFO

Article history:
Received 29 December 2009
Received in revised form
8 April 2010
Accepted 9 April 2010

Keywords:
Aerosols
Elevated aerosol layer
Depolarization ratio
Lidar
Aerosol radiative heating

ABSTRACT

Every year, during the pre-monsoon period (March–May), a pronounced increase in aerosol optical depth (AOD) is observed over the eastern Arabian Sea, which is attributed to the transport of continental aerosols. This paper presents the altitude distribution of tropospheric aerosols, characteristics of elevated aerosol layers and aerosol radiative heating of the atmosphere during the pre-monsoon season over Trivandrum (8.5°N, 77°E), a station located at the southwest coast of Indian peninsula which is covered by the eastern Arabian Sea plume. Altitude profiles of aerosol backscatter coefficient (β_a) and linear depolarization ratio (LDR) reveal two distinct aerosol layers persisting between 0–2 km and 2–4 km. The layer at 2–4 km, which contributes about 25% of the AOD during polluted conditions, contains significant amount of non-spherical aerosols. This layer is prominent only when the advection of dry airmass occurs from the northern parts of the Indian subcontinent and northern Arabian Sea. Role of long-range transport in the development of this aerosol layer is further confirmed using latitude–altitude cross-section of β_a observed by CALIPSO. Aerosol content in the layer below 2 km is large when advection of air occurs from the north and east Arabian Sea and is significantly small when it occurs from the southwest Arabian Sea or Indian Ocean. During the highly polluted conditions, aerosols tend to increase the diurnal mean atmospheric radiative heating rate by ~0.8 K day^{-1} at 500 m and 0.3 K day^{-1} at 3 km, which are about 80% and 30% of the respective radiative heating in the aerosol-free atmosphere.

1. Introduction

Atmospheric aerosols significantly influence the radiation budget of the earth-atmosphere system, cloud properties, hydrological cycle and earth's climate. During the northern-hemispheric winter (November–February) and pre-monsoon (March–May) seasons, oceanic regions around Indian subcontinent are significantly influenced by long-range transport of continental aerosols from Arabia, Indian subcontinent and Southeast Asia, producing considerable perturbations in the radiation budget of the earth-atmosphere system (Ramanathan et al., 2001; Rajeev and Ramanathan, 2001; Ramachandran and Jayaraman, 2002). Multi-year satellite observations show that transport of aerosols from the Asian continent over to the adjoining oceanic regions increases from winter to pre-monsoon season, leading to a well-defined aerosol plume over the eastern Arabian Sea that extend to more than 1000 km from the west coast of Indian Peninsula (Nair et al., 2005). Detailed investigations on the physical, chemical and radiative properties of aerosols over the Arabian Sea were conducted during the Indian Ocean Experiment (INDOEX) (Ramanathan et al., 2001) and the Integrated Campaign for Aerosols, gases and Radiation Budget (ICARB) (Moorthy et al., 2008), which revealed the presence of elevated aerosol layers and significant amount of black carbon in the atmosphere. Vertical profiles of aerosols over Maldives (4.1°N, 73.3°E), an Indian Ocean Island, revealed the presence of an aerosol layer in the altitude band of 1.5–3.5 km during February–March period (Ansmann et al., 2000; Muller et al., 2001). Shipborne and airborne lidar observations showed the presence of an elevated aerosol layer over a wide region in the Arabian Sea during the above period (Léon et al., 2002; Welton et al., 2002). Airborne lidar observations conducted on 23 April 2006 over the Southeast Arabian Sea within ~350 km from the Indian coast also revealed an aerosol layer extending up to about 2.7 km (Satheesh et al., 2009). However, the above observations were either focused on the vertical distribution of aerosols over the Arabian Sea during the February–March period or based on data during a very short period. Systematic observations of the altitude distribution of aerosols over the west coast of Indian peninsula are still lacking.

* Corresponding author. Tel.: +91 471 2563886; fax: +91 471 2706535.
E-mail address: k_rajeev@vssc.gov.in (K. Rajeev).

1352-2310/$ – see front matter © 2010 Elsevier Ltd. All rights reserved.
doi:10.1016/j.atmosenv.2010.04.014

This paper presents the altitude distribution of aerosols over Trivandrum (8.5°N, 77°E) during the pre-monsoon season based on observations carried out using a Micropulse Lidar (MPL). During this season, as the eastern Arabian Sea plume (EASP) extends to south of Trivandrum, the lidar observations at this site are very conducive for investigating the altitude structure of the EASP. Altitude profiles of aerosol backscatter coefficient (β_a) and linear depolarization ratio (LDR) during less, moderate, and highly polluted conditions are investigated. As the value of LDR increases with non-sphericity of aerosols (e.g., Sakai et al., 2000), this parameter is a potential tool for differentiating the type of aerosols at different altitudes. The long-range transport of aerosols is examined using air back-trajectory analysis and satellite observations of aerosol distribution. The radiative heating of the atmosphere due to these aerosols is estimated using radiation transfer computations.

2. Experimental methods, data and method of analysis

2.1. Micropulse lidar system and inversion of lidar data

A Micropulse Lidar with dual polarization capability (model: MPL-4B of Sigma Space Corporation, USA) is operated regularly from 25 March to 31 May 2008 to study the altitude structure of aerosols during the development phase of the EASP. This system consists of a diode-pumped frequency-doubled solid state Nd:YAG laser transmitter emitting laser pulses at the wavelength of 532 nm having a pulse width of 7 ns. The pulse repetition frequency is 2500 Hz and maximum pulse energy is 8 μJ. A Maksutov–Cassegrain type telescope with 178 mm diameter is used for transmitting the laser beam as well as receiving the backscattered radiation. Two identical interference filters (each having an FWHM of 0.14 nm and out-of-band rejection of 10^5) are used in cascade to limit the background radiation to a minimum. This makes the MPL suitable for daytime operation also. The detector is a Silicon Avalanche Photodiode (Si-APD) operated in photon counting mode. Observations are made with a range resolution of 30 m and time integration of 60 s. Polarization measurements are achieved using an actively controlled liquid crystal retarder by alternating between two polarization states and a polarizing beam splitter. Details of the depolarization measurements of the backscattered signal using MPL and estimation of the linear depolarization ratio (LDR) are explained in detail by Flynn et al. (2007). The lidar system alternates between the two states of polarization (co-polarized and cross-polarized) at an interval of 60 s. The raw data are subsequently corrected for the detector noise and geometrical correction factors following the method described by Welton et al. (2002). The dead-time correction for the APD detector is carried out using the calibration curve provided by the manufacturer.

For each profile, the average photon count observed between the altitudes of 50–60 km is considered as the background, which is subtracted from the measured signal to estimate the true backscattered signal. Extreme care is taken to avoid the cloud-contaminated data. Lidar data with clear sky condition prevailing at least upto an altitude of 6 km and for a minimum period of 30 min only are used to derive the altitude profile of aerosol backscatter coefficient (β_a) using Fernald's method (Fernald, 1984). Earlier observations (Franke et al., 2001; Welton et al., 2002) showed that the extinction-to-backscattered ratio (S) of aerosols over the Arabian Sea during January–March period generally varied in the range 20–70 Sr with a clustering around 30–50 Sr. Based on these, in the present study, a mean value of 40 Sr is adopted for S. The molecular backscattering and extinction coefficients are estimated using mean standard atmospheric model of pressure and temperature for the respective month applicable for Trivandrum. During night, the reference altitude (Z_R) is fixed at 20 km (where β_a is assumed to be zero). During the daytime, due to the relatively low signal-to-noise ratio (S/N), the maximum altitude upto which useful lidar signal could be available (and hence Z_R) decreases to ~6–8 km (~5 km during noon). Presence of clouds further decreases Z_R. In such cases, the boundary condition for β_a at Z_R is obtained from the prior or later profiles of β_a which extends to higher altitudes.

Sensitivity analysis (for the typical variations in the assumed value of S, and the boundary condition of β_a at Z_R) shows a maximum uncertainty of ~20% in the derived β_a. However, due to the geometrical correction of the lidar signal below 1 km (larger correction factor at lower altitudes), and the sea breeze circulation which might cause variations in the advected aerosol properties and the value of S (e.g., Raman et al., 2002), the uncertainty in β_a below 1 km is relatively larger: ~50% below 700 m and progressively decreasing to ~20% at 1 km. Utilization of the same telescope and detector system for the measurement of co- and cross-polarized signal reduces the uncertainty in LDR. The overall uncertainty of LDR below 5 km is <40%. However, above ~5 km, the strength of the cross-polarized lidar signal due to scattering by aerosols is very weak, and the uncertainty in LDR will be >50%. In the present study, LDR is used only as a qualitative index for the discrimination of highly non-spherical aerosols from the relatively spherical aerosols.

2.2. Measurement of aerosol optical depth

Aerosol optical depth (τ) during clear sky days were observed using a sunphotometer (Microtop-II, Solar Light Co.). This instrument provides AOD at five wavelengths: 440, 500, 675, 936 and 1020 nm. This is a calibrated system (periodic calibration using Langley-Bouger technique did not show any significant departure in the one-year old factory calibration) and the maximum uncertainty in the derived AOD is ±0.04. The aerosol optical depth at the MPL wavelength of 532 nm is estimated by fitting a power law type variation of AOD in these wavelengths. In order to minimize errors due to uncertainty in the parameters assumed in the lidar data inversion, the profiles of aerosol extinction and backscatter coefficients are further weighed by AOD observed at 532 nm.

3. Results and discussions

3.1. Spatial distribution of the East Arabian Sea plume

Fig. 1 shows the monthly mean regional distribution of AOD (τ at 550 nm) over the Arabian Sea, Bay of Bengal and equatorial Indian

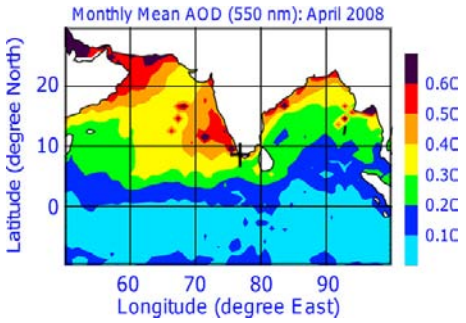

Fig. 1. Monthly mean regional distribution of MODIS-derived AOD (550 nm) over the Arabian Sea, Bay of Bengal and equatorial Indian Ocean during April 2008. Location of Trivandrum is marked with '+' symbol.

Ocean, extracted from the Terra-MODIS data (Moderate Resolution Imaging Spectroradiometer: MOD08_D3.005 product) during April 2008. Error in the MODIS-retrieved AOD is $0.03 \pm 0.05\tau$ over ocean. The objective of Fig. 1 is to show the spatial distribution of the EASP, which is manifested as a region of high AOD over the eastern Arabian Sea adjoining west coast of India. It spreads over most parts of the eastern Arabian Sea with its core located between ~7°N and ~20°N latitude. Values of AOD exceed 0.5 over a significantly large region near the west coast of India and the largest values of AOD are observed between 10 and 15°N. Trivandrum is located at the southern part of the EASP. Spatial variation of AOD over the Arabian Sea during March and May 2008 are similar to that of April, though the monthly mean AOD over most part of the plume is <0.4 in March and <0.5 in May 2008. Mean values of AOD over the Arabian Sea adjacent to Trivandrum are respectively 0.27, 0.41, and 0.50 during March, April, and May 2008, which are in agreement (within ±0.04) with the mean values of AOD observed using sunphotometer at Trivandrum during these months. This shows that the AOD variations of EASP are well represented in the observations made at Trivandrum.

3.2. Altitude variation of attenuated backscatter signal

Fig. 2 shows the co-polarized component of the attenuated lidar backscatter signal, ψ (after applying geometrical and detector corrections) and LDR observed on 26 March (representing a less polluted day with mean τ at 532 nm, $\tau_{532} = 0.21$), 4 April (a moderately polluted day with mean $\tau_{532} = 0.40$), and 8 May 2008 (a highly polluted day with mean $\tau_{532} = 0.52$). On 26 March, ψ is high and did not show significant altitude variation up to around 1 km, which corresponds to the aerosol mixing height (Hm) associated with the atmospheric boundary layer. Above the mixing height, ψ decreases rather monotonically with increase in altitude with no prominent layered structure. On 4 April, the altitude variation of ψ shows three distinct layers: (i) below Hm at ~1 km, (ii) between Hm and 2 km, and (iii) a rather weak but broad layer between 2 and 4 km. On 8 May, the altitude variation of ψ is more-or-less similar to that during 4 April, but the elevated layer (at 2–4 km) became more pronounced and merged with lower layer just above Hm. It is interesting to note that, on this day, the value of ψ decreased very sharply above 4 km and LDR associated with the elevated layer is significantly large. On average, the altitude variations of ψ and LDR observed on almost all the days during the pre-monsoon season can be categorized broadly into one of the three types described above (Fig. 2). Below ~1 km, the variation of Hm and the sea breeze circulation modulate the time-altitude variation of ψ and LDR on a diurnal scale (e.g., Raman et al., 2002) which is not considered in this study based on daily mean profiles.

3.3. Altitude profiles of β_a and LDR

The altitude profiles of β_a is estimated from the lidar data on all the 48 days during the period 25 March–31 May 2008. Based on the altitude variations of β_a and the observed AOD, the data are grouped into three different categories: (a) less polluted period (25–27 March, 7–11 April, 21–23 May) with mean $\tau_{532} = 0.22$, (b) moderately polluted period (28 March–6 April, 14–18 April) with mean $\tau_{532} = 0.41$, and (c) highly polluted period (21–30 April, 1–16 May) with mean $\tau_{532} = 0.55$. The time-altitude cross-sections of mean ψ observed for the above three categories are similar to those shown as typical examples in Fig. 2 for 26 March, 4 April and 8 May respectively. Fig. 3 shows the mean altitude profiles of β_a (left panels) and the corresponding profiles of LDR (right panels) for these three categories. The less polluted periods are characterized by an almost exponential decrease of β_a with altitude, notwithstanding the fact that a few relatively small peaks are observed around 2 km. During the moderately polluted period, β_a, in general, shows a distinct aerosol layer between the surface and 2 km, followed by an almost exponential decrease above. In general, the altitude profiles of β_a are distinctly different after 21 April compared to the period before. A rather weak altitude variation of β_a up to 4 km, which is followed by a sharp decrease above is observed during the highly polluted period of 21 April–16 May. A markedly less polluted condition, having significantly reduced aerosol content at all altitudes, was observed during 21–23 May ($\tau_{532} = 0.23$). During 27–30 May, though the mean AOD was only 0.27, the altitude variation of β_a is more-or-less similar to that of the highly polluted period. The decrease in AOD during this period can be attributed to the decrease in β_a in the aerosol layer below 2 km.

Overall, the value of LDR below 1 km shows a decreasing trend from March to May. Altitude profiles of LDR (Fig. 3) clearly show the presence of two distinct layers with relatively large value of LDR (0.06–0.1) between 2 and 4 km during 21 April–31 May. Though less prominent, this layer can be observed even during the less polluted period of 21–23 May. Below 2 km, the values of LDR on the less and moderately polluted days during March–May are generally <0.05. Extremely small values of LDR (<0.01) below 2 km during 21–23 May (period of less pollution) are particularly notable, indicating the highly spherical nature of aerosols. During the highly polluted period (21 April–16 May), the value of LDR below 2 km (typically ~0.08) is comparable to that of the elevated aerosol layer. However, the value of LDR in the 0–2 km region during the highly polluted periods are larger (outside the uncertainty limits) than that during the less and moderately polluted periods. Furthermore, during less and moderately polluted days of 21–30 May, the value of LDR associated with the layer at 2–4 km are larger than that of the 0–2 km region (outside the uncertainty limits). High value of LDR indicates significant amount of non-spherical aerosols. During the less and moderately polluted periods, aerosols below 2 km altitude are highly spherical in nature.

3.4. Normalized cumulative contribution of aerosols

In order to quantify the percentage contribution of aerosols in each altitude band to the total aerosol content in the atmosphere, the normalized cumulative contribution of aerosols (NCC) is estimated as a function of altitude (Z) by integrating β_a between the surface and 'Z' and normalizing with the total column integrated backscatter coefficient (IBC). Mean altitude variation of NCC during the less, moderate, and highly polluted periods discussed above are shown in Fig. 4. During the less polluted period, average contribution to IBC from the altitude region <1 km is 64% and that from <2 km is 88%. The corresponding contributions during the moderately polluted periods are 58% at <1 km and 88% at <2 km. Contribution of the elevated aerosol layer to IBC is largest (25%) during the highly polluted period when the contributions due to aerosols at <1 km and <2 km are reduced to 48% and 75% respectively. Weighting the contributions from different altitude bands with the observed mean value of τ_{532} shows a layer-integrated optical depth of 0.13 in the altitude band of 2–4 km during the highly polluted period, which is ~4 times larger than the corresponding value during the less polluted period (0.03).

3.5. Altitude structure of meteorological parameters

Fig. 5 shows the mean altitude profiles of relative humidity (RH), temperature, wind speed and wind direction obtained from radiosonde observations at Trivandrum during less, moderate, and highly polluted periods. Averages of the standard errors (<SE>) in the respective parameters between 0 and 6 km are also shown in

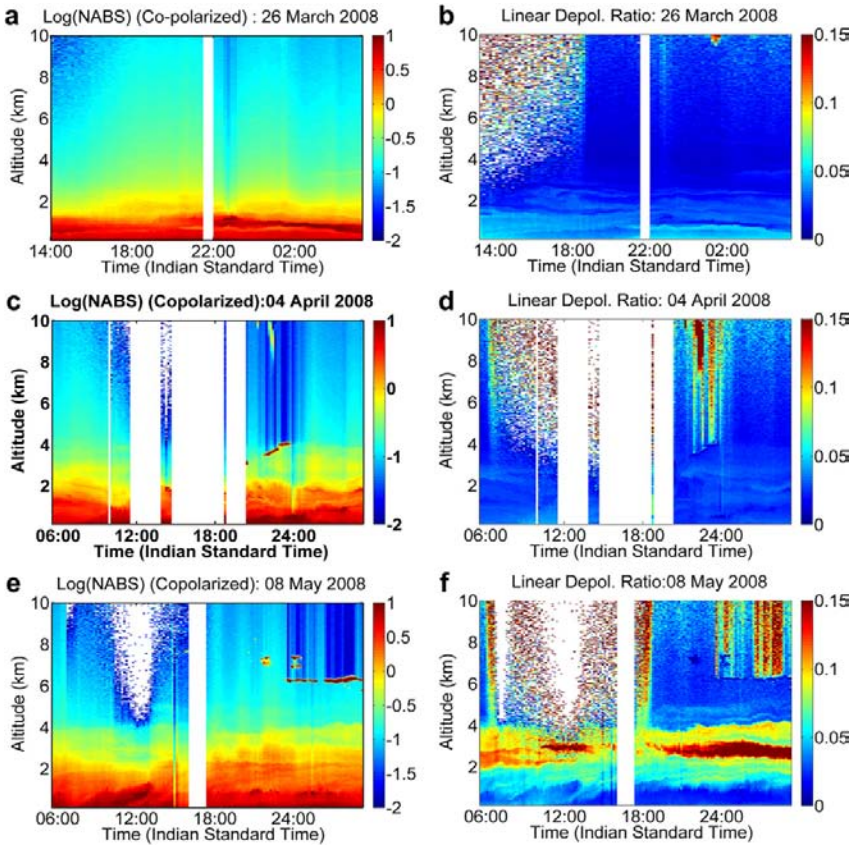

Fig. 2. (a) Time-altitude variations of the normalized co-polarized lidar backscatter signal (ABS) during 26 March 2008, (b) same as (a) but for linear depolarization ratio. (c,d) and (e,f) are same as (a,b), but for 4 April, and 8 May 2008 respectively.

Fig. 5. Vertical variation of the meteorological properties show three distinct altitude bands: (i) 0 to ~1.5–2 km, (ii) 2–4.5 km, and (iii) >4.5 km. The northwesterly wind (from the Arabian Sea) in the lowest layer changes to northeasterly (from the continental regions) above 1.5–2 km. During the highly polluted period, wind speed shows significant peaks (~6.5 m s^{-1}) at 800 m and 3 km and wind shear at the base and top of the layer at 2–4 km is more prominent. Wind speed is generally < 4 ms^{-1} during the less polluted period. The lower layer is highly humid (RH > 80%, with higher values during the moderate and highly polluted periods) while the layer at 2–4 km is rather dry (RH~50–60%). The value of RH decreases to <50% above 4.5 km. The temperature lapse rate is the least at ~2 km and ~4.5 km. On average, the lapse rate between 2 and 4 km is ~0.7 K km^{-1} larger than that below and above. The decrease in RH and change in lapse rate above ~4 km are associated with the trade wind inversion, which might have caused the drastic decrease in β_a observed above 4 km. Large relative humidity below ~2 km paves way for hygroscopic growth of aerosols in this layer (which will also be modulated by sea breeze circulation), leading to the formation of nearly spherical aerosols. This might have resulted in the relatively low values of LDR observed below 2 km. Aerosols within the dry layer between 2 and 4 km are unlikely to have significant hygroscopic growth and could be more non-spherical in nature (indicated by the large value of LDR). These two air masses meet at ~1.5–2 km, which is manifested with a temperature inversion. This prevents upward mixing of aerosols from below 2 km, while the slow gravitational settling of aerosols from the layer above might take place.

3.6. Air back-trajectory analysis

Effect of long-range transport in modulating the altitude profiles of β_a and AOD are investigated based on the 7-day air back-trajectories obtained using the NOAA – ARL – HYSPLIT transport dispersion model. Fig. 3 shows that the aerosol loading below 2 km during the moderate and highly polluted periods (28 March–6 April, 14 April–16 May) is significantly more than that during the less polluted periods (25–27 March, 7–11 April, and 21–30 May). The 7-day air back-trajectories ending at 1 km over Trivandrum during these moderate and highly polluted periods are shown in Fig. 6a while those during the less polluted periods are shown in Fig. 6b. Most of the 7-day back-trajectories at 1 km during the moderate and highly polluted periods have originated from the north and central Arabian Sea and traversed through the eastern Arabian Sea before reaching Trivandrum. Few of them started from the Peninsular India and coastal Arabia. Regional distribution of aerosols derived from satellite data over the Arabian Sea (Fig. 1) shows that AOD is highest over the eastern and northern Arabian Sea during the pre-monsoon season. Fig. 6b shows that almost all the trajectories ending at 1 km during the less polluted periods

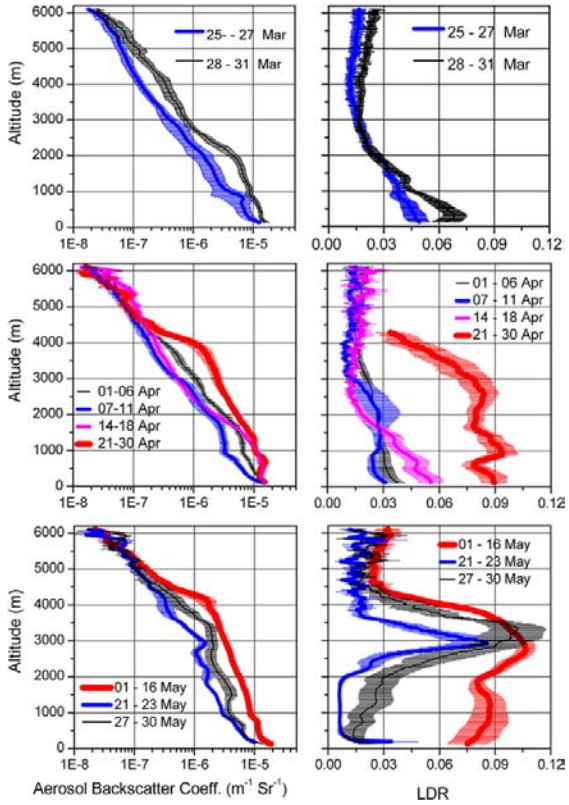

Fig. 3. The mean altitude profiles of βa (left panels) and linear depolarization ratio (right panels) for different conditions of AOD during March (top), April (middle) and May (bottom) months of 2008. The horizontal lines show standard errors. See text for details.

originate from the south Indian Ocean, southwest Arabian Sea or south Bay of Bengal, which are relatively clean (Fig. 1). The particles associated with these air masses could be mostly of oceanic origin (sea salt), which are basically hygroscopic in nature. Note that the

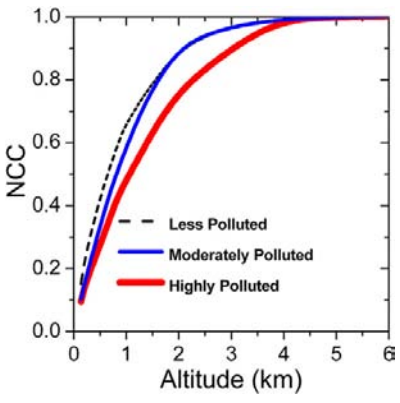

Fig. 4. Mean altitude variation of the normalized cumulative contribution of aerosols (NCC) to the total AOD during the less, moderate, and highly polluted periods.

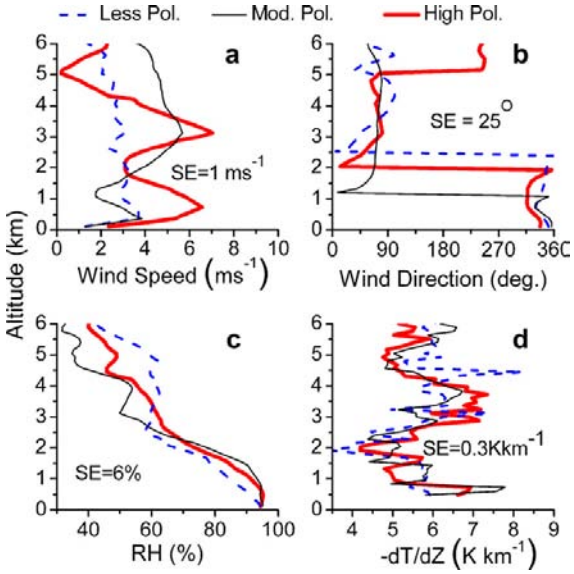

Fig. 5. Mean altitude profiles of (a) wind speed, (b) wind direction, (c) relative humidity, and (d) temperature lapse rate during less, moderate, and highly polluted periods. Values of <SE> shown in each panel are the averages of the standard errors in the respective parameters between 0 and 6 km.

values of LDR during less polluted days (21–23 May) are considerably small when the back-trajectories originate from pristine oceanic regions. This shows that transport of aerosols from the northern part of Arabian Sea is mainly responsible for the relatively high aerosol concentration observed below 2 km over Trivandrum during the moderate and highly polluted periods.

Fig. 7a shows the 7-day back-trajectories ending at 3.5 km at Trivandrum when the aerosol layer at 2–4 km was prominent (21 April-16 May, 27–30 May), while Fig. 7b shows the same during the days on which this layer was less prominent (25 March–18 April, 21–23 May). During the period of 21 April-16 May and 27–30 May, when the elevated aerosol layer with high depolarization was prominent up to 4 km, almost all the back-trajectories ending at 3.5 km over Trivandrum originated at the northwestern parts of the Indian subcontinent, north Arabian Sea or Arabia and traversed through central and east Peninsular India. Strikingly, during 25 March–18 April and 21–23 May, when the elevated layer at 2–4 km was absent or rather weak, most of the trajectories (Fig. 7b) originated from the southwest Arabian Sea, southeast Bay of Bengal or southeast Asia and none of them are from north of 15°N over the Indian subcontinent. This clearly shows that the elevated aerosol layer with considerable depolarization observed between 2 and 4 km during 21 April–16 May and 27–31 May is due to the long-range transport of continental aerosols (which are more non-spherical), most probably from the northwestern parts of the subcontinent. It would be interesting in this context to note that the aerosol loading over Kanpur, a station located in north India, showed predominant annual variation with maximum aerosol abundance occurring in the April–May period (Singh et al., 2004). High AOD and elevated aerosol layer are observed in the northern parts of the Indian subcontinent since late winter (Jayaraman et al., 2006; Tripathi et al., 2007). Similar aerosol layers associated with the long-range transport from the Arabian region and the Indian subcontinent over to the east coast of Peninsular India (adjoining Bay of Bengal) during the March–April period was reported by

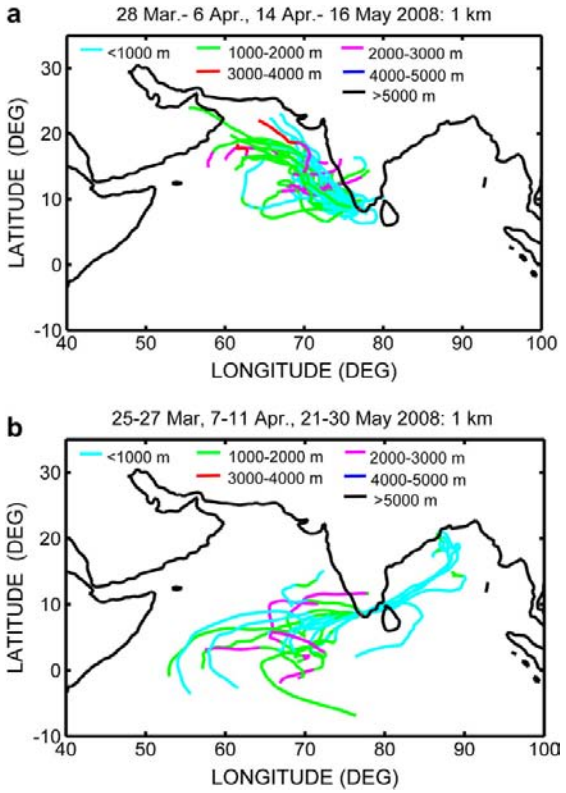

Fig. 6. The 7-day air back-trajectories ending at Trivandrum at 1 km during different periods in March, April, and May 2008. See text for details.

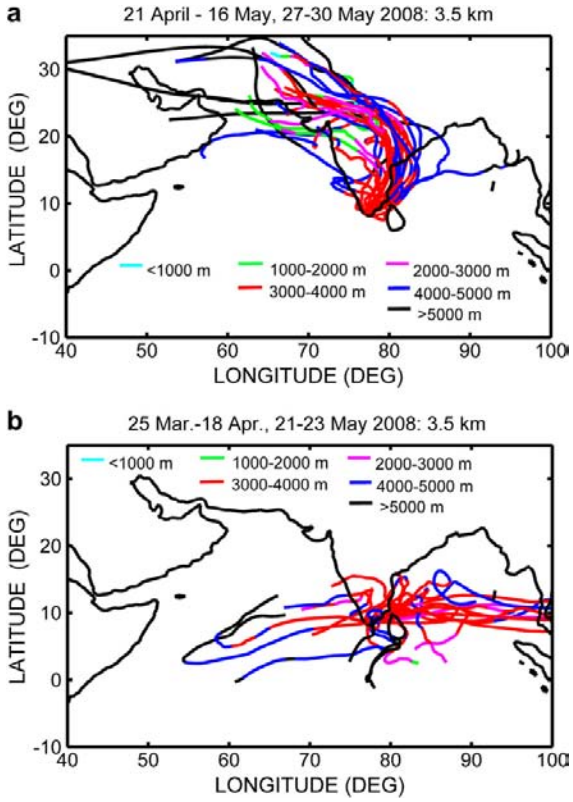

Fig. 7. The 7-day air back-trajectories ending at Trivandrum at 3.5 km during different periods in March, April, and May 2008. See text for details.

Niranjan et al. (2007). The present results are also in agreement with the observations over Maldives Island during February–March period, which showed elevated aerosol layers with relatively large values of Angstrom exponent and low single scattering albedo when the airmass was advected from the northern parts of the Indian subcontinent (Franke et al., 2003; Müller et al., 2003).

3.7. Latitude–altitude cross-section of β_a observed using CALIPSO

The long-range transport mechanism proposed above can cause the elevated aerosol layer over Trivandrum only if the northern parts of Indian subcontinent or Arabian Sea have significant aerosol loading up to about 4–5 km during this period. This aspect is examined using the altitude profiles of β_a observed using the Cloud Aerosol Lidar Pathfinder Satellite Observation (CALIPSO), which provides a comprehensive set of observations on aerosols and clouds on a global scale (Winker et al., 2007), but limited to the sub-satellite track. The altitude profiles of β_a observed at 532 nm (level 2 data having horizontal resolution of 40 km and altitude resolution of 120 m) are used for this purpose. Fig. 7a shows that the back-trajectories are spread over a wide longitude band of 70–85°E in the northwestern parts of the Indian subcontinent. Due to this reason, the monthly mean latitude–altitude cross-section of β_a obtained by averaging all the CALIPSO-derived aerosol backscatter profiles in the longitude band of 70–85°E during each month is considered here. Fig. 8 shows the monthly mean latitude–altitude cross-section of β_a during April and May 2008, both showing a significant increase in β_a from 5°N to ~15–20°N. The maximum altitude up to which this increase is significant extends upto ~5 km around 15–20°N which decreases to ~4 km at 5–10°N. Observations of significant aerosol amount up to ~4 km at ~4°N were also reported by Franke et al. (2003). Fig. 8 shows that an airmass originating from the north of 15°N in the longitude band of 70–85°E has the potential to transport significant amount of aerosols. This feature, along with the air back-trajectories (Fig. 7) unambiguously show that the elevated aerosol layers observed at 2–4 km over Trivandrum is caused by the transport of aerosols from the northwestern parts of the Indian subcontinent and north Arabian Sea. Furthermore, the elevated aerosol layer was considerably weak (or absent) when the back-trajectories originated from south of ~10°N (Fig. 7b) where the aerosol loading above ~3 km is significantly small.

3.8. Aerosol radiative heating of the atmosphere

Impact of the observed altitude distribution of aerosols on short-wave (wavelength band of 300–4000 nm) aerosol radiative heating of the atmosphere over Trivandrum during the pre-monsoon season is estimated by incorporating the observed altitude distribution of aerosols into the Santa Barbara DISORT Atmospheric Radiative Transfer Model (SBDART) (Richiazzi et al., 1998). The approach is given in Rajeev et al. (2008). The spectral radiative properties of aerosols required for these computations are obtained from the polluted continental aerosol model of the OPAC (Optical

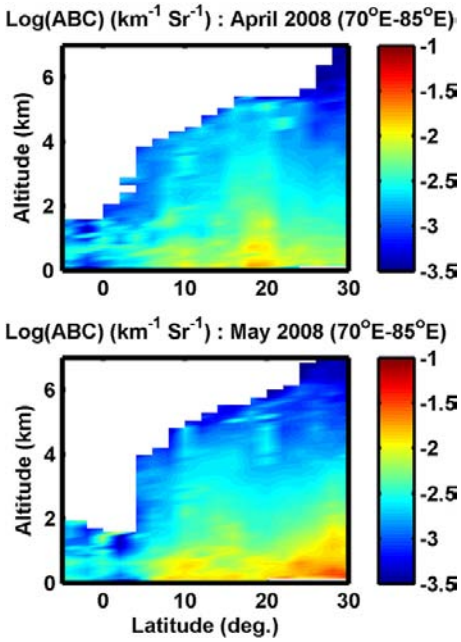

Fig. 8. Monthly mean latitude–altitude cross-sections of aerosol backscatter coefficient obtained from CALIPSO data in the longitude band of 70–85°E during April and May 2008.

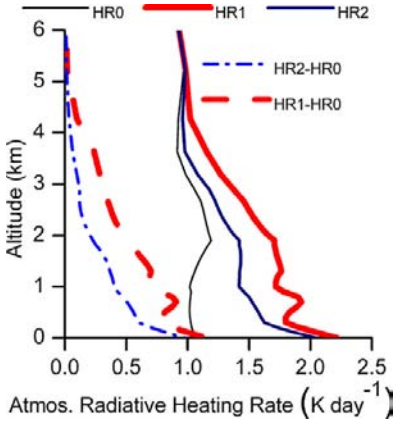

Fig. 9. Altitude variation of the diurnal mean atmospheric radiative heating rate for the background atmosphere (no aerosols, denoted as HR0) and highly polluted conditions (AOD = 0.52, denoted as HR1). The corresponding heating rate for AOD = 0.28 is denoted by HR2. Profiles of HR1-HR0 and HR2-HR0 are also shown for comparison.

Properties of Aerosols and Clouds) database (Hess et al., 1998), but for an Angstrom exponent of 0.9 (the mean value observed at Trivandrum during the pre-monsoon season), which is also comparable to that reported for the EASP (Kalapureddy and Devara, 2008). Altitude profile of aerosol single scattering albedo (ω_a) associated with EASP (in the visible band) during February–March is generally in the range 0.80–0.90 (Muller et al., 2001). Relatively smaller mass abundance of black carbon (0.9–2.2%) observed near the surface over the Arabian Sea during April–May (Babu et al., 2004; Nair et al., 2008) indicates that ω_a will be around 0.90–0.93 during the April–May period. In the adopted aerosol model, the values of ω_a is 0.90 at 500 nm and asymmetry parameter is 0.70 (which can vary by ±0.03 due to variations in aerosol composition and humidity). However, the value of ω_a during less polluted days might be larger than that during the highly polluted periods. Considering the potential sources of errors in the scattering and absorption properties of aerosols and meteorological parameters, the overall uncertainty in the estimated altitude profile of atmospheric heating rate due to aerosols is about 35%.

Altitude profile of the diurnal mean atmospheric radiative heating rate for the background (no aerosols, denoted as HR0) and highly polluted (with mean AOD = 0.52, denoted as HR1) atmospheric conditions over Trivandrum during the pre-monsoon season are shown in Fig. 9. The heating rate profile representing the average of less and moderately polluted conditions (AOD = 0.28, denoted as HR2) is also shown in Fig. 9 for comparison. In general, both HR1 and HR2 decrease monotonically with increase in altitude above 2 km. The increase in the atmospheric heating rate due to aerosols alone for highly polluted condition (HR1-HR0) is approximately 0.8 K day^{-1} at 500 m, 0.5 K day^{-1} at 2 km, and 0.3 K day^{-1} at 3 km, which are respectively 80%, 40%, and 30% of the corresponding values of HR0. The effect of aerosols on the radiative heating of the atmosphere is insignificant above 4 km. Average difference between the atmospheric heating rates for AOD = 0.52 and AOD = 0.28 (HR1–HR2), is around 0.3 K day^{-1} in the altitude band of 0–2 km. Note that this is in agreement (within the uncertainty limits) with the directly observed enhancement of 0.4 K day^{-1} in the atmospheric heating rate for an increase of 0.22 in AOD observed over the Indian Ocean during March 2006 (Ramanathan et al., 2007).

4. Conclusions

Altitude distribution of aerosols over Trivandrum, which is located at the southern parts of the East Arabian Sea plume during the pre-monsoon season, is investigated using Micropulse Lidar observations of aerosol backscatter coefficient and linear depolarization ratio during the March–May period of 2008. This study shows that distinctly different altitude profiles of aerosols prevail during the less (mean AOD~0.22), moderate (mean AOD~0.41) and highly (mean AOD~0.52) polluted conditions. A persistent elevated aerosol layer, which contributes ~25% of the column integrated AOD, is observed in the altitude region of 2–4 km throughout the period of 21 April-30 May 2008. The high values of LDR associated with this relatively dry layer (with RH ~50–60%) indicate that the aerosols in this layer might have significant non-sphericity. Altitude variation of meteorological properties and air back-trajectory analysis show that this layer is caused by the long-range transport of airmass from the northwestern parts of the Indian subcontinent and north Arabian Sea. When this layer is absent, the back-trajectories are distinctly different and originate from the southwest Arabian Sea or Bay of Bengal. A prominent aerosol layer extending from surface to ~2 km is observed during the moderate and highly polluted conditions, which is closely associated with the advection of air from the north and east Arabian Sea, where the AOD associated with EASP is largest. In contrast, during the less polluted period, the airmass originates mostly from the oceanic regions over the southwest Arabian Sea and Indian Ocean. High relative humidity (RH~80–97%) and the relatively low values of LDR (<0.05) associated with this layer suggest that the particles prevailing in this layer might be more hygroscopic and spherical in nature. During the highly polluted conditions, the trapping of solar radiation increase the atmospheric heating rate by about 0.8 K day^{-1} at

500 m and 0.3 K day^{-1} at 3 km, which are respectively ~80 and 30% of the atmospheric radiative heating rate in the aerosol-free atmosphere. This heating can lead to increase in atmospheric stability in the region very near to the surface, leading to inhibition of convection.

Acknowledgements

The authors acknowledge the NOAA Air Resources Laboratory (ARL) for the provision of the HYSPLIT transport and dispersion model and READY website (http://www.arl.noaa.gov/ready.html) used in this publication. MODIS AOD data used in this paper were obtained from the Giovanni online data system, developed and maintained by the NASA GES DISC. CALIPSO data was obtained from LaRCAtmospheric Sciences Data Center (http://eosweb.larc.nasa.gov/). Radiosonde data was obtained from the University of Wyoming (http://weather.uwyo.edu). K. Parameswaran acknowledges CSIR for providing support under the Emeritus Scientist scheme. We thank the reviewers for their constructive suggestions.

References

Ansmann, A., Althausen, D., Wandinger, U., Franke, K., Miiller, D., Wagner, F., Heintzenberg, J., 2000. Vertical profiling of the Indian aerosol plume with six-wavelength lidar during INDOEX: a first case study. Geophys. Res. Lett. 27 (7), 963–966.

Babu, S.S., Moorthy, K.K., Satheesh, S.K., 2004. Aerosol black carbon over Arabian Sea during intermonsoon and summer monsoon seasons. Geophys. Res. Lett. 31, L06104. doi:10.1029/2003GL018716.

Fernald, F.G., 1984. Analysis of atmospheric lidar observations: some comments. Appl. Opt. 23, 652–653.

Flynn, C.J., Mendoza, A., Zheng, Y., Mathur, S., 2007. Novel polarization-sensitive micropulse lidar measurement technique. Opt. Express 15 (6), 2785–2790.

Franke, K., Ansmann, A., Muller, D., Althausen, D., Wagner, F., Scheele, R., 2001. One year observations of particle lidar ratio over the tropical Indian Ocean with Raman Lidar. Geophys. Res. Lett. 28, 4559–4562.

Franke, K., Ansmann, A., Müller, D., Althausen, D., Venkataraman, C., Reddy, M.S., Wagner, F., Scheele, R., 2003. Optical properties of the Indo-Asian haze layer over the tropical Indian Ocean. J. Geophys. Res. 108 doi:10.1029/2002JD002473.

Hess, M., Kopke, P., Schult, I., 1998. Optical properties of aerosols and clouds: the software package opac. Bull. Am. Meteorol.Soc. 79, 831–844.

Jayaraman, A., Gadhavi, H., Ganguly, D., Misra, A., Ramachandran, S., Rajesh, T.A., 2006. Spatial variations in aerosol characteristics and regional radiative forcing over India: measurements and modeling of 2004 road campaign experiment. Atmos. Environ. 40, 6504–6515.

Kalapureddy, M.C.R., Devara, P.C.S., 2008. Characteristics of aerosols over oceanic regions around India during pre-monsoon 2006. Atmos. Environ. 42, 6816–6827.

Léon, J.-F., Chazette, P., Pelon, J., Dulac, F., Randriamiarisoa, H., 2002. Aerosol direct radiative impact over the INDOEX area based on passive and active remote sensing. J. Geophys. Res. 107 doi:10.1029/2000JD000116.

Moorthy, K.K., Satheesh, S.K., Babu, S.S., Dutt, C.B.S., 2008. Integrated Campaign for Aerosols, gases and Radiation Budget (ICARB): an overview. J. Earth Syst. Sci. 117 (S1), 243–262.

Muller, D., Franke, K., Wagner, F., Althausen, D., Ansmann, A., Heintzenberg, J., 2001. Vertical profiling of optical and physical particle properties over the tropical Indian Ocean with six wavelength lidar, 1, seasonal cycle. J. Geophys. Res. 106, 28,567–28,575.

Müller, D., Franke, K., Ansmann, A., Althausen, D., Wagner, F., 2003. Indo-Asian pollution during INDOEX: microphysical particle properties and single-scattering albedo inferred from multiwavelength lidar observations. J. Geophys. Res. 108 doi:10.1029/2003JD003538.

Nair, S.K., Parameswaran, K., Rajeev, K., 2005. Seven-years satellite observations of the mean structure and variabilities in the regional aerosol distribution over the oceanic areas around the Indian subcontinent. Ann. Geophysicae 23, 2011–2030.

Nair, V.S., Babu, S.S., Moorthy, K.K., 2008. Aerosol characteristics in the marine atmospheric boundary layer over the Bay of Bengal and Arabian Sea during ICARB: spatial distribution and latitudinal and longitudinal gradients. J. Geophys. Res. 113, D15208. doi:10.1029/2008JD009823.

Niranjan, K., Madhavan, B.L., Sreekanth, V., 2007. Micro pulse lidar observation of high altitude aerosol layers at Visakhapatnam located on the east coast of India. Geophys. Res. Lett. 34, L03815. doi:10.1029/2006GL028199.

Rajeev, K., Ramanathan, V., 2001. Direct observations of clear-sky aerosol radiative forcing from space during the Indian Ocean experiment. J. Geophys. Res. 106, 17,221–17,236.

Rajeev, K., Parameswaran, K., Nair, S.K., Meenu, S., 2008. Observational evidence for the radiative impact of Indonesian smoke in modulating the sea surface temperature of the equatorial Indian Ocean. J. Geophys. Res. 113, D17201. doi:10.1029/2007JD009611.

Ramachandran, S., Jayaraman, A., 2002. Premonsoon aerosol mass loadings and size distributions over the Arabian Sea and the tropical Indian Ocean. J. Geophys. Res. 107 (D24), 4738,. doi:10.1029/2002JD002386.

Raman, S., Niyogi, D.S., Simpson, M., Pelon, J., 2002. Dynamics of the elevated land plume over the Arabian Sea and the Northern Indian Ocean during north-easterly monsoons and during the Indian Ocean experiment (INDOEX). Geophys. Res. Lett. 29 doi:10.1029/2001GL014193.

Ramanathan, V., et al., 2001. Indian Ocean Experiment: an integrated analysis of the climate forcing and effects of the great Indo-Asian haze. J. Geophys. Res. 106, 28,371–28,398.

Ramanathan, V., Ramana, M.V., Roberts, G., Kim, D., Corrigan, C., Chung, C., Winker, D., 2007. Warming trends in Asia amplified by brown cloud solar absorption. Nature 448 doi:10.1038/nature06019.

Richiazzi, P., Yang, S., Gautier, C., Sowle, D., 1998. SBDART: A research and teaching software tool for plane-parallel radiative transfer in the Earth's atmosphere. Bull. Amer. Meteor. Soc. 79, 2101–2114.

Sakai, T., Shibata, T., Kwon, S.-A., Kim, Y.-S., Tamura, K., Iwasaka, Y., 2000. Free tropospheric aerosol backscatter, depolarization ratio, and relative humidity measured with the Raman lidar at Nagoya in 1994–1997: contributions of aerosols from the Asian Continent and the Pacific Ocean. Atmos. Environ. 34, 431–442.

Satheesh, S.K., Moorthy, K.K., Babu, S.S., Vinoj, V., Nair, V.S., Beegum, S.N., Dutt, C.B.S., Alappattu, D.P., Kunhikrishnan, P.K., 2009. Vertical structure and horizontal gradients of aerosol extinction coefficients over coastal India inferred from airborne lidar measurements during the Integrated Campaign for Aerosol, Gases and Radiation Budget (ICARB) field campaign. J. Geophys. Res. 114, D05204.

Singh, R.P., Dey, S., Tripathi, S.N., Tare, V., Holben, B., 2004. Variability of aerosol parameters over Kanpur, north India. J. Geophys. Res. 109 doi:10.1029/2004JD004966.

Tripathi, S.N., Pattnaik, A., Dey, S., 2007. Aerosol indirect effect over Indo-Gangetic plain. Atmos. Environ. 41, 7037–7047.

Welton, E.J., Voss, K.J., Quinn, P.K., Flatau, P.J., Markowicz, K., Campbell, J.R., Spinhirne, J.D., Gordon, H.R., Johnson, J.E., 2002. Measurements of aerosol vertical profiles and optical properties during INDOEX 1999 using micropulse lidars. J. Geophys. Res. 107, 8019. doi:10.1029/2000JD000038.

Winker, D.M., Hunt, W.H., McGill, M.J., 2007. Initial performance assessment of CALIOP. Geophys. Res. Lett. 34, L19803. doi:10.1029/2007GL030135.

JOURNAL OF GEOPHYSICAL RESEARCH, VOL. 115, D05205, doi:10.1029/2009JD011802, 2010

Regional distribution of deep clouds and cloud top altitudes over the Indian subcontinent and the surrounding oceans

S. Meenu,[1] K. Rajeev,[1] K. Parameswaran,[1] and Anish Kumar M. Nair[1]

Received 26 January 2009; revised 23 October 2009; accepted 2 November 2009; published 10 March 2010.

[1] The Bay of Bengal (BoB) and the east equatorial Indian Ocean are among the most intense deep convective regions over the tropics. Long-term monthly mean distributions of deep clouds and the regional differences in the cloud top brightness temperature (CTBT) over the Indian subcontinent and the surrounding oceanic regions (the northern and eastern BoB, the southeast Arabian Sea, and the eastern equatorial Indian Ocean) are derived using National Oceanic and Atmospheric Administration Advanced Very High Resolution Radiometer data for a period of 10 years and are compared with the direct observations of cloud top altitude (CTA) using Cloud-Aerosol Lidar and Infrared Pathfinder Satellite Observation (CALIPSO). The deepest clouds are found to occur over the northern BoB (NBoB) during the June–August period. The most probable CTBT in this region is ~12 K lower than that over the other deep convective regions. CALIPSO observations also show that the frequency of occurrence of CTA peaks at an altitude of ~16.5 km over the NBoB, which is ~1 km higher than that over the other regions. Strong convergence of horizontal wind between the surface and ~200 hpa level and large divergence above, combined with the most favorable sea surface temperature (>28°C), might be mainly responsible for the highest CTA being observed over the NBoB. The annual variation of the base altitude and thickness of the tropical tropopause layer (TTL) and the upper tropospheric temperature are closely associated with the corresponding variations in the deep cloud fraction. Considerable fraction of deep clouds occurs within the TTL over the BoB during the June–August period.

Citation: Meenu, S., K. Rajeev, K. Parameswaran, and A. K. M. Nair (2010), Regional distribution of deep clouds and cloud top altitudes over the Indian subcontinent and the surrounding oceans, *J. Geophys. Res.*, *115*, D05205, doi:10.1029/2009JD011802.

1. Introduction

[2] Deep convection over the tropics is a crucial element in driving the large-scale atmospheric circulation, redistribution of energy and moisture, maintenance of the hydrological cycle, and the overall climate of the Earth-atmosphere system. Release of latent heat associated with deep convection heats the entire tropospheric column, and the large anvils emanating from the active convective clouds influence the synoptic and mesoscale radiation balance [*Ramanathan et al.*, 1989; *Grossman and Garcia*, 1990]. Deep convection is the most effective mechanism for the transport of heat and moisture from the atmospheric boundary layer to the upper troposphere. Occasionally, deep convective clouds can penetrate into the upper troposphere and lower stratosphere (UTLS), transporting humid surface air parcels rapidly upward. The structure of the tropical tropopause layer (TTL) is at least partly controlled by the vertical variation in mixing induced by penetrating convection [*Dessler*, 2002].

[3] *Wylie and Menzel* [1999] observed that the frequency of cloud detection (above 6 km altitude) in the High-Resolution Infrared Sounder field of view is >50% over the Indian subcontinent and the adjoining oceanic regions during June to August, while such high frequency of occurrence of clouds are mainly confined to the equatorial Indian Ocean during the winter months. The frequency of occurrence of deep convective clouds exceeds ~25% over the Bay of Bengal during July and over the equatorial Indian Ocean during January [*Roca and Ramanathan*, 2000]. During the June to August period, the convective areas over the tropical Indian Ocean stand out for the presence of deep precipitating clouds with cloud top height >11.5 km [*Haynes and Stephens*, 2007].

[4] The regional distribution of clouds over the Indian subcontinent and the adjoining oceanic regions are unique in several ways. Over the entire tropics, the most frequent deep convection occurs over the Bay of Bengal, the eastern equatorial Indian Ocean and the western Pacific [*Newell and Gould-Stewart*, 1981; *Gettelman et al.*, 2002]. In contrast to the near-cancellation of the longwave and shortwave cloud radiative forcing at the top of the atmosphere over the tropics [*Kiehl*, 1994], the net cloud radiative forcing over this region is negative during the June–September period (Asian

[1] Space Physics Laboratory, Vikram Sarabhai Space Centre, Thiruvavanthapuram, India.

0148-0227/10/2009JD011802$09.00

summer monsoon season) [*Rajeevan and Srinivasan*, 2000]. The Intertropical Convergence Zone (ITCZ), where deep convective clouds are prominent, shows its largest annual migration (from ~10°S to ~30°N) over this region. Understanding the role of deep convection in determining the state of the UTLS region requires an extensive survey of the deep cloud characteristics and the vertical distribution of clouds. While several studies have been pursued in the past on this aspect [e.g., *Fu et al.*, 1990; *Mapes and Houze*, 1993; *Zhang*, 1993; *Hall and Vonder Haar*, 1999; *Gettelman et al.*, 2002; *Hong et al.*, 2007; *Rossow and Pearl*, 2007], most of them were either focused on the Pacific region or the tropics as a whole. Only a limited number of investigations targeting deep clouds over the Indian subcontinent and the surrounding oceanic regions exist [e.g., *Grossman and Garcia*, 1990; *Gambheer and Bhat*, 2000; *Rajeevan and Srinivasan*, 2000; *Roca et al.*, 2002; *Zuidema*, 2003; *Sathiyamoorthy et al.*, 2004]. Furthermore, quantitative estimates of the cloud top altitudes and studies of the influence of deep clouds on the tropical tropopause layer over this intense convective region are rather sparse. The main objective of the present study is to fill this gap.

[5] This study focuses on the annual variation in the monthly mean regional distribution of deep clouds and the vertical distribution of cloud top altitudes over the Indian subcontinent and the surrounding oceanic regions. The distribution of cloud top altitude inferred from long-term cloud top brightness temperature data are compared with the more reliable direct observations of cloud top altitude using Cloud-Aerosol Lidar and Infrared Pathfinder Satellite Observation (CALIPSO). The role of deep clouds in the annual variations in tropospheric temperature and the characteristics of the tropical tropopause layer are investigated. Though the diurnal variation of cloud occurrence is also important over the tropical oceans, this aspect is not considered in the present study.

2. Data and Method of Analysis

[6] Monthly mean regional distributions of the frequency of occurrence of high-altitude clouds and the corresponding cloud top brightness temperatures (CTBT) for a period of 10 years between 1996 and 2007 (except for a 17-month period of January 2004 to May 2005) are obtained by analyzing National Oceanics and Atmospheric Administration (NOAA) 14–, 16–, and 18–Advanced Very High Resolution Radiometer (AVHRR) level 1b global area coverage (GAC) data of the afternoon satellite passes in the geographical region between 30°S to 30°N in latitude and 40°E to 100°E in longitude. Characteristics of the AVHRR sensor and the method of processing the data are given in the NOAA *Polar Orbiter User's Guide* (http://www2.ncdc.noaa.gov/docs/intro.htm). The pixel resolution of AVHRR is about 4 km at nadir. The method for the detection of clouds from the AVHRR data employed in this study are similar to those described by *Meenu et al.* [2007]. High-altitude clouds are identified using the threshold method applied to the brightness temperature (BT) from channel 4 (wavelength band of 10.30–11.30 μm). This is quite adequate to detect all the cloud-filled pixels containing high-altitude clouds, which is the focus of the present study. The pixels having BT < 245 K are considered to contain high-altitude clouds. Those pixels with BT < 235 K and BT < 210 K are further divided into deep and very deep clouds, respectively. These threshold temperatures for the classification of the deep and very deep clouds are similar to those generally used in the literature [*Mapes and Houze*, 1993; *Zuidema*, 2003]. The fraction of high-altitude, deep, and very deep clouds together with their corresponding values of CTBT derived from the pixel-level satellite data are grouped into a uniform geographical grid of size 0.25° × 0.25° on a daily basis, which form the basic data for this study. The fraction of high-altitude, deep and very deep clouds (F_h, F_d, and F_v, respectively) at each grid point are obtained by dividing the number of pixels containing the respective cloud types by the total number of pixels in the grid box. The monthly mean cloud fraction of each cloud type is obtained by averaging the respective daily mean cloud fraction in that month.

[7] The Cloud-Aerosol Lidar with Orthogonal Polarization (CALIOP) onboard the CALIPSO [*Winker et al.*, 2007] provides the vertical profiles of the total backscatter in two wavelengths (532 and 1064 nm) and linear depolarization at 532 nm from a near-nadir viewing geometry. From these data, the aerosol and cloud profiles can be derived. The CALIOP inversion method, feature detection, determination of layer properties, and the associated uncertainties are given in detail in the CALIOP algorithm theoretical basis document [*Vaughan et al.*, 2005]. The CALIPSO level 2 cloud layer product, which contains information on the properties of cloud layers gridded at 5 km horizontal resolution (along the satellite track), is used in the present study. However, the diameter of the transmitted laser beam is about 70 m at the Earth's surface, which is the horizontal resolution of the Lidar data perpendicular to the satellite track. The altitude resolution of the lidar data is 30 m and 60 m in the altitude regions of 0–8.2 km and 8.2–20.2 km, respectively. The CALIPSO level 2 cloud layer product provides the geodetic latitude and longitude, number of cloud layers identified within each grid, layer optical properties, layer top and base altitudes, and a cloud-aerosol discrimination (CAD) score. The CAD score is an indicator of the confidence in the layer classification. Only those layers having a CAD score in the range of 80–100 are used in the present study. Owing to attenuation of the backscattered signal, detection of lower layers in a multilayer scene becomes difficult with increasing optical depth of the layers above. Similarly, detection of cloud base is complicated when the cloud optical depth is very large. We concentrate here on the cloud top altitude (CTA) of the topmost cloud layer obtained from CALIPSO, which is a highly reliable parameter in comparison with the derived optical properties. In order to avoid semitransparent cirrus clouds and to focus on the convectively produced clouds (which may also include convectively produced anvils), only those cloud layers having cloud optical depth (COD) more than 2.5 are considered in the present study.

[8] The NOAA-AVHRR provides data over the entire region every day, while the CALIPSO observations are confined to a vertical cross-sectional view along the subsatellite track. The longitudinal coverage of CALIPSO observation is rather limited since the equatorial crossing longitudes of two consecutive orbits are separated by about 25°. Furthermore, the CALIPSO observations are available only from June 2006. Owing to these reasons, the AVHRR

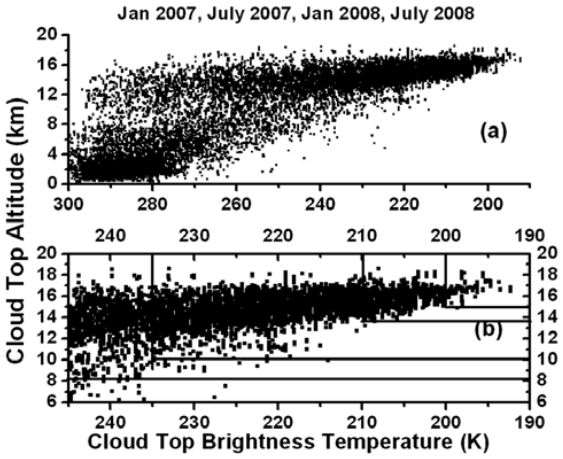

Figure 1. (a) Scatterplot of cloud top altitude (CTA) observed from Cloud-Aerosol Lidar and Infrared Pathfinder Satellite Observation with the corresponding cloud top brightness temperature (CTBT) observed from the Advanced Very High Resolution Radiometer during July and January 2007 and 2008. (b) Enlarged version of Figure 1a for CTBT < 245 K and CTA > 6 km.

data are mainly used to study the long-term climatology of cloud top distribution, while the results obtained from AVHRR are intercompared with direct observations of CTA using CALIPSO.

3. Results

[9] In order to find a relationship between the cloud top altitude and the cloud top brightness temperature, the values of CTA for the top layer cloud (with COD > 2.5) observed by CALIPSO are compared with the corresponding colocated values of CTBT observed by AVHRR. Figure 1a shows a scatterplot of CTA and the corresponding CTBT during the July and January months of 2007 and 2008. Figure 1b is an enlarged version of Figure 1a for CTBT < 245 K and CTA > 6 km. Considerable scatter is seen in Figure 1, with a wide range of values of CTBT associated with a given value of CTA and vice versa. The data separated into different regions or individual months also showed similar scatter. The spatial resolution of the AVHRR pixel (GAC data) is 4 km at nadir (and increases with the satellite zenith angle of the pixel), while that of the CALIPSO level 2 cloud layer product (which has only near-nadir view and gridded at 5 km resolution) is about 70 m × 5 km. Thus the fine features of the clouds will be better resolved by CALIPSO, while AVHRR pixel provides an integrated picture over a significantly larger area. For those clouds having spatial extent much less than the size of an AVHRR pixel, there will be a significant difference in the cloud characteristics derived from CALIPSO and AVHRR. It would be worth in this context to note that deep convective towers can have horizontal scales less than 10 km [*Fujita*, 1992]. Furthermore, the differences in the orbital characteristics and the viewing geometry of NOAA18-AVHRR and CALIPSO can produce a time difference (0 to 50 min) between spatially colocated observations of CTBT and CTA. Part of the scatter seen in Figure 1 could be attributed to these differences in the spatial resolutions and the difference in the time of the two observations. In addition, semitransparent cirrus clouds also might contribute to the observed scatter, since such clouds allow the infrared radiation emitted by the Earth's surface or lower-layer clouds to pass through and thereby increase the brightness temperature observed by the satellite [e.g., *Rajeev et al.*, 2008]. Relationship between the infrared brightness temperature and the cloud top altitude is influenced by several factors including within-pixel cloud heterogeneity, finite cloud emissivity, IR scattering, differences in visible extinction and IR absorption cross sections, nonlinear emission profile, cloud-environment temperature differences, and stray light in the infrared optics [*Sherwood et al.*, 2004]. For optically thick ice clouds with visible band cloud optical depth greater than 8, *Minnis et al.* [2008] showed a more robust relationship between cloud top altitude (derived from the CALIPSO data) and infrared effective radiating height (derived from the Moderate-Resolution Imaging Spectroradiometer having a spatial resolution of 1 km). Significantly large scatter observed in Figure 1 compared to that reported by *Minnis et al.* [2008] might be mainly contributed by coarser resolution of AVHRR pixels and semitransparency of clouds. (Note that Figure 1 represents clouds with visible band cloud optical depth greater than 2.5). It is highly probable that, at a given altitude, the low values of CTBT represent optically thick clouds with large spatial extent (at least for those completely filling the AVHRR pixel) while those with higher values of CTBT represent the clouds which do not completely fill the AVHRR pixel or that are semitransparent. Owing to the large scatter of points in Figure 1, a regression relationship between CTBT and CTA is not reliable. Nevertheless, the following features are clearly seen in Figures 1a and 1b: (1) for all the pixels with CTBT < 210 K the value of CTA is > 13.5 km and for those with CTBT < 200 K the value of CTA > 15 km and (2) for more than 95% of the pixels with CTBT < 235 K, the value of CTA is > 10 km and for those with CTBT < 245 K the value of CTA is > 8 km. These conclusions are found to be valid even when the data are analyzed after separating them into different seasons or regions. Thus, the high-altitude, deep and very deep clouds classified using the AVHRR have cloud top altitudes >8, >10, and >13.5 km, respectively.

[10] The long-term (1996–2007) monthly mean regional distributions of the high-altitude cloud fraction (F_h) over the study region obtained from the AVHRR data are shown in Figure 2. High values of F_h (~20%–40%) observed during January to March are closely associated with the ITCZ, which is manifested (in Figure 2) as a longitudinally extended and latitudinally confined band (latitudinal width ~10°) of high-altitude clouds around 10°S over the western tropical Indian Ocean and around the equator over the eastern Indian Ocean. During this period, the value of F_h is lowest (<5%) in the latitude band of 10°N–20°N (over the Arabian Sea, the Indian landmass, and the Bay of Bengal) and poleward of ~20°S over the eastern Indian Ocean. By April–May, as the ITCZ moves northward, F_h generally increases over a wide latitudinal band on both sides of the

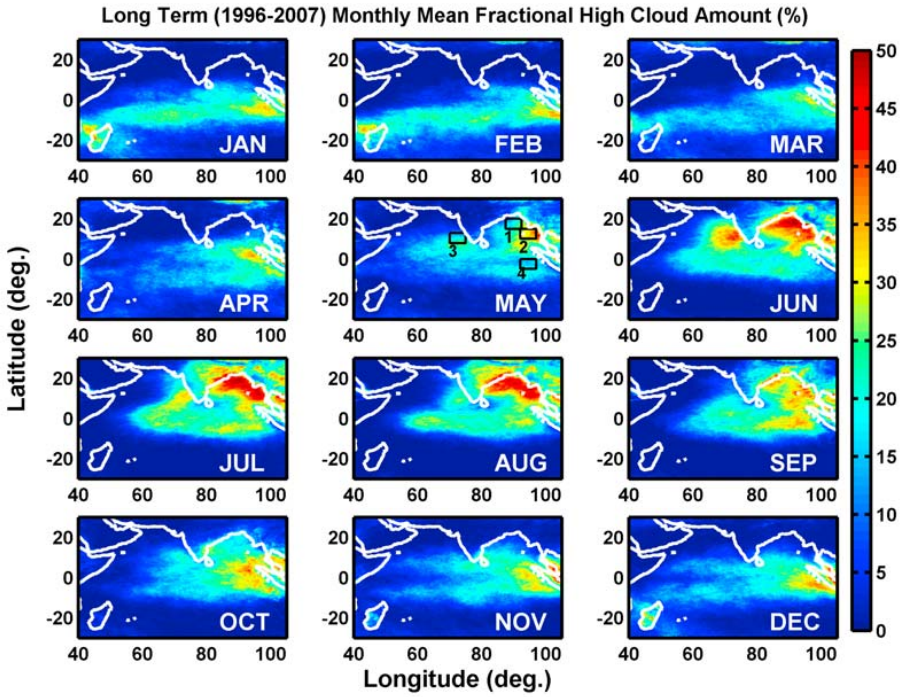

Figure 2. Annual cycle of the long-term (1996–2007) monthly mean spatial distribution of the high-altitude cloud fraction (expressed in percentage). The boxes shown for the month of May, numbered 1, 2, 3, and 4, represent the geographical regions of northern Bay of Bengal (NBoB), eastern Bay of Bengal (EBoB), southeast Arabian Sea (SEAS), and east equatorial Indian Ocean (EEIO), respectively.

equator in the eastern parts of the equatorial Indian Ocean. In May, F_h increases considerably over the southeast Arabian Sea and the Bay of Bengal. Climatologically, the Asian summer monsoon reaches the southern Arabian Sea and the Bay of Bengal by the end of May. Figure 2 shows that the spatial distributions of F_h are somewhat similar for all the months during the Asian summer monsoon season (June–September). The high-altitude cloud fraction during this period is larger over the oceanic regions close to the Indian landmass, while it is significantly smaller over the western Arabian Sea and the South Indian Ocean. The highest value of F_h during the Asian summer monsoon season is observed over the northern and eastern Bay of Bengal (NBoB and EBoB, respectively), followed by the southeast Arabian Sea (SEAS). Strong land-sea contrast is observed in the high-altitude cloud fraction over NBoB, EBoB, and SEAS during the Asian summer monsoon season. Temporal variation of F_h over the eastern equatorial Indian Ocean is significantly different from that over the Arabian Sea and the Bay of Bengal. Two bands of enhanced high-altitude cloud fraction appear between the 5°–10° latitude on either side of the equator during November and December, which is attributed to the manifestation of the double ITCZ [*Meenu et al.*, 2007].

[11] On the basis of the above analysis, four regions (with a spatial extent of 5° × 5°) which show significantly large high-altitude cloud fraction are identified for further analysis. They are (1) NBoB, 15°N–20°N, 87.5°E–92.5°E; (2) EBoB, 10°N–15°N, 92°E–97°E; (3) SEAS, 8°N–13°N, 70°E–75°E; and (4) east equatorial Indian Ocean (EEIO), 5°S–0°, 92°E–97°E. These regions are shown in Figure 2 (month of May). The most probable altitude of the cloud top over each region is investigated using the monthly mean frequency distribution of CTBT obtained from the daily AVHRR data. Figure 3 shows the long-term (1996–2007) average of the monthly mean histograms of CTBT (for CTBT < 260 K, at an interval of 3 K) over each of the above regions during January–December. Since the cloud fraction varies considerably over space and time (Figure 2) and the present study is focused only on the structure of the histogram to identify the preferred CTBT, each histogram is normalized with respect to the histogram mode for a given month.

[12] In general, low values of CTBT represent higher cloud top altitudes (Figure 1). Figure 3 shows that over NBoB, EBoB, and SEAS, the probability of occurrence decreases monotonically with decrease in CTBT during January–March. In April, over EBoB, the frequency of occurrence of CTBT around 220 K is high as indicated by a crest in the histogram. Similar crests are seen over NBoB, EBoB, and SEAS in May. By June, prominent crests appear around 200–225 K in the histograms of CTBT in all the above regions. This feature is very pronounced during July–August and starts diminishing from September onward. Over EEIO, the crest is present throughout the year and is more prominent during the September–January period.

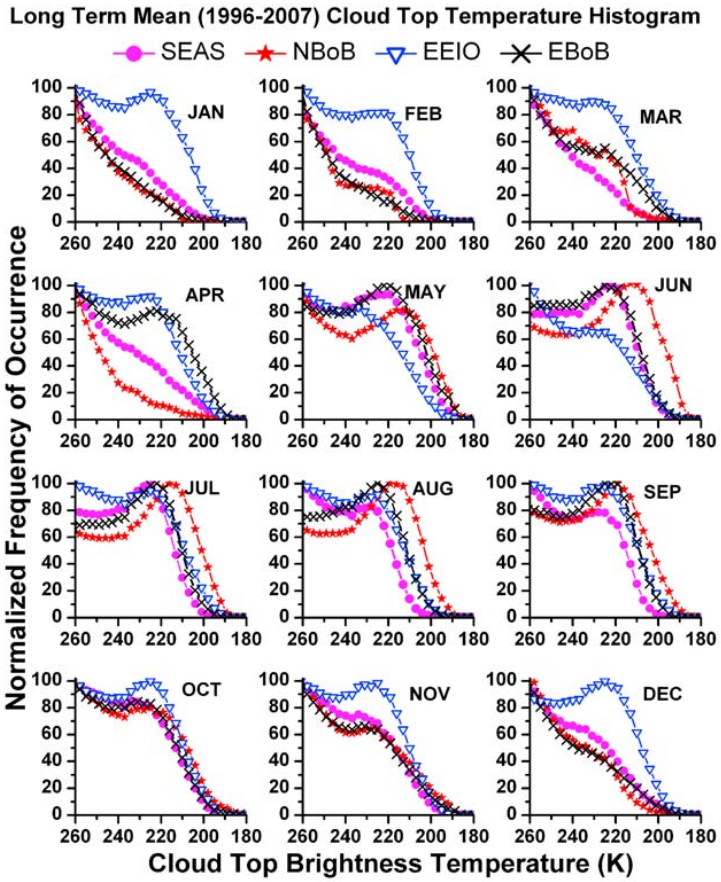

Figure 3. Long-term (1996–2007) average monthly mean normalized histograms of the cloud top temperature observed over selected deep convective regions: NBoB, EBoB, SEAS, and EEIO.

[13] The most notable feature in Figure 3 is that the crest in the histogram observed during the June–August period over NBoB is around 210 K while it is around 220–225 K over EBoB and SEAS. Furthermore, during this period, the frequency of occurrence of clouds with CTBT < 210 K is significantly higher over NBoB than over the other regions. Over EEIO, the most probable occurrence of CTBT in the upper troposphere is around 220–225 K throughout the year. Thus the most probable value of CTBT in the upper troposphere over NBoB during the June to August period is ~12 K lower than that over the other regions. As seen in the NCEP reanalysis, during this period the spatial variation in the upper tropospheric temperature is very small (<5 K) in these regions. Under the assumption that the cloud emissivity does not deviate significantly over the regions considered here, the above observations suggest that among the Indian subcontinent and the surrounding oceanic regions (including the EEIO), the most probable cloud top altitude is the highest over the NBoB region, and is at least 1 km above that over the rest of the regions.

[14] Direct measurements of CTA over these regions using CALIPSO during July 2006–December 2007 are used to check and ascertain the accuracy of the above inferences derived from the climatological mean CTBT. Figure 4 shows the histogram of the regional mean cloud top altitude over NBoB, EBoB, SEAS, and EEIO averaged for the 2006–2007 period during months of July (representing the Asian summer monsoon) and December (representing the Northern Hemisphere winter). For a direct comparison, the histograms of CTBT for the corresponding periods are also presented in Figure 4. It is important to note that the observations of CTA obtained from CALIPSO are very accurate (within 60 m in the altitude interval between 8.2 and 20.2 km), while the values of CTBT obtained from AVHRR depend on several cloud parameters (such as cloud optical depth, cloud fraction within the pixel, and cloud emissivity). The overall structure of these histograms of CTA is similar to those of CTBT. In July, over NBoB, CTA shows a prominent peak around 16.5–17.5 km, while over EBOB, SEAS, and EEIO the peak in the histogram is down by ~1 km (at ~15.5 km). In December, the frequency of occurrence of deep clouds is the highest over EEIO where the peak in the histogram appears between 15.5 and 16.5 km. On average, the peak in the histogram of CTA over

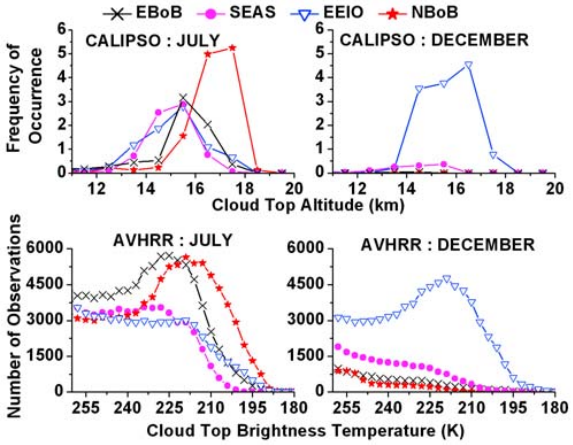

Figure 4. (top) Mean frequency of occurrence of the CTA over NBoB, EBoB, SEAS, and EEIO during July and December (2006–2007 average). (bottom) Histograms of the CTBT over NBoB, EBoB, SEAS, and EEIO for the corresponding periods (2006–2007 average).

EEIO in December is lower than that in the corresponding histogram over NBoB in July by ~1 km. This confirms the inference derived from the analysis of CTBT that the mean cloud top altitude is the highest over NBOB during June–August, which is >1 km above that over the other regions during any season.

[15] The long-term monthly mean variations of the fraction of high-altitude, deep and very deep clouds averaged over NBoB, EBoB, SEAS, and EEIO are shown in Figure 5. The cloud fraction with CTBT < 200 K (referred hereafter as the cloud fraction of near-tropopause clouds, F_{tp}) is also shown in Figure 5. As seen from Figure 1, F_{tp} represents the clouds with CTA > 15 km, and hence it is generally < 2.5 km below the cold point tropopause in this region. Figure 5 shows that, over NBoB, the deep and very deep clouds are present mainly during the May–November period. The peak cloud fraction over NBoB occurs during the June–August period (when F_d is about 35%–40% and F_v is 10%–13%). Over EBoB, the deep cloud fraction shows a broad peak from May to September, with a value of F_d in the range 25%–35% and F_v in the range 7%–10%. Over SEAS, deep clouds are mainly present during the May–December period, with a maximum cloud fraction occurring in June (F_d is ~26%). However, the fraction of very deep clouds over SEAS is <5% even in June. Seasonal variation of the deep and very deep cloud fractions is less pronounced over EEIO. In this region, the value of F_d is the largest during September–January (F_d ~ 22%) and the lowest during May–June (F_d ~ 14%). Though the very deep clouds prevail in this region throughout the year, its fraction is always <5%. This shows that, during the June–August period, fractions of the deep and very deep clouds over NBoB are more or less comparable to that over EBoB. These cloud fractions are about 40% and 100% larger than the highest values of the respective cloud fractions observed over the other regions in any season. Remarkably, the value of F_{tp} (i.e., clouds with CTA > 15 km) is significant (~5%) only over the NBoB region during June–July. This is significantly more than the value of F_{tp} observed over EBoB where the values of F_d and F_v are almost comparable to that over NBoB.

[16] Earlier studies, however, showed that the sea surface temperature (SST) in excess of a critical threshold value of ~27.5°C is required for the occurrence of large-scale deep convection [*Graham and Barnett*, 1987]. In those regions where sea surface temperature (SST) exceeds this critical value, surface moisture convergence is closely associated with the presence of deep convection [*Fu et al.*, 1990; *Zhang*, 1993]. Climatologically, over the Bay of Bengal, SST is >28°C during April–October and is <27°C during December–February, while the SST is >27.5°C over EEIO and SEAS almost throughout the year. This shows that SST is favorable for the formation of deep convection over all the regions considered here, except over the Bay of Bengal from December to February. The fractions of high-altitude and deep convective clouds are insignificant over the Bay of Bengal during the December–February period, when SST is <27°C. Though the deep clouds occur over the warm SST regions, the fraction of deep clouds is not directly proportional to the SST. This is in agreement with the earlier observations, which suggested that, over the Indian Ocean, the intensity of convection is rather insensitive to increase in SST above ~27.5°C [*Gadgil et al.*, 1984; *Graham and Barnett*, 1987]. Over the warm regions with SST > 27.5°C, as the top altitude of deep clouds are poorly correlated with SST, the additional mechanism responsible for the highest cloud top altitude in the NBoB is examined based on the dynamics of the troposphere. Figure 6 shows the altitude profiles of the monthly mean divergence of horizontal wind in the troposphere over NBoB, EBoB, SEAS, and EEIO in July (for the period of 1996–2007) obtained from the NCEP reanalysis [*Kalnay et al.*, 1996]. A convergence in the

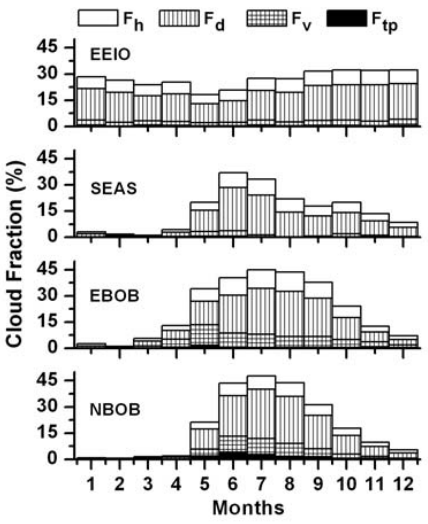

Figure 5. Long-term (1996–2007) average monthly mean fraction of high-altitude (F_h), deep (F_d), very deep (F_v), and near-tropopause (F_{tp}) clouds over NBoB, EBoB, SEAS, and EEIO.

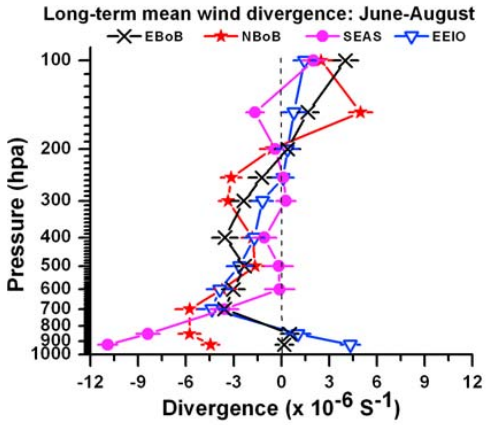

Figure 6. Altitude profiles of the long-term (1996–2007) seasonal mean divergence of horizontal wind over NBoB, EBoB, SEAS, and EEIO during the June–August period.

horizontal wind between the surface and ~250–200 hpa level is observed in all these regions, which is very crucial for driving the deep convection. On average, the wind convergence is stronger in the NBoB region, though it is not appreciably larger than the other regions. The upper tropospheric divergence, which is very strong over NBoB, further aids the convection from below. This, together with the favorable range of SST (typically around 28.5°C–29.5°C) leads to large convergence (and accumulation of waver vapor) between the surface and ~200 hpa level, and might be mainly responsible for the formation of deep convection over NBoB. The upstream orographic lifting of air also could be crucial for the highest cloud top altitude observed over this region during the June–August period [*Grossman and Garcia*, 1990].

[17] Net cloud radiative forcing and the latent heat release during cloud formation can influence the tropospheric temperature. This in turn can influence the characteristics of the tropical tropopause layer [*Gettelman and de F. Forster*, 2002]. Figure 7 shows the long-term (1996–2007) month-altitude cross sections of the deviations (dT) of the monthly mean temperature from the annual mean temperature over NBoB, EBoB, SEAS, and EEIO. This is obtained from the NCEP Reanalysis data by subtracting the annual mean altitude profile of temperature over each region from the monthly mean temperature profiles over that region. The altitude of the monthly mean cold point tropopause (averaged for 2002–2008) obtained from the GPS radio occultation observations (details presented in the following section) are also shown in Figure 7 for delineating the troposphere and stratosphere. Over the NBoB region, the annual variation in dT in the upper troposphere is generally large. Maximum variation is observed between 400 hpa and 200 hpa levels, where its value varies from about −2.5 K during January–March to 3 K during June–August. Similar annual variations in dT are observed in the upper troposphere over EBoB and SEAS also, even though the amplitude of these variations are relatively small. Note that the annual variation in dT over all these regions are in phase with the corresponding annual variation in the deep cloud fraction over the respective regions (Figures 2 and 5). The range of the annual variation in dT in the upper troposphere is closely associated with the corresponding range in the deep cloud fraction over the respective regions. It is largest over NBoB, which is followed by EBoB and SEAS, respectively. Over EEIO, the amplitudes of the annual variations in dT and the deep cloud fraction are considerably smaller and are less correlated. Another notable feature in Figure 7 is the prominent annual variation (~6 K) in the lower stratospheric temperature (above ~80 hpa level), the phase of which is remarkably the same over all the regions (with the maximum occurring in the July–September period). Annual variations of the lower stratospheric temperature and the altitude of the cold point tropopause have opposite phases over all the regions (Figure 7). Temperature of the lower stratosphere is determined by a balance between the adiabatic cooling produced by the upward movement of air parcels near and above the tropopause and the net radiative heating of the atmosphere. The annual variation in the lower stratospheric temperature is mainly produced by the corresponding variation in the upward movement of air parcels near and above the tropopause (and the adiabatic cooling) and has an opposite phase relation with the cold point tropopause throughout the tropics [*Reid and Gage*, 1981].

[18] The tropical tropopause layer is the region where convection overshoots the level of neutral buoyancy [*Sherwood and Dessler*, 2001]. The influence of the deep clouds on the TTL characteristics is investigated here. The level of minimum potential temperature lapse rate is a good indicator for the maximum influence of convection [*Gettelman and de F. Forster*, 2002] and hence the base of TTL. The altitude of the cold point tropopause (H_{CPT}) is the upper boundary of TTL. The altitude profiles of temperature derived from the GPS radio occultation (GPSRO) data from the CHAMP [*Hajj*

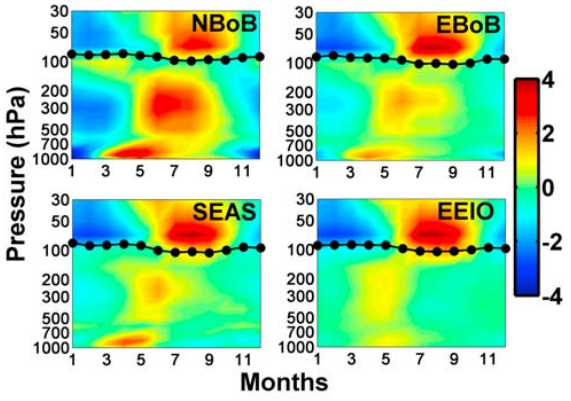

Figure 7. Month-altitude cross sections of the temperature differences (dT) obtained from National Centers for Environmental Prediction reanalysis data by subtracting the annual mean temperature profile from the monthly mean temperature profiles over NBoB, EBoB, SEAS, and EEIO. Filled circles show the monthly mean cold-point tropopause level obtained from the GPS radio occultation observations.

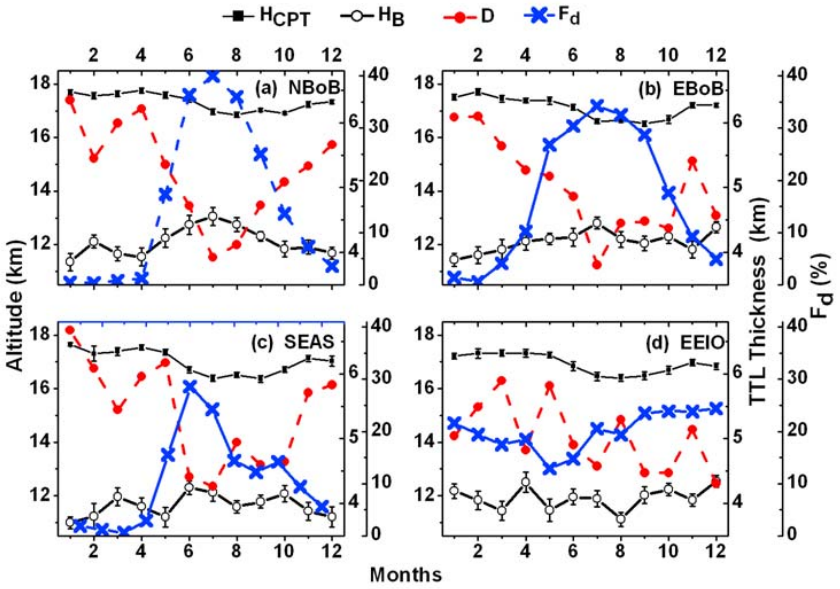

Figure 8. Long-term (2002–2008) monthly mean variations of H_{CPT}, H_B, tropical tropopause layer (TTL) thickness, and the deep cloud fraction (F_d) over (a) NBoB, (b) EBoB, (c) SEAS, and (d) EEIO. The vertical bars (in H_{CPT}, H_B) indicate the standard errors. The y axes on the left-hand side represent H_{CPT}, H_B. The first y axes on the right-hand side correspond to the TTL thickness, and the second y axes on right-hand side correspond to F_d.

et al., 2004] and COSMIC [*Wang and Lin*, 2007] satellites provide a fairly good vertical resolution (the gridded data resolution is 100 m) for deriving the TTL characteristics very accurately, even though the frequency of GPSRO observation is rather low compared to the NCEP reanalysis data. A description of the GPSRO technique for deriving the atmospheric temperature, the long-term stability of the data and the sources of errors are summarized elsewhere [e.g., *Kuo et al.*, 2004]. The overall accuracy of the temperature derived from GPSRO is comparable to or better than those obtained from radiosonde [*Kuo et al.*, 2005]. The temperature profiles obtained from the CHAMP data during 2002–2008 and COSMIC data during 2006–2008 are used in the present study. The base of TTL (H_B) is identified from the individual temperature profiles as the altitude level at which the potential temperature lapse rate is a minimum (H_{LRM}) and is less than 5 K/km [*Mehta et al.*, 2008]. When multiple minima are seen in the potential temperature lapse rate, the first minimum below the cold point tropopause is considered as the base of TTL.

[19] Figure 8 shows the monthly mean variations in H_{CPT}, H_B and the TTL thickness ($D = H_{CPT} - H_B$) over NBoB, EBoB, SEAS, and EEIO for the period 2002–2008. The vertical bars indicate the standard error. The mean standard errors of H_{CPT}, H_B, and TTL thickness are 0.11 km, 0.29 km, and 0.31 km, respectively. The monthly variations in the deep cloud fraction (F_d) over each region are also presented in Figure 8 for a direct comparison. Overall, H_{CPT} shows a broad maximum during January–March and minimum during July–September over all these locations. The annual mean value of H_{CPT} averaged for all these regions is 17.07 ± 0.82 km, which is very close to the climatological annual mean value of 16.9 km reported by *Seidel et al.* [2001] over the tropics. The average range of the annual variation in H_{CPT} is 1.07 km. The amplitude and phase of the annual variation in H_{CPT} is in agreement with the earlier observations over tropics reported in the literature [e.g., *Reid and Gage*, 1981; *Seidel et al.*, 2001; *Gettelman and de F. Forster*, 2002; *Mehta et al.*, 2008]. The values of H_B and TTL thickness averaged over NBoB, EBoB, SEAS and EEIO are 11.92±0.91 km, and 5.15±1.21 km, respectively, and are comparable to the corresponding values reported over the other tropical stations [*Gettelman and de F. Forster*, 2002; *Mehta et al.*, 2008]. Unlike H_{CPT}, the phase of the annual variation in H_B, which is highly coherent with the corresponding variation of F_d, varies from one region to the other. Over NBoB, H_B varies between 11.3 km and 13.0 km, with its minimum occurring during the December–April period and maximum during the June–August period. Over EBoB and SEAS, the annual variation of H_B is somewhat similar to that over NBoB, though the range of the variation is rather small (1.37 and 1.30 km over EBoB and SEAS, respectively). Over SEAS, the largest values of both H_B and F_d are observed in June, while over NBoB and EBoB their peak values are observed in July. Over EEIO, the deep cloud fraction is large throughout the year and the annual variations in H_B and F_d are considerably small and less correlated. The influence of the deep clouds in pushing up the H_B is more pronounced over NBoB, where F_d shows maximum annual variation, which is followed by EBOB and SEAS. The value of H_B over NBoB is larger than that over the other regions during the June–August period. The TTL

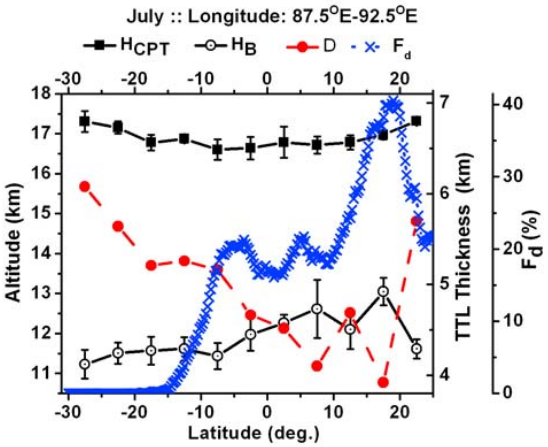

Figure 9. Latitude variations of H_{CPT}, H_B, TTL thickness, and F_d in the longitude band of 87.5°E–92.5°E in July. The vertical bars indicate the corresponding standard errors.

thickness is generally small during the June–September period over all these regions. The lowest value (~3.8 km) of TTL is encountered in July and the highest (~6.5 km) value in January over NBoB and EBoB. The nearly out-of-phase annual variations of H_{CPT} and H_B over the Arabian Sea and the Bay of Bengal increase the range of the variation in the TTL thickness. Over NBoB, where the annual variation in the TTL thickness is ~2.7 km, the corresponding variation in H_B is only ~1.7 km. Over EEIO, the annual variation in the thickness of TTL is mainly governed by the corresponding variation in H_{CPT}.

[20] Over NBoB, the value of H_{CPT} is comparable to that over the other regions during November–March, but is distinctly high during the June–September period compared to that over EBoB, SEAS and EEIO by 0.34, 0.58, and 0.53 km, respectively. Thus the large-scale deep convection also plays a role in increasing the altitude of H_{CPT} by around 300–500 m, as is observed during the June–September period over NBoB, when the deep cloud fraction is the largest. During the June–August period, the value of H_{CPT} over EBoB is less than that over NBoB by ~340 m, but more than that over SEAS by ~240 m. Note that during this period F_d is the largest over NBoB, which is followed by EBoB and SEAS. This also points to the potential influence of the deep clouds in modulating H_{CPT}.

[21] Influence of deep clouds on TTL characteristics are further investigated by analyzing the latitude variations of H_{CPT}, H_B, TTL thickness and F_d in the longitude band of 87.5°E–92.5°E (same as that of the NBoB longitude) during July, the results of which are presented in Figure 9. This longitude band and the period of the year are selected based on the fact that the largest latitude variation of the high-altitude cloud fraction is observed in this region in the month of July (Figure 2). The vertical bars indicate the standard error. The average standard error in H_{CPT} is 0.20 km and that of H_B is 0.36 km. The value of H_B is 13.05 km at 17.5°N which is ~1.5 km larger than the mean value of H_B observed between 7.5°S and 27.5°S. Correspondingly, the thickness of TTL decreases from a mean value of ~5.5 km between 7.5°S and 27.5°S to 3.9 km at 17.5°N. The value of H_B increases significantly only at the north of 7.5°S and is clearly associated with the increase in F_d. The decrease in the values of H_B and F_d north of 17.5°N are also notable in Figure 9. This further confirms that the increase in H_B and decrease in the TTL thickness are significantly influenced by the increase in F_d.

4. Discussion

[22] The spatiotemporal variations of the deep clouds observed in the present study are in agreement with that reported from the highly reflective cloud data set [*Grossman and Garcia*, 1990]. In the tropical region, the high-altitude clouds mainly prevail over the ITCZ, the South Pacific Convergence Zone (SPCZ), the Indian Ocean, and the tropical regions of Africa and America [*Hong et al.*, 2007]. CloudSat observations reveal that, during June–August, the occurrence of high-altitude clouds in the Indian region and the western Pacific Ocean is significantly more frequent compared to other regions, with a distinct peak around 12–15 km in its altitude of occurrence [*Haynes and Stephens*, 2007]. The present study shows that, among the Indian subcontinent and the adjoining oceans, the deepest clouds are observed over the northern Bay of Bengal region during the June–August period with a mean cloud top altitude which is ~1 km larger than that over the other regions.

[23] A 6-year climatology of the global vertical distributions of the thin cirrus clouds presented by *Wang et al.* [1996] showed that the eastern equatorial Indian Ocean, the Bay of Bengal, and the western equatorial Pacific are among those regions where the frequency of occurrence of thin cirrus clouds is very high. Over the Indian region, the maximum cloud occurrence is found during the June–August period. However, it is important to note that these observations based on solar occultation are biased toward clouds having very low optical depth. Even then, the overall characteristics of the distribution and the spatiotemporal variability of cirrus clouds reported by *Wang et al.* [1996] are in agreement with the corresponding variations of high-altitude clouds observed in the present study. Moreover, the lidar observations of cirrus clouds from a tropical location, Gadanki (13.5°N, 79.2°E), near the east coast of the peninsular India also revealed a high frequency of occurrence of cirrus, especially thicker ones, during the Asian summer monsoon period [*Sunilkumar et al.*, 2003]. The occurrence of the largest fraction of cirrus clouds in the 15.5–17.5 km altitude region over the north Bay of Bengal and the adjoining Indian landmass during June–August reported by *Wang et al.* [1996] as well as that revealed from the lidar observations from the Indian subcontinent are in good agreement with the distribution of the deep and very deep clouds observed in the present study, suggesting that the sources of both these cloud types could be similar. This inference is also supported by *Rajeev et al.* [2008], who showed that thin semitransparent cirrus clouds observed over the Indian subcontinent are mainly originating from deep convective outflows.

[24] *Zuidema* [2003] noted that the eastern Bay of Bengal experiences most rainfall from frequent convective systems which are relatively small and short-lived, while the convective activity over northwestern Bay of Bengal is more

organized into much larger and longer-lived systems. *Rossow and Pearl* [2007] observed that deep penetrating convection originate predominantly from the large organized convective systems. These studies also support the present observations showing the greater dominance of deep and very deep clouds over NBoB compared to the other regions.

[25] The level of maximum upper tropospheric divergence (Figure 6) is almost same as the altitude of the minimum potential temperature lapse rate (Figure 8). This implies that the level of the minimum potential temperature lapse rate is closely associated with the level of the major convective outflow. *Mehta et al.* [2008] showed that the altitude of prominent convective outflow obtained from the radar (the convective tropopause) and that of minimum potential temperature lapse rate match well with a rms difference of 1.14 km. The outbreak of deep convection is accompanied by diabatic heating below ~150–200 hpa (and by diabatic cooling at higher levels) which serves as a heat source for the environment below the level of neutral buoyancy (heat sink at higher levels) [*Salby et al.*, 2003]. The present study shows that, over the Bay of Bengal and the Arabian Sea, the annual variation in the upper tropospheric temperature below ~150 hpa level is mainly associated with the heating of the atmosphere by the deep clouds. This will have significant impact on the thermal structure of the upper troposphere and the Hadley circulation.

[26] The altitude of the cold point tropopause depends on the heating of the stratosphere internally by the direct absorption of solar radiation and the net heating of the troposphere from below by the Earth's surface. *Reid and Gage* [1981] showed that the annual variation in the tropical tropopause is a direct response to the annual variation in the average surface insolation, which produces an annual variation in the sea surface temperature. The SST variation produces a corresponding variation in the absolute humidity, latent heat release and the upper tropospheric potential temperature. Over the tropics, the upper tropospheric potential temperature generally maximizes around March [*Krishna Murthy et al.*, 1986], thus producing a high tropopause altitude during this period. The annual variation in the latent heat release produces a corresponding variation in the upward velocity of the air parcels near the tropopause and the lower stratosphere. The phase of the annual variation of temperature in the lower stratosphere is opposite to that of the temperature variation in the tropopause. This is due to the fact that the mechanisms responsible for the maximum tropopause potential temperature (i.e., SST and moisture content in the tropics) consequently produce a maximum in the buoyancy forces and hence the adiabatic cooling of the lower stratosphere, which leads to a minimum in the lower stratospheric potential temperature [*Reid and Gage*, 1981]. This explains the consistency in the phase of the annual variation observed in the lower stratospheric temperature over all the regions considered in the present study (Figure 7) and its out-of-phase relationship with the cold point tropopause altitude (Figures 7 and 8).

[27] The present study shows an in-phase relationship between the deep cloud fraction and the base altitude of TTL over NBoB, EBoB, and SEAS, where the annual variation in the deep cloud fraction is quite significant. Among the Indian subcontinent and the surrounding oceanic regions, the mean base altitude of TTL is the highest (13 km) over NBoB during July, which is also closely associated with the largest deep cloud fraction and the highest cloud top altitude in this region. This is in agreement with *Gettelman and de F. Forster* [2002] who showed that the potential temperature at the altitude of minimum potential temperature lapse rate over the North Bay of Bengal in July is about 356 K, which is the highest value observed at any particular location over the globe. The altitudes of the base and top of TTL over the Bay of Bengal and the Arabian Sea show nearly out-of-phase variations. This results in the amplification of the annual variation of TTL thickness over these regions, with a minimum value (3.8 km) during the Asian summer monsoon season and a maximum value (~6 km) during the northern hemispheric winter.

5. Conclusions

[28] Spatial distributions of the high-altitude, deep and very deep clouds over the Indian subcontinent and the surrounding oceanic regions are derived from the pixel-level brightness temperature measured by AVHRR on board the NOAA satellites. The vertical distribution and the preferential altitude of cloud top are inferred based on a histogram analysis of the cloud top brightness temperature. This is further ascertained by comparing it with the direct observations of cloud top altitude (of optically thick clouds) from the CALIPSO data. This study shows that the deepest clouds over the entire region occur over the northern Bay of Bengal during June–August, where the cloud top brightness temperature is about 12 K lower than the coldest cloud top brightness temperature over the other deep convective regions in the Bay of Bengal, the Arabian Sea and the Indian Ocean in any season. The CALIPSO measurements also show that the frequency of occurrence of the cloud top altitude peaks at about 16.5 km over the northern Bay of Bengal, which is ~1 km higher than that over the other regions. Over the northern Bay of Bengal, the highest fractions of deep clouds (35%–40%) and very deep clouds (10%–13%) occur during the June–August period. A combination of the strong convergence of horizontal wind between surface and ~200 hpa level followed by large divergence above and the favorable range of SST (typically around 28.5°C–29.5°C) might be mainly responsible for this feature.

[29] The annual variation of temperature in the upper troposphere below ~150 hpa level over the deep convective regions closely follows the corresponding variation in the deep cloud fraction. The annual variation in the upper tropospheric temperature is the largest (~6 K) over the northern Bay of Bengal, with the warm phase maximizing in the June–August period. The base altitude of TTL shows significant regional differences which are closely associated with the variations in the regional mean deep cloud fraction. The annual variation in the base altitude of TTL has an in-phase relationship with the corresponding variation of the deep cloud fraction. In general, the base altitude of TTL over the Bay of Bengal and the Arabian Sea peaks during the June–August period. Within the study region, the monthly mean base altitude of TTL is maximum (13.05 km) over the northern Bay of Bengal during July. The cold point tropopause shows a broad maximum during January–March and

minimum during July–September in all the regions. The nearly out-of-phase relationship between the annual variations of convective and cold point tropopause altitudes over the Arabian Sea and the Bay of Bengal increases the magnitude of the annual variation of the TTL thickness. In general, the monthly mean TTL thickness is small during the June–September period over the entire study region and the smallest (3.8 km) in July over the northern Bay of Bengal.

[30] The present observations show that, during the June–August period, significant fraction of deep and very deep clouds occur in the tropical tropopause layer, particularly over the northern and eastern Bay of Bengal. Role of these deep clouds in the moisture budget of the UTLS region needs to be investigated.

[31] **Acknowledgments.** The level 1b AVHRR data are obtained from NOAA-NESDIS through their Web site at http://www.class.noaa.gov. CALIPSO data were obtained from LaRC Atmospheric Sciences Data Center (ASDC) through their Web site at http://eosweb.larc.nasa.gov/. NCEP-NCAR Reanalysis wind data were provided by the NOAA-CIRES Climate Diagnostics Center, Boulder, Colorado, through their Web site at http://www.cdc.noaa.gov/. The COSMIC and CHAMP data were provided by the UCAR/COSMIC program through CDAAC (http://cosmic-io.cosmic.ucar.edu/cdaac). K.P. is an emeritus scientist supported by a CSIR grant. The authors are thankful to the three anonymous reviewers for their valuable suggestions.

References

Dessler, A. E. (2002), The effect of deep tropical convection on the tropical tropopause layer, *J. Geophys. Res.*, *107*(D3), 4033, doi:10.1029/2001JD000511.

Fu, R., A. D. Del Genio, and W. B. Rossow (1990), Behavior of deep convective clouds in the tropical Pacific deduced from ISCCP radiances, *J. Clim.*, *3*, 1129–1152, doi:10.1175/1520-0442(1990)003<1129:BODCCI>2.0.CO;2.

Fujita, T. T. (1992), The mystery of severe storms, *WRL Res. Pap. 239*, Wind Res. Lab., Univ. of Chicago, Chicago, Ill.

Gadgil, S., P. V. Joseph, and N. V. Joshi (1984), Ocean-atmosphere coupling over monsoon regions, *Nature*, *312*, 141–143, doi:10.1038/312141a0.

Gambheer, A. V., and G. S. Bhat (2000), Life cycle characteristics of deep cloud systems over the Indian region using INSAT-1B pixel data, *Mon. Weather Rev.*, *128*, 4071–4083, doi:10.1175/1520-0493(2000)129<4071:LCCODC>2.0.CO;2.

Gettelman, A., and P. M. de F. Forster (2002), A climatology of the tropical tropopause layer, *J. Meteorol. Soc. Jpn.*, *80*, 911–924, doi:10.2151/jmsj.80.911.

Gettelman, A., M. L. Salby, and I. Sassi (2002), Distribution and influence of convection in the tropical tropopause region, *J. Geophys. Res.*, *107*(D10), 4080, doi:10.1029/2001JD001048.

Graham, N. E., and T. P. Barnett (1987), Sea surface temperature, surface wind divergence and convection over tropical oceans, *Science*, *238*, 657–659, doi:10.1126/science.238.4827.657.

Grossman, R. L., and O. Garcia (1990), The distribution of deep convection over ocean and land during the Asian summer monsoon, *J. Clim.*, *3*, 1032–1044, doi:10.1175/1520-0442(1990)003<1032:TDODCO>2.0.CO;2.

Hajj, G., C. O. Ao, B. A. Iijima, D. Kuang, E. R. Kursinski, A. J. Mannucci, T. K. Meehan, L. J. Romans, M. de la Torre Juarez, and T. P. Yunck (2004), CHAMP and SAC-C atmospheric occultation results and intercomparisons, *J. Geophys. Res.*, *109*, D06109, doi:10.1029/2003JD003909.

Hall, T. J., and T. H. Vonder Haar (1999), The diurnal cycle of west Pacific deep convection and its relation to the spatial and temporal variation of tropical MCSs, *J. Atmos. Sci.*, *56*, 3401–3415, doi:10.1175/1520-0469(1999)056<3401:TDCOWP>2.0.CO;2.

Haynes, J. M., and G. L. Stephens (2007), Tropical oceanic cloudiness and the incidence of precipitation: Early results from CloudSat, *Geophys. Res. Lett.*, *34*, L09811, doi:10.1029/2007GL029335.

Hong, G., P. Yang, B. C. Gao, B. A. Baum, Y. X. Hu, M. D. King, and S. Platnick (2007), High cloud properties from three years of Terra and Aqua Collection-4 Data over the tropics, *J. Appl. Meteorol. Climatol.*, *46*, 1840–1856.

Kalnay, E., et al. (1996), The NCEP/NCAR Reanalysis 40-year Project, *Bull. Am. Meteorol. Soc.*, *77*, 437–471, doi:10.1175/1520-0477(1996)077<0437:TNYRP>2.0.CO;2.

Kiehl, J. T. (1994), On the observed near cancellation between longwave and shortwave cloud forcing in tropical regions, *J. Clim.*, *7*, 559–565, doi:10.1175/1520-0442(1994)007<0559:OTONCB>2.0.CO;2.

Krishna Murthy, B. V., K. Parameswaran, and K. O. Rose (1986), Temporal variations of the tropical tropopause characteristics, *J. Atmos. Sci.*, *43*, 914–922, doi:10.1175/1520-0469(1986)043<0914:TVOTTT>2.0.CO;2.

Kuo, Y. H., T. K. Wee, S. Sokolovskiy, C. Rocken, W. Schreiner, and D. Hunt (2004), Inversion and error estimation of GPS radio occultation data, *J. Meteorol. Soc. Jpn.*, *82*, 507–531, doi:10.2151/jmsj.2004.507.

Kuo, Y. H., W. S. Schreiner, J. Wang, D. Rossiter, and Y. Zhang (2005), Comparison of GPS radio occultation soundings with radiosondes, *Geophys. Res. Lett.*, *32*, L05817, doi:10.1029/2004GL021443.

Mapes, B. E., and R. A. J. Houze (1993), Cloud clusters and superclusters over the oceanic warm pool, *Mon. Weather Rev.*, *121*, 1398–1415, doi:10.1175/1520-0493(1993)121<1398:CCASOT>2.0.CO;2.

Meenu, S., K. Rajeev, K. Parameswaran, and C. Suresh Raju (2007), Characteristics of the double intertropical convergence zone over the tropical Indian Ocean, *J. Geophys. Res.*, *112*, D11106, doi:10.1029/2006JD007950.

Mehta, S. K., B. V. Krishna Murthy, D. N. Rao, M. V. Ratnam, K. Parameswaran, K. Rajeev, C. Suresh Raju, and K. G. Rao (2008), Identification of tropical convective tropopause and its association with cold point tropopause, *J. Geophys. Res.*, *113*, D00B04, doi:10.1029/2007JD009625.

Minnis, P., C. R. Yost, S. Sun-Mack, and Y. Chen (2008), Estimating the top altitude of optically thick ice clouds from thermal infrared satellite observations using CALIPSO data, *Geophys. Res. Lett.*, *35*, L12801, doi:10.1029/2008GL033947.

Newell, R. E., and S. Gould-Stewart (1981), A startospheric fountain?, *J. Atmos. Sci.*, *38*, 2789–2796, doi:10.1175/1520-0469(1981)038<2789:ASF>2.0.CO;2.

Rajeev, K., et al. (2008), Observational assessment of the potential of satellite-based water vapor and thermal IR brightness temperatures in detecting semitransparent cirrus, *Geophys. Res. Lett.*, *35*, L08808, doi:10.1029/2008GL033393.

Rajeevan, M., and J. Srinivasan (2000), Net cloud radiative forcing at the top of the atmosphere in the Asian monsoon region, *J. Clim.*, *13*, 650–657, doi:10.1175/1520-0442(2000)013<0650:NCRFAT>2.0.CO;2.

Ramanathan, V., R. D. Cess, E. F. Harrison, P. Minnis, B. R. Barkstrom, E. Ahmad, and D. Hartmann (1989), Cloud-radiative forcing and climate: Results from the Earth Radiation Budget Experiment, *Science*, *243*, 57–63, doi:10.1126/science.243.4887.57.

Reid, G. C., and K. S. Gage (1981), On the annual variation in height of the tropical tropopause, *J. Atmos. Sci.*, *38*, 1928–1938, doi:10.1175/1520-0469(1981)038<1928:OTAVIH>2.0.CO;2.

Roca, R., and V. Ramanathan (2000), Scale dependence of monsoonal convective systems over the Indian region, *J. Clim.*, *13*, 1286–1297, doi:10.1175/1520-0442(2000)013<1286:SDOMCS>2.0.CO;2.

Roca, R., M. Viollieer, L. Picon, and M. Desbois (2002), A multisatellite analysis of deep convection and its moist environment over the Indian Ocean during the winter monsoon, *J. Geophys. Res.*, *107*(D19), 8012, doi:10.1029/2000JD000040.

Rossow, W. B., and C. Pearl (2007), 22-year survey of tropical convection penetrating into the lower stratosphere, *Geophys. Res. Lett.*, *34*, L04803, doi:10.1029/2006GL028635.

Salby, M., F. Sassi, P. Callaghan, W. Read, and H. Pumphrey (2003), Fluctuations of cloud, humidity and thermal structure near the tropical tropopause, *J. Clim.*, *16*, 3428–3446, doi:10.1175/1520-0442(2003)016<3428:FOCHAT>2.0.CO;2.

Sathiyamoorthy, V. P., K. Pal, and P. C. Joshi (2004), Influence of the upper-tropospheric wind shear upon cloud radiative forcing in the Asian monsoon region, *J. Clim.*, *17*, 2725–2735, doi:10.1175/1520-0442(2004)017<2725:IOTUWS>2.0.CO;2.

Seidel, J. D., R. J. Ross, J. K. Angell, and G. C. Reid (2001), Climatological characteristics of the tropical tropopause as revealed by radiosondes, *J. Geophys. Res.*, *106*, 7857–7878, doi:10.1029/2000JD900837.

Sherwood, S. C., and A. E. Dessler (2001), A model for transport across the tropical tropopause, *J. Atmos. Sci.*, *58*, 765–779, doi:10.1175/1520-0469(2001)058<0765:AMFTAT>2.0.CO;2.

Sherwood, S. C., J.-H. Chae, P. Minnis, and M. McGill (2004), Underestimation of deep convective cloud tops by thermal imagery, *Geophys. Res. Lett.*, *31*, L11102, doi:10.1029/2004GL019699.

Sunilkumar, S. V., K. Parameswaran, and B. V. Krishna Murthy (2003), Lidar observations of cirrus cloud near the tropical tropopause: General features, *Atmos. Res.*, *66*, 203–227, doi:10.1016/S0169-8095(02)00159-X.

Vaughan, M. A., D. M. Winker, and K. A. Powell (2005), CALIOP algorithm theoretical basis document, Part 2: Feature detection and layer properties algorithms, *Rep. PC-SC1-202 Part-2*, NASA Langley Res. Cent., Hampton, Va.

Wang, K.-Y., and S.-C. Lin (2007), First continuous GPS soundings of temperature structure over Antarctic winter from FORMOSAT-3/COSMIC constellation, *Geophys. Res. Lett.*, *34*, L12805, doi:10.1029/2007GL030159.

Wang, P. H., P. Minnis, M. P. McCormick, G. S. Kent, and K. M. Skeens (1996), A 6-year climatology of cloud occurrence frequency from Stratospheric Aerosol and Gas Experiment II observations (1985–1990), *J. Geophys. Res.*, *101*, 29,407–29,429, doi:10.1029/96JD01780.

Winker, D. M., B. Hunt, and M. McGill (2007), Initial performance assessment of CALIOP, *Geophys. Res. Lett.*, *34*, L19803, doi:10.1029/2007GL030135.

Wylie, D. P., and W. P. Menzel (1999), Eight year of high cloud statistics using HIRS, *J. Clim.*, *12*, 170–184.

Zhang, C. (1993), On the annual cycle in highest, coldest clouds in the tropics, *J. Clim.*, *6*, 1987–1990, doi:10.1175/1520-0442(1993)006<1987:OTACIH>2.0.CO;2.

Zuidema, P. (2003), Convective clouds over the Bay of Bengal, *Mon. Weather Rev.*, *131*, 780–798, doi:10.1175/1520-0493(2003)131<0780:CCOTBO>2.0.CO;2.

S. Meenu, A. K. M. Nair, K. Parameswaran, and K. Rajeev, Space Physics Laboratory, Vikram Sarabhai Space Centre, Thiruvavanthapuram 695 022, India. (k_rajeev@vssc.gov.in)